

Lecture Notes in Mechanical Engineering

L. Vijayaraghavan  
K. Hemachandra Reddy  
S. M. Jameel Basha *Editors*

# Emerging Trends in Mechanical Engineering

Select Proceedings of ICETME 2018

 Springer

# **Lecture Notes in Mechanical Engineering**

**Lecture Notes in Mechanical Engineering (LNME)** publishes the latest developments in Mechanical Engineering - quickly, informally and with high quality. Original research reported in proceedings and post-proceedings represents the core of LNME. Volumes published in LNME embrace all aspects, subfields and new challenges of mechanical engineering. Topics in the series include:

- Engineering Design
- Machinery and Machine Elements
- Mechanical Structures and Stress Analysis
- Automotive Engineering
- Engine Technology
- Aerospace Technology and Astronautics
- Nanotechnology and Microengineering
- Control, Robotics, Mechatronics
- MEMS
- Theoretical and Applied Mechanics
- Dynamical Systems, Control
- Fluid Mechanics
- Engineering Thermodynamics, Heat and Mass Transfer
- Manufacturing
- Precision Engineering, Instrumentation, Measurement
- Materials Engineering
- Tribology and Surface Technology

To submit a proposal or request further information, please contact the Springer Editor in your country:

**China:** Li Shen at [li.shen@springer.com](mailto:li.shen@springer.com)

**India:** Dr. Akash Chakraborty at [akash.chakraborty@springernature.com](mailto:akash.chakraborty@springernature.com)

**Rest of Asia, Australia, New Zealand:** Swati Meherishi at [swati.meherishi@springer.com](mailto:swati.meherishi@springer.com)

**All other countries:** Dr. Leontina Di Cecco at [Leontina.dicecco@springer.com](mailto:Leontina.dicecco@springer.com)

To submit a proposal for a monograph, please check our Springer Tracts in Mechanical Engineering at <http://www.springer.com/series/11693> or contact [Leontina.dicecco@springer.com](mailto:Leontina.dicecco@springer.com)

**Indexed by SCOPUS. The books of the series are submitted for indexing to Web of Science.**

More information about this series at <http://www.springer.com/series/11236>

L. Vijayaraghavan · K. Hemachandra Reddy ·  
S. M. Jameel Basha  
Editors

# Emerging Trends in Mechanical Engineering

Select Proceedings of ICETME 2018



Springer

*Editors*

L. Vijayaraghavan  
Indian Institute of Technology Madras  
Chennai, Tamil Nadu, India

K. Hemachandra Reddy  
JNTUA College of Engineering  
Anantapur, Andhra Pradesh, India

S. M. Jameel Basha  
Srinivasa Ramanujan Institute  
of Technology  
Anantapur, Andhra Pradesh, India

ISSN 2195-4356

ISSN 2195-4364 (electronic)

Lecture Notes in Mechanical Engineering

ISBN 978-981-32-9930-6

ISBN 978-981-32-9931-3 (eBook)

<https://doi.org/10.1007/978-981-32-9931-3>

© Springer Nature Singapore Pte Ltd. 2020

This work is subject to copyright. All rights are reserved by the Publisher, whether the whole or part of the material is concerned, specifically the rights of translation, reprinting, reuse of illustrations, recitation, broadcasting, reproduction on microfilms or in any other physical way, and transmission or information storage and retrieval, electronic adaptation, computer software, or by similar or dissimilar methodology now known or hereafter developed.

The use of general descriptive names, registered names, trademarks, service marks, etc. in this publication does not imply, even in the absence of a specific statement, that such names are exempt from the relevant protective laws and regulations and therefore free for general use.

The publisher, the authors and the editors are safe to assume that the advice and information in this book are believed to be true and accurate at the date of publication. Neither the publisher nor the authors or the editors give a warranty, expressed or implied, with respect to the material contained herein or for any errors or omissions that may have been made. The publisher remains neutral with regard to jurisdictional claims in published maps and institutional affiliations.

This Springer imprint is published by the registered company Springer Nature Singapore Pte Ltd. The registered company address is: 152 Beach Road, #21-01/04 Gateway East, Singapore 189721, Singapore

# Committees

## National Advisory Board

Dr. Rajiv Tiwari, Professor, rotor dynamics, vibrations, IIT Guwahati

Dr. K. S. R. Krishna Murthy, Professor, fracture mechanics, IIT Guwahati

Dr. Ravi Kant, Assistant Professor, manufacturing, IIT Ropar, Punjab

Dr. Sachin Kumar Singh, Assistant Professor, acoustics, vibrations, IIT (ISM) Dhanbad, Jharkhand

Dr. Vinod Yadav, Assistant Professor, manufacturing, FEM, NERIST, Itanagar

Dr. Mohit Lal, Assistant Professor, bearings, industrial engineering, NIT Rourkela, Odisha

Dr. S. Venkataramanaiah, Professor, operations management, IIM Lucknow

Dr. N. Shiva Kumar, Principal Research Scientist, design and manufacturing, IISc Bangalore

Dr. V. Hari Kumar, Assistant Professor, geometric modeling for CAD, finite element/isogeometric analysis, robotics and applied optimization, NIT Warangal

Dr. G. Raghavendra, Assistant Professor, composites, nano-materials, tribology, polymer composites, NIT Warangal

Dr. Seikh Mustafa Kamal, Assistant Professor, FEM, metal forming, Tezpur University

Dr. G. Rakesh Mote, Assistant Professor, mechanical engineering, IIT Bombay

Dr. S. Subramanyam, Assistant Professor, aerospace engineering, IIT Kanpur

Dr. Ajay M. Sidpara, Assistant Professor, IIT Kharagpur

Dr. K. Sreenivas Reddy, Professor, heat transfer, thermal engineering, IIT Madras

Dr. G. S. V. L. Narasimham, Professor, heat and mass transfer, CFD, HVAC, refrigeration, cryogenics, IISc Bangalore

Dr. Ravi Shankar, Assistant Professor, composite materials, machining, IIT Guwahati

Dr. B. Karunakar, Associate Professor, Mfg science, FEM in Mfg, IIT Roorkee

Dr. Anil Kumar, Associate Professor, IIT Tirupati

Dr. Veeresh Babu A., Assistant Professor, IC engines, alternate fuels, emission control, NIT Warangal  
 Dr. K. Kiran Kumar, Assistant Professor, heat transfer; nanofluids; refrigeration and air-conditioning; CFD; non-conventional energy sources, NIT Warangal  
 Dr. S. Syed Ismail, Assistant Professor, tribology; surface texturing; lubrication; nano-lubricant, NIT Warangal  
 Dr. V. Ganesan, Professor, IC engines, CFD, IITM  
 Dr. K. Vijaya Kumar Reddy, Professor, IC engines, JNTU Hyderabad  
 Dr. S. Manzoor Hussain, Professor, production, JNTU Hyderabad  
 K. Hemachandra Reddy, Professor, thermal, JNTU Anantapur  
 Dr. Kallol Mondal, Professor, mechanical engineering, IIT Kanpur  
 Dr. Balakrishnan Narayanarao, Professor, IISC Bangalore  
 Dr. Anantasuresh, Professor, compliant mechanisms, MEMS, kinematics of mechanisms, proein design, micromanipulation and biomechanics, IISc Bangalore  
 Dr. Amirtham Rajagopal, Associate Professor, FEM, composites, IIT Hyderabad  
 Dr. N. Venkaiah, Associate Professor, MMM, machining, optimization, IIT Tirupati  
 Dr. B. S. V. Prasad Patnaik, Professor, IIT Madras  
 Dr. A. ElayaPerumal, Professor, vibrations, composites, Anna University  
 Dr. M. Pradeep Kumar, Associate Professor, composite machining, unconventional machining, FEM, Anna University  
 Dr. N. Arunachalam, Assistant Professor, manufacturing, IITM  
 Dr. G. B. Bhaskar, Associate Professor, composites, manufacturing, Anna University  
 Dr. L. Vijayaragavan, Professor, manufacturing, IITM

## **International Advisory Board**

Dr. N. Subba Reddy, Associate Professor, material science and engineering, South Korea  
 Dr. Satya Pramod Jammy, Assistant Professor, thermal engineering, UK  
 Dr. Mekala Narasimha Rao, Assistant Professor, solid mechanics, composite materials, Germany  
 Dr. Moola Mohan Reddy, Professor, Malaysia  
 Dr. J. Paulo Davim, Professor, machining and tribology, Portugal  
 Dr. Chan-Hee Park, Senior Researcher, South Korea  
 Dr. Zhang Shunqi, Associate Professor, vibrations, composite materials, China  
 Dr. Min Chen, Assistant Professor, industrial design, China  
 Seung-Yong Yang, Associate Professor, material science and engineering, South Korea  
 Dr. Jeoung-Han Kim, Associate Professor, material science and engineering, South Korea

## **Organizing Committee**

### **Chief Patron**

Mrs. J. Padmavathy, Chairperson

### **Patron**

Mr. A. Sambasiva Reddy, Correspondent and Secretary

### **Co patrons**

Mr. K. Jagan Mohan Reddy, Chief Executive Officer

Mr. M. Ranjit Reddy, Chief Administrative Officer

Dr. Hitendra Sarma, Principal

### **Conference Chair**

Dr. L. Vijayaraghavan, Professor, IIT Madras

### **Conference Co-chair**

Dr. K. Hemachandra Reddy, Professor, JNTU Anantapur

### **Program Chair**

Dr. S. M. Jameel Basha, Professor

### **Organizing Chair**

Mr. A. Venkata Dhanunjaya Reddy, Assistant Professor



## **Organizing Committee**

Dr. K. Subba Reddy, Professor  
Dr. D. Sai Chaitanya Kishore, Associate Professor  
Mr. K. Bharani Kumar Reddy, Assistant Professor  
Mr. Y. Rama Mohan Reddy, Assistant Professor

## **Registration Committee**

Mrs. V. Arundhati, Assistant Professor  
Ms. M. Usha Rani, Assistant Professor  
Mrs. P. Pranitha, Assistant Professor

## **Publication Committee**

Mr. N. Vikram Manoj Kumar, Assistant Professor  
Mr. G. Sreenivasa Kumar, Assistant Professor  
Mr. K. John Samuel, Assistant Professor  
Mr. K. Kiran Kumar, Assistant Professor

## **Hospitality Committee**

Mr. K. Neelakanta, Assistant Professor  
Mr. L. Vamsi Krishna Reddy, Assistant Professor  
Mr. V. Viswanatha Chari, Assistant Professor  
Mr. Ch. Joseph Sundar, Assistant Professor  
Mr. B. Sreenivasulu, Assistant Professor  
Mr. R. Sudheer Kumar, Assistant Professor  
Mr. M. Irfan Ahmad, Assistant Professor  
Mr. R. S. Mohammad Jaffar, Assistant Professor

## **International Reviewers**

Dr. N. Subba Reddy, Associate Professor, material science and engineering,  
Gyeongsang National University, South Korea

Dr. Satya Pramod Jammy, Assistant Professor, thermal engineering, University of Southampton, UK

Dr. Mekala Narasimha Rao, Assistant Professor, solid mechanics, composite materials, RWTH Aachen University, Germany

Dr. Moola Mohan Reddy, Professor, mechanical engineering, Curtin University, Malaysia

Dr. Zhang Shunqi, Associate Professor, vibrations, composite materials, Shanghai University, China

Dr. Seung-Yong Yang, Associate Professor, material science and engineering, Korea University of Technology and Education, South Korea

## **National Reviewers**

Dr. Rajiv Tiwari, Professor, rotor dynamics, vibrations, IIT Guwahati, India

Dr. K. S. R. Krishna Murthy, Professor, fracture mechanics, IIT Guwahati, India

Dr. Ravi Kant, Assistant Professor, manufacturing, IIT Ropar, Punjab, India

Dr. Sachin Kumar Singh, Assistant Professor, acoustics, vibrations, IIT (ISM) Dhanbad, Jharkhand, India

Dr. Vinod Yadav, Assistant Professor, manufacturing, FEM, NERIST, Itanagar, India

Dr. Mohit Lal, Assistant Professor, bearings, industrial engineering, NIT Rourkela, Odisha, India

Dr. S. Venkataramanaiah, Professor, operations management, IIM Lucknow, India

Dr. N. Shiva Kumar, Professor, design and manufacturing, IISc Bangalore, India

Dr. V. Hari Kumar, Assistant Professor, geometric modeling for CAD, finite element/isogeometric analysis, robotics and applied optimization, NIT Warangal, India

Dr. G. Raghavendra, Assistant Professor, composites, nano-materials, tribology, polymer composites, NIT Warangal, India

Dr. Seikh Mustafa Kamal, Assistant Professor, FEM, metal forming, Tezpur University, India

Dr. G. Rakesh Mote, Assistant Professor, mechanical engineering, IIT Bombay, India

Dr. Ajay M Sidpara, Assistant Professor, mechanical engineering, IIT Kharagpur, India

Dr. B. Srinivasa Prasad, Associate Professor, mechanical engineering, GITAM, Vizag, India

Dr. Anil Kumar, Associate Professor, mechanical engineering, IIT Tirupati, India

Dr. Veeresh Babu A., Assistant Professor, IC engines, alternate fuels, emission control, NIT Warangal, India

Dr. K. Kiran Kumar, Assistant Professor, heat transfer; nanofluids; refrigeration and air-conditioning; CFD; non-conventional energy sources, NIT Warangal, India

Dr. V. Ganesan, Professor, IC engines, CFD, IITM, India

Dr. K. Durga Prasad, Professor, IC engines, JNTU Anantapur, India  
Dr. B. Anjaneya Prasad, Professor, thermal, composites, JNTU Hyderabad, India  
Dr. A. Aruna Kumari, Professor, thermal, JNTU Hyderabad, India  
K Govinda Rajulu, Professor, thermal, composites, JNTU Anantapur, India  
Chandra Mohan Reddy, Assistant Professor, production, industrial engineering and design, JNTU Anantapur, India  
V. Venugopal Reddy, Professor, CAD/CAM, JNTU Pulivendula, India  
Srinivasan, Professor, thermal, JNTU Kalikiri, India  
Kalyani Radha, Assistant Professor, thermal, JNTU Anantapur, India  
V. Diwakar Reddy, Professor, design, SV University, India  
Pandu Rangadu, Professor, thermal, JNTU Anantapur, India  
Bala Krishna, Professor, thermal, JNTU Kakinada, India  
Garlapati Nagababu, Assistant Professor, design, solar, PDPU Gandhinagar, India  
Jaykumar J. Vora, Assistant Professor, welding, PDPU Gandhinagar, India  
Kush P. Mehta, Assistant Professor, welding, PDPU Gandhinagar, India  
Nirav P. Patel, Assistant Professor, optimization, FEM, composites, PDPU Gandhinagar, India  
Pavan Kumar Gurrula, Assistant Professor, 3D printing, reverse engineering, PDPU Gandhinagar, India  
Dr. A. ElayaPerumal, Professor, vibrations, composites, Anna University, India  
Dr. M. Pradeep Kumar, Associate Professor, composite machining, unconventional machining, FEM, Anna University, India  
Dr. N. Arunachalam, Assistant Professor, manufacturing, IITM, India  
Dr. G. B. Bhaskar, Associate Professor, composites, manufacturing, Anna University, India  
Dr. L. Vijayaragavan, Professor, manufacturing, IITM, India  
Dr Jaydeep Patel, Assistant Professor, Optimization, renewable energy, PDPU Gandhinagar, India  
Dr. S. M. Jameel Basha, Professor, thermal engineering, SRIT Anantapur, India  
Dr. D. Sai Chaitanya Kishore, Associate Professor, manufacturing, SRIT Anantapur, India

# Preface

The first International Conference on Emerging Trends in Mechanical Engineering (ICETME-2018) is being organized by Department of Mechanical Engineering, Srinivasa Ramanujan Institute of Technology, Anantapur, Andhra Pradesh, India, with Springer as the publisher for the conference proceedings in Lecture Notes in Mechanical Engineering (LNME). This conference is organized to fulfill the objectives such as

- To have peer interaction among the researchers.
- To expose and deliberate the recent happenings and developments in technology.
- To listen to the keynote lectures delivered by the professors and researchers both at national and international level in the field of the eminence of mechanical engineering.
- To discuss the challenges and threats pertaining to the technology and place them for the discussion before academicians, scientists and industry persons.

The conference is a right forum to discuss the bottlenecks cropping up in the path of research and remove the technological anomalies which may be possible only through proper interaction with the eminent personalities who actively involved in the research.

The total number of papers received is 175. After undergoing a plagiarism check and a thorough review process, 61 papers are accepted for presentation. All the papers reflect recent and advanced research in the field of mechanical engineering.

On behalf of the Department of Mechanical Engineering, SRIT, we profusely thank all the concerned for their kind cooperation toward organizing this conference. We also express sincere thanks to the National and International Advisory Board Members, Reviewers for scrutiny of the papers, Keynote Speakers, Session Chairs and Faculty of this Department who are behind the success of this conference.

We hope that the proceedings in this Lecture Notes in Mechanical Engineering (LNME) should prove to be one of the best references for the researchers in the field of mechanical engineering.

Anantapur, India  
Anantapur, India  
Chennai, India

Prof. S. M. Jameel Basha  
Prof. K. Hemachandra Reddy  
Prof. L. Vijayaraghavan

# Keynote Speakers

Prof. V. Ganesan, Recent Trends In Automotive Engines, IIT Madras

Mr. N. Divakar Reddy, Current Trends and Opportunities in Commercial Vehicle Industry, Ashok Leyland

Prof. Jeoung Han Kim, Thermal Joining of Carbon Fiber Reinforced Plastic to AZ31 Alloy Sheet, Hanbat National University, Korea

Prof. N. Subba Reddy, Application of Artificial Neural Networks in Materials Science Research, Gyeongsang National University, Korea

Prof. G. Ananthasuresh, Tools and Techniques for Mechano-Diagnostics, IISc Bangalore

Prof. Rajiv Tiwari, Emerging Technology in Condition Monitoring of Rotating Machinery, IIT Guwahati

# Contents

<b>Parametric Optimization of Nd:YAG Laser Microgrooving of Alumina Ceramic Using Integrated RSM-PSO Approach . . . . .</b>	<b>1</b>
Anil Swain, Santosh Kumar Sahu, Anisha Ekka and Sudhansu Ranjan Das	
<b>Optimization of Valve-Train Components for Durability Analysis by Using Finite Element Analysis Method . . . . .</b>	<b>11</b>
Anuradha J. Thakare and Ashok J. Keche	
<b>Stratification by Fuel Injection and Positive Ignition . . . . .</b>	<b>25</b>
V. V. Prathibha Bharathi	
<b>Analysis of Miniature Loop Heat Pipe Under Varying Working Fluids and Wick Materials at Low Heat Inputs . . . . .</b>	<b>33</b>
V. Murali Krishna and Mechiri Sandeep Kumar	
<b>Computational Design and Analysis of a Piston with Different Head Thicknesses and Top Land Widths . . . . .</b>	<b>43</b>
Rayapati Subbarao and Mukul Kashiwal	
<b>Development and Fabrication of Smart Waste Segregator . . . . .</b>	<b>55</b>
R. Harshith, Y. Karthik, Pruthvishri Hegde, Sharma B. N. Tejas, D. Shivalingappa and H. S. Kumarswamy	
<b>Influence of Heat Index on Tensile Properties and Formability of Friction Stir Dissimilar Welded Blanks . . . . .</b>	<b>65</b>
Bhanodaya Kiran Babu Nadikudi	
<b>Convective Heat Transfer on the Optimum Spacing of High Heat Dissipating Heat Sources—A Numerical Approach . . . . .</b>	<b>73</b>
K. Mathew and Naveen Patil	

<b>Effect of Alkali Treatment on Mechanical Properties of Tapsi Fiber Reinforced Polyester Composites</b> .....	85
R. Meenakshi Reddy, D. Mohana Krishnudu, B. Madhusudhan Reddy and P. Venkateshwar Reddy	
<b>Finite Element Analysis and Theoretical Wear Behaviour for Total Hip Replacement</b> .....	93
Shaik Akbar Basha and Debasish Sarkar	
<b>Characteristics of Mixed Convective Flowover Fins for Automobile Application</b> .....	105
D. Sanjana Reddy, Y. Ranjani, M. Mukeshanand, M. Sudharshan Srinivas, D. Lalith Kumar and L. Dineshkumar	
<b>A Study on Implementation of Simulation at Operational Level in Manufacturing System</b> .....	115
Manohar V. Pattar, Vinayak N. Kulkarni, Sanjay V. Kulkarni and B. B. Kotturshettar	
<b>Productivity Improvement at Actuator Assembly Section Using Manual and Video Work Study Techniques</b> .....	123
Rohini P. Tippannavar, Vinayak N. Kulkarni and V. N. Gaitonde	
<b>Development and Characterization of Polyamide Fiber Composite Filled with Fly Ash for Wind Turbine Blade</b> .....	131
J. Joy Mathavan and Amar Patnaik	
<b>Stereomicroscopic Analysis of Fracture Surfaces of Cold Drawn Steel Wires</b> .....	141
S. S. Bargujer, Vikas Dagar and Pankaj Chandna	
<b>Comparison of Thermo-Physical and Tribological Characteristics of Nanolubricant</b> .....	153
Md Mansoor Ahamed, S. M. Jameel Basha and B. Durga Prasad	
<b>Predictive Modeling and Optimization of Technological Response Parameters in Nd:YAG Laser Microgrooving of Titanium Alloy Using Combined RSM-PSO Approach</b> .....	165
Samir Kumar Panda, Sudhansu Ranjan Das and Debabrata Dhupal	
<b>Application of Taguchi's Orthogonal Array and Overall Evaluation Criteria in Turning of AISI D2 Steel in Dry and Forced Air-Cooled Environment</b> .....	177
S. K. Rajbongshi and D. K. Sarma	
<b>Rearranging and Optimizing of Butterfly Valve Manufacturing Layout Using Simulation</b> .....	187
Shridevi V. Patil, V. N. Gaitonde, Vinayak N. Kulkarni and Sanjay V. Kulkarni	



<b>A Comparative Analysis of Annular Fin Array Under Multi-objective Optimization</b> .....	195
Abhijit Deka and Dilip Datta	
<b>A Novel Discount Mechanism for Buy Online PickUp in Store (BOPS)</b> .....	205
Vinay Surendra Yadav and A. R. Singh	
<b>Investigation of Fracture Parameters of Jute/Glass Reinforced Hybrid Composite and Analysis by Using FEA</b> .....	215
Venkata Sushma Chinta, P. Ravinder Reddy, Koorapati Eshwara Prasad and Krishna Sai Vadapally	
<b>Optimization of Machining Parameters During Dry Cutting of Ti6Al4V Using Taguchi’s Orthogonal Array</b> .....	229
P. Kumar and J. P. Misra	
<b>Makespan Optimization in Open Shop Scheduling</b> .....	245
Prakash Kesarawani, Neeraj Kumar and Abhishek Mishra	
<b>Assessment of Manufacturing Process Through Lean Manufacturing and Sustainability Indicators: Case Studies in Indian Perspective</b> .....	253
Vikas Swarnakar, A. R. Singh and Anil Kr. Tiwari	
<b>Effects of Graphite Particles in Titanium Metal Matrix Developed by Spark Plasma Sintering Process</b> .....	265
T. Vishnu Vardhan, S. Marichamy, S. Sathees Kumar and B. Sridhar Babu	
<b>Effect on Bearings in Rotating Components by Vibration Analysis: A Case Study in Steel Plant</b> .....	275
B. K. Pavan Kumar, Yadavalli Basavaraj and M. J. Sandeep	
<b>Multi-objective Optimization of Photochemical Machining Parameters Using Taguchi Grey Relational Analysis</b> .....	283
Rashed Mustafa Mazarbhuiya and Maneswar Rahang	
<b>Experimental Investigations on Microstructure, Mechanical and Wear Behavior Under Dry Sliding of Al6061 with Particulate-Reinforced SiC and TiB<sub>2</sub> Metal Matrix Composite Developed by Stir Casting</b> .....	293
G. Srinivas Kumar, Y. V. Mohan Reddy and B. Chandra Mohan Reddy	
<b>Investigations on Material Removal Rate During Wire Electrodischarge Machining of Nickel–Titanium Alloy</b> .....	305
Vinayak N. Kulkarni, V. N. Gaitonde, Rohit Sureban and M. S. Patil	
<b>A Study on the Development of Aluminum Alloys Using the Mechanical Surface Improvement Method Using the Taguchi Method</b> .....	315
Suleyman Cinar Cagan, Bellam Venkatesh and Berat Baris Buldum	

<b>A Review on 4D Printing—the Next Industrial Revolution</b> . . . . .	325
L. Vamsi Krishna Reddy and Kode Jaya Prakash	
<b>Parametric Investigations on Friction Stir Welding of Aluminium Alloys</b> . . . . .	333
Bazani Shaik, G. Harinath Gowd and B. Durgaprasad	
<b>A Study of Direct and Inverse Problems in Force Sensing of Elastic Bodies</b> . . . . .	347
Saurav Kumar Dutta, Annem Narayana Reddy and Santosha Kumar Dwivedy	
<b>Linear Heat Transfer and Structural Analysis of a Railway Wheel</b> . . . .	357
A. N. Borade and A. J. Keche	
<b>Performance Optimization of VCR Diesel Engine Using Soybean Oil-Based Biodiesel</b> . . . . .	365
Hrushikesh B. Kulkarni and Pravin R. Kubade	
<b>Vibration Response of Sandwich Beam with Viscoelastic Core and FGM Face Sheets Using Finite Element Method</b> . . . . .	377
I. Ramu, M. Raghuraman and K. V. G. R. Seshu	
<b>Heat Transfer Enhancement with Different Nanofluids in Heat Exchanger by CFD</b> . . . . .	387
T. Sreedhar, B. Nageswara Rao and D. Vinay Kumar	
<b>Adopting SDR Fluctuations to Non-premixed Turbulent Combustion by Varying Swirl Ratio</b> . . . . .	399
S. M. Jameel Basha	
<b>Flat-Fire Trajectory Simulation of AK-47 Assault Rifle 7.82-mm Bullet</b> . . . . .	415
D. Siva Krishna Reddy, Bibhu Prasad Padhy and Bharani Kumar Reddy	
<b>Optimum Annular Plane Fin Profile with Uniformly Varying Thickness</b> . . . . .	427
Abhijit Deka and Dilip Datta	
<b>Experimental Study on Effect of Green Cutting Fluid and Surfactant on Temperature in Turning Operation</b> . . . . .	437
Rahul Katna, Mohammed Suhaib, Narayan Agrawal, Swati Jain, Kanwarjeet Singh and S. Maji	
<b>Comparative Investigation of Alloy Plates Against Ballistic Impact, Blast, and Fire Loading</b> . . . . .	451
Jaykumar Gadhiya, Rahul Singh Dhari, Milanpuri Goswami and Nirav Patel	

**Inverse Kinematics and Trajectory Planning of Planar Redundant Manipulators in Cluttered Workspace** ..... 461  
 V. V. M. J. Satish Chembuly and Hari K. Voruganti

**Investigation on Mechanical Properties of Equal Channel Angular Formed Al6061 and Graphite Metal Matrix Composite** ..... 471  
 M. K. Ravishankar, H. R. Vitala and B. P. Dileep

**The Effect of Heat Treatment on Mechanical Properties of Aluminium Alloy 7075 with Nano B<sub>4</sub>C** ..... 481  
 T. H. Manjunatha, Yadavalli Basavaraj, V. Venkataramana and Madeva Nagaral

**Comparison of Various Types of Lubrication During Hard Turning of H13 Tool Steel by Analysing Flank Wear Using ANOVA** ..... 489  
 Anil Raj, K. Ramesha, Joel U. Sajan, Danish Mohammed Khan and U. A. Varshini

**Study of Wear Properties of Vinyl Ester Polymer Filled with Micro-Gr-Nano-CuO Particles** ..... 499  
 S. N. Vasantha Kumar, Govardhan Goud and P. C. Sharath

**Experimental Modeling of EDMed Aluminum Metal Matrix Composite: A Review** ..... 511  
 Rama Nand Yadav, Rajesh Kumar Porwal and J. Ramkumar

**Numerical Simulation of Transient Temperature and Stresses During Friction Stir Welding of AA 7075 T651** ..... 519  
 Md. Parwez Alam and A. N. Sinha

**Energy Production Through Gasification of Waste Biomass in Punjab Region** ..... 529  
 Rohtash Goswami, Sunirmit Verma and Ranjan Das

**Image Correlation Technique for Slope and Curvature of a Cantilever Beam Using Light Intensity** ..... 539  
 M. Raghuraman and I. Ramu

**Influence of the Notch Length on the Optimal Radial Location of Strain Gage in a Single Edged Notched Plate** ..... 549  
 Pranjol Paul, K. S. R. K. Murthy and Debabrata Chakraborty

**Mathematical Prediction of Thermal Runaway Conditions During the Nitration of DNT to TNT** ..... 561  
 Md. Touseef Ahamad, A. Seshu Kumar and A. M. K. Prasad

**Flow Physics Analysis on the Effect of Cambered Airfoil Blades on Vertical Axis Wind Turbines Using CFD** ..... 575  
 Kanthala Uma Reddy, Bachu Deb, Bidesh Roy and Sheikh Mohammad Rashid

<b>Application of Additive Dispersed Green Cutting Fluids in Machining</b> .....	583
R. Padmini and Vivek Balakrishnan	
<b>Investigating the Effect of Metal Working Fluid in Orthogonal Cutting of AISI 420 Stainless Steel Using 3-Dimensional Finite Element Model</b> .....	593
Madan Mohan Reddy Nune and Phaneendra Kiran Chaganti	
<b>Free and Forced Vibration Analysis of Functionally Graded Beams Using Finite Element Model Based on Refined Third-Order Theory</b> .....	603
M. Altaf Khan, M. Y. Yasin, Mirza Shariq Beg and A. H. Khan	
<b>A Statistical Analysis to Optimize Wear Properties of Hybrid Polymer PTFE Composites</b> .....	613
G. Harish, P. Harsha Vardhan and Y. P. Deepthi	
<b>Recent Advances in the Development of Aluminium Matrix Composites (AMCs)</b> .....	619
V. Anand, M. N. Akshay, S. Abhilash and G. Deepak	
<b>A Comparative Analysis of LiDAR and Wind Mast Measured Wind Data with the Reanalysis Datasets for an Offshore Location of Gujarat</b> .....	627
Hardik K. Jani, Garlapati Nagababu, Ravi P. Patel and Surendra Singh Kachhwaha	

## About the Editors

**Dr. L. Vijayaraghavan** is a retired professor, Department of Mechanical Engineering at the Indian Institute of Technology (IIT) Madras. He received his B.E. (Mechanical Engineering) in 1974 from Annamalai University, Tamil Nadu and his masters in machine tool engineering in 1976 from Madras University, Coimbatore. He completed his Ph.D in metal cutting from IIT Madras in 1983. He has published more than 80 journal articles and 140 conference papers in machine tools design. Dr. Vijayaraghavan has also been invited as a guest lecturer to numerous universities across the globe. He has successfully completed several sponsored and research based industrial consultancy projects. More than 20 students have been awarded their doctoral degrees under his guidance. His major research interests include machine tools and metal cutting, CAD-CAM, condition monitoring, grinding, and machining of composites.

**Dr. K. Hemachandra Reddy** is a senior professor in the Department of Mechanical Engineering at JNTUA College of Engineering, Ananthapuramu, India. He received his bachelors (Mechanical Engineering) in 1988 from Sri Venkateswara University, Andhra Pradesh and his masters in heat power engineering in 1991, from Jawaharlal Nehru Technological University, Hyderabad. He completed his Ph.D in 2001, in IC engines from Jawaharlal Nehru Technological University, Hyderabad. He has published more than 135 journal and 75 conference papers. He has also delivered more than 30 invited talks on thermal engineering and more than 100 lectures on personality development, career counseling, goal setting and achievement motivation in various academic institutions and public platforms. He has served as a National Executive Council Member of ISTE, New Delhi, for two terms and was nominated to the National Council of Institution of Engineers (India) for the year 2015 and as Secretary, ISTE Andhra Pradesh section for a period of three years. He has acted as a member of more than 10 state level committees on higher education and also acted as the chairman of Board of Studies,

Director of Academic Planning and Registrar of JNTUA. Dr. Hemachandra Reddy has guided more than 30 doctoral students. His research interests include CFD, IC engines, heat transfer, pollution mitigation, materials and alternative sources of energy.

**Dr. S. M. Jameel Basha** is a professor in the Department of Mechanical Engineering at Srinivasa Ramanujan Institute of Technology, Ananthapuramu, India. He received his bachelors in Mechanical Engineering from Gulbarga University, Karnataka, and his masters in heat transfer from Jawaharlal Nehru Technological University, Hyderabad. He completed his Ph.D in IC Engines from JNTUA University, Ananthapuramu. He has published more than 30 journal articles and 15 conference papers in the field of thermal engineering. Dr. Jameel Basha is a member of IEI India and a life member of ISTE. He has a long teaching experience of more than 20 years and has also successfully served in various academic and administrative roles during this time. His research interests include IC engines and heat transfer.

# Parametric Optimization of Nd:YAG Laser Microgrooving of Alumina Ceramic Using Integrated RSM-PSO Approach



Anil Swain, Santosh Kumar Sahu, Anisha Ekka and Sudhansu Ranjan Das

**Abstract** In order to manufacture various products with well-suited quality by machining, appropriate choice of process parameters is of prime importance. Hence, the present work focuses on modeling and optimization during Nd:YAG laser microgrooving of K-60 alumina ceramic material with an objective to find the optimum process parameters settings for minimizing the upper width deviation. The experiments are performed as per Box–Behnken design of experiments (BBDOEs) with four process parameters (diode current, pulse frequency, scanning speed, and number of passes) for parametric optimization in order to control the technological response characteristic (upper width deviation) of the precision microgrooves on K-60 alumina. Analysis of variance (ANOVA), response surface methodology (RSM), and particle swarm optimization (PSO) are subsequently proposed for predictive modeling and process optimization. Result shows the optimal setting of machining variables in laser microgrooving of K-60 alumina ceramic at pulse frequency of 4.4 kHz, diode current of 17 amp, scan speed of 35 mm/s, number of passes as 12, with estimated groove upper width deviation of 0.02669  $\mu\text{m}$ . The methodology described here is expected to be highly beneficial for manufacturing industries.

**Keywords** Laser microgrooving · K-60 alumina ceramic · ANOVA · RSM · PSO

## 1 Introduction

The recent technology has been advancing to infinite extent in search of newer materials and alloys with high hardness, strength, and less weight which are very difficult to be machined with the conventional machining processes for achieving

---

A. Swain · A. Ekka · S. R. Das (✉)  
Department of Production Engineering, VSSUniversity of Technology, Burla 768018, India  
e-mail: [das.sudhansu83@gmail.com](mailto:das.sudhansu83@gmail.com)

S. K. Sahu  
Department of Mechanical Engineering, VSS University of Technology, Burla 768018, India

the required accuracy and precision. Nowadays, there is a vast demand for the well-finished products of alumina ceramic materials with high accuracy and complex integrated designs. Such features on a component can be achieved only through the advanced manufacturing process, especially by laser beam machining. In case of micromachining, the feature size is less than 1 mm. Hence, lasers are increasingly employed for a precise micromachining because their beams can be focused accurately on microscopic areas, and attributed to a number of advantages which are normally applicable to whole range of the materials processing applications, like, non-contact processing, high productivity, eradication of the finishing operations, minimized cost of processing, and enhanced the quality of product, maximise material utilization, green manufacturing and minimize the heat affected zone [1]. The above-cited advantages can only be obtained with appropriate selection of process parameters. Researchers have employed various methods: multiple regression analysis (MRA) [2, 3] and artificial neural network (ANN) [4–6] for mathematical modeling in order to predict the responses and Taguchi method [7–9], response surface method (RSM) [10–12], genetic algorithm (GA) [13–15], particle swarm optimization (PSO) [16, 17] for optimization the controlled process parameters during laser micromachining process that have been explored as productivity and reliable tool in advanced computing technology for high-quality frameworks since it gives a straightforward, skilled, and systematically optimize the output, such as cost, quality, and performance. The proper utilization along with appropriate adjustment of machining controllable process parameters is of main importance for achieving fine grade of microgrooves, which generally utilize proper time and effort due to the frequently changing behavior of the laser micromachining process. Thus, the present study focuses on development of mathematical model and response parametric optimization during laser microgrooving of alumina ceramic using statistical approach such as RSM followed by computational approach like PSO.

## 2 Experimental Procedure

A 75-W diode-pumped Nd:YAG laser (make: Sahajanand, model: SPRIGO LD) was used to conduct the experiments which has assist gas supply unit. During experiment, the laser beam (focal length of 77 mm) has been set at surface of the workpiece as the focal plane which resulted in laser beam spot size around 21  $\mu\text{m}$ . In the present research, K-60 alumina ceramic plate of dimension (25 mm \* 25 mm \* 4 mm) is considered as the workpiece material for experimentation, subjected to microgrooving by multiple laser pulses (DPSS Nd:YAG laser treatment) with actual peak power vary between 0.7 and 5 kW. In the current investigation diode current, pulse frequency, scan speed, and number of pass are considered as the input process parameters which influence the technological performance of laser microgrooving such as upper width deviation. The different process parameters and their values are shown in Table 1.

Using the above-mentioned process parameters (4) each with four different levels, a well-designed experimental layout is formulated in conformance with



**Table 1** Process parameters and levels

Control parameters	Symbols	Units	Levels				
			-2	-1	0	1	2
Diode current	$I$	amp	17	19	21	23	25
Pulse frequency	$F$	kHz	2.8	3.2	3.6	4.0	4.4
Scan speed	$S$	mm/s	35	45	55	65	75
Number of passes	$N$		8	9	10	11	12

Box–Behnken design of experiments (BBDOEs) which is consisting of thirty one (31) number of trials. Design of experimental plan with actual value of process parameters and measured response is presented in Table 2. The upper width deviation (UWD) of machined microgroove is measured by utilizing optical microscope (model: STM6, make: Olympus). The schematic view of experimental work and methodology proposed in the current study is presented in Fig. 1.

For parametric optimization, particle swarm optimization (PSO) approach has been employed, which is a biographically inspired stochastic population-based computational approach, which simulates the collective social–psychological behavior of animals such as fish schooling, bird flocking in order to provide the sufficiently good solution to a complex optimization problem. It is a search algorithm for minimizing the functions where each member of the population is called swarm. This method is much powerful and very popular because of its simplicity of execution as well as ability to briskly converge to good solution. Every particle is considered as a point in  $N$ -dimensional space that modifies its “flying” to its own flying experience as well as experience of flying other particles. A PSO system integrates local search methods with global search methods aiming to stabilize exploitation and exploration. PSO algorithm maintains multiple potential solutions at one time. The basic computational principle includes evaluating the present position of the particle, comparing it with personal best as well as global best and imitate self and others. The position of every particle in the swarm is influenced both by best optimist position through its own movement and surroundings. During each iteration of the algorithm, each solution is evaluated by an objective function to determine its fitness. All the particles are initiated randomly and evaluated by finding the  $p_{\text{best}}$  (best value of each particle) and  $g_{\text{best}}$  (best value in the entire swarm). In basic PSO method, the velocity of particle is evaluated mathematically by:

$$v_i^{k+1} = wv_i^k + C_1R_1(p_{\text{best}_i} - x_i^k) + C_2R_2(g_{\text{best}} - x_i^k) \quad (1)$$

Mathematically, the update position of every particle can be described by using the following equation:

$$x_i^{k+1} = x_i^k + v_i^{k+1} \quad (2)$$

where  $v_i^k$  and  $x_i^k$  are the  $i$ th particle’s velocity and update position at iteration  $k$ th w.r.t. search space;  $R_1$  and  $R_2$  are two random numbers fall in between 0 and 1;  $C_1$

**Table 2** Design of experimental plan associated with results

Run	Coded values			Actual settings				Response	
	<i>I</i>	<i>F</i>	<i>S</i>	<i>N</i>	Diode current (amp)	Pulse frequency (kHz)	Scan speed (mm/s)		No. of passes
1	1	1	-1	-1	23	4.0	45	9	0.07017
2	0	0	0	-2	21	3.6	55	8	0.037225
3	-1	-1	1	1	19	3.2	65	11	0.039325
4	-1	1	-1	-1	19	4.0	45	9	0.032250
5	0	0	0	0	21	3.6	55	10	0.053233
6	0	0	0	2	21	3.6	55	12	0.066
7	0	-2	0	0	21	2.8	55	10	0.05315
8	-1	1	1	-1	19	4.0	65	9	0.027662
9	-1	0	1	1	19	3.6	65	11	0.02373
10	-1	-1	-1	-1	19	3.2	45	9	0.021243
11	0	0	0	0	21	3.6	55	10	0.029759
12	0	0	0	0	21	3.6	55	10	0.028759
13	2	0	0	0	25	3.6	55	10	0.110604
14	-1	-1	1	-1	19	3.2	65	9	0.036215
15	1	-1	-1	-1	23	3.2	45	9	0.063806
16	1	-1	-1	1	23	3.2	45	11	0.072296
17	0	0	0	0	21	3.6	55	10	0.053152
18	1	-1	1	-1	23	3.2	65	9	0.06485
19	0	0	2	0	21	3.6	75	10	0.036153
20	-1	1	-1	1	19	4.0	45	11	0.031877

(continued)

Table 2 (continued)

Run	Coded values			Actual settings				Response	
	I	F	S	N	Diode current (amp)	Pulse frequency (kHz)	Scan speed (mm/s)		No. of passes
21	0	0	0	0	21	3.6	55	10	0.038259
22	-1	-1	-1	1	19	3.2	45	11	0.017
23	0	0	0	0	21	3.6	55	10	0.040386
24	0	0	-2	0	21	3.6	35	10	0.046825
25	-1	1	-1	-1	19	4.0	45	11	0.032880
26	1	-1	1	-1	23	3.2	65	11	0.066986
27	0	2	0	0	21	4.4	55	10	0.024494
28	1	1	1	1	23	4.0	65	11	0.074431
29	0	0	0	0	21	3.6	55	10	0.005296
30	1	1	1	-1	23	4.0	65	9	0.057
31	-1	0	0	0	17	3.6	55	10	0.002151

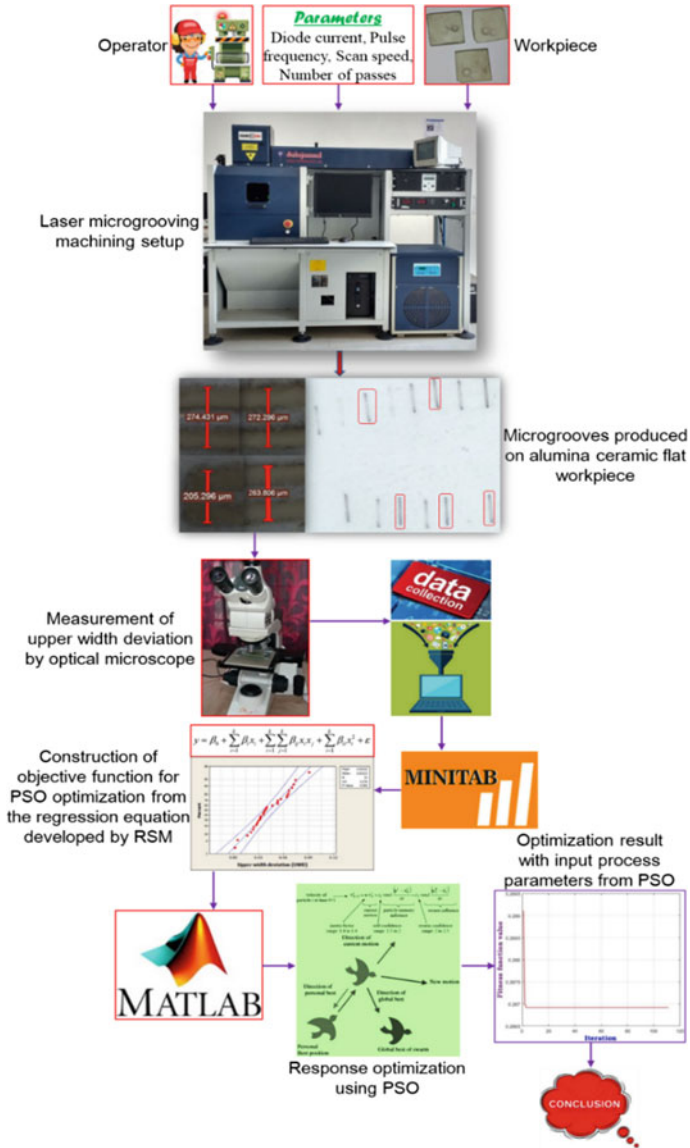


Fig. 1 Schematic of methodology and experimental setup proposed

and  $C_2$  are the acceleration coefficients correspond to  $p_{\text{best}}$  and  $g_{\text{best}}$ , respectively; and  $w$  is the inertia weight can be assessed by the following equation:

$$w = w_{\text{max}} - \left[ \frac{w_{\text{max}} - w_{\text{min}}}{\text{iter}_{\text{total}}} \times \text{iter}_{\text{current}} \right] \quad (3)$$

### 3 Results and Discussion

#### 3.1 Development of Predictive Model

The results of response characteristic, i.e., upper width deviation (UWD) which were obtained in accordance of BBDOEs, were analyzed in Minitab16 through response surface methodology (RSM), developed the mathematical model to find out the best fit of correlation between the upper width deviation of the microgrooved component with the input parameters such as diode current ( $I$ ), pulse frequency ( $F$ ), scanning speed ( $S$ ), and number of passes ( $N$ ). Regression equation in the second order (i.e., quadratic model) for the response UWD is presented by:

$$\begin{aligned} \text{UWD} = & 0.874829 - 0.045604 * I - 0.090648 * F + 0.007902 * S \\ & - 0.109260 * N + 0.001069 * I^2 + 0.009591 * F^2 + 0.00000 * S^2 \\ & + 0.003086 * N^2 + 0.001689 * IF - 0.000200 * IS + 0.001723 * IN \\ & - 0.0011363 * FS + 0.004777 * FN - 0.000033 * \text{SNR}^2 \\ = & 91.11\%, R^2(\text{adj.}) = 83.34\% \end{aligned} \quad (4)$$

To avoid the misleading conclusion, statistical analysis is performed for the proposed RSM model (UWD) by employing ANOVA in order to check its adequacy and validity, as shown in Table 3. The estimate F-value of the model for UWD is 11.72, which shows the excellent significance of model because of lower magnitude of  $F$ -table value (2.46) at 95% of confidence level. Moreover, the suggested quadratic model is noticed statistically significant as the P-value is under 0.05. Particularly, the model explains the  $R^2$  value (i.e., coefficient of determination) of 0.91 which is very close to unity (1) ensuring the excellent fit for the model with better predictive ability. Finally, normal probability plot combined with Anderson–Darling test for UWD is illustrated in Fig. 2 and confirms the residuals are distributed nearly close to a straight line revealing that the errors are dispersed normally and specifying that the terms corresponding to the model are significant. With  $P$ -value (0.392 for UWD) received from Anderson–Darling test is greater than significance level value (0.05), which confirms the adequacy of model as no reason was observed for the rejection of null hypothesis. Hence, the proposed predictive model can be utilized as objective function for particle swarm optimization.

**Table 3** Results of ANOVA for response model, UWD

Source	DF	Seq. SS	Adj. SS	Adj. MS	F	P	Remark
Regression	14	0.012878	0.012878	0.000920	11.72	0.000	Significant
Linear	4	0.011633	0.000709	0.000177	2.26	0.108	
Square	4	0.000629	0.000739	0.000185	2.35	0.098	
Interaction	6	0.000553	0.000553	0.000092	1.17	0.368	
Residual error	16	0.001256	0.001256	0.000079			
Lack of fit	10	0.000658	0.000658	0.000066	0.66	0.733	
Pure error	6	0.000598	0.000598	0.000100			
Total	30	0.014135					

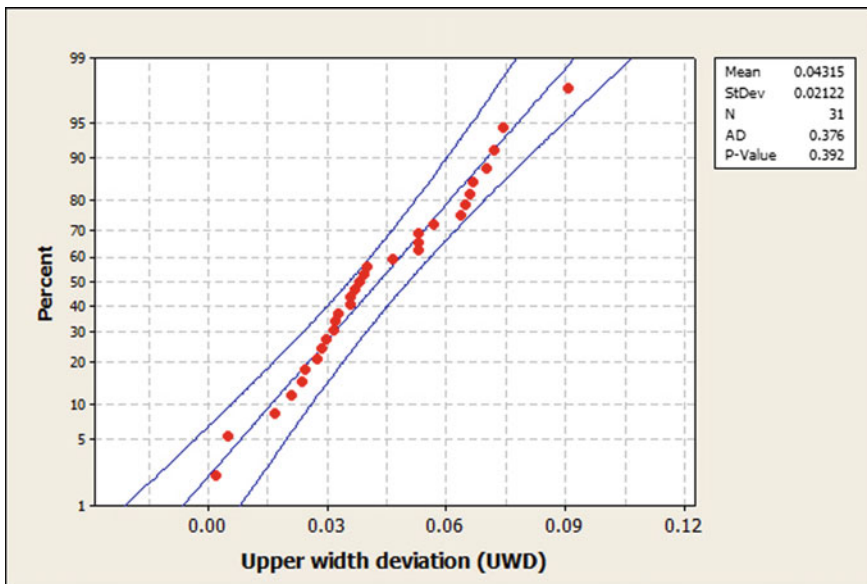
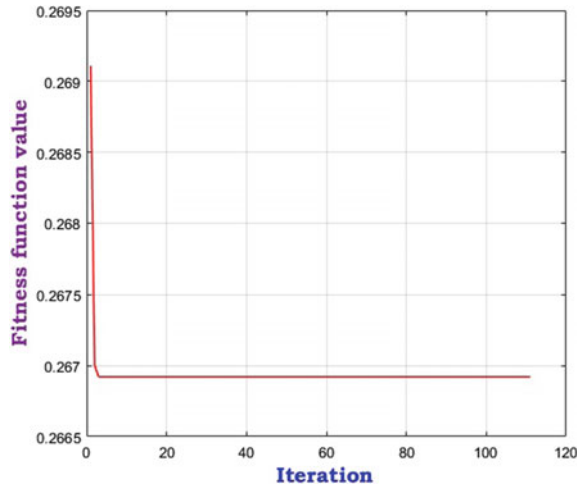


**Fig. 2** Normal probability plot for UWD

### 3.2 Response Optimization Using PSO

The predictive mathematical model for upper width deviation developed by RSM, shown in Eq. (4), is considered as an objective function for particle swarm optimization. Figure 3 presents the convergence plot, which aims to minimize the above-mentioned response in the existence of PSO algorithm-specific parameters. In this work, the critical parameters are considered about the population size of 120, acceleration factors ( $C_1$  and  $C_2$ ) of 1.2, maximum number of iterations equal to 200, minimum and maximum values of inertia weights of 0.35 and 0.5, respectively. By

**Fig. 3** Convergence curve for PSO algorithm



using PSO, the optimal microgrooving settings in laser machining of K-60 alumina ceramic are diode current 17 amp, pulse frequency 4.4 kHz, scan speed 35 mm/s, number of passes as 12, with estimated groove upper width deviation (UWD) of 0.02669  $\mu\text{m}$ .

## 4 Conclusion

Empirical models proposed for the technological response characteristic such as upper width deviation have  $R$ -Square value close to one and  $P$ -value less than 0.05, which ensured the greater statistical significance with the excellence of fit for the model. The normal probability plot ensures that the residuals distributed fairly near to a straight line showing the normality dispersion of errors as well as implying the sources associated with the model are significant. Anderson–Darling test for model shows adequate, as  $P$ -value is over 0.05 at 95% confidence level. Response optimization employing PSO technique shows the optimal setting of machining variables in laser microgrooving of K-60 alumina ceramic at pulse frequency of 4.4 kHz, diode current of 17 amp, scan speed of 35 mm/s, number of passes as 12, with estimated groove upper width deviation of 0.02669  $\mu\text{m}$ . The suggested multiple approaches (experimental, statistical, and computational) are reliable methodologies for improving laser microgrooving process and can be used in model predictive control, real-time process monitoring, and optimization in different machining processes.

## References

1. Darwish SMH, Ahmed N, Al-Ahmari AM (2017) Laser beam micro-milling of micro-channels in aerospace alloys. Springer Nature Singapore, pp 15–80. <https://doi.org/10.1007/978-981-10-3602-6> (2017)
2. Dhupal D, Doloi B, Bhattacharyya B (2009) Modeling and optimization on Nd:YAG laser turned micro-grooving of cylindrical ceramic material. *Opt Lasers Eng* 47:917–925
3. Kibria G, Doloi B, Bhattacharyya B (2013) Predictive model and process parameters optimization of Nd:YAG laser micro-turning of ceramics. *Int J Adv Manuf Technol* 65:213–229
4. Biswas R, Kuar AS, Biswas SK, Mitra S (2010) Artificial neural network modelling of Nd:YAG laser microdrilling on titanium nitride—alumina composite. *J Eng Manuf* 224:473–482
5. Kibria G, Doloi B, Bhattacharyya B (2014) Modelling and optimization of Nd: YAG laser micro-turning process during machining of aluminum oxide ( $Al_2O_3$ ) ceramics using response surface methodology and artificial neural network. *Manuf Rev* 1:1–8
6. Dixit SR, Das SR, Dhupal D (2018) Parametric optimization of Nd:YAG laser microgrooving on aluminum oxide using integrated RSM-ANN-GA approach. *J Ind Eng Int* <https://doi.org/10.1007/s40092-018-0295-1> (2018)
7. Kuar AS, Acherjee B, Ganguly D, Mitra S (2012) Optimization of Nd:YAG Laser parameters for microdrilling of alumina with multiquality characteristics via grey-Taguchi method. *Mater Manuf Processes* 27:329–336
8. Mohammed M, Umer U, Rehman A, Al-Ahmari A, El-Tamimi A (2018) Microchannels fabrication in alumina ceramic using direct Nd:YAG laser writing. *Micromachines* 9:371
9. Yang K, Xia Y, Li L, He N, Zhang Y, Zhang T, Wang Y (2018) Experimental study on hybrid machining of laser irradiation and grinding for sharpening of a CVD diamond micro-milling tool. *Int J Adv Manuf Technol*. <https://doi.org/10.1007/s00170-018-1624-7> (2018)
10. Kibria G, Doloi B, Bhattacharyya B (2012) Optimisation of Nd: YAG laser micro-turning process using response surface methodology. *Int. J. Precis Technol* 3:14–36
11. Biswas R, Kuar AS, Mitra S (2015) Process optimization in Nd:YAG laser microdrilling of alumina–aluminium interpenetrating phase composite. *J Mater Res Technol* 4:323–332
12. Kibria G, Doloi B, Bhattacharyya B (2013) Investigation and analysis on pulsed Nd:YAG laser micro-turning process of aluminium oxide ( $Al_2O_3$ ) ceramic at various laser defocusing conditions. *Int. J Adv Manuf Technol* 76:17–27
13. Nandi S, Kuar AS (2015) Parametric optimisation of Nd:YAG laser micro-drilling of alumina using NSGA II. *Int. J Mach Machinability Mater* 17:1–21
14. Mohammed MK, Umer U, Al-Ahmari A (2017) Optimization of laser micro milling of alumina ceramic using radial basis functions and MOGA-II. *Int J Adv Manuf Technol* 91:2017–2029
15. Abdo BMA, El-Tamimi AM, Anwar S, Umer U, Alahmari AM, Ghaleb MA (2018) Experimental investigation and multi-objective optimization of Nd:YAG laser micro-channeling process of zirconia dental ceramic. *Int J Adv Manuf Technol* 98(5–8):2213–2230
16. Kalita K, Shivakoti I, Ghadai RK (2017) Optimizing process parameters for laser beam micro-marking using genetic algorithm and particle swarm optimization. *Mater Manuf Processes* 32:1101–1108
17. Dhupal D, Mohanty S, Dixit SR, Das SR, Nanda BK (2018) Micromachining on Al-SiC based metal matrix composite using DPSS laser. *Mater Today Proc* 5:11304–11318



# Optimization of Valve-Train Components for Durability Analysis by Using Finite Element Analysis Method



Anuradha J. Thakare and Ashok J. Keche

**Abstract** For improved engine performance, the valve-train components must concern the parameters durability, environmental norms, the shorter valve response time, and lightweight design solution. In the valve-train system for designers and manufacturers, the stress concentrations accumulated on the valve due to the partial contact, which further cause failures in the valve. The partial contact between the valve, insert, and guide becomes uneven because of the thermal distortion load of the valve insert and guide. This paper proposes a detailed engineering analysis using finite element method of an automotive engine valve-train system using lightweight titanium for intake and exhaust valve. The complete structural virtual simulation assessment, the 3D linear heat transfer, and stress–strain approach used to get thermo-mechanical loading effect on valve-train system. The simultaneous comparative evaluation of existing steel grade material with proposed titanium material as a tensile test results benchmark. In addition, to define the material life characteristic the fatigue factor of safety evaluated by using Soderberg stress-life cycle in terms of both materials. Thus, the titanium alloy has enough potential as an optimal better material and high strength-to-weight ratio for the improved engine performance in compared to steel alloy.

**Keywords** Valve-train components · Finite element method · Ti6al4v · Durability analysis · Fatigue assessment

## 1 Introduction

The valve-train components of the automotive engine are a device to control the operation of valves. The main function of the valve is sealing the gas in the cylinder. It is closely related to the flow efficiency and the performance of the engine. Since the automotive industry is increasingly demanding higher durability and reliability

---

A. J. Thakare (✉) · A. J. Keche  
Department of Mechanical Engineering, Maharashtra Institute of Technology (MIT), Aurangabad,  
Maharashtra 431001, India  
e-mail: [anuradhathakare293@gmail.com](mailto:anuradhathakare293@gmail.com)

© Springer Nature Singapore Pte Ltd. 2020  
L. Vijayaraghavan et al. (eds.), *Emerging Trends in Mechanical Engineering*,  
Lecture Notes in Mechanical Engineering,  
[https://doi.org/10.1007/978-981-32-9931-3\\_2](https://doi.org/10.1007/978-981-32-9931-3_2)

of the engine valve, a critical component of the IC engine system [1]. Additionally, the focus of greater environmental and pollution control norms make the scope for use of titanium material as a solution to high-performance durability requirement. During the engine running, the valves are subjected to various loads of combustion pressures, a spring force, thermal loads, and the impact force due to valve-closing speed. The various combined loads and repeated cycling induce stresses to lead to a valve fracture. A valve failure occurs when the accumulated fatigue damage to the valve is over the fatigue strength of the valve material [2–5]. In case of valve breaks, the engine loses its function and stops. Thus, it is necessary for an advance to check the durability of the valve.

The design of a valve and its application to the engine are as important as the selection of the alloys. Titanium grade 5 (Ti6Al4V) is viewed as the ultimate valve alloy material because of its lightness and superior high-temperature strength. It is about 40% lighter than steel making it a good alternative for high revving engines. The major aim of selecting titanium is to achieve better sealing, flexibility, and uniform stress distribution. Also, the recent trends in high-speed and high-performance sports vehicles demand in advance lightweight design support fluctuation from acceleration to normal phase of speed [6].

There are two different kinds of steels grade material, used for making valves martensitic alloys and austenitic alloy. Austenitic stainless steel can handle high temperature, but the steel is softer at lower temperature than low carbon alloy martensitic steel which loses hardness and strength at above 1000 °F. For this reason, it is only used for intake valves. Intake valves are cooled by the incoming air–fuel mixture and typically run around less than 450 °C in light-duty spark-ignition engines and 550 °C in heavy-duty compression engines. Austenitic exhaust valve operating temperatures are as hot as around 850 °C [7].

In the present study, the general discussion on stress, strain and heat transfer FEA, fatigue factor of safety, and design of safety with their governing equations supported by physical testing conducted on steel material for intake valve design EN-52 and for exhaust valve design 21-4N with titanium valves for material modeling were presented.

## 2 Finite Element Modeling

A finite element model was created to simulate an engine valve titanium and steel which undergoes fatigue fracture during durability cycles. To provide ideal virtual simulation interaction, the finite element model builds for assembly consisting valve, guide, and seat insert. The geometrical dimensions were obtained from a common vehicle real system. The Finite element model of valve-train component is given below in Fig. 1.

The procedure carried out through valve-train design and analysis is shown by following Fig. 2. The analysis of the model has executed through Abaqus at normal engine operating conditions.

**Fig. 1** Finite element model of valve-train component

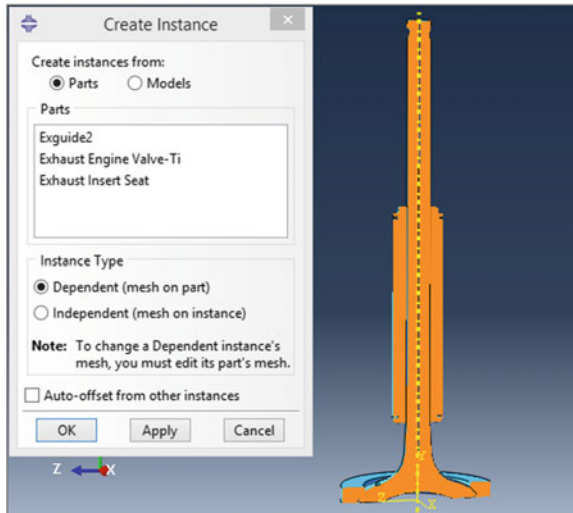


**Fig. 2** Procedure of valve-train design and analysis

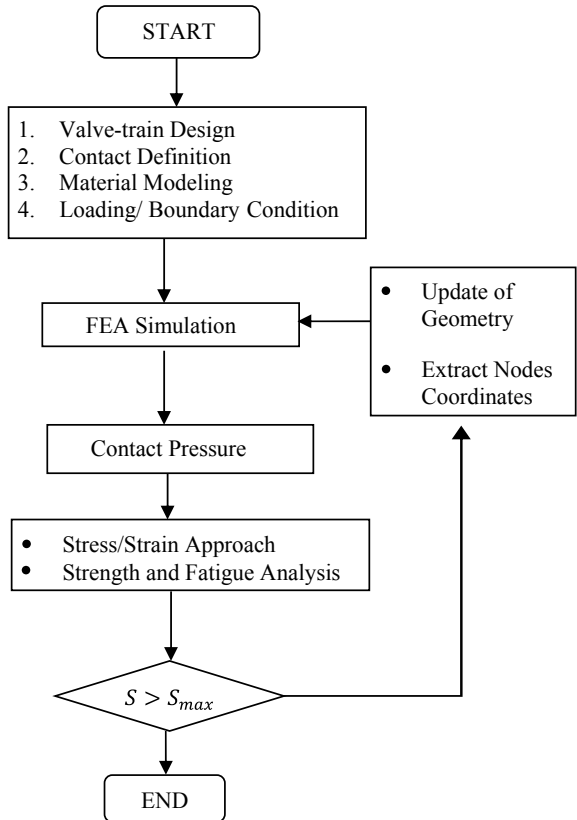


**Table 1** Mechanical and thermal properties of existing steel alloy 21-4N and EN-52 valve material

Specification data	21-4N	EN-52
Young's modulus (GPa)	211	207
Thermal conductivity (W/m K)	18.7	21
Poisson's ratio	0.3	0.31
Density (g/cm <sup>3</sup> )	7.65	7.75
Specific heat (J/g K)	0.49	0.46
Expansion coefficient (10 <sup>6</sup> /K <sup>-1</sup> )	16.5	12–14
Yield Strength (MPa)	580	565

**Table 2** Mechanical and thermal properties of proposed titanium alloy valve material

Specification	Guide	Insert	Titanium valve
Yield strength (MPa)	285	350	880
Young's modulus (GPa)	212	117	113.8
Poisson's ratio	0.33	0.34	0.34
Density (g/cm <sup>3</sup> )	8.84	8.94	4.43
Thermal conductivity (W/m K)	28.7	28.5	6.7
Specific heat (J/g K)	0.5	0.52	0.52
Expansion coefficient (10 <sup>6</sup> /K <sup>-1</sup> )	13.95	16.2	16.2

The valve material input data used for titanium (grade 5) alloy and 21-4N, and EN-52 along with seat insert, a guide is given in Tables 1 and 2.

The design for the proposed reference boundary condition of basic equations used to dimension the valve-train components. Then in the model, 3D solid element meshing was built in a valve body. Meshing has to be fine along the seat area to ensure better results of deformation. A load is distributed along the valve head area, and thus, the meshing along the face area should be uniform so that the combustion pressure strikes all the parts of the angular region of the valve head. The meshed model of the valve-train is as shown in the diagram (see Fig. 3).

### 3 General Discussion on Virtual Experimental Plan

Thermal stress on valve we get through the analysis of a 3D linear steady-state thermal analysis. During the combustion process, the operating temperature in the intake valves reaches up to 500 °C–600 °C and of the exhaust valves is between 700 °C–850 °C, and at this temperature, the thermal analysis is carried out. The surface to surface interactions is given between the master surface guides or insert and slave surface valve. The load is impacting on a face and guide with uniform

**Fig. 3** Finite element  
Meshed model of the valve



distribution along with boundary condition is applied at the guide and insert with 350 magnitudes. The friction coefficient for the titanium valve is 0.05 and for steel valve is 0.15. The temperatures for both alloys in case of intake and exhaust valves are as shown below from Figs. 4, 5, 6, and 7.

**Case I: Titanium Valve** (Fig. 4 and 5)

**Case II: Steel Valve** (Fig. 6 and 7)

The absorbed heat is cooled by the valve seat and guide that contact to the valve. The maximum temperature is indicated at valve neck as shown from Figs. 4, 5, 6, and 7 for both alloys in case of intake and exhaust diagram where the failure is occurred. The material strength is deteriorated due to this high temperature.

#### (A) Thermo-Mechanical Stress Analysis Results

For static structural analysis, the combustion pressure of 200 Mpa applied on the face of the valve-keeping seat and guide constrained in all directions and rotation. The Lancaster is applied under boundary condition between the guide and insert which were kept fixed. Tie constraints are applied in between the valve insert and valve guide. For more accurate results, we had coupled stresses with heat transfer, Fig. 8, showing the predefined condition. The thermo-mechanical coupled analysis results for both alloys in case of intake and exhaust diagram are as shown below from Figs. 9, 10, 11, and 12.

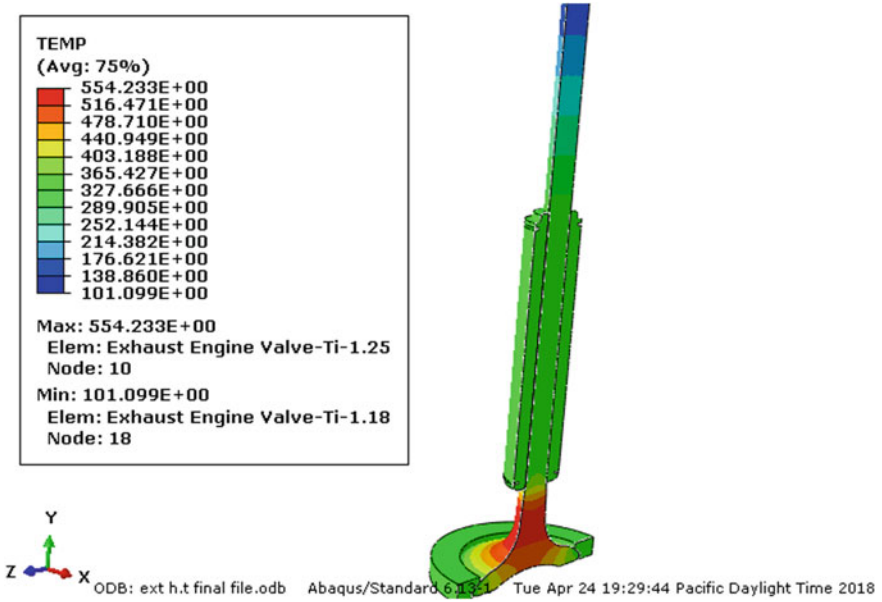


Fig. 4 Titanium exhaust valve temperature value

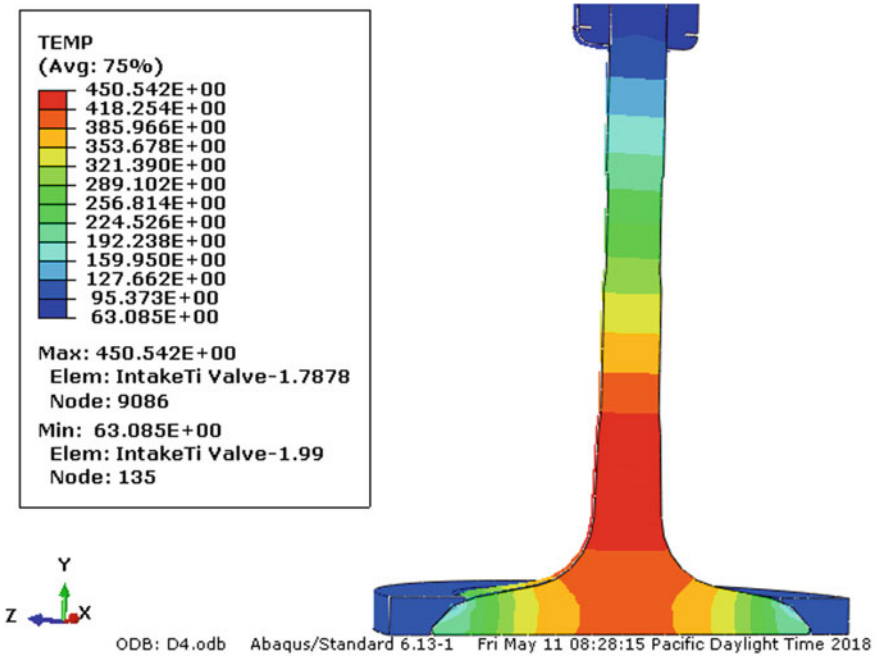


Fig. 5 Titanium intake valve temperature value

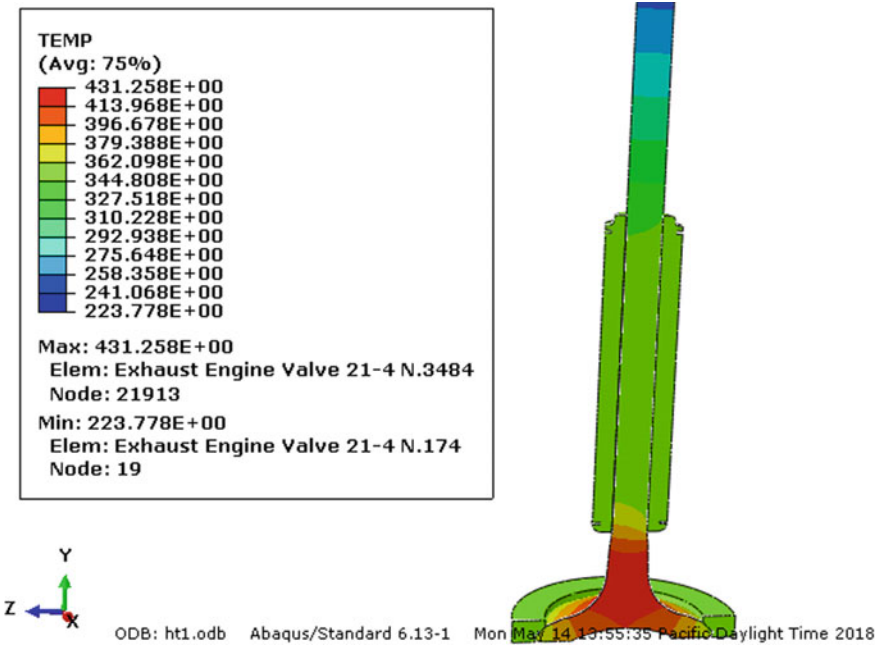


Fig. 6 21-4N steel alloy exhaust valve temperature

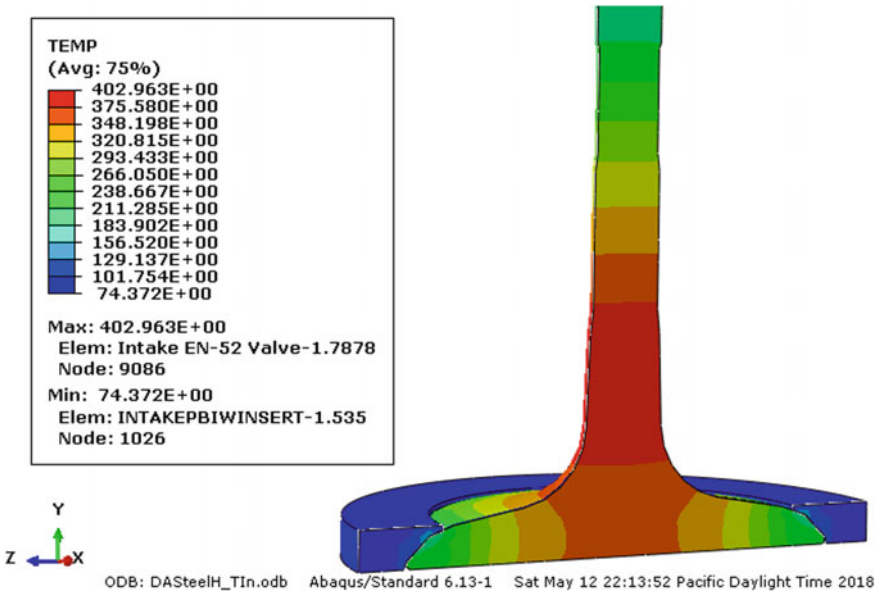


Fig. 7 EN-52 steel alloy intake valve temperature

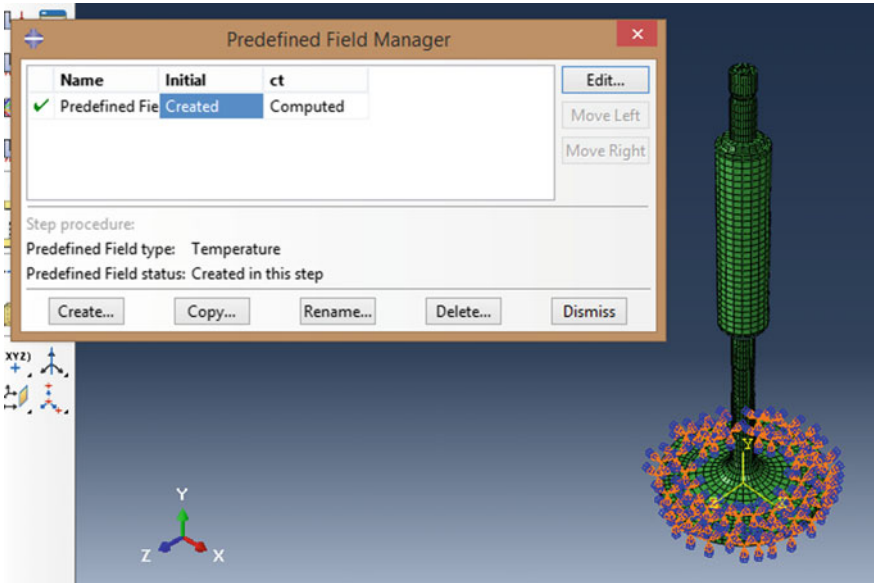


Fig. 8 FEM predefined loading condition

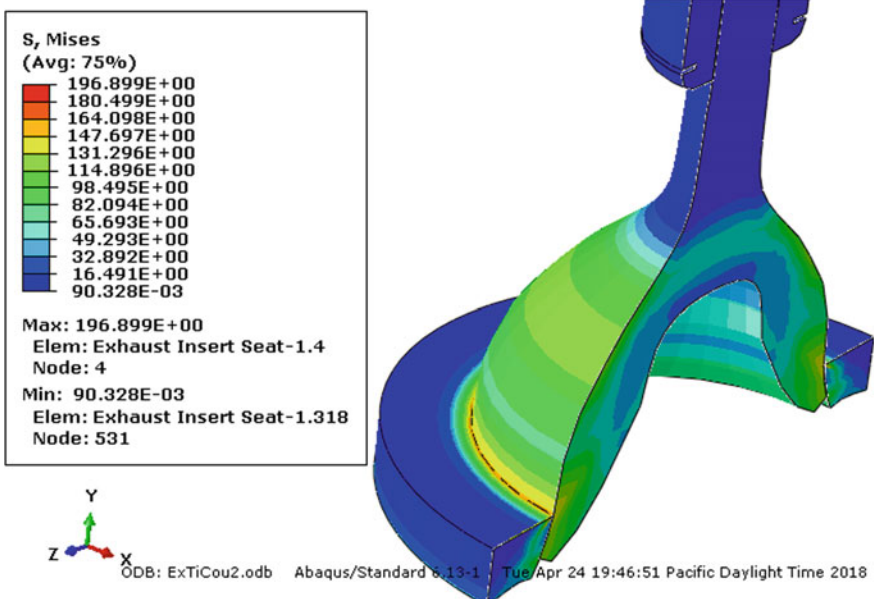


Fig. 9 Thermo-mechanical max working stress showing on titanium exhaust valve-train components



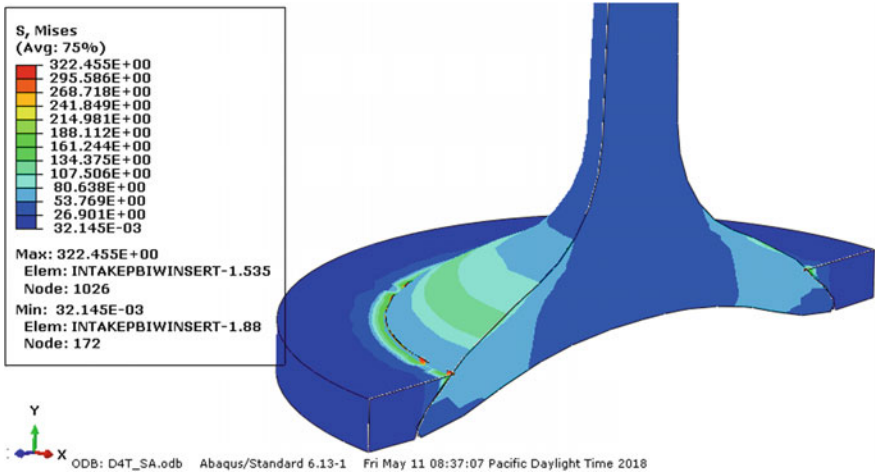


Fig. 10 Thermo-mechanical max working stress showing on titanium intake valve-train components

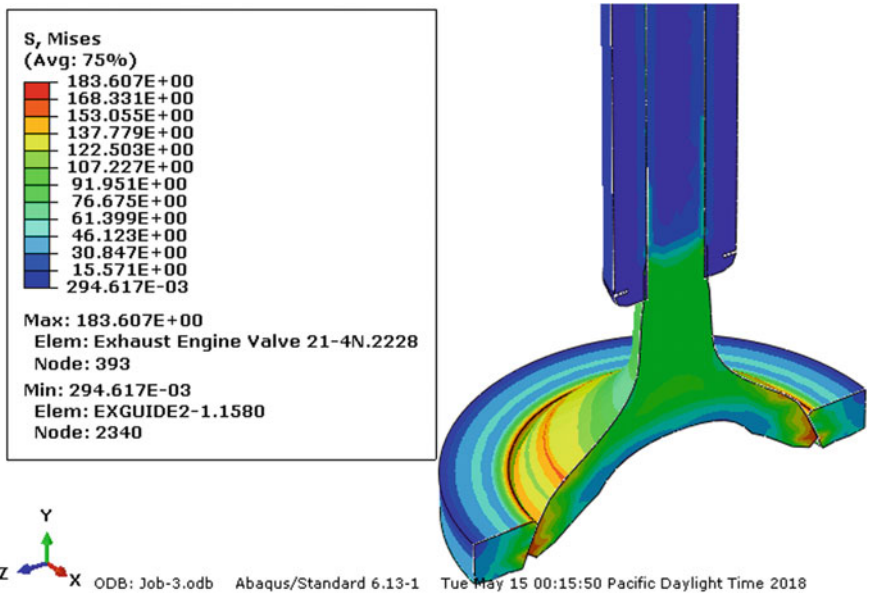


Fig. 11 Thermo-mechanical max working stress showing on 21-4N exhaust valve-train components

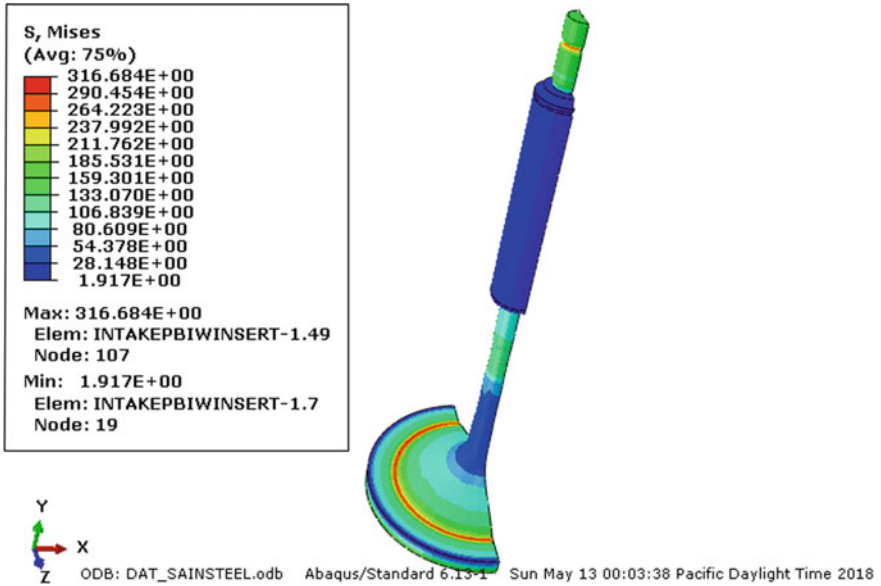


Fig. 12 Thermo-mechanical max working stress showing on EN-52 Intake valve-train components

**Case I: Thermocouple Titanium Results** (Figs. 9, 10)

**Case II: (a) Thermo-Mechanical Coupled Steel Results** (Figs. 11, and 12)

The maximum stress distribution in both cases intake and exhaust for titanium and steel alloy is shown in Figs. 9, 10, 11, and 12. A maximum stress occurs at the periphery of the valve.

**(B) Fatigue Assessment and Design Safety Factors:**

For engine valve manufacturers, it is necessary to have a valve fatigue life assessment model which can be further used in future product design to ensure a high probability to move the product test cycles. This is one of the objectives of this present work. Before modeling on valve fatigue, a detailed stress analysis work by finite element was conducted under mechanical loads. The fatigue life varies usually from  $10^5$  cycles to  $10^7$  cycles. The design factor is defined for an application and is not an actual calculation; the safety factor is a ratio of maximum strength to the intended load for the actual item that was designed. By this definition, a structure with a FOS of exactly 1 will support only the design load and no more. Any additional load will cause the structure to fail. A structure with a FOS of 2 will fail at twice the design load [8–11].

**Stress-Life Approach**

In the stress-life approach, the equivalent value of fully reversed cycling in Soderberg curve is used to find the valve fatigue life and design of safety factor.

The equivalent Soderberg's equation:

$$N_{fs} = \frac{YS}{\sigma_{mean} + \sigma_r K_f \frac{YS}{\sigma_e}} \tag{1}$$

$$\sigma_a = \frac{\sigma_{max} - \sigma_{min}}{2} \tag{2}$$

$$\sigma_m = \frac{\sigma_{max} + \sigma_{min}}{2} \tag{3}$$

Following are the fatigue graphs for steel and titanium as shown in (Figs. 13, 14, 15, and 16).

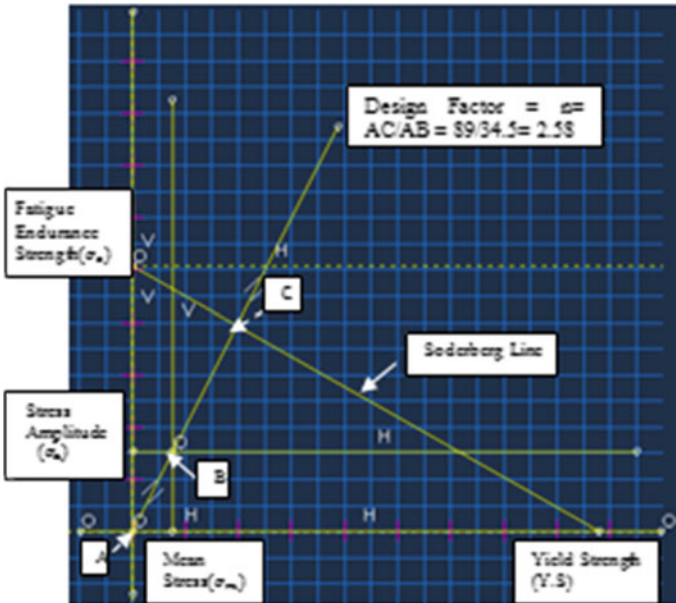
**Analysis Results**

Table 3 given below shows the heat transfer and thermo-mechanical coupled analysis results for both steel and titanium.

The predicted total fatigue life for the titanium and steel valves are computed and tabulated in Table 4 where Y.S,  $\sigma_m$ ,  $\sigma_r$ ,  $\sigma_e$  are yield strength, mean stress, reversing stress, and endurance stress. Table 4 shows fatigue calculation.

**Conclusions**

Following conclusions are drawn from the results obtained:



**Fig. 13** Titanium exhaust valve fatigue behavior

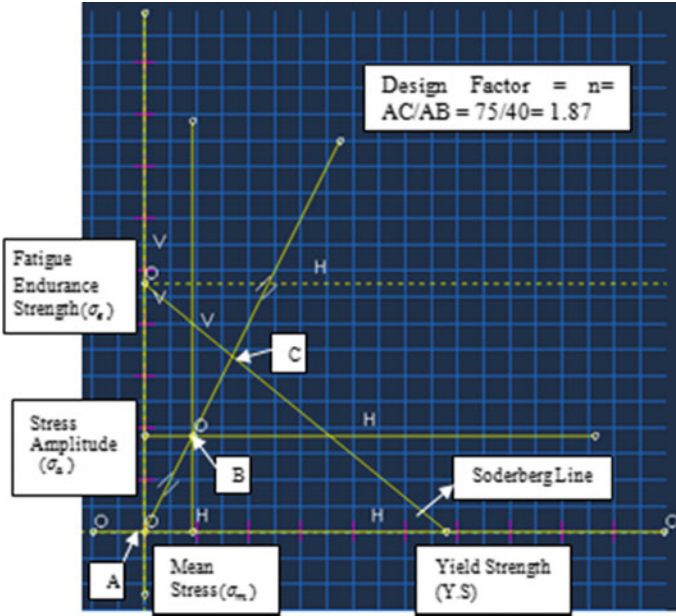


Fig. 14 21-4N exhaust valve fatigue behavior

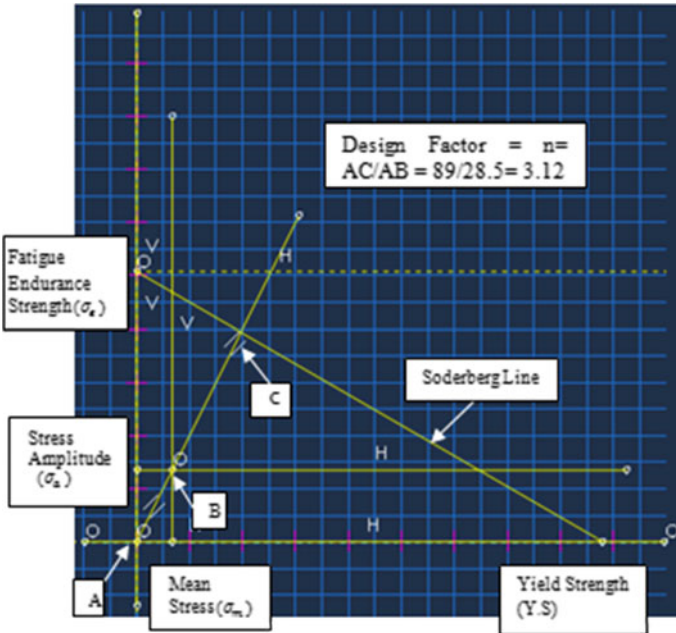


Fig. 15 Titanium intake valve fatigue behavior

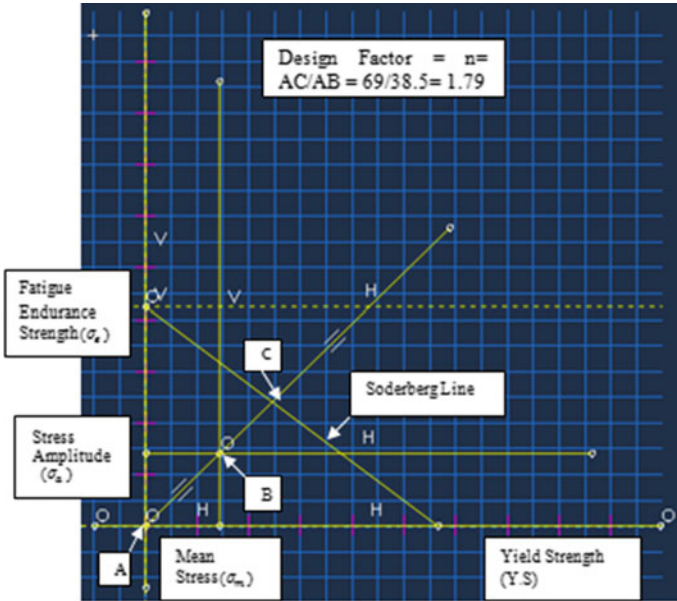


Fig. 16 EN-52 intake valve fatigue behavior

Table 3 Finite element analysis results for steel and titanium

		Thermal results (°C)	Thermo-mechanical coupled results (MPa)
Steel	Intake (EN-52)	402.96	316.68
	Exhaust (21-4N)	431.26	183.61
Titanium	Intake	450.54	322.45
	Exhaust	554.23	196.89

Source Computed data using FEA solver

Table 4 Fatigue factor calculation

		$\sigma_e$	$\sigma_m$	$\sigma_{max}$	$\sigma_a$	$N_{fs}$
Steel	Intake (EN-52)	425	143.22	283.76	140.5	1.79
	Exhaust (21-4N)	475	91.8	183.61	183.61	1.87
Titanium	Intake	507.5	67.33	134.66	134.66	3.12
	Exhaust	507.5	76.19	152.38	152.38	2.58

- (1) Valve fatigue life can be reasonably assessed by using the SN method which is the main purpose of life prediction.
- (2) Design safety factor of Titanium for both Exhaust and Inlet valve is high in compare to Steel alloy (En-52 & 21-4N) valve. Thus, it is also proved that the titanium alloy has enough potential as an optimal better material for the engine valve in comparing to 21-4 N and EN-52 steel alloy to improve engine performance.
- (3) It is found that the durability of the valve neck is subjected to various factors such as partial contact due to the thermal deformation of the seat and the degradation of material strength due to high temperature and the static load when the valve moves.

**Acknowledgements** The authors are highly grateful to Maharashtra Institute of Technology, Aurangabad, Maharashtra, India, for providing financial support.

## References

1. Pang ML, Smith SP, Herman R, Buuck B (2005) Stress analysis of an automotive engine valve by finite element methods. SAE International Paper No. 06P-78
2. de Cassia R, de Araujo Nunes MA, Oliveira ABS (2011) Dynamical simulation of a valve-train mechanism: an engineering education approach. In: 21st Brazilian Congress of Mechanical Engineering, 24–28 Oct 2011
3. Gawale Snehal S, Shelke SN (2016) Diesel engine exhaust valve design and optimization. IQSR J Mech Civ Eng. 13(04):85–93
4. Arul Murugan P, Ranganathan S (2015) New thermo mechanical analysis of engine valve using a multi-field approach. IJEDR 3(2):958–961
5. Londhe Rohit T, Kshirsagar JM (2014) Experimental analysis of valve and valve seats wear in gases (CNG) fuelled engine. IQSR J Mech Civ Eng 11(04):56–62
6. SAE J 775- Engine Poppet valve Information Report- SAE International, Surface Vehicle Information Report, Issued 1961-06, revised 2004-1.1
7. Kolchin A, Demidov V (1984) Design of automotive systems. Authors of the book-first edition
8. Pang ML, Smith SP, Herman R, Buuck B (2006) Fatigue life assessment on an automotive engine exhaust valve. SAE International Paper No. 06M-47
9. Torres MAS, Voorwald HJC (2002) An evaluation of shot peening, residual stress and stress relaxation on the fatigue life of AISI 4340 steel. Int J Fatigue 24:877–886
10. Khan MI, Khan MA, Shakoor A (2018) A failure analysis of the exhaust valve from a heavy-duty natural gas engine. Eng Fail Anal 85:77–88
11. Voorwald HJC, Caisse RC, Cioffi MOH (2011) Fatigue Strength of X45CrSi93 stainless steel applied as internal combustion engine valves. Procedia Eng 10:1256–1261

# Stratification by Fuel Injection and Positive Ignition



V. V. Prathibha Bharathi

**Abstract** Of many types of IC Engines, two types, namely diesel and petrol engines, are well established. Each one of them has certain limitations. The full load power characteristics of petrol engine are very good, but the degree of air utilization is also high. Diesel engines have part load characteristics but have poor air utilization. Comparatively, the emission characteristics for the diesel and petrol engines are poor due to the high peak temperatures. In the actual operation, basing on the stoichiometric fuel–air mixture ignition the fuel efficiencies are very much lowered in both the engines. From the observation, we see that the engine runs at part load and max power conditions. Therefore, an engine is to be developed, which can combine the advantages of diesel and petrol engine and also avoid the many of their disadvantages. In that course of action stratified charge engine is one, which is midway of the heterogeneous CI engine and homogeneous SI engine. Here an overview of stratified charge engine working and its combustion by fuel injection with positive ignition method is presented.

**Keywords** Engine · Load power · Ignition

## 1 Introduction

Ricardo, around 1922, made the first attempt to obtain the charge stratification. Later in October 1972, the President of Honda Motor Company Mr. Soichiro Honda introduced the “compound vortex-controlled combustion—stratified charge engine”. A type of IC Engine wherein the combustion chamber, the different fuel–air mixture strengthens at various places relatively too rich mixture at the end of the spark plug and a lean mixture in the rest of the chamber. The overall mixture is rather lean where the whole fuel mixture in the combustion chamber is distributed in layers of different mixture strengths. In the spark ignition IC engine, near the spark plug the mixture

---

V. V. Prathibha Bharathi (✉)

Department of Mechanical Engineering, Anurag Group of Institutions (Autonomous), Ghatkesar, Venkatapur, Hyderabad, Telangana, India  
e-mail: [prathibhaseenu@gmail.com](mailto:prathibhaseenu@gmail.com)

© Springer Nature Singapore Pte Ltd. 2020

L. Vijayaraghavan et al. (eds.), *Emerging Trends in Mechanical Engineering*,  
Lecture Notes in Mechanical Engineering,  
[https://doi.org/10.1007/978-981-32-9931-3\\_3](https://doi.org/10.1007/978-981-32-9931-3_3)

is richer than that in the combustion chamber, then this would be a stratified charge engine which burns the leaner over all fuel mixtures.

The main objective of stratified engine feeds the rich mixture through a separate inlet valve to generate a swirl in the combustion chamber. By this, weak mixture enters the cylinder in general and then the vortex comprising alternate layers of rich and lean mixtures are formed [1]. As the rich mixture is directed on to the spark plug points which ignites and burns the mixture throughout the cylinder. This stratified engine concentrates on the mixture near the spark plug whose AF ratio is  $<14:1$  and the remaining mixture in the cylinder which is a lean mixture whose AF ratio is  $\geq 50:1$ . As like the direct ignition system in the diesel, here it uses the same process to run at high compressions. However, to gain the ability of quick mixing and clean burning to avoid the poor combustion it relies on gasoline-like Otto cycle which is found in the diesel.

## 2 Stratified Engine Construction and Its Working

The combustion chamber is designed in such a way that at the spark plug a pre-combustion chamber is created which helps to produce a rich mixture close to the spark plug. For this modification, piston head is also done and where the cavity which is in the form of a toroidal and imparts swirling movement to the air in the cylinder during compression. It is also provided with a thin fan-shaped fuel spray (see Fig. 1).

In this, through the transfer system, the engine pulls only the air and the fuel injector which is placed at the top of the cylinder head will inject the required amount of fuel for the combustion in the form of a fuel cloud (see Fig. 2) into the cylinder.

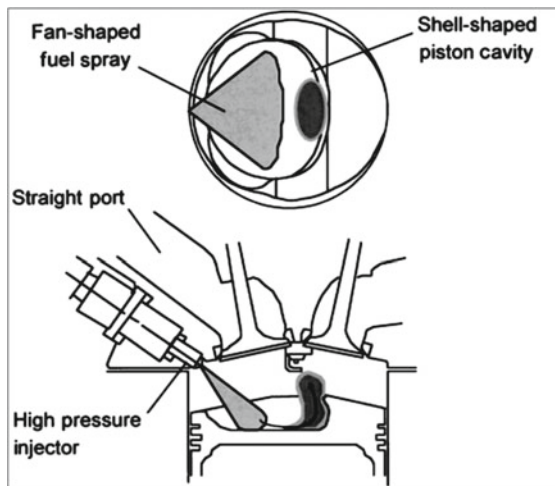


**Fig. 1** Fan-shaped fuel spray



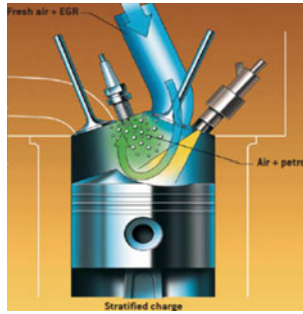


Fig. 2 Modified piston head

When the cloud is ignited and burn, the air which is already pulled through transfer system surrounding the fuel cloud provides the complete combustion before the opening of exhaust port. Here the fuel is injected just before ignition to get the higher compression ratios without knock.

### 3 Method of Fuel Injection and Positive Ignition

#### 3.1 Approach

The schematic representation of the Ricardo charge stratification plan and elevation which shows the fuel spray arrangement is shown in figures (see Figs. 3 and 4). By

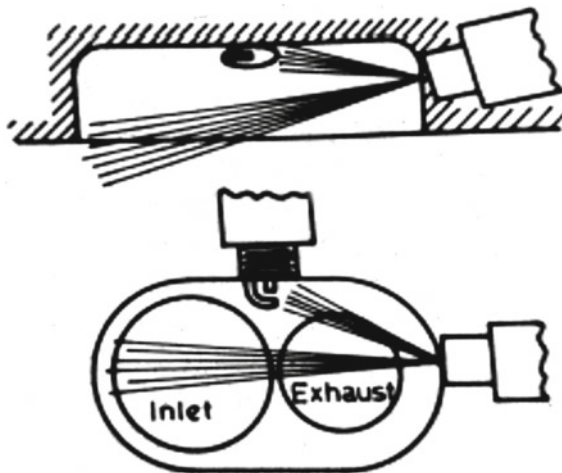
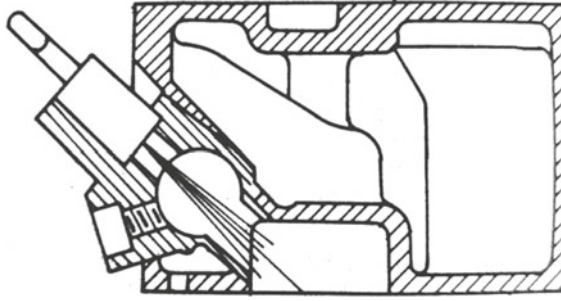


Fig. 3 Ricardo's first charge stratification approach



**Fig. 4** Ricardo's prechamber stratification

an auxiliary spray at the spark plug a rich mixture was formed, while on the other hand along the major axis of the combustion chamber, a spray was injected to form a leaner mixture.

The engine operation gives the efficiencies as high as 36% because of this arrangement [2]. Due to the too rich mixture near the spark plug, the full load of the engine does not work properly about the load of 50% where the range is limited to higher speeds.

Ricardo made some modification by fitting a small prechamber with injector and the spark plug for the above arrangement where a rich mixture is formed near the spark plug and a lean mixture is supplied to the combustion chamber through carburetor. The lean mixture present in the chamber burns with the burning of auxiliary charge in the prechamber before it issues out through its throat. Problems of engine operation are involved in this approach. At the full load range, getting good performance is not achieved due to the improper combustion of fuel at full load [3]. We can see that at part loads the lean mixtures are burned effectively, but at full loads, the rich mixture is not burned properly due to the incomplete scavenging of the prechamber and the improper fuel distribution. Loss of thermal efficiency due to throttling can be achieved by means of prechamber [4]. To avoid an over-rich mixture and for good fuel distribution in prechamber to provide regular injection at low fuel deliveries, the fuel injection system has to be highly sophisticated.

### **3.2 Volkswagen PCI Stratified Charge Engine**

The figure illustrates the Volkswagen PCI stratified charge engine (see Fig. 5). The spherical unscavenged prechamber comprises approximately 25–30% of the compression volume and by means of a relatively large flow transfer passage is linked to the main combustion chamber. The shape of the main combustion chamber is of disc-like one and contains no squish surfaces but a slight swirl is induced by the intake port [2].

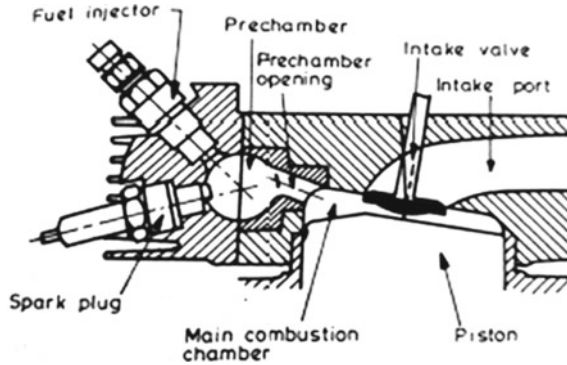


**Fig. 5** Volkswagen PCI stratified charge engine

The arrangement of the injection nozzle and the spark plug is in sequence in the direction of flow so that the mixture produced by blending of the incoming air is received by the spark plug to avoid over richment at the spark plug. The total volume of fuel is partly injected into the prechamber and partly into the intake manifold, with a relatively rich mixture at spark plug under all operating conditions. By adjusting, the mixture strength which is introduced into the combustion chamber the load regulation is achieved.

One major advantage of this system is that, unlike other stratification processes, the fuel injection timing does not need to be varied. This is a considerable simplification. Its octane requirement is comparatively low, in a particular, at high speeds. It can be easily operated on very lean mixtures (relative air–fuel ratios larger than 2) which is also advantageous from exhaust emission point of view.

### **3.3 Broderson Method of Stratification**

The gap between the part-load and full-load performance problems can be solved with the use of two alternatives. One is by injection timings, the mixture strengths in auxiliary and combustion chamber are controlled.

Another is to obtain stratification by carburetion alone, i.e. by replacement of carburetion. The Broderson method of stratification is shown in figure (see Fig. 6) where we see the engine with a divided combustion chamber. The fuel is injected into the prechamber where the prechamber contains the spark plug, injector and intake valve.

During this methodology, the premise of charge stratification is formed as the piston passes bottom dead centre position in the combustion chamber; there will be change in the direction of airflow. Before BDC, the fuel injected into the main chamber is carried by air where it is mixed in the chamber with all the air present in it due to the suction effect. Because of the reversal of airflow direction, the fuel which is

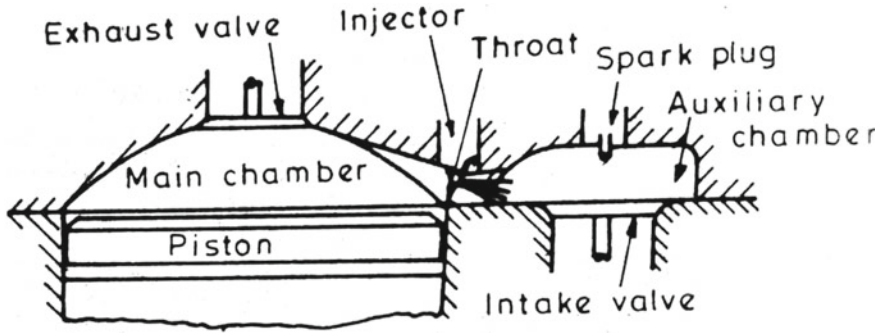


**Fig. 6** Broderson method of charge stratification

injected after BDC will remain in the prechamber by forming a combustible mixture near the spark plug [5]. It is evident that desired mixture ratio can be achieved by varying the beginning timing of injection and duration of injection.

After the start of compression stroke, air is moving from the main chamber to the prechamber and all the fuel entered into it will remain to form an ignitable mixture at the spark plug where the lean mixture is present in the main chamber. Due to the torch effect from the prechamber, the lean mixture in the main chamber is burnt. For fast and whole burning of the charge in the main chamber, it has to be designed to witness satisfactory turbulence and mixing in it. During the suction stroke before BDC at full load, the fuel is injected and is mixed with the air to affect a uniform strength throughout the combustion space. Thus, as like the normal spark-ignition operation here also the flame is spread over both the chambers.

The method invented by Broderson retains the favourable condition by avoiding the pumping losses caused by throttling and carburettor venturi. In accrual, the high part load efficiency is achieved by lean mixture burning at full load with some knock resistance. When compared with the Otto engines, this will dispense lower exhaust temperatures. This engine gives good air pollution characteristics due to the pure air present in the main chamber at part load.

The divided-chamber, stratified-charge engine can burn propane, kerosene, diesel and gasoline fuels and shows little sensitivity to octane number, i.e. it has multi fuel capability inherent in it. The disadvantages of this method are as follows:

- (i) The injection and ignition equipment should be carefully observed to commensurate with the prechamber and main chamber design.
- (ii) The tendency of noise increases with the load increase, i.e. sound produced due to rapid expulsion of gasses at idling from the prechamber.

### 3.4 Swirling Effect

Due to swirling, the fuel vapour was distributed around the cylinder wall in a doughnut-like shape because the fuel vapour was rotated along the cylinder wall by the swirling flow [6]. In other words, the swirl intensity can enhance stratification degrees that directly affect the lean limit range by diffusing amount of fuel to form stoichiometric mixture in the wider area.

#### Characteristics of Stratified Charge Engines

- (i) Full load performance is slightly deputy to petrol engine but have a good part load efficiency.
- (ii) Comparable all the stratification processes have built in tendency of knock resistance, multi-fuel capability and smooth combustion. It can also operate at low octane fuel depending on the respective design.
- (iii) The un-throttled engines have comparatively higher volumetric efficiencies than the carburetted engines.
- (iv) Most of the stratification engines have good schemes of exhaust emission.

#### Applications

The characteristics troth that these engines are bright future one as of its design, weight, fuel economy, speed, multi-fuel capability, load range, etc. In October 1972, Honda Motor Company laid the foundation for CVCC stratified charge engine and following in 1976 introduced world's first stratified charge engine car. Today, several stratified engines are in the markets which run on using about 15–20% less fuel comparatively with non-stratified engine design. A number of companies are actively working on this engine for automotive applications.

#### Advantages and Disadvantages

##### Advantages

- (i) Leaner mixture has the higher value of  $\gamma$  which results in better part load efficiencies. Comparatively for the same pressure ratio, the part load efficiency of lean charge engine is much better than petrol engine.
- (ii) The amount of oxides of nitrogen and CO release is reduced.
- (iii) The quenching at walls reduce drastically on the use of charge stratification.
- (iv) The losses due to throttling are avoided.
- (v) The emission levels are low, capable of wide quality of fuels, and moreover, it can be manufactured with the existing technology.

##### Disadvantages

- (i) For a given size, the power resulted with charge stratification is reduced.
- (ii) It has a higher HC emission than that of conventional engine.
- (iii) Its manufacture is more complex, and hence, its manufacturing cost is higher.
- (iv) Its reliability is yet to be well established.

## 4 Conclusion

On comparison, stratified charge direct injection engines possess redolently higher fuel economy than conventional throttled engines. The heat losses can be decreased in such way that because of stratifying the fuel–air mixture will be in the centre of the combustion chamber which will keep the burnt products away from the walls. These all show the sign of reduced fuel consumption which leads to a reduction in the engine exhaust emissions. According to the present scenario, reduction in emissions is encouraged, and so these types of engines with necessary developments are to be implemented.

### Future Scope

For the practical work on stratified charge engine, the theoretical approach carried in this paper and may help in the form of a brief study. By this base study, the practical work on the stratified charge engine by making the experimental optical stratification engine sets up to perform ignition performance research, including data acquisition system with the diagnostic and techniques of optical measurement for various studies can be carried.

## References

1. Heywood JB (1989) Internal combustion engines. Mc Grawhill
2. Mathur ML, Sharma RP (1994) A course in internal combustion engines. Dhanpat Rai & Sons, New Delhi
3. Brandstetter WR, Decker G (1975) Fundamental studies on the volkswagen stratified charge combustion process. *Combust Flame*
4. Green RK, Zavier CC (1992) Charge stratification in a spark ignition engine. *Proceedings of the institution of mechanical engineers. Part A: J Power Energy* 206(1):59–64
5. Zanforlin S, Gentili R (2004) Stable fuel confinement in stratified charge GDI engines, internal combustion engine division fall technical conference ICEF2004-0919, ASME, pp 363–372
6. Blair GP (1990) The design of two-stroke engines, society of automotive engineers. Warrendale, Pennsylvania, pp 672, SAE ref no.: R-104, ISBN 1-56091-008-9

# Analysis of Miniature Loop Heat Pipe Under Varying Working Fluids and Wick Materials at Low Heat Inputs



V. Murali Krishna and Mechiri Sandeep Kumar

**Abstract** In modern electronic equipment, the use of heat pipes is steadily increasing as they have maximum heat transport capability per unit area. The driving mechanism in heat pipe is the capillary forces developed in fine porous wick to circulate the fluid. The heat transfer in heat pipe is by both condensation and evaporation. Loop heat pipe is one such kind, which has two-phase heat transfer. In this device, the working fluid is circulated due to surface tension forces formed in wick. It can be operated against gravity and can possess flexible transport lines. In the present work, the performance of loop heat pipe is investigated using different working fluids and wick materials. The results are obtained for low heat input ranging from 5 to 12 W. Results show that acetone fluid had better thermal performance when compared to other fluids as it has very low thermal resistance, which is almost half of the thermal resistance of water. As the heat load increased, the temperature difference also increased between the evaporator and condenser. A better thermal performance was obtained with nickel as wick material.

**Keywords** Miniature loop heat pipe · Wick materials · Working fluids

## 1 Introduction

One of the major concerns in several electronics applications, process industries, and power generation is cooling. Cooling can be addressed by selecting an appropriate heat pipe. A loop heat pipe (LHP) is one such device, which possesses a two-phase cooling system with high density of heat dissipation. The quantity of working fluid is fixed, and great amount of heat is transferred by both condensation and evaporation. LHP has the advantage of operating against gravity and higher heat transfer capacity.

---

V. Murali Krishna (✉) · M. S. Kumar  
Department of Mechanical Engineering, B. V. Raju Institute of Technology, Narsapur,  
Medak 502313, India  
e-mail: [mk\\_vemula@rediffmail.com](mailto:mk_vemula@rediffmail.com)

M. S. Kumar  
e-mail: [sand.mechiri@gmail.com](mailto:sand.mechiri@gmail.com)

© Springer Nature Singapore Pte Ltd. 2020  
L. Vijayaraghavan et al. (eds.), *Emerging Trends in Mechanical Engineering*,  
Lecture Notes in Mechanical Engineering,  
[https://doi.org/10.1007/978-981-32-9931-3\\_4](https://doi.org/10.1007/978-981-32-9931-3_4)

The heat can be transferred to longer distance with least temperature drop. Faghri and Parvani [1] made a numerical study on performance of heat pipe with double wall for various heating as well as cooling loads in laminar flow. An analytical study also conducted to calculate the pressure loss and velocity variation. They observed reverse flow at high rate of condensation. Faghri and Buchko [2] made a numerical and experimental study on heat pipe, to find out the effect of heat load dissemination with several heat sources. An increase in heat capacity was found with rearrangement of heat loads.

Muraoka et al. [3] made both theoretical and experimental study for enhancement of condenser performance by substituting a tube condenser with a condenser having porous wick arrangement. They found substantial betterment in performance. Kaya and Hoang [4] proposed a mathematical model and validated it by performing experiments on two different LHPs for different sink temperatures and heights. They found 5% deviation between theoretical and experimental results. A mathematical model was developed by Muraoka et al. [5] to find the fluid flow and heat transfer characteristics of LHP with porous elements in evaporator and condenser to increase startup stability. An improvement in the performance was noticed compared to their previous work [3]. But effective parting of vapor from liquid was not found due to establishment of liquid layer over the porous element. An analytical model was proposed for looped and un-looped pulsating heat pipes by Shafii et al. [6]. In this model, multiple liquid slugs and vapor plugs were also considered. The heat transport rate enhanced with increase in diameter and also due to temperature difference between heating and cooling walls. They also found that the gravity did not play any substantial effect on the efficiency of un-looped heat pipe.

Kaya and Ku [7] conducted a theoretical and experimental investigation to determine the performance of a small LHP. The parameters considered were heat loads, sink temperatures, and orientations. They observed that with increase in heat load, there was a variation in the working fluid arrangement and increase in pressure loss. A theoretical model developed by Launay et al. [8] to predict the fluid flow and thermal behavior of LHP under oscillating heat loads. The validation of the model was done by experimental data and found a good agreement between them. Qu and Ma [9] conducted a theoretical study to determine the influence of various parameters on startup features of pulsating heat pipe. Their results stated that capillary wall state and kind of working fluid significantly influence the startup characteristics. Kaya et al. [10] made simulation studies to find dynamic behavior of LHP at ambient and vacuum states. They stated that there is a need for empirical correlations at low powers.

Chernysheva and Maydanik [11] performed numerical simulations in a cylindrical evaporator during the startup of LHP. The parameters considered are heat loads, wick materials, and working fluids. They found that the LHP can be started effectively only after formation of vapor from the liquid in the channels. The influence of wick material on the performance miniature heat pipe was deliberated by Singh et al. [12]. They found from their experimental study that the thermal performance of heat pipe was greater with copper wick compared to nickel wick. Kiseev et al. [13] proposed a methodology to design the capillary arrangement for upturned meniscus evaporators



of LHPs. Li and Peterson [14] conducted a theoretical study to investigate the heat and mass transport in a square flat evaporator of LHP with a fully saturated wick. The model developed was precisely predicting the performance of LHP particularly at low heat loads.

Zhang et al. [15] developed a three-dimensional model to investigate fluid flow and heat transfer in the flat evaporator of miniature LHP at the specified heat flux. They found that the heat transfer is less for the fully saturated wick compared to vapor groove inside the sintered wick. Mameli et al. [16] developed non-dimensional heat transfer correlations suitable for different working fluids. The numerical data obtained was validated with experimental data available in the literature for a single loop pulsating heat pipe and found reasonably good agreement. Wu et al. [17] investigated the effect of evaporation surface area on the performance of LHP. Their results indicated that the cooling capability of LHP was increased with increase in surface area. Nishikawara and Nagano [18] developed a mathematical model to determine the effect of micro-gap between the case and wick of the evaporator. The influence of heat load, wick shape working fluid, and wick material on heat transport was studied. They observed an enhancement in heat transfer and reduction in hysteresis of liquid-vapor interface in a porous structure. Recently, Nishikawara and Nagano [19] proposed a model to optimize wick shape in the evaporator of LHPs by using the length of three-phase contact line (TPCL). They observed increase in heat transfer rate up to certain TPCL length, and thereafter, it was decreased due to increase in pressure loss in vapor grooves. It was found that no simulation work is reported in the literature on thermal performance of closed-loop heat pipe at very low heat inputs. Microelectronic devices used in certain applications generate lower heat inputs. So in view of the importance, CFD analysis is made on a miniature loop heat pipe for heat inputs ranging from 5 to 12 W. The heat transfer performance of heat pipe considered was found for five different working fluids namely water, acetone, methyl alcohol, ammonia, and ethyl alcohol. The wick materials considered were nickel and ultra-high molecular weight (UHMW) polyethylene, with fill ratios of 55–85%. Also, variation of evaporator temperature was studied. The loop heat pipe was designed in CATIA V6, and the CFD analysis was made on ANSYS CFD academic research version 19.2.

## 2 Physical Model

The schematic outline of the loop heat pipe considered is shown in Fig. 1. The evaporator section has a central porous wick through which a volatile working liquid circulates. A reservoir, also called as compensator, is attached on left side of the evaporator tube. The reservoir supplies the working fluid to the evaporator without any interruption. The diameter of porous wick is slightly less than that of the evaporator tube. The space between the cylindrical wick and evaporator tube provides the path for flow of vapor in the evaporator tube. The evaporator tube is exposed to the heat source. The working fluid receives the heat falling on the evaporator tube. The

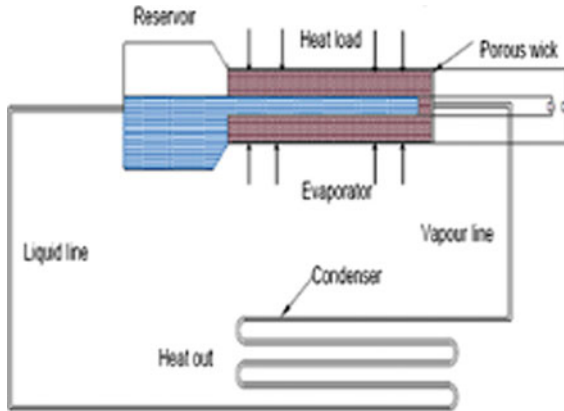


**Fig. 1** Loop heat pipe

working fluid in the porous wick vaporizes by receiving the heat, flows through the space between the wick and evaporator tube, leaves the evaporator, and enters into the condenser tube. The condenser section is a coil heat exchanger. Water is circulated over the coil to condense the vapor flowing in the tube. There is a two-phase flow of a mixture of vapor and liquid in the condenser tube. The condensed liquid goes to the compensator from where it is sent to the evaporator tube.

The inner and outer diameters of the copper evaporator are 10 and 20 mm, respectively, and length of the evaporator is 1000 mm. The size of the condenser considered has a coil diameter of 12.5 mm and length 1000 mm. The physical model considered is modeled in CATIA V6 software.

### 3 Results and Discussion

The model created in CATIA is imported in ANSYS workbench. The model developed is simulated to determine the thermal performance of loop heat pipe considered using Fluent software by applying appropriate boundary conditions. The numerical study is made on the closed-loop heat pipe with five different working fluids and two different wick materials for heat inputs ranging from 5 to 12 W. The fill ratios of 55–85% were considered in the present work, as the heat pipe has better heat transfer performance at lower inputs [20]. The working fluids considered in the present study are water, acetone, methyl alcohol, ammonia, and ethyl alcohol, and wick materials considered are nickel and ultra-high molecular weight (UHMW) polyethylene. The properties of working fluids are listed in Table 1. The heat transfer coefficient ( $h$ ) is calculated using the equation given below.

$$h = \frac{Q}{A(T_E - T_C)} \quad (1)$$

**Table 1** Properties of working fluids at 20 °C

Name	Density (kg/m <sup>3</sup> )	Viscosity (mPa s)	Thermal conductivity (W/m K)	Specific heat (KJ/kg K)
Acetone	784	0.306	0.1642	2.15
Ammonia	682	0.138	0.5210	4.74
Ethanol	789	1.150	0.179	2.40
Methanol	792	0.544	0.2040	2.46
Water	998	0.890	0.561	4.18

where  $Q$  is the heat input ( $W$ ),  $A$  is the surface area of the evaporator,  $T_E$  is the evaporator average temperature ( $^{\circ}C$ ), and  $T_C$  is the condenser average temperature ( $^{\circ}C$ ).

### 3.1 Variation of Heat Transfer Coefficients for Different Working Fluids and Fill Ratios with Nickel as Wick Material

The variation of heat transfer coefficient (HTC) at fill ratio of 55% for working fluids as acetone, ammonia, ethanol, methanol, and water for different heat inputs with nickel as wick material is shown in Fig. 2a. An increase in HTC with increase in heat input for all the working fluids can be witnessed. This is due to improvement of heat transfer rates in condenser and evaporator with increase in heat input. At fill ratio of 55%, the increase in HTC with increase in heat input for water is not significant. The value of HTC increases very gradually with the rise in heat input for water as working fluid, escalates gradually for methanol, ethanol, and ammonia, and escalates very quickly for acetone as working fluid.

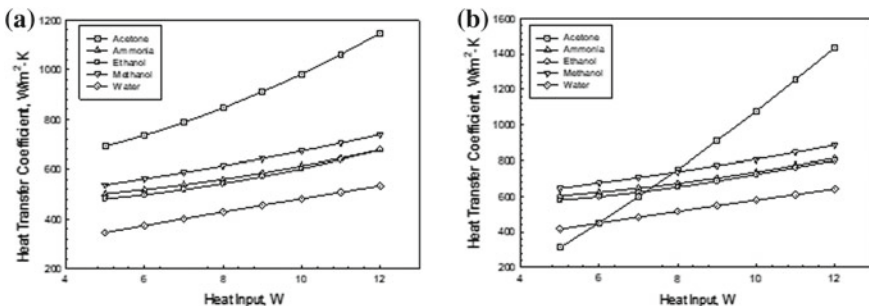


**Fig. 2** Variation of heat transfer coefficient with heat input with nickel wick at **a** 55% fill ratio and **b** 85% fill ratio

The variation of HTC with heat input for different working fluids at fill ratio of 85% is shown in Fig. 2b. The values of HTCs escalate with rise in fill ratio for all the working fluids. For 85% fill ratio, the working fluids ammonia, ethanol, methanol, and water display nearly similar pattern of HTC. But acetone shows very high HTCs for greater heat inputs. The repetitive tendency of increasing value of HTC with rise in heat load is restricted by the burn out at maximum heat input. At this state, the amount of condensate coming back is not as much of the rate of evaporation.

### 3.2 Variation of HTCs for Different Working Fluids and Fill Ratios with UHMW Polyethylene Wick

Metal, ceramic, and plastic materials are used for the preparation of wicks. The thermal conductivity for plastic wicks is very low. The wick with low thermal conductivity enhances the performance of LHP by inhibiting heat transfer from the evaporator to the reservoir section through the wick. So, the numerical results are also obtained with UHMW wick with the same working fluids for different fill ratios and heat loads. Figure 3a. shows the variation of HTC for different heat loads and working fluids at fill ratio of 55%. Among the fluids considered, acetone has maximum value of HTC, and water has least value of HTC. This is due to better flow of acetone compared to other fluids due to low density, surface tension, saturation temperature, and latent heat of evaporation.

As discussed in the previous section, the magnitude of HTC is also enhanced in rise in fill ratio for all the working fluids with UHMW wick. The same can be witnessed from the Fig. 3b. At upper heat loads, acetone has very high HTCs due to quicker bubble creation with enhancement in heat input compared to ammonia, ethanol, methanol, and water.

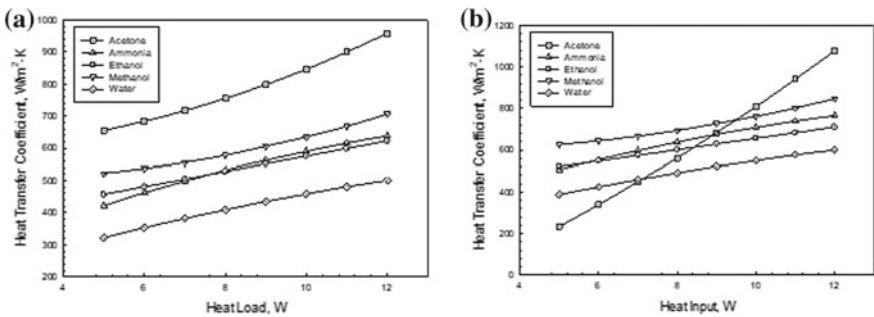


Fig. 3 Variation of HTC with heat input with UHMW wick at fill ratio of a 55% and b 85%

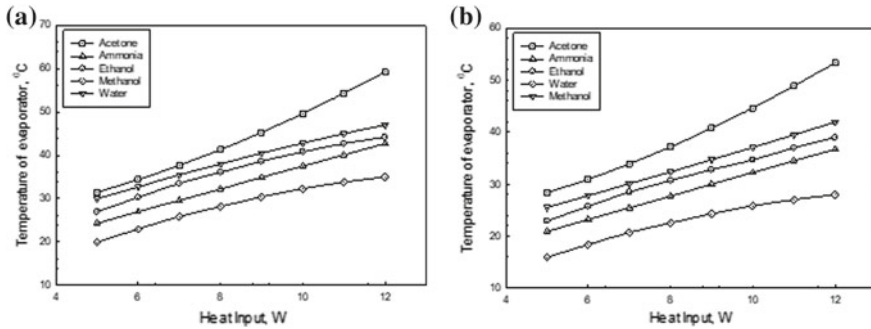


Fig. 4 Effect of heat load on ET at fill ratios of a 55% and b 85% for with nickel wick

### 3.3 Variation of Evaporator Temperature for Different Working Fluids and Fill Ratios with Nickel as Wick Material

The variation of average steady temperature of evaporator with heat input for acetone, ammonia, ethanol, methanol, and water with nickel wick at fill ratio of 55% is shown in Fig. 4a. The steady-state average temperature of evaporator is enhanced for all the working fluids with rise in heat load. The evaporator temperature (ET) is maximum for acetone and bottommost for water at the steady state. This can be attributed to rapid bubble progression for acetone due to low latent heat of evaporation and saturation temperature. Figure 4b shows the effect of heat load on average ET at the fill ratio of 85%. The working fluids acetone, ammonia, ethanol, methanol, and water displays almost comparable pattern of ET for 85% fill ratio. But the magnitudes of ET are less for all the working fluids due to increase in fraction of the evaporator volume that is occupied by the working fluid.

### 3.4 Variation of Evaporator Temperature for Different Working Fluids and Fill Ratios with UHMW Polyethylene Wick

The usage of wicks made of UHMW Polyethylene is increasing in heat pipes due to its outstanding machinability and low thermal conductivity. So, the variation of ET with UHMW Polyethylene wick for various heat loads at 55% fill ratio is shown in Fig. 5a from the results attained. The steady-state average ET is enhanced for all the working fluids with increase in heat load. The effect of ET at fill ratio of 85% is depicted in Fig. 5b. The ET is diminished with rise in fill ratio. The constraint of plastic wick is low porosity, which limits the maximum operating temperature.

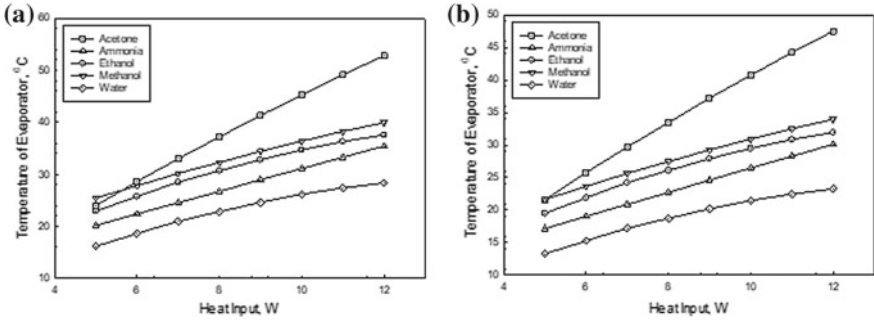


**Fig. 5** Variation of ET with heat input for UHMW wick at fill ratio of **a** 55% and **b** 85%

### 4 Conclusions

In the present work, the heat transfer performance of loop heat pipe was investigated using different working fluids with different wick materials at different heat inputs and fill ratios. It is found that the acetone fluid indicated better thermal performance when compared to other fluids. It is due to the thermal resistance of acetone is very low, which is nearly half of the thermal resistance of water. It was found that as the heat load increases the difference in temperature between the condenser and evaporator also increased. Also found from the results that using nickel as wick material compared to UHMW Polyethylene shows improved performance in terms of heat transfer. It has been observed that the heat transfer coefficient enhances with increase in fill ratio due to decrease in temperature change between the evaporator and condenser, fluids used in loop heat pipe and their specific heat, viscosity, density.

### References

1. Faghri A, Parvani S (1988) Numerical analysis of laminar flow in a double-walled annular heat pipe. *J Thermophys Heat Transfer* 2:165–171
2. Faghri A, Buchko M (1991) Experimental and numerical analysis of low-temperature heat pipes with multiple heat sources. *J Heat Transfer* 113:728–734
3. Muraoka I, Ramos FM, Vlassov VV (1998) Experimental and theoretical investigation of a capillary pumped loop with a porous element in the condenser. *Int Comm Heat Mass Transfer* 25(8):1085–1094
4. Kaya T, Hoang TT (1999) Mathematical modeling of loop heat pipes and experimental validation. *J Thermo-Phys Heat Transfer* 13(3):314–320
5. Muraoka I, Ramos FM, Vlassov VV (2001) Analysis of the operational characteristics and limits of a loop heat pipe with porous element in the condenser. *Int J Heat Mass Transfer* 44(12):2287–2297
6. Shafii MB, Faghri A, Zhang Y (2001) Thermal modeling of unlooped and looped pulsating heat pipes. *ASME J Heat Transfer* 123:1159–1172
7. Kaya T, Ku J (2003) Thermal operational characteristics of a small-loop heat pipe. *J Thermo-Phys Heat Transfer* 17(4):464–470

8. Launay S, Platel V, Dutour S, Joly JL (2007) Transient modeling of loop heat pipes for the oscillating behavior study. *J Thermo-Phys Heat Transfer* 21(3):487–495
9. Qu W, Ma HB (2007) Theoretical analysis of startup of a pulsating heat pipe. *Int J Heat Mass Transfer* 50:2309–2316
10. Kaya T, Pérez R, Gregori C, Torres A (2008) Numerical simulation of transient operation of loop heat pipes. *Appl Therm Eng* 28:967–974
11. Chernysheva MA, Maydanik YF (2008) Numerical simulation of transient heat and mass transfer in a cylindrical evaporator of a loop heat pipe. *Int J Heat Mass Transfer* 51:4204–4215
12. Singh R, Akbarzadeh A, Mochizuki M (2009) Effect of wick characteristics on the thermal performance of the miniature loop heat pipe. *J Heat Transfer* 131(8):082601
13. Kiseev VM, Vlassov VV, Muraoka I (2010) Optimization of capillary structures for inverted meniscus evaporators of loop heat pipes and heat switches. *Int J Heat Mass Transfer* 53(9–10):2143–2148
14. Li J, Peterson GP (2011) 3D heat transfer analysis in a loop heat pipe evaporator with a fully saturated wick. *Int. J. Heat and Mass Transfer* 54:564–574
15. Zhang X, Li X, Wang S (2012) Three-dimensional simulation on heat transfer in the flat evaporator of miniature loop heat pipe. *Int J Therm Sci* 54:188–198
16. Mameli M, Marengo M, Zinna S (2012) Thermal simulation of a pulsating heat pipe: effects of different liquid properties on a simple geometry. *Heat Trans Eng* 33:1177–1187
17. Wu SC, Wang D, Gao JH, Huang ZY, Chen YM (2014) Effect of the number of grooves on a wick's surface on the heat transfer performance of loop heat pipe. *Appl Therm Eng* 71(1):371–377
18. Nishikawara M, Nagano H (2016) Numerical simulation of capillary evaporator with micro-gap in a loop heat pipe. *Int J Therm Sci* 102:39–46
19. Nishikawara M, Nagano H (2017) Optimization of wick shape in a loop heat pipe for high heat transfer. *Int J Heat Mass Transfer* 104:1083–1089
20. Wang Y (2015) Experimental investigations on operating characteristics of a closed loop pulsating heat pipe. *Front Energy* 9:134–141

# Computational Design and Analysis of a Piston with Different Head Thicknesses and Top Land Widths



Rayapati Subbarao and Mukul Kashiwal

**Abstract** The objective of this work is to check the structural performance of the piston, while changing some of its design parameters. This paper describes the modelling and analysis of piston, which has been done using Solid Edge and Ansys 16.0. Analysis was performed on the piston with different head thicknesses ( $T_H$ ) and top land widths ( $b_1$ ) to observe its structural performance. The comparison has been done by using different materials (Grey Cast Iron FG 200, Aluminium 4032 and AISI 1020 Steel) for the same geometry to observe the consequences. The deformation in the piston has increased slightly when we decreased the piston head thickness and top land width. Thorough observation has been done with respect to equivalent stresses and we found that AISI 1020 Steel is a better material for the piston among the three materials considered but the stresses are lowest in Aluminium 4032. For piston of 12 mm head thickness and top land width, the equivalent stresses and deformation are found to be maximum for all the three materials used and are minimum when the piston head thickness and top land width are 19 mm.

**Keywords** Piston head thickness · Analysis of a piston · Deformation · Equivalent stresses · Top land width

## 1 Introduction

Piston is the main part of an engine, which conveys the impulse received from the gases expanding within the cylinder to the crankshaft through the connecting rod. While designing the piston, two main aspects must be considered, one is structural and other is thermal, which form the base for the mechanical and thermal performance evaluation. During the combustion process, when the piston is subjected to static loading, piston undergoes an alteration due to the energy stored inside the piston

---

R. Subbarao  
NITTTR, Kolkata, India

M. Kashiwal (✉)  
Indian Maritime University, Kolkata, India  
e-mail: [mukulkashiwal@gmail.com](mailto:mukulkashiwal@gmail.com)

© Springer Nature Singapore Pte Ltd. 2020  
L. Vijayaraghavan et al. (eds.), *Emerging Trends in Mechanical Engineering*,  
Lecture Notes in Mechanical Engineering,  
[https://doi.org/10.1007/978-981-32-9931-3\\_5](https://doi.org/10.1007/978-981-32-9931-3_5)



and this energy is the determination factor of the yield and failure of the piston. The reason for the piston failure may be wear, temperatures and fatigue-related. But the failure of the piston is mainly due to the stress occurrence, which is either mechanical or thermal in nature.

The pressures occurring on the piston top due to gas is generally 3–5 MPa for gasoline engines and 6–9 MPa for diesel engines. There are only a few research works, proposing engine piston's new dimensions, materials and manufacturing techniques. Wang et al. [1] used FEM for a piston and discussed various parameters. Kakaee et al. [2] performed thermo-mechanical analysis of an SI engine piston using different boundary condition treatments. Cioatã et al. [3] did mechanical and thermal analysis of internal combustion engine piston using Ansys. Grzegorz and Andrzej [4] analysed the effect of gaps in the lock of sealing rings and nominated sizes of belt on the piston-ring-cylinder seal. Even, a recent review paper by Misra and Agrawal [5] gave the importance of such studies and described the design of a piston using composite material. So, it requires a thorough examination of the smallest details. In this context, present work primarily aims at studying the use of three different materials for the piston of same dimensions by changing the piston head thickness and top land width to assess the effect on structural performance, which has not been done before.

## 2 Methodology

Piston of the engine must have tremendous strength so that it can withstand high gas pressures or inertia forces and also it should possess minimum mass so that the inertia forces can be minimised. In the construction phase of piston, proper measure should be taken towards the gas and oil sealing of the cylinder and provide sufficient bearing area to prevent failures. It is becoming essential as the materials might act as the base for making the piston. Materials of lightweight have high specific strength, high hardness, wear resistance, low friction coefficient and thermal expansion, high thermal conductivity, high heat-absorbing ability and good ability in abatement. The dimensions of the piston are calculated for the Grey Cast Iron FG 200 and used for the other two materials too. Materials selected for the piston in this work and their properties are given in Table 1. Density, tensile strength (yield) and moduli are high for AISI 1020 Steel. Grey Cast Iron has high tensile strength (ultimate), which is commonly used piston material. This work compares the stress and deformation aspects of these materials.

Piston has been modelled in Solidedge, according to the dimensions given in Table 2. For modelling, a 2D sketch with the help of calculated dimensions was drawn and defined by dimensions and constraints. Then the 2D drawing has been converted into 3D model using certain tools available in the package. The piston shape is found to be uneven because of the presence of various curved surfaces in the inner cavity, which may affect the results if the structure is not subdivided into equal-sized elements before analysis. So, the simple shape of the piston has been subdivided into a mesh of finite-sized elements. The tetrahedral mesh is used

**Table 1** Material properties

Property	Grey Cast Iron FG 200	Aluminium 4032	AISI 1020 steel
Density (kg/m <sup>3</sup> )	7100	2690	7800
Young's modulus (GPa)	114	73	350
Poisson's ratio	0.26	0.33	0.25
Bulk modulus (MPa)	79,167	71,569	233,330
Shear modulus (MPa)	45,238	27,444	140,000
Tensile strength (yield) [MPa]	200	320	350
Tensile strength (ultimate) [MPa]	720	390	420

**Table 2** Piston dimensions

Thickness of piston head	16.0	mm
No. of rings	4	
Radius of cup	70.0	mm
Piston ring radial thickness	3.4	mm
Piston ring axial thickness	3.0	mm
Top land width	16.0	mm
Lands between the ring grooves	2.5	mm
Thickness of piston barrel (maximum)	11.3	mm
wall thickness (towards the open end)	3.4	mm
Skirt length	87.0	mm
Piston length	125.5	mm
Piston pin outside diameter	35.0	mm

for the piston. Tetra meshing provides a robust smoothening procedure for mesh refinement. The total number of elements generated in meshing is 249,317 and nodes are 421,616 as shown in Fig. 1c. Structural problems are usually modelled through a displacement-based mode and are often based on formulation, which includes relative rotations, whose numerical resolution requires non-linear shape functions in the finite element approximation. Boundary condition is defined as the load and support in static structural analysis. Frictionless support was provided for the limiting motion at the piston pin support area and 5 MPa pressure has been applied on the piston head top as shown in Fig. 1d.

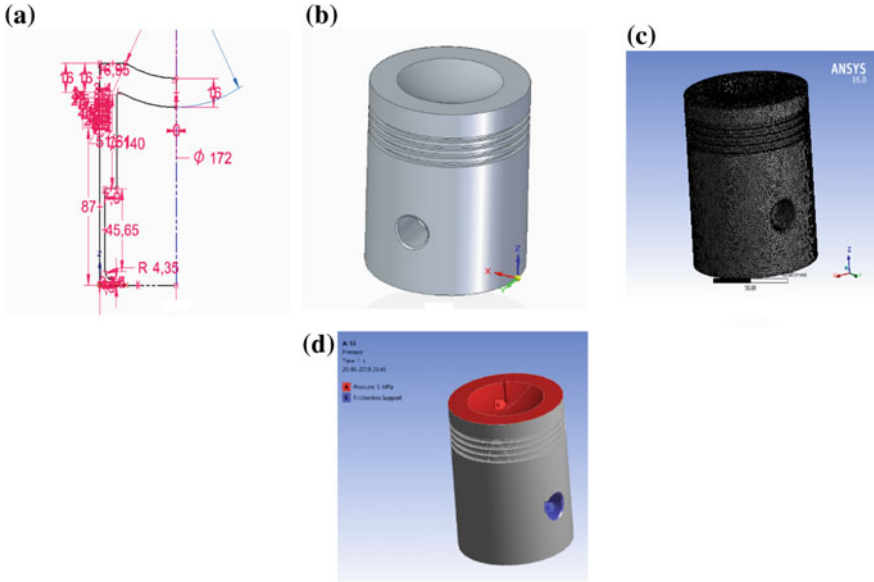


**Fig. 1** Modelling and boundary conditions, **a** 2D sketch, **b** 3D model, **c** meshed model, **d** pressure and frictionless support

### 3 Results and Discussion

See Table 3.

**Table 3** Deformation and equivalent stresses for the different materials

Head thickness/top land width (mm)	Deformation (in mm) for			Equivalent stresses (in MPa) for		
	Grey Cast Iron FG 200	Aluminium 4032	AISI 1020 Steel	Grey Cast Iron FG 200	Aluminium 4032	AISI 1020 Steel
19	0.03662	0.05691	0.01193	143.15	139.93	143.75
18	0.03683	0.05725	0.01200	151.74	146.49	152.45
17	0.03707	0.05766	0.01208	156.33	150.67	157.11
16	0.03730	0.05802	0.01215	151.51	147.18	152.26
15	0.03766	0.05861	0.01227	146.41	141.93	147.06
14	0.03793	0.05905	0.01236	155.34	149.89	156.16
13	0.04014	0.06210	0.01309	151.15	145.76	151.89
12	0.04344	0.06714	0.01416	152.75	147.47	153.48

### 3.1 Structural Analysis

#### 3.1.1 Deformation and Equivalent Stresses on Piston of Aluminium 4032

Figure 2 shows the deformation for different head thicknesses and top land widths of piston, which is made of Aluminium 4032. The maximum and minimum deformations are easily distinguished from the figure. The deformation in different locations of the piston found is from 0.0569 to 0.0671 mm. An increasing trend of equivalent stresses has been observed for the piston of Aluminium 4032 when piston head thickness and top land width are decreased. The maximum deformation occurred at the top of the piston, as practically the largest portion of the product of combustible mixture acts on the head of the piston.

The minimum deformation has been observed at the piston pin support. At the lowest portion of the piston skirt, the maximum deformation too was observed. The maximum deformation location is the base for the component failure.

Figure 3 shows the equivalent stresses for pistons of different head thicknesses and top land widths. The equivalent stresses found in the different locations of the piston, varied from 139.93 to 147.47 MPa. An increasing trend in equivalent stresses has been observed for the piston of Aluminium 4032 with reverse trend of piston

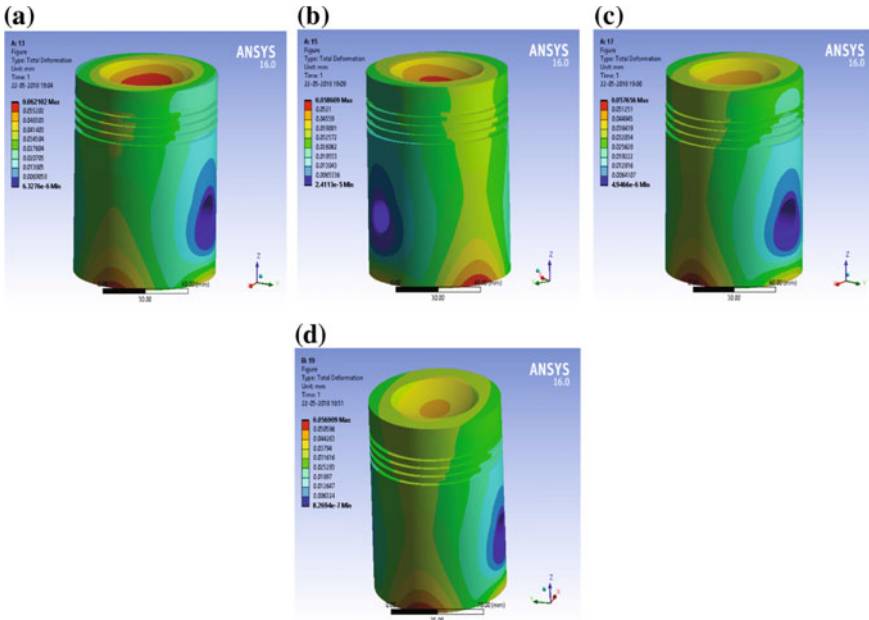
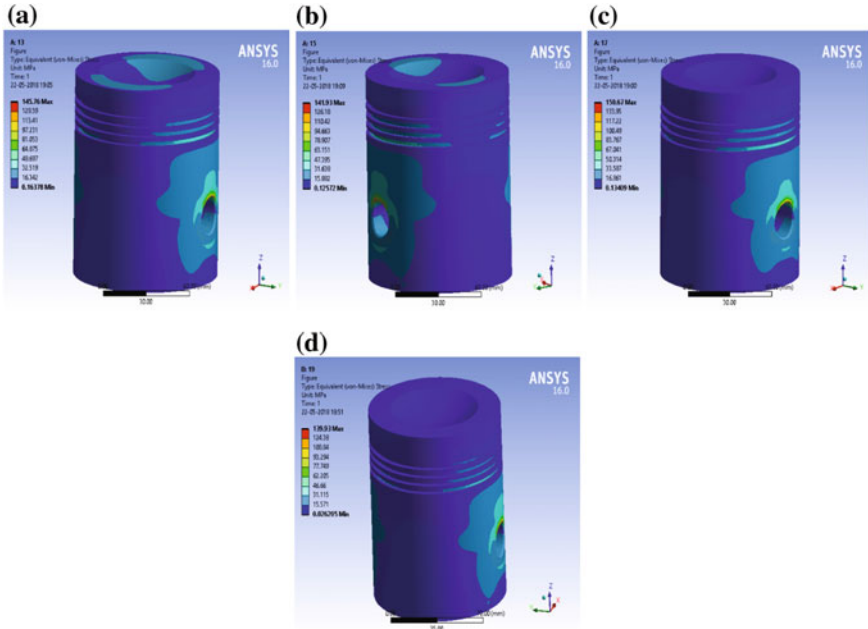


Fig. 2 Deformation on piston of Aluminium 4032 for a 13 mm, b 15 mm, c 17 mm and d 19 mm head thicknesses ( $T_H$ ) and top land widths ( $b_1$ )



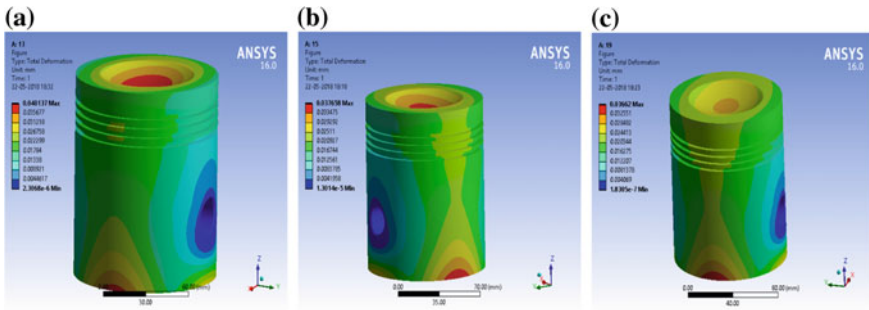
**Fig. 3** Equivalent stresses on piston of Aluminium 4032 for **a** 13 mm, **b** 15 mm, **c** 17 mm and **d** 19 mm head thicknesses ( $T_H$ ) and top land widths ( $b_1$ )

head thickness and top land width. The maximum stress at the piston pin support and minimum stress occurred at the upper portion of the piston has been observed. The maximum stress, which was observed at the upper portion of the piston, is under the yield tensile strength of the Aluminium 4032, which provides a good factor of safety.

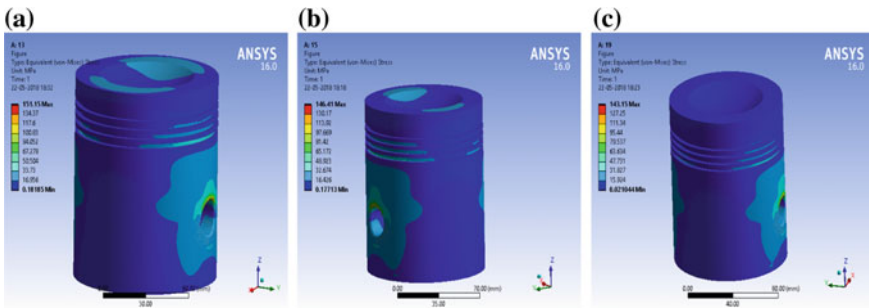
### 3.1.2 Deformation and Equivalent Stresses on the Piston of Grey Cast Iron FG 200

Figure 4 shows the deformation for different head thicknesses and top land widths of piston, which is made of Grey Cast Iron FG 200. The deformation from 0.0366 mm to 0.0434 mm in different locations of the piston and an increasing trend of equivalent stresses for piston of Grey Cast Iron FG 200 has been observed, when the piston head thickness and top land width are decreased. The maximum deformation occurred at the top of the piston and the minimum deformation occurred at the piston pin support as shown in Fig. 4a, b, respectively.

Figure 5 shows the equivalent stresses for different head thicknesses and top land widths of piston, which is made of Grey Cast Iron FG 200. An increasing trend in equivalent stresses has been observed with decreasing piston head thickness and



**Fig. 4** Deformation on a piston of Grey Cast Iron FG 200 for **a** 13 mm, **b** 15 mm and **c** 19 mm head thicknesses ( $T_H$ ) and top land widths ( $b_1$ )



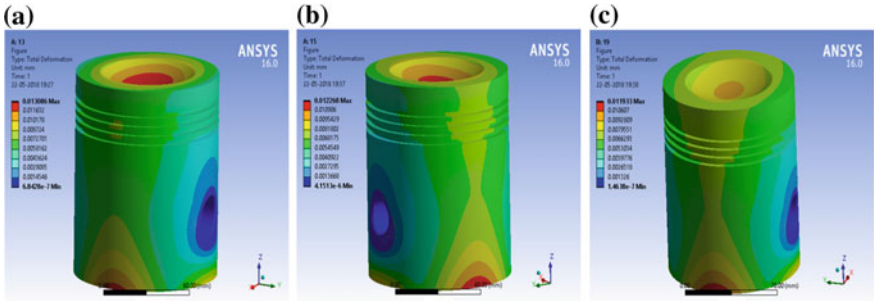
**Fig. 5** Equivalent stresses on a piston of Grey Cast Iron FG 200 for **a** 13 mm, **b** 15 mm and **c** 19 mm head thicknesses ( $T_H$ ) and top land widths ( $b_1$ )

top land width. The stresses have been found to vary from 143.15 to 152.75 MPa at different locations of the piston. The maximum stress occurred at the piston pin support area. The minimum stress 143.15 MPa occurred at top of the piston. The maximum stress found to be acting on the piston is under yield tensile strength of the Grey Cast Iron FG 200. The maximum and minimum stresses for the piston of Grey Cast Iron FG 200 are higher than that of Aluminium 4032 piston.

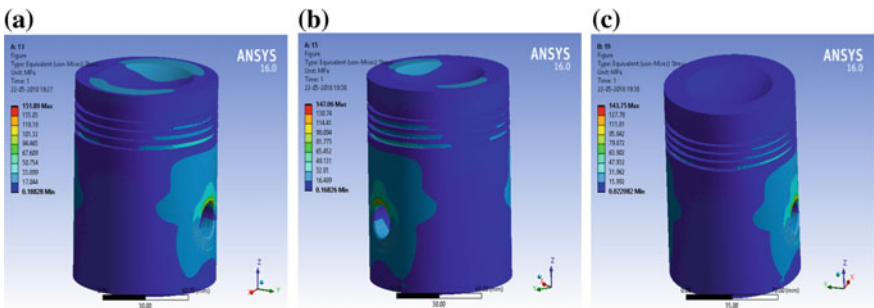
**3.1.3 Deformation and Equivalent Stresses on Piston of Steel**

Figure 6 shows the deformation for different head thicknesses and top land widths of piston, which is made of steel. The deformation in the different locations of the piston from 0.0119 mm to 0.0141 mm and maximum deformation at the top of the piston has been observed, as the largest portion of the product of combustible mixture acts on the head of the piston. The minimum deformation was at the piston pin support. Piston made of steel showed the lowest deformation among all the three materials.

Figure 7 shows the equivalent stresses for different head thicknesses and top land



**Fig. 6** Deformation on a piston of steel for **a** 13 mm, **b** 15 and **c** 19 mm head thicknesses ( $T_H$ ) and top land widths ( $b_1$ )



**Fig. 7** Equivalent stresses on a piston of steel for **a** 13 mm, **b** 15 mm and **c** 19 mm head thicknesses ( $T_H$ ) and top land widths ( $b_1$ )

widths of piston, which is made of steel. The maximum stress 153.48 MPa, at the piston pin support area and the minimum stress of 143.75 MPa, at the upper portion of the piston has been observed. The maximum stress acting on the piston is under the yield tensile strength of the Grey Cast Iron FG 200. The maximum and minimum stresses for the piston of steel are slightly higher than that of stresses in Grey Cast Iron FG 200.

The equivalent stresses for all the three materials used are shown in Fig. 8. The stresses for the piston made of AISI 1020 Steel are the highest and for Aluminium 4032 are lowest. In the range of decreasing head thickness and top land width, two points of 19 mm and 15 mm piston head thickness from, where the stresses begin to rise and a point of 17 mm has been observed from, where the stresses fall till 15 mm head thickness. The stresses at 17 mm piston head thickness and top land width are found to be even greater than that at 12 mm.

All the materials used presents similar pattern of increase in deformation with reducing head thickness, except that the gap between the minimum and maximum value of deformation. For the steel, it is very small, when compared to other two materials. Maximum deformation has been found for the piston made of Aluminium

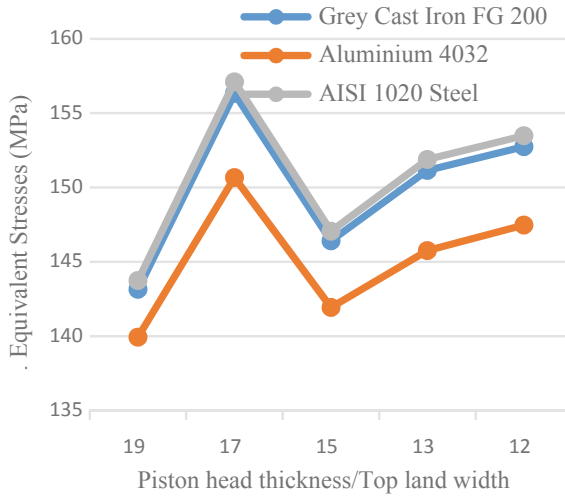


**Fig. 8** Piston head thickness/top land width versus equivalent stresses

4032 and minimum deformation for the piston made of steel. Hike in the deformation takes place when piston head thickness was reduced further after 14 mm. It is clear from Fig. 9 that deformation graph from the head thickness 19–14 mm is almost similar.

As all the three materials used here displayed a similar trend of equivalent stresses, it can be concluded that the sudden rise in the equivalent stresses for the 17 mm head thickness piston as shown in Fig. 8 is not due to the material properties. But it is

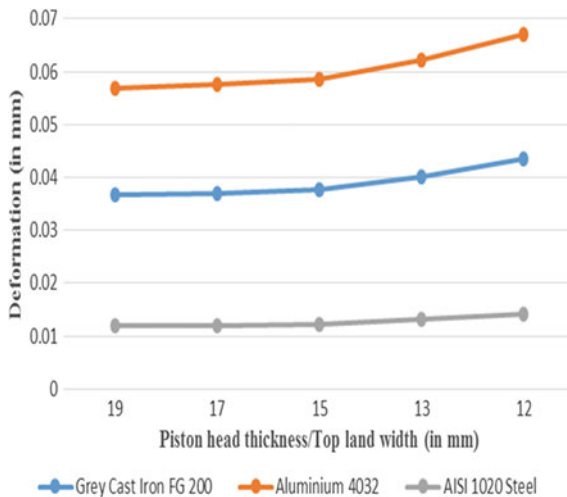


**Fig. 9** Piston head thickness/top land width versus deformation



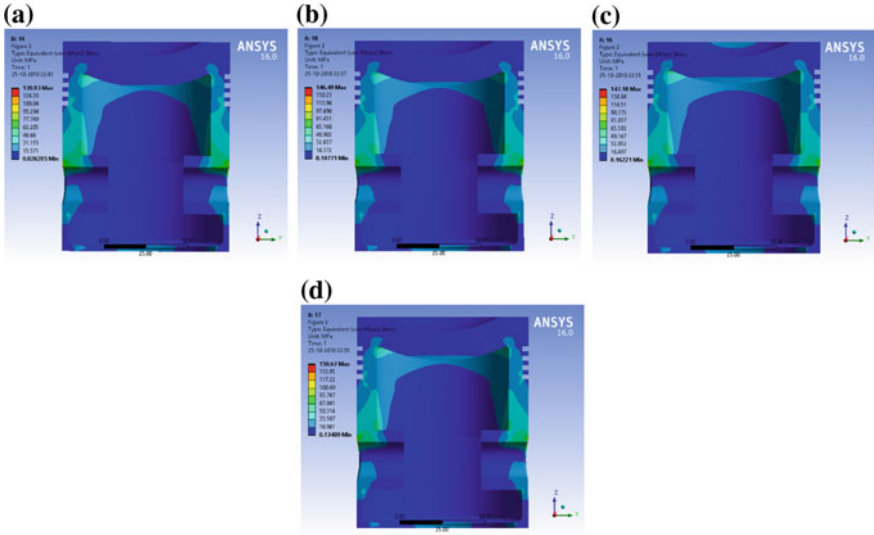


**Fig. 10** Section view of equivalent stresses on a piston of aluminium for **a** 19 mm, **b** 18 mm and **c** 17 mm, **d** 16 mm head thicknesses ( $T_H$ ) and top land widths ( $b_1$ )

because of the respective positions of the piston ring grooves, top land and piston head cup. When pressure is applied on the piston, stresses start building up from the piston head top as shown in Fig. 10. The inner edge of the piston head cup has been kept filleted so that the stress concentration does not occur in that area. The stress concentrations are observed at the piston pin bore edge, where the pressure forces meet the reaction forces. The respective position of the piston ring grooves, piston head cup and top land for 16 mm head thickness piston is almost similar to 19 mm head thickness piston, in which the stresses have been spread in all the ring grooves. But in the piston of 17 mm head thickness, the stresses got spread in 2–3 ring grooves only and stress concentration occurred at the piston pin bore edge. Figure 9 shows that the stresses are decreasing with increase in the piston head thickness. The deformation in the piston of 19 mm head thickness has been observed at the bottom of the piston skirt. But it was less, as the stress distribution was more on the upper area of the piston. As we decrease the piston head thickness, stress gets concentrated at the piston pin bore edge and deformation starts increasing towards that side.

### 4 Conclusions

Computational design and analysis of a piston are carried out with different head thicknesses and top land widths. The structural performance of the piston has been checked, when changes are made in its design parameters. Different piston materials

like Grey Cast Iron FG 200, Aluminium 4032 and AISI 1020 Steel are picked for computation. The equivalent stresses and deformation increase, when the piston head thickness and top land width have reduced. Comparison was made and it has been found that the piston with 19 mm head thickness and 19 mm top land width experiences the lowest deformation and equivalent stresses. For the width of 12 mm, piston experiences maximum deformation and equivalent stresses. The piston made of AISI 1020 Steel experiences the lowest deformation for the same boundary conditions, but highest stresses among the materials used. For all the materials, similar pattern of deformation and stress changes has been observed. Hence, it can be concluded that for the same geometry of piston, if the steel is used, the lowest deformation has obtained. If Aluminium 4032 is used, lowermost stresses can be achieved. Also, there is an increasing trend in deformation and equivalent stresses with reducing piston head thickness and top land width. Results, thus, confirm the necessity of finalising the head thickness and top land width for piston, before finalising the engine requirements.

## References

1. Wang YX, Liu YQ, Shi HY (2010) Finite element static and dynamic analysis for a piston. *Adv Mater Res* 97–101:3323–3326
2. Kakaee A-H, Gharloghi J, Foroughifar A, Khanlari A (2015) Thermo-mechanical analysis of an SI engine piston using different boundary condition treatments. *J Central South Univ* 22(10):3817–3829
3. Cioată VG, Kiss I, Alexa V, Rațiu SA (2017) Mechanical and thermal analysis of the internal combustion engine piston using Ansys. *IOP Conf Ser: Mater Sci Eng* 163:012043
4. Koszalka G, Suchecki A (2017) Analysis of design parameters of pistons and piston rings of a combustion engine, vol 118. In: VII International Congress on combustion engines, p 00013
5. Misra S, Agrawal A (2018) Design and analysis of piston by Al-GHS 1300, Al-GHY 1250, Al-Si-C, A6061 and A4032 composite material: a review. *IOP Conf Ser.: Mater Sci Eng* 1953:130004

# Development and Fabrication of Smart Waste Segregator



R. Harshith, Y. Karthik, Pruthvishri Hegde, Sharma B. N. Tejas,  
D. Shivalingappa and H. S. Kumarswamy

**Abstract** The magnitude of waste disposal in public areas is increasing due to increase in population, change in the lifestyle of the human beings, and improper measures for reducing and recycling of waste. There is an urgent need for creating awareness among the public and spread motivation among the youth of the country. The problem can be overcome by segregation at source. The main motto of the project work is to develop a smart waste segregator to collect recyclable and reusable waste. It tries to reduce human interference by automating the system to the maximum extent possible. The model is developed and fabricated to meet the requirements for separating different kinds of wastes using various mechanisms and electronic circuits which include conveyor, Arduino board, sensors, motors, etc. It involves various mechanical operations for setting up the system and programming to make the electronic circuits work. The model can segregate wet waste, dry waste, and metal waste. The mechanical part of the system involves preparing conveyor frame and mechanisms for material transfer, whereas the electronic circuits include programming the movement of various mechanical elements to perform their jobs automatically. Waste alignment will happen with the help of resistance plates provided at both ends of the conveyor belt. Sensors with specific applications are used

---

R. Harshith · Y. Karthik · P. Hegde · S. B. N. Tejas (✉) · D. Shivalingappa · H. S. Kumarswamy  
Department of Mechanical Engineering, BNM Institute of Technology, Bengaluru 560070, India  
e-mail: [tejas.sharma1996@gmail.com](mailto:tejas.sharma1996@gmail.com)

R. Harshith  
e-mail: [harshithramaiah@gmail.com](mailto:harshithramaiah@gmail.com)

Y. Karthik  
e-mail: [karthikkirbe@gmail.com](mailto:karthikkirbe@gmail.com)

P. Hegde  
e-mail: [pruthvipruthhegde@gmail.com](mailto:pruthvipruthhegde@gmail.com)

D. Shivalingappa  
e-mail: [dsivadvg@gmail.com](mailto:dsivadvg@gmail.com)

H. S. Kumarswamy  
e-mail: [kumarhs89@gmail.com](mailto:kumarhs89@gmail.com)

to identify wet, dry, and metal wastes. Bins are monitored using sensors to avoid overflowing of waste.

**Keywords** Smart waste segregator · Recyclable and reusable waste · Conveyors · Arduino board · Sensors · Motors

## 1 Introduction

The magnitude of waste disposal in public areas is increasing due to increase in population, change in the lifestyle of the human beings, and improper measures for reducing and recycling of waste. Dumping wastes in open sites result in deterioration of soil quality affecting vegetation adversely [1]. Rats, flies, and other insects which carry diseases such as malaria, dengue fever, etc. are attracted toward these sites which infect people around. Dumping waste in crowded areas increases the vulnerability of spreading more diseases. In general, to reduce the waste disposal in public, the government has arranged bins at several places, vehicles for collecting waste on daily basis, etc. [2]. Further development measures are undertaken by setting up segregation and waste management plants where different kinds of wastes are separated manually or using mechanical components and recycled in respective plants [2].

There is a need for a system which can segregate different types of waste at the source so that the wastes which are recyclable and reusable can be processed further and turned out into useful end products [3]. The waste segregation system has a very good scope for development in the current situation of the country in terms of waste management and awareness of people toward it. A system can be built with an application of multiple branches of engineering. Both mechanical and electronics play a vital role in building this system and proper research and survey are required to get better ideas about the requirements and specifications of the model that is concentrated on.

Samreen et al. [4] have developed a method for Automation of Waste material Segregation (AMS) in scrap industry. It was designed to sort the trash into metallic waste, plastic waste, and glass waste. The method uses inductive sensors for metallic items and capacitive sensors to distinguish between plastic and glass waste. Experimental results show that the waste segregation is successfully implemented using the Automation of material segregation (AMS) method.

Aleena et al. [5] tried to implement an automatic waste segregation system. The machine was designed to sort different categories of waste classified into metallic, organic, and plastic. Ultrasonic sensors were also used to monitor the waste collection system.

Baishya et al. [6] built a machine for segregation of waste based on the size as small-sized, bigger-sized lightweight, and heavy materials. The machine is made of declined roller conveyor which is setup with blower and hopper. Various weights

of different materials are recorded before and after segregation and waste recovery amounts are calculated and efficiency of the machine is tabulated.

Chowdhury et al. [7] discussed about the development of a waste sorter which can separate different dry wastes. The waste sorter was developed using an electromechanical system using a microcontroller and operational amplifier which can sort various materials.

Various researchers have proposed different approaches to initiate awareness among the people and to develop systems for achieving a solution to the problem. With reference to the previous work done on the waste management and segregation and its techniques, the information is available on segregating either for dry waste or wet waste. Though systems are available for the concerned problem, the systems are not considerably efficient; therefore, effective separation and segregation of waste are predominant.

## 2 Methodology

Generally, wastes are classified into various types based on different parameters. We can classify wastes as dry wastes and wet wastes. Separation of waste is a major concern in the society. The machine developed can be of prime use to separate the wet waste from dry waste. Further, metals are separated from dry waste. The development of the machine involves various equipment such as conveyor, DC motors, high torque low-speed-gear DC motor, conveyor rollers, bearings, hopper, sensing table, sheet metal, MS tubes, and sensors. Figure 1 shows the work flow of the smart waste segregator.

- The hopper is a conical passage where the waste is dropped initially and stored during the operation of the mechanism.
- A controlled flow of waste from the hopper onto the conveyor is achieved using an additional mechanism.

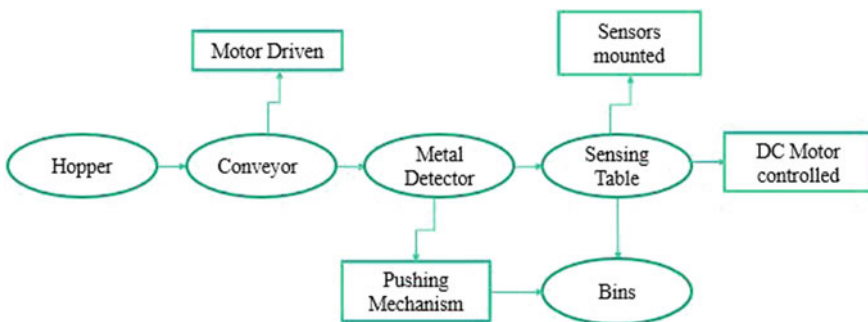


Fig. 1 Work flow of the smart waste segregator

- The conveyor is driven by the rollers specifically designed for the conveyor and the velocity required for carrying out the operation. The rollers are driven by a geared DC motor which can help to step down the speed and provide high torque required to drive the belt conveyor.
- The motor is connected to the conveyor by means of sprockets. Both ends are coupled with sprockets of different teeth and are made to rotate by means of a chain drive.
- The conveyor carries all the waste throughout the length and drops it on the sensing table.
- The sensing table consists of the sensors to detect the wet waste and dry waste. If the moisture sensor and IR sensors are activated, then the waste is pushed into the wet waste bin. If only IR sensor is activated, the waste is considered to be dry waste.
- At the end of the conveyor, a metal detector is used to identify metals. A mechanical arm is used to push the metals out of the belt. The arm is actuated by the motor and is programmed to traversing the arm forward and reverses to the desired span.
- The waste is made to fall into the bins, which are manually fabricated as per the ratios of the amounts of classified wastes.
- A pushing ring is used to push the wastes into respective bins by moving the ring to either side of the sensing table.
- The whole process is controlled by an Arduino board which has analogue and digital input ports in which sensors and motors can be mounted and programmed to achieve required movements and operations.

Figure 2 shows the initial conceptual design of the smart waste segregator. As research was carried on sensor specifications and dimension constraints, the concept design was found to have little technical and practical infeasibilities. Thus, modifications were incorporated in the fabricated model to improve the effectiveness of the system.

### 3 Development and Fabrication

#### 3.1 *Materials and Equipment*

The machine is supported completely on the frame. It is made of mild steel pipes which are welded or fastened together to form a rigid structure which supports the complete setup and bear the loads acting on the system. The conveyor belt is the key component of the machine which carries the waste onto the sensing table placed at the end of the conveyor. The conveyor is powered by a high torque low-speed-geared DC motor which drives the rollers coupled to the gearbox of the DC motor and in turn connected on to the conveyor belt.

Low-capacity DC motors are used for the functioning of the mechanical arm, pushing ring of the sensing table, and to control the waste flow at the hopper. Bearings are used to support the rollers and reduce the load on the motor. The HTLS DC motor



**Fig. 2** Conceptual design of the smart waste segregator

used in the setup has to transmit torque and provide movement to the conveyor, which is done by the chain sprockets. A less toothed sprocket is coupled to a motor and a sprocket with more teeth is fixed to the conveyor roller shaft to step down the speed.

A metal detector, IR sensors, and moisture sensors are used in the setup to monitor the segregation process. A metal detector is placed under the conveyor to identify metals. The mechanical arm pushes the metals out of the conveyor. The sensing table consists of a grid of moisture sensors to detect wet waste and IR sensors to detect the presence of materials on the table. A pushing ring is used to push the waste on either side depending on whether the material present is wet or dry.

Some major electronic components include the Arduino board and motor driver. Arduino board is the brain of the system which automates the whole system. All the sensors and motors are integrated with the Arduino and are programmed to the requirements. The motor driver is used for the forward and reverse rotation of the DC motors which is again integrated with the Arduino.

### **3.2 Specifications**

Various materials are selected on the basis of certain requirements. Specifications of major components are mentioned below:

- The HTLS-g geared DC motor: It is a high-speed motor stepped down to 10 rpm with the help of worm gears.
- Low-capacity DC motors: Two 10 rpm motors are used. One for the mechanical arm movement and the other for the pushing ring at the sensing table. A 500 rpm motor is used to lift the hopper plate.
- The top end diameter of the hopper is 15 in. and the bottom end diameter is 9 in. Two bins of 1 sq. ft. and one bin of 2 sq. ft. each with 24 in. height are used to collect the waste.
- The diameter of the pushing ring inside which waste falls is of 9 in. diameter. It is considered to be equal to the bottom end diameter of the hopper.
- The conveyor roller is of 3.5 in. diameter. On the basis of the required conveyor speed, the suitable roller diameter is considered.
- The Arduino board used to control all the circuits is “Arduino UNO.” The motor driver used in the electronics setup is “L298n.”
- The metal detector used is MD-300 and the moisture sensor used is a grid type raindrop sensor module.

### 3.3 Mechanisms

**Waste Flow Control Mechanism** The waste which is thrown into the hopper moves on to the belt conveyor. To control the amount of waste flow, a mechanism is used. The bottom end of the hopper is grooved and a plate is placed which can traverse in the direction parallel to the cross section of it. The plate movement is provided using a DC motor which is mounted directly to the hopper bottom end. The motor shaft is coupled with a screw rod rigidly, which makes the screw rod to rotate at the speed of the motor. The mechanism of the waste flow control is shown in Fig. 2. The plate creates buffer storage inside the hopper when it is in a closed position. Once the motor starts rotating, the plate widens the path for waste by moving above.

**Mechanical Arm** A mechanical arm shown in Fig. 3 is mounted near the sensing table end of the belt conveyor which is used to push the metals out of the belt region to the dustbin. The metal detector is placed below the belt and arm right above the detector area. When the sensor detects the metal, the motor will run, which simultaneously rotates the mechanical arm fixed to the motor shaft.

**Separating Mechanism** A pushing ring is used over the sensing table to separate wet waste from dry waste. The pushing ring is fixed through a slider to move to either side of the table. A slider is a fixture for the pushing ring which acts as horizontal support and driver, while the motor spindle is vertical. The slider is rigidly mounted between the motor shaft and the pushing ring end enabling it to slide left and right of the sensing table. The Separating mechanism is as shown in Fig. 4.



**Fig. 3** Waste flow control mechanism



**Fig. 4** Mechanical arm



## 4 Results and Discussion

The working model of smart waste segregator shown in Fig. 5 has been developed and fabricated. It is a compact and efficient system to segregate metal, wet and dry wastes. The machine was tested to check its effectiveness in segregating the wastes of three kinds.

The sliding mechanism of hopper plate is used to allow materials of different sizes onto the conveyor. The baffle plates on the conveyor frame are used to align the wastes as it passes on the conveyor belt. The metal detector detects metals of various sizes if the field produced is above the threshold magnetic field strength of the detector. It is found that the mechanical arm setup used to push metals detected by a metal detector kept below the belt is capable of pushing approximately 150–200 g.

The ring slides over the sensing table after the moisture sensor, mounted on the table, and the IR sensor gives an output to the Arduino which rotates the motor to the predefined angle to segregate wet and dry waste. Sensors with specific applications are used to identify wet, dry, and metal wastes. IR Sensors have maximum range of 6 in. within which the materials are detected. Bins are monitored using sensors to avoid overflowing of waste. The system requires lesser power for its operation (Fig. 6).

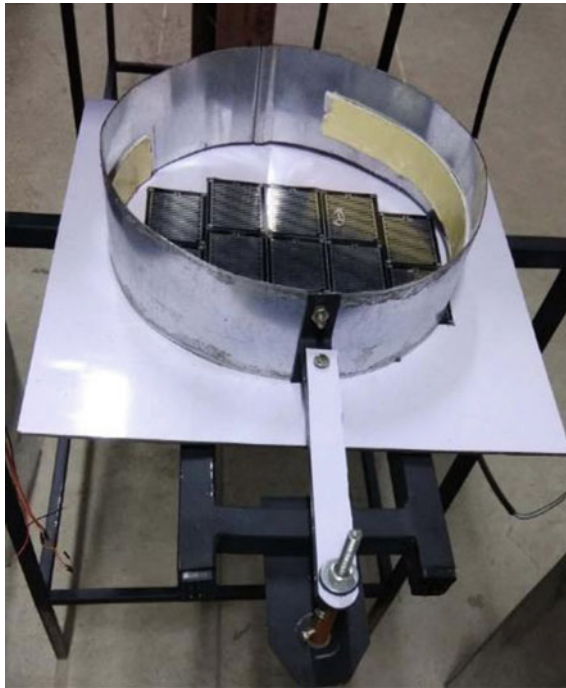


**Fig. 5** Separating mechanism



**Fig. 6** Working model of the smart waste segregator

The advantages of the smart waste segregator over other existing systems are:

1. The system is developed to be compact, user-friendly, and flexible. It is easy to transport the machine and relocate based on the space constraints.
2. The machine is completely customizable. The user can operate and control the machine as he/she wants it to, by modifying the program code fed into the Arduino board.
3. The sensors mounted on the sensing table can separate wet and dry wastes, while existing segregators can only categorize dry wastes.
4. The model is a small-scale development explaining the concept for a larger scale model. The performance of the machine is competitive with already existing machines, advantage being the lower cost.

## 5 Conclusions

The fabricated working model of smart waste segregator will be useful to the society to overcome the problem of waste segregation by segregating wastes at the source. It reduces the human interference as much as possible since the system is automated to the maximum possible extent. This project creates awareness among people about the need to segregate wastes and avoid pollution by dumping wastes in the open. Certain wastes which are segregated can be recycled. Instead of burning garbage, separation would reduce this problem which causes pollution. Since waste generation cannot be avoided, one can only try to find cost-effective solutions to this problem.

The waste segregator will be a good solution for waste segregation as it segregates the waste at the source level itself. Almost all the metallic wastes can be segregated

and, in turn, can be recycled into consumer goods. By streamlining and simplifying the waste segregation process through one central system in offices, apartments, and similar such places, one can effectively implement the waste segregation process through this type of waste segregator. We have made an attempt to reach “Zero Waste to Land Fill” targets that are part of the sustainable initiative and also this working model is an eco-friendly system as it uses electrical power.

## References

1. Delgermaa G, Matsumoto T (2016) A study of waste management of households in Ulaanbaatar on questionnaire surveys. *Int J Environ Sci Dev* 7(5):368–371
2. Agarwal R, Chaudhary M, Singh J (2015) Waste management initiatives in India for human well-being. *Eur Sci J* 105–127. ISSN: 1857-7881
3. Jain S, Jain M (2015) Municipal solid wet waste management by public participation. *Soc Issues Environ Probl* 3:1–4. ISSN: 2350-(O), ISSN: 2394-3629(P)
4. Samreen SM, Gadgay B, Pujari V, Pallavi BV (2017) Automatic metal, glass and plastic waste sorter. *Int J Res Appl Sci Eng Technol* 5: 884–889
5. Aleena VJ, Balakrishnan K, Rosmi TB, Swathy Krishna KJ, Sreejith S, Subha TD (2016) Automatic waste segregator and monitoring system. *J Microcontrol Eng Appl* 3:1–7. ISSN: 2455-197X
6. Baishya P, Singh SB, Mahanta DK (2015) Fabrication & testing of dry waste sorting machine. *Int Res J Eng Technol (IRJET)* 2:2248–2251
7. Chowdhury MH, Mahmudul Hasan Russel Md, Mehdi Masud Talukder Md (2013) Development of automatic smart waste sorter machine. In: *International Conference on Mechanical, Industrial and Materials Engineering 2013 (ICMIME2013)*, pp 1–7

# Influence of Heat Index on Tensile Properties and Formability of Friction Stir Dissimilar Welded Blanks



Bhanodaya Kiran Babu Nadikudi

**Abstract** In friction stir welding process, developed heat is considered as an important factor because it strongly influences the properties of welding. In this study, the effect of heat index on tensile properties and forming behaviour of friction stir welded joints were studied. The influence of grain size on the hardness is also studied. Microhardness and grain size relationship of the welded blanks is expressed in the Hall–Petch equation. It was observed that the mechanical properties and hardness were better at lower rotational speed. An improved formability is achieved at the lower tool rotational speed rather than the high rotational speeds due to refinement of grains occurred at lower heat input.

**Keywords** Aluminium alloys · Friction stir welding · Heat index

## 1 Introduction

Aluminium alloys are well known with their predominant high strength and less weight properties when compared with the other engineering materials. These properties are attracting various industries such as ship building, aerospace and automobile sectors, and these aluminium alloy blanks are used as tailor welded blanks (TWBs). In the fabrication of body components, the automobiles need the materials made with different materials which can give different strengths at different places with local stiffness. This kind of TWBs can be made with combinations of materials with various thicknesses. By applying these variations in material combinations, we get many advantages such as high and moderate strength of the parts, results in reduction in overall cost and enhancement in the local stiffness of the fabricated parts.

---

B. K. B. Nadikudi (✉)

Mechanical Engineering Department, Sreenidhi Institute of Science and Technology, Hyderabad, India

e-mail: [uday.nadikudi@gmail.com](mailto:uday.nadikudi@gmail.com)

Generally, aluminium alloy blanks can be welded with conventional fusion welding techniques, but they present low weldability, and in the same time, cracks are formed during the solidification of the weld zone. Friction stir welding (FSW) is a very popular non-fusion kind of technique, and it is proven as the best welding method to join aluminium blanks [1–5]. This welding technique is also considered as a relatively better joining process for designers and manufacturers when compared with conventional fusion welding techniques [6–8]. This joining technique was started using in the replacement of fusion welding techniques holding numerous advantages like no porosity, distortion, energy-efficient, environmental friendly and more versatile [9, 10]. Therefore, many researchers are applying FSW to weld similar and dissimilar materials [11, 12]. On the other hand, recrystallized and fine equiaxed grain structure is obtained at stir zone. It is a very well known that the developed microstructure at weld zone is transformed into equiaxed grains through dynamic recrystallization [13–17]. The development of heat generation is directly influenced by tool rotational speed and welding speed [18]. During welding, the developed heat can be expressed with the heat index parameter and is the ratio of rotational speed to the welding speed ( $\omega^2/\nu$ ). In FSW process, this heat index is considered to be an important parameter in the development of welded blanks. A significant effect of heat index in friction stir welding process is that it significantly controls the mixing and flow of material during stirring. It is also considered that the heat index is influencing the formability of welded blanks. Few researchers have used FSW process to weld the aluminium alloy blanks and formed in limiting dome height (LDH) test to determine the formability of welded blanks [19, 20]. The present study is aimed to weld two dissimilar (AA6061 and AA2014) aluminium alloy blanks; the mechanical properties are evaluated with tensile test, and formability behaviour is evaluated with LDH test, developing a correlation of weld grain size with the hardness values with Hall–Petch equation

## 2 Experimental Procedure

The base materials selected for the present investigation were 3-mm-thick aluminium alloys of AA6061 and AA2014. The blanks were cut into 300 mm long and 75 mm wide. Friction stir welding was performed on blanks in the FSW set-up (Fig. 1), and the experiments were performed according to the full factorial design array with two FSW parameter factors such as rotational speed ( $\omega$ ) and welding speed ( $\nu$ ) with three levels. Having decided to vary the two process parameters at three levels, a full factorial Design of Experiments (DoE) was selected for experimental design, so that experimental region is systematically explored.

**Fig. 1** FSW set-up

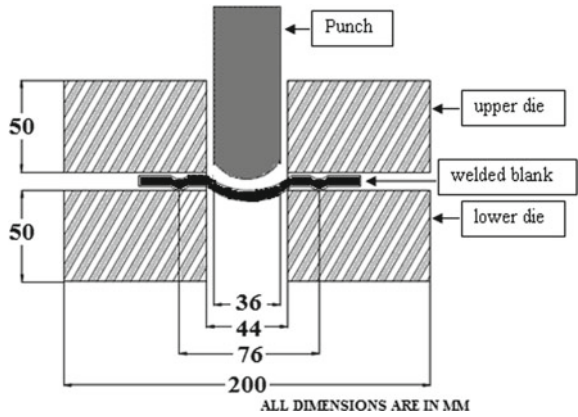


**Table 1** Influence of process parameters on the heat index

Run	Rotational speed, $\omega$ (RPM)	Welding speed, $v$ (mm/min)	Heat index $\omega^2/v$
1	900	16	50,625
2	900	24	33,750
3	900	32	25,312
4	1150	16	82,656
5	1150	24	55,104
6	1150	32	41,328
7	1400	16	122,250
8	1400	24	81,666
9	1400	32	61,250

The layout of standard full factorial DoE and heat index at different levels is shown in Table 1. As shown, the DoE consists of two three-level columns arranged in nine rows or combinations. The factors assigned to the columns and rows show the combination of factors' level for single experiment. The welding range of the tool rotational speed varied between 900 and 1400 rpm, whereas the welding speed varied from 16 to 32 mm/min. Tensile test was performed after welding to access the tensile properties of welded blanks. Samples for hardness were extracted from welded blanks, and values are measured with the help of Vickers hardness tester with the dwell period of 10 s with load of 200 g. LDH test was performed to analyse the formability behaviour of welded blanks using a 50 ton hydraulically operated press with a 36-mm-diameter hemispherical punch as shown in Fig. 2. Samples of size 100 × 100 mm were prepared from the welded blanks for limiting dome height test.

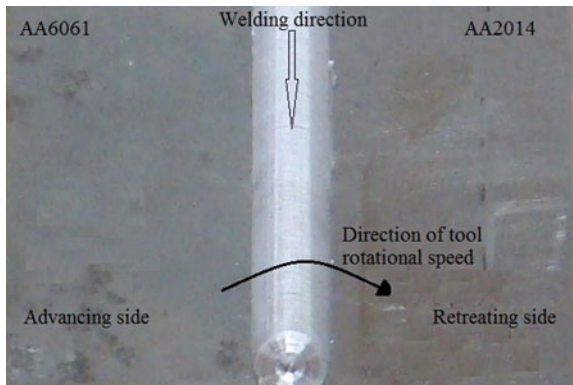
Fig. 2 Schematic diagram of the LDH test



### 3 Results and Discussions

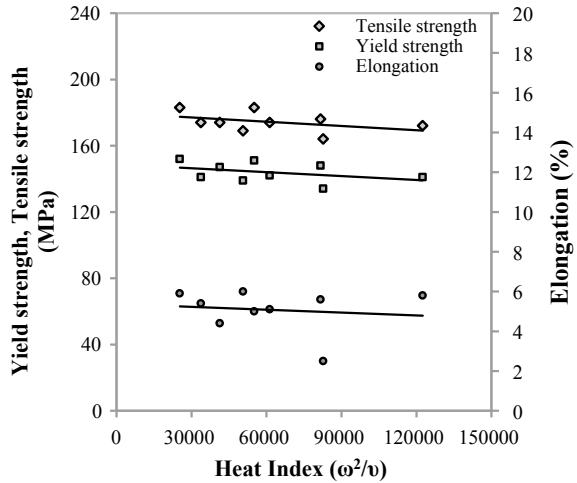
Aluminium alloy joints were made successfully with the variation in FSW process parameters, and surface of a welded blank is shown in Fig. 3. The variation of tensile strength, yield strength and elongation with a heat index ( $\omega^2/v$ ) for the welded blanks made at different process parameters is shown in Fig. 4. It can be observed that the yield strength and tensile strength were decreased with increase in heat index. In addition, the elongation also decreases with increase in heat input. At lower rotational speed of 900 rpm, the tool develops a sufficient heat input that is enough to soften the material around the tool pin and also proper flow of plasticized material that led to a huge plastic deformation during welding. The increased heat input decreases the mechanical properties which are due to grain growth after refinement [21]. The grain size at stir zone becomes larger with increase in the heat index, which supports the grains' growth after recrystallization [22].

Fig. 3 Welded blank





**Fig. 4** Variation of yield strength, tensile strength, elongation with heat index

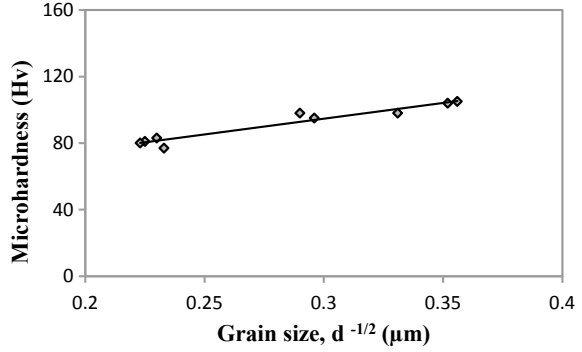


Generally, in FSW welding process, the heat index is playing a major role in the stirring of the material around the tool and mixing and material flow rate during welding. The properties obtained from the welded blanks depend on the rotational speed and welding speeds led through generation of heat input. It is known that the heat development in FSW process is considered as a function of tool rotational speed and welding speeds. The heat input index is found to be high at rotational speed of 900 rpm and welding speed of 16 mm/min and is reduced while increasing the welding speed from 16 to 32 mm/min. This is mainly due to sufficient heat generation and sufficient deformation occurred and results more homogeneous microstructure.

At 900 rpm and welding speed from 16 to 32 mm/min, enhanced mechanical properties of welded blanks are achieved by providing a sufficient heat to plasticize the materials. To achieve complete deformation with the proper plastic material flow around the tool pin and grain refinement of the joint through the dynamic recrystallisation mechanism by providing a proper heat input, these can be achieved at rotational speed of 900 rpm and welding speed from 16 to 32 mm/min. A high heat input and slow cooling are introduced with increase in tool rotational speed (900–1400 rpm) and at welding speeds (16–32 mm/min) leads to welding zone allows enough time available for the grains to grow which decreases the tensile properties. An optimal rotational speed is needed to stop growing the grains after crystallization, and these can be achieved at 900 rpm to obtain better tensile properties and formability.

The relationship of grains size and microhardness of the welded zone can be represented with the help of Hall–Petch equation by slope change; the microhardness ( $H_v$ ) is proportional to the reciprocal square root of grain size ( $1/\sqrt{d}$ ) as shown in Fig. 5. The variations of grain size on the microhardness can be drawn using microhardness ( $H_v$ ) data and the grain size ( $d$ ). The Hall–Petch equation relates the hardness with grain size through the following equation.

**Fig. 5** Relationship between the microhardness and grain size of welded blanks



$$H_v = H_0 + K_h d^{-1/2} \tag{1}$$

The slope of the line in Fig. 5 represents the hardness which increases with a reduction in the grain size. The slope gives the values as  $H_0 = 37.7 H_v$  and  $K_h = 189.8 H_v \mu\text{m}^2$ . Decrease in the heat input leads to refining the grain structure [21]. The curve shows finer grain size results in high hardness as well as high strength; this is due to the existence of fine grains, in which normally, grains are associated with more boundary interaction with other grains which acts as obstacles to the slip during deformation [23].

The formed welded blank in biaxial forming condition is shown in Fig. 6. The variation of formability with the heat index ( $\omega^2/\nu$ ) for dissimilar welded blanks is shown in Fig. 7. It can be observed that the formability is better at lower tool rotational speed (900 rpm), and it decreased while increasing in the rotational speed

**Fig. 6** Formed welded blank in biaxial condition

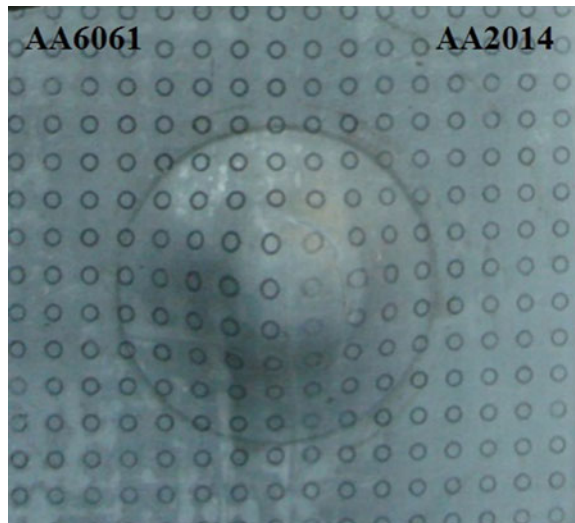
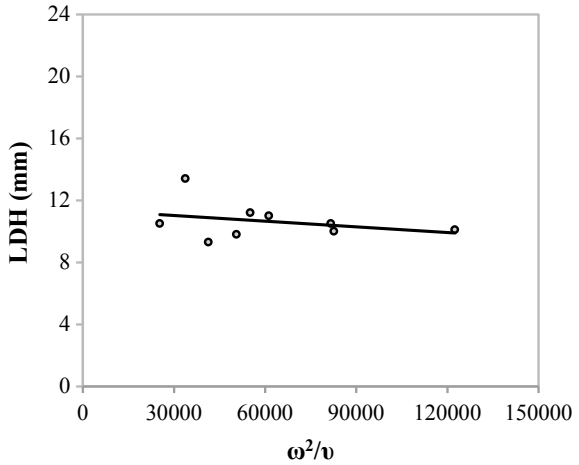


**Fig. 7** Variation of formability with heat index



from 900 to 1400 rpm. A better refinement of grains occurred at lower heat input rather than the higher heat input. High heat input generation leads to grain growth after refinement occurred during dynamic recrystallization [21] which leads to decrease in the formability.

#### 4 Conclusions

With the use of friction stir welding technique, it is possible to weld different aluminium alloy blanks. Variation in tool rotational speed and welding speed generates different heat inputs, and this influences the tensile properties and formability of welded blanks. The strength and hardness were improved at lower heat index through FSW process due to refinement of grains at weld zone. On the other hand, formability better is at lower heat input rather than the higher heat inputs.

#### References

1. Mishra RS, Mahoney MW (2007) Friction stir welding and processing. ASM International, pp 1–5
2. Hassan AM, Qasim T, Ghaithan A (2012) Effect of pin profile on friction stir welded aluminium matrix composites. *Mater Manuf Process* 27:1397–1401
3. Govindaraju M, Kandasamy J, Manzoor Hussain M, Prasada Rao K (2012) Some aspects of cross butt friction stir weldments of rare earth magnesium alloys: novel attempts in Friction stir welding. *J Appl Sci* 12(10):1043–1047
4. Joshi V, Balasubramaniam K, Prakash RV (2011) Optimization of friction stir welding parameters for AA5083 by radiography and ultrasonic technique. In: IEEE international ultrasonic symposium proceedings, pp 1920–1923 (2011)

5. Mohanty HK, Venkateswarlu D, Mahapatra MM, Kumar P, Mandal NR (2012) Modeling the effects of tool probe geometries and process parameters on friction stirred aluminium welds. *J Mech Eng Autom* 2(4):74–79
6. Prado RA, Murr LE, Shindo DJ (2001) Tool wear in the friction stir welding of aluminum alloy 6061+20%  $AL_2O_3$ , a preliminary study. *Scrip Mater* 45:75–80
7. Prado RA, Murr LE, Soto KF (2003) Self optimization in tool wear for friction stir welding of Al 6061+20%  $AL_2O_3$  MMC. *Mater Sci Eng A* A349:156–165
8. Sato YS, Park SHC, Michiuchi M (2004) Constitutional liquation during dissimilar friction stir welding of Al and Mg alloys. *Mater Sci Eng A* 50:1233–1236
9. Palanivel R, Koshy Mathews P (2011) The tensile behaviour of friction-stir welded dissimilar aluminium alloys. *Mater Technol* 45(6):623–626
10. Hirata T, Oguri T, Hagino H, Tanaka T, Chung SK, Takigawa Y, Higashi K (2007) Influence of friction stir welding parameters on grain size and formability in 5083 aluminium alloy. *Mater Sci Eng A* 456:344–349
11. Shukla RK, Shaw PK (2010) Comparative study of friction stir welding and tungsten inert gas welding process. *Indian J Sci Technol* 3(6):667–671
12. Chien C-H, Lin W-B, Chen T (2012) Optimal FSW process parameters for aluminium alloys AA5083. *Chin Inst Eng* 34(1):99–105
13. Xu X, Ynag X, Zhou G, Tan B (2012) The mixing condition and mechanical property on friction stir welded dissimilar formed 3003 and 60601 aluminium alloys. *Adv Mater Res* 418–420:1346–1350
14. Subbaiah K, Geetha M, Govindaraju M, Rao SK (2012) Mechanical properties of friction stir welded cast Al-Mg-Sc alloys. *Trans Indian Inst Metals* 65(2):155–158
15. Vagh AS, Pandya SN (2012) Influence of process parameters on the mechanical properties of FSWed AA2014-T6 alloy using Taguchi orthogonal array. *Int J Eng Sci Emerg Technol* 2(1):51–58
16. Palanivel R, Koshy Mathews P, Muragan N (2010) Influences of tool pin profile on the mechanical and metallurgical properties of friction stir welding of dissimilar aluminium alloys. *Int J Eng Technol* 2(2):109–2115
17. Aissani M, Gachi S, Boubenider F, Benkedda Y (2010) Design and optimization of friction stir welding tool. *Mater Manuf Process* 25:1199–1205
18. Moreira PMGP, Santos T, Tavares SMO, Richter-Trummer V, Vilaca P, de Castro PMST (2008) Mechanical characterization of friction stir welds of two dissimilar aluminium alloys of the 6xxx series. *Mater Sci Forum* 587–588:430–434
19. Leitao C, Emílio B, Chaparro BM, Rodrigues DM (2009) Formability of similar and dissimilar friction stir welded AA 5182-H111 and AA 6016-T4 tailored blanks. *Mater Des* 30:3235–3242
20. Miles MP, Melton DW, Nelson TW (2005) Formability of friction-stir-welded dissimilar-aluminium-alloy sheets. *Metall Mater Trans A* 36A:3335–3342
21. Motaleb-Nejad P, Saeid T, Heidarzadeh A, Darzi K, Ashjari M (2014) Effect of tool pin profile on microstructure and mechanical properties of friction stir welded AZ31B magnesium alloy. *Mater Des* 59:221–226
22. Lee W-B, Kim J-W, Yeon Y-M, Jung S-B (2003) The joint characteristics of friction stir welded AZ91D magnesium alloy. *Mater Trans* 44(5):917–923
23. Afrin N, Chen DL, Cao X, Jahazi M (2008) Microstructure and tensile properties of friction stir welded AZ31B magnesium alloy. *Mater Sci Eng A* 472:179–186

# Convective Heat Transfer on the Optimum Spacing of High Heat Dissipating Heat Sources—A Numerical Approach



K. Mathew and Naveen Patil

**Abstract** The paper emphasizes the numerical investigation to analyse the three modes of conjugate convective heat transfer characteristics from seven non-identical heat sources (Aluminium) mounted on a substrate board (Bakelite). The objective is to determine the best mode of heat transfer which suits for cooling of ICs (heat sources), also temperature is non-dimensionalized as ( $\theta$ ), and it is predicted by applying fuzzy logic control. To accomplish this, numerical simulations are carried out using ANSYS Icepak to estimate the temperature distribution of the IC chips. Results suggest that the mixed convection is the better mode of heat transfer and the temperature of heat sources is reduced. Temperature of the heat sources is a strong function of their size and position on the substrate board. There is a strong agreement between the numerical values of ANSYS Icepak and predicted values obtained from fuzzy logic.

**Keywords** CFD simulations · Fuzzy logic · Heat sources · Convective modes of heat transfer · Optimal arrangement

## 1 Introduction

Present-day electronic equipment is working under highly demanding conditions, with satisfactory performance depending on the operating temperature. Effective cooling is required to keep this equipment within safe temperature limits of 85 °C. For low and medium heat-generating devices, air cooling is widely used. Though natural convection cooling does not require additional devices to create air movement, the rate of heat removal is much lower. Forced convection cooling is preferred whenever high heat transfer rates are required. It confirms from the literature that, the various factors responsible for the failure of electronic components [1] are humidity (16%), vibration (24%), dust (6%) and temperature (54%). This clearly indicates that

---

K. Mathew (✉)

MIT School of Engineering, MIT-ADT University, Pune, India

e-mail: [mathew.karvinkoppa@mituniversity.edu.in](mailto:mathew.karvinkoppa@mituniversity.edu.in)

N. Patil

Vellore Institute of Technology, Vellore, Tamil Nadu, India

© Springer Nature Singapore Pte Ltd. 2020

L. Vijayaraghavan et al. (eds.), *Emerging Trends in Mechanical Engineering*,

Lecture Notes in Mechanical Engineering,

[https://doi.org/10.1007/978-981-32-9931-3\\_8](https://doi.org/10.1007/978-981-32-9931-3_8)

temperature leads the chart for the failure of electronic equipment and must have to be controlled with great interest. The electronic industries are facing a stiff challenge for maintaining the component temperature below 85 °C.

## 2 Background Study

Due to the rapid development of an integrated circuit technology, miniaturization will lead to gradual increase in circuit densities, and rate of heat dissipation increases tremendously; hence, the cooling of electronic components has become challenging. As the extent of electronic parts ends up littler, the area accessible for heat dissipation is reducing which leads to more challenging effective cooling systems. Numerical investigation was conducted to estimate the optimize positions of ICs on the SMPS board under mixed convection [2]. They found that the temperature variation of the ICs is a strong function of their size, position and heat flux. They proposed a correlation for these parameters. The optimum distribution of discrete heat sources was determined experimentally [3]. They used a robust hybridization technique (ANN and GA) to determine the optimal configuration of ICs and also they suggested that this will give better results than regular optimization techniques. Analysed experimentally and numerically forced convection cooling of ICs arranged optimally on the substrate board [4]. They suggest a correlated non-dimensional temperature ( $\theta$ ) in terms of Reynolds number (Re) and thermal conductivity ( $K$ ). Steady-state experiments were conducted on five non-identical protruding discrete ICs under natural, mixed convection heat transfer medium [5]. Their goal is to find the rate of heat dissipation from ICs, keeping at the lowest bottom of the PCB and to compare both modes of heat transfer for cooling of heat sources. A complete review of the cooling on discrete heated modules under a different mode of heat transfer [6]. They suggested the choice of working fluid based on the operating level of heat flux ranges. Numerical investigation has been carried out to determine the three-dimensional natural convective heat transfer on flush mounted in the horizontal cavity filled with air [7]. They concluded the walls at the outer side are strongly affected by the convection. Studied the cooling performance of multiple protruding ICs mounted in the horizontal channel under forced convection, they found that heat transfer is maximum by 33.15% at Re 3428 [8]. They proposed the correlation for the average Nusselt number and the dimensionless temperature is maximum which is a function of the Richardson number. Optimal arrangement of rectangular ICs mounted on PCB is studied experimentally and numerically [9]. They used COMSOL MULTIPHYSICS and suggested a correlation for dimensionless temperature ( $\theta$ ) in terms of heat flux ( $q_{max}$ ), geometric distance parameter ( $\lambda$ ) and thermal conductivity of the substrate board ( $K_{the}$ ), and it is observed that heat transfer rate is increased by arranging the ICs with optimal spacing. To estimate the array size and condition of heat substrate board with heat sources on the enhancement of rate, heat transfer was studied numerically and experimentally [10]. They proposed an empirical relation for evaluating the Nusselt number under different thermal conditions for array substrate board geometries.

From glance of literature review, many of the work has been focused on the single mode of heat transfer [2, 7, 9] and some of the studies were pertinent two modes of heat transfer [5, 6, 10] for the cooling of discrete heated modules, and ANSYS FLUENT and COMSOL MULTIPHYSICS are used for analysis of ICs. However, is clear that numerical analysis using ANSYS Icepak scarres. Hence, the present analysis emphasizes on numerical simulation on optimal configuration of non-dimensional geometric parameter distance  $\lambda = 1.3$  under three different modes of conjugate convective heat transfer (free, forced and mixed convection). Fuzzy logic control is used to predict the temperature of heat sources (ICs). This will give a clear insight into the electronic cooling engineers regarding the selection of the mode of convective heat transfer for the cooling of electronic components. Hence, the study is critical for the thermal management designers.

### 3 Methodology

#### 3.1 Numerical Simulation

Numerical simulation is carried out using ANSYS Icepak (R-16) for cooling of seven non-identical protruded ICs mounted on a substrate board under all the three-mode convective heat transfer (free, forced and mixed convection) for optimal configuration  $\lambda = 1.3$  as reported in [9]. The ANSYS Icepak is an object-based modelling software with pre-defined electronic components and has specific applications in the electronics industry. Once the modelling is done, the Icepak uses FLUENT solver for the thermal and fluid flow calculation. However, all the set-ups are carried out using Icepak, and then the Icepak uses FLUENT to solve the governing equation such as the conservation equations of mass, momentum, energy and other scalars such as turbulence if needed. The FLUENT solver uses the schemes called control volume technique.

The dimensions of all the components for  $\lambda = 1.3$  are depicted in Figs. 1 and 2. The heat sources are denoted by  $AI_{1, \text{and}}$  the subscript stands for the position of heat sources.

#### Governing Equation

ANSYS Icepak solves the Navier–Stokes equations for transport of mass, momentum and energy for the laminar fluid flow and heat transfer. The equations are written as follows

The conservation equation of mass is given in Eq. 1.

$$\frac{\partial \rho}{\partial t} + \frac{\partial(\rho u)}{\partial x} + \frac{\partial(\rho v)}{\partial y} + \frac{\partial(\rho w)}{\partial z} = 0 \quad (1)$$

For an incompressible fluid, the value of density  $\rho$  is constant, and Eq. 1 reduces to the form Eq. 2.

**Fig. 1** Components used for present computational study

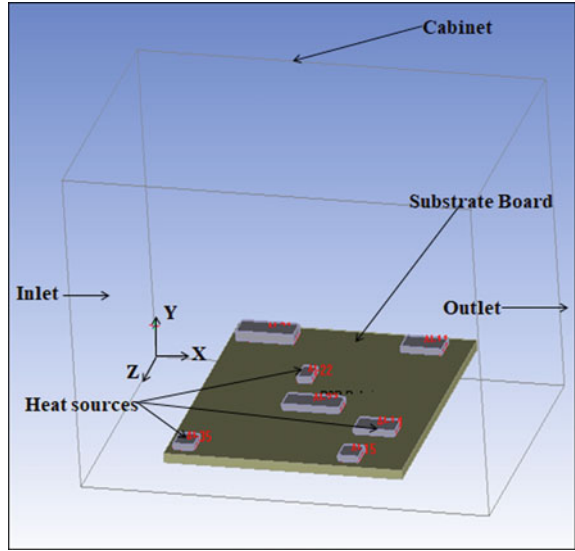
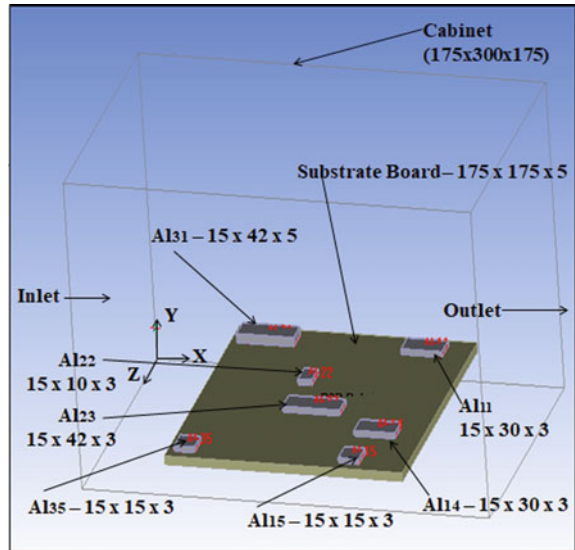


**Fig. 2** Dimensions and locations of ICs (all dimensions are in mm)



$$\frac{\partial u}{\partial x} + \frac{\partial v}{\partial y} + \frac{\partial w}{\partial z} = 0 \tag{2}$$

The momentum principle describes the relationship between the velocity, pressure and density of a moving fluid. The general form of the momentum equation (Navier–Stokes equation) for natural convection is given in Eqs. [3–5].



$$\frac{\partial u}{\partial t} + u \frac{\partial u}{\partial x} + v \frac{\partial u}{\partial y} + w \frac{\partial u}{\partial z} = -\frac{1}{\rho} \frac{\partial p}{\partial x} + \nu \left( \frac{\partial^2 u}{\partial x^2} + \frac{\partial^2 u}{\partial y^2} + \frac{\partial^2 u}{\partial z^2} \right) + \rho \beta (T_{\max} - T_{\text{amb}}) \quad (3)$$

$$\frac{\partial v}{\partial t} + u \frac{\partial v}{\partial x} + v \frac{\partial v}{\partial y} + w \frac{\partial v}{\partial z} = -\frac{1}{\rho} \frac{\partial p}{\partial y} + \nu \left( \frac{\partial^2 v}{\partial x^2} + \frac{\partial^2 v}{\partial y^2} + \frac{\partial^2 v}{\partial z^2} \right) + \rho \beta (T_{\max} - T_{\text{amb}}) \quad (4)$$

$$\frac{\partial w}{\partial t} + u \frac{\partial w}{\partial x} + v \frac{\partial w}{\partial y} + w \frac{\partial w}{\partial z} = -\frac{1}{\rho} \frac{\partial p}{\partial z} + \nu \left( \frac{\partial^2 w}{\partial x^2} + \frac{\partial^2 w}{\partial y^2} + \frac{\partial^2 w}{\partial z^2} \right) + \rho \beta (T_{\max} - T_{\text{amb}}) \quad (5)$$

The above equation (Eq. 3–5), the buoyancy term  $[\rho \beta (T_{\max} - T_{\text{amb}})]$ , is zero for the forced convection case. Applying the first law of thermodynamics to a small control volume of an incompressible fluid, the final form of the energy equation in 3D can be written, as given in Eq. 6.

$$\frac{\partial T}{\partial t} + u \frac{\partial T}{\partial x} + v \frac{\partial T}{\partial y} + w \frac{\partial T}{\partial z} = \frac{k}{\rho c} \left( \frac{\partial^2 T}{\partial x^2} + \frac{\partial^2 T}{\partial y^2} + \frac{\partial^2 T}{\partial z^2} \right) + q_g + \emptyset \quad (6)$$

where  $q_g$  is the heat generation,  $C$  is the specific heat and  $\emptyset$  is the viscous dissipation, which is further written in the form as given in Eq. 7.

$$\emptyset = 2\mu \left[ \left( \frac{\partial u}{\partial x} \right)^2 + \left( \frac{\partial v}{\partial y} \right)^2 + \left( \frac{\partial w}{\partial z} \right)^2 \right] + \mu \left[ \left( \frac{\partial u}{\partial x} + \frac{\partial v}{\partial y} \right)^2 + \left( \frac{\partial v}{\partial y} + \frac{\partial w}{\partial z} \right)^2 + \left( \frac{\partial w}{\partial z} + \frac{\partial u}{\partial x} \right)^2 \right] \quad (7)$$

For natural convection, driving force for working fluid is due to the difference in density. The boundary conditions for the natural convection, forced convection and mixed convection are mentioned in Table 1. The mixed convection velocity is calculated (Appendix) in such a way that, the maximum temperature of the ICs should not exceed 85 °C.

**Table 1** Boundary conditions for different modes

Locations	Natural convection	Mixed convection	Forced convection
Inlet, $X = 0$	$V = 0.1 \text{ m/s}$ $T = T_{\infty} = 29 \text{ }^{\circ}\text{C}$ $\frac{\partial T}{\partial y} = \frac{\partial T}{\partial z} = 0$	$V = 0.78 \text{ m/s}$ $T = T_{\infty} = 29 \text{ }^{\circ}\text{C}$ $\frac{\partial T}{\partial y} = \frac{\partial T}{\partial z} = 0$	$V = 0.45 \text{ m/s}$ $T = T_{\infty} = 29 \text{ }^{\circ}\text{C}$ $\frac{\partial T}{\partial y} = \frac{\partial T}{\partial z} = 0$
Outlet, $X = L$	$p = p_{\infty}$ , lateral boundary conditions are adiabatic		

**Table 2** Mesh independency study

S. No.	Nodes	Hexa	Quads	$T_{\max}$ (°C)
1	19,348	17,296	533	56.84
2	11,836	10,388	3859	57.11
3	<b>29,660</b>	<b>26,890</b>	<b>7029</b>	<b>56.31</b>
4	89,532	83,540	15,170	56.45

**Table 3** Validation of experimental and numerical results

$\lambda = 1.3$	Temperature °C	$q = 1500 \text{ W/m}^2$		$q = 2000 \text{ W/m}^2$	
		Experimental	Numerical	Experimental	Numerical
Natural convection	$T_{\text{excess,max}}$	36.6	39.85	50	50.61
Forced convection $V = 0.45 \text{ m/s}$	$T_{\text{excess,max}}$	26.5	23.61	30	31.48

### Mesh Sensibility Study

The grid independence study has been carried out for ( $\lambda = 1.3$ ) on basis keeping the temperature limit  $85 \text{ }^\circ\text{C}$ . The grid independence study for configuration  $\lambda = 1.3$  is given in Table 2. The grid sensitivity study is done with reference to Roache [11] for the present study. The grid size (Nodes, Hexas and Quads) is selected on the basis of the convergence criteria for mass, momentum (in  $x$ -,  $y$ - and  $z$ -direction) as well as energy balance equation. The safe temperature limit for the heat sources, i.e  $85 \text{ }^\circ\text{C}$  is also kept in mind during the grid independence study. Hence, Table 3 represents the mesh independence of the based that 29,660 Nodes, Hexa 26,890 and Quads 7029 are selected for simulation. The convergence criteria  $1e^{-6}$  for energy equation and  $1e^{-6}$  for continuity and momentum equations are set. The mesh profile for mixed convection mode of heat transfer for configuration with  $\lambda = 1.3$  is shown in Fig. 3.

### 3.2 Fuzzy Logic

In this study, the fuzzy system has been utilized keeping in mind the end goal to show and anticipate the numerical outcomes. A basic fuzzy comprises four noteworthy parts: Fuzzy interface, rules, and defuzzification interface. It has the impact of changing fresh information into fuzzy sets and connects between input and output with rules. For example, if  $x$  is  $A$  then  $y$  is  $B$ . Each fuzzy set is described by appropriate membership function. In the present investigation, Mamdani fuzzy modelled is used with the sources of inputs are  $\lambda$ ,  $k^*$ ,  $q^*$  and  $Re$  and yield  $\theta$  as output. The defuzzification interface blends and changes over fuzzy sets into noteworthy numerical yields (Fig. 4).

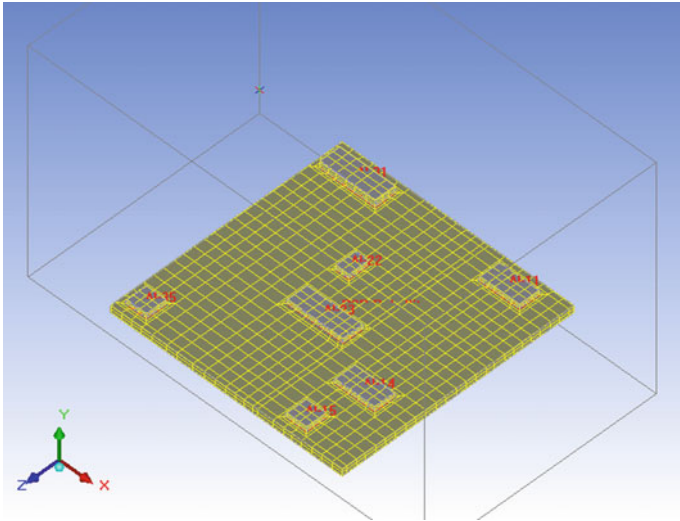


Fig. 3 Mesh sensibility for configuration  $\lambda = 1.3$

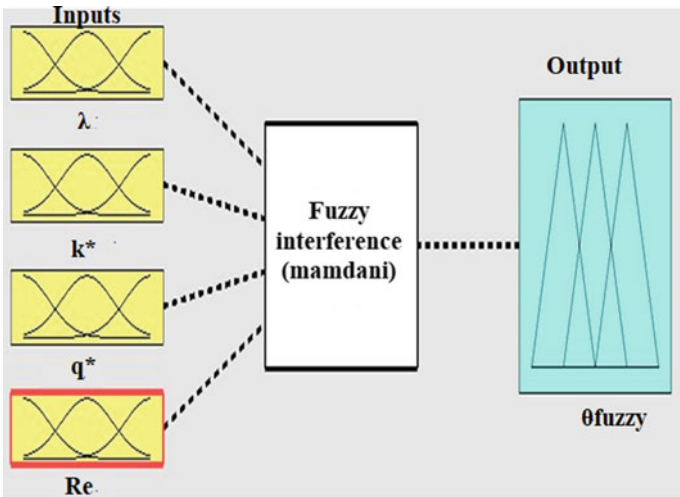


Fig. 4 Fuzzy inference system with inputs and output

## 4 Result and Discussion

### 4.1 Validation of Numerical Results

Seven non-identical rectangular ICs are placed on the substrate board (Bakelite). Diverse blend is workable for keeping ICs on the substrate board and the optimal set-up is obtained utilizing heuristic non-dimensional geometric separation parameter  $\lambda$ , as revealed in [9]. Numerical analysis is carried on optimal configuration  $\lambda = 1.3$  for three modes of convective heat transfer (free, forced and mixed convection) by supplying constant heat flux of  $q = 1500 \text{ W/m}^2$  and  $q = 2000 \text{ W/m}^2$ . It was observed that there is a strong agreement between the experimental values and numerical values for natural convection and forced convection as shown in the table. The experimental values were obtained from [9].

Figure 5 shows the temperature distribution of heat sources for optimal configuration  $\lambda = 1.3$  for three modes of convective heat transfer. Figure 5a depicts the temperature of heat sources for constant heat flux of  $1500 \text{ W/m}^2$ . It is clearly seen that for natural (free) convection heat transfer, the temperature of all heat sources is maximum and minimum for mixed convection heat transfer. Heat source number 2, located at 11, has the maximum temperature among all heat sources for all three-mode convective heat transfer. The maximum temperature of the heat source is  $49.48 \text{ }^\circ\text{C}$  for mixed convection, which is the minimum in comparison with natural and forced convection as shown in Fig. 5a. In a similar manner, Fig. 5b shows the temperature of heat sources for constant heat flux of  $2000 \text{ W/m}^2$ . The maximum temperature of the heat source is  $53.59 \text{ }^\circ\text{C}$  for mixed convection located at 11 positions, which is the minimum in comparison with natural and forced convection as shown in Fig. 5b. From Fig. 5a and b, it is evident that the heat sources with maximum temperature is placed at the lower edge of the substrate board stating further that the temperature of heat sources is minimum for mixed convection heat transfer in both

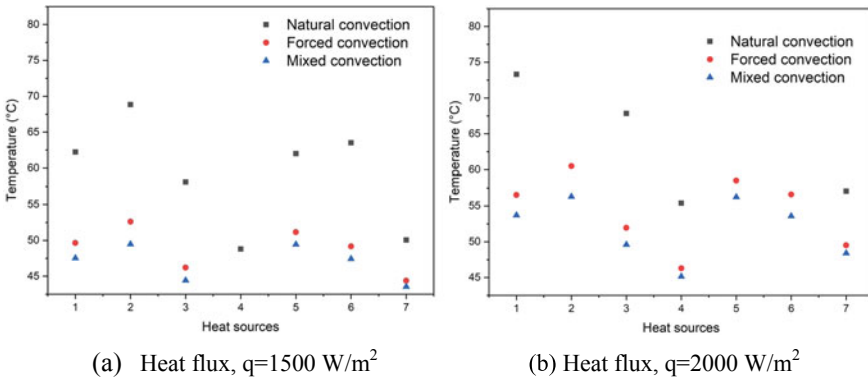
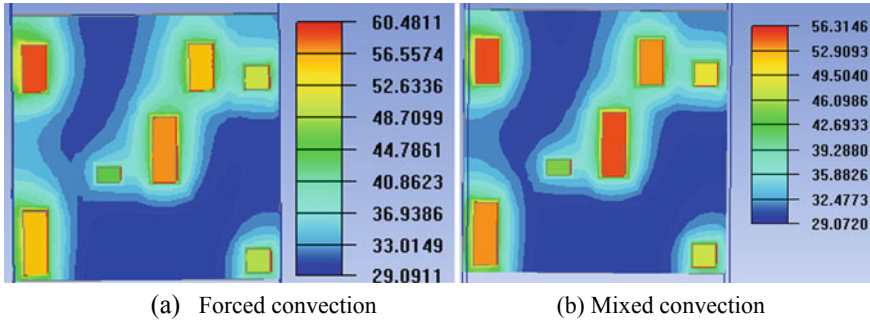


Fig. 5 Temperature of heat sources for optimal configuration  $\lambda = 1.3$



**Fig. 6** Temperature contours of ICs for  $q = 2000 \text{ W/m}^2$

the case of constant heat flux supplied of 1500 and 2000  $\text{W/m}^2$ . Figure 6a and b shows the temperature distribution for forced convection and mixed convection heat transfer with constant heat flux 2000  $\text{W/m}^2$ , respectively.

Fuzzy logic control is applied to the forced convection correlation proposed by Durgam et al. [9] for non-dimensional temperature, which is function of non-dimensional heat flux ( $q^*$ ), non-dimensional thermal conductivity ( $k^*$ ) and non-dimensional geometric parameter distance ( $\lambda$ ), given in Eq. 8

$$\theta = 8.34 \times 10^{-6} q^* + 0.11 k^* - 0.35 \lambda \tag{8}$$

Equation 8 is valid for the range of parameters,  $0.41 \leq \lambda \leq 1.63$ ,  $11.21 \leq k^* \leq 330$ ,  $1176 \leq q^* \leq 76,542$  and  $1125 \leq Re \leq 2625$ . The values of all the parameters ( $\lambda$ ,  $k^*$ ,  $q^*$  and  $Re$ ) are interpolated for 47 values between the range at equal intervals and the non-dimensional temperature correlation ( $\theta_{\text{corr}}$ ) is calculated. The rules of the fuzzy logic control are defined on the basis of the variation of all independent variables on  $\theta_{\text{corr}}$  as shown in Fig. 7. Figure 8 shows the parity plot of  $\pm 12\%$  between  $\theta_{\text{corr}}$  and predicted values of  $\theta_{\text{fuzzy}}$ .

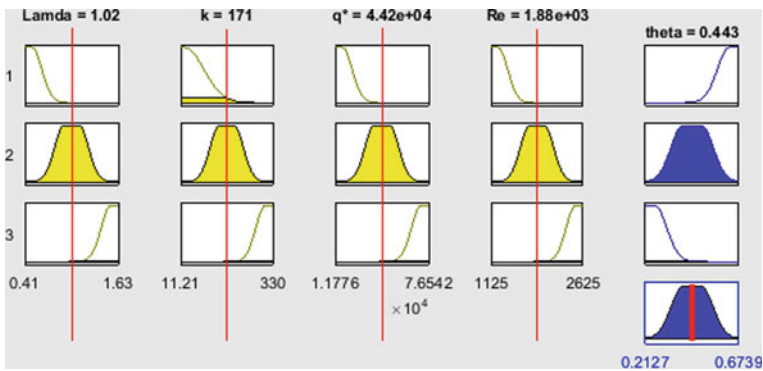


**Fig. 7** Rule chart for predicting non-dimensional ( $\theta_{\text{fuzzy}}$ )

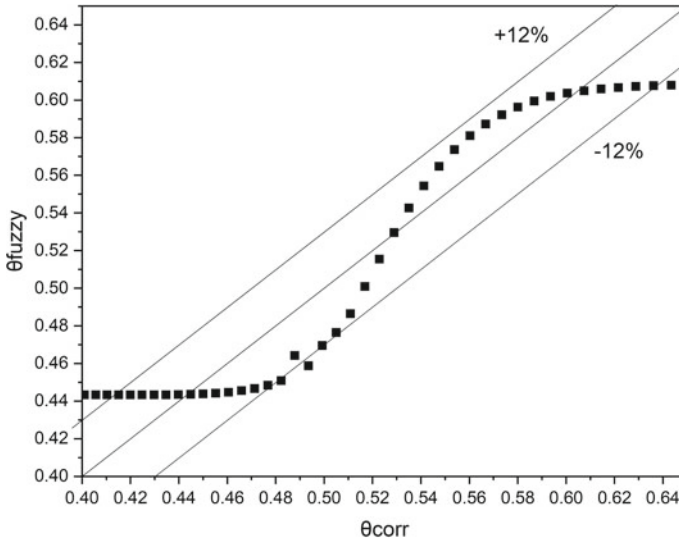


**Fig. 8** Parity plot, showing the agreement between temperature  $\theta_{corr}$  and  $\theta_{fuzzy}$

## 5 Conclusion

A numerical investigation for natural, forced and mixed convection heat transfer on seven non-identical heat sources (Aluminium) mounted on substrate board (Bakelite) is conducted on the optimal configuration of  $\lambda = 1.3$  as reported in the literature. It is observed that mixed convection heat transfer as the minimum of maximum temperature of ICs of  $53.59\text{ }^{\circ}\text{C}$  as compared to natural and forced convection heat transfer. It is also seen that the ICs with maximum temperature should be placed at the lower side of substrate, which results in more interaction of heat source with cooling air. The experiment results from literature are in strong agreement with the numerical results. An attempt is made to apply fuzzy logic control to predict the temperature of heat sources for forced convection. There is strong agreement between the numerical values of ANSYS Icepak and predicted values obtained from fuzzy logic with  $\pm 12\%$  error. Fuzzy logic is an innovative way to predict the temperature of ICs for the electronic cooling engineers and the selection of mode of convective heat transfer for the cooling of electronic components. Hence, the study is critical for the thermal management designers.

## Appendix

$$1 = \frac{Gr}{Re^2} = Ri$$

$$Gr = \frac{g\beta\Delta T_{ref}H^3}{\nu^2}, Re = \frac{uL_h}{\nu}$$

$$\beta = \frac{1}{T_{mean}} = \frac{1}{(55 + 273)} = 3.04878 \times 10^{-3} K^{-1},$$

$$L_h = \frac{4A}{P} = \frac{4 \times (0.042 \times 0.015)}{2(0.042 + 0.015)} = 22.1052 \times 10^{-3} m$$

$$\Delta T_{ref} = \frac{qL}{K_{Al}} = \frac{2000 \times 0.042}{230} = 0.3652 K$$

$$1 = \frac{9.81 \times 3.04878 \times 10^{-3} \times 0.365 \times 0.3^3}{(u \times 22.105 \times 10^{-3})^2}$$

$$u = 0.7768 \approx 0.78 \text{ m/s}$$

## References

1. Reynell M (1990) Major causes for failure of electronic components. U.S. Air Force Avionics Integrity Program
2. Mathew VK, Hotta TK (2018) A Numerical investigation on the optimal arrangement of IC chips mounted on an SMPS board cooled under mixed convection. *Therm Sci Eng Prog* 7:221–229
3. Hotta TK, Balaji C, Venkateshan SP (2015) Experiment driven ANN-GA based technique for optimal distribution of discrete heat sources under mixed convection. *Exp Heat Transf* 28:298–315
4. Durgam S, Venkateshan SP, Sundararajan T (2018) A novel concept of discrete heat source array with dummy components cooled by forced convection in a vertical channel. *Appl Therm Eng* 129:979–994
5. Hotta TK, Venkateshan SP (2012) Natural and mixed convection heat transfer cooling of discrete heat sources placed near the bottom on a PCB. *Int J Mech Aersp Eng* 6:266–273
6. Patil NG, Hotta TK (2018) A review on cooling of discrete heated modules using liquid jet impingement. *Front Heat Mass Transf* 11
7. Gavara M, Kanna PR (2014) A three-dimensional study of natural convection in a horizontal channel with discrete heaters on one of its vertical walls. *Heat Transf Eng* 35:1235–1245
8. Sultan GI (2000) Enhancing forced convection heat transfer from multiple protruding heat sources simulating electronic components in a horizontal channel by passive cooling. *Micro-electr J* 31:773–779
9. Durgam S, Venkateshan SP, Sundararajan T (2017) Experimental and numerical investigations on optimal distribution of heat source array under natural and forced convection in a horizontal channel. *Int J Therm Sci* 115:125–138

10. Yadav V, Kant K (2007) Air cooling of variable array of heated modules in a vertical channel. *J Electron Packag* 129:205
11. Roache P, Perspective J. A method for uniform reporting of grid refinement studies. *J Fluid Eng* 116: 405–413



# Effect of Alkali Treatment on Mechanical Properties of Tapsi Fiber Reinforced Polyester Composites



R. Meenakshi Reddy , D. Mohana Krishnudu ,  
B. Madhusudhan Reddy  and P. Venkateshwar Reddy 

**Abstract** These days, NFCs are accentuating the greatest potential for engineers in numerous applications. A natural fiber polymer composite (NFC) offers the designer to acquire the fundamental properties in a munificent degree by the choice of fibers and matrix. Tapsi fiber reinforced polyester composites were made up with a statute of blends. The tensile, flexural, and impact properties of Tapsi fiber reinforced polyester composites were studied. The mechanical properties such as tensile strength, flexural strength, and impact strength of the Tapsi fiber reinforced polyester composites were assessed according to the ASTM guidelines. The impacts of alkali treatment (NaOH) of the fibers on these properties were likewise studied. It was observed that the mechanical properties of the polyester composite improved with increment in the fiber content. These properties were observed to be far and away superior when alkali-treated tapsi fibers were utilized as a part of the composites.

**Keywords** Tapsi fiber · Tensile strength · Flexural strength · Impact strength

## 1 Introduction

The research area of natural fiber composites (NFC) is aggravating rapidly in comparison with the synthetic fibers such as glass, owing to its several diversified applications—low cost, bio-degradability, low environmental impact, and wide range of other applications. NFCs are having the greatest potential for engineers in many applications. A NFC offers the designer to obtain the essential properties in an extensive extent by the choice of fibers and matrix. Many studies on the composites made from polyester matrix and natural fibers were reported in the literature [1]. Wong et al. [2] investigated the failure initiation of the short bamboo fiber reinforced polyester composites and noticed that the strength of the specimen increased with increase in fiber content of the specimen. Satishkumar et al. [3] studied and compared the tensile

---

R. Meenakshi Reddy (✉) · D. Mohana Krishnudu · B. Madhusudhan Reddy ·  
P. Venkateshwar Reddy  
G Pulla Reddy Engineering College, Kurnool, Andhra Pradesh 518007, India  
e-mail: [rmreddy123@gmail.com](mailto:rmreddy123@gmail.com)

© Springer Nature Singapore Pte Ltd. 2020  
L. Vijayaraghavan et al. (eds.), *Emerging Trends in Mechanical Engineering*,  
Lecture Notes in Mechanical Engineering,  
[https://doi.org/10.1007/978-981-32-9931-3\\_9](https://doi.org/10.1007/978-981-32-9931-3_9)

properties of the snake grass fiber with the traditional natural fibers. Mohan Rao et al. [4] fabricated the composite specimens of grass stalk fibers using retting and chemical (NaOH) extraction processes, the fibers were incorporated into a polyester matrix, and the tensile properties of fibers were determined. Obuko et al. [5] investigated on the development of eco-friendly composites using bamboo fibers by evaluating the basic mechanical properties and reported that the steam explosion technique is essential to extract the bamboo fibers. Osorio et al. [6] studied the morphological aspects of both treated and untreated bamboo fiber composites and reported that the treated fibers have good mechanical strengths when compared to the untreated fiber composites. Varadharajulu et al. [7] investigated on the chemical resistance of epoxy-coated bamboo fibers. Mandal and Alam [8] investigated on the dynamic mechanical properties and morphology of short glass/bamboo fiber reinforced polyester composites by varying the fiber content and percentage of glass fiber by bamboo fiber. Oushabi et al. [9] studied the mechanical, chemical, thermal, and morphological properties of the palm fibers and reported that the alkali treatment improves the thermal resistance of date palm fibers. Krishnudu et al. [10, 11] investigated on mechanical properties of natural fiber like coir-Luffa cylindrical and prosperous juliflora hybrid composites. In the present work, investigation is carried out to know the mechanical properties of tpsi fiber composites such as tensile, flexural, and impact strength. Study on these properties is vital in comparison with physical properties.

## 2 Materials and Methods

The following subsections deal with the Materials and methods used in the current study.

### 2.1 Matrix

In this work, unsaturated polyester bechances as a matrix and Methyl ethyl ketone peroxide transpires as a catalyst and cobalt naphthenate as an accelerator. The fundamental element of this resin is possession of fantastic mechanical and dynamic quality. It has a span of realistic usability of two years; the tpsi fibers utilized as a part of the present study were acquired from the Tripura state in INDIA in dried form. To evacuate hemi-cellulose and oily nature of these fibers, they are soaked in 5% NaOH solution for 1 h and then washed with water altogether. Tpsi fiber is acquired from the Tungabhadra waterway of Andhra Pradesh. A similar strategy is taken after for both the fibers for alkali treatment.

## 2.2 Alkali Treatment

Tapsi fibers underwent treatment with 10% sodium hydroxide (NaOH) solution at 30 °C, maintaining a ratio of 15:1 and immersed in the alkali solution for one hour. The fibers were then initially washed with tap water repetitively to eliminate NaOH, neutralized with acetic acid and again, finally, washed thoroughly with distilled water, and dried in a hot air oven at 100 °C for a period of 24 h.

## 2.3 Preparation of the Composite and Test Specimen

For preparing the composite, molding box is arranged at first with a glass of size 200 mm × 200 mm × 3 mm. The shape is covered with a fine layer of fluid arrangement of polyvinyl alcohol (PVA) that acts as a releasing specialist; further, a thin covering of hard wax is covered over it, and in conclusion, another fine layer of PVA was covered. Each coat was allowed to dry for 30 min at room temperature. A 3 mm thick plate was produced using the mix of polyester, catalyst, and accelerator. At that point, the molding box was stacked with the blend of matrix and taps fibers in arbitrary orientation with shifting rate and was set in vacuum broiler, which is kept up at 70 °C for three hours to finish the curing, a great many cures the plate was expelled from the molding box with simple tapering method. The samples are fabricated by varying weight % of fibers that are designated as C5 (5 wt% of tapsi fiber), C10 (10 wt% of tapsi fiber), C15 (15 wt% of tapsi fiber), C20 (20 wt% of tapsi fiber), and C25 (25 wt% of tapsi fiber). It was cut into samples for tensile tests with measurements of 150 × 15 × 3 mm<sup>3</sup> according to ASTM-D 3039-76 determinations. The gauge length of the samples was kept up at 100 mm for this test. For both tensile and flexural tests, 50 kN load cell sample sizes are cut in accordance with ASTM-D 618 (i.e., 150 mm × 15 mm × 3 mm) for flexural testing. The impact testing specimens (62.5 mm × 12.7 mm × 3 mm) were prepared. The sample was tested by utilizing INSTRON 3369 universal testing machine with the crosshead speed kept up at 5 mm/min. The temperature and humidity of this test were kept up at 22 °C and 50%, respectively. For each test, five samples were tested, and the average value was noted. For correlation purpose, the specimens of matrix material were also prepared in similar lines.

### 3 Results and Discussion

#### 3.1 Tensile Load Measurement

The composite specimens C5, C10, C15, C20, and C25 are tested for tensile properties in a universal testing machine (UTM). The tensile strength was determined using INSTRON-3369 model UTM. The crosshead speed for tensile test was maintained at 10 mm/min. The temperature and humidity of this test were maintained at 18 °C and 50%, respectively. In each case, five samples were tested, and average values were calculated. The tensile strength for five samples is shown in Fig. 1. It is observed that the tensile strength of composite is increased as the fiber weight increases in the composite sample for both treated and untreated. Treated samples possess elevated tensile strength when compared to untreated samples, and a maximum of 78 MPa is observed for both C20 and C25 treated samples.

#### 3.2 Flexural Strength Measurement

The composite specimens C5, C10, C15, C20, and C25 are tested for flexural properties (three-point bend test) in a universal testing machine (UTM) and, a span length of 10 cm was maintained. The flexural strength was determined using INSTRON-3369 model UTM. The crosshead speed for flexural test was maintained at 10 mm/min.

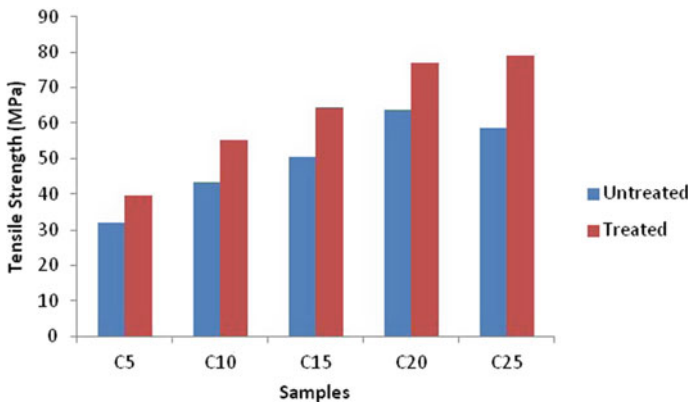


**Fig. 1** Variation of maximum tensile strength with tpsi fibers reinforced polyester composites for both treated and untreated samples

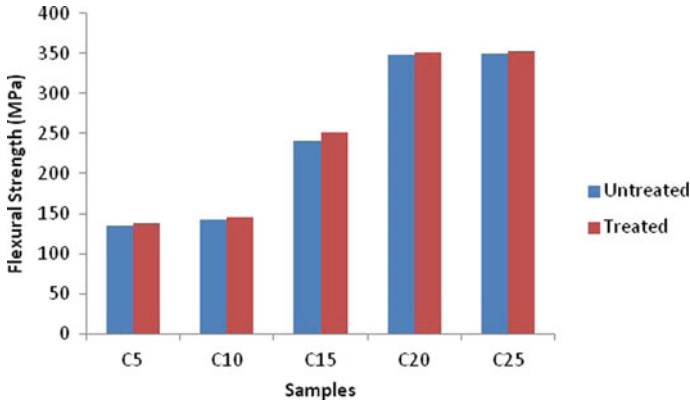


**Fig. 2** Variation of maximum flexural strength with tapsi fibers reinforced polyester composites for both treated and untreated samples

The temperature and humidity of this test were maintained at 18 °C and 50%, respectively. In each case, five samples were tested, and average values were calculated and is shown in Fig. 2. The increase in fiber weight content in the matrix system offered better stiffness to the samples, which in turn provide enhanced flexural resistance of the composite sample. However, the flexural strength of the composite samples C20 and C25 attained an equal amount of flexural strength (350 MPa). This is due to inadequate matrix to hold the bulky weight fraction of fibers.

### 3.3 Impact Strength Measurement

The composite specimens C5, C10, C15, C20, and C25 are tested for impact strength in an impact tester. The impact strength was determined using IZOD impact testing machine. In each case, five samples were tested, and average values were calculated and is shown in Fig. 3. From Fig. 3, it was observed that impact strength increases with fiber content. It was also observed from Fig. 3 that treated hybrid composites have more impact strength when compared to untreated hybrid composites. Improvement of impact properties for treated composites is due to the removal of hemi-cellulose and lignin.

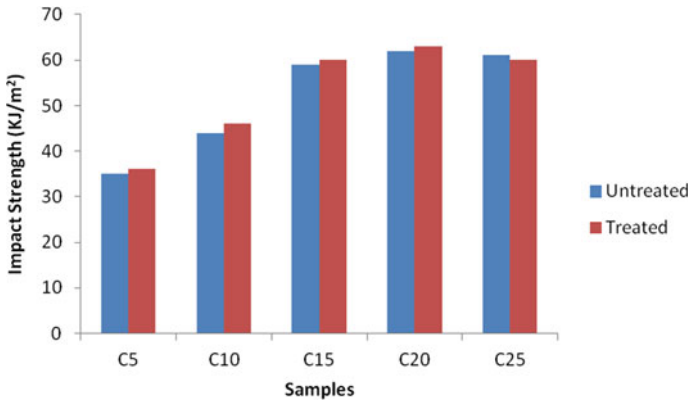


**Fig. 3** Variation of maximum impact strength with tapsi fibers reinforced polyester composites for both treated and untreated samples

## 4 Conclusion

The hybrid composites of tapsi fiber reinforced polyester were readied, and their mechanical properties were studied. The impact of tapsi fiber percentage on these properties was studied. These hybrid composites with treated fiber composite samples were found to display great mechanical properties. It was discovered that treated fibers have good bonding between matrix and fibers. The hybrid composites with treated tapsi fibers were found to have superior mechanical properties because of the disposal of undefined powerless hemi-cellulose segments from the tapsi fibers might be in charge of this conduct. The maximum tensile strength of the composite samples C20 and C25 is almost equal to 72.62 MPa, which is higher in comparison with remaining three samples. Likewise, the maximum flexural and impact strengths of the composite samples are almost equal for both C20 and C25 samples during their corresponding tests.

## References

1. Mohan Rao KM, Rao KM, Prasad AR (2010) Fabrication and testing of natural fibre composites: Vakka, sisal, bamboo and banana. *Mater Des* 31(1):508–513. <https://doi.org/10.1016/j.matdes.2009.06.023>
2. Wong K, Zahi S, Low K, Lim C (2010) Fracture characterisation of short bamboo fibre reinforced polyester composites. *Mater Des* 31(9):4147–4154. <https://doi.org/10.1016/j.matdes.2010.04.029>
3. Sathish Kumar T, Navaneethakrishnan P, Shankar S (2012) Tensile and flexural properties of snake grass natural fiber reinforced isophthallic polyester composites. *Compos Sci Technol* 72(10):1183–1190. <https://doi.org/10.1016/j.compscitech.2012.04.00>

4. Rao KM, Prasad AV, Babu MN, Rao KM, Gupta AVSSKS (2007) Tensile properties of elephant grass fiber reinforced polyester composites. *J Mater Sci* 42(9):3266–3272. <https://doi.org/10.1007/s10853-006-0657-8>
5. Okubo K, Fujii T, Yamamoto Y (2004) Development of bamboo-based polymer composites and their mechanical properties. *Compos Part A Appl Sci Manuf* 35(3):377–383. <https://doi.org/10.1016/j.compositesa.2003.09.017>
6. Osorio L, Trujillo E, Vuure AV, Verpoest I (2011) Morphological aspects and mechanical properties of single bamboo fibers and flexural characterisation of bamboo/epoxy composites. *J Reinf Plast Compos* 30(5):396–408. <https://doi.org/10.1177/0731684410397683>
7. Rajulu AV, Reddy KH, Reddy GR (2010) Chemical resistance and tensile properties of glass and bamboo fibers reinforced polyester hybrid composites. *J Reinf Plast Compos* 29(14):2119–2123. <https://doi.org/10.1177/0731684409349520>
8. Mandal S, Alam S (2012) Dynamic mechanical analysis and morphological studies of glass/bamboo fiber reinforced unsaturated polyester resin-based hybrid composites. *J Appl Polym Sci* 125(S1). <https://doi.org/10.1002/app.36304>
9. Oushabi A, Sair S, Hassani FO, Abboud Y, Tanane O, Bouari AE (2017) The effect of alkali treatment on mechanical, morphological and thermal properties of date palm fibers (DPFs): study of the interface of DPF–polyurethane composite. *South Afr J Chem Eng* 23:116–123. <https://doi.org/10.1016/j.sajce.2017.04.005>
10. Krishnudu DM, Sreeramulu D, Reddy PV, Rao HR (2018) Effect of alkali treatment on mechanical properties of *Prosopis Juliflora* hybrid composites. *Int J Appl Eng Res* 13(5):2933–2935
11. Krishnudu DM, Sreeramulu D, Reddy PV (2018) Optimization the mechanical properties of coir-luffa *Cylindrica* filled hybrid composites by using Taguchi method. In AIP conference proceedings, vol 1952, No 1. AIP Publishing, p. 020058

# Finite Element Analysis and Theoretical Wear Behaviour for Total Hip Replacement



Shaik Akbar Basha and Debasish Sarkar

**Abstract** In consideration of total hip replacement (THR) and theoretical life estimation, we extensively performed finite element analysis and predicted the wear behaviour of different head sizes of 28, 30 and 32 mm and two bearing systems namely ZTA head—ZTA liner and Ti6Al4V head—UHMWPE liner. Static but stance activity was encountered for the 100 kg subject, where the ZTA head—ZTA liner combination exhibit less von mises stress compared to Ti6Al4V head—UHMWPE liner bearing. Interestingly, 30 mm femoral head experiences more jump distance (JD) and more range of motion (ROM) in comparison of the 28 mm femoral head, and less deformation compares to 32 mm femoral head. The wear behaviour is estimated using Archard's law and predicted wear depth is around 600  $\mu\text{m}$  for 15 years for 30 mm femoral head during articulating motion with identical tribocouple.

**Keywords** Total hip replacement (THR) · Static analysis · ZTA · Wear rate

## 1 Introduction

The natural hip joint is an assembly of ball and socket, where the ball represents femoral head and socket represents acetabulum. The hip joint helps in mobility and support the weight of the human body during static (standing) and dynamic (walking and running) loading conditions. A surgical procedure used to remove the diseased cartilage and bone of the hip joint and replace with artificial hip joint components is called total hip replacement (THR). The failure of THR is mainly due to instability and dislocation. The dislocation rate in primary THR is 0.5–10% [1] and revision THR 10–25% [2]. The dislocation occurred in THR is mainly two types, early and late dislocation. Due to the impingement of the femoral neck from the acetabular

---

S. A. Basha (✉) · D. Sarkar (✉)

Department of Ceramic Engineering, National Institute of Technology, Rourkela, Odisha 769008, India

e-mail: [akbar3406@gmail.com](mailto:akbar3406@gmail.com)

D. Sarkar

e-mail: [dsarkar@nitrkl.ac.in](mailto:dsarkar@nitrkl.ac.in)

© Springer Nature Singapore Pte Ltd. 2020

L. Vijayaraghavan et al. (eds.), *Emerging Trends in Mechanical Engineering*,

Lecture Notes in Mechanical Engineering,

[https://doi.org/10.1007/978-981-32-9931-3\\_10](https://doi.org/10.1007/978-981-32-9931-3_10)



liner cup lip causes early dislocation, the impingement of early dislocation is due to the limitation of a range of motion. The late dislocation was due to wear rate of femoral head and acetabular liner. The paper is a target to generate von mises stresses in the artificial hip joint assembly and to predict the wear rate of the head and liner. The finite element was generated, which consists of components femoral stem, femoral head, acetabular liner and acetabular socket. The femoral stem fixed in femoral bone F, and the acetabular socket fixed in acetabular bone A. The static analysis was performed stance activity (shifting weight from both to one leg and back).

## 2 Finite Element Modelling of an Artificial Hip Joint

The finite element method used in science and industry for stress analysis. FEA software analyses used for implants like hip, knee and dental. The FEA results generated mainly depend on many individual factors, boundary conditions, material properties, interface and approach to the model. The present model was on the approximation of the clinical situation. Modelling the exact geometry of the bone is complex. Hence, in the present study, many assumptions are made during the development of the model.

The artificial hip joint model was developed using CATIA V5R17 modelling software as shown in Fig. 1. All components of the artificial hip joint femoral stem, femoral head, an acetabular liner, acetabular socket, femur bone (bone F) and acetabular bone (bone A) are separately built and assembled using CATIA V5R17 assembly. For analysis and comparison three different hip joint models developed in CATIA V5R17, they are 28 mm head THR model, 30 mm head THR model and 32 mm head THR model.

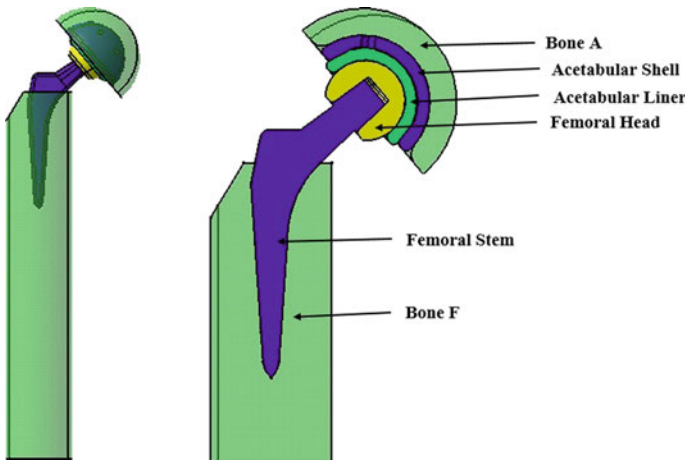
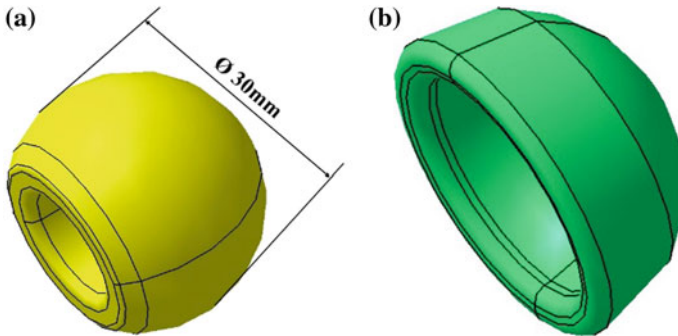


Fig. 1 Schematic representation of the THR model system



**Fig. 2** **a** Femoral head CAD model and **b** acetabular liner CAD model

The three femoral head of size 28, 30 and 32 mm are accompanied by acetabular liners with inner and outer diameter 28.02/38 mm, 30.02/40 mm and 32.02/42 mm, respectively, with a radial clearance of 20  $\mu\text{m}$  between the femoral head and acetabular liner. The 30 mm femoral head and acetabular liner are shown in Fig. 2.

The dimensions of femoral stem designed with stem length 81.73 mm, taper 12/14 and neck-shaft angle 130°. The inner and outer dimensions of the acetabular socket for 28, 30 and 32 mm femoral head are 38.02/48 mm, 40.02/50 mm and 42.02/52 mm, respectively, with a radial clearance of 20  $\mu\text{m}$  between the acetabular liner and acetabular socket. All the three models exported into ANSYS 17.2. THR models finely mesh through ANSYS 17.2. with element size as 2.5 mm and tetrahedral elements. The meshed 28 mm, 30 mm and 32 mm THR models has nodes 4,21,960 and elements 2,90,078, nodes 4,30,105 and elements 2,95,434 and nodes 4,39,268 and elements 3,01,434, respectively.

### 3 Material Properties of THR Model

For comparison, two bearings are considered for analysis, i.e. Ti6Al4V head/UHMWPE liner and ZTA head/ZTA liner. The materials used are ceramic—ZTA composite (95 wt%  $\text{Al}_2\text{O}_3$ , 5 wt% 3YSZ), metal-Ti6Al4V and polyethylene-UHMWPE for two bearings femoral head and acetabular liner. All materials are assumed to be homogeneous, isotropic and linear elastic. The rule of the mixture was used to calculate Young's modulus—375 GPa and Poisson's ratio—0.3 of ZTA composite. The material properties used for FEM analysis tabulated in Table 1.

**Table 1** Properties of materials for FEM analysis [3]

S. No.	Material	Young's modulus (GPa)	Poisson's ratio	Mass density (g/cm <sup>3</sup> )	Yield strength (MPa)
1.	Alumina (Al <sub>2</sub> O <sub>3</sub> )	380	0.3	3.95	665
2.	Zirconia (ZrO <sub>2</sub> )	210	0.3	6.05	711
3.	Ti-6Al-4V	110	0.3	4.5	800
4.	UHMWPE	1	0.4	0.93	23.56
5.	Simulative bone	20	0.3	1.932	–

## 4 Loading and Boundary Conditions

For static analysis average human load of 100 kg is considered. The static load is determined from experimental observations of Bergmann et al. [4]. The static stance load is when a person is shifting weight from both to one leg and back. The static load and boundary conditions are applied in this work are normal to hip joint. The high contact forces and friction moments in the joints cause the fixation of the acetabular socket, the failure of hip implants is due to cup loosening [5–7]. To identify the effect of cup fixation moments is used in the static load. Not only the load and moments, but also the coefficient of friction between the hip assembly components affects the THR assembly. The stance force of 3340.5 N and 1.03 Nm applied on the femoral head. The stance force is shown in Table 2.

From Tsouknidas et al. [8]. An abductor muscle force of 703 N applied on bone F to counter the static force, the top surface of bone A and base surface of bone F are fixed in all directions. Static loading and boundary conditions of the THR model are shown in Fig. 3.

According to Bergmann et al. the coefficient of friction between metal on the metal bearing is 0.1–0.2 [9], the coefficient of friction between ceramic on the ceramic bearing is 0.05 by Fialho et al. [10]. The coefficient of friction between porous-surfaced metal and tibial cancellous bone is 0.3–1.3 by Rancourt et al. [11], the coefficient of the surface between alumina on alumina bearing 0.05–0.1 [12]. The coefficient of friction between Ti6Al4V and UHMWPE under bovine serum is 0.55 [13].

In the present study, therefore, the coefficient of friction between metal and simulative bone and coefficient of friction between ZTA and ZTA bearing was considered as 0.2. The coefficient of friction between Ti6Al4V and UHMWPE bearing as 0.15 is considered for static analysis.

**Table 2** Stance and abductor muscle force for FEM analysis

S. No.	Force	$F_x$ (N)	$F_y$ (N)	$F_z$ (N)	$F_{res}$ (N)	$M_x$ (Nm)	$M_y$ (Nm)	$M_z$ (Nm)	$M_{res}$ (Nm)
1.	Stance force	945.59	-198.39	-3197.72	3340.5	0.18	0.57	0.83	1.03
2.	Abductor muscle force	86.18	161.05	679.04	703	-	-	-	-

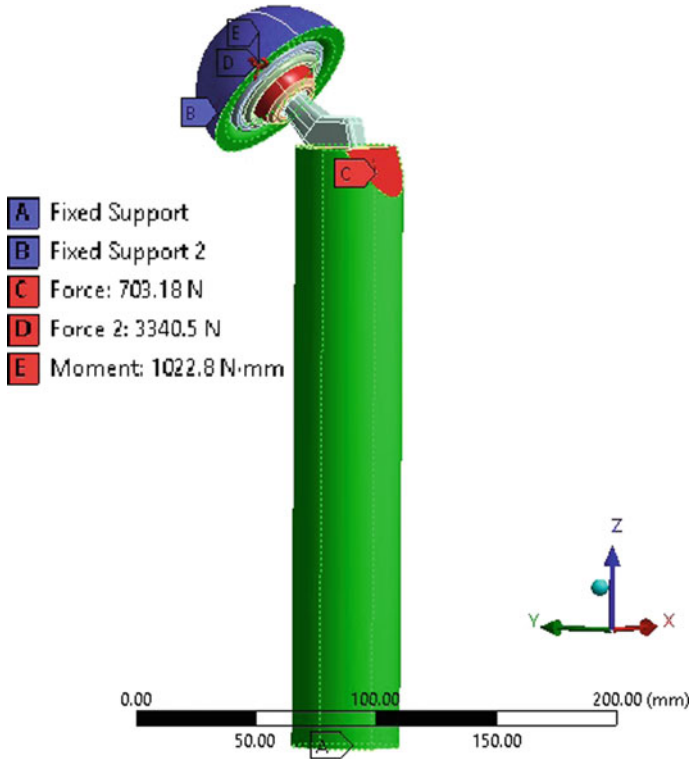


Fig. 3 Loads and boundary conditions on THR model system

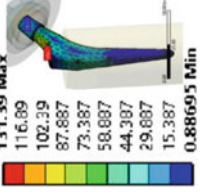
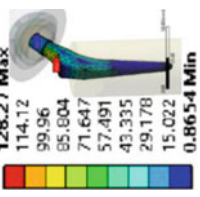
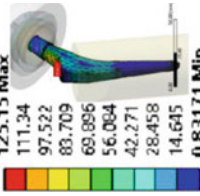
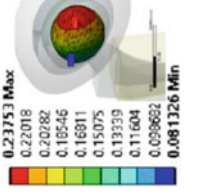
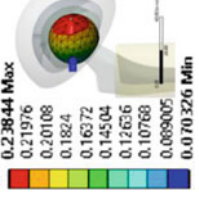
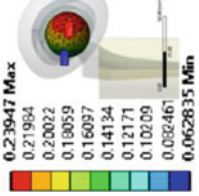
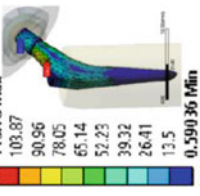
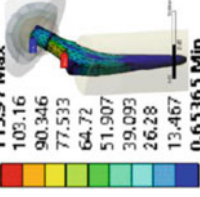
### 5 Results for Static Analysis

From the static analysis, the ZTA/ZTA bearing generates less von mises stress compared to Ti6Al4V/ UHMWPE bearing. The von mises stress generated in both bearings is less than the yield strength of the prosthesis material used. For both bearings, the maximum von mises stress is concentrated on the upper portion of femoral stem neck. The von mises stress is decreased with the increase of the head size as the bearing load area increased (see Table 3).

Jump distance (JD) is the femoral head centre translation distance required for a head to dislocate from a socket. Prosthetic hips with less JD are more likely to dislocate than hips with more JD. The range of motion (ROM) of the THA implant depends on the femoral head diameter, head neck ratio and neck length of the stem. Increased ROM the stability of THA increase and increased the risk of impingement. The impingement occurs between the femoral stem neck and acetabular liner.

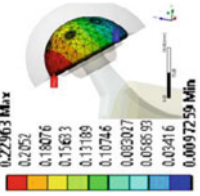
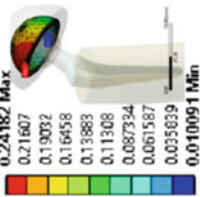
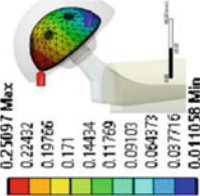
In THA, if the femoral head and femoral stem neck ratio are less than two, then there is significantly less in ROM and increased risk of impingement. The femoral head and femoral stem neck ratio for 28 mm, 30 mm and 32 mm THA models are

**Table 3** Static analysis: The von mises stress and total deformation of three 28, 30 and 32 mm THR models with two bearings

	28 mm	30 mm	32 mm
Ti6Al4 V/UHMWPE bearing	 <p>131.39 Max 116.89 102.39 87.887 73.387 58.887 44.387 29.687 15.387 0.88665 Min</p>	 <p>128.27 Max 114.12 99.96 85.804 71.647 57.491 43.335 29.178 15.022 0.8654 Min</p>	 <p>125.15 Max 111.34 97.522 83.709 69.896 56.064 42.271 28.458 14.645 0.83171 Min</p>
	 <p>0.23753 Max 0.22018 0.20282 0.18546 0.16911 0.15075 0.13359 0.11604 0.09862 0.081326 Min</p>	 <p>0.23844 Max 0.21976 0.20108 0.1824 0.16372 0.14504 0.12636 0.10768 0.089005 0.070326 Min</p>	 <p>0.23947 Max 0.21984 0.20022 0.18059 0.16097 0.14134 0.12171 0.10209 0.082461 0.062835 Min</p>
	von mises stress (MPa)	 <p>116.78 Max 103.87 90.96 78.05 65.14 52.23 39.32 26.41 13.5 0.59036 Min</p>	 <p>115.97 Max 103.16 90.346 77.533 64.72 51.907 39.093 26.28 13.467 0.65365 Min</p>
ZTA/ZTA bearing	von mises stress (MPa)		

(continued)

Table 3 (continued)

		28 mm	30 mm	32 mm
	Total deformation (mm)	 <p>0.22963 Max 0.2052 0.18076 0.15633 0.13189 0.10746 0.083047 0.058693 0.03416 0.0097259 Min</p>	 <p>0.24182 Max 0.21607 0.19032 0.16458 0.13883 0.11308 0.087334 0.061587 0.035639 0.010091 Min</p>	 <p>0.25097 Max 0.22432 0.19766 0.171 0.14434 0.11769 0.09103 0.064373 0.037716 0.011058 Min</p>

2.15, 2.31 and 2.46, respectively. The ROM for 28 mm, 30 mm and 32 mm THA models are  $110^\circ$ ,  $116^\circ$  and  $120^\circ$ , respectively. The ROM of THA models increased with the increase of femoral head size.

From the two bearings, the ZTA/ZTA bearing is considered as the best choice as it generates less von mises stress. Among the three femoral heads, 30 mm ZTA femoral head is considered as optimum, as it generates less von mises stress, more JD and more range of motion compared to lower size 28 mm head under continuous activity, but higher size 32 mm experience more deformation compare to other sizes.

## 6 Wear of 30 mm ZTA/ZTA Bearing Total Hip Replacement

Wear is the gradual removal of material from the surface of the body. The wear of hip prosthesis is due to contact of components, sliding distance and tribological properties of materials used. Wear is a remarkable phenomenon for the failure of THA implants; the factors influence the wear are femoral head size, the bearing material used and patient factors (age, sex, weight and activity level). Volumetric wear is the amount of material removed from the surface of the bearing.

Archard's law was used to estimate the wear [14].

$$V = K_w \times dS \times P_c$$

where  $V$  is volume of wear debris,  $K_w$  is wear coefficient,  $dS$  is sliding distance and  $P_c$  is the contact pressure.

$$dV = \Delta Adh = K_w \times \sigma \times A \times dS, \quad \text{Wear depth } (dh) = K_w \times \sigma \times dS.$$

Wear coefficient ( $K_w$ ) is a volume of material loss per unit distance; it was measured experimentally. Wear coefficient of  $\text{Al}_2\text{O}_3$  and ZTA combination obtained from the ball on disk experiment is  $5.3\text{E}-8 \text{ mm}^3/\text{Nm}$  [15]. The maximum contact pressure from the static analysis ( $\sigma$ ) = 35.73 MPa (see Fig. 4). From a sliding distance ( $dS$ ) the wear depth ( $dh$ ) is calculated.

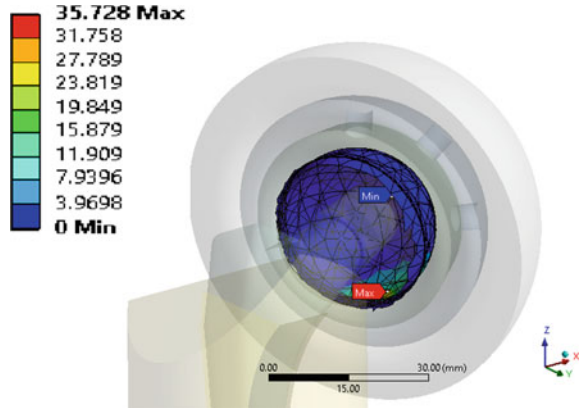
The sliding distance was calculated from the walking cycle of human which consists of motions flexion, extension, adduction, abduction and internal-external rotation. Among the motions flexion and extension have more effect during walking hence, during half walking cycle the flexion and extension angle is  $23^\circ$  and  $17^\circ$ , respectively. For the complete walking cycle, hip joint rotates at an angle of  $80^\circ$ . In the present study, the radius of femoral head 15 mm is considered for analysis.

$$\text{For one cycle total hip rotation} = 80^\circ = 1.396 \text{ rad.}$$

$$\begin{aligned} \text{Sliding distance } (dS) &= \text{femoral head radius} \times \text{hip rotation angle} \\ &= 15 \times 1.396 = 20.94 \text{ mm} = 20.94\text{E}-3 \text{ m.} \end{aligned}$$



**Fig. 4** Contact pressure of ceramic head and ceramic acetabular liner bearing



By using Archard's law,

$$\begin{aligned}
 \text{Wear depth } (dh) &= K_w \times \sigma \times dS. \\
 &= 5.3E-8 \times 35.73 \times 20.94E-3 \\
 &= 3.965E-8 \text{ mm/cycle.}
 \end{aligned}$$

Average human takes one million steps in one year; the wear rate was estimated to be 0.04 mm/year. After 15 years 600  $\mu\text{m}$  of wear depth takes place at a constant point. Under dynamic analysis, the wear depth of 0.062 mm/year is obtained [16].

## 7 Conclusion

The static analysis was conducted for THR model with three different femoral head sizes 28, 30 and 32 mm along with two bearings ZTA/ZTA and Ti6Al4V/UHMWPE. A 100 kg human performing stance activity, i.e. a person shifting weight from both to one leg and back is considered for static analysis. The von mises stress generated in THR components is less than the yield strength of the prosthesis material used. Hence, the design is safe in the human body. The high stresses are observed in the femoral stem neck region. The 30 mm femoral head is considered as the optimum head as it has less von mises stress, more JD distance and more ROM compared to 28 mm femoral head and less deformation than the 32 mm femoral head. The wear is estimated by using Archard's law, wear depth of 0.04 mm/year has calculated for the 30 mm femoral head of ZTA material. Based on the wear of femoral head it is assumed that the hip joint is safe for 15 years.

**Acknowledgements** The current research project is financially supported by the Department of Biotechnology (DBT), Government of India (GOI) (Grant No. BT/PR13466/COE/34/26/2015).

## References

1. Sariali E, Leonard P, Mamoudy P (2008) Dislocation after total hip arthroplasty using Hueter anterior approach. *J Arthroplasty* 23(2):266–272
2. Alberton GM, High WA, Morrey BF (2002) Dislocation after revision total hip arthroplasty: an analysis of risk factors and treatment options. *J Bone Joint Surg Am* 84(10):1788–1792
3. Askari Ehsan, Flores Paulo, Dabirrahmani Danè, Appleyard Richard (2016) A review of squeaking in ceramic total hip prostheses. *Tribol Int* 93:239–256
4. Bergmann G, Bender A, Dymke J, Duda G, Damm P (2016) Standardized loads acting in hip implants. *PLoS ONE* 11(5):e0155612
5. Bergen H (2010) Annual Report 2010, Norwegian Arthroplasty Register. Norwegian Arthroplasty Register
6. David D, Graves S, Tomkins A (2013) Annual Report 2013 Australian Orthopaedic Association National Joint Replacement Registry
7. Garellick G, Karrholm J, Rogmark C, Rolfson O, Herberts P (2011) Annual Report 2011. Swedish Hip Arthroplasty Register
8. Tsouknidas Alexander, Anagnostidis Kleovoulos, Maliaris Georgios, Michailidis Nikolaos (2012) Fracture risk in the femoral hip region: a finite element analysis supported experimental approach. *J Biomech* 45:1959–1964
9. Bergmann G, Deuretzbacher G, Heller M, Graichen F, Rohlmann A, Strauss J, Duda GN (2001) Hip contact forces and gait patterns from routine activities. *J Biomech* 34:639–642
10. Fialho JC, Fernandes PR, Eca L, Folgado J (2007) Computational hip joint simulator for wear and heat generation. *J Biomech* 40:2358–2366
11. Rancourt D, Shirazi-Adl A, Drouin G et al (1990) Friction properties of the interface between porous-surfaced metals and tibial cancellous bone. *J Biomed Mater Res* 24:1503–1519
12. Khademhosseini A (2008) *Micro and nanoengineering of the cell microenvironment: technologies and applications*. Artech House Publishers
13. Park J (2008) *Bioceramics: properties, characterizations, and applications*. Springer
14. Wu JS, Hung J, Shu C, Chen J (2003) The computer simulation of wear behavior appearing in total hip prosthesis. *Comput Methods Program Biomed* 70:81–91
15. Strey NF, Scandian C (2017) Tribological transitions during sliding of zirconia against alumina and ZTA in water. *Wear* 376–377:343–351
16. Shaik AB, Sarkar D (2019) Dynamic analysis and life estimation of the artificial hip joint prosthesis. In: *Advances in Intelligent Systems and Computing*, vol 949, Springer, pp 265–274

# Characteristics of Mixed Convective Flowover Fins for Automobile Application



D. Sanjana Reddy, Y. Ranjani, M. Mukeshanand, M. Sudharshan Srinivas,  
D. Lalith Kumar and L. Dineshkumar 

**Abstract** Enhancement of heat transfer rate in automobiles is one of the key research areas currently. To address one such heat transfer issue, the authors have attempted a detailed study about mixed convection heat transfer for a fluid in a lid driven square cavity with different blockages placed at the center of cavity and are maintained at constant wall temperature at a steady state condition. The fluid flow is due to the top wall which is in motion while the other walls are kept stationary. The governing differential equations are solved for a range of dimensionless constants like Reynolds number from 1 to 1000, Prandtl number from 1 to 100 and Grashof's number from 0 to  $10^5$ . It is observed that the heat transfer is more in triangular blockage when compared to that of square and cylindrical blockages. Also, in case of blockages with grooves, more heat transfer is observed in triangular blockage than square and cylindrical ones with grooves. Out of all cases studied in the current work, heat transfer rate is found to be better in triangular blockage with grooves.

**Keywords** Heat flux · Mixed convection · Blockage · Viscosity · Mesh convergence · Heat transfer

## 1 Introduction

Heat transfer is a phenomenon that plays a major role in the world of thermodynamics [1]. In automobiles, heat transfer from the engine is a very vital phenomenon. There is the challenge of removing excess of heat with the help the fins from the engine to increase engine's efficiency. This paper attempts to properly design and optimize a fin using Finite volume analysis to increase heat transfer rate.

The most common type of mode of heat transfer in fluids is convection. Convection takes place due to the movement of molecules. When the movement of these molecules takes place without any external source, it is called natural convection.

---

D. Sanjana Reddy · Y. Ranjani · M. Mukeshanand · M. S. Srinivas · D. Lalith Kumar ·  
L. Dineshkumar (✉)  
Amrita School Engineering, Amrita Vishwa Vidyapeetham, Bengaluru, India  
e-mail: [L\\_dineshkumar@blr.amrita.edu](mailto:L_dineshkumar@blr.amrita.edu)

© Springer Nature Singapore Pte Ltd. 2020  
L. Vijayaraghavan et al. (eds.), *Emerging Trends in Mechanical Engineering*,  
Lecture Notes in Mechanical Engineering,  
[https://doi.org/10.1007/978-981-32-9931-3\\_11](https://doi.org/10.1007/978-981-32-9931-3_11)

And when it happens with the aid of external source, it is called forced convection. When both these mechanisms act together to transfer heat i.e., when there is an interaction between buoyant and pressure forces, it is called mixed convection. To achieve mixed convection, a lid driven cavity is used where natural convection is obtained by maintaining the temperatures of walls of the cavity at different temperatures and forced convection is obtained with the help of the top wall of the cavity which moves with a certain velocity. In case of constant wall temperature (CWT), the surface wall has the same temperature throughout, but the flow of heat per unit area through the walls is different. And in case of constant heat flux (CHF), the wall temperature may not be uniform throughout but the rate of flow of heat per unit area through the wall surface remains same. Grashof's number is the ratio of buoyancy to viscous forces acting on the fluid. With the help of Grashof's number, one can predict if natural convection or forced convection is dominant. Prandtl number is the ratio of momentum diffusivity to thermal diffusivity [2–6]. It can be used to determine the thermal conductivity of gases at high temperature. It also provides information about thermal and hydrodynamic boundary layer. Reynold's number is the ratio of inertial forces to viscous forces in a fluid flow. It helps us to predict the patterns in fluid's behavior. For  $Gr = 0$ , it becomes purely forced convection and for  $Gr = 10^5$ , natural convection is predominant. It has been observed that, when flow advances towards purely natural or purely forced convection, heat transfer rate increases. Also, an obstacle in the cavity helps in offering resistance to flow which increases heat transfer. Therefore, an obstacle is placed at the center of the cavity and the pattern of heat transfer is observed. For a range of dimensionless parameters mentioned as follows ( $1 \leq Re \leq 1000$ ;  $1 \leq Pr \leq 100$ ;  $0 \leq Gr \leq 10^5$ ), the heat transfer rate in the lid driven cavity for Constant Wall Temperature (CWT) has been analyzed with a triangular, circular and square obstacle placed one at a time at the center of the cavity and is maintained at a higher temperature. Surface roughness can also improve heat transfer. Therefore these obstacles were then replaced by the obstacles with same dimensions but with rough surfaces [1, 5, 7–10]. Heat transfer rate has been analyzed for the same set of conditions as in the previous case and results have been compared.

## 2 Problem Statement

A square cavity of side 1 m in length containing fluid with top wall moving is considered for the numerical analysis as shown in the Fig. 1. The length of the lid is considered as the reference length. Since in this study the non-dimensional analysis was carried out from an application point of view, the driving velocity of lid is not specified. But still the velocity of the lid can be calculated using no-slip condition [i.e. the first layer of the liquid molecule in contact with the lid will have the velocity same as lid, and the velocity of liquid can be calculated using Reynolds number (a non-dimensional number)].

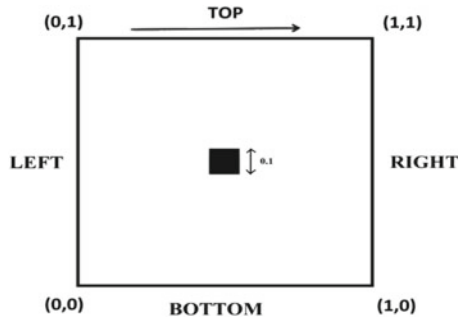


**Fig. 1** Domain of problem, all dimensions are in meters

A blockage of characteristic length of the side 0.1 m with constant surface temperature is placed at the center of the cavity. This blockage may be of the following shapes like square, triangle or cylinder. For the range of values of Prandtl number (1, 50, 100), Reynold’s number (1, 100, 1000), and Grashof’s number (0,  $10^3$ ,  $10^5$ ), a different combination of these dimensionless quantities is used to assess the heat transfer and rate of convection in the system. The blockage may be smooth or may have surface roughness.

The effects of the temperature difference, force and different values of dimensionless quantities like Reynolds number, Grashof’s number and Prandtl number on the rate and amount of heat transfer, and the ability of the fluid to absorb heat from the objects of different shapes is studied, so as to find the most suitable object of a fixed dimension to be used as a fin.

### 3 Numerical Methodology

Numerical simulations help researchers to explain various phenomena and solve various kinds of problems involving heat transfer [11, 12]. Finite volume method is used to solve the governing equations such as continuity, momentum and energy. Initially the flow domain was discretized using quadrilateral elements and a solution was obtained. In order to reduce the computational time without compromising on accuracy of the solution, a converged solution was attained by changing the mesh element to triangle and reducing the number of elements. A mesh convergence was attained for the simulation using triangular elements. Further, changing the number of triangular elements did not affect the solution and thus the attained solution was considered to be mesh converged solution.

Figure 2 represents the domain of the problem after meshing. Both mesh convergence and solution convergence study have been done and validated as reported in the earlier paper [13]. The solution iteration is terminated for the convergence

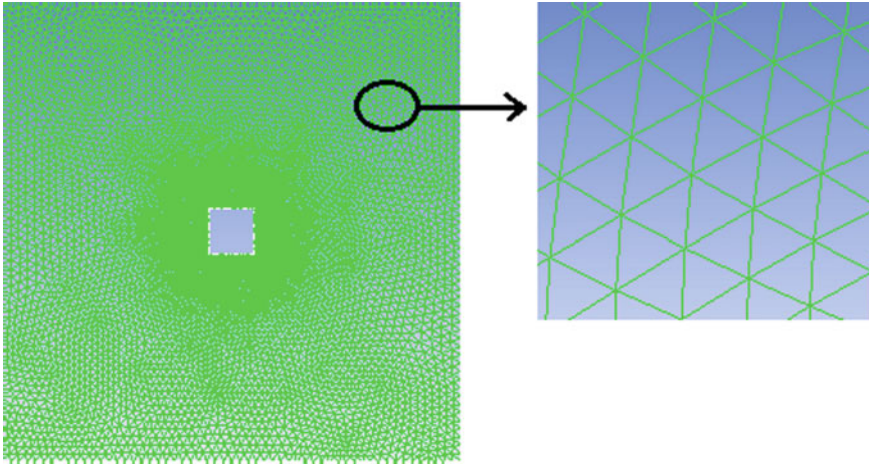


**Fig. 2** Surface mesh with a smooth square fin of 10% blockage

criterion of  $10^{-8}$  for continuity equation and  $10^{-6}$  for  $x$  and  $y$  momentum and energy equations. The continuity, momentum and energy equations are expressed as follows:

Continuity equation:

$$\frac{\partial}{\partial x}(\rho u) + \frac{\partial}{\partial y}(\rho v) = 0 \quad (1)$$

$x$ -momentum equation:

$$\frac{\partial}{\partial x}(\rho uu) + \frac{\partial}{\partial y}(\rho vu) = \sum F_x \quad (2)$$

$y$ -momentum equation:

$$\frac{\partial}{\partial x}(\rho uv) + \frac{\partial}{\partial y}(\rho vv) = \sum F_y \quad (3)$$

Energy equation:

$$\frac{\partial T}{\partial x}(u) + \frac{\partial T}{\partial y}(v) = (\text{Re} * \text{Pr})^{-1} \left( \frac{\partial T^2}{\partial x^2} + \frac{\partial T^2}{\partial y^2} \right) \quad (4)$$

where,

$\rho$  is density,  $u, v$  are the velocities in  $x$  and  $y$  direction respectively.  $\sum F_x$  and  $\sum F_y$  are the resultant forces acting in  $x$  and  $y$  direction respectively.

Re—Reynolds number

Pr—Prandtl Number

Gr—Grashof’s Number

T—Temperature in Kelvin dependent on  $x, y$ .

The above equations are solved for the following boundary conditions:

- Left and right walls are stationary having constant temperature.
- Top wall is moving with certain velocity (say  $v_{lid} = 1$  m/s) and heat flux through the wall is zero.
- The bottom wall is stationary with zero heat flux.
- The fin (blockage) placed at the center of cavity is considered to have a uniform temperature throughout the surface.

## 4 Results and Discussions

In the present section, the results surrounding the effects of the above-mentioned parameters on heat transfer characteristics (heat signature diagrams or isotherms) are shown. Here the mixed convection takes place at CWT condition for varying Reynolds, Grashof’s and Prandtl numbers. Figures 3 and 4 show the isotherms for  $Re = 1, 100, 1000$ ;  $Gr = 0, 10^3, 10^5$ ;  $Pr = 1, 50, 100$ . Here dynamic viscosity of the water is taken at  $20\text{ }^\circ\text{C}$  to be  $1.002$ . And velocity of the flow at  $Re = 100$  is found to be  $1.004\text{ e} - 4$ ; from the formula:

$$Re = (\rho * v * L) / \mu \tag{5}$$

where

$\rho$  density of water at  $20\text{ }^\circ\text{C}$  is  $998.21\text{ kg/m}^3$ ;

$v$  velocity of the flow m/s

$L$  characteristic length (length of the lid)

$\mu$  dynamic viscosity of water in Pa s.

Similarly, other velocities can be obtained.

Initially the fluid moves along the direction of top plate since Reynolds number is very low, because of which the convective zone stays above the blockage. But once the Reynolds number increases the convective zone moves to the right a little and then starts moving towards the blockage. With increase in Reynolds number the convection changes from natural to forced convection. But for triangular blockage we can observe more forced convection than in that of other two blockages. With increase in Reynolds number the fluid circulates properly around the blockage taking

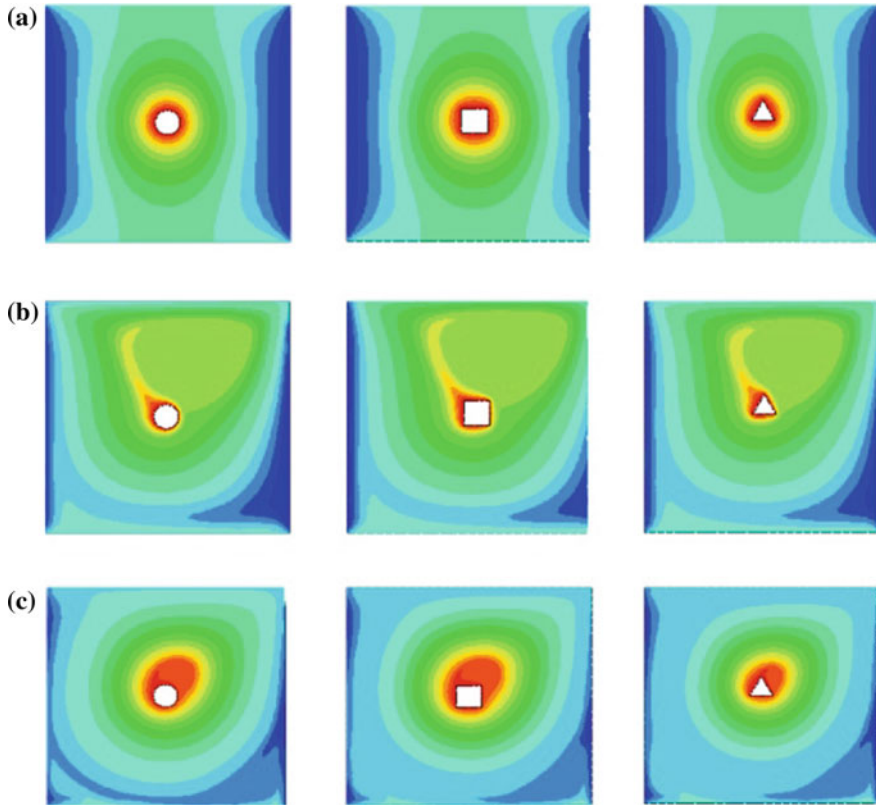


**Fig. 3** Isotherm patterns for different parameters **a**  $Pr = 1$ ,  $Re = 1$ , **b**  $Pr = 50$ ,  $Re = 100$ , **c**  $Pr = 100$ ,  $Re = 1000$  at  $Gr = 0$  and constant wall temperature

away more heat. With increase in Prandtl number the heat capacity of water increases and because of which convection occurs at a faster rate. The difference between the square and triangular blockage is only with the presence of inclined edge for the triangular the blockage. Sharper the edge more is the convection rate because the fluid interacts with the surface for a considerable time as it comes to rest at that edge and it enhances heat transfer. Roughness are modeled in fluent with varying the wall roughness factor. The intensity of the wall roughness can be varied from 0 to 100%. Here, in this study, wall roughness factor of 50% is used for the entire simulation. As the roughness of the surface increases the fluid momentarily comes to rest at that place. Due to which the fluid gets more time to take heat from the surface of the blockage. Also, as roughness increases area of contact also increases simultaneously, which is also a reason for increase in convection.

In Fig. 3, the temperature distribution becomes more even with the increase in Re number for every case. As the Re number increases the convective zone first becomes parallel to the moving lid direction and then surrounds the blockage in both



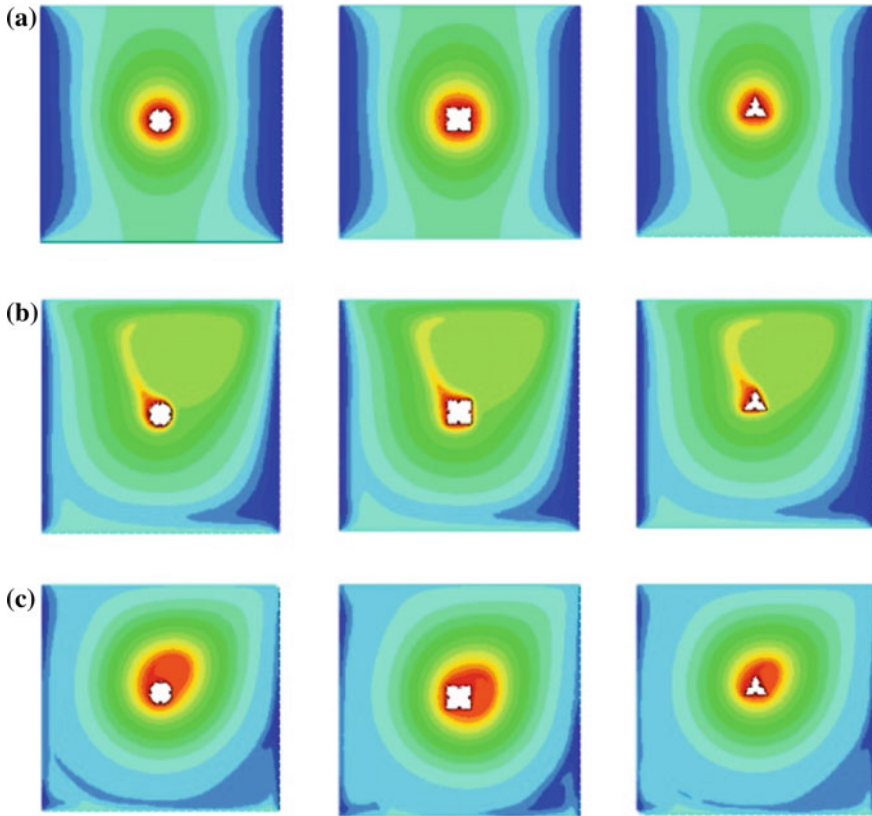


**Fig. 4** Isotherm patterns for different parameters **a**  $Pr = 1, Re = 1$ , **b**  $Pr = 50, Re = 100$ , **c**  $Pr = 100, Re = 1000$  at  $Gr = 10^3$  and constant wall temperature

the cylindrical and triangular blockage and for each  $Re$  number the convective zone appears to be nearly the same for all the blockages of different shape. But for the triangular blockage the temperature region is more uniform and this is true in every case. The convective zone is always surrounding the blockage for all the blockages but the change in convective zone is very small when compared to the increase in  $Re = 1$  to  $Re = 1000$ . Compared to  $Re = 1000$ , for  $Re = 1$  the convective zone is spread, whereas in  $Re = 1000$  the convective zone surrounds the blockage. The convection in this case and remaining cases is higher because of the roughness on the surface of the blockages.

In Fig. 3, the convective zone first becomes parallel to the moving lid direction and then surrounds the blockage. For lower  $Re$  numbers the convective zone is nearly the same. Then at higher  $Re$  numbers the convective zone is concentrated around the blockage. Not much difference is seen in the convective zones at higher  $Re$  numbers. At  $Re = 1, Pr = 1$  and since  $Gr = 10^5$  the buoyant force is high, because of which more of natural convection is observed. Convection occurs faster for triangular blockage

only in (a) and (c), whereas, in (b) the fluid portion below the blockage is completely cooled compared to the other two blockages.

Isotherm contours for the different values of Reynolds number, Prandtl number and Grashof's number are shown for the different blockages. As velocity of the top lid increases, under the forced convection case, fluid close to the lid is being dragged by the lid. But as Grashof's number increases, natural convection starts to take over, and there is heat transfer between the blockage and side wall which produces parallel isotherm lines.

## 5 Conclusions

Mixed convective heat transfer for a fluid in a lid driven square cavity with different blockages retained at constant wall temperature and at a steady state condition was studied. The governing equations are solved for a range of constants like Reynolds number from 1 to 1000, Prandtl number from 1 to 100 and Grashof's number from 0 to  $10^5$ . It is observed that the heat transfer is more in triangular blockage when compared to square and cylindrical blockage. Also, in case of blockages with grooves, more heat transfer is observed in triangular blockage than square and cylindrical ones with grooves. Out of all, heat transfer is better in triangular blockage with grooves.

## References

1. Indukuri JV, Maniyeri R (2017) Numerical simulation of oscillating lid driven square cavity. Alexandria Eng J
2. Elsherbiny SM, Teamah MA, Moussa AR (2017) Natural convection heat transfer from an isothermal horizontal square cylinder. Alexandria Eng J 56(1):181–187
3. Gangawane KM, Manikandan B (2017) Mixed convection characteristics in lid-driven cavity containing heated triangular block. Chin J Chem Eng 25(10):1381–1394
4. Islam AW, Sharif MAR, Carlson ES (2012) Mixed convection in a lid driven square cavity with an isothermally heated square blockage inside. Int J Heat Mass Transf 55(19):5244–5255
5. Abdelkhalek MM (2008) Mixed convection in a square cavity by a perturbation technique. Comput Mater Sci 42(2):212–219
6. Oztop HF, Dagtekin I (2004) Mixed convection in two-sided lid-driven differentially heated square cavity. Int J Heat Mass Transf 47(8):1761–1769
7. Cheng TS (2011) Characteristics of mixed convection heat transfer in a lid-driven square cavity with various Richardson and Prandtl numbers. Int J Therm Sci 50(2):197–205
8. Cheng TS, Liu W-H (2014) Effects of cavity inclination on mixed convection heat transfer in lid-driven cavity flows. Comput Fluids 100:108–122
9. Warriar HU, Kotebavi VM (2016) Heat transfer enhancement in solar air heater duct fitted with punched hole delta winglets. IOP Conf Ser Mater Sci Eng 149(1)
10. Doreti LK, Dineshkumar L (2018) Control techniques in flow past a cylinder—a review. IOP Conf Ser Mater Sci Eng 377:12144
11. Adsul PP, Dineshkumar L (2018) On code verification of 2D transient heat conduction in composite wall. IOP Conf Ser Mater Sci Eng 377:12128

12. Bharathwaj R, Giridharan P, Karthick K, Prasath CH, Prakash Marimuthu K (2016) Computational study of Coanda based Fluidic Thrust Vectoring system for optimising Coanda geometry. IOP Conf Ser Mater Sci Eng 149(1)
13. Mohammed AN, Jithin EV, Dineshkumar L, Ratna Kishore V, Mohammad A (2018) Tip opening of burner-stabilized flames. Energy Fuels 32(2):2344–2354

# A Study on Implementation of Simulation at Operational Level in Manufacturing System



Manohar V. Pattar, Vinayak N. Kulkarni, Sanjay V. Kulkarni  
and B. B. Kotturshettar

**Abstract** Manufacturing simulation has a greater role to play in this era of smart manufacturing. Global competency can be achieved when industries are able to execute planned strategies at an operational level. Over the years simulation has been extensively used at strategic levels, where decisions concerning productivity, design, process reengineering, alternative model selection to be made, have long term effects. Many research experts have pointed at the need to use simulation at an operational level in manufacturing system. This paper explains the significance of simulation at an operational level. In order to analyze the above said research problem, a tin container production line in LVT containers plant unit at Hubballi, Karnataka, India was considered for the study. The main objective in this study is to maximize production rate through minimizing serious bottlenecks identified at various stages by proposing several scenarios without altering existing facility.

**Keywords** Manufacturing simulation · Strategic level · Bottlenecks · Productivity

## 1 Introduction

Rapid growth of expertise and constant change in the customer requirement have decreased product life cycle. Nowadays industries are driven by customers unlike old traditional hierarchy rules, wherein flow of control was from top to bottom. “Lean manufacturing” is what industries people refer to. Thus, the processes that are carried at an operational level play a significant role in the path of moving toward lean manufacturing. At the operational level, industries require to collect, merge, and analyze various data set generated on the floor from unit production to equipment operations data. The effective execution of real-time analytics and monitoring is possible through better-informed decision making. We know that physical implementation of change can be difficult task. But through simulation,

---

M. V. Pattar (✉) · V. N. Kulkarni · S. V. Kulkarni · B. B. Kotturshettar  
School of Mechanical Engineering, KLE Technological University, Hubballi, Karnataka 580031,  
India  
e-mail: [manohar.gdg@gmail.com](mailto:manohar.gdg@gmail.com)

© Springer Nature Singapore Pte Ltd. 2020  
L. Vijayaraghavan et al. (eds.), *Emerging Trends in Mechanical Engineering*,  
Lecture Notes in Mechanical Engineering,  
[https://doi.org/10.1007/978-981-32-9931-3\\_12](https://doi.org/10.1007/978-981-32-9931-3_12)

designer can actually test and verify several design alternatives as they would be having detail analysis of existing system's behavior over a period of time. Given that over the years simulation has been used mostly for decision support in situations that are several months and maybe years ahead. Simeonov and Simeonovova in their paper have considered a case study on coffee production describing potential uses of simulation for increasing productivity and profit [1]. Minegishi and Thiel explained simulation study on industrial management behavior in food industries [2]. But there has been too little concern toward implementing simulation in plans and schedules on a weekly or even daily basis from industry people.

In order to explore the effects of implementation of simulation at the factory floor, we conducted a simulation study at a tin container production line. The objective of the study was to maximize production rate through minimizing serious bottlenecks identified at various stages by proposing several scenarios without altering existing facility. Simulation study is carried out through several orientation visits to the plant and getting familiar with the system components [3, 4]. Among available simulation software's such as Arena 10.0, ProModel, Process model, etc., Arena 10.0 was used to run real-time simulation and build the system model. With the simulation run results, congestions in different stages on the production line were determined. Through simulation experiments, several scenarios were developed to identify feasible solution to increase production rate. Introduction of change into existing system always has a cost attached to it. Therefore, payback period of capital investment was also calculated [5].

## 2 Methodology

To accomplish the objective of the study detail analysis of requirements of simulation was carried out. All the stages, their processes, inter-arrival times, and resources are identified and reported. Then, a simulation model is built using modules of simulation software and it has to be verified and validated so that it represents true behavior of the existing system. Once we arrive at a validated model, it is used to conduct the simulation experiment to look for feasible solution which maximizes the productivity of the plant.

### 2.1 *Description of Production Process and Simulation Model*

The manufacturing process of the tin container at the LVT containers, Hubballi has five main stages, namely side seam welding, stretch forming, body flanging, top seaming, and bottom seaming. These stages have been adapted by LVT containers, and hence the simulation study has been carried out on same processes and same sequence has been used for analysis. The production starts with welding of tin sheet across its edge to form one enclosed material. Next stage is concerned with providing

the rectangular shape to the tin sheet which is called as stretch forming. Thereafter, it is body flanging stage in which the rectangular containers edges are tapped to form the flanges at the top and bottom side. Finally, top and bottom seaming stages are carried out to attach the plates at the respective ends. Top seaming and bottom seaming stages are shown under single block in Fig. 1.

During plant visit orientation, data on arrival rates, processing times of five stages, activity times, and breakdown times were obtained from observation data handbook of LVT containers. Further, for authentication purpose, obtained data was physically verified with the handbook data during actual operation of all processes. These were used as inputs for developing a simulation model. Table 1 shows the processing times of each stage with failure statistics.

For the simulation study Arena 10.0 software is used and based on the data distribution collected “As-is” model is developed as shown in Fig. 2.

**Verification and Validation:** For verification, Simulation software Arena was used to prove that movement of entities is same as the flow of the parts in the existing tin production line. Simulation model is a duplicate version of real system, whose

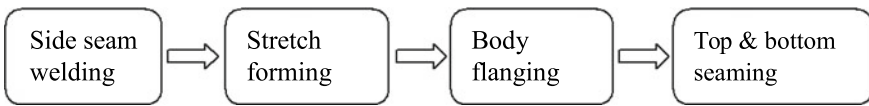


Fig. 1 Stages of tin container production line

Table 1 Data distribution table

Processing stages	Processing time (s)	Workstation breakdown	
		Uptime (s) (expo)	Repair (s) (uniform)
1	6	–	–
2	9.13	–	–
3	8.5	1800	120,240
4	9.39	–	–
5	9.55	–	–

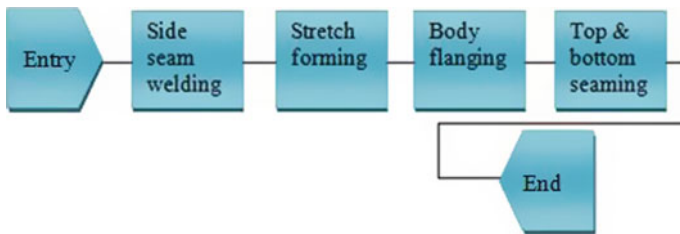


Fig. 2 “As-is” Arena model of current system in Arena software

**Table 2** Stage wise congestions observed

	Side seam welding	Stretch forming	Body flanging	Top seaming	Bottom seaming
Avg. no in queue	0	20.25	15.98	2.4	1.035
Avg. waiting time	0	30.15	22.39	12.44	6.01

behavior should match to that of system as much as possible [5]. Therefore, the validation of the Arena model is done, which requires model to show number of parts produced same as number of parts produced by real system. Through simulation run, the number of parts produced per day was 2280 and according to the plant records number of parts produced per day was 2100 which is acceptable.

### 3 Simulation Runs and Experiment

As-is model of the current system is analyzed thoroughly and for 8 h of plant operation average number of queues and average number of waiting time at each stage is noted down with the help of results obtained from simulation software.

The critical points to be measured were average number in queue and average waiting time. Through simulation run, values of these critical points were tabulated as shown in Table 2. As per our objective, we need to minimize the congestions at each stage starting with the most effecting productivity. A scenario is introduced in the exiting process line, which has the potential to eliminate the critical points, i.e., congestions. Two scenarios are being tested in the simulation software namely scenario number 1: elimination of jam failure at the third stage and scenario number 2: addition of side seam welding machine.

### 4 Results

It is clear from Table 3, the number of containers produced per day from scenario 2, which we assume as optimal scenario is 469 more than existing system production rates, i.e., 2569 containers per day. We can say that there was around 22% increase in production rate. The workstations utilization at each stage has also enhanced due to the changes tested in the production line.

To have a better understanding of impact of simulation study on the existing system of the tin production line, Table 4 provides a comparative statistics of current situation of the system and optimal scenario from the simulation study. Severe congestions

**Table 3** Outcomes after proposed scenarios from the simulation

Scenario		SSW	SF	BF	TS	BS	ANP
1	ANQ	0	14.90	11.65	1.47	0	2228
	AWT	0	23.71	16.18	5.41	0	
2	ANQ	0	10.11	7.37	0	0	2569
	AWT	0	18.04	8.23	0	0	

ANP Avg. number of containers produced, ANQ Avg. number in queue, AWT Avg. wait time, SSW side seam welding, SF stretch forming, BF body flanging, TS top seaming, BS bottom seaming

**Table 4** Comparative statistics

		SSW	SF	BF	TS	BS
Current situation	ANQ	0	20.25	15.98	2.4	1.035
	AWT	0	30.15	22.39	12.44	6.01
Optimal scenario (2)	ANQ	0	10.11	7.37	0	0
	AWT	0	18.04	8.23	0	0

observed at each stage have also been eliminated as average number in queue and average waiting time of parts are reduced.

## 5 Payback Period Calculation

The proposed scenario calls for additional cost to be invested. Hence, it is necessary to conduct cost analysis to check whether the change proposed to the system is economically viable or not. Table 5 shows days required to recover the capital invested for both scenarios 1 and 2.

## 6 Conclusion

Operational level management of many small scale industries run without proper guidance and perhaps less technologically supported. This particular study was successful in implementing simulation tool at an operational level, wherein the main objective of increasing the production rate was increased by almost 22% and reducing average waiting times and average number of queue at each stage of the production line. The number of days required to recover the capital invested for implementing proposed scenario is estimated to be 13 days.

The biggest challenge in implementation of simulation at an operational level is convincing the plant management that using simulation in this way, along with improvised computer tool support, has large impacts on plant itself. The technical



**Table 5** Cost table of scenarios

Scenarios	Cost of scenario (Rs)	Cost of labor (Rs/day)	Containers/day	Additional containers/day	Net profit of scenario/day (Rs)	Days required to recover scenario cost
	$C$	$X$	$y$	$z = y - 2100$	$p = 81z - x$	$d = c/p$
Current	-	-	2100	0	0	-
Scenario 1	200000	0	2228	128	10368	20
Scenario 2	500000	640	2569	469	37349	13

challenges hindering successful simulation study in this area are not be underestimated. But the development of integrated hardware and software tools, user-friendly graphic interface, have indeed created opportunities to explore more. People in these kinds of industries must be given training and education about simulation software and they should be encouraged to utilize such tools.

## References

1. Simeonov S, Simeonovová J (2002) Simulation scheduling in food industry application. *Czech J Food Sci* 20(1):31–37
2. Minegishi S, Thiel D (2000) System dynamics modeling and simulation of a particular food supply chain. *Simul Pract Theory* 8:321–339
3. Kulkarni RG, Kulkarni VN, Gaitonde VN (2018) Productivity improvement in assembly workstation of motor winding unit. *Mater Today Proc* 5(11):23518–23525
4. Kamble R, Kulkarni V (2014) Productivity improvement at assembly station using work study techniques. *Int J Res Eng Technol (IJRET)* eISSN, 2319–1163
5. Bhaskaran S (1998) Simulation analysis of a manufacturing supply chain. *Decis Sci* 29(3): 633–657

# Productivity Improvement at Actuator Assembly Section Using Manual and Video Work Study Techniques



Rohini P. Tippannavar, Vinayak N. Kulkarni and V. N. Gaitonde

**Abstract** Work study is one of the important productivity improvement tools in industrial engineering methods and practices, through which productivity of man and machine can be improved. Work study has two main approaches, one is method study and other being time and motion study. This paper focuses on improving the productivity by minimizing the time and cost in an assembly section of an organization with the help of both manual and video work study techniques. Results of both the methods are initially analyzed and compared at the end. The existing method followed to assemble the actuators was recorded, and improved method was proposed using industrial engineering methods and practices which consumed less time and also unnecessary movements are eliminated. By adapting the proposed method, productivity improvement of 41.66% is being observed, and the time saved for assembling actuator was found to be 4 min per actuator. Video work study is found to be more accurate than conventional manual work study.

**Keywords** Productivity · Work study techniques · Video work study · Manual work study · Industrial engineering

## 1 Introduction

Work study refers to investigation of work accomplished in an organization by efficiently using the procurable resources like materials, men, machines and capital in order to minimize the time and obtain the highest possible quality of work by causing less fatigue to the labors [1]. It is the basic technique for method study and work measurement. It is systematic both in problem investigation and in obtaining

---

R. P. Tippannavar (✉)

Department of Industrial and Production Engineering, B V B College of Engineering and Technology, Hubballi, Karnataka, India  
e-mail: [rohiniprakash062@gmail.com](mailto:rohiniprakash062@gmail.com)

V. N. Kulkarni · V. N. Gaitonde

School of Mechanical Engineering, KLE Technological University, Hubballi, Karnataka, India  
e-mail: [vinayak33me@gmail.com](mailto:vinayak33me@gmail.com)

© Springer Nature Singapore Pte Ltd. 2020

L. Vijayaraghavan et al. (eds.), *Emerging Trends in Mechanical Engineering*,  
Lecture Notes in Mechanical Engineering,  
[https://doi.org/10.1007/978-981-32-9931-3\\_13](https://doi.org/10.1007/978-981-32-9931-3_13)

the solution. It can be accomplished by uninterrupted analysis of work in the selected area where the activities are taking place [2]. Work study involves investigation of the work done in the organization to make the best possible use of the available resources [3]. Work study mainly focuses on simplifying the work which increases the productivity. It makes use of work measurement to evaluate the work content. Work study aims at eliminating the unnecessary time involved in the process [4]. Bon and Daim conducted a study which focuses on increasing the productivity by minimizing the costs. The results showed that the cost and time saved can be utilized further to develop the organization through different work study techniques [4]. Kulkarni et al. studied the cycle time of different work stations in an assembly unit and proposed a new better method for performing assembly operation by reducing unwanted motion involved in the operation by memo motion study [5]. Similarly, Kamble and Kulkarni suggested that the ineffective time and unwanted motions have to be observed and removed from any assembly section to improve the productivity through work study concepts [6]. Although some work has been done in the area of work study, time study and motion study in different industrial scenarios, there are very few works based on concentrated work on work study and ergonomics. Especially, the comparison between manual work study and video work study has not been concentrated in many areas of research works mentioned above. In the present study conducted, it was observed that more time was consumed to assemble an actuator due to unnecessary movement of the worker, affecting the productivity of the assembly unit. Systematic arrangements were not followed in the assembly section of an electrical actuator unit, and hence the time consumed to assemble was more. Therefore, the objective of the present study is to “study and improve the existing method of assembling electrical actuators by suggesting improved method so as to simplify the work and eliminate the inappropriate time involved in the assembling process.” The following sections of the paper explain the application of manual work study technique and video work study technique for studying the existing method and proposing new method for improving the productivity of assembly unit. Video work study used in this project is one of the easiest and simplest methods for work study purpose. The results obtained through video work study are more accurate than manual work study. This method consumes less time, and hence it is an effective and quick way for improving the operations in any organization.

## 2 Methodology

The methodology starts from conducting structured interviews and ends with comparing the manual and video work study. The following section discusses the details of methodology adapted for this project work (Fig. 1).

The study represents the application of work study techniques to improve the productivity. During the initial field survey, the plant layout was studied. The selected industry was small and medium scale (SME) that involved the manufacturing of actuators. The problems were identified in the assembly section. It was observed that

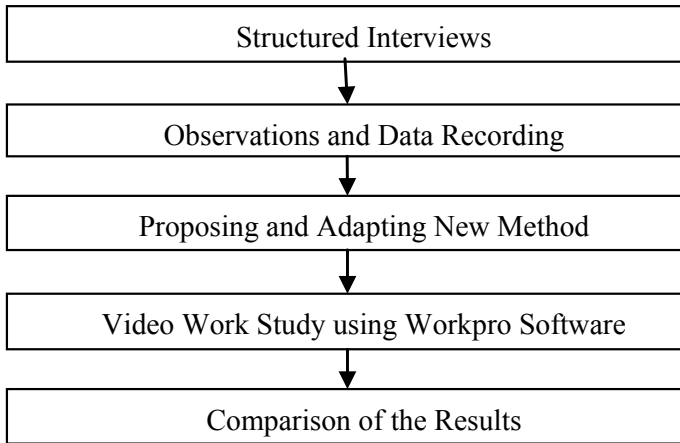


**Fig. 1** Methodology

many operations were repeated which consumed lot of time. There was unnecessary movement of workers to pick the materials which also resulted in consumption of extra time. This affected the productivity of worker. Hence the further section of this paper highlights the methodology used to address the above use.

- **Structured interviews regarding the existing method:** Details of the existing method in the assembly section of the organizations were discussed with the production manager, supervisors and the workers. Several basic questions were asked during the interviews. The discussion was followed by both formal and informal sessions. The higher managers along with workers were involved in the discussions before proceeding to observation and recording section.
- **Observations and data recording of the existing method:** The existing process of assembly was observed and recorded. All the relevant data were collected to examine. A manual flow process chart of workers assembly work was drafted. The identified problems in existing method for assembling were analyzed with the help of work study techniques, i.e., method study and work study. Method study is where the production methods are improved, and work measurement where the human activities are assessed [7]. The assembly section had the fastener tray which consisted of variety of fasteners which were not sorted. It had no compartments, and hence time consumed while searching for a particular type of fastener was more. Different cylinders were all kept together near the assembly area which made the area messier. Connecting wires were all kept on the table without separating. During the final step of assembling, the tightening of nuts was made with spanner which consumed extra time. This caused fatigue to the worker since he had to bend every time as observed.
- **Proposing and adapting new method:** Considering all the circumstances of the existing method and through a detailed analysis of flow process chart of existing method, a new method for assembling the actuators has been proposed which not

only reduces the ineffective time and reduces the fatigue of the workers but also is economical. A new flow process chart was drafted where the unnecessary operations were eliminated. The fastener tray was designed with several compartments. The assembly components with stand were made accessible near the assembly section which helped eliminate the unnecessary movement of the worker. For the cylinders, a separate rack was made in a single stand and different cylinder sections were named, and the cylinders were kept in the respective racks. This made the assembly section spacious and clean. The connecting wires were stored in different bins. Instead of spanner, an air gun bush was given which made the tightening of nuts quicker, and fatigue of the worker was also reduced. The assembling time was reduced. Suggestions to vary the method of assembling steps were also given which helped to reduce the cycle time. The proposed method was presented to all the members of the organization using demonstrations.

- **Video work study using WorkPro software:** Video work study involves the use of video to study the selected work. During manual work study, there are many situations which are difficult to observe because of the high-speed activities or complexity of the operation, and to avoid those situations, video work study is adapted [8]. In this study, the video work study was done at the assembly section which involved a lot of hand motions and movement of the worker. Video work study was carried out for both existing and proposed methods. The equipments used for this study were Nikon L-120 camera and a tripod stand. The tripod was placed at the right place with the camera, and the video was taken. The video was later extracted for the analysis. The analysis of the video was done by the WorkPro software. Video work study which is profitable is one of the easiest and simplest methods for work study purpose. This method consumes less time to give the results, and hence it is an effective and quick way for improving the operations in any organization. It uses multi-media and database technologies to do the Video Time Study (VTS) and Video Method Study (VMS) which are helpful in manufacturing and allied sectors to set the new records.
- **Comparison of the results between manual and video work study:** After the results are obtained from the software, a comparison is made with the manual work study results. It also compares activity between machines and workers hence providing accurate results. There are many in detail and in depth analysis that can be obtained through video work study.

### 3 Data Analysis and Results

Analyzing data is important to obtain the desired results. Based on the data collected, the analysis is carried out. Manual work study data was obtained using stopwatch and paper. A flow process chart was plotted based on the data collected. Video work study gives the flow process chart, standard time and delay analysis charts through WorkPro software. The comparison of manual work study of existing and proposed

**Table 1** Comparison of existing and proposed methods of manual method

Activity	Existing (s)	Proposed (s)	Savings (s)
Operation	321.7	209.7	112
Inspection	26.04	29.57	-3.53
Transportation	228.6	62.12	166.48
Delay	5.97	9.89	-3.92
Total	582.31	311.28	271.03

**Table 2** Comparison of existing and proposed methods of video work study method

Activity	Existing (s)	Proposed (s)	Savings (s)
Operation	330.32	209.94	120.38
Inspection	29.12	29.271	-0.15
Transportation	178.64	61.051	117.58
Delay	6.02	9.82	-3.8
Total	544.100	310.082	234.018

**Table 3** Comparison of manual and video work study

Work study type	Existing (s)	Proposed (s)	Savings (s)
Manual work study	582.31	311.28	271.03
Video work study	544.100	310.082	234.018

methods is as shown in Table 1. The comparison of manual and video work study is shown in Table 2.

From Table 1, it is seen that the work study is analyzed in the form of operation, inspection, transportation and delay activities. It can be observed that the transportation consumes 228.6 s because of improper work layout. Operations consume 321.7 s since there are many unnecessary movements involved. Table 2 shows the analysis of video work study where the time consumed is more accurately obtained. In Table 3, it is seen that by implementing the suggested method, the overall time to assemble the actuator is reduced to 311.28 s from 528.31 s. Hence 271.03 s of time is saved. From Table 2, it is seen that the assembly time in video work study for existing method is 544.100 s, whereas for proposed, it consumed 310.082 s by saving 234.018 s of time.

### 3.1 Video Work Study for Existing Method

See Figs. 2, 3 and 4.

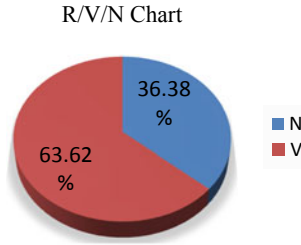


Fig. 2 R/V/N chart for existing method

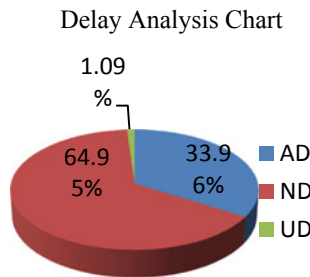


Fig. 3 Delay analysis chart for existing method

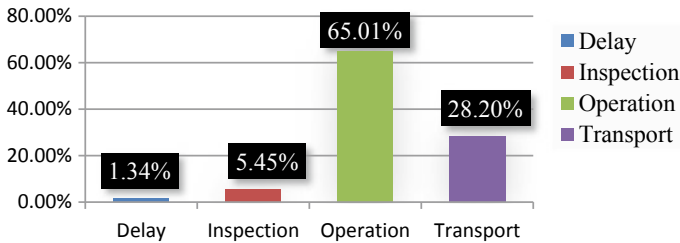


Fig. 4 Flow analysis chart for existing method

### 3.2 Video Work Study for Proposed Method

Figure 2 is the R/V/N chart of existing method where R stands for required non-value added time. V stands for value added time which is 63.62% and N stands for non-value added time which is 36.38%. Figure 3 represents the delays involved during the assembly process. The avoidable delay (A) occurred is 33.96%, no delay (ND) occurred is 64.95% and unavoidable delay (UD) occurred is 1.09%. Figure 4 represents the flow analysis chart where the time consumed by various activities is recorded. In the existing method, the transportation involved is 28.20%. Figure 5 represents the R/V/N chart of proposed method where the value added time is improved



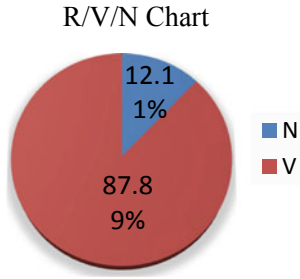


Fig. 5 R/V/N chart for proposed method

to 87.89%, and non-value added time is reduced to 12.11%. Figure 6 represents the delay analysis chart of proposed chart where the avoidable delay (AD) is 39.64%, no delay (ND) is 58.02% and unavoidable delay (UD) is 2.34%. In Fig. 7, the flow analysis chart of proposed method shows the transportation is reduced to 19.92%.

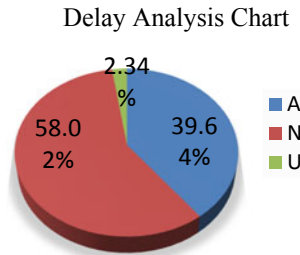


Fig. 6 Delay analysis chart for proposed method

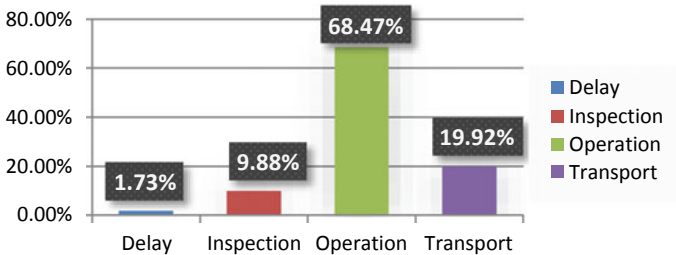


Fig. 7 Flow analysis chart for proposed method

## 4 Conclusions

Elimination of unnecessary time was possible by proposing new method. Reduction of unnecessary movements was observed by rearranging the assembly layout and also by designing of fastener tray with different compartments, storage bins for different wires, and the working area was rearranged by systematically placing the cylinders in the shelf. By adapting the proposed new method, the inappropriate or any repeated operations were eliminated which resulted in saving time. Productivity improvement of 41.66% was seen. Therefore, it can be observed that a good profit can be obtained to the organization by using the work study techniques as the productivity of the labor increases. Also, work layout changes make worker more comfortable while working on assembly section. After the comparison of existing method and proposed method was made, it was observed that the time taken to assemble one eight-inch actuator per day was 9.7 min in existing method and was reduced to 5.7 min. The actuators assembled per day by per worker were increased from 24 actuators to 34 actuators. Hence the productivity of actuators per day with two workers was observed from 48 actuators to 68 actuators. From the obtained data, it was found that the profit from one model of eight-inch actuator is Rs. 240. Productivity improvement per day has increased to 68 actuators from 48 actuators. Hence the total profit per day for the improved productivity is  $20 * 240 = \text{Rs. } 4800$  per day. If the proposed method is adopted, then the profit for the company can go up to Rs. 14,40,000 per year (considering 25 days working per month). After adapting the proposed method, increased efficiency in productivity was observed which helped in enhancing the industry's profitability.

## References

1. Singh MP, Hemant Y (2016) Improvement in process industries by using work study methods: a case study. *Int J Mech Eng Technol*, 426–436
2. Parthiban P, Raju R (2012) Productivity improvement in shoe making industry by using method study. *IOSR J Mech Civil Eng*, 1–8
3. Mwanza BG, Mbohwa C (2016) Application of work study for productivity improved: a case study of a brewing company. *Int Conf Ind Eng Oper Manag*, 296–305. Kuala Lumpur, Malaysia
4. Bon AT, Daim D (2010) Time motion study indetermination of time standard in manpower process. In: 3rd Engineering Conference on Advancement in Mechanical and Manufacturing for Sustainable Environment
5. Kulkarni RG, Kulkarni VN, Gaitonde VN (2018) Productivity improvement in assembly workstation of motor winding unit. *Mater Today Proc* 5(11):23518–23525
6. Kamble R, Kulkarni V (2014) Productivity improvement at assembly station using work study techniques. *Int J Res Eng Technol* 3. eISSN: 2319-1163
7. Bagri GP, Raushan P (2014) Productivity improvement of forging section using work study and automation in existing axle manufacturing plant. *Int J Mech Prod Eng* 2. ISSN: 2320–2092
8. Malhar S, Kulkarni V, Gaitonde VN (2017) Ergonomics work standardization study for identifying and improving critical work stations using lean manufacturing concept—a case study on LCV assembly shop. *Int J Darshan Inst Eng Res Emerg Technol* 6(2):18–26

# Development and Characterization of Polyamide Fiber Composite Filled with Fly Ash for Wind Turbine Blade



J. Joy Mathavan and Amar Patnaik

**Abstract** Proposing a suitable material for wind turbine blade is discussed in this paper. Low weight, high stiffness, high strength, and long durability are some of the salient features a material should possess to act as the wind turbine blade. Carbon fiber, glass fiber, and aramid fiber are used as blade materials in these days because they meet most of these features. In addition to, fly ash as filler material with polyamide fiber is discussed in this paper. The specimens were prepared by hand layup process. Erosion test is performed in air-jet erosion tester. The graphs are drawn according to smaller the better criteria of Taguchi L25 orthogonal array of two factors and five variables. Graphs obtained from dynamic mechanical analyzer for tensile test and three-point bending test are compared for different specimens. Hardness values are calculated by Rockwell hardness tester, and densities are calculated to analyze the void content.

**Keywords** Aramid fiber · Fly ash · Tensile strength · Wind turbine blade

## 1 Introduction

Getting rid of dependency on fossil fuel is an important objective for all the nations of the world today. The concentration is pointed on renewable sources of energy to achieve this target. Wind energy is an important source of renewable energy, and it is an environment-friendly way of obtaining energy [1]. So, it is important to utilize it and obtain a maximum use of it. Wind turbine is a method of converting wind power into energy. Proposing a suitable material for wind turbine blade is discussed in this paper. One of the main objectives of wind turbine blade research is to keep the weight of the blade under control [2]. Because the weight of the blade

---

J. Joy Mathavan (✉)

Faculty of Technology, University of Jaffna, Jaffna, Sri Lanka

e-mail: [joymathavan1991@gmail.com](mailto:joymathavan1991@gmail.com)

A. Patnaik

Malaviya National Institute of Technology, Jaipur, India

e-mail: [patnaik.amar@gmail.com](mailto:patnaik.amar@gmail.com)

© Springer Nature Singapore Pte Ltd. 2020

L. Vijayaraghavan et al. (eds.), *Emerging Trends in Mechanical Engineering*,

Lecture Notes in Mechanical Engineering,

[https://doi.org/10.1007/978-981-32-9931-3\\_14](https://doi.org/10.1007/978-981-32-9931-3_14)

theoretically increases with the cube of its length, the power output only increases with the square of the length [1]. This is the reason why more attention is paid to the weight of the blade. To achieve this target, in the field of wind energy, a new material composite has been fabricated and tested for erosion in air-jet erosion tester. The erosion of turbine blade material is unavoidable, which in turn decreases the efficiency, reliability, and operating life of turbine blades. However, excessive erosion may lead to lack of performance. In order to minimize the erosion, extensive developments have been carried out for past few years by material researchers. The major areas of consideration when talking about windmill are the material used to make blade and rotor, shape of the blade, the coatings used on blades, and the optimum length of blade [3]. With the development in technology, different materials including carbon fiber, glass fiber, and aramid fiber are tested for wind turbine blade material considering its expected qualities like low weight, high stiffness, long fatigue life, high strength, long durability, and electrical and thermal resistance [4].

## 2 Research Background

Wind turbine blades were made up of aluminum and its alloys at the initial stage. But, thermal damage due to lightning strike [5], poor resistance due to corrosion and vibration of blade by wind load when it rotates were some problems accompanied and, in turn, resulted in the failure of the above-mentioned material [1]. Wind turbine blades made up of coated timber were used in developing countries, (mostly in remote areas of those countries) because of their economic conditions. It could be made by local carpenters is an additional advantage of this material. But, the blade material was limited for certain kinds of timbers, and the length of the blade was small [6]. It was used for small-level necessities. Currently, carbon-fiber-reinforced polymer, glass-fiber-reinforced polymer, and aramid-fiber-reinforced polymer are being used for manufacturing wind turbine blades [2]. Compared to aluminum alloys and coated timbers, the weight of these fibers is very low [7]. These fibers have high stiffness-to-density ratio, high strength-to-density ratio, and good fracture toughness [8]. According to the past studies, glass fiber has good electrical and mechanical properties and also has high heat resistance [9]. But, they are dielectric in nature [5]. Carbon fiber has an outstanding combination of high stiffness, light weight, high strength, and low density [9]. But, they are electrically conductive in nature [5]. Carbon fibers are three times stiffer, two times stronger, and also five times costlier than glass fibers [10]. Aramid fiber (aromatic polyamide) has admirable environmental and thermal stability, static and dynamic fatigue resistance, wear resistance and impact resistance [9].

Aramid fiber has the highest specific tensile strength (strength/density ratio) among all commercially existing continuous-filament yarn. They have very low densities [9]. But all of them (glass and aramid fibers for small blade and carbon fiber for long blade) are used across the world today [11]. It is anticipated that the addition of inorganic filler material will help to improve the required qualities of the fiber

composite to be used as wind turbine blade. In this study, fly ash is added in different percentages with polyamide fiber and polyester resin combination and tested for erosion behavior under air-jet erosion tester. It is noticeable that the tests performed for hydraulic turbine blade material having granite dust as a filler material gave good results while considering stability and durability [12].

### 3 Experimental Procedure

#### 3.1 Preparation of the Specimens

The composition of wind turbine blade material contains a polymer matrix (organic part), inorganic filler particles (distributed part), and an adhering agent to bind filler with matrix (interface). Here, polyamide needle fiber considered as the base material, fly ash is the filler material, and polyester resin is taken as adhering agent. Incorporating inorganic fillers to the fiber composites results in increment in mechanical properties (such as hardness, density, and tensile strength) [12].

Addition of any filler which can work on the perception of resistance to erosion and good in mechanical properties will be beneficial for the researches in the field of wind turbine blade material. In the current work, it is fly-ash-filled with polyamide needle fiber. The major elemental constituents of fly ash are Si, Al, Fe, Ca, C, Mg, K, Na, S, Ti, P, and Mn, and it has a specific gravity of 1.22–1.225 g/cm<sup>3</sup> [13]. So, it can enhance the erosion resistance and hardness values which will satisfy the requirements along with better physical, mechanical, and tribological properties. We can study the preparation and testing procedures in three steps. First step is preparing composite material, i.e., the fabrication of polyamide fiber composite filled and unfilled with fly ash. Second step is testing the prepared composite material samples for erosion properties. This includes the determination of erosion rate with its impact factors such as impingement angle and percentage addition of fly ash. Third step is experimenting with mechanical properties. It includes the characterization of physical (density), mechanical, and thermo-mechanical properties (hardness, tensile strength, and three-point bending) of polyamide fiber composite samples filled and unfilled with fly ash.

The designation and composition of samples are shown in Table 1. Hand layup method is used to prepare the specimens. In this method, polyamide fiber gets added layer by layer and polyester resin mixed with fly ash used as the matrix to adjoin and strengthen the composite. Specimens of 20 \* 10 cm were prepared, and they were cut into necessary dimensions according to the requirement of the tests performed.

**Table 1** Sample designation and composition

Sample designation	Composition
Specimen 1	Polyamide fiber + polyester resin
Specimen 2	Polyamide fiber + polyester resin + 5% fly ash
Specimen 3	Polyamide fiber + polyester resin + 10% fly ash
Specimen 4	Polyamide fiber + polyester resin + 15% fly ash
Specimen 5	Polyamide fiber + polyester resin + 20% fly ash

### 3.2 Description about the Tests

The samples were tested for erosion in air-jet erosion tester (TR-871-400) as per the standards of ASTM G76 international test method. The experiments were conducted under air-jet velocity of 60 m/s because 56 m/s is the maximum normal wind velocity measured on earth. To test the variation of impingement angle, there are specimen holders of five different angles 30°, 45°, 60°, 75°, and 90°. The specimens were cut in a shape of 25 \* 25 mm to fit into the specimen holder. The feed rate of erodent was fixed at 5 g/min. The erodent used for the experiment was 50-micron-sized normal sand (SiO<sub>2</sub>) because most of the erodent particles that strike the wind turbine blades mixed with wind are of this category. The experiments were conducted at 40 °C average temperature. The erodent feed rate and velocity of the air jet in air-jet erosion tester kept constant throughout the experiments. Weights of the samples were weighed by Precisa 125 A balance. Its least count is 1 mg and the range is 0–450 g. The samples were cleaned before and after the experiments, and the weight loss was calculated. The tensile test is conducted in dynamic mechanical analyzer (DMA 8000). The maximum thickness of the sample is 3 mm and length can be varied in between 10 and 20 mm to suit the machine standards. The width is kept around 5 mm; because if we increase the width, it may result in an improper holding of the sample in the clamp. Hardness test is performed in Rockwell hardness tester according to ASTM E-18 standard. An average of ten independent tests were performed and the average of them taken into account.

## 4 Results and Discussion

### 4.1 Erosion Analysis

Taguchi orthogonal array is used to analyze the erosion rate. In a Taguchi designed experiment, we manipulate noise factors to force variability to occur and from the

results, identify optimal control factor settings that make the process robust to variation from the noise factors [14]. This is known as signal-to-noise (SN) ratio. Lower the erosion rate, better to be used in our applications. Based on this, smaller is better criteria in Taguchi table was chosen, and the equation for it is shown below. Here, n is the simulation repetition number under the same design parameter conditions and Y is the measured results.

$$S/N = -10 \log \left[ \frac{\sum (Y^2)}{n} \right] \tag{1}$$

The results attained from Taguchi analysis table of L25 orthogonal array, 5 \* 2 (5 factors and 2 variables) are shown in Figs. 1 and 2. The percentage addition of fly ash and the angle of impingement are the two variables here. The signal-to-noise ratio for angle of impingement shows 90° is the best applicable angle to minimize erosion and 75° stands the next. The Taguchi graph shows that the erosion rate is

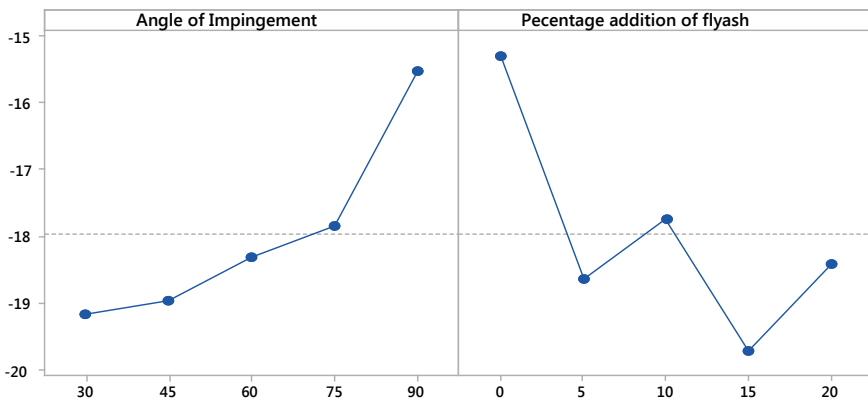


Fig. 1 Results of erosion analysis—mean of SN ratios

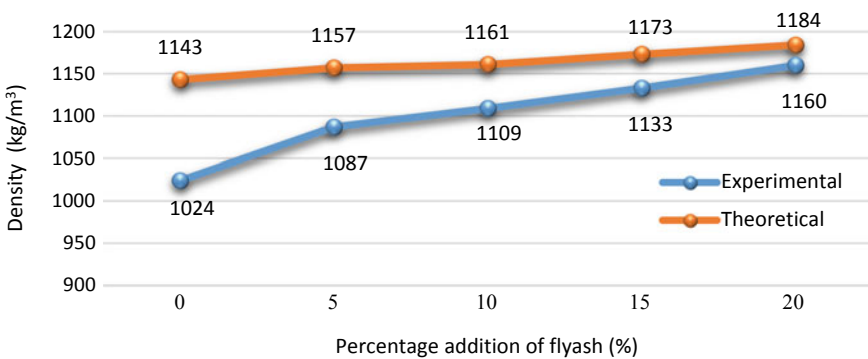


Fig. 2 Theoretical and experimental density comparison

decreasing generally when we increase the impingement angle. While we consider the percentage addition of fly ash, pure polyamide fiber sample and 10% fly ash added fiber are good for the application because both of them are above the mean line. It can be noticed that both 5 and 15% fly-ash-added specimens show low erosion resistance.

## 4.2 Density Analysis

The density analysis is a major component to be considered while discussing the material selection for wind turbine blade material. High stiffness-to-density ratio and high strength-to-density ratio are desirable characters of a material to be used in this field. Carbon fiber, glass fiber, and aramid fiber already possess these qualities [8]. Generally, the theoretical density can be found for any composite material in terms of weight fraction by the equation given below [15].

$$\rho_{cm} = 1 / [(w_p / \rho_p) + (w_m / \rho_m) + (w_f / \rho_f)] \quad (2)$$

Here,  $w$  denotes weight fraction and  $\rho$  denotes density.

The suffixes denote the individual constituents used here. (p—polyamide fiber, m—matrix, f—fly ash, and cm—composite material). There are three constituents in this composite, which are matrix-polyester resin, polyamide fiber, and particulate filler-fly ash. Traditional water immersion method is used to find the actual density ( $\rho$ ) of the composite experimentally. From the graph, it can be observed that the density values are increasing with the increase in percentage addition of fly ash. The volume fraction of voids getting reduced with the increase in the percentage addition of fly ash. Void content is the difference between theoretical and practical density values.

## 4.3 Hardness Test (RHB)

Hardness is the measure of resistance of a material to localized plastic deformation. As defined in ASTM E-18, the Rockwell hardness test is used to find the hardness of the samples. Several scales may be used from possible combinations of indenters and loads, which permit the testing of all metal alloys and polymers. Indenters include spherical and hardened steel balls having diameters of 1/16, 1/8, 1/4, and 1/2 inch. Conical hard steel with indenter size of 1/16" was used in this experiment. The applied load is 100 kgf. The graph shows the variation of RHB value with the percentage addition of fly ash to the composite. With the addition of fly ash, the hardness values are increasing subsequently (Fig. 3).



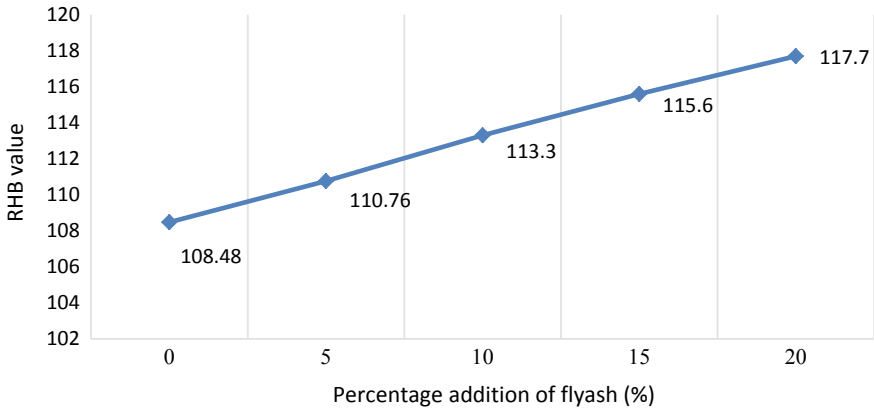


Fig. 3 Rockwell hardness test (B test)

### 4.4 Tensile Test

Tensile test is also done through dynamic mechanical analysis. The samples were cut in the size of 2 \* 3 \* 12 mm in order to keep them in the space provided in DMA. The graph of tensile analysis was drawn for modulus vs temperature. The graphs which are drawn for samples with a different percentage addition of fly ash are then compared. As like the three-point bending test, the peak temperature was fixed at 120 °C. The rate of change of temperature is kept at 3 °C per minute.

Loss modulus means being proportional to the energy dissipated during one loading cycle. For example, it can be said that energy lost as heat and is a degree of vibration energy that has been converted during vibration. It cannot be recovered. Figure 4 represents the variation of storage modulus with temperature. We can see

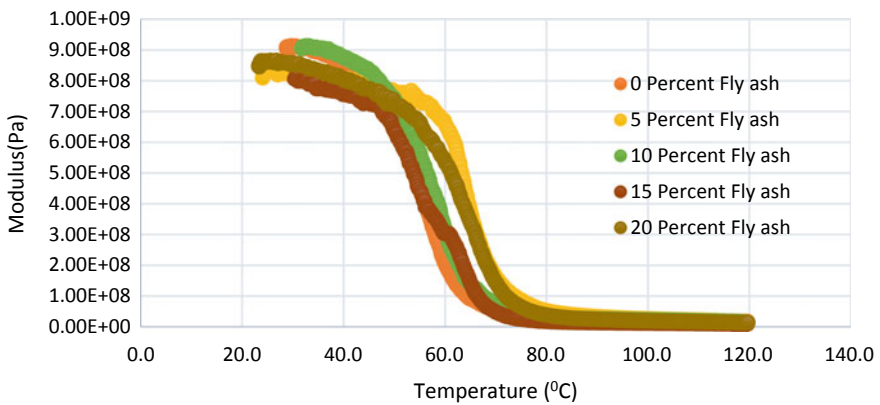


Fig. 4 Variation of modulus with temperature

that there are three significant regions in this graph. There is a zone from 20<sup>0</sup>C to 50<sup>0</sup> C where the modulus values are high; from 50<sup>0</sup>C to 80<sup>0</sup>C there is transmission region where a significant reduction in the storage modulus occurs; and from 80<sup>0</sup>C to 120<sup>0</sup>C the graph shows elastic behavior where the deterioration is severe. It can also be noticed from the graph that 10% granite-dust-added sample has a high modulus of 900 Mpa and 15% granite-dust-added sample has minimum of 800 MPa. All the samples show above 800 MPa, and the range is between 800 and 900 MPa.

## 5 Conclusion

- (1) The impingement angle is a deciding factor in erosion rate. Highest erosion occurred in the angle of 30° and the lowest erosion occurred in the angle of 90°. Erosion rate generally decreasing with increase in angle from 30° to 90°.
- (2) Percentage addition of fly ash is another factor which influences the erosion rate. Lowest erosion occurred in 0% fly-ash-added sample, and it is followed by 10% fly-ash-added sample. Highest erosion occurred when we add 15% fly ash and is followed by 5% fly ash. Since it is showing a zig-zag pattern in this region, further study may give an exact percentage addition of this filler material.
- (3) Density values are increasing with the increase in percentage addition of fly ash. A small deviation observed between the experimental and theoretical densities. The deviation might be occurred because of the absorption of water molecules by the sample when we tested it for practical density. The volume fraction of voids getting reduced with the increase in the percentage addition of fly ash.
- (4) With the increase in the percentage addition of fly ash, the hardness values are increasing.
- (5) When we consider tensile analysis, all the specimens are showing a tensile value above  $8 \times 10^8$  Pa while 10% fly-ash-added sample shows a highest value of  $9 \times 10^8$  Pa. All of them are deteriorating in the region around 60 °C.

The established wind turbine blade composite material shows better tribological, mechanical, and physical characteristics. The erosion resistance of the above composite increases its durability. Its weight is also very less compared to alloys. Hence, in long term, the cost of the proposed material will be reasonable and worthwhile.

## References

1. Kumar A, Dwivedi A, Paliwal V, Patil PP (2014) Free vibration analysis of Al 2024 wind turbine blade designed for Uttarakhand region based on FEA. *Procedia Technol* 14:336–347
2. Ashwill TD, Paquette JA (2008) Composite materials for innovative wind turbine blades. *Wind Energy Technology Department Sandia National Laboratories Albuquerque, NM* 87185

3. Mandell JF, Samborsky DD, Agastra P (2012) Composite materials fatigue issues in wind turbine blade construction. Department of Chemical and Biological Engineering, Montana State University, Bozeman, MT 59717
4. Chen X, Zhao W, Zhao XL, Xu JZ (2014) Preliminary failure investigation of a 52.3 m glass/epoxy composite wind turbine blade. *Eng Fail Anal* 44:345–350
5. Wang Y, Zhupanska OI (2015) Lightning strike thermal damage model for glass fiber reinforced polymer matrix composites and its application to wind turbine blades. *Compos Struct* (in press)
6. Mishnaevsky L Jr, Freere P, Sinha R, Acharya P, Shrestha R, Manandhar P (2011) Small wind turbines with timber blades for developing countries: materials choice, development, installation and experiences. *Renew Energy* 36:2128–2138
7. Jang YJ, Choi CW, Lee JH, Kang KW (2015) Development of fatigue life prediction method and effect of 10-min mean wind speed distribution on fatigue life of small wind turbine composite blade. *Renew Energy* 79:187–198
8. Mustafa G, Suleman A, Crawford C (2015) Probabilistic micromechanical analysis of composite material stiffness properties for a wind turbine blade. *Compos Struct* 131:905–916
9. Suresh Babu K, Subba Raju NV, Srinivasa Reddy M, Nageswara Rao D (2006) The material selection for typical wind turbine blades using MADM approach & analysis of blades. *MCDM* 2006, Chania, Greece, June 19–23
10. Wind turbine blade structural engineering, *WE Handbook-3-Structural Design*
11. Ancona D, McVeigh J (2001) Wind turbine—materials and manufacturing fact sheet. Prepared for the Office of Industrial Technologies, US Department of Energy by Princeton Energy Resources International, LLC, August 29
12. Mathavan JJ, Shrestha S, Kaifi R, Patnaik A (2019) Analysis of erosion properties of polymer composite filled with granite dust for hydraulic turbine blade material. In: Ghosh S (ed) *Waste management and resource efficiency*. Springer, Singapore
13. Arivumangai A, Felixkala T (2014) Strength and durability properties of granite powder concrete. *J Civil Eng Res* 4(2A)
14. Pouretedal HR, Damiri S, Shahsavvan A (2018) Modification of RDX and HMX crystals in procedure of solvent/anti-solvent by statistical methods of Taguchi analysis design and MLR technique. *Defence Technol* 14:59–63
15. Agarwal BD, Broutman LJ (1990) *Analysis and performance of fiber composites*. Wiley, New York

# Stereomicroscopic Analysis of Fracture Surfaces of Cold Drawn Steel Wires



S. S. Bargujer, Vikas Dagar and Pankaj Chandna

**Abstract** The investigation on the fractured surface of steel wires in the tensile test and torsion test has been carried out using stereomicroscopic technique. The analysis has been done on cold drawn wires subjected to different pass schedules. Investigation revealed that pass schedule having optimum true strain resulted in the best mechanical properties. Hot rolled piano wire rod having carbon percentage 0.87% has been used in the investigation. The fully pearlitic microstructure is developed during lead patenting process of wire rod at 950 °C. The wire rod has been reduced from 7.00 mm diameter to 2.6 mm wire diameter by subjecting it to three different pass schedules. The investigation revealed that highest UTS and TS properties are achieved in pass schedule-1 and pass schedule-2 respectively in the cold drawn wire of diameter 2.60 mm. The high reduction rate per die in pass schedule-1 has a negative effect on torsion strength whereas the low reduction rate per die in pass schedule-3 has negative effect on torsion strength as well as tensile strength.

**Keywords** Hypereutectoid steel wire · Reduction ratio per die · Torsion strength · Tensile strength

## 1 Introduction

The cold drawn hypereutectoid steel wires are widely used for the applications having requirements of ultra-high tensile strength along with high ductility. The ultra-high-strength in the cold drawn hypereutectoid steel wires can be achieved only if the microstructure in the material is fine pearlite. The best method to achieve the fine pearlitic microstructure is lead patenting. In lead patenting process, the hot-rolled piano wire rods are initially heated in austenitic zone up to 950 °C for 5 min approximately and then dipped in a lead bath temperature at 520 °C. The microstructure of

---

S. S. Bargujer · V. Dagar (✉)  
Ordnance Cable Factory, Plot No. 183, Industrial Area-I, Chandigarh 160002, India  
e-mail: [vikasdagar12@rediffmail.com](mailto:vikasdagar12@rediffmail.com)

P. Chandna  
National Institute of Technology, Kurukshetra, Haryana 136118, India

© Springer Nature Singapore Pte Ltd. 2020  
L. Vijayaraghavan et al. (eds.), *Emerging Trends in Mechanical Engineering*,  
Lecture Notes in Mechanical Engineering,  
[https://doi.org/10.1007/978-981-32-9931-3\\_15](https://doi.org/10.1007/978-981-32-9931-3_15)

**Table 1** Chemical composition of hot rolled piano wire rod

S. No.	Chemical element	Percentage (%)
1	Carbon	0.87
2	Manganese	0.56
3	Silicon	0.18
4	Sulphur	0.006
5	Phosphorus	0.007

hot rolled piano wire rods is changed into austenite phase during heating at 950 °C and thereafter changed into pearlite phase by dipping in the lead bath at 520 °C.

The pearlitic lead patented piano wire rods are cold drawn through a sequence of dies. The behavior of cold drawn wires is investigated after passing through three die pass schedules of different reduction rate per die. The quantitative analysis of cold drawn wires of these pass schedules is already reported by Bargujer et al. [1]. However, the qualitative analysis of cold drawn wires of these pass schedules is presented here to understand the role of different reduction rate in the conical converging dies. The stereomicroscopic images of fracture surface of tensile test and torsion test of cold drawn hypereutectoid steel wires are investigated. So far, the numbers of studies [2–10] are carried out to investigate the role of reduction ratio and other parameters [11] for different steel in a pass schedule. However, such detailed investigation of hypereutectoid steel wire is not reported, so far. The objective of this investigation is to further improve the mechanical properties of cold drawn hypereutectoid steel wires.

## 2 Material and Method

The hot-rolled piano wire rod having the chemical composition as mentioned in Table 1 has been used in the experiment.

The optical micrograph and SEM micrograph of lead patented piano wire rod is shown in Fig. 1 and it is confirmed that the microstructure developed in lead patented piano wire rod is fully pearlitic.

## 3 Results

The ultimate tensile strength (UTS) and torsion strength (TS) of cold drawn wires of different wire diameter ( $D_w$ ) against three pass schedules are mentioned in Table 2.

The numbers of conical converging dies used to reduce the wire diameter from 7.00 to 2.60 mm are seven numbers in the pass schedule-1, nine numbers in the pass schedule-2 and twelve numbers in the pass schedule-3. The reduction ratio per die is high, medium and low in pass schedule-1, pass schedule-2 and pass schedule-3

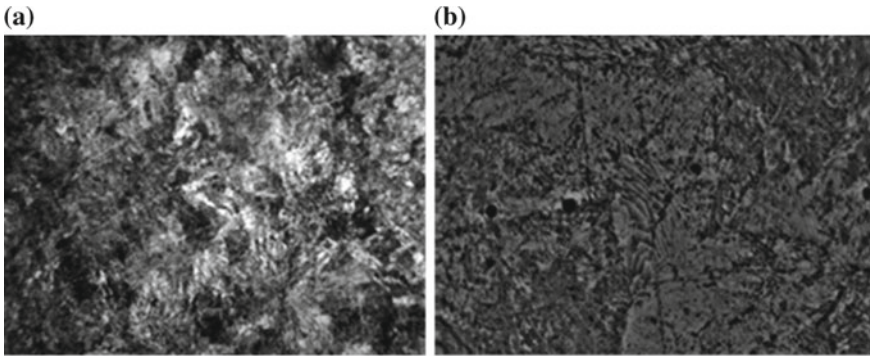


**Fig. 1** a Optical micrograph, b SEM micrograph

respectively. The highest UTS and TS properties are achieved in pass schedule-1 and pass schedule-2, respectively, in the cold drawn wire of diameter 2.60 mm.

### ***3.1 Pass Schedule-1***

The stereomicroscopic images of cup-cone fractured surfaces after UTS test for pass schedule-1 are as shown in Fig. 2.

The stereomicroscopic images of fractured surfaces after torsion test for pass schedule-1 are as shown in Fig. 3.

### ***3.2 Pass Schedule-2***

The stereomicroscopic images of cup-cone fractured surfaces after UTS test for pass schedule-2 are as shown in Fig. 4.

The stereomicroscopic images of fracture surfaces after torsion test for pass schedule-2 are as shown in Fig. 5.

### ***3.3 Pass Schedule-3***

The stereomicroscopic images of cup-cone fractured surface after UTS test for pass schedule-3 are as shown in Fig. 6.

The stereomicroscopic images of fractured surfaces after torsion test for pass schedule-3 are as shown in Fig. 7.

**Table 2** The UTS and TS of pass schedules

Die No.	Pass schedule-1			Pass schedule-2			Pass schedule-3		
	$D_w$ (mm)	UTS (N/mm <sup>2</sup> )	TS (Nos.)	$D_w$ (mm)	UTS (N/mm <sup>2</sup> )	TS (Nos.)	$D_w$ (mm)	UTS (N/mm <sup>2</sup> )	TS (Nos.)
0	7.00	1259.09	30	7.00	1259.09	30	7.00	1259.09	30
1	6.00	1437.16	28	6.00	1437.16	28	6.00	1437.16	28
2	5.00	1625.51	26	5.30	1516.90	48	5.60	1498.56	36
3	4.40	1715.32	38	4.70	1618.64	32	5.20	1560.43	42
4	3.80	1822.52	18	4.20	1733.41	42	4.80	1572.43	40
5	3.40	1889.50	44	3.80	1827.86	32	4.50	1634.16	28
6	3.00	2038.52	22	3.40	1939.85	18	4.20	1658.24	30
7	2.60	2195.65	23	3.10	1964.35	21	3.90	1741.11	30
8				2.80	1995.42	21	3.60	1851.48	32
9				2.60	2080.11	35	3.30	1905.31	16
10							3.00	1938.97	30
11							2.80	1975.62	35
12							2.60	2013.54	26

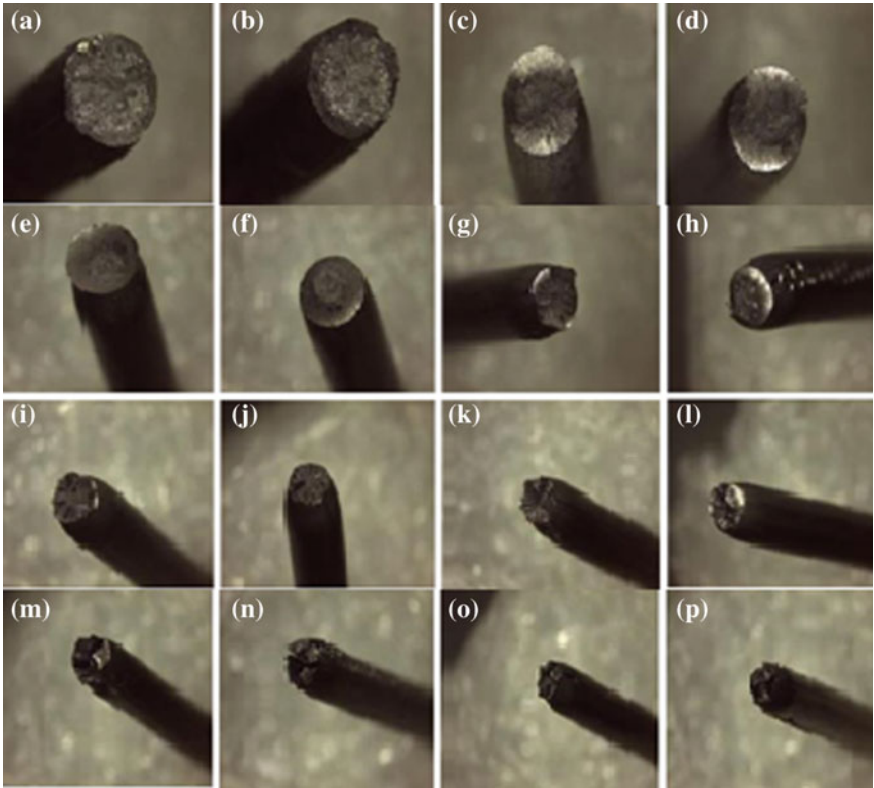


**Fig. 2** The stereomicroscopic images of cup-cone fracture after UTS test for pass schedule-1

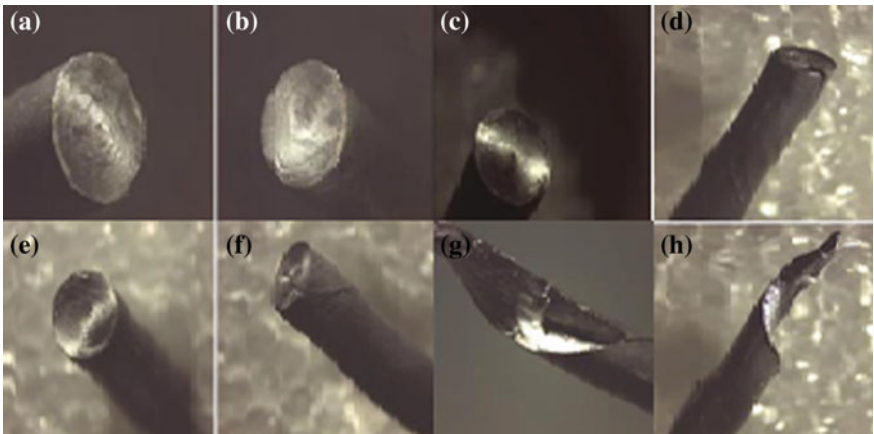


**Fig. 3** The stereomicroscopic images of fracture surfaces after torsion test for pass schedule-1



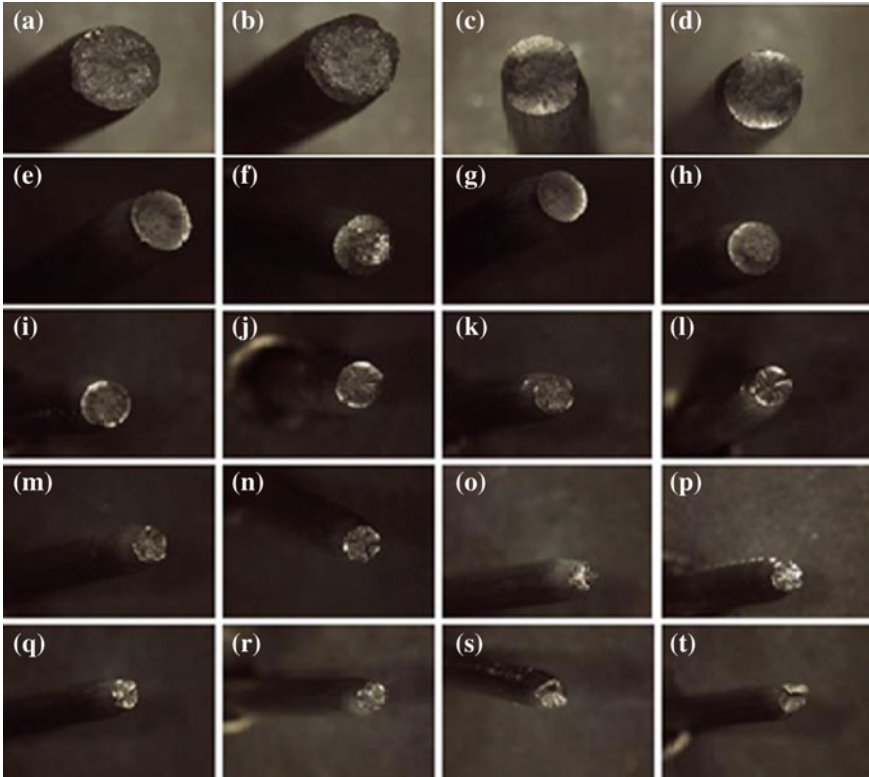


**Fig. 4** The stereomicroscopic images of cup-cone fracture after UTS test for pass schedule-2

## 4 Discussion

The detailed discussion is carried out on all three pass schedules to understand the change in ductility of cold drawn wires. The ductility of cold drawn wire is characterized by the shape of cup and cone obtained in tensile test and by analyzing the fracture surface in torsion test.

### 4.1 Pass Schedule-1

The images of cup-cone fractured surfaces of pass schedule-1 indicate that ductility is highest at third die. After third die, the ductility of the wire starts diminishing as it passes through subsequent dies. The images of fractured surface of pass schedule-1 in torsion indicate clearly that very clean fracture surface is achieved in third die but cracks generated on the surface in fourth die. The fractured surface after fifth die

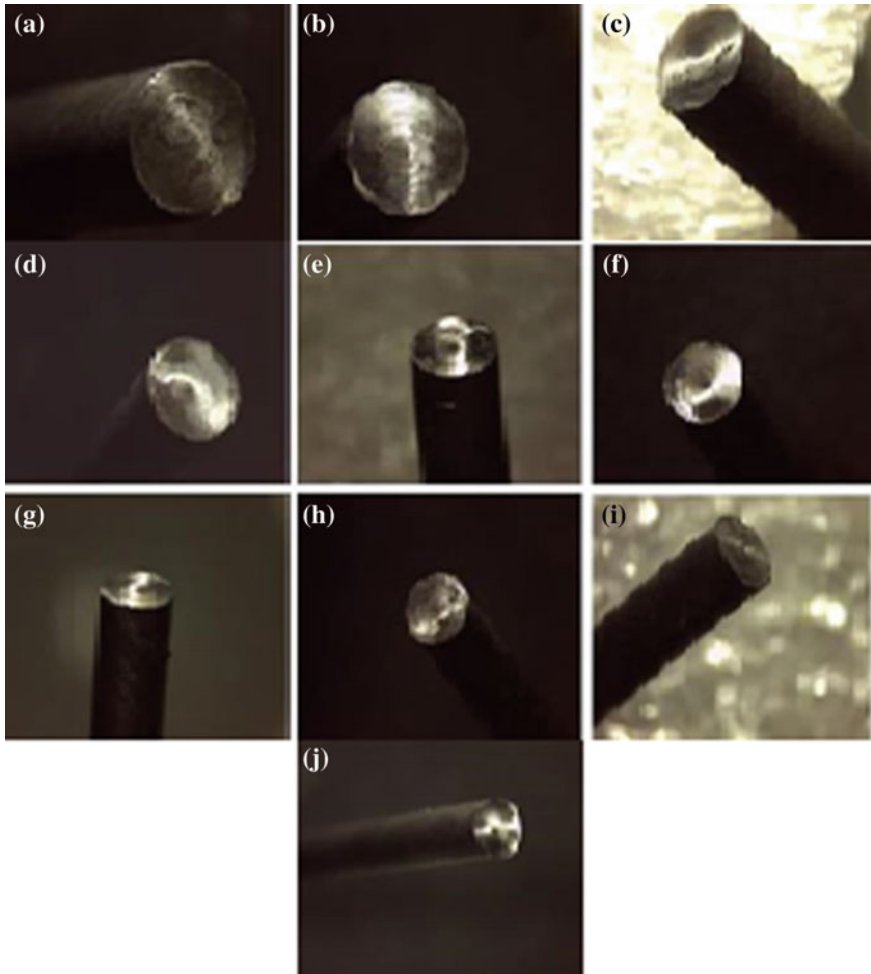


**Fig. 5** The stereomicroscopic images of fracture surfaces after torsion test for pass schedule-2

clearly indicates that wire becomes brittle and cracks are generated in lamellar structure during wire drawing. The degree of brittleness increases with further increase in cold work.

#### **4.2 Pass Schedule-2**

The images of cup-cone fractured surfaces of pass schedule-2 indicate that ductility of lead patented wire is little bit low as compare to ductility of cold drawn wire at third or fourth die. The images of cup-cone fractured surfaces of pass schedule-2 indicate

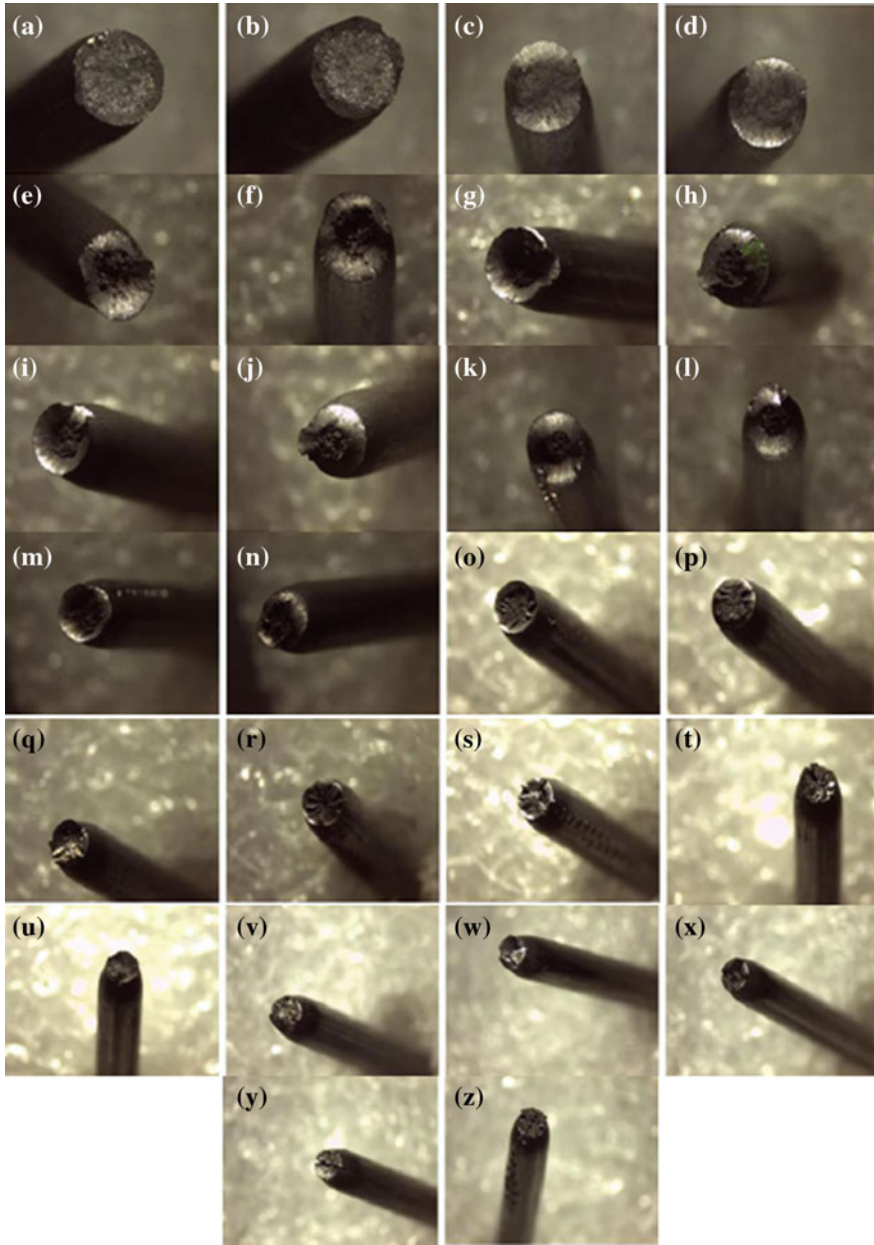


**Fig. 6** The stereomicroscopic images of cup-cone fracture after UTS test for pass schedule-3

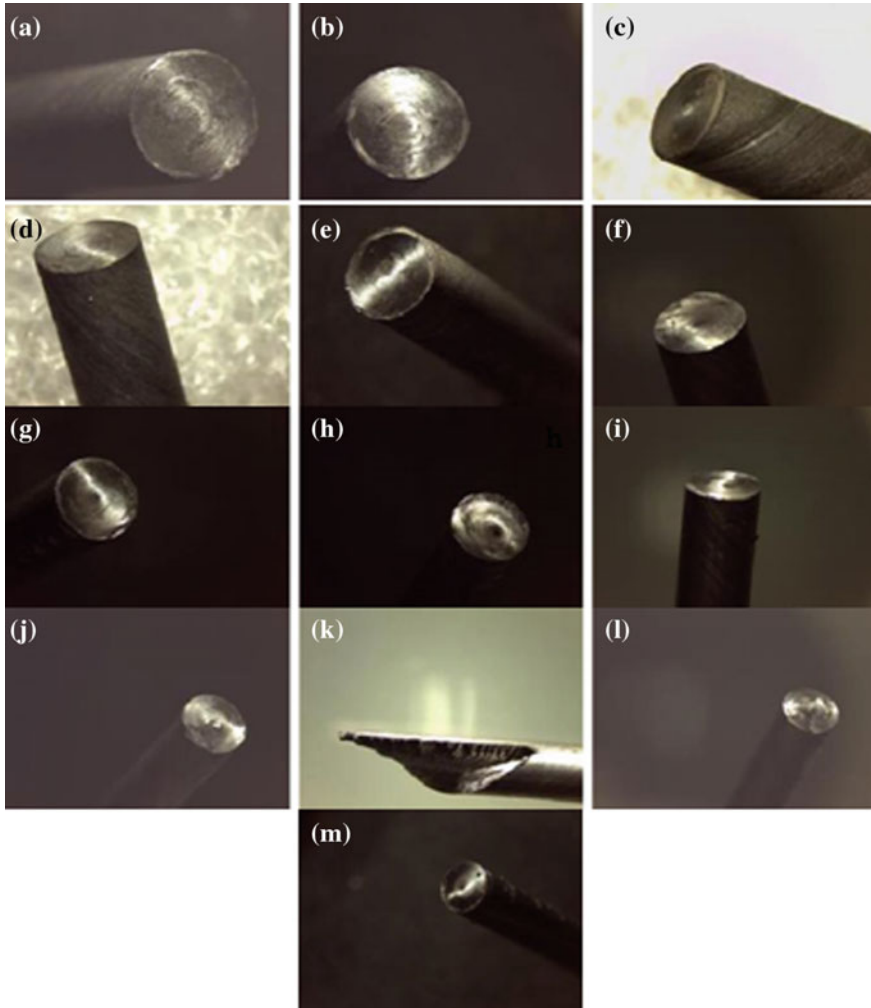


**Fig. 7** The stereomicroscopic images of fracture surfaces after torsion test for pass schedule-3

that ductility of cold drawn wire is maintained even after passing through the last die of pass schedule. The images of fractured surface of pass schedule-2 in torsion indicate that no crack is generated in the fracture surface as well as longitudinal surface of cold drawn wire. This clearly indicates that ductility of cold drawn wire is maintained throughout the pass schedule-2.

### 4.3 Pass Schedule-3

The images of cup-cone fractured surface of pass schedule-3 indicate that wire is able to maintain its ductility up to a reasonable level up to ninth die but minor cracks are developed in cup-cone fracture surface after ninth die. These cracks indicate the loss of ductility in cold drawn wire. The size of these minor crack increases at a slow rate with increases in degree of cold work. The images of fractured surface of pass schedule-3 in torsion indicate that cold drawn wire is able to maintain its ductility up to ninth die although the cleanliness of fracture surfaces is poor as compare to pass schedule-2. At tenth die, the fractured surface indicates that wire loses its ductility. The fractured surface becomes worst but longitudinal surface still stood good. At eleventh and twelfth die, the fractured surface becomes little better as compared to tenth die but quality of longitudinal surface decreases. So, after ninth die, the degree of brittleness increases with further increase in cold work.

The ductility of cold drawn wire changes with increase in degree of cold work. The profile of cup and cone fractured surface describes the changes in ductility of cold drawn wire. It is observed that profile of cup and cone in initial few dies is relatively poor. The profile improves with increase in number of die pass and attends its peak at intermediate die pass but profile diminishes with further increase in die pass. This indicates that ductility of wire increases with increase in cold work up to a stage but decreases with further increases in cold work. The degree of cleanness of fracture surface in torsion test indicates the ductility of cold drawn wire. The degree of cleanness of fracture surface of cold drawn wire of intermediate die is high as compared to initial dies and final dies of each pass schedules.

## 5 Conclusion

The investigation of fractured surfaces after tensile test and torsion test is carried out using M/s Leica make stereomicroscope. The following conclusions are drawn as:

1. The fully pearlitic microstructure is developed in lead patented hypereutectoid steel wires.
2. The highest UTS is achieved in pass schedule-1 but ductility reduces to such a low level that wire is practically of no use.
3. The highest TS is achieved in pass schedule-2 and UTS of cold drawn wire is marginally lower than pass schedule-1. So, cold drawn wire of ultra-high-strength along with very good ductility is achieved.
4. The cold drawn wire of pass schedule-3 is neither able to achieved ultra-high strength nor good ductility.
5. The ductility of cold drawn wire can be predicted by analyzing the cup-cone fractured surface in tensile test. However, the characterization of ductility of cold drawn wire by analyzing fractured surface of torsion test is much better as compare to cup-cone fractured surface analysis.

6. The high reduction rate per die in pass schedule-1 has negative effect on torsion strength. The low reduction rate per die in pass schedule-3 has negative effect on torsion strength as well as tensile strength. So, pass schedule-2 has optimum reduction rate per die.

## References

1. Bargujer SS, Singh P, Raizada V (2016) Thermoprocessing and wire drawing behavior of ultra high strength steel wires. *Perspect Sci* 8:554–557
2. Zelin M (2002) Microstructure evolution in pearlitic steels during wire drawings. *Acta Mater* 50:4431–4447
3. Takahashi T, Tashiro H, Nishida S, Ochiai I, Ohashi S, Tarui T (1995) Strengthening of steel wire for tire cord. *Nippon Steel Technical Report* 64
4. Raabe D, Choi PP, Li Y, Kostka A, Sauvage X, Lecouturier F, Hono K, Kirchheim R, Pippen R, Embury D (2010) Metallic composites processed via extreme deformation: towards the limits of strength in bulk materials. *MRS Bull* 36:982–991
5. Lee SK, Lee SB, Kim BM (2010) Process design of multistage wet wire drawing for improving the drawing speed for 0.72 wt% C steel wire. *J Mater Process Technol* 210:776–783
6. Kumar P, Guroa NP, Haldar A, Suwas S (2011) Progressive changes in the microstructure and texture in the pearlitic steel during wire drawing. *ISIJ Int* 51(4):679–684
7. Brandaleze E (2015) Structure evolution of pearlite in steels with different carbon content under drastic deformation during cold drawing. *Procedia Mater Sci* 8:1023–1030
8. Kapp MW, Hohenwarter A, Wurster S, Yang B, Pippan R (2016) Anisotropic deformation characteristics of an ultrafine and nanolamellar pearlitic steel. *Acta Mater* 106:239–248
9. Nematollahi GA, Grabowski B, Raabe D, Neugebauer J (2016) Multiscale description of carbon-supersaturated ferrite in severely drawn pearlitic wires. *Acta Mater* 111:321–334
10. Tanaka M, Saito H, Yasumaru M, Higashida K (2016) Nature of delamination cracks in pearlitic steels. *Scripta Mater* 112:32–36
11. Bargujer SS, Suri NM, Belokar RM (2015) X-ray diffraction analysis of severely cold deformed hypereutectoid steel wire. *Defence Sci J* 65(6):500–507

# Comparison of Thermo-Physical and Tribological Characteristics of Nanolubricant



Md Mansoor Ahamed, S. M. Jameel Basha and B. Durga Prasad

**Abstract** This paper presents the comparison of characterization and investigation on viscosity, thermal conductivity and friction coefficient of Silicon carbide (SiC), Silicon nitride ( $\text{Si}_3\text{N}_4$ ) and Magnesium oxide (MgO) nanolubricants for refrigeration applications. The characterization of nanoparticles was done by SEM, XRD and EDS tests. Nanopolyester oil samples were prepared by two-step method for different volume concentrations of 0.15, 0.3, 0.45 and 0.6%. Viscosity of the nanolubricants was measured for different volume concentration and at various temperatures. The experimental results found that the viscosity and thermal conductivity of the  $\text{Si}_3\text{N}_4$  nanolubricant is higher than the other nanolubricants. Also it is found that the coefficient of friction of  $\text{Si}_3\text{N}_4$  nano lubricant is lower than the other nanolubricants. The viscosity of the  $\text{Si}_3\text{N}_4$  nanolubricant has been enhanced by 41.6, 33.9, 31.2, and 37.1% at 0.6% volume concentration for 20, 30, 40, and 50 °C with respect to polyolester (POE) oil. The result displayed that the thermal conductivity of  $\text{Si}_3\text{N}_4$  nanolubricant was enhanced by 42.4, 46, 45.6, & 41.4% corresponding to 0.15, 0.3, 0.45 and 0.6% volume concentration with respect to pure POE oil. This paper also emphasis on the comparison of tribological behavior of the nanolubricant and pure POE oil. It is found that the coefficient of friction was reduced by 1.3 times lower at optimal concentration of 0.6%. These conclusions suggest that  $\text{Si}_3\text{N}_4$  nanoparticle as additives in the base POE oil can improve the lubrication and thermal properties of base lubricant and can be used for the refrigeration application.

**Keywords** Nanoparticles · Nanolubricant · Characterization · Thermo-physical properties · Tribological properties

---

M. M. Ahamed (✉) · B. D. Prasad  
Jawaharlal Nehru Technological University, Anantapur, India  
e-mail: [mansoorbe039@gmail.com](mailto:mansoorbe039@gmail.com)

S. M. J. Basha  
Srinivasa Ramanujam Institute of Technology & Sciences, Anantapur, India

© Springer Nature Singapore Pte Ltd. 2020  
L. Vijayaraghavan et al. (eds.), *Emerging Trends in Mechanical Engineering*,  
Lecture Notes in Mechanical Engineering,  
[https://doi.org/10.1007/978-981-32-9931-3\\_16](https://doi.org/10.1007/978-981-32-9931-3_16)

## 1 Introduction

In the countenance of alarming power resource crisis, there is call for budding thermal techniques which are energy efficient. Thermal devices like refrigerators and air conditioners utilize huge quantity of energy. So possibility of emerging energy economical appliances need to be discover. The fast development in nanotechnology has directed towards rising of novel generation of heat transfer fluids with disseminated nanosize particles called nanofluids had to be explore. Enhanced heat transfer of nanofluids depends on the potential upgrading in the thermal conductivity of the nanofluids. Hence, data on the thermo-physical properties for the POE oil + nanoparticles is essentially significant for assessment of the compressor system as well as for simulations of different heat transfer methods in refrigeration systems.

Eastman et al. [1] observed that thermal conductivity was increased by 40% by adding nanoparticles to a volume fraction of 0.4%. Chandrasekhar et al. [2] conclude that nanolubricants have superior heat transfer properties such as high thermal conductivity, good evenness, uniformity, minimum congestion in flow channels due to very miniature size and remarkable specific surface area of the nanoparticles compare to the base conventional heat transfer fluids. Bobbo et al. [3] studied that the dispersion of nanoparticles in POE oil increases the lubricity and solubility of lubricant and refrigerant. Venerus and Jiang [4] employed larger diameter nanoparticles in lubricant and observed higher thermal conductivity which also coincides with the one calculated by the classical Maxwell-Garnett model.

Kedzierski et al. [5] conducted experiment to find the thermo-physical properties of the POE + CuO nanolubricant and the result found that the kinematic viscosity and density of the nanolubricant has been enhanced with mass concentration at ambient pressure and in the temperature range of 288–318 K. Cremaschi [6] found that the enhancement of thermal conductivity and viscosity depends on the temperature, particle size and volume concentration of metal oxide nanoparticle in the base oil. Kedzierski [7] showed that the existence of the polymeric surfactants in the synthetic polyester oil +  $\text{Al}_2\text{O}_3$  nanoparticles directs to increase and decrease in viscosity and liquid density of the nano-oil with mass concentration and temperature, respectively.

Cremaschi et al. [8] revealed that the mixing of  $\text{Al}_2\text{O}_3$  nanoadditives to the POE oil amplifies the viscosity by 8–16% with nanoparticle concentration and decreases by 40–30% with an increase in temperature from 20 to 40 °C. Also it was found that thermal conductivity of the nanolubricant is 1.1 times larger at 5 °C and 1.4 times higher at 40 °C with  $\text{Al}_2\text{O}_3$  nanoparticles in the lubricant oil. Sharif et al. [9] found that the thermal conductivity and viscosity of the  $\text{Al}_2\text{O}_3$  + polyalkalyne glycol nanolubricant is enhanced by 1.04 times and 7.58 times larger than the pure polyalkalyne glycol lubricant at 1% and 0.4% concentration, respectively. Zawawi et al. [10] found that the enhancement in thermal conductivity and viscosity of  $\text{SiO}_2$ /PAG and  $\text{Al}_2\text{O}_3$ /PAG nanolubricant with volume fraction and reduced with temperature.

Wang and Xie [11] found the improvement in solubility between mineral oil and HFC refrigerant when  $\text{TiO}_2$  nanoparticles are mixed with mineral oil. Huang [12] found that the additives of graphene nanosheets of 500 nm in the paraffin oil improved



the anti-wear ability and load-bearing ability of paraffin oil. Lee et al. [13] illustrated the reduction in friction coefficient and less wear rate with the addition of graphite nanoparticles to the pure oil. Choi et al. [14] presented that the mixing of fullerene nanoparticles to the mineral oil reduces the friction coefficient by 90% at 0.1 vol% in contrast with pure lubricant, which directs us to the inference that nanoparticles can enrich the effectiveness and consistency of the compressor.

Hwang [15] obtained decrease in the friction and enhanced in the anti-wear properties by mixing spherical graphite nanoparticles in mineral oil. Li et al. [16] concluded that with  $ZrO_2/SiO_2$  composite nanoparticles can lucratively reduce the coefficient of friction by 16.24% for 0.1 wt%. Battez et al. [17] obtained that by adding CuO nanoparticles to the oil exhibits reduction in friction in contrast to the base oil. Padgurskas et al. and Wu et al. [18, 19] noticed that by mixing nanoparticles to the lubricating oil can improve tribological properties. Several researchers have worked with different nanoparticles and concluded that addition of nanoparticles to the lubricants can efficiently reduce wear and friction. Hence the aim of this work is to estimate the thermo-physical properties of the SiC, MgO and  $Si_3N_4$  nanoparticles in the suspended POE oil.

## 2 Materials and Preparation of Nanolubricant

### 2.1 Characterization of Nanoparticles

The morphology of SiC,  $Si_3N_4$  and MgO nanoparticles was examined by scanning electron microscope (SEM) as shown in Figs. 1 and 2. The X-Ray diffraction data (XRD) results revealed that the shapes of the SiC and  $Si_3N_4$  nanoparticles are hexagon (JCPDS card no. 89–3843 and 82–0697) and the shape of MgO nanoparticles are cubic shape (JCPDS card no. 65–0476). Further, the shapes of the nanoparticles are examined by the SEM image which is shown in Fig. 1a–c. The crystal size of SiC,  $Si_3N_4$  and MgO nanoparticles were found by X-Ray diffraction data (XRD) as shown in Fig. 2a–c.

The XRD results shows the diffractive peaks are in correspondence with the values of  $2\theta$  at  $35.7^\circ$ ,  $30.39^\circ$  and  $43.50^\circ$  for SiC,  $Si_3N_4$  and MgO nanoparticles as shown in Fig. 2d–f. According to the Scherrer's equation [20] it found that the average particle size of the SiC,  $Si_3N_4$  and MgO nanoparticles are 32 nm, 44 nm, and 37 nm, respectively. The chemical composition of the SiC,  $Si_3N_4$  and MgO nanoparticles were analyzed by the Energy Dispersive X-Ray Spectroscopy (EDS) test as shown in Fig. 2a–c. It is clear that silicon carbide nanoparticles is composed of silicon and carbon, silicon nitride nanoparticles are composed of silicon and nitrogen and Magnesium oxide nanoparticles is composed of magnesium and oxygen.

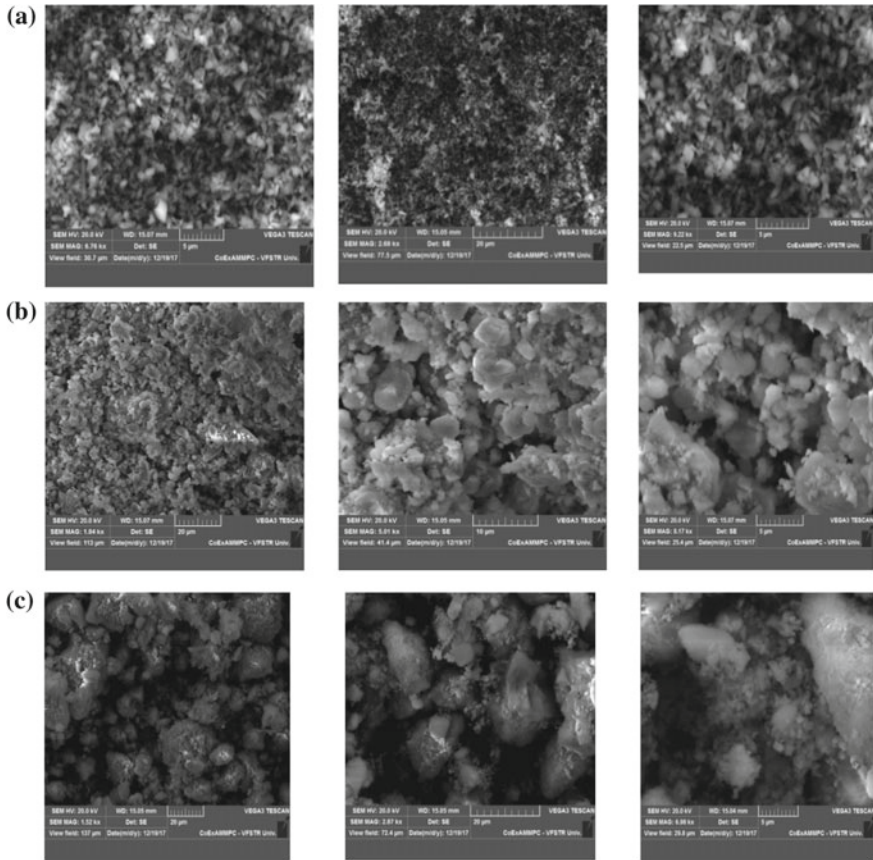


**Fig. 1** a SEM images of SiC nanoparticles at 6.76KX, 2.68KX, 9.22KX magnification. b SEM images of Si<sub>3</sub>N<sub>4</sub> nanoparticles at 1.54KX, 5.01 KX, 8.17KX magnification. c SEM images of MgO nanoparticles at 1.52KX, 2.87KX, 6.98KX magnification

## 2.2 Preparation of Nanolubricant

Nanolubricants can be primed using single-step or two-step methods. In the current investigation, two-step procedures are used. Commercially existing SiC, Si<sub>3</sub>N<sub>4</sub>, and MgO nanoparticles and polyolester (POE) oil were used for the preparation of nanolubricant. Nanolubricant samples were prepared by mixing nanoparticles to the base POE oil. The mass of nanoparticles according to the volume percentage were computed by using Eq. (1). Initially the mixture is stirred well by means of magnetic stirrer for 30 min and then mixed with probe type ultra sonicator for 3 h. Nanosamples of 0.15, 0.3, 0.45, and 0.6% by volume were prepared.

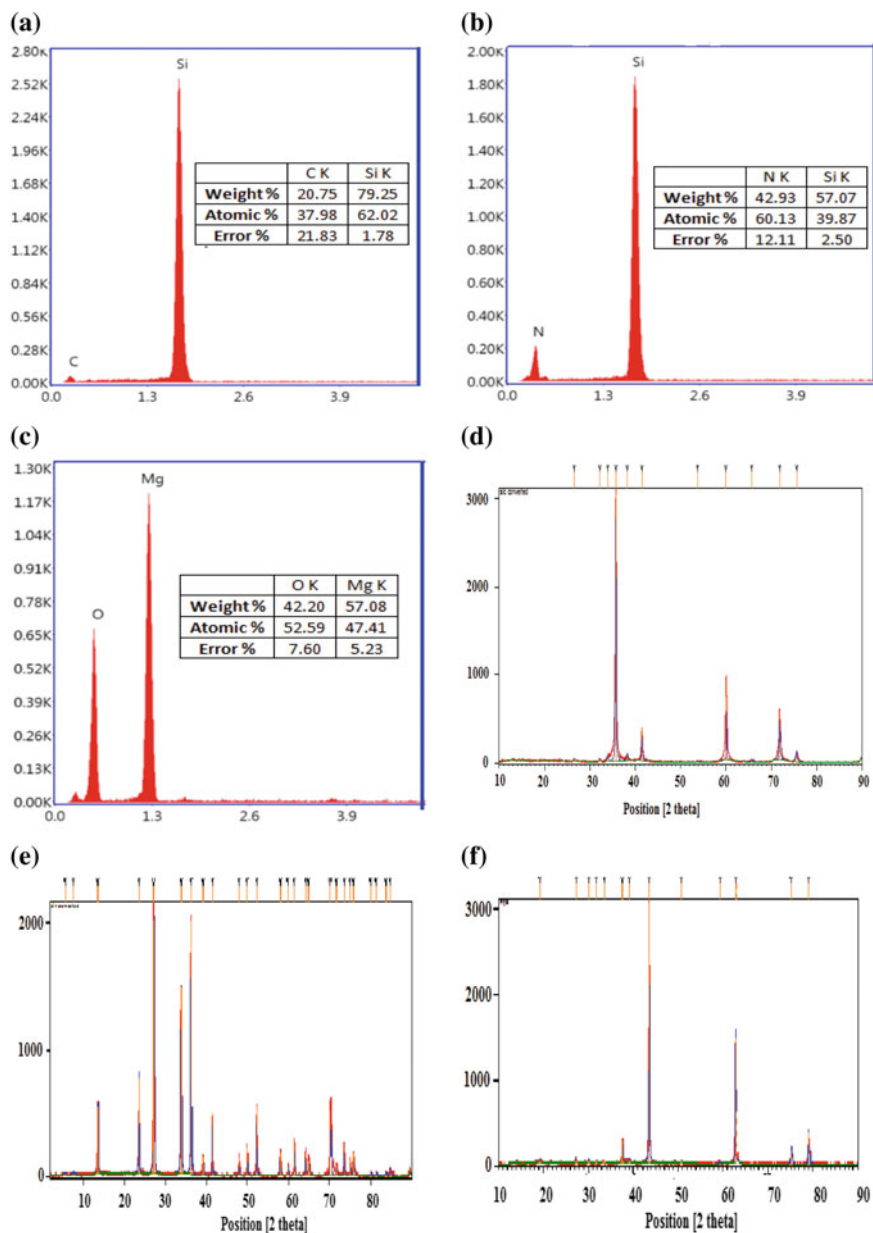


**Fig. 2** a Chemical composition of SiC nanoparticles. b Chemical composition of Si<sub>3</sub>N<sub>4</sub> nanoparticles. c Chemical composition of MgO nanoparticles. d XRD test of SiC nanoparticle. e XRD test of Si<sub>3</sub>N<sub>4</sub> nanoparticle. f XRD test of MgO nanoparticle

$$\varphi = \frac{\frac{m_{np}}{\rho_{np}}}{\frac{m_{np}}{\rho_{np}} + \frac{m_o}{\rho_o}} \quad (1)$$

### 2.3 Viscosity Measurement

Viscosity of lubricant oil affects directly the performance of the compressor. Addition of nanoparticles to the lubricating oil alters the viscosity and tribological properties. An optimal enhancement of viscosity will improve life and reduces the energy consumption of the compressor. The main aim of this work is to estimate the optimal percentage of nanoparticles in the POE oil, which improves the efficiency of the compressor. Viscosity of POE oil and nanolubricants were found by using redwood viscometer which works based on the method of laminar flow through a capillary tube of standard dimensions under falling head.

### 2.4 Thermal Conductivity Measurement

Thermal conductivity of the fluids plays a major role in heat transfer. It is evident from the literature that thermal conductivity of the fluid is enhanced by adding nano additives to the POE oil. In this work, thermal conductivity of nanolubricants was determined with KD2 Pro thermal analyzer at room temperature for different concentrations. The thermal conductivity of the nanolubricants was examined for four types of volume concentrations (0.15, 0.3, 0.45, and 0.6%) under the control of atmospheric temperature of  $26 \pm 1$  °C. The experimental procedure and attempt are as follows:

- (1) Put the nanolubricant sample in an ultrasonic vibrator and stir it for one hour.
- (2) Insert the test probe to the sample nanolubricant to note the readings.
- (3) Experimental readings were noted for time interval of 20 min and the readings are taken three times for the same sample to reduce the experimental errors.

### 2.5 Tribological Test

The tribological test of different nanolubricants and POE oil is measured with pin-on-disk wear apparatus. The nanolubricant sample is placed on a chuck which is rotated at a programmed rate. A static ball is made to contact with the rotating sample and therefore determines the tangential forces (friction) between sample and ball with a

sensor. The data attainment device records the frictional force as a function of data points.

In the investigational approach, the frictional force of all the four concentrations was recorded for a time of 20 min, at interlude of 5 min and the mean value was obtained for each concentration of nanoparticles. Each concentration was added for every 5 min. Coefficient of friction (COF) is calculated by using the given formula.

$$\text{COF} = \frac{\text{Friction force}}{\text{Load}} \quad (2)$$

### 3 Results and Discussion

#### 3.1 Viscosity

The rheological property of the POE oil, SiC, Si<sub>3</sub>N<sub>4</sub>, and MgO nanolubricants was estimated with Redwood viscometer. Figure 3a–d shows the assessment of dynamic viscosity of pure POE oil and modified POE oils at different temperature and concentration. It is obvious from the experimental results that the viscosity of customized POE oil is more than the pure POE oil and decreases with increase in temperature as expected. The finding signifies that the raise in viscosity due to the mixing of nanoparticles to the POE oil is more exceptional in the lower temperature range. It is also observed that for MgO nanolubricant the viscosity increases at lower temperature and decreases further compare to POE oil.

Inspite of this, it is essential to curtail or optimize the use of nanoparticles in the POE oil, so as to achieve the required significance without affecting the other properties. Figure 3a, b shows the effect of SiC and Si<sub>3</sub>N<sub>4</sub> nanoparticles in the viscosity of the POE oil. It is found that the viscosity has been enhanced and the enhancement is high at 0.3% and 0.6% vol. concentration for SiC and Si<sub>3</sub>N<sub>4</sub> nanolubricants, respectively. From Fig. 3a, b the maximum viscosity has been found to be increased by 31.7, 26, 11 and 20.9% for SiC nanolubricant and 41.6, 33.9, 31.2 and 37.1% for Si<sub>3</sub>N<sub>4</sub> nanolubricant in comparison with POE oil at 20, 30, 40 and 50 °C. Experimental result also shows the viscosity of MgO nanolubricant has been decreased than POE oil by 31, 29 and 0% corresponding to 30, 40 and 50 °C as shown in Fig. 3c. From Fig. 3d it is clear that the viscosity of the Si<sub>3</sub>N<sub>4</sub> nanolubricant is higher than the two nanolubricants.

Enhancement in viscosity of the nanolubricant is beneficial in terms of load capacity according to hydrodynamic lubrication, and also increases the solubility of refrigerant and lubricant in the compressor [21]. Thereby allows pure refrigerant to the condenser and evaporator which improves the rate of heat transfer and in turn increases the refrigeration effect in the evaporator. According to boundary lubrication, friction coefficient decreases due to increase in the viscosity. In order to

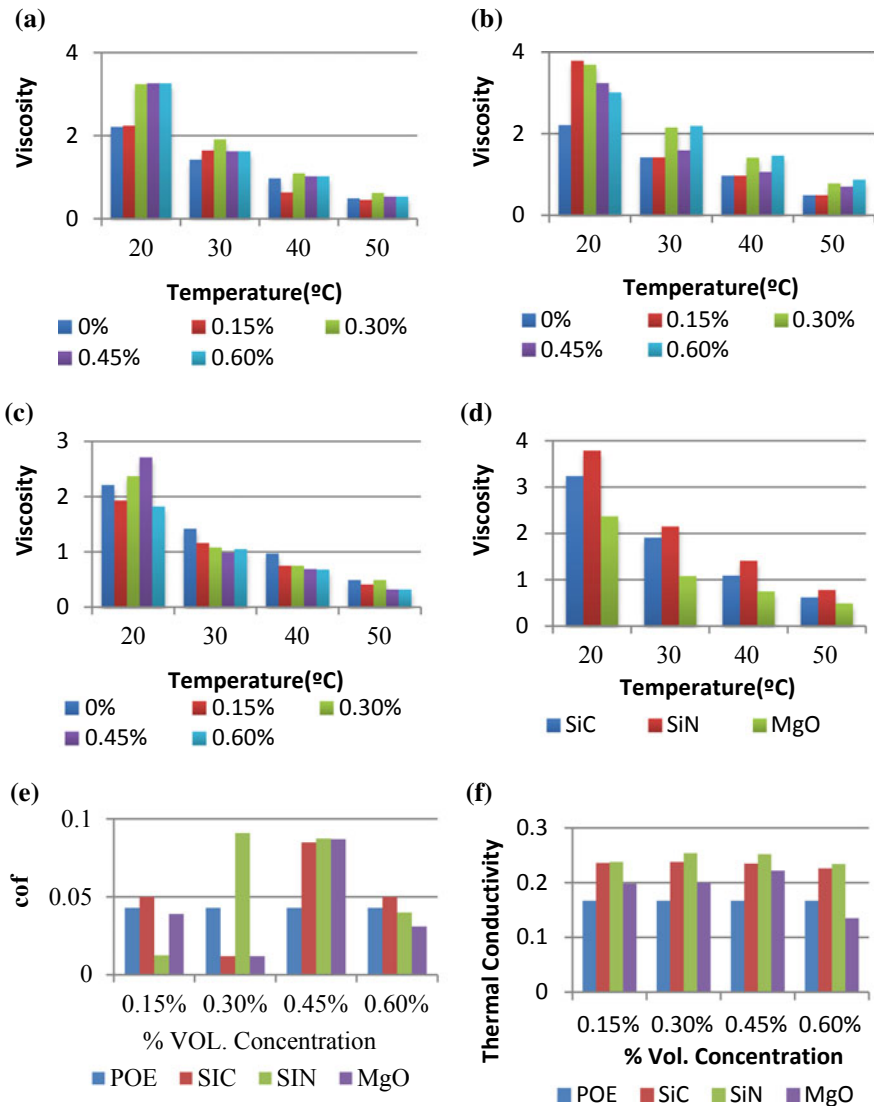


**Fig. 3** a Viscosity of SiC nanolubricant at different temperature and concentration. b Viscosity of Si<sub>3</sub>N<sub>4</sub> nanolubricant at different temperature and concentration. c Viscosity of MgO nanolubricant at different temperature and concentration. d Comparison of maximum viscosity of SiC, Si<sub>3</sub>N<sub>4</sub> and MgO nanolubricants at different temperature and concentration. e Comparison coefficient of friction of nanolubricants and POE oil at different volume concentration. f Variation of thermal conductivity with volume concentration

investigate further the optimal volume concentration of nanoparticles, the coefficient of friction was experimentally determined.

### 3.2 Coefficient of Friction

The findings from the viscosity test elucidated that the nanoadditives in the POE oil improves the viscosity. Examinations were carried out to know the influence of viscosity on the lubrication attributes. The coefficient of friction of the lubricants was ascertained by performing pin on disk tester, which was set to produce an actual boundary lubrication system. All the trails were performed in controlled room temperature. Figure 3e illustrates the deviation of the frictional forces between the pin and disc with the mixing of nanoadditives in the POE oil. It is evident from the results that the coefficient of friction reduces maximum where the viscosity is maximum.

Result shows that the coefficient of friction has been reduced by 66, 35 and 25% for SiC, Si<sub>3</sub>N<sub>4</sub> and MgO nanolubricants corresponding to the room temperature. Based on the viscosity and friction test the optimum concentration of the nanoparticles were concluded as 0.3, 0.6, and 0.3% volume concentration for SiC, Si<sub>3</sub>N<sub>4</sub>, and MgO nanolubricants. Experimental results of viscosity and coefficient of friction as shown in Fig. 3d, e concludes that the Si<sub>3</sub>N<sub>4</sub> nanolubricant can exhibit good tribological characteristics. It is seen from Fig. 3a–c that the viscosity improves with the increase of volume concentration which leads to decrease in the friction. This indicates the presence of volume fraction of nanoadditives in the lubricant can reduce the friction in the mating parts and thus reduces the energy consumption [22].

Figure 4a–c, and d represents the deviation of the frictional force between the pin on disc with regards to volume concentration and it is less at the point where the viscosity of the lubricant is higher. Initially in the experiment the pin and disk stay in direct contact and therefore the frictional force is high. Over time, the induction of the oil between the surfaces generates boundary lubrication, which reduces the frictional force. In the present work, experimentation recommends 0.3, 0.6 and 0.3% volume fraction for SiC, Si<sub>3</sub>N<sub>4</sub> and MgO nanolubricants, respectively, signifies a best-measured quantity which results in the minimum value of the friction coefficient. Result also reveals that the Si<sub>3</sub>N<sub>4</sub> nanolubricant exhibits the lowest coefficient of friction from the other two nanolubricants.

### 3.3 Thermal Conductivity

The thermal conductivity of POE oil, SiC, Si<sub>3</sub>N<sub>4</sub>, and MgO nano-oils at 299.16 K for 0.15–0.6% volume concentrations are represented in Fig. 3f. The experimental findings show that the improvement in the thermal conductivity depends on the presence of nanoadditives in the base oil and the same was reported by the many researchers. Experiment results illustrate that the maximum thermal conductivity is found to be

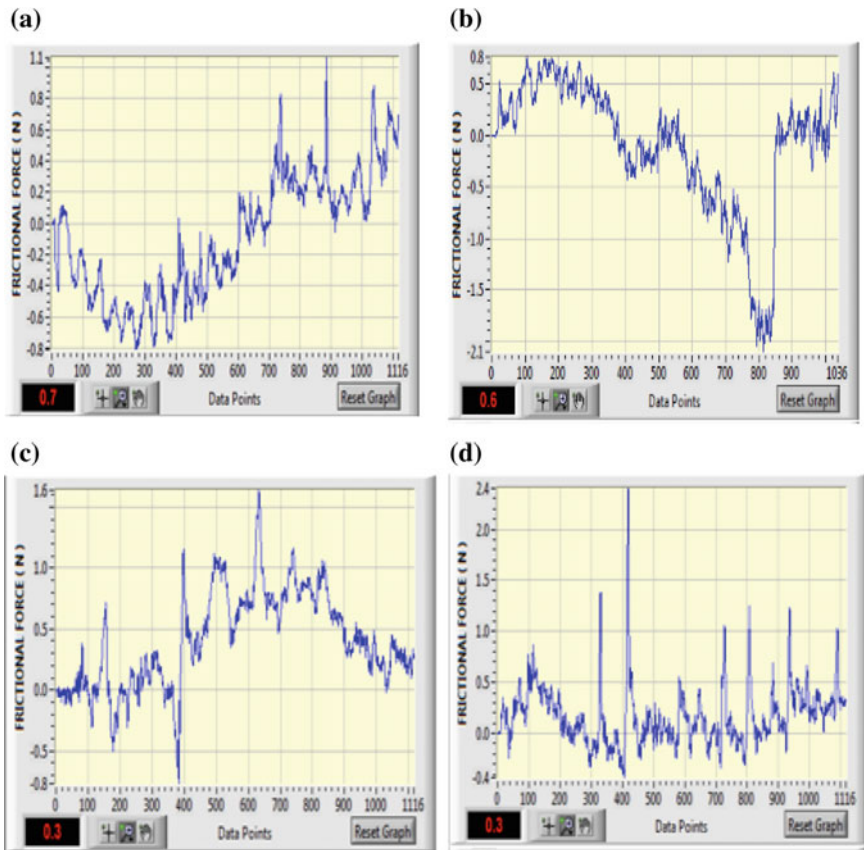


**Fig. 4** a Computer generated frictional force graph of POE oil alone. b Computer generated frictional force graph of SiC nanolubricant. c Computer generated frictional force graph of Si<sub>3</sub>N<sub>4</sub> nanolubricant. d Computer generated frictional force graph of MgO nanolubricant

at 0.3% vol. concentration for SiC, Si<sub>3</sub>N<sub>4</sub> nanolubricants and 0.45% for MgO nanolubricant. The thermal conductivity of the SiC, Si<sub>3</sub>N<sub>4</sub> and MgO nanolubricants were enhanced by 42%, 46%, and 38% respectively in comparison with POE oil.

Figure 3f shows that the thermal conductivity of Si<sub>3</sub>N<sub>4</sub> nanolubricant is higher than the other nanolubricants at all % volume concentration. Thermal conductivity results also reveal that the nanolubricant having highest thermal conductivity nanoparticles exhibits highest value. The enrichment in thermal conductivity of the nanolubricant, improves the rate of heat transfer from the compressor. Therefore, the discharge temperature of the compressor decreases which increase the life of the compressor.



## 4 Conclusions

Experimental investigation illustrates the additive of SiC, Si<sub>3</sub>N<sub>4</sub> and MgO nanoparticles in the POE oil enhances the viscosity, thermal conductivity and reduces the coefficient of friction. These results highly depend on the %volume fraction of the nanoparticles in the base oil and temperature. In this work, compared to all the three nanolubricants, the maximum viscosity of nanolubricant is found to be at 0.6% at all the temperatures for Si<sub>3</sub>N<sub>4</sub> nanolubricant and the coefficient of friction was also reduced by 7% at the same concentration. This is due to the fact that the high viscosity reduces the friction between the pin and disk. Also the maximum thermal conductivity is observed for Si<sub>3</sub>N<sub>4</sub> nanolubricant at all concentration. It is seen that the thermal conductivity has been enhanced by 42, 46, 45 and 41% at 0.15, 0.3, 0.45 and 0.6% volume concentration. Due to the above variation in the thermal properties the compressor life increases and works smoothly. The variation of various test results of the nanolubricant is in accordance with the literature survey. From the experimental results it is concluded that the best feasible volume fraction to be 0.6% for Si<sub>3</sub>N<sub>4</sub> nanolubricant and 0.3 vol% for SiC and MgO nanolubricant. Hence the experimental results recommend that the additives of SiC, Si<sub>3</sub>N<sub>4</sub> and MgO nanoparticles in the POE oil can improve the working of compressor in refrigeration and in turn improves the performance of the refrigeration system. Among the three, Si<sub>3</sub>N<sub>4</sub> nanolubricant shows better performance due to its enhanced properties.

## References

1. Eastman A, Choi SUS, Li S, Thompson LJ, Lee S (1996) Enhancement thermal conductivity through the development of nano fluids. In: Fall meeting of the Metals Research Society (MRS). Boston, USA
2. Chandrasekar M, Suresh S, Bose AC (2010) Experimental investigations and theoretical determination of thermal conductivity and viscosity of Al<sub>2</sub>O<sub>3</sub>/water nanofluid. *Exp Therm Fluid Sci* 34:210–216
3. Bobbo S, Fedele L, Fabrizio M, Barison S, Battiston S, Pagura C (2010) Influence of nanoparticles dispersion in POE oils on lubricity and R134a solubility. *Int J Refrig* 33:1180–1186
4. Venerus DC, Jiang Y (2011) Investigation of thermal transport inn colloidal silica dispersions. *J Nanoparticles Res* 13(7):3075–3083
5. Kedzierski MA (2012) Viscosity and density of CuO nanolubricant. *Int J Refrig* 35(7):1997–2002
6. Cremaschi L (2012) A fundamental view of the flow boiling heat transfer characteristics of nanorefrigerants. In: Proceedings of the ASMEIMECE 2012 international mechanical engineering congress and exposition, Houston, TX, USA
7. Kedzierski MA (2013) Viscosity and density of aluminum oxide nanolubricant. *Int J Refrig* 36(4):1333–1340
8. Cremaschi L et al (2014) Thermodynamic and heat transfer properties of Al<sub>2</sub>O<sub>3</sub> nanolubricant. International Refrigeration and Air conditioning conference, Purdue University
9. Sharif MZ, Azmi WH, Redhwan AAM, Mamat R (2016) Investigation of thermal conductivity and viscosity of Al<sub>2</sub>O<sub>3</sub>/PAG nanolubricant for application in automotive air conditioning system. *Int J Refrig*. <http://dx.doi.org/10.1016/j.ijrefrig.2016.06.025>

10. Zawawi NMM, Azmi WH, Redhwan AAM, Sharif MZ, Sharma KV (2017) Thermophysical properties of  $\text{Al}_2\text{O}_3$ - $\text{SiO}_2$ /PAG composite nanolubricant for refrigeration system. *Int J Refrig* 80:1–10
11. Wang RX, Xie HB (2003) A refrigerating system  $\text{uSi}_3\text{N}_4$  g HFC134a and mineral lubricant appended with  $\text{N-TiO}_2(\text{R})$  as working fluids. In: Proceedings of the 4th international symposium on HVAC, Tsinghua University
12. Huang HD, Tu JP, Gan LP, Li CZ (2006) An investigation on tribological properties of graphite nanosheets as oil additive. *Wear* 261(2):140–144
13. Lee K, Hwang YJ, Cheong S, Kwon L, Kim S, Lee J (2009) Performance evaluation of nanolubricants of fullerene nanoparticles in refrigeration mineral oil. *Curr Appl Phys* 9:128–131
14. Hwang YJ, Lee CG, Choi YM et al (2011) Effect of the size and morphology of particles dispersed in nano-oil on friction performance between rotating discs. *J Mech Sci Technol* 25(11):2853–2857
15. Lee C-G, Hwang Y-J, Choi Y-M, Lee J-K, Choi C, Oh J-M (2009) A study on the tribological characteristics of graphite nano lubricants. *Int J Precision Eng Manuf* 10(1):85–90
16. Li W, Zheng S, Cao B, Ma S (2011) Friction and wear properties of  $\text{ZrO}_2/\text{SiO}_2$  composite nanoparticles. *J Nanoparticle Res* 13:2129–2137
17. Battez AH, Viesca JL, Gonza lez R, Blanco D, Asedegbega E, Osorio A (2010) Friction reduction properties of a CuO nanolubricant used as lubricant for a NiCrBSi coating. *Wear* 268:325–328
18. Padgurskas J, Rkuiza R, Prosycevas L, Kreivaitis R (2013) Tribological properties of lubricant additives of Fe, Cu and Co nanoparticles. *Tribol Int* 60:224–232
19. Wu YY, Tsui WC, Liu TC (2007) Experimental analysis of tribological properties of lubricating oil with nanoparticles additives. *Wear* 262:819–825
20. Raman V, Bahl OP, Dhawan U (1995) *J Mater Sci* 30:2686
21. Wang RX, Xie HB (2003) A refrigerating system  $\text{uSi}_3\text{N}_4$  g HFC134a and mineral lubricant appended with  $\text{n-TiO}_2(\text{R})$  as working fluids. In: Proceedings of the 4th international symposium on HVAC pp. 888–892
22. Youbi-Idrissi Mohammed, Bonjour Jocelyn (2008) The effect of oil in refrigeration: current research issues and critical review of thermodynamic aspects. *Int J Refrig* 31:165–179

# Predictive Modeling and Optimization of Technological Response Parameters in Nd:YAG Laser Microgrooving of Titanium Alloy Using Combined RSM-PSO Approach



Samir Kumar Panda, Sudhansu Ranjan Das and Debabrata Dhupal

**Abstract** The present work focuses on modeling and optimization during Nd:YAG laser microgrooving of  $Ti_6Al_4V$  titanium alloy material with an objective to find the optimum process parameters settings for the groove upper width as well as depth and heat-affected zone. The experiments are performed as per Box–Behnken design of experiments (BBDOEs) with four process parameters (diode current, pulse frequency, scanning speed, and number of passes) for parametric optimization in order to control the technological response characteristics of the precision microgrooves on  $Ti_6Al_4V$  titanium alloy. Analysis of variance (ANOVA), response surface methodology (RSM) and particle swarm optimization (PSO) are subsequently proposed for predictive modeling and process optimization. The methodology described here is expected to be highly beneficial for manufacturing industries.

**Keywords** Laser microgrooving ·  $Ti_6Al_4V$  · ANOVA · RSM · PSO

## 1 Introduction

The recent technology has been advancing to infinite extent in search of newer materials and alloys with high hardness, strength and less weight which are very difficult to be machined with the conventional machining processes for achieving the required accuracy and precision. Nowadays, there is a vast demand for the well-finished products of titanium alloy materials with high accuracy and complex integrated designs. Such features on a component can be achieved only through the advanced manufacturing process, especially by laser beam machining. In case of micromachining the feature size is less than 1 mm. Hence lasers are increasingly employed for a precise micromachining because their beams can be focused accurately on microscopic areas, and attributed to a number of advantages which are normally applicable to whole range of the materials processing applications, like, non-contact processing,

---

S. K. Panda · S. R. Das (✉) · D. Dhupal  
Veer Surendra Sai University of Technology, Burla 768018, India  
e-mail: [das.sudhansu83@gmail.com](mailto:das.sudhansu83@gmail.com)

© Springer Nature Singapore Pte Ltd. 2020  
L. Vijayaraghavan et al. (eds.), *Emerging Trends in Mechanical Engineering*,  
Lecture Notes in Mechanical Engineering,  
[https://doi.org/10.1007/978-981-32-9931-3\\_17](https://doi.org/10.1007/978-981-32-9931-3_17)

high productivity, eradication of the finishing operations, minimized cost of processing, and enhanced the quality of product, maximize material utilization, green manufacturing and minimize the heat-affected zone. The above-cited advantages can only be obtained with appropriate selection of process parameters. Researchers have employed various methods MRA [1, 2] and ANN [3, 4] for mathematical modeling in order to predict the responses and Taguchi method [5], RSM [6, 7], GA [8, 9], PSO [10, 11] for optimization the controlled process parameters during laser micromachining process, that have been explored as productivity and reliable tool in advanced computing technology for high-quality frameworks since it gives a straight-forward, skilled, and systematically optimize the output, such as cost, quality, and performance. The proper utilization, along with appropriate adjustment of machining controllable process parameters are of main importance for achieving fine grade of microgrooves, which generally utilize proper time and effort due to the frequently changing behavior of the laser micromachining process. Thus, the present study focuses on development of mathematical models and multi-response parametric optimization during laser microgrooving of titanium alloy ( $\text{Ti}_6\text{Al}_4\text{V}$ ) through Nd:YAG laser treatment using statistical approach such as response surface methodology (RSM) followed by, computational approach like particle swarm optimization (PSO).

## 2 Experimental Procedure

A 75 W diode-pumped Nd:YAG laser (make: Sahajanand, model: SPRIGO LD) was used to conduct the experiments which has assist gas supply unit. During experiment, the laser beam (focal length of 77 mm) has been set at surface of the workpiece as the focal plane which resulted in laser beam spot size around 21  $\mu\text{m}$ . In the present research,  $\text{Ti}_6\text{Al}_4\text{V}$  titanium alloy plate of dimension (75 mm \* 25 mm \* 5 mm) is considered as the workpiece material for experimentation, subjected to microgrooving by multiple laser pulses (DPSS Nd:YAG laser treatment) with actual peak power vary between 0.7–5 kW.

In the current investigation diode current, pulse frequency, scan speed, and number of pass are considered as the input process parameters which influence the technological response characteristics of laser microgrooving such as, upper width, heat-affected zone and groove depth. The different process parameters and their values are shown in Table 1. Using the abovementioned process parameters (4) each with five different levels, a well-designed experimental layout is formulated in conformance with Box–Behnken design of experiments (BBDOEs) which is consisting of thirty-one (31) number of trials. Design of experimental plan with actual value of process parameters, measured response are presented in Table 2. All the experiential trials for laser engraving are performed with argon gas. The upper width (GWD), heat affected zone (HAZ) and groove depth (GD) of machined microgroove is measured by utilizing scanning electron microscope (make: Hitachi, model: SU3500).

**Table 1** Process parameters and levels

Parameters	Symbols	Units	Levels				
			-2	-1	0	1	2
Diode current	$X_1$	amp	18.5	20	21.5	23	24.5
Pulse frequency	$X_2$	kHz	28	31	34	37	40
Scan speed	$X_3$	mm/s	40	50	60	70	80
Number of passes	$X_4$		9	10	11	12	13

The schematic view of experimental work and methodology proposed in the current study, is presented in Fig. 1.

### 3 Results and Discussion

#### 3.1 Development of Response Model

The results of response characteristics, i.e., groove width (GWD), groove depth (GD) and heat-affected zone (HAZ) which were obtained in accordance of BBDOEs, were analyzed in Minitab 16 through response surface methodology (RSM) and developed the mathematical models to find-out the best-fit of correlation between the abovementioned response (GWD, GD, HAZ) of the microgrooved component with the input parameters such as diode current ( $X_1$ ), pulse frequency ( $X_2$ ), scanning speed ( $X_3$ ) and number of passes ( $X_4$ ). Regression equations in the second-order (i.e., quadratic model) for the responses are presented by:

$$\begin{aligned}
 Y_{\text{GWD}} = & -2663 + 37.6X_1 + 47.5X_2 - 1.29X_3 + 303.1X_4 + 2.199X_1^2 + 0.272X_2^2 \\
 & + 0.00573X_3^2 - 3.052X_4^2 - 1.458X_1X_2 - 0.1708X_1X_3 - 5.958X_1X_4 \\
 & + 0.0604X_2X_3 - 3.354X_2X_4 + 0.194X_3X_4
 \end{aligned} \tag{1}$$

$$\begin{aligned}
 Y_{\text{HAZ}} = & 1189 - 54X_1 - 2.93X_2 - 14.64X_3 - 15.2X_4 - 0.428X_1^2 \\
 & - 0.4888X_2^2 - 0.008X_3^2 - 1.4X_4^2 + 0.915X_1X_2 + 0.3287X_1X_3 \\
 & + 2.437X_1X_4 + 0.2694X_2X_3 - 0.073X_2X_4 - 0.0731X_3X_4
 \end{aligned} \tag{2}$$

$$\begin{aligned}
 Y_{\text{GD}} = & 2222 - 383.7X_1 + 166.7X_2 + 10.03X_3 - 238X_4 + 9.370X_1^2 \\
 & - 0.49X_2^2 - 0.1816X_3^2 + 20.09X_4^2 - 5.083X_1X_2 + 1.408X_1X_3 \\
 & + 7.58X_1X_4 + 0.521X_2X_3 - 4.71X_2X_4 - 3.088X_3X_4
 \end{aligned} \tag{3}$$

To avoid the misleading conclusion, statistical analysis is performed for the proposed RSM models (GUV, HAZ, and GD) by employing ANOVA in order to check

Table 2 Design of experimental plan and experimental results

Run	Coded values				Actual settings				Responses			
	X <sub>1</sub>	X <sub>2</sub>	X <sub>3</sub>	X <sub>4</sub>	Diode current (amp)	Frequency (kHz)	Scan speed (mm/s)	No. of passes	G UW (μm)	HAZ (μm)	GD (μm)	
1	1	1	-1	-1	23	37	50	10	334.0938	48.865	244.989	
2	0	0	0	-2	21.5	34	60	9	277.406	62.684	378.406	
3	-1	-1	1	1	20	31	70	12	309.968	36.978	252.364	
4	-1	1	-1	-1	20	37	50	10	303	41.787	295.25	
5	0	0	0	0	21.5	34	60	11	305.5	62.314	323.75	
6	0	0	0	2	21.5	34	60	13	297.781	58.471	457.197	
7	0	-2	0	0	21.5	28	60	11	301.281	52.196	291.781	
8	-1	1	1	-1	20	37	70	10	304.343	47.865	395.177	
9	-1	1	1	1	20	37	70	12	315.75	37.362	331.666	
10	-1	-1	-1	-1	20	31	50	10	258.468	71.265	240.197	
11	0	0	0	0	21.5	34	60	11	299.25	66.764	335.5	
12	0	0	0	0	21.5	34	60	11	292.25	64.764	327	
13	2	0	0	0	24.5	34	60	11	335.281	74.184	452.197	
14	-1	-1	1	-1	20	31	70	10	256.875	47.225	272.562	
15	1	-1	-1	-1	23	31	50	10	320	68.037	264.375	
16	1	-1	-1	1	23	31	50	12	329.718	71.378	425.177	
17	0	0	0	0	21.5	34	60	11	301.25	65.939	334.75	
18	1	-1	1	-1	23	31	70	10	310.968	58.190	387.677	
19	0	0	2	0	21.5	34	80	11	301.156	56.196	311.822	
20	-1	1	-1	1	20	37	50	12	301.093	32.953	352.677	

(continued)

Table 2 (continued)

Run	Coded values				Actual settings				Responses			
	X <sub>1</sub>	X <sub>2</sub>	X <sub>3</sub>	X <sub>4</sub>	Diode current (amp)	Frequency (kHz)	Scan speed (mm/s)	No. of passes	GUV (µm)	HAZ (µm)	GD (µm)	
21	0	0	0	0	21.5	34	60	11	300.75	69.014	304.75	
22	-1	-1	-1	1	20	31	50	12	312.5	70.862	355.687	
23	0	0	0	0	21.5	34	60	11	304.75	64.264	304.875	
24	0	0	-2	0	21.5	34	40	11	303.031	69.759	217.781	
25	1	1	-1	1	23	37	50	12	301.875	59.875	338.479	
26	1	-1	1	1	23	31	70	12	319.75	66.512	424.791	
27	0	2	0	0	21.5	40	60	11	317.906	44.959	347.822	
28	1	1	1	1	23	37	70	12	306.593	80.378	393.156	
29	0	0	0	0	21.5	34	60	11	303.25	63.239	341.375	
30	1	1	1	-1	23	37	70	10	319.25	74.537	413.354	
31	-2	0	0	0	18.5	34	60	11	303.906	50.471	391.406	

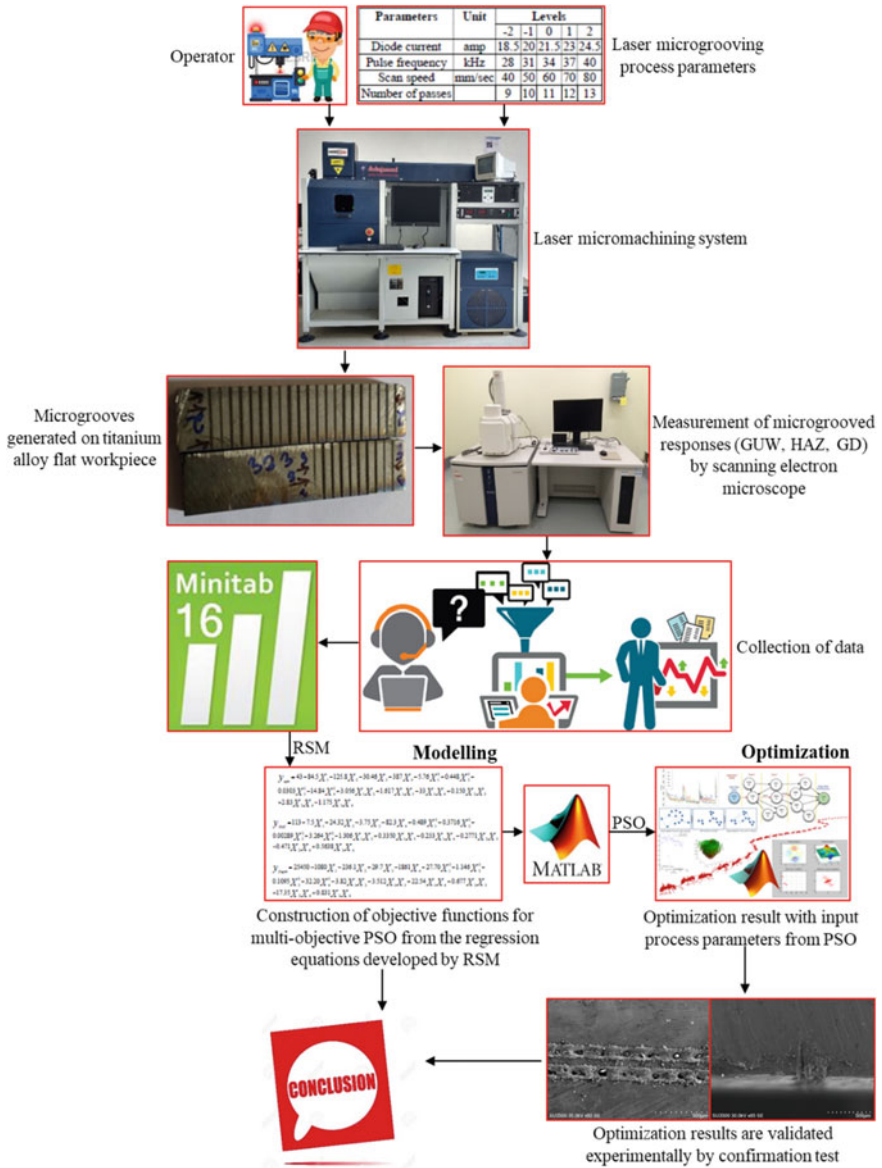


Fig. 1 Schematic layout of experimental setup and methodology proposed



their adequacy and validity, as shown in Table 3. The estimate  $F$ -value of the models for GUW, HAZ, and GD are 27.14, 25.15, and 31.05, respectively, which shows the excellent significance of model because of lower magnitude of  $F$ -table value (2.46) at 95% of confidence level. Moreover, it can be clearly seen that the developed quadratic models are statistically significant as the  $P$  (probability) value is under 0.05. Particularly, the model developed using RSM for groove width, groove depth and heat-affected zone explain the  $R^2$  values (i.e., co-efficient of determination) of 0.959, 0.956, and 0.964, respectively, which are very close to unity (1) ensuring the excellent fit for the model with greater statistical significance. Finally, normal probability plot combined with Anderson–Darling test for GUW, HAZ, and GD is shown in Fig. 2, which ensures that the residuals distributed fairly close to a straight line indicating that the errors are dispersed normally and specifying that the terms associated with the model are significant. With  $p$ -value (0.103 for GUW, 0.055 for HAZ, and 0.11 in case of GD) received from Anderson–Darling test is greater than significance level value (0.05), which confirms the adequacy of models as no reason was observed for the rejection of null-hypothesis. Hence, the proposed predictive can be utilized for particle swarm optimization.

### 3.2 Response Optimization Using PSO

Alternative method like GA, claimed to be more efficient for simultaneous optimization of multiple responses. However, the computational effort required by PSO to arrive to such high-quality solutions is less than the effort required to arrive at the same high-quality solutions by the GA, which pursuits us to consider PSO in the present study. PSO is a soft computing approach which relies on some programming commands to generate the global optimal result. The regression Eqs. (1)–(3) developed by RSM approach for groove width, heat affected zone thickness and groove depth are utilized in generation of objective function for PSO. The minimum and maximum values of the process parameters were used as constraints for the objective function. For multiple response optimizations using PSO, the following equation is proposed by taking into consideration of all the responses simultaneously optimized and optimum parameter settings can be considered by the objective function:

$$Z_{\text{GLOBALMIN}} = W_1 * \frac{Y_{\text{GWD}}}{Y_{\text{GWDMIN}}} + W_2 * \frac{Y_{\text{HAZ}}}{Y_{\text{HAZMIN}}} + W_3 * \frac{Y_{\text{GD}}}{Y_{\text{GDMIN}}} \quad (4)$$

Figure 3 presents the convergence plot, which aims to optimize the abovementioned three laser microgrooving responses in the presence of PSO specific parameters. Here, the initial swarm size is set at 50 with maximum number of iteration of 100. The constants  $C1$  and  $C2$  are taken as 2. By solving the optimization problem with PSO, it was found that the  $Z_{\text{MIN}}$  value is 0.2949, occurring at a weightage of 0.80 ( $W_1$ ) to upper width. Also 10% i.e. weightage of 0.1 ( $W_1$  and  $W_3$ ) equal importance has been given to other two responses (heat affected zone thickness and groove

**Table 3** Results of ANOVA for response model

Regression	Groove width (GWD)			HAZ			Groove depth (GD)					
	<i>F</i>	<i>P</i>	<i>R</i> <sup>2</sup>	<i>R</i> <sup>2</sup> (adj)	<i>F</i>	<i>P</i>	<i>R</i> <sup>2</sup>	<i>R</i> <sup>2</sup> (adj)	<i>F</i>	<i>P</i>	<i>R</i> <sup>2</sup>	<i>R</i> <sup>2</sup> (adj)
	27.14	0.000	95.96%	92.42%	25.15	0.000	95.65%	91.85%	31.05	0.000	96.45%	93.34%

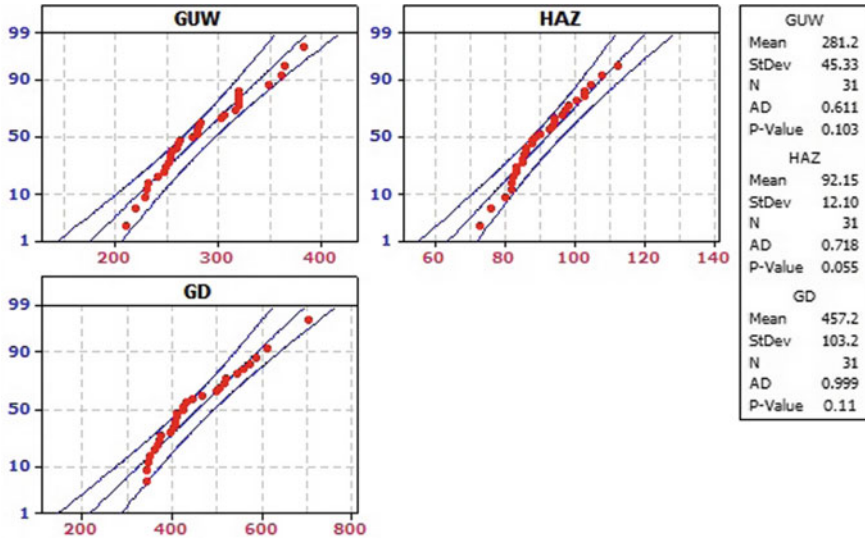


Fig. 2 Normal probability plot for technological response characteristics of laser microgroove

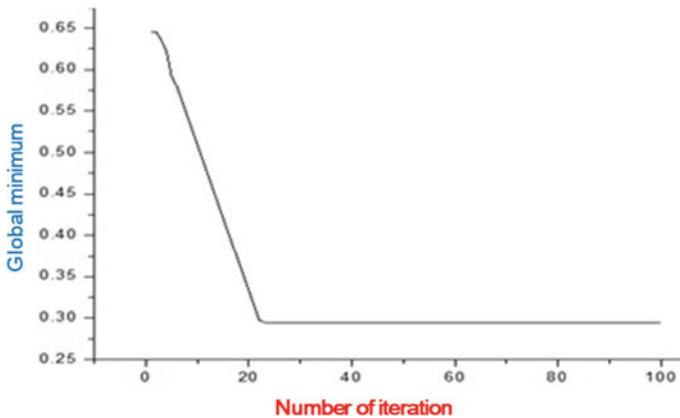
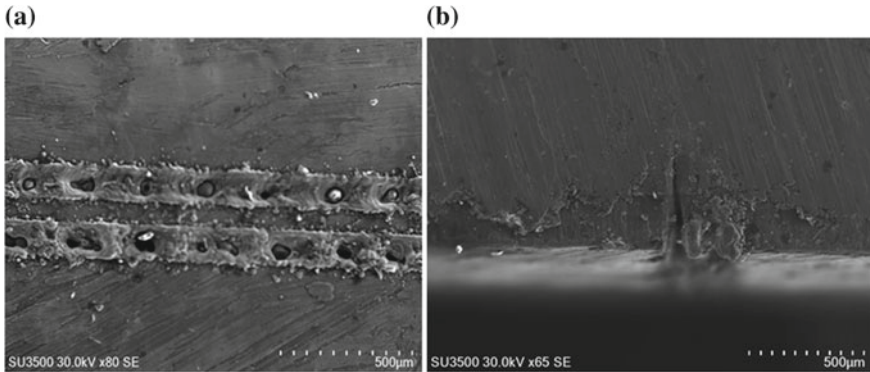


Fig. 3 Optimal convergence curve for multi-objective PSO

depth). Moreover, it can be concluded that the optimal solution occurs at sudden decrease in global minimum with a less processing time due to lesser complexity as well as significant improvement in computational efficiency of PSO algorithm. The optimal process parameters setting for microgrooving variables in laser machining of titanium alloy ( $Ti_6Al_4V$ ) are diode current 18.5 amp, pulse frequency 40 kHz, scan speed 40 mm/s, no. of passes 13, with estimated groove width (GWD) of 0.124 mm, heat affected zone (HAZ) of 0.123 mm and groove depth (GD) of 0.232 mm. Finally, an additional experiment is performed with the optimal configuration (suggested by



**Fig. 4** SEM micrograph showing machined surface under optimum cutting conditions

PSO) in order to observe the machined microgroove using scanning electron microscope (SEM), shown in Fig. 4.

## 4 Conclusions

In the present work, laser engraving has been carried out on  $Ti_6Al_4V$  substrate using argon gas. The experiments were modeled using CCD based RSM approach. Empirical models proposed for the technological response characteristics such as, groove upper width as well as depth and heat-affected zone have  $R$ -square value close to one and  $P$ -value less than 0.05, which ensured the greater statistical significance with excellence of fit for the model. The normal probability plot ensures that the residuals distributed fairly near to a straight line showing the normality dispersion of errors as well as implying the sources associated with the models are significant. Anderson–Darling test for model show adequate, as  $P$ -value is over 0.05 at 95% confidence level. The regression equations developed in RSM approach were used to generate the objective function for the PSO approach, which demonstrated the ability to optimize and to accurately model the technological response characteristics of microgroove through advances in computer technology. By solving the optimization problem with PSO, corresponds to optimal setting of process parameters (diode current = 18.5 amp, pulse frequency = 40 kHz, scan speed = 40 mm/s, number of passes = 13) with estimated upper width 0.124 mm, heat affected zone 0.123 mm and depth 0.232 mm. The suggested multiple approaches (experimental, statistical, and computational) are reliable methodologies for improving laser microgrooving process and can be used in model predictive control, real-time process monitoring, and optimization in different machining process.

## References

1. Dhupal D, Doloi B, Bhattacharyya B (2009) Modeling and optimization on Nd:YAG laser turned micro-grooving of cylindrical ceramic material. *Opt Lasers Eng* 47:917–925
2. Kibria G, Doloi B, Bhattacharyya B (2013) Predictive model and process parameters optimization of Nd:YAG laser micro-turning of ceramics. *Int J Adv Manuf Technol* 65:213–229
3. Biswas R, Kuar AS, Biswas SK, Mitra S (2010) Artificial neural network modelling of Nd:YAG laser microdrilling on titanium nitride—alumina composite. *J Eng Manuf* 224:473–482
4. Kibria G, Doloi B, Bhattacharyya B (2014) Modelling and optimization of Nd: YAG laser micro-turning process during machining of aluminum oxide ( $Al_2O_3$ ) ceramics using response surface methodology and artificial neural network. *Manuf Rev* 1:1–8
5. Kuar AS, Acherjee B, Ganguly D, Mitra S (2012) Optimization of Nd:YAG laser parameters for microdrilling of alumina with multiquality characteristics via Grey-Taguchi method. *Mater Manuf Processes* 27:329–336
6. Kibria G, Doloi B, Bhattacharyya B (2012) Optimisation of Nd: YAG laser micro-turning process using response surface methodology. *Int J Precis Technol* 3:14–36
7. Biswas R, Kuar AS, Mitra S (2015) Process optimization in Nd:YAG laser microdrilling of alumina–aluminium interpenetrating phase composite. *J Mater Res Technol* 4:323–332
8. Nandi S, Kuar AS (2015) Parametric optimisation of Nd:YAG laser micro-drilling of alumina using NSGA II. *Int J Mach Mach Mater* 17:1–21
9. Mohammed MK, Umer U, Al-Ahmari A (2017) Optimization of laser micro milling of alumina ceramic using radial basis functions and MOGA-II. *Int J Adv Manuf Technol* 91:2017–2029
10. Kalita K, Shivakoti I, Ghadai RK (2017) Optimizing process parameters for laser beam micro-marking using genetic algorithm and particle swarm optimization. *Mater Manuf Process* 32:1101–1108
11. Dhupal D, Mohanty S, Dixit SR, Das SR, Nanda BK (2018) Micromachining on Al-SiC based metal matrix composite using DPSS laser. *Mater Today: Proc* 5:11304–11318

# Application of Taguchi's Orthogonal Array and Overall Evaluation Criteria in Turning of AISI D2 Steel in Dry and Forced Air-Cooled Environment



S. K. Rajbongshi and D. K. Sarma

**Abstract** Optimization of process parameters is an important technique in machining sector. In the present work, an experimental study has been performed in turning of AISI D2 steel using coated carbide tool in dry and forced air-cooled environment. Taguchi's orthogonal array  $L_9$  has been used for running the experiments considering cutting speed, feed rate and depth of cut as process parameters and surface roughness, flank wear and cutting force as performance parameters. To optimize the performance parameters together in a single setting, an overall evaluation criterion (OEC) has been used. Analysis of variance (ANOVA) and average performance value of OEC is also analyzed. It is found that from the predicted setting of the average performance value of OEC, the surface roughness, flank wear and cutting force is reduced in both dry turning (DT) and forced air-cooled turning (ACT) as compared to the optimum value obtained from the experimental run.

**Keywords** Taguchi's overall evaluation criteria · Dry turning · Air-cooled turning

## 1 Introduction

The machining operation is an important area in manufacturing sector. In order to manufacture products at competitive price, selection of proper cutting tool as well as process parameter is an important aspect. The process parameter setting plays an important role in obtaining optimum values of performance parameters. The hard machining operations can provide equivalent surface finish with grinding and better complex parts in less time and cost as compared to grinding operations. The researchers have focused mainly on machining of hard materials using coated carbide, ceramics and CBN inserts, mentioned by Bartarya and Choudhury [1]. Shao et al. mentioned the machinability of stellite 12 alloys with the application of coated and uncoated carbide tools in dry environment [2]. They suggested that the coated carbide tool was better as compared to uncoated carbide tool in minimizing flank

---

S. K. Rajbongshi (✉) · D. K. Sarma  
NIT Meghalaya, Shillong, Meghalaya 793003, India  
e-mail: [sanjibraj09@gmail.com](mailto:sanjibraj09@gmail.com)

© Springer Nature Singapore Pte Ltd. 2020  
L. Vijayaraghavan et al. (eds.), *Emerging Trends in Mechanical Engineering*,  
Lecture Notes in Mechanical Engineering,  
[https://doi.org/10.1007/978-981-32-9931-3\\_18](https://doi.org/10.1007/978-981-32-9931-3_18)

wear. Strenkowski et al. used CBN and advanced ceramic cutting tool materials in machining hardened steel [3]. The different wear behaviors of CBN tool was studied by Chou et al. in machining of hardened AISI 52100 steel [4]. The authors reported that the performance of low CBN content tool was better in terms of surface roughness and flank wear as compared to high CBN content tool. The machinability of AISI 4340 steel and AISI D2 steel using coated carbide tool and mixed alumina insert, respectively, were studied by Lima et al. [5]. It was reported that machining of AISI D2 steel using mixed alumina inserts gave equivalent surface finish comparable to cylindrical grinding.

In machining, due to the high friction between the tool and work piece generates high strain rates. Due to this temperature, generation is high at the tool work piece junction. Generally, liquid coolants are applied at the tool work piece junction to minimize the heat as well as for lubrication purposes. Dry machining is an important aspect considering it to be environmentally friendly. Klocke and Eisenblatte worked on dry machining; Weinert et al. mentioned the concept of near-dry machining (NDM) [6, 7]. Dixit et al. mentioned the green manufacturing concepts and its application in manufacturing area [8]. Now a day, the use of forced air-cooling is a new alternative to avoid the use of harmful coolants in machining. Sarma and Dixit studied the application of compressed air in machining of grey cast iron with mixed oxide ceramic tool [9]. Air-cooled turning was found to be better in terms of machining performances than dry turning. Similar observation was mentioned by Liu et al. [10].

The use of statistical analysis is an important tool in machining sector. The statistical tool helps in modeling and optimizing the machining parameters. Among the different statistical tool, Taguchi's optimization technique is widely used by the researchers. It helps the experimenters to give an optimal solution with less number of experiments. Panda et al. used Taguchi's  $L_9$  orthogonal array in hard turning of EN 31 steel using multilayer coated carbide inserts [11]. The authors observed feed and depth of cut as the significant parameters. Das et al. found minimum tool wear using Taguchi's  $L_9$  orthogonal array in machining AISI D2 steel with coated carbide inserts at a cutting speed of 150 m/min, feed 0.25 mm/rev and depth of cut 0.5 mm [12]. Singh and Kumar used Taguchi's orthogonal array to reduce tool wear in machining EN 24 steel with coated carbide inserts [13].

From the above literature reviews, it has been observed that the researchers are mainly using ceramic and CBN tool in machining hard materials, although few researchers have used coated carbide tool. Due to the high cost of ceramic and CBN tool, in the present work, an effort has been made using coated carbide tool in machining of hardened AISI D2 steel to obtain the best results similar to ceramic and CBN. Also, very few works have been done in turning operation using forced compressed air as the medium of operation. So, in this present work forced compressed air is used as the medium of operation. For comparison, dry turning is also performed. It is also found that lot of researchers are using Taguchi's single response optimization technique in optimizing machining parameters. But multi-response optimization technique such as overall evaluation criteria (OEC) application is very limited in

machining area. With this regard, in this work OEC criterion is being applied in turning of hardened AISI D2 steel with coated carbide tool in dry and forced air-cooled environment.

## 2 Experimental Set Up

The equipments which are used for conducting the experiments are as follows:

- (i) For the turning operation, high-speed conventional lathe of Make: Tussor Machine Tools India Pvt. Ltd. & Model: SC250 is used. The motor power of the lathe is 5.5 kW and spindle speed is 40–2300 rpm.
- (ii) Surface roughness is measured using surface roughness tester of Make: Taylor Hobson & Model: S-128 is used. The gauge range is 0–400  $\mu\text{m}$  and sampling length are 0.25–8 mm.
- (iii) For tool flank measurement, optical microscope of Make: Olympus & Model: BX51 M is used. The magnification range is 50X–1000X.
- (iv) For measurement of cutting forces, lathe tool dynamometer of Make: Kistler & Model: 9257 B is used. The range of the cutting force is 0–10 KN.
- (v) Reciprocating compressed air of Make: Elgi & Model: TS03HN is used for generating compressed air. The power of the compressor is 3 HP and maximum pressure limit is 12  $\text{kg}/\text{cm}^2$ . Compressor air flow rate and pressure at the nozzle end are 0.00041  $\text{m}^3/\text{s}$  and 1.052 bar, respectively.
- (vi) The work piece is heat-treated up to 48 HRC in an electric muffle furnace of Make: Voltam furnace Industries. The temperature of the furnace is 1400  $^{\circ}\text{C}$  with digital PID controller.

Figure 1 shows the experimental set up along with the specimen (work piece).

## 3 Results and Discussions

In this section, the results obtained from turning AISI D2 steel (48 HRC) with coated carbide tool in dry and forced air-cooled environment are discussed. The experimental design, Taguchi's overall evaluation criteria (OEC), analysis of variance (ANOVA) and average performance values of OEC are analyzed in this section.

### 3.1 Experimental Design

In the present work, three process parameters viz. cutting speed, feed and depth of cut have been considered for the study. Each parameter has three levels. The performance parameters considered for the study are surface roughness (SR), flank wear (FW) and



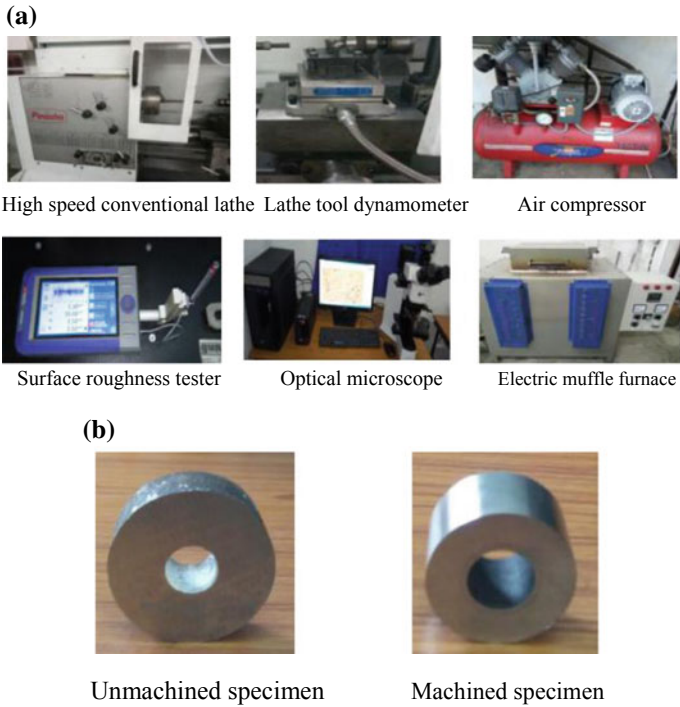


**Fig. 1** a Experimental set up. b Unmachined and machined specimen

cutting force (CF). The degree of freedom (DOF) of each parameter is 2. The total DOF for all the three parameters including the average is 7. Therefore, Taguchi’s orthogonal array (OA)  $L_9$  has been considered for the experimental design without considering the interaction effect. Table 1 shows the process parameters along with their levels and DOF.

**Table 1** Process parameters along with their levels and DOF

Parameters	Level			DOF
	1 (Low)	2 (Medium)	3 (High)	
$v$ (m/min)	100	125	150	2
$f$ (mm/rev)	0.05	0.10	0.15	2
$d$ (mm)	0.25	0.40	0.55	2

### 3.2 Overall Evaluation Criteria (OEC)

Taguchi's OA method, a fractional factorial design is useful in the sense that it selects particular settings of the parameters and gives the optimum value of the responses within that particular setting. This saves the time and cost of the experimenters without doing the full factorial design. In general, Taguchi's optimization method is applied to optimize single response at a time. This takes a lot of time and cost to optimize several responses separately. To overcome this problem, overall evaluation criteria (OEC) can be used to optimize the multiple responses obtained from Taguchi's OA table in one particular setting. This helps the experimenter to run only one confirmation experiment for the particular setting and to get the optimum value of the multi responses. In multi-objective optimization problems each response has different units, measurements, quality characteristics, and relative weight. To combine these different characteristics and criteria, the response values must be weighted and normalized accordingly. The formula for finding OEC is given as follows:

$$\begin{aligned} \text{OEC}_j = & [(S_{j1} - W_1)/(B_1 - W_1) \times R_1] + [(S_{j2} - W_2)/(B_2 - W_2) \times R_2] \\ & + [(S_{j3} - W_3)/(B_3 - W_3) \times R_3] \end{aligned} \quad (1)$$

Here,  $W$  represents worst value and  $B$  represents best value of a response,  $R$  represents relative weight of response,  $S$  means sample value,  $j = 1, 2, 3, \dots, 9$  in this experimental run. The indexes 1, 2, and 3 represent for surface roughness, flank wear and cutting force, respectively. The experimental run settings having higher OEC values give the optimum response values. Table 2 shows the Taguchi's OA  $L_9$  along with its response values and corresponding OEC values calculated using Eq. 1 in dry turning (DT) and air-cooled turning (ACT), respectively. The data for ACT is taken from author's previous work [14]. Here the values of  $R_1$ ,  $R_2$ , and  $R_3$  are taken as 40%, 40%, and 20%, respectively, for surface roughness, flank wear and cutting force considering the importance of responses.

### 3.3 Analysis of Variance (ANOVA)

ANOVA is a statistical analysis tool used for checking the influence of parameters in an experiment. In the present work, ANOVA is carried out for multi-objective optimization technique of OEC in DT and ACT. Tables 3 and 4 show the ANOVA for OEC in DT and ACT, respectively. From Table 3, it is observed that depth of cut and cutting speed are the most influential parameters for OEC as they have higher percentage contribution in OEC. Between depth of cut and cutting speed, depth of cut is found to be more significant as compared to the cutting speed because depth of cut has higher percentage contribution as compared to cutting speed in terms of OEC in DT. Feed has less influence for OEC in DT. Similarly from Table 4, cutting speed and depth of cut are the most significant parameters for OEC in ACT. Between

**Table 2** Taguchi's OA L<sub>9</sub> along with its response values and OEC in DT and ACT

Expt. No.	$v$ (m/min)	$f$ (mm/rev)	$d$ (mm)	SR ( $\mu\text{m}$ )		FW (mm)		CF(N)		OEC	
				DT	ACT	DT	ACT	DT	ACT	DT	ACT
1	100	0.05	0.25	1.44	1.77	0.15	0.10	113	48	71.36	78.42
2	100	0.10	0.40	1.38	1.61	0.22	0.19	176	235	61.68	59.94
3	100	0.15	0.55	1.33	1.53	0.43	0.27	202	299	35.55	48.38
4	125	0.05	0.55	1.36	1.57	0.40	0.29	182	163	38.11	54.45
5	125	0.10	0.25	1.30	1.36	0.23	0.18	102	99	82.17	85.26
6	125	0.15	0.40	1.33	1.64	0.35	0.28	189	182	48.75	50.58
7	150	0.05	0.40	1.30	1.42	0.35	0.30	102	79	65.03	67.70
8	150	0.10	0.55	1.55	1.93	0.40	0.40	178	225	10.51	15.89
9	150	0.15	0.25	1.57	2.12	0.38	0.30	55	96	27.14	29.50

**Table 3** ANOVA table for OEC in DT

Parameters	DOF	Sum of square (SS)	Mean sum of square (SS)	F-ratio	% Contribution
<i>v</i>	2	971.85	485.92	0.88	22.71
<i>f</i>	2	241.59	120.80	0.22	5.64
<i>d</i>	2	1963.69	981.84	1.79	45.91
Error (e)	2	1099.67	549.83		25.74
Total	8	4276.80			100

**Table 4** ANOVA table for OEC in ACT

Parameters	DOF	Sum of square (SS)	Mean sum of square	F-ratio	% Contribution
<i>v</i>	2	1266.31	663.15	1.76	32.55
<i>f</i>	2	869.25	434.62	1.21	22.34
<i>d</i>	2	1034.27	517.13	1.43	26.58
Error (e)	2	720.89	360.45		18.53
Total	8	3890.72			100

cutting speed and depth of cut, cutting speed is found to be more significant due to higher percentage contribution of cutting speed as compared to depth of cut for OEC in ACT. Feed has less influence as compared to cutting speed and depth of cut for OEC in ACT.

### 3.4 Average Performance Value of OEC

The average performance values are found out to evaluate the optimal process parameter combination to obtain the optimum response value (OEC). At first, OEC is found out for each experimental run for all the responses. Then OEC values are calculated based on the levels. The higher values of OEC for a particular parameter setting give the optimum value. Tables 5 and 6 show the average performance value with their optimal settings for OEC in DT and ACT, respectively. The bold letter indicates the optimum setting of the parameter value. From both Tables 5 and 6, the optimal

**Table 5** Average performance value and optimal parameter combination for OEC in DT

Parameter	Level		
	1	2	3
<i>v</i> (m/min)	56.19	<b>56.34</b>	34.22
<i>f</i> (mm/rev)	<b>58.17</b>	51.45	37.14
<i>d</i> (mm)	<b>60.22</b>	58.48	28.05

**Table 6** Average performance value and optimal parameter combination for OEC in ACT

Parameter	Level		
	1	2	3
$v$ (m/min)	62.24	<b>63.43</b>	37.69
$f$ (mm/rev)	<b>66.86</b>	53.70	42.82
$d$ (mm)	<b>64.39</b>	59.40	39.58

setting of the parameter for OEC in DT and ACT is  $v_2-f_1-d_1$ , i.e.,  $v = 125$  m/min,  $f = 0.05$  mm/rev,  $d = 0.25$  mm.

### 3.5 Comparison of Optimum Value of OEC from Experimental Run and Level Wise Optimum Parametric Average Performance Value of OEC

It is observed that the Expt. No. 5 has higher value of OEC for both DT and ACT, i.e., the setting is  $v_2-f_2-d_1$  from Table 2. The optimum value of average performance for OEC is found as  $v_2-f_1-d_1$  that represents in Tables 5 and 6. The confirmatory experiment for both these optimal settings of OEC is performed. The values of surface roughness, flank wear and cutting force using the predicted performance value of OEC are shown in Table 7 along with the comparison of optimal values from Expt. no 5 for both DT and ACT. Using the Taguchi’s OEC criteria and the average performance value, it is observed that the surface roughness, flank wear and cutting force is improved by 5.38%, 4.34%, and 22.54%, respectively, for DT. Similarly for ACT, surface roughness, flank wear and cutting force is improved by 4.41%, 16.67%, and 15.15%, respectively. From these results, it is found that the average performance value of OEC is higher in case of ACT as compared to that of DT which implies that ACT is better as compared to DT. From the comparison of

**Table 7** Comparison of experimental values of optimal experimental run and optimal average performance value of OEC in DT and ACT

Optimal machining parameters				
Condition	DT		ACT	
	Using optimal value in expt. no 5 from $L_9$ table	Using optimal average performance prediction value	Using optimal value in expt. no 5 from $L_9$ table	Using optimal average performance prediction value
Level	$v_2-f_2-d_1$	$v_2-f_1-d_1$	$v_2-f_2-d_1$	$v_2-f_1-d_1$
SR ( $\mu\text{m}$ )	1.30	1.23	1.36	1.30
FW (mm)	0.23	0.22	0.18	0.15
CF (N)	102	79	99	84

OEC value, it is observed that in ACT, the improvement rate of tool wear is better as compared to DT. But the improvement rate of surface roughness and cutting force is better in case of DT than ACT.

## 4 Conclusion

In this work, Taguchi's OA L<sub>9</sub> has been used for conducting the experiments in turning of AISI D2 steel using coated carbide tool in a dry and forced air-cooled environment. OEC technique is used for optimization of surface roughness, flank wear and cutting force at a single setting for both DT and ACT. The result obtained from Taguchi's analysis in both DT and ACT is summarized as follows:

- 1) From ANOVA, the depth of cut followed by cutting speed is the most influential parameter in terms of multi-optimization criteria in DT, whereas cutting speed followed by depth of cut are the most influential parameters in ACT. In both DT and ACT, feed rate has less significance for OEC.
- 2) The optimal experimental run has been found using higher OEC criteria which is found in experiment number 5 for both DT and ACT.
- 3) The optimal experimental run is compared with the optimal settings of the average performance value of OEC for both DT and ACT. There is an improvement of 5.38, 4.34, and 22.54% for surface roughness, flank wear and cutting force in DT using the optimal setting of average performance value in comparison to the experimental run 5. Similarly, for ACT; surface roughness, flank wear and cutting force is improved by 4.41%, 16.67%, and 15.15%, respectively.
- 4) From OEC, the improvement rate of tool wear is better in case of ACT than DT, but the improvement rate for surface roughness and cutting force is better in DT as compared to ACT.

## References

1. Bartarya G, Choudhury SK (2012) State of the art in hard turning. *Int J Mach Tools Manuf* 53(1):1–14
2. Shao H, Li L, Zhang SZ (2013) Study on machinability of stellite alloy with uncoated and coated carbide tools in turning. *J Manuf Process* 15(4):673–681
3. Strenkowski JS, Shih AJ, Lin JC (2002) An analytical finite element model for predicting three-dimensional tool forces and chip flow. *Int J Mach Tools Manuf* 42(6):723–731
4. Chou YK, Evans CJ, Barash MM (2002) Experimental investigation on CBM turning of hardened AISI 52100 steel. *J Mater Process Technol* 124(3):274–283
5. Lima JG, Avila RF, Abrao AM, Faustino M, Davim JP (2005) Hard turning: AISI 4340 high strength low alloy steel and AISI D2 cold work tool steel. *J Mater Process Technol* 169(3): 388–395
6. Klocke F, Eisenblatte G (1997) Dry turning. *CIRP Ann-Manuf Technol* 46 (2):519–526

7. Weinert K, Inasaki I, Sutherland JW, Wakabayashi T (2004) Dry machining and minimum quantity lubrication. *CIRP Ann-Manuf Technol* 53(2):511–537
8. Dixit US, Sarma DK, Davim JP (2012) *Environmentally friendly machining*, 1st edn. Springer-Verlag, New York
9. Sarma DK, Dixit US (2007) A comparison of dry and air-cooled turning of grey cast iron with mixed oxide ceramic tool. *J Mater Process Technol* 190(1–3):160–172
10. Liu M, Chiang KT, Hung CM (2013) Modelling and analyzing the effects of air-cooled turning on the machinability of Ti-6Al-4 V titanium alloy using the cold air gun coolant system. *Int J Adv Manuf Technol* 67(5–8):1053–1066
11. Panda A, Sahoo AK, Rout AK (2016) Investigations on surface quality characteristics with multi-response parametric optimization and correlation. *Alex Eng J* 55:1625–1633
12. Das SR, Nayak RP, Dhupal D (2012) Optimization of cutting parameters on tool wear and work piece surface temperature in turning of AISI D2 steel. *Int J Lean Think* 3:140–156
13. Singh H, Kumar P (2004) Tool wear optimization in turning operation by Taguchi method. *J Eng Mater Sci* 11:19–24
14. Rajbongshi SK, Sarma DK (2019) Process parameters optimization using Taguchi's orthogonal array and grey relational analysis during hard turning of AISI D2 steel in forced air-cooled condition. *IOP Conf Ser: Mater Sci Eng* 491(012032):1–6

# Rearranging and Optimizing of Butterfly Valve Manufacturing Layout Using Simulation



Shridevi V. Patil, V. N. Gaitonde, Vinayak N. Kulkarni  
and Sanjay V. Kulkarni

**Abstract** Most layouts are designed for the initial conditions of the business; however, as the company grows it has to adapt to internal and external changes; a redesign is necessary for plant layout. There should be a relationship between output, shop floor area and manufacturing process. This study is based on the analysis of the current layout of the butterfly valve in WEIR BDK Valves, Hubballi. The current layout measurement is noted in the initial stage with the current layout and proposed layout drawings with the help of CAD software, and the time study, arrangement of machines, productivity and material flow of current layout are analyzed. The aim of this project is to purpose a new and efficient layout to reduce travel time, to minimize material flow and to find out the most efficient arrangement of machines in the assembly unit of butterfly valve section. The new proposed layout is analyzed using the ARENA simulation software, and the same is implemented in the company. After implementing, the time study, material flow and arrangement of machines of proposed layout are analyzed. This study also illustrates how simulation technique helps in solving the problems in plant layouts. It also helps to modify the plant layout to improve the productivity and overall efficiency of company. The efficient redesign of plant layout is necessary for operations and management costs.

**Keywords** Plant layout · Butterfly valve unit · Cycle time · Productivity

## 1 Introduction

The design of a plant layout refers to the arrangement of the material, the machine and the human sequence inside the unit or plant to have the easiest and shortest material flow at the lowest cost and with the least amount of material processing process and to improve the delivery of finished products. There are two methods for layout improvement. The first is the re-routing of material flow in a given facility that

---

S. V. Patil (✉) · V. N. Gaitonde · V. N. Kulkarni · S. V. Kulkarni  
School of Mechanical Engineering, KLE Technological University, Hubballi, Karnataka 580031,  
India  
e-mail: [patilsv989@gmail.com](mailto:patilsv989@gmail.com)

© Springer Nature Singapore Pte Ltd. 2020  
L. Vijayaraghavan et al. (eds.), *Emerging Trends in Mechanical Engineering*,  
Lecture Notes in Mechanical Engineering,  
[https://doi.org/10.1007/978-981-32-9931-3\\_19](https://doi.org/10.1007/978-981-32-9931-3_19)



can improve the efficiency of material movement. When re-routing is not efficient, the other alternative is the redesign of the layout. In most of the cases, the redesign requires more time, effort and is more expensive [1]. Yadav and Sharma [2] conducted a study in B. Shankara Sales Organization, Agra, by creating several virtual options of layout without disturbing the original one, and this study gave a fantastic change in production rate, productivity plant efficiency with efficient utilization [2]. John and Jenson Joseph [3] focus to simulate the factory layout using the software ARENA (student's version) and came out with results that only properly laid out plant can ensure the smooth and rapid movement of material, from the raw material stage to the end product stage. Singh and Lal [4] focus on various techniques used in plant layout; these systems are utilized to enhance the efficiency of design.

This project focuses on the study of the flow in the production line of process layout as well as the shop floor layout of butterfly valve unit in the WEIR BDK Valves. Here, the first step is to examine the existing layout before modeling and simulating the plant layout in Arena software. This project aims to develop a process flow simulation model of the existing plant layout to identify problems in the production line and determine where the productivity improvement can be realized. Next step is to develop a proposed layout, the simulation software gives the details of productivity problems in the assembly line and several new plant layout designs are developed to encounter the problems occurred in the original plant layout. From the analysis and the simulation results, a summary of comparison of before and after layout results is made.

## 2 Methodology

To accomplish the objective of the study, initially the problem is identified in the current layout. Based on the problem identified, the literature survey has been done after which all the parameters like TAKT time (is the average between start of production of one unit to another next unit), cycle time (is the total time from the beginning to the end of the process, it includes all process times), material movement and volume of production of current layout are analyzed. Then, a proposed model is built by using CAD software for visual checking of layout and identified the difference between all parameters considered in current layout with proposed layout. The feasibility test of proposed layout is done with the help of Arena simulation software, and the proposed layout is implemented.

### 2.1 *Current Layout Data Analysis*

The current state production processes have 31 steps to manufacture a valve. The process map helps to identify the non-value-added activities in the process. There will be a different process map for different size of valves. This particular process map

is used to analyze the valve size of DN40-150. The steps involved in the particular process map initially start with cleaning the cast body, and next steps are as follows: inserting the seat inside the body, hammering the seat, fixing of bush to the stem, stem matching with the disk, applying grease inside the seat and on disk, disk inserting in the seat, bottom stem assembly, disk for symmetry with screwdriver, applying grease to the top stem, top stem assembly, fixing of plate with two Allen bolts, fixing of bottom cap by two hex bolts, fixing of throttle plate by two hex nut and bolts with washers, lever fixing, final tightening of nuts and bolts, checking proper sealing of disk with the seat by operating lever, moving the assembled valve to testing input area, searching and placing of test plates, keeping the valve in the fixture and filling water for cell testing, setting up a pressure for cell testing, shell leak observation, drain the pressure, arrangements for seat test, closing the fixture, applying pressure for seat test, seat leak observation, releasing pressure, removing valve from the test fixture, at last tagging and packing should done.

While taking the measurements and identifying the bottlenecks in the current layout, the data of TAKT time, cycle time and distance traveled by the materials were collected to analyze the difference between these parameters after implementing the proposed layout. Table 1 shows the cycle time and distance traveled for different size of valves.

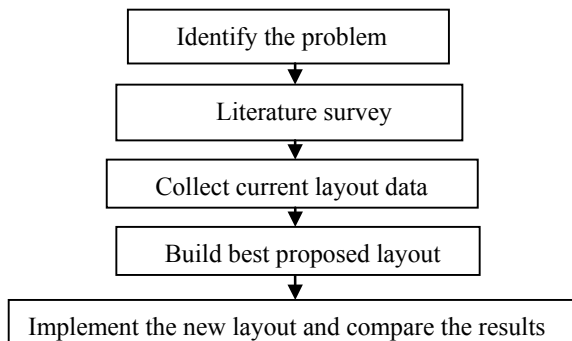
Figure 1 shows the total number of valve seized or attended by each worker at each process stage. It is clear from the figure that the workers at stages 1, 3, 8, 13, 17, 21 attended the more number of valves.

From Fig. 2, it is evident that motion and movement contribute to 45% of the waste followed by over processing with 35% contribution.

**Table 1** Data distribution table (before)

Size	Distance travel (m)	Time (s)	
		Cycle time	TAKT time
DN40-100	50	1032	645
DN125-150	50	1017	645

**Fig. 1** Flow chart of methodology



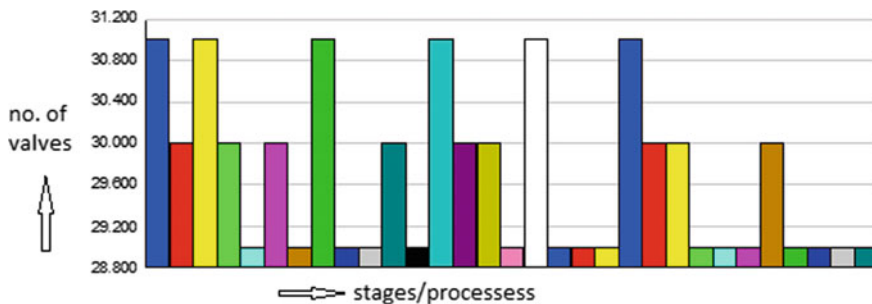


Fig. 2 Total number seized (before)

### 2.2 After Layout Data Analysis

After analyzing the current layout, the proposed layout is checked for feasibility using Arena simulation. After that some time-consuming activities which are marked as wastes like clean the cast body, stem matching with disk, disk for symmetry with screwdriver, final tightening of nuts and bolts, moving the body, searching of test plates, keeping the valve in the fixture and water filling activity are removed. Thus, the simulation model of proposed layout is built which contains 23 steps by eliminating non-value-added steps from 31 steps of current layout [5, 6].

The data observed after implementing proposed layout and after checking feasibility of proposed layout in Arena simulation are listed in Table 2.

Figure 3 indicates the wastes identified in the process. From Fig. 4 it is clear that the number of valves seized by worker is more (88) at stage 15, i.e., shell test stage.

## 3 Results

From Tables 1 and 2, it can be seen that before the changes in layout, the cycle time for size DN40-100 is 1032 s and for size DN125-150 is 1017 s which means the cycle time for both sizes exceeds the TAKT time 645 s. After implementation, the cycle time is reduced for all sizes, i.e., for size DN40-65 is 620 s, DN80-100 is 614 s, for DN125-150 is 634 s. It is also seen that the distance traveled is reduced from 50 to 20 m.

Table 2 Data distribution table (after)

Size	Distance travel (m)	Time (s)	
		Cycle time	TAKT time
DN40-65	20	620	645
DN80-100	20	614	645
DN125-150	20	634	645

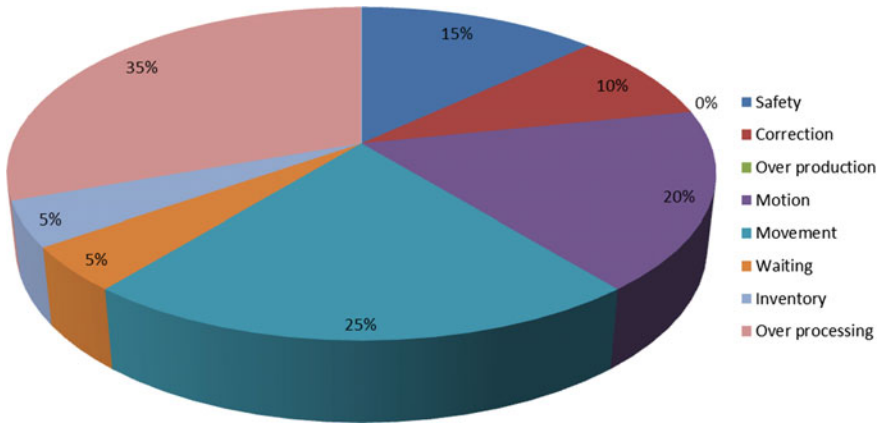


Fig. 3 Waste identification chart

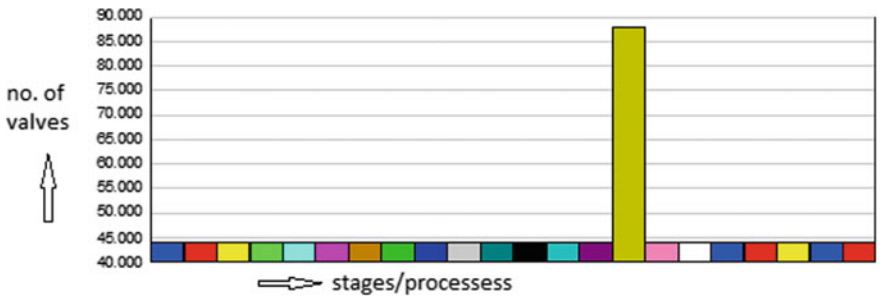


Fig. 4 Total number seized (after)

### 3.1 Comparison of Productivity (Volume of Production)

The total available time per day or per shift is 30,300 s, i.e., 505 min

$$\text{Valves/shift} = \frac{\text{total available time in sec}}{\text{time to produce one valve in sec}}$$

From Table 3, it is clear that the volume of production is increased from 29 valves per shift to 44 valves per shift.

Table 3 Comparison of productivity

	No. of products/shift	No. of products/month
Before	29	870
After	44	1320

**Table 4** Comparison of machine utilization

	VA time	NVA time	Wait time	Transfer time	Total time	TMU
Before	0.06213	0.01939	0.00795	0.00	0.08947	0.3159
After	0.07418	0.00	0.00069	0.00	0.07488	0.3915

Time is in hours

VA time value-added time, NVA time non-value-added time, TMU total machine utilization

### 3.2 Percentage Improvements

$$\% \text{ increase} = \frac{\text{new value} - \text{initial value}}{\text{initial value}} \times 100$$

$$\% \text{ reduce} = \frac{\text{initial value} - \text{new value}}{\text{initial value}} \times 100$$

The percentage improvements are as follows:

1. % reduction in distance traveled = 60%
2. % reduction in cycle time = 39.9%
3. % increase in machine utilization = 23.93%
4. % increase in productivity = 51.72%.

### 3.3 Machine Utilization

From Table 4, it can be seen that the value-added time to manufacture a valve is increased from 0.06213 h of current layout to 0.07418 h of proposed layout. The non-value-added time and total time required to manufacture valve are reduced from 0.01939 to 0 h and 0.08947 to 0.07488 h, respectively. The total machine utilization is improved from 31.59 to 39.15% after implementing a new or proposed layout of butterfly valve unit.

## 4 Conclusions

For the efficient production of the components in the industry, it is desirable to have a good disposition to reduce the material handling time, the cost, the production time, etc., since this project simulates the location of the existing plant. Then, the best alternative design was determined using a simulation technique using Arena software. The purpose of redesigning an existing design is to ensure that the company has a competitive advantage. This is the most important objective for any organization.

After the implementation of the proposed design and after verifying the feasibility of the design in the Arena simulation, it can be said that the objectives of the study are met.

- The distance travel by the material is reduced to 60% after implementing new plant layout.
- There is 39.9% reduction in cycle time of proposed layout.
- The machine utilization is found to be increased by 23.93% in proposed layout.
- The productivity is maximized from current layout to proposed layout by 51.72%.

## References

1. Zhang M, Batta R, Nagi R (2011) Designing manufacturing facility layouts to mitigate congestion. *IIE Transactions*, 43(10):689–702
2. Yadav P, Sharma S (2016) A case study of plant layout: to compare production efficiency of manual plant layout and computerized plant layout using ARENA software. *General Sci* 4(4) (July–August)
3. John B, Jenson Joseph E (2013) Analysis and simulation of factory layout using ARENA. *Int J Sci Res Publ* 3(2), (February)
4. Tejinder S, Harvinder L (2016) Various techniques used in plant layout. *Int J Res Mech Eng Technol* 6(1):33–34. ISSN: 2249-5770
5. Kulkarni RG, Kulkarni VN, Gaitonde VN (2018) Productivity improvement in assembly workstation of motor winding unit. *Mater Today: Proc* 5(11):23518–23525
6. Ravikumar K, Vinayak K (2014) Productivity improvement at assembly station using work study techniques. *Int J Res Eng Technol* 3(September) eISSN: 2319-1163

# A Comparative Analysis of Annular Fin Array Under Multi-objective Optimization



Abhijit Deka and Dilip Datta 

**Abstract** This study presents a comparative analysis of different optimum annular fin arrays, which involve fins of constant thickness, nonlinearly varying thickness, and step change in thickness. The designs of the fin arrays are formulated as multi-objective optimization problems aiming at maximizing the heat dissipation rate and surface efficiency while minimizing the total fin volume. Computing the heat dissipation rate through the hybrid spline difference method (HSDM), the multi-objective optimizer NSGA-II is utilized for optimizing the considered three-objective functions in various combinations. Finally, to facilitate one in selecting a compromise fin array configuration out of multiple trade-off alternatives, a comparative analysis is performed among the trade-off solutions obtained for the considered three types of fin arrays.

**Keywords** Annular fin array · Heat dissipation · Multi-objective optimization

## 1 Introduction

The heat dissipation from a heat exchanger having a cylindrical primary surface can be increased by attaching an annular fin array to it. However, the requirement of additional material and fabrication for the fin array increases the overall cost of the heat exchanger, thus demanding the optimum design of the fin array.

A very few number of works dealing with optimization of annular fin array could be found in specialized literature, the majority of which are concerned with annular fin arrays with fins of constant thickness [1, 2]. A fin array with fins of constant thickness has the simplest design, but the material near its tip is not fully utilized

---

A. Deka (✉) · D. Datta  
Department of Mechanical Engineering, Tezpur University,  
Tezpur 784028, India  
e-mail: [adeka13@tezu.ernet.in](mailto:adeka13@tezu.ernet.in)

D. Datta  
e-mail: [ddatta@tezu.ernet.in](mailto:ddatta@tezu.ernet.in)

© Springer Nature Singapore Pte Ltd. 2020  
L. Vijayaraghavan et al. (eds.), *Emerging Trends in Mechanical Engineering*,  
Lecture Notes in Mechanical Engineering,  
[https://doi.org/10.1007/978-981-32-9931-3\\_20](https://doi.org/10.1007/978-981-32-9931-3_20)

in heat dissipation, thus encourages fin arrays with stepped fins or fins of thickness decreasing gradually in the outward direction [3–5].

On the other hand, the design of fins is usually limited only to single-objective optimization, where the heat dissipation rate is maximized considering either a pre-defined fixed volume [6] or a fixed total height of the fin array [7]. In practice, the heat dissipation rate through a fin array conflicts with fin volume and surface efficiency, i.e., an optimized solution favorable for one is unacceptable in terms of the other and *vice-versa*. Hence, design of a fin array essentially becomes a multi-objective optimization problem. However, no work in specialized literature could be found comparing performances of different annular fin arrays under multi-objective optimization. Inspired by such research gap, this work puts forward a comparative analysis of the optimal scenarios of different annular fin arrays, which would facilitate one to adopt a suitable solution out of multiple alternatives based upon the availability of information and resources.

## 2 Problem Statement and Formulation

Figure 1 shows the schematic diagrams of annular fin arrays having fins of different profiles (namely fins of constant thickness, nonlinearly varying thickness (e.g., parabolic, hyperbolic etc.), and step change in thickness) where  $r$  represents the radial distance of a fin with  $r_b$  and  $r_o$  being its base and tip values, respectively, and  $s_b$  is the interspacing at the base of two fins. For a fin of constant thickness as shown in Fig. 1a,  $t_b$  is the half thickness of the fin. In Fig. 1b,  $t$  represents the half thickness of a fin of nonlinearly varying thickness with  $t_b$  and  $t_o$  being its base and tip values, respectively. On the other hand,  $t_1$  and  $t_2$  in Fig. 1c are the half thicknesses of the two rectangular steps of a stepped fin while  $r_1$  is the radius at the point of step change in thickness.

### 2.1 Heat Dissipation Model

In this study, the thermal conductivity  $k$  is considered to be varying linearly with temperature  $T_i$  as given by Eq. (1) [8],

$$k = k_a \{1 + \beta (T_i - T_\infty)\} \quad (1)$$

where  $T_\infty$  is the ambient temperature,  $k = k_a$  at  $T_i = T_\infty$ , and the parameter  $\beta$  controls the variation in  $k$ . Furthermore,  $T_i = T$  for constant and nonlinearly varying thickness fins, while  $i$  in  $T_i$  indicates the steps in a stepped fin ( $i = 1$  for the step near the base and  $i = 2$  for the step near the tip). For air flowing through two consecutive fins, the average natural convective heat transfer coefficient  $h$  can be given by Eq. (2) [9],



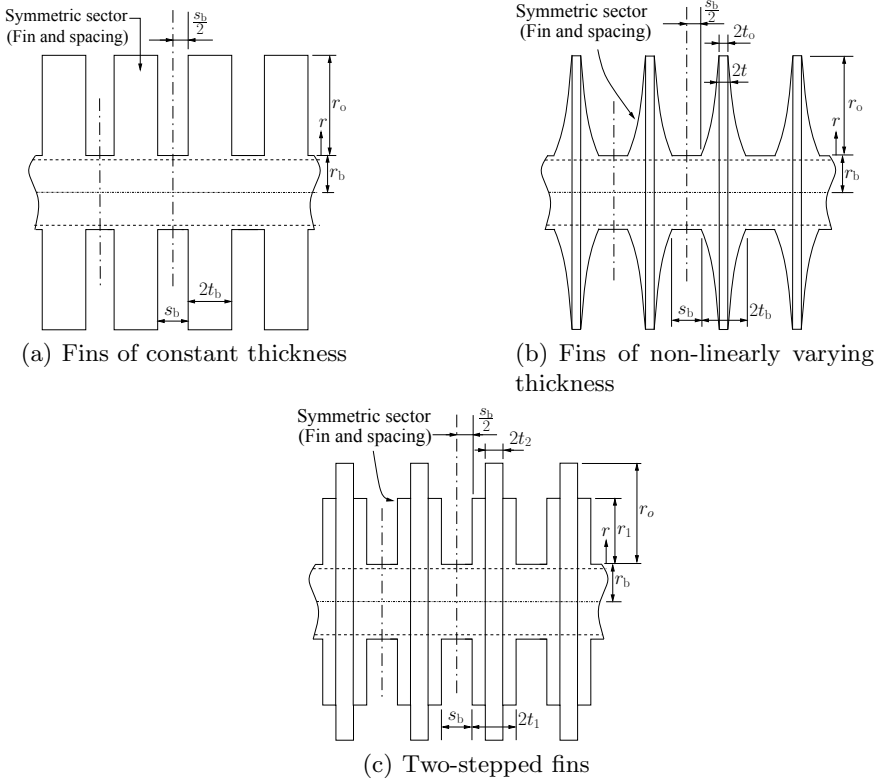


**Fig. 1** Arrays of annular fins with fins of different profiles

$$\left. \begin{aligned}
 h &= \frac{k}{s_m} \left\{ c_0 + c_1 Ra^{a_0} \left( \frac{r_o}{r_b} \right)^{a_1} + c_2 Ra^{a_2} + c_3 \left( \frac{r_o}{r_b} \right)^{a_3} \right\} \\
 \text{where, } Ra &= \frac{g \beta_e (T_b - T_\infty) s_m^4}{2 \nu_s \alpha_s r_o} \\
 c_0 &= -3.827 ; \quad c_1 = 0.047 ; \quad c_2 = 1.039 ; \quad c_3 = 2.548 \\
 a_0 &= 0.348 ; \quad a_1 = 0.173 ; \quad a_2 = 0.175 ; \quad a_3 = 0.009
 \end{aligned} \right\} \quad (2)$$

where  $s_m$  is the mean fin interspacing, and  $Ra$  is the Rayleigh number in the laminar range of  $[5, 10^8]$ . The properties are evaluated at the film temperature of  $(T_b + T_\infty) / 2$ ,  $T_b$  being fin base temperature.  $g$  is acceleration due to gravity while  $\nu_s$ ,  $\beta_e$ , and  $\alpha_s$  are, respectively, kinematic viscosity, thermal expansion coefficient, and thermal diffusivity of air.

Various assumptions made in this study are as follows: (a) fin base temperature ( $T_b$ ) is constant, (b) flow of heat through the fin is one-dimensional (since, the fin thickness is considered to be very small as compared to its outer radius) and in steady state, (c) heat loss from a fin array takes place by natural convection only, (d) no internal

heat is generated, (e) fin arrays are in the horizontal orientation making the gravity forces parallel to the fins, and (f) the thermal behavior of a fin array is equivalent to that of a repetitive sector containing a fin and interspacing as shown in Fig. 1. With such assumptions, the governing equation and boundary conditions for constant and nonlinearly varying thickness fins of annular fin arrays can be given by Eqs. (3) and (4), respectively.

$$\frac{d}{dr} \left[ r \{1 + \beta (T - T_\infty)\} \frac{dT}{dr} \right] + \left[ r \{1 + \beta (T - T_\infty)\} \frac{dT}{dr} \right] \frac{t'}{t} - \frac{hr}{k_a t} (T - T_\infty) \left(1 + t'^2\right)^{\frac{1}{2}} = 0 \tag{3}$$

$$T = T_b ; \quad \text{at } r = r_b \tag{4a}$$

$$-k_a \{1 + \beta (T - T_\infty)\} \frac{dT}{dr} = h (T - T_\infty) ; \quad \text{at } r = r_o \tag{4b}$$

Similarly, the energy balance governing equation and boundary conditions for stepped fins of an annular fin array can be given by Eqs. (5) and (6), respectively.

$$\text{where, } \left. \begin{array}{l} \frac{d}{dr} \left[ r \{1 + \beta (T_i - T_\infty)\} \frac{dT_i}{dr} \right] - \frac{hr}{k_a t_i} (T_i - T_\infty) = 0 \\ r_b \leq r \leq r_1 ; \quad \text{for } i = 1 \\ r_1 \leq r \leq r_o ; \quad \text{for } i = 2 \end{array} \right\} \tag{5}$$

$$T_1 = \begin{cases} T_b ; & \text{if } r = r_b \\ T_2 ; & \text{if } r = r_1 \end{cases} \tag{6a}$$

$$-k_a \{1 + \beta (T_2 - T_\infty)\} \frac{dT_2}{dr} = h (T_2 - T_\infty) ; \quad \text{at } r = r_o \tag{6b}$$

$$-t_1 k_a \{1 + \beta (T_1 - T_\infty)\} \frac{dT_1}{dr} = -t_2 k_a \{1 + \beta (T_2 - T_\infty)\} \frac{dT_2}{dr} + h (t_1 - t_2) (T_1 - T_\infty) ; \quad \text{at } r = r_1 \tag{6c}$$

### 3 Optimization Modeling of Annular Fin Arrays

The performance analysis of the considered annular fin arrays is carried out in different combinations of three-objective functions, namely the total heat dissipation rate ( $f_1$ ), total fin volume ( $f_2$ ), and surface efficiency ( $f_3$ ). The fin arrays are accordingly formulated as multi-objective optimization problems.

### 3.1 Fin Arrays with Constant and Nonlinearly Varying Thickness Fin

The nonlinearly varying thickness profile of the fin is defined by a B-spline curve, where the coordinates of the  $m$  number of control points of the B-spline curve,  $P_i(x_i, y_i)$  ( $i = 1$  to  $m$ ), are considered as the design variables of the fin array as depicted in Fig. 1b with  $x$  values representing the radial distances of a fin from its base and  $y$  values as the corresponding half thicknesses of the fin. A fin of constant thickness, as depicted in Fig. 1a, can be expressed by such a single point with  $m = 1$ , i.e., by  $P_1(x_1, y_1)$  with  $x_1$  representing the outer radius of the fin and  $y_1$  as its half thickness. The number of fins in a fin array,  $n_{fin}$ , is taken as another design variable in these two fin arrays. Accordingly, a common multi-objective optimization problem can be formulated for the above-mentioned fin arrays as given by Eq. (7).

$$\left. \begin{array}{l} \text{Determine} \\ \text{to maximize} \\ \text{minimize} \\ \text{subject to} \end{array} \right\} \begin{array}{l} \mathbf{x} \equiv \{n_{fin}, P_i(x_i, y_i) | P_i(x_i, y_i); i = 1 \text{ to } m\}^T \\ \mathbf{z}(\mathbf{x}) \equiv \{f_1(\mathbf{x}), f_3(\mathbf{x})\}^T \\ \mathbf{f}(\mathbf{x}) \equiv \{f_2(\mathbf{x})\}^T \\ g_1(\mathbf{x}) \equiv x_1 < x_2 \leq \dots \leq x_m \\ g_2(\mathbf{x}) \equiv \frac{W}{4} \geq y_1 \geq y_2 \geq \dots \geq y_m \\ g_3(\mathbf{x}) \equiv \left\lfloor \frac{W}{2y_1 + s_{max}} \right\rfloor \leq n_{fin} \leq \left\lfloor \frac{W}{2y_1 + s_{min}} \right\rfloor \\ s_{max}, s_{min} \geq 0 \end{array} \quad (7)$$

In Eq. (7), constraint  $g_1(\mathbf{x})$  ensures that the control points of the B-spline curve (i.e., their  $x$  values) are distributed in the radial outward direction of a fin, while constraint  $g_2(\mathbf{x})$  makes the corresponding  $y$  values non-increasing (note that constraints  $g_1(\mathbf{x})$  and  $g_2(\mathbf{x})$  are not applicable in the case of the fins of constant thickness). In constraint  $g_2(\mathbf{x})$ , the upper limit of  $y_1$  (i.e.,  $y_1 \leq \frac{W}{4}$ ) ensures that the fin array is formed with a minimum of two fins within the predefined fixed length ( $W$ ) of the heat exchanger primary surface. On the other hand, constraint  $g_3(\mathbf{x})$  sets the lower limit of  $n_{fin}$  to two and the upper limit to such a value to avoid the excess number of fins over length  $W$ . Further, in constraint  $g_3(\mathbf{x})$ , the range of fin interspacing at the base,  $(s_{min}, s_{max})$ , is to be so chosen that  $Ra$  in Eq. (2) remains within its laminar range.

### 3.2 Fin Arrays with Fin of Step Change in Thickness

For fin array with two-stepped rectangular fins, the optimization problem can be formulated as in Eq. (8) by taking number of fins in the array ( $n_{fin}$ ), outer radii and half thicknesses of the two steps of a fin ( $r_1, r_o, t_1$ , and  $t_2$ ) as design variables.

$$\left. \begin{array}{l}
 \text{Determine} \quad \mathbf{x} \equiv (n_{\text{fin}}, r_1, r_o, t_1, t_2)^T \\
 \text{to maximize} \quad \mathbf{z}(\mathbf{x}) \equiv \{f_1(\mathbf{x}), f_3(\mathbf{x})\}^T \\
 \text{minimize} \quad \mathbf{f}(\mathbf{x}) \equiv \{f_2(\mathbf{x})\}^T \\
 \text{subject to} \quad g_1(\mathbf{x}) \equiv r_1 > r_b \\
 \quad \quad \quad g_2(\mathbf{x}) \equiv r_o > r_1 \\
 \quad \quad \quad g_3(\mathbf{x}) \equiv t_1 \leq \frac{W}{4} \\
 \quad \quad \quad g_4(\mathbf{x}) \equiv t_1 > t_2 \\
 \quad \quad \quad g_5(\mathbf{x}) \equiv \left[ \frac{W}{2t_1 + s_{\text{max}}} \right] \leq n_{\text{fin}} \leq \left[ \frac{W}{2t_1 + s_{\text{min}}} \right] \\
 \quad \quad \quad r_1, r_o, t_1, t_2 \geq 0 .
 \end{array} \right\} \quad (8)$$

In Eq. (8), constraint  $g_1(\mathbf{x})$  ensures the existence of a fin by making  $r_1 > r_b$ , while constraint  $g_2(\mathbf{x})$  ensures that the fin is of two steps by making  $r_o > r_1$ . Constraint  $g_4(\mathbf{x})$  makes the outer step of a fin thinner than its inner step. The purposes of constraints  $g_3(\mathbf{x})$  and  $g_5(\mathbf{x})$  are similar, respectively, to the conditions in constraint  $g_2(\mathbf{x})$  (i.e.,  $y_1 \leq \frac{W}{4}$ ) and constraint  $g_3(\mathbf{x})$  of Eq. (7).

### 3.3 Formulation of Objective Functions

In accordance with the thermal modeling of the fin array as given in Sect. 2, the three-objective functions in Eqs. (7) and (8), i.e.,  $f_1(\mathbf{x})$ – $f_3(\mathbf{x})$ , can be given by Eq. (9).

$$f_1(\mathbf{x}) = n_{\text{fin}} \times \left\{ -kA_b \left. \frac{dT_i}{dr} \right|_{r=r_b} + 2\pi hr_b s_b (T_b - T_\infty) \right\} \quad (9a)$$

$$f_2(\mathbf{x}) = V \quad (9b)$$

$$f_3(\mathbf{x}) = \frac{1}{n_{\text{fin}}} \times \frac{f_1(\mathbf{x})}{hA_s (T_b - T_\infty) + 2\pi hr_b s_b (T_b - T_\infty)} \quad (9c)$$

where  $A_b = \begin{cases} 4\pi r_b t_1 ; & \text{for stepped fins} \\ 4\pi r_b t_b ; & \text{for fins of constant and nonlinearly varying thicknesses} \end{cases} \quad (9d)$

The fin volume  $V$  in Eq. (9b) and the heat dissipation surface area  $A_s$  in Eq. (9c) for fins of nonlinearly varying thickness are evaluated using the Simpson’s  $\frac{1}{3}$  rule for numerical integration, while the same for constant thickness and stepped fins are evaluated from the fin geometry [10].

### 4 Experimentation and Discussion

The multi-objective optimization models of the fin design problems, as formulated by Eqs. (7) and (8), are solved using the non-dominated sorting genetic algorithm II (NSGA-II) [11]. In each cycle of NSGA-II, the hybrid spline difference method (HSDM) [8] is employed for evaluating the heat dissipation rate, i.e.,  $f_1(x)$  in Eq. (9a), using Eqs. (3) and (4) for fins of constant and nonlinearly varying thicknesses, while using Eqs. (5) and (6) for stepped fins [10]. Using C programming language, the proposed procedure is coded; the validation of which is conducted through the step fin tip temperature and its efficiency. The numerical results of HSDM exactly match with those of Kundu et al. [12], thus validating the numerical code for the direct problem used in this study.

The operating conditions and fin material properties, as well as the fin array geometry, considered for numerical experimentation, are given in Table 1. Based on some trial runs, the considered algorithmic parameter settings for NSGA-II are as follows: a population of size 100 is evolved over 400 generations with crossover probability of 90% and random mutation probability in the range of (0, 1%]. With such experimental setup, the multi-objective optimization problems in Eqs. (7) and (8) are studied under two combinations of the three-objective functions:  $f_1$ -vs- $f_2$  and  $f_1$ -vs- $f_3$ .

The comparison of the Pareto fronts obtained by simultaneously maximizing  $f_1$  and minimizing  $f_2$  is shown in Fig. 2, where it is found that  $f_1$  conflicts with  $f_2$ . It is also observed that the values of  $f_1$  at lower values of  $f_2$  are almost similar for all the three fin arrays. However, in terms of the  $f_1$  values at higher values of  $f_2$ , the fin array with fins of nonlinearly varying thickness comes out to be the best fin array, while the fin array with fins of constant thickness is the worst one.

**Table 1** Input data related to operating conditions, material properties, and fin array geometries

Parameter	Value/range of value
Ambient temperature, $T_\infty$	300 K
Fin base temperature, $T_b$	373 K
Thermal conductivity of the fin material at $T_\infty$ , $k_a$	186 W/mK
Variable thermal conductivity parameter, $\beta$	-0.00018 K <sup>-1</sup>
Base radius of fins, $r_b$	2.0 cm
Outer radius of fins, $r_o$	2.5–6.0 cm
Fin half thickness, $t$ (for fins of constant/varying thickness)	0.01–0.2 cm
Radius of step change in thickness, $r_1$ (for stepped fin)	2.5–6.0 cm
Half thickness of the step near the base, $t_1$ (for stepped fin)	0.01–0.2 cm
Half thickness of the step near the tip, $t_2$ (for stepped fin)	0.01–0.2 cm
Length of the primary cylinder, $W$	40.0 cm
Fin interspacing at base, $s_b$	[0.36, 18.0] cm

**Fig. 2** Pareto fronts of  $f_1$  and  $f_2$

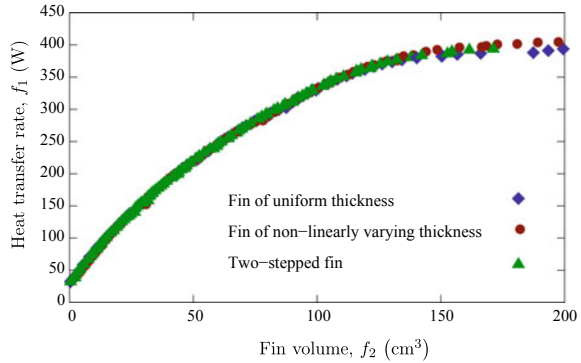
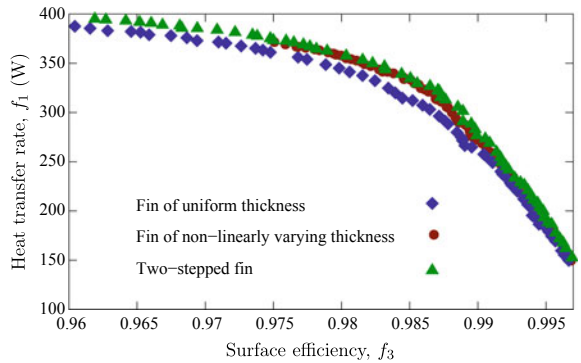


**Fig. 3** Pareto fronts of  $f_1$  and  $f_3$



The comparison of the Pareto fronts obtained by simultaneously maximizing  $f_1$  and  $f_3$  is shown in Fig.3, where it is found that  $f_1$  conflicts with  $f_3$  also. Further, it is observed that for similar values of  $f_1$ , the values of  $f_3$  are almost indifferent in the case of fin arrays with fins of nonlinearly varying thickness and stepped fins, and the same for the fin array with fins of constant thickness is the lowest.

### 5 Conclusion

This work presents a comparative investigation of multi-objective design optimization of three annular fin arrays. Maximizing the heat dissipation rate separately with minimization of total fin volume and maximization of fin surface efficiency, it is observed that the annular fin array with fins of nonlinearly varying thickness has a higher heat dissipation rate per unit fin volume, followed by those of the fin array with stepped fins. Further, for similar heat dissipation rate, the surface efficiency of fin array with fins of constant thickness is the lowest while it is almost similar in the case of fin arrays with fins of nonlinearly varying thickness and stepped fins.

## References

1. Bar-Cohen A, Iyengar M, Kraus AD (2003) Design of optimum plate-fin natural convective heat sinks. *J Electron Packag* 125:208–216
2. Lai CY, Kou HS, Lee JJ (2006) Optimum thermal analysis of annular fin heat sink by adjusting outer radius and fin number. *Appl Therm Eng* 26:927–936
3. Deka A, Datta D (2017) Geometric size optimization of annular step fin using multi-objective genetic algorithm. *J Therm Sci Eng Appl* 9:0210131–0210139
4. Deka A, Datta D (2017) B-spline curve based optimum profile of annular fins using multiobjective genetic algorithm. *J Therm Stress* 40:733–746
5. Deka A, Datta D (2018) Multi-objective optimization of annular fin array with B-spline curve based fin profiles. *J Therm Stress* 41:247–261
6. Kundu B, Lee KS, Campo A (2012) Exact and approximate analytic methods to calculate maximum heat flow in annular fin arrays with a rectangular step profile. *Int J Thermophys* 33:1314–1333
7. Kundu B, Das PK (2009) Performance and optimum design analysis of convective fin arrays attached to flat and curved primary surfaces. *Int J Refrig* 32:430–443
8. Wang CC, Liao WJ, Yang CY (2013) Hybrid spline difference method for heat transfer and thermal stresses in annular fins. *Numer Heat Transf Part B* 64:71–88
9. Senapati JR, Dash SK, Roy S (2016) Numerical investigation of natural convection heat transfer over annular finned horizontal cylinder. *Int J Heat Mass Transf* 96:330–345
10. Deka A, Datta D (2017) A comparative investigation of annular fins of different profiles using multi-objective genetic algorithm. In: 2017 international conference on advances in mechanical, industrial, automation and management systems (AMIAMS), Allahabad, India, IEEE, pp 74–79
11. Deb K, Pratap A, Agarwal S, Meyarivan T (2002) A fast and elitist multi-objective genetic algorithm: NSGA-II. *IEEE Trans Evol Comput* 6:182–197
12. Kundu B, Lee KS, Campo A (2015) An ease of analysis for optimum design of an annular step fin. *Int J Heat Mass Transf* 85:221–227

# A Novel Discount Mechanism for Buy Online PickUp in Store (BOPS)



Vinay Surendra Yadav  and A. R. Singh 

**Abstract** Buy online pickup in store (BOPS) is one of the omnichannel fulfillment strategies which is gaining lots of popularity among omnichannel stakeholders. For this purpose, few large retailers have adopted BOPS strategy while many more are in queue to adopt for BOPS's benefits to expand their business. To attract the customer to use BOPS environment, retailers often offer various discounts on products and services. In this paper, a novel discount strategy is proposed under BOPS environment to benefit both consumers and retailers. In this mechanism, the customer would be delighted through different discount categories which are based on travel distance to pick their order. To get depth insight into this strategy, a numerical illustration is enumerated. This strategy would be useful to the new market entrant in this area for expanding their business through leveraging such BOPS schemes.

**Keywords** BOPS · Discount mechanism · Omnichannel · Optimization

## 1 Introduction

The emergence of omnichannel has redefined the retail industry to a great extent. Consumers have transformed themselves into omnichannel consumers who believe to enjoy seamless experience. This demand to have frictionless service is making life difficult for retailer. Since this is an era of digital information, even a slight mistake by retailer in expectation fulfillment of consumer can cause a loss of many valuable customers. Thus, retailers are forced to restructure and reconfigure their strategy in order to match omnichannel expectation. Few of important ones are changed in structure of distribution network, information system, application programmable interface, channel collaboration, etc. These changes have brought many interesting intervention in today's retail industry. Few of them are buy online pickup in store

---

V. S. Yadav (✉) · A. R. Singh  
National Institute of Technology Raipur, Raipur, India  
e-mail: [vinaysyadav93@gmail.com](mailto:vinaysyadav93@gmail.com)

A. R. Singh  
e-mail: [amitrajsingh1@gmail.com](mailto:amitrajsingh1@gmail.com)

© Springer Nature Singapore Pte Ltd. 2020  
L. Vijayaraghavan et al. (eds.), *Emerging Trends in Mechanical Engineering*,  
Lecture Notes in Mechanical Engineering,  
[https://doi.org/10.1007/978-981-32-9931-3\\_21](https://doi.org/10.1007/978-981-32-9931-3_21)



(BOPS), reserve online pickup and pay in store (ROPS), ship to store (STS), ship from store (SFS), etc. Out of these, BOPS is most popular due win-win situation for both retailer as well as customer. These could be seen in terms of large retailer, i.e., 42% of them provide options of BOPS [1]. This strategy has been very effective in terms of its sales and providing better customer satisfaction. For example, BOPS accounted for almost a third (30.2%) of Sam's Club e-commerce sales in 2015 while in case of Kmart it was 22.6% [2]. Adoption of BOPS could be seen in the Nielsen report of 2015 [3] on the future of grocery. BOPS has many benefits such as it reduces congestion at store and thus saves the time of consumer. It is also cost effective due to reduced cost of last mile fulfillment which accounts for 28% of total delivery cost [4]. As due to pickup by consumer in case of BOPS, this major cost could be saved and in return some discount may be offered to consumer to motivate for BOPS. BOPS also offer quality check of the product at the time of pickup at store. BOPS is also very useful in increasing in-store sales through cross-selling at the time of pickup. Also, it overcomes the major disadvantage of online shopping issues like late delivery and returns management through its structure of collecting and returning product at the store.

BOPS being a very recent and novice phenomenon in today's retail industry, it possesses few shortcomings in its operations. JDA and Centrio (2016) [5] reported that about 16% of online consumer finds it difficult to locate their appropriate order picking store because of distance issues. This drawback in the form of "unreasonable store recommendation" is a serious issue which keeps 62% of consumer away [6], and these issues have not been reported much in the literature. Jin et al. [7] tried to answer this query by deciding optimal strategy by trade-off between retailer costs and BOPS service area. We answer this gap by designing a distribution network for deciding optimal BOPS service area based on a discount mechanism keeping both consumer and retailer interest in mind. To the best of our knowledge, such discount mechanism keeping both retailer and consumer has not been reported in the literature yet.

This section dealt with the introduction to omnichannel and its interesting invention in today's retailing world. Next section deals with the literature review regarding related work in the field of omnichannel and BOPS. Section three is concerned with formulation of proposed mathematical model while section four deals with a numerical illustration for the same. Finally, section five puts forward a concluding remark of the proposed study.

## 2 Literature Review

This section is mainly concerned with two domains of literature related to our work, namely omnichannel retailing and BOPS.

## 2.1 Omnichannel Retailing

Rigby [8] was the person to coin the term omnichannel which is concerned with integration of all available channels to make the consumer's shopping experience as seamless and frictionless. These channels may be bricks and mortar shops, kiosks, websites, direct mail and catalogs, home services, call centers, social media, televisions, mobile devices, networked appliances, gaming consoles and more [8]. Broadly, they may be grouped as online and offline but nowadays physical boundaries between them are diminishing due to integration into one single channel, i.e., omnichannel [9]. Retailers are making use of this integration to shape strategy for their business activities. Some other retailing channels also exist such as multi-channel and cross-channel. A clear distinction of these could be found in the work of Beck and Rygl [10]. The strength and weakness concerning these channels could be found in the work of Chopra [11].

Yadav et al. [12] designed a distribution system for omnichannel environment where consumer had the flexibility to choose the desired channel as per their wish. However, due to flexibility, demand uncertainty exists in such distribution system which was dealt by Yadav et al. [13]. Saghiri et al. [14] developed a three-dimensional conceptual framework for omnichannel systems and also reviewed the enablers for the same; whereas, Ailawadi and Farris [15] developed a framework for managing demand distribution in omnichannel systems and suggested various metrics for increasing supply chain efficiency. Few empirical studies also are reported in the literature. Bell et al. [16] conducted quasi-experimental studies to understand the effect offline showrooms of Warby Parker's and found that having offline stores for order fulfillment could improve both operational efficiency and demand as well. Gao and Su [17] investigated omnichannel self-ordering technologies through a theoretical model which enables customer to choose their orders themselves. Results obtained in their studies suggest that omnichannel self-ordering technologies have capability to reduce waiting cost, meanwhile employment level, demand and labor cost would increase. Deutsch and Golany [18] designed solution to last mile problem in the form of parcel locker networks. The objective of their model was to maximize the profit comprised of revenue earned through sales minus fixed cost of establishing locker, discount cost for customers who were willing to travel to pick their parcel and opportunities lost cost due to lost sales who did not travel to pick their order. Gao and Su [19] studied the impact of providing omnichannel information on online returns and store inventory level through three mechanisms (i.e., virtual showrooms, physical showrooms and information availability). The above literature suggests that most of the studies were in the field of information mechanism of omnichannel strategy while order fulfillment area is not focused much. In this work, one of the ordering mechanisms of omnichannel in the form of BOPS is briefly dealt.

## 2.2 BOPS

Few variant of emerging omnichannel ordering strategies is reported in the literature. These are buy online pickup in store (BOPS), reserve online and pickup in store (ROPS), ship from stores (SFS) and ship to store (STS). BOPS is so popular that most of the global giant had started to adopt the philosophy of BOPS to reap its benefits [6]. About 42% of the larger retailers are seen with providing the option of BOPS to the customers [6]. Gallino and Moreno [20] carried an empirical investigation and reported that BOPS increases store sales while reduces online sales. Gao and Su [21] reported the limitation of BOPS that it is not profitable in case of implementation for those products which sells well in stores and in case where store fulfillment is cost effective. However, to motivate customer for using BOPS, there is a need to provide some forms of incentive to the customer. The incentive mechanism could be in terms of discounts, coupons, etc., so that the customer agrees to travel a certain distance to pick their order. In this work, a distribution network is designed for deciding optimal BOPS service area based on a discount mechanism keeping both consumer and retailer interest in mind.

## 3 Problem Environment

Few assumptions are made in formulating the proposed model. These are as follows:

Assumptions:

1. Location of each DC and demand of each DC are known in advance.
2. Model is formulated for a single period.
3. The capacity of DC is assumed to be infinite since it is assumed that DCs are replenished as the inventory drops below a particular level.

The proposed model aims at two aspects. First one is to design discount mechanism for BOPS, and second aspects are to maximize revenue for DCs.

Notations used in the proposed model are as follows:

$f_i$	fixed cost of setting up $i$ th facility i.e. DC here
$D_i$	demand at $i$ th DC in each period
$R_i$	revenue generated per order in each period
$A_i$	minimum distance from nearest DC to order point
dc	total number of DC
$m$	number of demand points
$P_{\min}$	minimum number of DCs to be opened.

Decision variable used in the proposed model

$$y_i = \begin{cases} 1 & \text{if } i\text{th facility is open} \\ 0 & \text{otherwise} \end{cases}$$

$$x_{ij} = \begin{cases} 1 & \text{if } j\text{th order is fulfilled from } i\text{th DC} \\ 0 & \text{otherwise} \end{cases}$$

### 3.1 Discount Mechanisms

Suppose  $A$  is the minimum distance to the nearest DC and order point. Now, this distance could be anything from zero up to maximum distance  $A_{\max}$ . This distance could be categorized as follows:

$$A_1 < A_2 < \dots < A_{\max} \quad (1)$$

Any order less than  $A_1$  unit distance would be considered in the category of  $A_1$  discount and so on. Also this  $A_1$  category discount could be defined in terms of average distance covered by the all customers of this region in that period.

$$\text{Average distance}_{i\text{th period}} = \frac{\text{total distance covered by all the customer in } i\text{th period}}{\text{number of customer in the } i\text{th period}} \quad (2)$$

Based on this average distance, some discount may be offered depending on the policy of distribution center and let us denote it by  $C_i$  here. Also, this mechanism is very easy to implement for distribution center as the BOPS customer location could be easily traced when he/she is making an order through GPS location of the phone or laptop. Similarly for other category, discount could also be modeled. Thus, from this approach, the different discount could be obtained, and once it is finalized it would remain constant for that period. Such type of discount mechanism based on travel distance will be very effective and fair as the person traveling longer distance must get higher benefits. Also, such mechanism is beneficial in retailer regards too since the average distance is considered. The retailer could accordingly share his profit made from BOPS customer travel.

### 3.2 Maximizing Revenue for DC

The objective of maximizing profit for DC could be achieved by minimizing the total cost incurred in selling the products to the consumer since revenue generated per order would be constant.

$$\text{Max Profit} = \text{Revenue generated} - \text{total cost incurred} \quad (3)$$

Here, minimizing total cost would be comprised of two parts where the first part denotes the fixed cost incurred in setting up a facility while the second part is discount offered to the BOPS customers. This is shown in Eq. 4.

$$\text{Min } \sum_{i=1}^{dc} f_i y_i + \sum_{i=1}^{dc} \sum_{j=1}^m D_j C_i x_{ij} \tag{4}$$

s.t.:

$$\sum_{i=1}^{dc} x_{ij} = 1 \quad \forall j \in m \tag{5}$$

$$\sum_{j=m} D_j x_{ij} - y_i \geq 0 \quad \forall i \in dc \tag{6}$$

$$\sum_{i=1}^{dc} y_i \geq P_{\min} \tag{7}$$

$$y_i, x_{ij} \in \{0, 1\} \tag{8}$$

The fixed cost is comprised of cost incurred in erecting a facility and varying cost like rental, maintenance of facility, electricity, labor cost of officials and more (all these costs are normalized per demand period and here one single demand period is considered). While the second part of equation consists of discount offered to customer which is the product of total demand and discount offered to the consumer for each demand.

Constraint 5 ensures that one market demand is supplied from a single DC only, and order splitting is not allowed. Constraint 6 is linking constraint to maintain the flow of products. Constraint 7 ensures that minimum number of DCs must operate as per strategy of retailer to fulfill required service level within the region. Constraint 8 forces the allocation and opening of DC as a binary variable. The above problem turns out to be un-capacitated plant location model which could be solved through MS-Excel Solver.

### 4 Numerical Illustration

The location of distribution center is considered within a 100 \* 100 coordinate scheme. Five DCs (namely P, Q, R, S and T) are considered in this problem, and these DCs are situated as such that it should have maximum demand coverage. Also, some of the cost data are generated similar to Deutsch and Golany [18]. The fixed cost for single day is assumed to be 2000 units for four corner DCs while 6000 units for central DC (see Fig. 1). Central DC's fixed cost is high as it is in the middle of city so

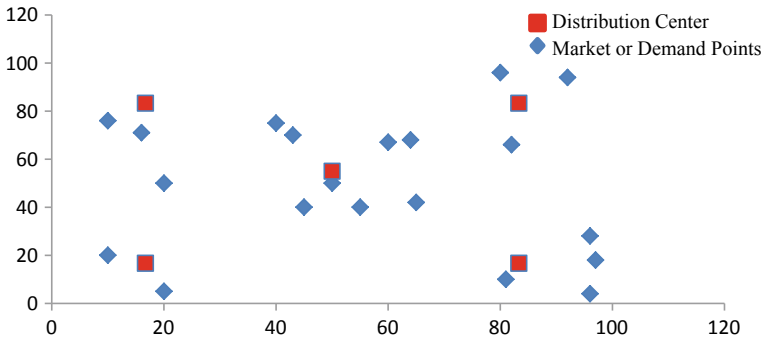


Fig. 1 Schematic of DCs and demand points for the considered problem

often faces high demand and thus needs larger space to accommodate more products. Twenty random demand points have been generated in 100 \* 100 coordinate schemes and discount matrix  $C_i$  which is mentioned in Table 1. Three categories of discount are taken here where nearest distance less than 25 unit is categorized in discount category 1, more than 25 units but less than 50 units is in category 2, and more than 50 units is under category 3. Discounts offered to category 1, category 2 and category 3 are 1 unit, 2 units and 3 units, respectively. Demand is generated through RANDBETWEEN function of MS-Excel under lower bound as 25 units and higher bound as 75 units. Revenue generated per order is considered as 5 units. In case of BOPS, generally customer prefers to order at any time of day from office and pick up the order while returning to home. The other cases may be customer has gone to area near to DCs for other personal work and may pick up order at that point of time. Thus, the consumers need not to travel extra for shopping.

Solving this model results in minimum cost of 15,300, and all DCs are open as we could see from Fig. 1. DC P fulfills the demand of markets D2, D3, D5, D8, D12, D15, D16, D17 and D18. DC Q fulfills the demand of market D9 and D14. DC R fulfills the demand of D10 and D13. DC S fulfills the demand of market D6, D7 and D11. DC T fulfills the demand of market D1, D4, D19 and D20. More details could be seen in Fig. 1.

### 4.1 Managerial Insights

With the increasing demand for BOPS services and meeting the competitive need of the organization, managers are often asked for extra efforts in terms of strategies to fulfill these needs. The proposed model is one such kind which would be helpful to the managers in deciding their BOPS strategies. The discount proposed in our model to consumer is allocated based on the consumer’s distance to the nearest distribution center, and also the maximum discount is fixed, so the possibility of consumer to

**Table 1** Discount matrix for demand points

	D1	D2	D3	D4	D5	D6	D7	D8	D9	D10	D11	D12	D13	D14	D15	D16	D17	D18	D19	D20
P	2	1	2	3	1	2	2	1	2	3	2	1	3	3	3	1	1	1	3	3
Q	3	3	2	3	3	3	3	2	1	3	3	3	3	1	3	3	3	2	3	3
R	2	2	3	3	3	3	3	3	1	3	3	3	3	1	3	3	3	3	3	3
S	3	2	2	3	2	1	1	3	3	3	1	2	3	3	3	3	2	3	3	3
T	1	2	3	1	1	3	3	3	3	3	3	2	3	3	3	2	2	3	1	3
Demand	48	71	45	40	29	25	46	64	27	46	57	27	48	25	45	61	69	56	58	30

leverage this distance mechanism would be based on the strategies and policies of organization and are governed by the managerial vision.

## 5 Conclusion

BOPS requires capital investment initially in form of investments in information and labor but still it is profitable due to many advantages like reduced cost of last mile fulfillment which is one of the major cost in delivery, increased in-store sales through cross-selling at the time of pickup, reduced congestion at store, time saving of both consumer and retailers, availability of quality checks at the time of pick from store and easy returns. It also overcomes the major disadvantage of online shopping issues like late delivery and returns management through its structure of collecting and returning product at store. But to motivate customers to migrate to BOPS, motivation is need in the form of discounts and seamless services.

In this work, a novel discount mechanism for BOPS environment is proposed where BOPS user gets the discount based on their travel distance. Such kind of mechanism is very effective and fair as both BOPS retailers and customers through sharing BOPS benefits among them. This makes a win-win situation for both parties. Here, the discount mechanism is based on the average travel distance of BOPS customer from nearest DC.

However, the model is illustrated through a hypothetical example which is one of the limitations of this work. In case of bigger and complex problems since exact solver may not be suitable, heuristic or metaheuristic is suggested in future work. Also, web or phone-based application could be made in near future for real-time suggestive discount mechanism for future purchase in BOPS environment.

## References

1. <https://www.emarketer.com/Article/Gap-Between-Online-Offline-Commerce-Shrinking/1014575>. Last accessed 2018/08/01
2. <https://s3.amazonaws.com/slice-intelligence-prod/whitepapers/downloads/Its-Prime-Time-for-Need-It-Now-Slice-White-Paper.pdf>. Last accessed 2018/08/01
3. [https://www.nielsen.com/content/dam/niensglobal/vn/docs/Reports/2015/Nielsen%20Global%20ECommerce%20and%20The%20New%20Retail%20Report%20APRIL%202015%20\(Digital\).pdf](https://www.nielsen.com/content/dam/niensglobal/vn/docs/Reports/2015/Nielsen%20Global%20ECommerce%20and%20The%20New%20Retail%20Report%20APRIL%202015%20(Digital).pdf). Last accessed 2018/08/01
4. Goodman R (2005) Whatever you call it, just don't think of last-mile logistics, last. *Glob Logist Supply Chain Strateg* 9(12):46–51
5. JDA and Centrio (2016) Customer pulse report Germany 2016. <https://www.centrio.com/centrio-jda-customer-pulse-report-2016>. Last accessed 2018/08/01
6. eMarketer (2012) Innovation in buy online, pick up in-store services. <http://www.emarketer.com/newsroom/index.php/order-online-pick-instore-servicesbring-consumers-worlds/>. Last accessed 2018/08/01
7. Jin M, Li G, Cheng TCE (2018) Buy online and pick up in-store: design of the service area. *Eur J Oper Res* 268(2):613–623



8. Rigby D (2011) The future of shopping. *Harvard Bus Rev* 89(12)
9. Brynjolfsson E, Hu YJ, Rahman MS (2013) Competing in the age of omnichannel retailing. *MIT Sloan Manag. Rev.* 54(4):23–29
10. Beck N, Rygl D (2015) Categorization of multiple channel retailing in multi-, cross-, and omni-channel retailing for retailers and retailing. *J Retail Consum Serv* 27:170–178
11. Chopra S (2015) How omni-channel can be the future of retailing. *Decision* 43(2):135–144
12. Yadav VS, Tripathi S, Singh AR (2017) Exploring omnichannel and network design in omni environment. *Cogent Eng* 4(1)
13. Yadav VS, Tripathi S, Singh AR (2018) Bi-objective optimization for sustainable supply chain network design in omnichannel. *J Manuf Technol Manag*
14. Saghiri S, Wilding R, Mena C, Bourlakis M (2017) Toward a three-dimensional framework for omni-channel. *J Bus Res*
15. Ailawadi KL, Farris PW (2017) Managing multi-and omni-channel distribution: metrics and research directions. *J Retail* 93(1):120–135
16. Bell DR, Gallino S, Moreno A (2017) Offline showrooms in omnichannel retail: demand and operational benefits. *Manage Sci* 64(4):1629–1651
17. Gao F, Su X (2017) Omnichannel service operations with online and offline self-order technologies. *Manage Sci* 64(8):3595–3608
18. Deutsch Y, Golany B (2018) A parcel locker network as a solution to the logistics last mile problem. *Int J Product Res* 56(1–2):251–261
19. Gao F, Su X (2016) Online and offline information for omnichannel retailing. *Manuf Serv Oper Manage* 19(1):84–98
20. Gallino S, Moreno A (2014) Integration of online and offline channels in retail: the impact of sharing reliable inventory availability information. *Manage Sci* 60(6):1434–1451
21. Gao F, Su X (2016) Omnichannel retail operations with buy-online-and-pick-up-in-store. *Manage Sci* 63(8):2478–2492

# Investigation of Fracture Parameters of Jute/Glass Reinforced Hybrid Composite and Analysis by Using FEA



Venkata Sushma Chinta, P. Ravinder Reddy, Koorapati Eshwara Prasad and Krishna Sai Vadapally

**Abstract** These days the interest of people has shifted toward using natural fibers as reinforcement in the preparation of polymer composite material. Having superior properties such as lower density, higher stiffness, better mechanical properties and since the natural fibers are abundantly available, being renewable and biodegradable, the natural fiber-based composite preparation has become a wide area for research activity. This paper deals with the testing and analysis of the single edge notch bend specimen for the estimation of fracture toughness of the material. Six SENB hybrid composite specimens made of glass fibers, jute fibers and epoxy are prepared as per ASTM D-5045. Then, the models of hybrid composite are created in ANSYS to find  $J$ -integral and stress intensity factor. The purpose is to retain sufficient mechanical properties by adding layers of glass fiber, at the same time ensuring a lower cost and lower weight by reinforcing intermediate layers of jute fiber in it. Determining the mechanical characteristics of hybrid composite laminate was carried out by three-point bending test so as to compare it with ASTM D-5045 test method's manual. Wherein, the results of the test specimens have satisfied the necessary conditions put forth by the test manual. Mechanical characteristics obtained with hybrid jute reinforced glass laminates enable the substitution of glass fiber by other natural fibers for moderately loaded applications to combine performance and economy.

**Keywords** Jute/glass fiber · Hybrid composite · SENB ·  $J$ -integral · Stress intensity factor

---

V. S. Chinta (✉) · P. Ravinder Reddy · K. S. Vadapally  
Chaitanya Bharathi Institute of Technology (A), Hyderabad, Telangana, India  
e-mail: [venkatasushmachinta@gmail.com](mailto:venkatasushmachinta@gmail.com)

P. Ravinder Reddy  
e-mail: [reddy.prr@gmail.com](mailto:reddy.prr@gmail.com)

K. S. Vadapally  
e-mail: [kvodapally1997@gmail.com](mailto:kvodapally1997@gmail.com)

K. E. Prasad  
Siddhartha Institute of Engineering and Technology, Hyderabad, Telangana, India  
e-mail: [epkoorapati@gmail.com](mailto:epkoorapati@gmail.com)

## 1 Introduction

In the last twenty years, the use of natural fibers had an increase in its use for reinforcement in the composite materials. These natural fibers are abundantly available at a lower cost, with lightweight and satisfactory-specific properties. These materials are quickly replacing metal or ceramic materials, wood, with their lower weight, higher strength-to-weight ratio and stiffness properties. The purpose here is to overcome the rarefaction of fossil resources and weight reduction up to 60–80% of the component weight. Though the ultimate strength and Young's modulus of jute are lower than glass fiber, its specific modulus is comparable with glass fiber, and based on modulus per cost basis, jute is far more better than glass fiber. Accordingly, where high strength is not a requirement, jute is used fully or partially, to replace the glass fiber. Apart from being available at a lower price, its renewability and lower energy required for its production (only 2% of that for glass) make it almost applicable reinforcement in composites.

Numerous research studies done over the last few years have reported the successful use of natural fibers, as reinforcement to enhance the mechanical characteristics of glass fiber matrix.

Muthuvel [1] has done investigation of jute, glass and chopped fiber of different lengths hybrid composite by simple hand layup resulting in the improvement of material properties which are greatly influenced by fiber lengths and the aspect ratio of fiber. Venkata Sushma Chinta [2] has done a study on bidirectional carbon/glass reinforced epoxy hybrid composites discussing the effect of stacked layer's orientation on tensile, shear and flexural properties. Sudeep Deshpande [3] has carried out an investigation on glass/jute fiber reinforced epoxy composed of varying concentration of bone powder and coconut shell, fabricated by hand layup process. It discussed the effect of volume % of the constituents on material properties, which were far better than the properties of conventional composites. Hamza Bouguessir [4] has found out that the hybrid fibers are sufficiently stiff and strong to be reinforced in the composite laminates with thermosetting matrix, giving better mechanical properties than the conventionally prepared laminate. Mazharul Islam [5] investigated the stacking of jute and glass mat on mechanical characteristics of the hybrid by studying the fracture features and crack profiles using scanning electron microscopy. Water absorption (%) of the hybrid was found to be negligible, hybrid composite degraded moderately and pure glass degraded the least. Sanjay [6] has made an effort in stacking up the sequence of the glass and jute fiber layers, where the pure jute specimen showed poor results among all, while pure glass specimen was at the top. However, the one with jute fibers in between the glass fibers showed better results. Hari Krishnan [7] has studied the effect of varying concentration on the opening mode of fracture toughness of the jute/glass composite by compact tension experimentation and finite element analysis. The finite element analysis results indicate that there is very less discrepancy. Gujjala Raghavendra [8] investigated the jute fiber reinforced epoxy composites to study the jute fiber properties when reinforced into epoxy matrix. Thermo gravimetric analysis revealed that the reinforcement of jute

fiber improved the tribological properties that may stop the crack to propagate and control the deformation. Maneesh Tewari [9] studied the effect of adding bagasse into the glass fiber composite. The addition of glass fiber and bagasse improved the modulus of elasticity further and also improved its impact strength and water absorption capacity. Yongli Zhang [10] has studied the behavior of unidirectional flax, glass fiber reinforced with phenolic resin to investigate the hybrid effects of laminates made by natural and synthetic fibers whose stacking sequence influenced the tensile properties, fracture toughness and inter-laminar shear strength.

All the previous work [11–23] showed the fundamental understanding of their behavior as reinforcement for composites. Though effort was made to test the glass/jute composite specimen, many were limited to evaluating the tensile, shear, flexural properties, etc. The main criterion for the components to fail during operation is fracture, thus it becomes important to estimate the fracture toughness, which very few people have done so far. The availability of natural jute fiber at very low cost and as to find an alternative to decrease the after effects of glass fiber on environment, research has been undertaken to develop hybrid fiber reinforced polymer (HFRP) composites. In the present study, fracture toughness of jute/glass hybrid composite for different dimensions of the specimen is found out theoretically by single edge notch bend geometry as per ASTM 5045. Then, finite element analysis is performed using ANSYS software, and then the comparisons between theoretical and experimental results were made.

## 2 Experimentation

### 2.1 Materials

Woven roving bidirectional glass fibers of 0.3 mm thickness is shown in Fig. 1. The woven jute sheet was collected from a local market that is used for the purpose of making bags used for packaging rice grains. The jute sheet that was used for the reinforcement is shown in Fig. 2. Epoxy resin (EP-306 grade epoxy resin & EH-758 grade hardener) as shown in Fig. 3 is selected as a matrix. Epoxy resins are expensive

**Fig. 1** Woven roving glass

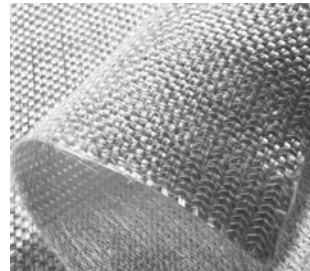


**Fig. 2** Woven jute



**Fig. 3** Epoxy and hardener



**Table 1** Mechanical properties of glass fiber, jute fiber and epoxy

Properties	Glass fiber	Jute fiber	Epoxy resin
Young's modulus (GPa)	72.4	28	3.45
Density (gm/cc)	2.6	1.45	1.14
Rigidity modulus (GPa)	29.67	0.35	1.277
Poisson's ratio	0.22	0.37	0.35

than polyester, but possess better mechanical properties like dynamic strength and fatigue resistance, so as to impart good inter-laminar strength to the composite.

Properties of the constituents are shown in Table 1.

### 2.2 Specimen Fabrication

The fabrication of a single edge notch bend (SENB) specimen is done to determine the fracture toughness of the material. SENB is preferred keeping in mind our further area of research to apply this material for cooling tower fan blades.

### 2.3 *Estimation of the Weight of the Fibers, Epoxy-Hardener Mixture*

For a sample of dimensions  $120 \times 120 \times 10 \text{ mm}^3$ , the corresponding volume of the sample is equal to 144 cc. Assuming the volume fraction of the fiber as 0.55, the corresponding volume of the fabric becomes 79.2 cc. The density of the glass fabric is 2.6 g/cc and jute fabric is 1.45 g/cc. The theoretical weight of the glass fabric becomes 109.82 g and jute fiber becomes 53.59 g. The alternate layers of glass and jute are stacked as per the requirement. The weight of resin is estimated as 73.87 g. To compensate for the beaker loss, brush loss and oozing out of matrix due to tightening 2.5 times more resin have been taken in which 10% is hardener. A 166 ml epoxy is taken separately and then mixed with 16.6 ml of hardener. In this study, an EH-758 grade of hardener is used to mix with epoxy resin in 1:10 proportions in the process of manufacturing of composite and obtain an optimum matrix composition.

### 2.4 *Fabrication Procedure*

Hand layup procedure is followed for fabrication of composite laminate plate as shown in Fig. 4. To start with, a nonsticking release wax is applied on the mold plate surface to avoid the sticking of the fiber to it. Glass and jute fibers are cut as per the mold size. Roving glass sheet is then placed on the mold plate, over which resin is applied with the help of the brush so as to spread it uniformly over the surface. Then, the jute layer is placed and by using a roller, mild pressure is applied to remove the excess epoxy present and the air trapped. The stacking is repeated till the required number of layers is achieved. After this wax is applied on the inner surface of the top mold plate and is clamped together tightly using bolts. After curing at room temperature for about two days, the composite plate is taken out and is further processed. Normal curing time at room temperature is 24–48 h for

**Fig. 4** Preparation of hybrid composite plate



epoxy-based composite laminates. The composite plate is further allowed to cure for a week before cutting is done.

### 2.5 Preparation of Standard Test Specimen

The plate is cut according to the bend test specimen [24] to estimate stress intensity factor and strain energy release rate of jute/glass hybrid composite. Specimens are cut as per the requirement to use it in three-point bending test. Specimens of dimensions  $116 \times 24 \times 13 \text{ mm}^3$  are cut from the plate on the surface grinding machine in our institution, and their dimensions are mentioned in Table 2. The specimen  $GJ_1$  and its dimensions are shown in Fig. 5.

### 2.6 Single Edge Notch Bending Test

Single edge notch bending test was performed to find maximum load taken by the specimens and stress intensity factor at the cracked tip, strain energy release rate so as to define the toughness in terms of critical stress intensity factor. In the SENB test,

**Table 2** Dimensions of the SENB specimens

Specimen designation	Sample dimensions (mm)			Crack length (mm) ( $a$ )	$a/W$ ratio
	Length ( $L$ )	Width ( $W$ )	Thickness ( $B$ )		
$GJ_1$	116.08	24.02	13.50	11.60	0.48
$GJ_2$	116.12	24.14	13.25	11.66	0.48
$GJ_3$	116.16	24.20	13.35	11.72	0.48
$GJ_4$	116.28	24.74	12.95	11.82	0.48
$GJ_5$	116.30	24.82	13.15	11.94	0.48
$GJ_6$	116.80	24.88	13.45	11.96	0.48

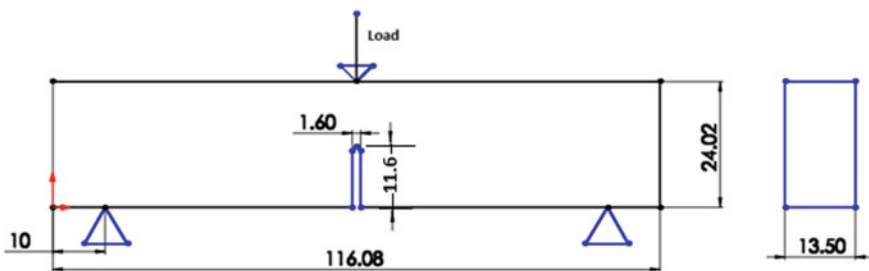


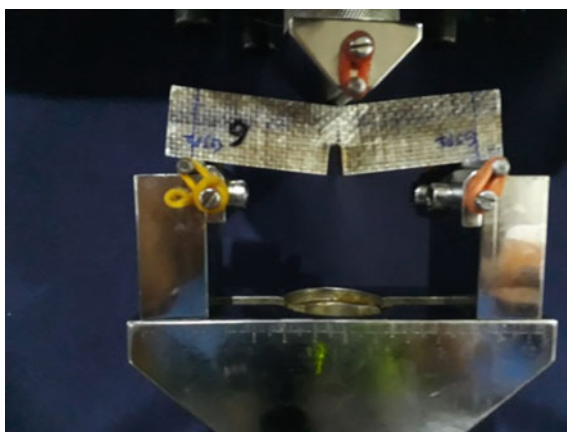
**Fig. 5** Specimen and notch dimensions of  $GJ_1$

load is applied on the specimen, to propagate the already created cracked notch. The test was performed according to ASTM D-5045 test standard [24] using universal testing machine (UTM) in CBIT. Bending test fixtures are used to fix the specimen, and the load is applied at the mid-way between support rollers. The experimentation setup for specimen  $GJ_1$  is shown in Fig. 6. The machine has the maximum capacity of 25 KN. Load is applied, and the feed rate is set as 2 mm per minute. The load at which the crack propagates is noted from the computer attached to the UTM. Figure 7 shows crack mouth opening for specimen  $GJ_6$ .

**Fig. 6** Experimental setup for specimen  $GJ_1$



**Fig. 7** Crack opening at failure for specimen  $GJ_6$





### 2.6.1 Measurement of Compliance for Specimen $GJ_1$ and Estimation of Load $P_Q$

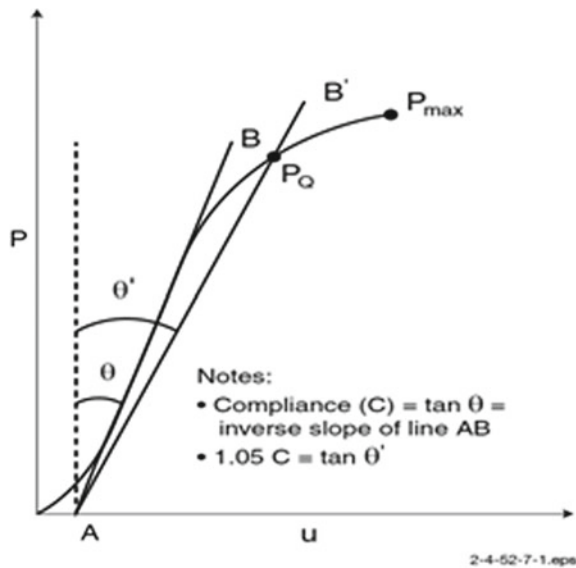
The following conditions should be satisfied by the specimen as per ASTM D-5045 to conduct the test. For  $GJ_1$  specimen, the thickness of the specimen is 13.5 mm. Single edge notch bend is recommended with small thickness to achieve plane strain. The crack length is measured using optical microscope.

- For straight through the notch  $1 \leq \frac{W}{B} \leq 4$ , for  $GJ_1$  specimen  $\frac{W}{B} = \frac{24.02}{13.5} = 1.78$  is satisfied
- The notch width  $N < \frac{W}{10}$ , for  $GJ_1$  specimen  $1.6 < 2.402$  is satisfied

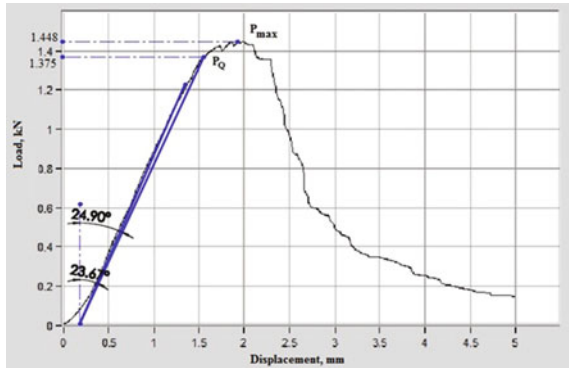
To determine the initial compliance  $C$ , best straight line (AB) is drawn passing through maximum of the interpolating points.  $C$  is calculated as the reciprocal of slope of the line (AB). Then interpolate a second line (AB') with a compliance of 5% more than that of the line (AB). If the maximum load ( $P_{max}$ ) on the specimen falls within the region of lines (AB) and (AB'), use it to calculate  $K_1$ . If  $P_{max}$  falls outside the region of lines (AB) and (AB'), then use the intersection of line (AB') and the load curve as  $P_Q$ , and further, if  $P_{max}/P_Q < 1.1$ , use  $P_Q$  in the calculation of  $K_1$ . However, if  $P_{max}/P_Q > 1.1$ , the test turns out to be not valid.

Figure 9 is load VS displacement curve obtained for bending test for  $GJ_1$  specimen. By the procedure from Fig. 8 and the Fig. 9 shows value of  $P_Q$  for specimen  $GJ_1$  is 1.375 KN. The maximum load taken by the specimen  $P_{max}$  is 1.448 KN.  $P_{max}/P_Q$  for specimen  $GJ_1$  is 1.06, which is less than 1.1, so the test was found to be valid. Stress intensity factor can be considered as an estimate of fracture toughness. The critical stress intensity factor ( $K_Q$ ) is given by the equation:

**Fig. 8** Compliance from ASTM D-5045



**Fig. 9** Estimation of  $P_Q$  for specimen  $GJ_1$



$$K_Q = (P_Q/BW^{1/2})f(x) \tag{1}$$

where  $f(x) = (2 + x)(0.886 + 4.64x - 13.32 \times 2 + 14.72 \times 3 - 5.6 \times 4)$ ,  $P_Q$  = load at which crack propagates in N,  $B$  = thickness of the specimen in mm,  $W$  = width of the specimen in mm,  $a$  = length of the crack in mm,  $x = a/W$ .

The strain energy release rate ( $G_Q$ ) is given by the equation:

$$G_Q = (1 - \nu^2)K_{IC}^2/E \tag{2}$$

By using Eq. 1, for specimen  $GJ_1$  at the maximum load of 1375 N, the stress intensity factor is calculated as 211.11 MPa mm<sup>1/2</sup>. The value of equivalent Young’s modulus is 20.7 GPa and Poisson’s ratio is 0.172. By using Eq. 2, the strain energy release rate is calculated as 2.09 kJ/m<sup>2</sup>.

### 3 Finite Element Analysis

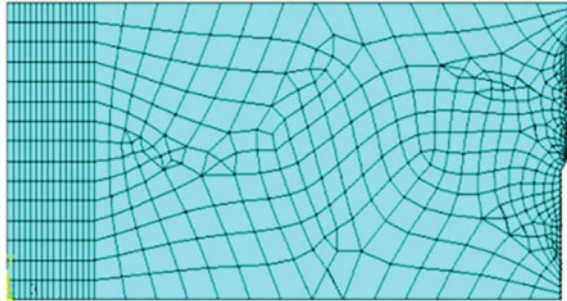
Finite element analysis was performed using analysis software ANSYS 19. A finite element model was created using ANSYS, Mechanical APDL. The element type used was SHELL 281, and a model of required dimension was created. Six such models were created as per the specimens that were put into the three-point bending test. The thickness of each glass, jute layer is estimated based on number layers used in fabrication of specimen. In analysis, each particular stack layer was inputted with its respective orthotropic properties and that are as are shown in Table 3.

Create key points based on the geometry of specimen; only half of the model is created based on symmetry. Then, areas are created by joining the key points, and sizing of each line is done as per mesh requirement. Stress concentration is defined on the key point at the crack tip [25, 26]. Later, the areas are meshed to obtain mesh as shown in Fig. 10. The specimen has 2128 nodes and 686 elements. Figure 11 shows mesh at the vicinity of the crack tip. Then, boundary conditions like constraints,

**Table 3** Properties of glass and jute epoxy

Properties	Properties of glass epoxy	Properties of jute epoxy
$E_1$	26,536.3 MPa	14,030.3 MPa
$E_2$	26,536.3 MPa	14,030.3 MPa
$E_3$	11,002.6 MPa	8909.85 MPa
$\nu_{12}$	0.112	0.241
$\nu_{23}$	0.348	0.431
$\nu_{13}$	0.348	0.431
$G_{12}$	3878.53 MPa	3198.9 MPa
$G_{23}$	3845.67 MPa	3123.7 MPa
$G_{13}$	3845.67 MPa	3123.7 MPa

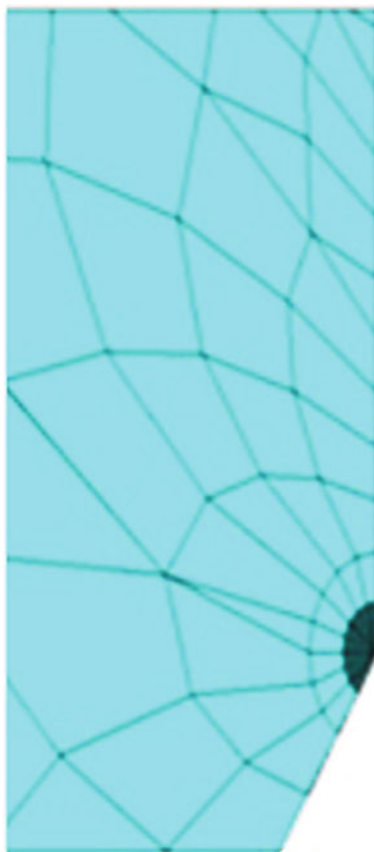
**Fig. 10** Element plot for SENB specimen  $GJ_1$



symmetry conditions and load are applied. The  $P_{max}$  that is obtained from SENB test is used as load value for specimen. Then, the problem is solved in ANSYS. Under post processing, a path is defined around crack tip and a subroutine is used to estimate parameters like  $J$ -integral and stress intensity factor.

From Fig. 12, we can observe that  $K_{IC}$  from ANSYS for  $GJ_1$  specimen is  $204.9 \text{ MPa mm}^{1/2}$ .

**Fig. 11** Element plot in the vicinity of crack for  $GJ_1$  specimen



## 4 Results and Discussion

From Table 4, strain energy release rate evaluated from experiment and ANSYS is listed. The maximum value of strain energy release rate from experiment is  $2.53 \text{ kJ/m}^2$  at a load of 1498 N. From Table 5, stress intensity factor evaluated from experiment and ANSYS is listed. The maximum value of stress intensity factor from experiment is  $232.11 \text{ MPa mm}^{1/2}$  at a load of 1498 N. Deviation is observed in the estimation of strain energy release rate because a more generalized approach mentioned in ASTM D-5045 has been adopted while conducting the experimental analysis.

**Fig. 12** Critical stress intensity factor

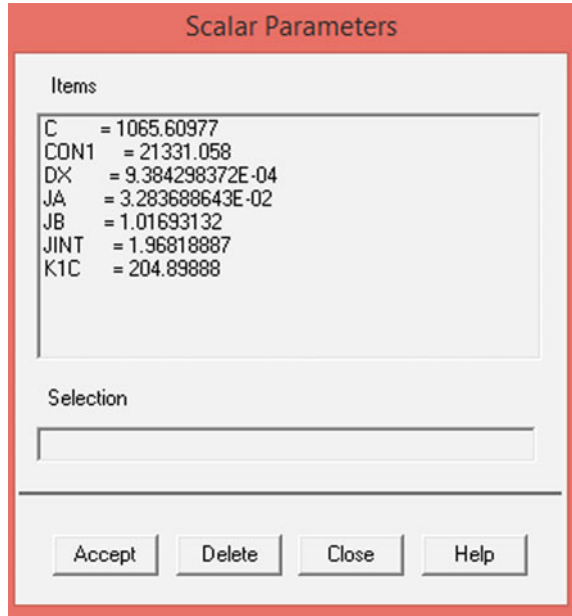


**Table 4** Comparison of strain energy release rate

Specimen designation	Load $P_{max}$ (N)	Strain energy release rate $G_{Ic}$ (kJ/m <sup>2</sup> )		
		Experiment	Ansys	% of deviation
$GJ_1$	1448	2.09	1.968	5.8
$GJ_2$	1468	2.29	1.983	13.4
$GJ_3$	1475	2.40	2.089	12.9
$GJ_4$	1481	2.42	2.141	11.5
$GJ_5$	1491	2.54	2.251	11.4
$GJ_6$	1498	2.53	2.273	10.2

**Table 5** Comparison of stress intensity factor

Specimen designation	Load $P_{max}$ (N)	Stress intensity factor $k_{Ic}$ (MPa mm <sup>1/2</sup> )		
		Experiment	Ansys	% of deviation
$GJ_1$	1448	211.11	204.90	2.9
$GJ_2$	1468	221.04	205.72	6.9
$GJ_3$	1475	226.10	211.14	6.6
$GJ_4$	1481	227.36	213.71	6.0
$GJ_5$	1491	232.74	219.15	6.2
$GJ_6$	1498	232.11	220.19	5.1

## 5 Conclusion

All specimens showed expected behavior during the process of fracture as mentioned in the ASTM D-5045. The strain energy release rate from experiment and ANSYS showed higher deviation than expected. There is a good agreement between the stress intensity factor values obtained experimentally and by ANSYS. Results of FEA are found to be close with the experimental results. The use of jute fibers as reinforcement with glass fibers gives a promising solution to replace the pure glass fiber composites, resulting in the reduction of cost and environmental decomposition problems.

## References

1. Muthuvel M, Ranganath G (2013) Characterization study of jute and glass fiber reinforced hybrid composite material. *Int J Eng Res Technol* 2(4):335–344
2. Chinta VS, Nagini Y, Sandhya V (2018) Investigation of mechanical properties of bidirectional carbon/glass reinforced epoxy hybrid composites. *Int J Mech Prod Eng Res Dev* 8(3):449–456
3. Sudeep D, Rangaswamy T (2014) Effect of fillers on E-glass/jute fiber reinforced epoxy composites. *Int J Eng Res Appl* 4(8):118–123
4. Hamza B, Elhaddi H (2016) Hybrid jute/glass reinforced laminate mechanical properties. *J Civil Environ Eng* 6(4):1–5
5. Mazharul I (2016) Fabrication and characterization of jute-glass fiber reinforced polyester hybrid composites. *Int J Sci Eng Res* 7(9):1708–1719
6. Sanjay MR, Yogesha B (2016) Studies on mechanical properties of jute/E-glass fiber reinforced epoxy hybrid composites. *J Miner Mater Charact Eng* 4(1):15–25
7. Harikrishnan KR, Deviprasad V (2015) Mode I fracture toughness of jute/glass fiber hybrid composite—an experimental and numerical study. *Int J Eng Trends Technol* 28(6):307–310
8. Raghavendra, G., Ojha S (2013) Jute fiber reinforced epoxy composites and comparison with the glass and neat epoxy composites. *J Compos Mater* 48(20):2537–2547
9. Maneesh T, Singh VK (2012) Evaluation of mechanical properties of Bagasse-glass fiber reinforced composite. *J Mater Environ Sci* 3(1):171–184
10. Zhang Y, Li Y (2013) Tensile and interfacial properties of unidirectional flax/glass fiber reinforced hybrid composites. *Compos Sci Technol* 88(2013):172–177
11. Bindal A, Singh S (2013) Development of glass/jute fibers reinforced polyester composite. *Indian J Mater Sci* 1–6
12. Rafiqzaman Md, Mahbuba Z (2017) Jute-glass fiber based composite for engineering application. *Eur J Adv Eng Technol* 4(7):510–515
13. Ramesh M, PalaniKumar K (2013) Mechanical property evaluation of sisal-jute glass fiber reinforced polyester composites. *Compos Part B Eng* 48(48):1–9
14. Ansar MA, Singh D (2013) Fatigue analysis of glass fiber reinforced composites. *Int J Eng Res Appl* 3(3):588–591
15. Jagannatha TD, Harish G (2015) Mechanical properties of carbon/glass fiber reinforced epoxy hybrid polymer composites. *Int J Mech Eng Robot Res* 4(2):131–137
16. Patil D (2013) Mechanical property of glass fiber reinforcement epoxy composites. *Int J Sci Eng Res* 1(4):6–9
17. Natarajan K, Padma CB (2014) Study of mechanical and morphological properties of glass fiber reinforced modified epoxy composites. *Int J Res Eng Technol* 3(1):1–6
18. AkmSamsur R (2015) Thermal and mechanical properties of woven glass fiber reinforced epoxy composites with carbon nano tubes grown in-situ. *The Int J Eng Sci* 4(12):54–61

19. SrikanthRao D, Ravinder Reddy P (2016) Determination of mode I Fracture toughness of epoxy-glass fiber composite laminate. In: 11th international symposium on plasticity and impact mechanics, implast vol 173, pp 1678–1683
20. Hana J, Yonjig K (2015) Mode I fracture toughness of carbon-glass/epoxy inter ply hybrid composites. *J Mech Sci Technol* 29(5):1955–1962
21. Hatice T, Ayşegül A (2017) Development of carbon-glass fiber reinforced hybrid composites by vacuum infusion technique. *J Turkish Chem Soc* 1(2):35–42
22. Bakker Ad (1982) Elastic-plastic fracture mechanics analysis of an SENB specimen. *Int J Press Vessels Pip* 10(6):431–449
23. Cicero S, Madrazo V (2012) Estimation of fracture toughness by testing notched fracture specimens and applying the theory of critical distances. *Int Sch Res Not* 1–8
24. ASTM D-5045 Standard Test Methods for Plane Strain Fracture Toughness and Strain Energy Release Rate of Plastic Materials
25. Sushma CV, Ravinder Reddy P, Rama Lakshmi P (2013) Investigation of fracture parameters of compact tension specimen by FEA. *Int J Eng Res Technol* 2(6):1587–1591
26. Sushma CV, RavinderReddy P, Rama Lakshmi P (2013) Investigation of stress intensity factor of aluminium plate by FEA. In: Proceedings of national conference on advances in mechanical engineering & renewable energy, March 2013, CBIT

# Optimization of Machining Parameters During Dry Cutting of Ti6Al4V Using Taguchi's Orthogonal Array



P. Kumar  and J. P. Misra 

**Abstract** The present study assessed the effect of control parameter, i.e. approach angle ( $A$ ), cutting speed ( $B$ ), depth of cut ( $C$ ) and feed ( $D$ ) on the response characteristics, i.e. material removal rate (MRR) and surface roughness (SR) during machining of titanium alloy using Taguchi technique. Experimental trials were performed on the lathe machine using the  $L_9$  orthogonal array. Statistical analysis carried out to know the contribution and effect of cutting parameters on response characteristics. From the analysis, it was found that the feed ( $D$ ) was the most influential factor followed by approach angle ( $A$ ) which affects the surface roughness (SR) while cutting speed ( $B$ ) had a most significant effect on the material removal rate (MRR). Subsequently, an optimal control parameter was obtained and modelled for response characteristics.

**Keywords** Taguchi approach · ANOVA · Orthogonal array · Surface roughness · Material removal rate · Titanium alloy · Pooling · Regression

## 1 Introduction

Titanium and its alloys are having wide application areas including aerospace and marine industries, petroleum and chemical industries and bio-medical industry owing to its unique characteristics: high specific strength, strong corrosion-resistance, low fracture resistance and capability to hold high strength at high temperatures, etc. But their metallurgical characteristics make them more difficult to machine material.

Owing to poor machinability, many companies are compelled to focus on developing techniques to minimize machining cost and achieve reasonable production rates. Turning is most commonly used in traditional machining processes to machine titanium alloys. Cutting speed, feed rate, depth of cut, tool geometry, workpiece material and cutting environment are the machining parameters which extremely change the quality of the machined part. Cutting fluid plays a significant role in metal cutting,

---

P. Kumar (✉) · J. P. Misra  
Department of Mechanical Engineering, National Institute of Technology Kurukshetra,  
Kurukshetra, Haryana 136119, India  
e-mail: [pawank76@gmail.com](mailto:pawank76@gmail.com)

© Springer Nature Singapore Pte Ltd. 2020  
L. Vijayaraghavan et al. (eds.), *Emerging Trends in Mechanical Engineering*,  
Lecture Notes in Mechanical Engineering,  
[https://doi.org/10.1007/978-981-32-9931-3\\_23](https://doi.org/10.1007/978-981-32-9931-3_23)



namely: cooling, lubrication and chip transport actions. Taylor emphasized that use of cutting fluids to get high material removal rate as it permits high cutting speeds by prolonging cutting tool life [1].

But, cutting fluid costs about 3–4 times of the cutting tool's cost and which is also about 15% of the metal cutting cost. Moreover, environmental issues/law and economical desirability make machining without cutting fluids (i.e. *green machining*) a future trend for manufacturing industries.

Dry machining is generally performed at lower cutting speed to prolong tool life which reduces production rate [2]. In dry machining as compared to wet machining, large friction and cutting temperature are produced which drastically reduce tool life and cause dimensional deviations and inferior surface quality in the machined part [3]. So, proper selection of machining parameter is vital. It is the necessity of this process to select suitable machining parameter settings to produce good quality product at a reasonable cost and production rate. The cutting parameters of any machining process are generally guidelines provided by manufacturers, or they are operator's knowledge-based. Yet, it is very hard to pick up the most favourable machining conditions to meet industry and consumer's requirements [4].

Taguchi method is very simple and efficient method to optimize the designs for quality and cost. In contrast to full factorial design which tests all possible combination in design space, the Taguchi method only tests some pair of combinations. This approach hence saves resources (time and cost) as fewer experiments are required to fulfil the same purpose [5]. The collection of crucial data also helps to determine that which parameter is mainly affecting the part quality significantly.

In recent study, researchers [6] used textured tool for titanium machining and observed a decrease in cutting temperature by 103 °C as compared to the traditional plane cutting tool. Another group of researchers examined the influence of cutting speed and feed rate on the tangential cutting force in the orthogonal turning of Ti–6Al–4V. Depth of cut was kept constant in their experimentation. They used response surface methodology (RSM) to design experiments and developed a mathematical model whose adequacy was proved by analysis of variance (ANOVA) [7]. Recently, for the micro-end milling of titanium alloy, the influence of tool signature on wear resistance and the part surface was examined by using PCD tool [8]. They included the subsurface microstructure alteration as an important index to measure the performance of PCD tools. In another work for finish turning of CP-Ti grade 2, cutting force, tool wear, friction coefficient, chip morphology, chip reduction coefficient, micro-hardness of machined surface, surface roughness and machining temperature were reported. The machining was performed under different machining environments (dry, flood and MQL) using carbide inserts. Turning was performed at different combinations of cutting speeds (51, 67 and 87 m/min) while keeping feed rate and depth of cut constant at 0.12 mm/rev and 0.5 mm, respectively [9].

In this experimental investigation, turning operation was performed on titanium alloy (Ti–6Al–4V) using DOE on a conventional lathe. Uncoated tungsten carbide (WC-Co) inserts were used for the machining as they perform better as compared to coated inserts. Using design of experiments, approach experiments were planned and Taguchi's  $L_9$  orthogonal array was selected found suitable for the study to obtain large

information with minimum resource utilization. The four factors, viz. approach angle (*A*), cutting speed (*B*), depth of cut (*C*) and feed (*D*) were taken for the experimental study and their influence on surface roughness (SR) and material removal rate (MRR) was examined. ANOVA analysis was also carried out to know the relative significance of parameters and then optimal combination was obtained. Furthermore, empirical modelling was also carried out to predict response characteristics for the turning process.

## 2 Experimental Procedures

In this experimental study, the experiments were performed according to Taguchi's ( $L_9$ ) orthogonal array. Turning operation was performed on heavy-duty lathe machine NH22 (HMT, make) as shown in Fig. 1.

### 2.1 Selection of Material

Ti6Al4V alloy was selected as work material for the present study due to its vast application area. The elemental composition of the alloy was found using EDX test.

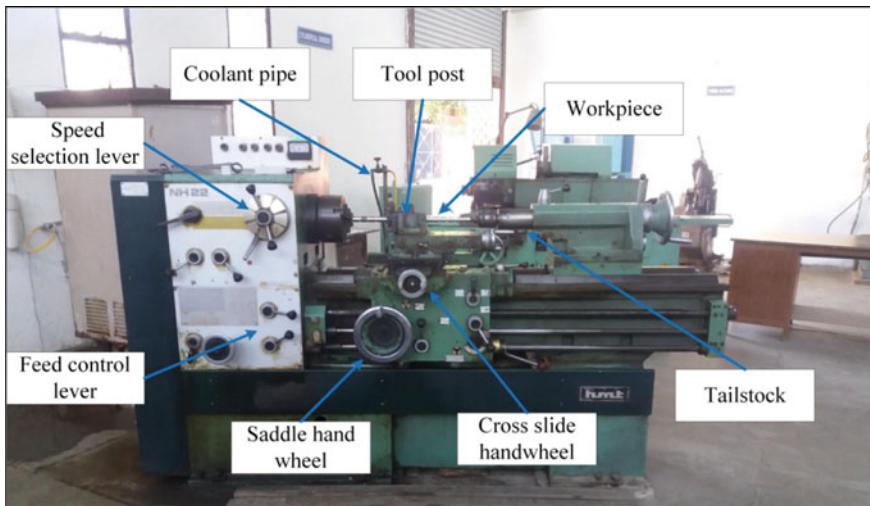


Fig. 1 Lathe machine

**Table 1** Cutting factors and their levels

Cutting parameter	Symbol	Unit	Level		
			1	2	3
Approach angle	<i>A</i>	degree	50	70	90
Cutting speed	<i>B</i>	rpm	174	420	930
Depth of cut	<i>C</i>	mm	0.4	0.6	0.8
Feed	<i>D</i>	mm/rev	0.08	0.28	0.52

## 2.2 Selection of Cutting Tool

Uncoated tungsten carbide (WC-Co) cutting inserts TNMG160408MS (Widia) were used for the experimentation. These inserts having a triangular shape with 60° geometry and 0.4 mm nose radius. To clamp these inserts, MTJNR 2020K16 (Widia) tool holder was used.

## 2.3 Experimental Plan and Procedure

To carry out the statistical analysis, the degree of freedom of input factors must be less than or at least equal to the selected OA. The OA selected in this study meets this requirement.

A commercially available Ti6Al4V rod with a 25 mm diameter was used to perform turning experiments. Before performing experiment rod was prepared for turning operation by removing its surface layer to the obtained fresh cylindrical surface. After that rod was grooved to distinguish different machining areas, each having a 25 mm length. The four controllable factors considered in this study are approach angle (*A*), cutting speed (*B*), depth of cut (*C*) and feed (*D*). Different levels of cutting parameters taken for the study are tabulated in Table 1 below.

## 2.4 Measurement of Performance Characteristics

The average surface roughness of the turned surface was measured with the help of surface analyser SURFCOM FLEX 114 (Carl Zeiss make). A cut-off length ( $\lambda_c$ ) of 2.5 mm was chosen for the surface roughness measurement of the machined part. Average of two sampling readings was taken as a final surface roughness measurement value. The MRR was determined using the weight loss method. Material removed was collected for each trial run and weighed using a digital weighing balance GR-202 (Essae make) having an accuracy of 0.01 mg.

### 3 Results and Discussion

The experimental layout and result so obtain after experimentation are shown in Table 2. After the experimentation, the results were analysed using various statistical tools. Statistical software MINITAB 17 was used for data analysis. ANOVA analysis was carried out to know the percentage contribution of input parameters on the response characteristics. The results of Taguchi experiments were elaborated and modelled here with statistical significance.

To know the statistical significance of each input variable, its variability is separated from the total variability. By using the following Eq. (1), the total sum of the squared deviations  $SS_T$  from the total mean is calculated

$$SS_T = \sum_{j=1}^p (\gamma_j - \gamma_m)^2 \tag{1}$$

where,

- $p$  number of experiment in the orthogonal array
- $\gamma_m$  mean of the experiments.

which are sum of the squared deviations from the total mean of the input variables.

The main effect plots for S/N ratio of MRR and SR are presented in Fig. 2. It is depicted that the S/N ratio for MRR increases with increasing approach angle ( $A$ ), cutting speed ( $B$ ), depth of cut ( $C$ ), and feed ( $D$ ). The S/N ratio for SR remains almost constant with increasing cutting speed ( $B$ ), and depth of cut ( $C$ ) while, it decreases with increasing approach angle ( $A$ ) and feed ( $D$ ).

The response results for the S/N ratio of MRR are shown in Table 3. It can be observed that the desired setting of cutting speed ( $B$ ) for maximizing the MRR is

**Table 2** Experimental design using an  $L_9(3^4)$  orthogonal array

Exp. no.	Cutting parameter level				Response parameter		S/N ratio	
	A	B	C	D	SR	MRR	SR	MRR
	Approach angle	Cutting speed	Depth of cut	Feed	( $\mu\text{m}$ )	( $\text{gm/s}$ )	(dB)	(dB)
1	50	175	0.4	0.08	0.681	0.012151	3.337058	-38.3076
2	50	420	0.6	0.28	2.229	0.146111	-6.9622	-16.7064
3	50	930	0.8	0.52	4.249	0.613728	-12.5657	-4.24049
4	70	175	0.6	0.52	5.3595	0.040582	-14.5825	-27.8333
5	70	420	0.8	0.08	0.7025	0.117128	3.067073	-18.6268
6	70	930	0.4	0.28	3.3345	0.157378	-10.4606	-16.0611
7	90	175	0.8	0.28	3.7905	0.106213	-11.5739	-19.4764
8	90	420	0.4	0.52	6.488	0.213877	-16.2422	-13.3967
9	90	930	0.6	0.08	0.766	0.148556	2.315425	-16.5622

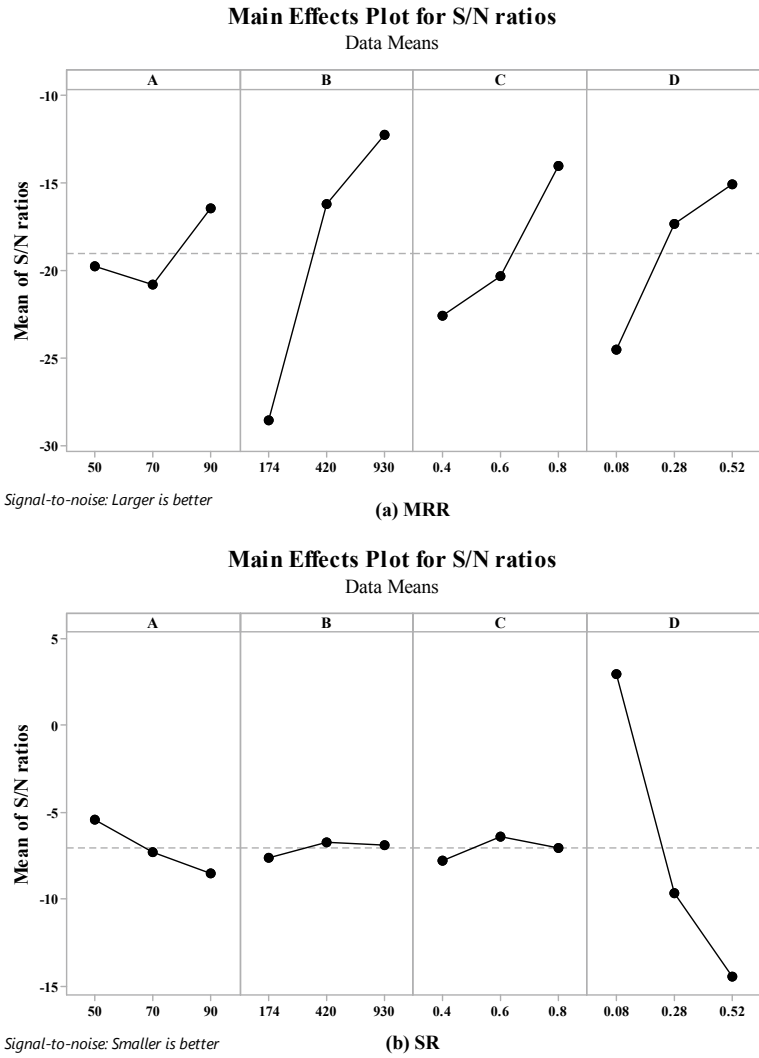


Fig. 2 Main effects plot of S/N ratio

Table 3 Response table for the S/N of MRR

Cutting parameter	Symbol	Level			Max–Min	Rank
		1	2	3		
Approach angle	A	−19.75	−20.84	−16.48	4.36	4
Cutting speed	B	−28.54	−16.24	−12.29	16.25	1
Depth of cut	C	−22.59	−20.37	−14.11	8.47	3
Feed	D	−24.5	−17.41	−15.16	9.34	2

at highest level 3 (930 rpm). Likewise, the feed ( $D$ ) and depth of cut ( $C$ ) should be set at the 0.52 mm/rev and 0.8 mm, respectively, which is also at highest level 3 to maximize the MRR. Besides that, ranking shown in Table 3 describes the relative significance of the input parameter towards the output response. From this ranking, it implies that cutting speed ( $B$ ) influences the MRR the most as it is ranked 1 followed by feed ( $D$ ), depth of cut ( $C$ ).

On the other hand, SR is under the direct influence with approach angle ( $A$ ) and feed ( $D$ ). Table 4 shows the response results for S/N ratio of SR. It is apparent that the desired level of approach angle ( $A$ ) for minimizing the SR is at the lowest level which is level 1( $50^0$ ). Similarly, the feed setting at level 1, which is 0.08 mm/rev is the most appropriate setting to minimize the SR. The ranking shown in the response Table 4 describes the relative significance of the input parameter for the SR. Feed ( $D$ ) is given rank 1, means it is the most influential factor affecting the SR which is further followed by approach angle ( $A$ ).

Table 5 shows the results of ANOVA for MRR.  $F_A (V_A/V_e)$  is undefined because of  $V_e = 0$ . Similarly,  $F_B$  and  $F_C$  are also undefined. As approach angle ( $A$ ) is having very less contribution (4.29%), the sum of squares for this factor can be combined with the error,  $S_e$ . This process of combining the contributions of the one factor to other factor is known as *pooling*. So,  $V_e$  can be joint (pooled) with another small

**Table 4** Response table for the S/N of SR

Cutting parameter	Symbol	Level			Max–Min	Rank
		1	2	3		
Approach angle	$A$	−5.397	−7.325	−8.5	3.103	2
Cutting speed	$B$	−7.606	−6.712	−6.904	0.894	4
Depth of cut	$C$	−7.789	−6.41	−7.024	1.379	3
Feed	$D$	2.907	−9.666	−14.463	17.37	1

**Table 5** ANOVA results, MRR

Cutting parameter	Symbol	Degree of freedom	Sum of squares	Mean squares ( $V$ )	$F$	Pure Sum of squares	Contribution (%)
Approach angle	$A$	2	30.9249	15.46245	Undefined	Undefined	4.29
Cutting speed	$B$	2	430.9333	215.4667	–	–	59.83
Depth of cut	$C$	2	115.8379	57.91895	–	–	16.08
Feed	$D$	2	142.5569	71.27845	–	–	19.79
Error		0	0	0/0	–	–	
Total		8	720.253				100

variance,  $V_A$ , to compute a new error  $V_e$  which can be used to make some significant results.

It is evident from pooled ANOVA Table 6 of MRR that the cutting speed ( $B$ ) followed by feed ( $D$ ) and depth of cut ( $C$ ) are considered as the most significant factor as they represent 55.54, 15.50 and 11.79% of the contribution to the experimental outcome, respectively. On the other hand, error represents 17.17% of contribution to the experimental outputs.

Similarly, Table 7 shows ANOVA results for SR.  $F_A (V_A/V_e)$  is undefined because of  $V_e = 0$ . Similarly,  $F_B, F_C$  and  $F_D$  are also undefined. As input parameters, cutting speed ( $B$ ) and depth of cut ( $C$ ) both cumulatively have less than one per cent (0.84% only) contribution on output response (SR), they can be pooled. So, a new error  $V_e$  calculated and used to draw some significant results.

The pooled ANOVA results for the SR are shown in Table 8. After pooling, it was observed that the feed ( $D$ ) has the highest contribution (95.39%) on the new surface generated during machining. Approach angle ( $A$ ) has only 2.10% contribution, which

**Table 6** Pooled ANOVA results, MRR

Cutting parameter	Symbol	Degree of freedom	Sum of squares	Mean squares ( $V$ )	$F$	Pure sum of squares	Contribution (%)
Approach angle	$A$	–	Pooled	–	–	–	–
Cutting speed	$B$	2	430.9333	215.4667	13.93483	400.0084	55.54
Depth of cut	$C$	2	115.8379	57.91895	3.74578	84.91297	11.79
Feed	$D$	2	142.5569	71.27845	4.609778	111.632	15.50
Error		2	30.9249	15.46245		92.77469	17.17
Total		8	720.253				100

**Table 7** ANOVA results, SR

Cutting parameter	Symbol	Degree of freedom	Sum of squares	Mean squares ( $V$ )	$F$	Pure sum of squares	Contribution (%)
Approach angle	$A$	2	14.7294	7.364701	Undefined	Undefined	2.94
Cutting speed	$B$	2	1.329742	0.664871	–	–	0.27
Depth of cut	$C$	2	2.86303	1.431515	–	–	0.57
Feed	$D$	2	482.7943	241.3972	–	–	96.23
Error		0	0	0/0	–	–	
Total		8	501.7165				100

**Table 8** Pooled ANOVA results, SR

Cutting parameter	Symbol	Degree of freedom	Sum of squares	Mean squares (V)	F	Pure sum of squares	Contribution (%)
Approach angle	A	2	14.7294	7.364701	7.02609	10.53663	2.10
Cutting speed	B	–	Pooled	–	–	–	–
Depth of cut	C	–	Pooled	–	–	–	–
Feed	D	2	482.7943	241.3972	230.298	478.6016	95.39
Error		4	4.192772	1.048193		8.385544	2.51
Total		8	501.7165				100

is not of much significance. On the other hand, error represents 2.51% of contribution only on several experimental outputs, which is under the acceptable statistical limit.

So after obtaining the optimal parameter settings for MRR and SR, the improved response characteristics were predicted and further verified using the optimal parametric settings. The estimated optimal response by using the optimal level of the machining parameters can be calculated as

$$Y_o = \bar{T} + \sum_{i=1}^n (X_i - \bar{T}) \tag{2}$$

where,

$Y_o$  estimated performance at optimal condition

$\bar{T}$  average performance

$X$  contributing parameters

$n$  number of process parameters having significant contribution in multiple performance characteristics.

The predicted or estimated output response (optimal) is equal to the mean performance plus the summation of the difference between the overall mean performance and the contributing parameters for each of the factors at an optimal level.

Using the above Eq. (2) and optimal levels of machining parameters, the optimal values of MRR and SR (Ra) are calculated as given by Eqs. (3) and (4), respectively.

$$MRR = \bar{T} + (B_3 - \bar{T}) + (C_3 - \bar{T}) + (D_3 - \bar{T}) = -116.91 \text{ dB} \tag{3}$$

$$SR = \bar{T} + (A_1 - \bar{T}) + (D_1 - \bar{T}) = 11.55201 \text{ dB} \tag{4}$$

According to these predictions, it can be inferred that the maximum and minimum values of MRR and SR are  $-116.9$  dB and  $11.55$  dB, respectively, which are the values within the obtained experimental results.



### 3.1 Confidence Interval

Confidence interval (CI) is an interval which provides a significance level that the estimated parameter lies within the range. It is calculated from the data obtained through experimentation. It is used as an indicator of reliability for the predicted parameter [10]. Uncertainty about the predicted parameter magnitude is well recognized by the width of the confidence interval so obtained. Wider the interval, more probable to definite the parameter estimate or, in another word, more experimental data is required for a closer estimate. The CI for MRR and SR was calculated using Eq. (5).

$$\text{C.I.} = \sqrt{\frac{F_{\alpha v_1 v_2} \times V_e}{N_e}} \quad (5)$$

where,

$$N_e = \frac{N}{(1 + DoF_{\text{eff}})}$$

From the above relations, the value of confidence interval (CI) for optimal MRR and SR model is as follows,

MRR

$$V_e = 92.77469, N_e = 9/(1 + 6) = 1.2857143$$

$$F(1, 2) = 8.5263, \text{CI} = (615.2415)^{1/2} = 24.8040$$

Hence, the 90% confidence interval of the optimal MRR in confirmation test is,  $-116.91 \pm 24.8040$  dB.

SR

$$V_e = 8.385544, N_e = 9/(1 + 4) = 1.8$$

$$F(1, 4) = 7.7086, \text{CI} = (35.91155)^{1/2} = 5.9926$$

Hence, the 95% confidence interval of the optimal SR in the confirmation test is,  $11.55201 \pm 5.9926$  dB.

Confirmation run was conducted at the optimal condition of MRR (A3B3C3D3) and SR (A1B2C2D1) obtained through experimental data analysis and it is found that the results for both the responses are within the predicted limit. The SR and MRR obtained were  $0.602 \mu\text{m}$  and  $0.053 \text{ mg/s}$ , respectively.

### 3.2 Empirical Modelling

After completing the experimental data analysis, the next step for any nonlinear and uncertain process could be modelling of response parameter. The predictive model helps a lot for parameter selection for the desired response. Regression is one of a fundamental technique to fulfil this purpose. As this technique build a relation between different input and output variables, it becomes quite easy to predict the output response. Hence, manufacturing industries can be benefitted using this kind of models for process data description, parameter estimation, and control [11]. The criteria for fitting the best line through the data in simple linear regression are to minimize the sum of squares of residuals. The linear fit is expressed as shown in Eq. (6),

$$y = a_0 + a_1x \quad (6)$$

where  $y$  is the value of response and  $x$  is the value of the variable.

The empirical equations of the fitted models for the different quality characteristics are shown in Eqs. (7) and (8).

$$\text{MRR} = -0.177 - 0.00253 A + 0.000328 B + 0.378 C + 0.453 D \quad (7)$$

$$\text{SR} = -1.071 + 0.03238 A - 0.000660 B - 1.468 C + 10.526 D \quad (8)$$

where  $A$  is approach angle,  $B$  is cutting speed,  $C$  is the depth of cut and  $D$  is feed.

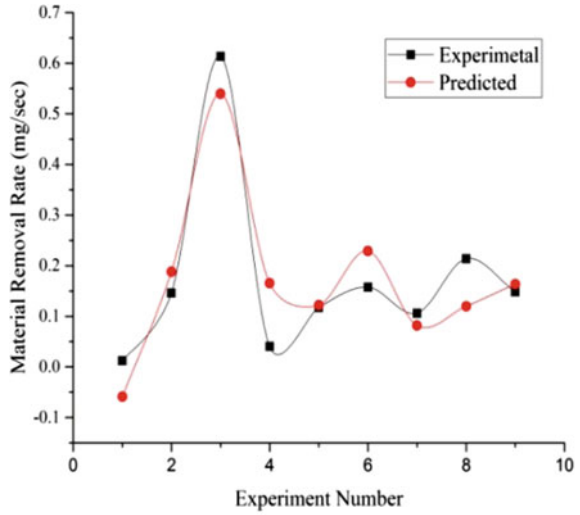
From the linear regression models developed for predicting, it is found that the feed is the most significant parameter affecting both response characteristics. The regression plot obtained during generation of multiple regression models for MRR and SR is shown in Fig. 3.

Residuals versus fits graph are shown in Fig. 4. These graphs representing the random scattering of residuals about zero and there no pattern is observed. That is good sign for any model.

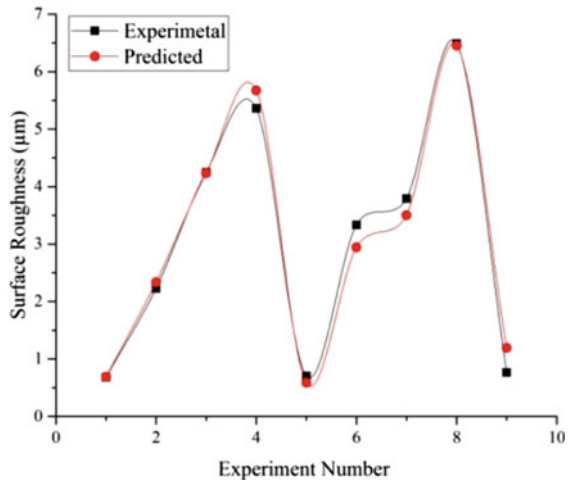
The graph shown in Fig. 5 below is representing the efficiency of the empirical model developed.  $R$ -square value was used for this purpose which is also known as “coefficient of determination”. Its value ranges between 0 and 1. Higher is the  $R$ -square, better is the response. The MRR and SR models having  $R$ -squared values 0.83 and 0.99, respectively, mean both models are adequate for prediction.

The correlation between the experimental and predicted models was also calculated to know the nature of the relation between observed and predicted values. The value of “Pearson’s  $r$ ” ranges between  $-1$  and  $+1$ . Here, a strong positive correlation for the both MRR (0.91) and SR (0.99) model for their respective experimental and modelled (predictive) results was observed.

**Fig. 3** Experimental versus predicted values



(a) MRR

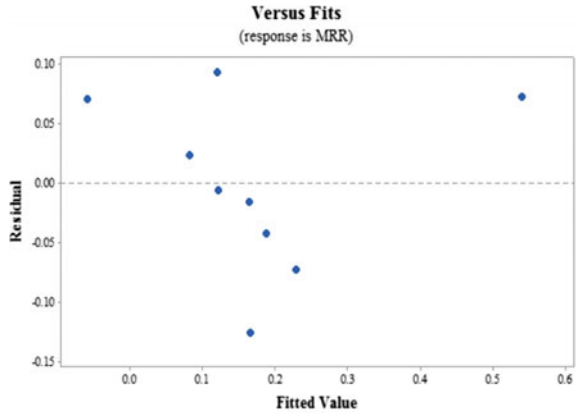


(b) SR

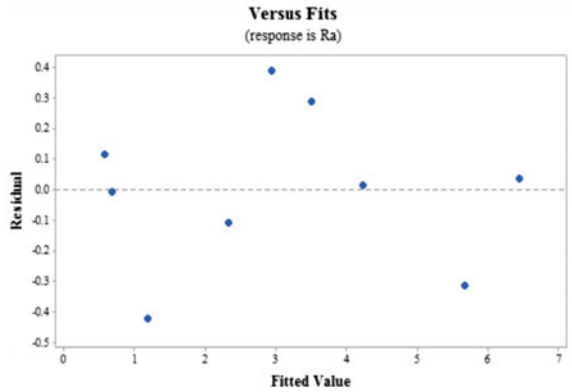
### 4 Conclusions

- The Taguchi technique is used to evaluate the multiple performance characteristics through ANOVA. It makes the determination of optimal analysis more efficient and can greatly simplify the optimization procedure for the complex machining responses.

Fig. 4 Residual plot



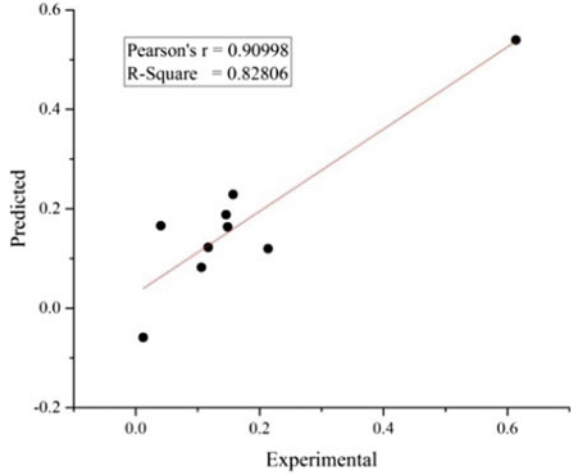
(a) MRR



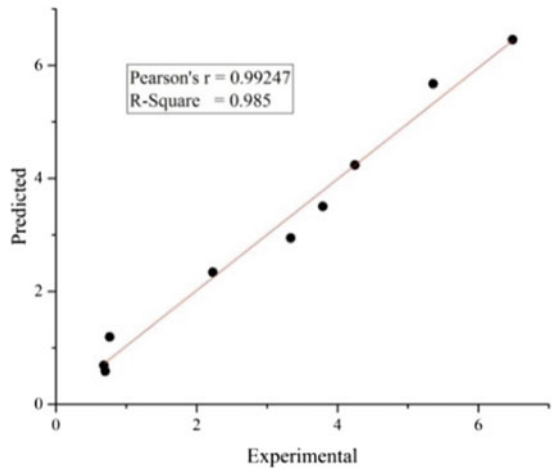
(b) SR

- For turning titanium alloy (grade-5) with uncoated WC-Co tool, the optimal level setting of machining parameters are B3, C3 and D3 for maximizing MRR and A1 and D1 for minimizing the SR according to the results of response table and response graph.
- ANOVA results show that parameter B (cutting speed), parameter C (depth of cut) and parameter D (feed) affect the MRR by 55.54, 11.79 and 15.50% in the turning process, respectively. SR is affected by parameter A (approach angle) and parameter D (feed rate) with 2.10 and 95.39% contribution, respectively.
- Based on the optimal levels of machining parameters, the surface roughness (Ra) and MRR obtained were 0.602  $\mu\text{m}$  and 0.053 mg/s, respectively. It can be concluded that the required performance characteristics have been improved through Taguchi technique.
- Prediction of MRR and SR is carried out by the developed empirical model using linear regression models for various input process variables. Both models found

Fig. 5 Correlation graph



(a) MRR



(b) SR

adequate having *R*-squared values 0.83 and 0.99 for MRR and SR model, respectively.

- The reliability of the optimal results is determined by calculating the confidence interval. The 95% confidence interval for SR and 90% for MRR obtained from confirmation test are found to be within the limits.

## References

1. Avuncan G (1998) Machining economy and cutting tools. Makine Takim Endustrisi Ltd. Publication, Istanbul, pp 375–403
2. Groover MP (2010) Fundamentals of modern manufacturing: materials, processes, and systems. Wiley, Danvers, MA
3. Kumar P, Misra JP (2019) Modelling of tool wear for Ti64 turning operation. Mater Sci Forum 969:750–755. <https://doi.org/10.4028/www.scientific.net/MSF.969.750>
4. Abhang LB, Hameedullah M (2012) Determination of optimum parameters for multi-performance characteristics in turning by using grey relational analysis. The Int J Adv Manuf Technol 63(1–4):13–24. <https://doi.org/10.1007/s00170-011-3857-6>
5. Pawan K, Misra JP (2018) A surface roughness predictive model for DSS longitudinal turning operation. DAAAM International Scientific Book, Chapter 25, pp 285–296
6. Xie J, Luo MJ, Wu KK, Yang LF, Li DH (2013) Experimental study on cutting temperature and cutting force in dry turning of titanium alloy using a non-coated micro-grooved tool. Int J Mach Tools Manuf 73:25–36. <https://doi.org/10.1016/j.ijmachtools.2013.05.006>
7. Boujelbene M (2018) Investigation and modeling of the tangential cutting force of the Titanium alloy Ti–6Al–4V in the orthogonal turning process. Procedia Manufacturing, Maharashtra, India, pp 571–577
8. Bai J, Bai Q, Tong Z (2018) Experimental and multiscale numerical investigation of wear mechanism and cutting performance of polycrystalline diamond tools in micro-end milling of titanium alloy Ti–6Al–4V. Int J Refract Metals Hard Mater 74:40–51. <https://doi.org/10.1016/j.ijrmhm.2018.03.007>
9. Khan A, K Maity (2018) Influence of cutting speed and cooling method on the machinability of commercially pure titanium (CP-Ti) grade II. J Manuf Process 31:650–661. <https://doi.org/10.1016/j.jmapro.2017.12.021>
10. Montgomery DC, Runger GC (2010) Applied statistics and probability for engineers. Wiley
11. Montgomery DC (2017) Design and analysis of experiments. Wiley

# Makespan Optimization in Open Shop Scheduling



Prakash Kesarawani, Neeraj Kumar and Abhishek Mishra

**Abstract** In today's rapid production scenario, scheduling plays a dynamic role in planning. In this work, open shop scheduling problem related to a copper flexible braids manufacturing company is considered. In a scheduling problem, the purpose is to find the orders of jobs on specific machines with an objective to optimize the makespan. Scheduling can be either manual or automatic. Manual scheduling of operations is a difficult task. Hence, computational methods are used to automate and simplify the process. In this work, integer programming and constraint programming-based mathematical models are developed to tackle this problem. The branch-and-bound (B&B) algorithm is applied for integer programming model, and branch-and-cut (B&C) algorithm is applied for constraint programming model in order to get optimized makespan. A comparison of results obtained from both mathematical models is done for selection of optimized makespan and identification of model.

**Keywords** Open shop scheduling (OSS) · Integer programming · Constraint programming

## 1 Introduction

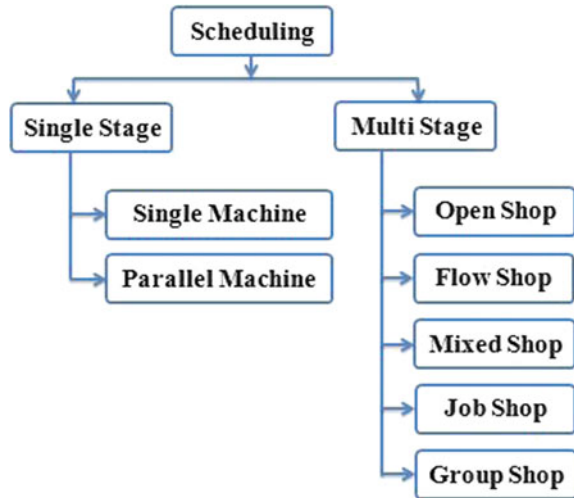
Scheduling deals with the allocation of the resources or the arrangement of resources. It is a wider term used in number of industrial problems. For example, scheduling of jobs in industry for obtaining the optimum makespan time. Figure 1 represents the classification of scheduling. To perform the scheduling, the very first thing is to get the information about the availability of resources. When the scheduler gets all the information on available resources, the second step is to allocate the available resources for performing specified tasks. For this, the scheduler first constructs a tentative schedule chart and then evaluates it. After the completion of evaluation, scheduler conveys the plan to user. User may or may not be satisfied by the results

---

P. Kesarawani · N. Kumar · A. Mishra (✉)  
Department of Mechanical Engineering, National Institute of Technology Delhi, New Delhi  
110040, India  
e-mail: [abhishekmishra@nitdelhi.ac.in](mailto:abhishekmishra@nitdelhi.ac.in)

© Springer Nature Singapore Pte Ltd. 2020  
L. Vijayaraghavan et al. (eds.), *Emerging Trends in Mechanical Engineering*,  
Lecture Notes in Mechanical Engineering,  
[https://doi.org/10.1007/978-981-32-9931-3\\_24](https://doi.org/10.1007/978-981-32-9931-3_24)

**Fig. 1** Classification of scheduling



obtained by the tentative scheduling plan and can alter some resources to get the more efficient and accurate output. Widely, scheduling is classified as  $\alpha/\beta/\gamma$  types; where  $\alpha$  represents job environment,  $\beta$  indicates job characteristics and  $\gamma$  signifies the optimality criterion.

In the present work,  $n$  number of jobs along with  $m$  number of machines is considered. Hence, it comes under the multi-stage scheduling as mentioned in Fig. 1. In open shop scheduling process, the sequence of jobs on machines is not defined and aim is to determine the time at which each job needs to be processed at each workstation. The first exact technique for solving the open shop problem depends on resolution of one machine problem having negative and positive time lags [1]. Some authors have considered the objective of open shop scheduling problem as minimizing the makespan. They established a model using constraint programming to solve the problem and tested the results with the existing literature [2].

For solution of open shop scheduling problem, many metaheuristic algorithms have been introduced in last few years. Some of the current and successful metaheuristic algorithms are ant colony optimization [3], genetic algorithm [4], and particle swarm optimization [5]. From the literature, it can be concluded that most of the heuristic techniques rapidly give good results. Most of them are constructive techniques and belong to three major groups: matching algorithms, priority dispatching rules, and insertion and appending actions joint with beam search. Open shop scheduling was explored with dynamic shortest processing time (DSPT), which considered the scheduling of  $n$  jobs and  $m$  machines [6]. A heuristic for minimizing the makespan was proposed and a new lower bound presented for schedule. It was verified with the experiments.



## 2 Methodology

In the present work, industrial problems were considered, and models for open shop scheduling problem were developed in integer programming using B&B algorithm, as well as in constraint programming using B&C algorithm.

### 2.1 Integer Formulation of Problem

In open shop scheduling, there are no restrictions of sequence of machines as well as order of jobs. Sequence of machines and order of jobs are open to schedule for optimization of time. The time of processing of each job on each machine is known. The only objective is to find the optimal sequence so that makespan or maximum completion time can be minimized. Some assumptions are made for the open shop scheduling problems such as every job can be operated only once on certain machine, and all jobs are prepared for processing at initial time zero (Fig. 2).

Equation (1) shows the optimality criterion, used for minimizing the makespan or maximum completion time for open shop scheduling problem satisfying all the constraints such as feasibility, precedence as well as non-negativity for  $M_{\max}$ .

$$\text{Minimum } M_{\max} \tag{1}$$

#### 2.1.1 Branch and Bound

The branch-and-bound technique is a solution method specially used to solve integer programming problems. The B&B algorithm is a solution technique that divides the practical solution space into minor subsets of solution. These minor subsets can be calculated systematically until the best feasible solution is found. B&B requires an initial lower bound on each machine processing time to begin the algorithm. A tighter bound, however, can be found for each processing time. In addition to lower bounds on processing times, beginning of the algorithm needs primary feasible schedule.

### 2.2 Constraint Programming

For solving scheduling problem, constraint programming techniques are extensively used. A Constraint Satisfaction Problem (CSP) involves a set of constraints, a variables set ( $V$ ) defined by an equivalent set of possible values known as domain ( $D$ ). The feasible solution of the problem is to assign a value to each variable in such a way that all constraints get simultaneously satisfied. A circulation or propagation

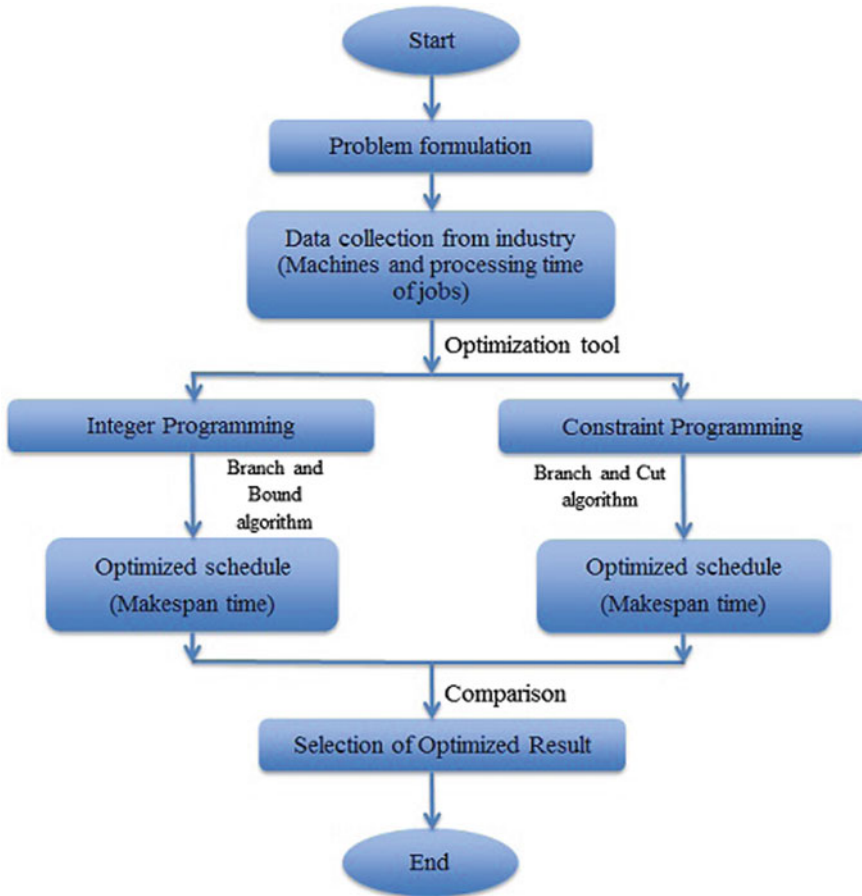
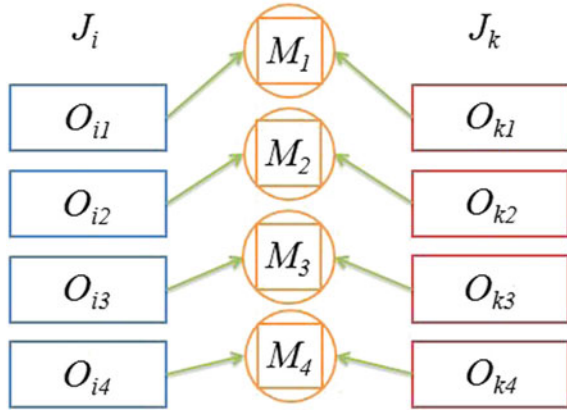


Fig. 2 Flowchart for open shop scheduling problem

mechanism is used to handle the constraints which allow the decrease of the set of domains of variables, as well as the trimming of the search tree. A circulation mechanism attached to a backtracking system permits the search space to be explored in a broad manner. Constraint programming techniques used to solve scheduling problem by using specialized global constraints, which permits modeling resource limitations such as cumulative global constraints or unary resource constraints [7].

Constraint programming (CP) models in the task of scheduling generally represent a non-preemptive task  $T_{i,j}$  with the help of three non-negative integer variables indicating the start of task ( $S_{i,j}$ ), required duration ( $P_{i,j}$ ), and end of the task ( $E_{i,j}$ ), so that  $S_{i,j} + P_{i,j} = E_{i,j}$ . In open shop scheduling problems, duration  $P_{i,j}$  is a constant and is known in advance. The head of a task  $EST T_{i,j} = INF S_{i,j}$  represents the earliest possible starting date of the task, whereas the tail  $LC T_{i,j} = SUP E_{i,j}$  is the latest completion time. The open shop scheduling problem presents that only one

**Fig. 3** Open shop scheduling



task of a job or machine can be processed at any given time as shown in Fig. 3. These constraints are modeled with the unary resource global constraint. In the end, some temporal constraints are used for making the decision process such as precedence between tasks for the taken problem.

**2.2.1 Branch and Cut**

The branch-and-cut algorithm is used in one of the optimization tools to obtain the solution of open shop scheduling problem based on formulation. In this algorithm, initial set of inequalities is generated and solved by linear programming relaxation. If the solution to the linear programming relaxation is an integer, an optimal solution has been reached. If it is not an integer, an enumeration tree is created and an effort is made to produce those valid inequalities which failed to comply at every node of this tree. Hence, when the linear programming bound is calculated at a specified node of the tree, the linear program includes all the cuts produced so far. Before beginning the branch-and-cut (B&C) method, an upper bound is calculated with the heuristic search. This upper bound is used to cut the enumeration tree every time the solution value at a specified node surpasses that of the upper bound.

**3 Result and Discussion**

In this work, we have solved the industrial problem of a copper flexible braids manufacturing company. The integer linear programming model (ILP) programmed in the optimization solver which is based on branch-and-bound (B&B) algorithm.

Second optimization tool that is used here works on the branch-and-cut (B&C) algorithm which reduced the unnecessary iterations by cutting the non-feasible

branches and gives the solution very fast. Given problem is manufacturing of copper flexible braids. There are various types of copper flexible braids used in power transmission. Processing time of each job on different machines is given in Table 1. Objective value is 540 s. It shows that for completion of one job, it will take 540 s (i.e., 9 min). Given solution is feasible. Objective bound 480 shows that the minimum time for completing the jobs could be 480 s. It is the lowest limit of makespan time. Now, the second problem is manufacturing of copper flexible braids. According to the layers of braids, we considered four different products. Table 2 shows the processing time of each job on each machine.

The objective value is 960 s. It shows that for completion of one job, it will take 960 s. The results obtained by the branch-and-bound (B&B) algorithm for OSP are close to the upper bounds of optimal makespan. The B&B is compared with branch-and-cut (B&C) for these two industrial problems. It is observed from the results that makespan time obtained by B&B is equal to makespan time obtained by B&C. The best solution and makespan values obtained by B&C and the proposed B&B are listed in Table 3. The result shows that B&C takes less computational time than B&B (Figs. 4, 5 and Table 4).

**Table 1** Notations used for integer formulation of open shop scheduling

Symbol definition	Problem parameters	Decision parameters
$j_i$ = job number $i$ ; $m_k$ = machine number $k$ ; $N_i$ = total number of operations of job $j_i$ $O_{iJk}$ = Operation number $j$ of job $i$ at machine $k$ ;	$B$ = a large number; $n$ = number of jobs; $m$ = number of machines; $S_{iJk}$ = Starting time of operation $O_{iJk}$ ; $p_{iJk}$ = Processing time of job $i$ at machine $k$ ;	$M_{\max}$ = Maximum makespan time or maximum completion time Therefore, $M_{\max} = \sum_{i=1}^n M_i$ ; $\alpha_{iJk} = 1$ , if job $i$ is scheduled at $j$ th number at machine $k$ , otherwise 0; $\gamma_{ijj'k}^k = 1$ , if operation $O_{iJk}$ precedes the operation $O_{i'J'k}$ , otherwise 0;

**Table 2** Processing time at each machine (case 1)

Job	Machine	Processing time (s)
1	M1, M2, M3, M4, M5	16, 90, 60, 50, 120
2	M1, M2, M3, M4, M5	10, 120, 72, 80, 180
3	M1, M2, M3, M4, M5	20, 90, 72, 80, 180
4	M1, M2, M3, M4, M5	10, 30, 3, 10, 60

**Table 3** Processing time at each machine (case 2)

Job	Machine	Processing time (s)
1	M1, M2, M3, M4, M5, M6, M7	4, 60, 240, 120, 3, 60, 2
2	M1, M2, M3, M4, M5, M6, M7	16, 60, 240, 120, 3, 90, 3
3	M1, M2, M3, M4, M5, M6, M7	20, 60, 240, 120, 3, 120, 5
4	M1, M2, M3, M4, M5, M6, M7	42, 60, 240, 120, 3, 240, 20

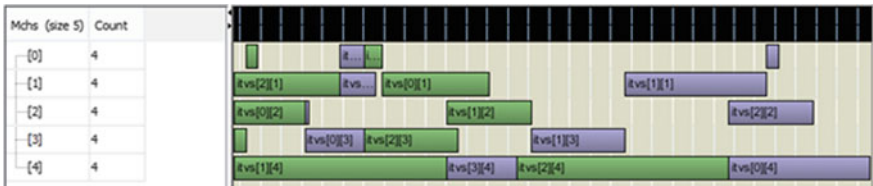


**Fig. 4** Optimum makespan for the industrial problem (case 1)

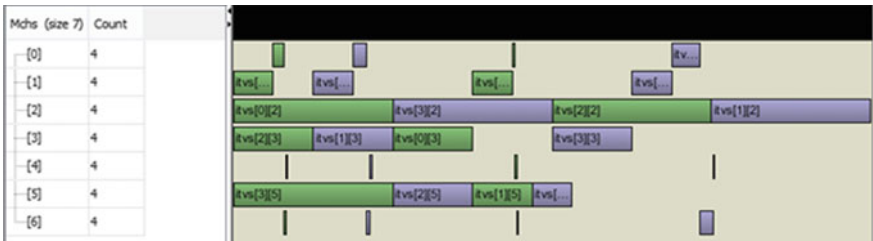


**Fig. 5** Optimum makespan for the industrial problem (case 2)

**Table 4** Comparative results of algorithms for real industrial problem

Problem size (Job × machine)	Makespan from B&B (in s)	Makespan from B&C (in s)	Computation time (in s)
4 × 5	540	540	B&B-754828.9 B&C-0.37
4 × 7	960	960	B&B-2841570.9 B&C-0.78

## 4 Conclusions

In the present work, a mathematical model is proposed for  $n$  job,  $m$  machine for open shop scheduling. This model used the criterion of minimization of makespan time. This model is further programmed in two optimization tools, which computationally help to solve the problem. A similar model can also be used for other objective functions such as minimum tardiness, minimization of mean flow time with slight modification in the mathematical model. The future work may be conducted to develop new metaheuristics techniques and mixed integer linear programming (MILP) for solving open shop scheduling problem.

## References

1. Brucker P, Hilbig T, Hurink J (1996) A branch and bound algorithm for scheduling problems with positive and negative time-lags. Technical report, Osnabrueck University
2. Malapert A, Cambazard H, Guéret C, Jussien N, Langevin A, Rousseau LM (2012) An optimal constraint programming approach to the open-shop problem. *INFORMS J Comput* 24(2): 228–244
3. Blum C (2005) Beam-ACO—hybridizing ant colony optimization with beam search: an application to open shop scheduling. *Comput Oper Res* 32(6):1565–1591
4. Prins C (2000) Competitive genetic algorithms for the open-shop scheduling problem. *Math Methods Oper Res* 52(3):389–411
5. Sha DY, Hsu CY (2008) A new particle swarm optimization for the open shop scheduling problem. *Comput Oper Res* 35(10):3243–3261
6. Bai D, Tang L (2013) Open shop scheduling problem to minimize makespan with release dates. *Appl Math Model* 37(4):2008–2015
7. Beldiceanu N, Carlsson M, Demassey S, Petit T (2006) Graph properties based filtering. In: International conference on principles and practice of constraint programming. Springer, Berlin, pp 59–74 (2006)

# Assessment of Manufacturing Process Through Lean Manufacturing and Sustainability Indicators: Case Studies in Indian Perspective



Vikas Swarnakar , A. R. Singh  and Anil Kr. Tiwari 

**Abstract** Due to the government pressure and public awareness, industries are bound to incorporate sustainability in their manufacturing process. In this context, the concept of lean manufacturing and value stream mapping (VSM) process has been used widely in various manufacturing industries to minimize the waste in their production process. The objective of this study is to propose a conceptual model for the integration of VSM tool integrated with various sustainability indicators. The proposed model is capable to assess the manufacturing process into three sustainability dimensions such as economic, social, and environmental. This methodology was applied to two different manufacturing industries such as automotive component manufacturing organization and PVC pipe manufacturing organization, situated in India. The result demonstrated that the proposed methodology identified the areas of improvement after applying these integrated methodologies and clearly enabled the opportunities for improvements in both manufacturing organizations.

**Keywords** Lean manufacturing · Sustainability indicators · Manufacturing process · Value stream mapping

## 1 Introduction

The operation management frameworks have been developed to adopt the new changes in the market with certain changes in customer demands. During the twentieth century, the increase in demands for quality of products thus various management

---

V. Swarnakar (✉) · A. R. Singh · A. Kr. Tiwari  
National Institute of Technology Raipur, Raipur, India  
e-mail: [vikkiwarnakar@gmail.com](mailto:vikkiwarnakar@gmail.com)

A. R. Singh  
e-mail: [amitrajsingh1@gmail.com](mailto:amitrajsingh1@gmail.com)

A. Kr. Tiwari  
e-mail: [anil.kr.tiwari@gmail.com](mailto:anil.kr.tiwari@gmail.com)

frameworks have come into the competitive market to fulfill the customer needs. This framework was developed based on the analysis of standard time, methods, and operations. In the end of the twentieth century, the demand of the quality product was in hike due to globalization, and resulted various manufacturing processes had been managed according to quality, delivery time, cost of the product, flexibility, reliability, and speed indicators [8]. Lean manufacturing approach is widely applied for the management of manufacturing process. The objective of lean manufacturing is to eliminate waste from the production process and enhance the operational improvement of the organization. The various improvements can be found after the successful implementation of the LM concept such as reduction in cycle time, waiting time, inventory level, number of employees; this can directly help in the improvement of quality, cost, and delivery time of the product. Ultimately, these improve customer satisfaction level of industry in the competitive market. This study introduces a new group of sustainability indicators integrated with three dimensions such as economic, social, and environmental key performance index (KPI), and these indicators are integrated with lean manufacturing tools VSM (lean KPIs) to develop a conceptual method for assessing sustainability of the manufacturing process.

## **2 Literature Review**

### ***2.1 Reviews on Adoption of Lean Manufacturing***

Lean manufacturing (LM) is defined as a methodology which eliminates waste from manufacturing process through reduction in non-value-added activities and improves bottom-line results. Eatock et al. [4] defined that the lean manufacturing is a set of principles, procedures, methods which helps to reduce waste and improve the production process. The study highlighted the value stream mapping tool is a most powerful tool among the other lean tools and also stated that this tool provides a holistic view and is highly used in several organizations. Chen et al. [2] presented an implementation process of lean manufacturing in a factory with the help of a case study. Kuhlman et al. [9] proposed the concept of extended value stream mapping (EVSM). The EVSM consisted of transport indicators and allowed this for the development of future scenario for the improvement in manufacturing process. Dües et al. [3] analyzed the relation between green and lean manufacturing practices in the area of supply chain management (SCM).



## 2.2 *Reviews on Sustainability Indicators*

Sustainability can be defined as is the ability to maintain organization profit (expected by shareholders) in the manufacturing of goods or services without affecting the environment [6]. Hueting [7] explored that the environmental sustainability is an action which protects the essential environmental functions for future generation. Strezov et al. [11] elaborated that each sustainability dimension consisted of sustainability indicators which easily asses the sustainable performance of any organization. Faulkner and Badurdeen [6] developed a conceptual model of sustainable value stream mapping (Sus-VSM) integrated with various sustainability indicators. Brown et al. [1] applied the same model developed by Faulkner and Badurdeen [6] in three different manufacturing industries with a different process such as flow shop, job shop, and manufacturing cells. Roufechaei et al. [10] highlighted the concept of economic sustainability developed based on the ratio of investment and return as per expectation of shareholder. The study also stated that the use of economic indicators in value stream mapping tool contributes to the assessment of economic characteristics in their manufacturing process.

From the above review, there is a need to develop the method for assessment of the manufacturing process. In this work, our aim is to integrating the new group of sustainability indicators (economic, social, and environmental) into lean manufacturing tools (VSM) to assess the manufacturing process of Indian manufacturing industry.

## 3 **Methodology**

The methodology used in this study is clearly presented with the help of flow diagram and shown in Fig. 1. In this diagram, the first step is method is separated into two stages. The first stage needs to review the literature regarding sustainability indicators, and in the second stage we need to categorize the group of sustainability indicators that compose the assessment method used to assessing the sustainable

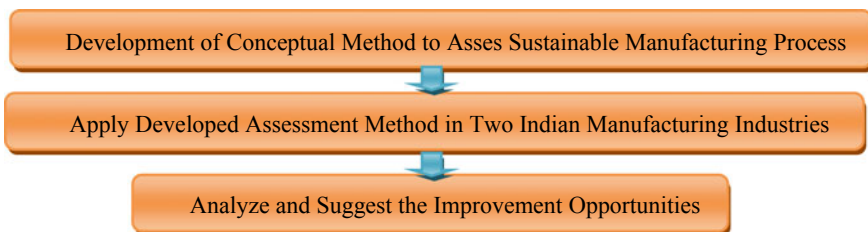


**Fig. 1** Applied methodology

manufacturing process. The objective of this first step is to define a new group of sustainability indicators which integrated with three dimensions such as economic, social, and environmental, and these indicators are integrated with lean manufacturing tools (VSM) to develop a conceptual method for assessing sustainability in the manufacturing process. This concept was developed based on valuation models presented by Kuhlman et al. [9].

The sustainability indicators are identified with experts' opinion and literature review from 2009 to 2017 searched by the following keywords: sustainability indicators, lean manufacturing, value stream mapping. In step 2, need to apply the assessment method in two Indian manufacturing industries. The data were collected through direct observation of the shop floor and detailed discussion with senior management, employees, and operators.

## **4 Development of a Conceptual Method to Assess the Sustainability in the Manufacturing Process**

The conceptual method for assessing sustainability in the manufacturing process through the integration of sustainability indicators with VSM tool was developed. In this context, new group of sustainability indicators was developed based on triple bottom line (TBL) concept and various reviewed literatures.

### ***4.1 Development of Key Performance Index Based on TBL Concept***

The three KPIs have been developed according to Eccles et al. [5], and the study stated that both social and environmental dimensions are directly associated with expected payback period. In India, most of the manufacturing industries do not have exact knowledge about suitable metrics for measuring the cost-benefits of sustainability. The conceptual method is proposed to integrate lean manufacturing and sustainability indicators to assess the manufacturing process. In this study, a new group of KPIs has been developed through the literature review and experts' opinion. The experts are having more than 15 years of industrial experience. In this context, each manufacturing operation is calculated using various formulas which are clearly presented in Table 1. In this study, six sustainability indicators have been considered and all are having equal weights and importance.

**Table 1** Various KPIs used in lean manufacturing tool VSM

Dimension	Field/area	Sustainability indicators	Formula used for calculation
Economic	Cost management	Operational cost	OC (Rs.) = cycle time (labor cost + management cost + depreciation cost)
		Effective cost	Operational cost/overall equipment effectiveness
Social	Satisfaction level	Absent rate	Abs (%) = total absentee time (in h)/total working time (in h)
		Accident rate	Total no. of accidents/total employees
Environmental	Quality and health	Electric consumption	Calculate based on predefined reference
	Consumption	Water consumption	Calculate based on predefined reference

## 5 Case Study

The pilot test was performed in two Indian manufacturing organizations. The first test was performed in one automotive component manufacturing organization named as ABC situated in Tamil Nadu, India, and second was in polyvinyl chloride (PVC) pipe manufacturing organization named as XYZ situated in Chhattisgarh, India. Due to non-disclosure agreement terms, we cannot mention the exact name of the companies. The conceptual method was applied in both organizations that have the high maturity of both lean and sustainable practices. Both manufacturing processes are characterized as flow shop and manufacturing high volume and low variety products. The data are as follows.

### 5.1 Pilot Test at an Automotive Component Manufacturing Organization

The customer demand for case product was 8000 pieces per day. The total available time was 480 min/day, and actual production time was 420 min/day. Thus, Takt time can be calculated as 9.45'' per piece. The manufacturing process is shown in Fig. 2. The data have been collected from shop floor observation and proper meeting with workers, and management persons. The VSM is developed and calculated with the

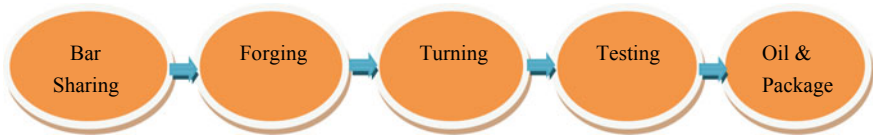


Fig. 2 Automotive component manufacturing process

integration of sustainability indicators and shown in Fig. 3. The Takt time was calculated as 10.8'' (process cycle time is less than or equal to Takt time) that meets the customer demand and is considered as sustainable. The high inventory level in the process leads to high lead time (16.2 days). This VSM integrated with economic, social, and environmental indicators. The reference value is necessary to calculate the bottleneck operation in manufacturing process and obtained through an interview with production and human resources department peoples. In this study, two sustainability indicators are considered under economic dimensions such as operational cost and effective cost. The operational cost is calculated for each process, and it observed the highest relative cost of 29.85% for forging operation in the manufacturing process and is considered as bottleneck operation. The effective cost calculated and observed the highest relative cost of 24.77% for testing operation in all process and thus is also considered as bottleneck operation.

The two sustainability indicators are considered under social dimension such as absent rate and accident rate. The absent rate has calculated and identified highest relative rate of 33.33% for bar shearing operation, and accident rate has observed high relative rate of 85.71% for forging operation in all manufacturing processes. In an analysis of environmental dimension, two sustainability indicators are considered as electric consumption and water consumption. The high electric consumption has been observed (relative cost of 20.22%) in forging operation and is considered as

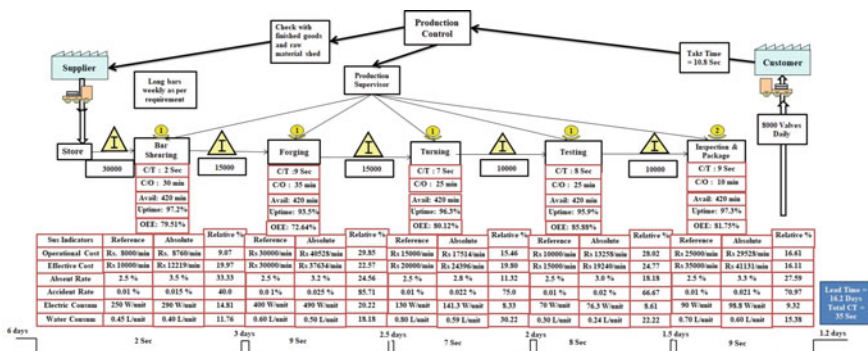


Fig. 3 Sustainability indicators in VSM applied in automotive component manufacturing organization

bottleneck operation. The high water consumption has been observed (relative cost of 30.22%) in turning operation, and this process is also considered as a bottleneck operation.

### 5.2 Pilot Test at PVC Pipe Manufacturing Organization

The customer demand for case product was 15,000 pieces per day. The total available time was 480 min/day, and actual production time was 420 min/day. Thus, Takt time can be calculated as 5.76" per piece. The manufacturing process is shown in Fig. 4. The data have been collected from shop floor observation and proper meeting with workers, and management persons. The VSM is developed and calculated with integration of sustainability indicators and shown in Fig. 5. The Takt time was calculated as 5.76" (process cycle time is less than or equal to Takt time) that meets the customer demand and is considered as sustainable. The high inventory level in the process leads to high lead time (18.2 days). This VSM integrated with economic, social, and environmental indicators. The reference value is necessary to calculate the bottleneck operation in manufacturing process and obtained through an interview



Fig. 4 PVC pipe manufacturing process

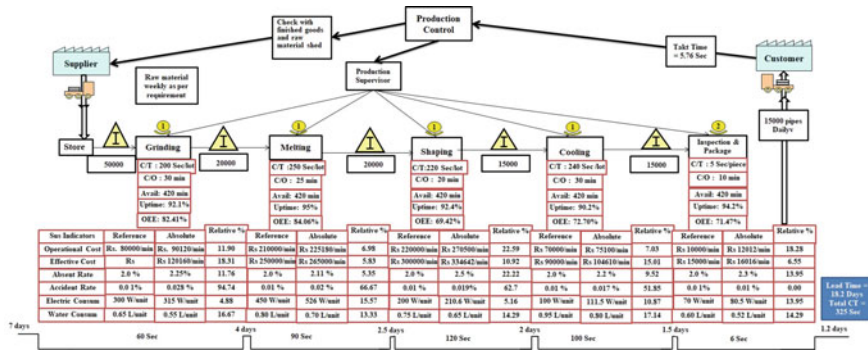


Fig. 5 Sustainability indicators in VSM applied in PVC pipe manufacturing organization

with production and human resources department peoples. In this study, two sustainability indicators are considered under economic dimensions such as operational cost and effective cost. The operational cost is calculated for each process, and it observed the highest relative cost of 22.59% for shaping operation in the manufacturing process and is considered as bottleneck operation. The effective cost calculated and observed the highest relative cost of 18.31% for grinding operation in all processes and thus is also considered as bottleneck operation.

The two sustainability indicators are considered under social dimension such as absent rate and accident rate. The absent rate has calculated and identified highest relative rate of 22.22% for shaping operation, and accident rate has observed high relative rate of 94.74% for grinding operation in all manufacturing processes. In an analysis of environmental dimension, two sustainability indicators are considered as electric consumption and water consumption. The high electric consumption has been observed (relative cost of 15.57%) in melting operation and is considered as bottleneck operation. The high water consumption has been observed (relative cost of 17.14%) in cooling operation, and this process is also considered as bottleneck operation.

### 5.3 Opportunity for Improvements Observed in Case Studies

The result has been obtained from the case study and summarized in Table 2. It can be clearly observed that the developed conceptual method for manufacturing process assessment is applicable in these case studies. It can be also observed that the various bottleneck operations are fluctuated according to sustainability dimension. Thus, the improvements can be developed with the different bottleneck operations. The various improvement actions have been identified and suggested for further improvements in manufacturing process and shown in Table 3.

**Table 2** Summarized result for the assessment of manufacturing process

Case	Economic dimension (bottleneck operations)		Social dimension (bottleneck operations)		Environmental dimension (bottleneck operations)	
	Operational cost	Effective cost	Absent rate	Accident rate	Electric consumption	Water consumption
1	Forging	Testing	Bar shearing	Forging	Forging	Turing
2	Shaping	Grinding	Shaping	Grinding	Melting	Cooling

**Table 3** Opportunities for improvements

S. no.	Action taken	Case	Dimension	Sustainability indicators	Opportunities for improvement
1	1	1;2	Economic	Overall equipment effectiveness	To improve the OEE% need to improve three key metrics which are availability; performance; and quality. The availability can be improved with the use of total productive maintenance tools and techniques; performance can be improved with the use of setup time reduction tools; quality can be enhanced with the use of reducing defects and eliminate waste from the process
2	2	1;2	Economic	Inventory	The inventory can be reduced using Kanban techniques
3	3	1;2	Economic	Operational cost	Operational cost can be reduced by reducing the cycle time of the process using lean Six Sigma tools which reduce the waste and reduce the variation in customer demands
4	4	1;2	Economic	Effective cost	To reduce the effective cost need to improve OEE% and reduce the operational cost using above technique
5	5	1;2	Social	Absent rate	To reduce the absent rate need to develop environment-friendly work environment and adopt some employee motivation technique
6	6	1;2	Social	Accident rate	To reduce the accident rate need to develop safety departments and organize safety program and time-to-time proper training is required related safety precautions. Also, adopt structured safety rules in the organization
7	7	1;2	Environmental	Electric consumption	To reduce the electric consumption in forging and melting process with change the machine parameter using discrete event simulation model and DOE technique
8	8	1;2	Environmental	Water consumption	To reduce the consumption of water using filtration techniques and reuse of water which is used in cooling and turning operation

## 6 Conclusion

The concept of integrating lean manufacturing tool, value stream mapping (VSM), with sustainability indicators to assess the manufacturing process has been recently discussed in the literature by various authors. However, development of a conceptual model for the integration of VSM tools with various sustainability indicators in the assessment of the manufacturing process that efficiently contributing the increased level of sustainability in any manufacturing process is in the initial stage. Thus, the main objective of this study is to discuss the obtained result and improvements identified in the two industrial case studies related to the assessment of manufacturing process through integration of VSM and sustainability indicators. The case studies are presented for assisting the new direction for improvement and future research in the field of lean manufacturing (LM) and sustainability. This methodology brings the new group of sustainability indicators under the three dimensions that are economic; social; and environmental. Two sustainability indicators have been considered under each dimension through developed assessment mode and the reviewed literature on sustainability indicators. The opportunities for improvements have been identified and presented clearly. After successful implementation of actions, various improvements can be observed toward the assessment of manufacturing process.

The study has been pilot tested in two manufacturing organizations situated in India with few sustainability indicators. In the future, it can be tested in more than two manufacturing organizations with a new group of sustainability indicators to assess the manufacturing process.

## References

1. Brown A, Amundson J, Badurdeen F (2014) Sustainable value stream mapping (Sus-VSM) in different manufacturing system configurations: application case studies. *J Clean Prod* 85:164–179
2. Chen JC, Li Y, Shady BD (2010) From value stream mapping toward a lean/sigma continuous improvement process: an industrial case study. *Int J Prod Res* 48(4):1069–1086
3. Dries CM, Tan KH, Lim M (2013) Green as the new lean: how to use lean practices as a catalyst to greening your supply chain. *J Clean Prod* 40:93–100
4. Eatock J, Dixon D, Young T (2009) An exploratory survey of current practice in the medical device industry. *J Manuf Technol Manage* 20(2):218–234
5. Eccles RG, Ioannou I, Serafeim G (2012) The impact of a corporate culture of sustainability on corporate behavior and performance (No. W17950). National Bureau of Economic Research, Cambridge, MA, USA
6. Faulkner W, Badurdeen F (2014) Sustainable Value Stream Mapping (Sus-VSM): methodology to visualize and assess manufacturing sustainability performance. *J Clean Prod* 85:8–18
7. Hueting R (2010) Why environmental sustainability can most probably not be attained with growing production. *J Clean Prod* 18(6):525–530
8. Kim DB, Shin SJ, Shao G, Brodsky A (2015) A decision-guidance framework for sustainability performance analysis of manufacturing processes. *Int J Adv Manuf Technol* 78(9–12):1455–1471



9. Kuhlant P, Edtmayr T, Sihh W (2011) Methodical approach to increase productivity and reduce lead time in assembly and production-logistic processes. *CIRP J Manuf Sci Technol* 4(1):24–32
10. Roufechaei KM, Bakar AHA, Tabassi AA (2014) Energy-efficient design for sustainable housing development. *J Clean Prod* 65:380–388
11. Strezov V, Evans A, Evans T (2013) Defining sustainability indicators of iron and steel production. *J Clean Prod* 51:66–70

# Effects of Graphite Particles in Titanium Metal Matrix Developed by Spark Plasma Sintering Process



T. Vishnu Vardhan , S. Marichamy, S. Sathees Kumar  
and B. Sridhar Babu

**Abstract** In recent days, the requirement of advanced materials plays an important role in the engineering field. Simultaneously, material properties have been fulfilled the demand for industrial applications. Advanced new materials are to be achieved through one or more materials combined with each other. Composite materials have been satisfied all kinds of applications. Due to their excellent properties, they are used in various fields such as aerospace, automobile, medical, communication, electrical and electronics fields. Titanium–graphite metal matrix provides excellent properties such as strength, hardness, corrosion resistance, thermal and electrical conductivities. Titanium–graphite composite samples with the volume fraction of graphite in the mixture are 3, 5 and 10% prepared by spark plasma sintering (SPS) process. It has been observed that addition of graphite into titanium provides higher amount of density and hardness. Metal matrix characterization has been studied through scanning electron microscope (SEM) and X-ray diffraction (XRD). Titanium–graphite composite has been machined by electrical discharge machining (EDM) process.

**Keywords** Titanium–graphite composite · Spark plasma sintering (SPS) · Scanning electron microscope (SEM) · X-ray diffraction (XRD) · Electrical discharge machining (EDM) process

## 1 Introduction

In recent advancement of materials, titanium matrix composites are playing an important role due to its outstanding properties such as high Young's modulus, strength, hardness, corrosion, and temperature resistance [1–4]. Titanium matrix composites (TMCs) have an isotropic characteristics and better creep resistance [5]. Compared to other methods, powder metallurgy technique is the optimal method to fabricate the titanium matrix composites. This method has provided more desirable fabrication

---

T. Vishnu Vardhan (✉) · S. Marichamy · S. Sathees Kumar · B. Sridhar Babu  
Department of Mechanical Engineering, CMR Institute of Technology, Kandlakoya Village,  
Medchal, Hyderabad, India  
e-mail: [crsh318@gmail.com](mailto:crsh318@gmail.com)

© Springer Nature Singapore Pte Ltd. 2020  
L. Vijayaraghavan et al. (eds.), *Emerging Trends in Mechanical Engineering*,  
Lecture Notes in Mechanical Engineering,  
[https://doi.org/10.1007/978-981-32-9931-3\\_26](https://doi.org/10.1007/978-981-32-9931-3_26)

265

parameters such as processing temperature, pressure, holding time, and heating rate [6–8]. Improved properties have been found out on titanium–aluminium metal matrix using spark plasma sintering process [9]. The desirable strength and grain interface structure has been achieved on titanium–aluminium–vanadium composites [10]. In spark plasma sintering process, temperature distribution has been studied based on thermal conductivity [11]. The effect of particle has been investigated under various range of temperature and pressure and concluded that deformation was observed due to an increase in the particle size [12]. High amount of heating rate leads to non-uniform densification, and cracks are also formed during sintering process [13]. The properties of W–Cu alloy have been evaluated by varying the sintering temperature and achieved the desirable mechanical properties [14]. Hardness and tensile strength have been increased by the addition of  $TiB_2$  content [15]. Carbides and borides have been widely used as reinforcements [16–19].

The aim of the present work is synthesis and characterization of titanium–graphite metal matrix by spark plasma sintering process with the volume fraction of graphite in the mixture is 3, 5 and 10%. Metal matrix characterization has been studied through scanning electron microscope (SEM) and X-ray diffraction (XRD). Density and hardness are also studied with their effects of graphite particles. Material removal rate is also measured by machining of EDM process. The graphite that present in the titanium MMC plays a vital role in improving mechanical and machining characteristics at specific percentages by volume. The range is specified from 3 to 10% of graphite as it starts the improvement in either mechanical or machining characteristics at 3% and the phenomenon of embrittlement after 10%.

## 2 Material Fabrication

The spark plasma sintering (SPS) is one of the processes used to fabricate the metal matrix. The main advantages of SPS have enhanced the material properties: higher process efficiency, lower processing temperature and time. It provides high sintering rate and uniaxial pressure to merge the powders. Graphite powders are mixed with titanium, and the volume fractions of graphite in the mixture are 3%, 5% and 10%, respectively. The mixed powders have been placed inside the SPS chamber. The rectangular shape and size of the SPS pallets are  $60 \times 50 \times 8$  mm. The rate of mixing mainly depends on the homogeneity of the powders [20]. During spark plasma sintering process, relocation and bulk deformation of the particles can be controlled [21, 22]. The process parameters are temperature (800 °C), pressure (40 MPa), heating rate (150 °C) and holding time (15 min) that have been considered. Before SPS process, a vacuum has been developed inside the chamber to avoid the reaction. The specimen is maintained for 15 min when it has been reached the above process parameters. After that, it has been cooled for 45 min before removed from the die unit.

### 3 Analysis of Titanium–Graphite Powders

The shape and size of the titanium–graphite powders are characterized by SEM analysis. Figure 1 shows the microstructure of the titanium–graphite powders. SEM image that indicates the crystal structure of titanium is shown in Fig. 1a, and the irregular shape of graphite powder is shown in Fig. 1b. Figure 2 shows that the particles size distribution of the titanium and graphite powders. It can be observed that the median size of 40  $\mu\text{m}$  has been achieved for titanium and graphite powders.

#### 3.1 XRD Analysis

XRD plots of titanium–graphite composite samples with the volume fraction of graphite in the mixture are 3, 5 and 10% prepared by SPS are shown in Fig. 3. From XRD plot, a high peak shows that titanium whereas, a smaller peak shows that

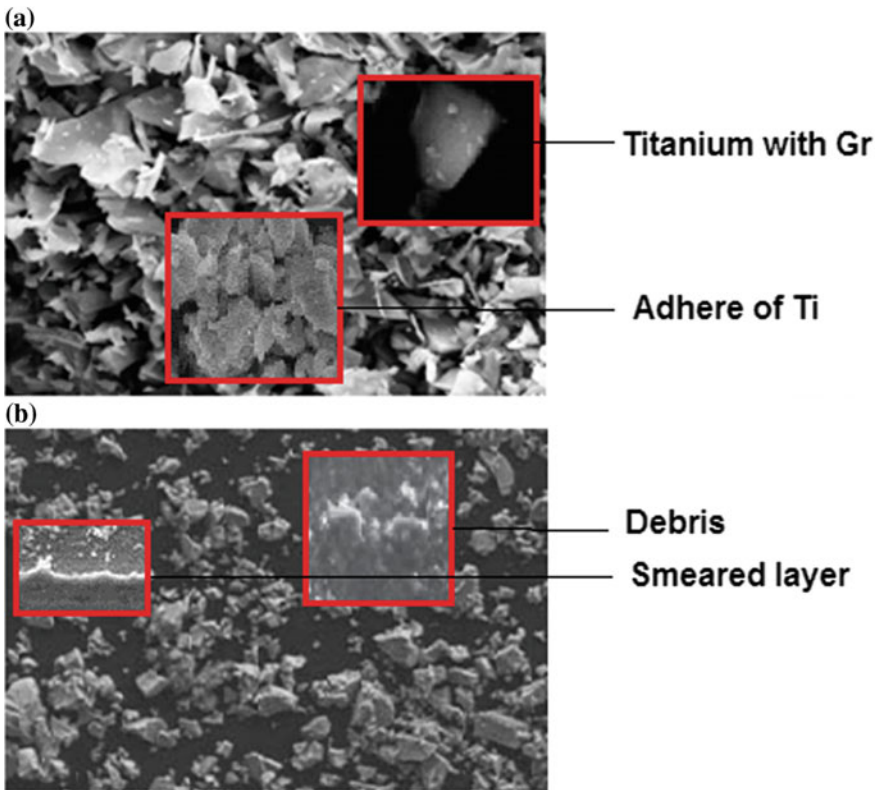


Fig. 1 SEM image of a titanium, b graphite

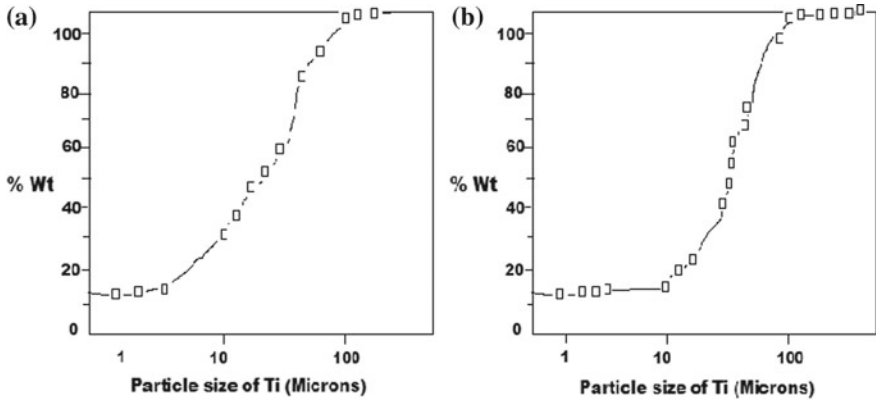


Fig. 2 Particles size distribution of a titanium, b graphite

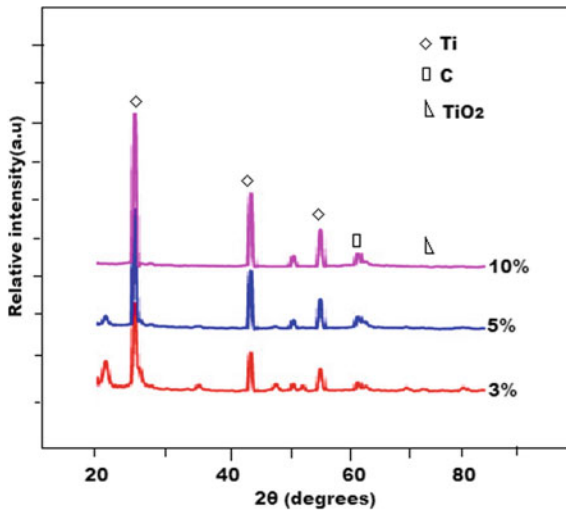


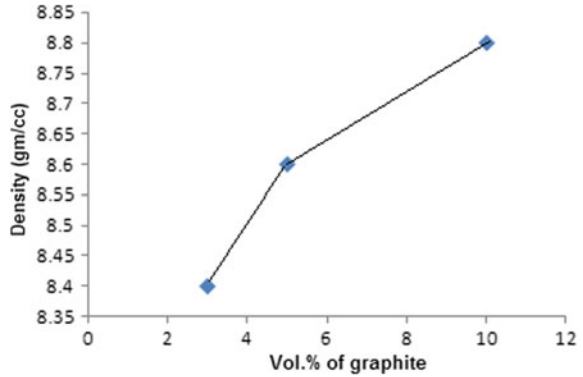
Fig. 3 XRD plots of titanium-graphite composite

graphite and also less amount of titanium dioxide are noticed. It may be formed due to titanium chemically react with atmospheric oxygen.

### 3.2 Density Measurement

Figure 4 shows the variation of density with volume percentage of graphite in the samples. Density increases with the increase in the volume percentage of graphite. Due to the addition of graphite, density and strength of the reinforcement have been

**Fig. 4** Density plots of titanium-graphite composite

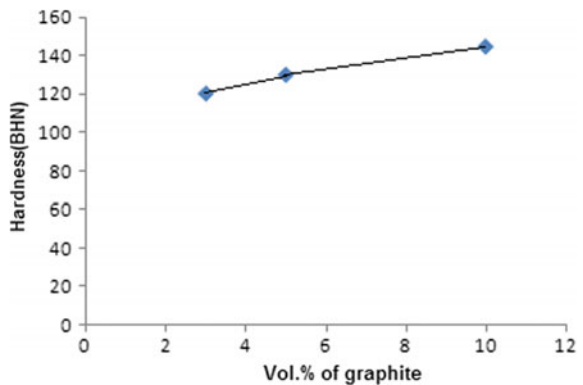


increased. The contacts of the interface between the particles have been increased. The increase in density and hardness is due to the intensification of graphite and dispersion of grains.

### 3.3 Hardness Measurement

Figure 5 shows the variation of hardness with volume percentage of graphite in the samples. Hardness increases with the increase in the volume percentage of graphite. Due to the intensification of graphite, hardness and dispersion of grains have been increased.

**Fig. 5** Hardness (BHN) plots of titanium-graphite composite



### 3.4 SEM Analysis

The morphology of the titanium–graphite composite samples with the volume fraction of graphite in the mixture is 3, 5 and 10% prepared by SPS process is shown in Fig. 6.

The graphite particles (dark region) have been uniformly distributed along with the material structures. The dark regions have been increased with increase in the percentage of graphite particles. The placements of graphite particles are high in 10% volume fraction of graphite. The glowing of particle contact between tungsten and graphite is also obtained. No gaps have been found out in the material structure. Grain growth has been observed when increase in temperature and densification of the material [23].

Figure 7 shows the good interface and compatibility of titanium–graphite composite. No voids or cracks have observed on the boundary layer.

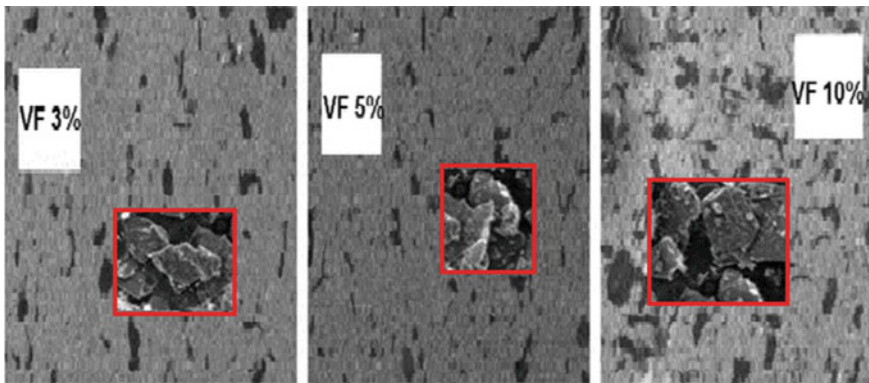


Fig. 6 SEM images of titanium–graphite composite with 3, 5 and 10% volume fraction of graphite

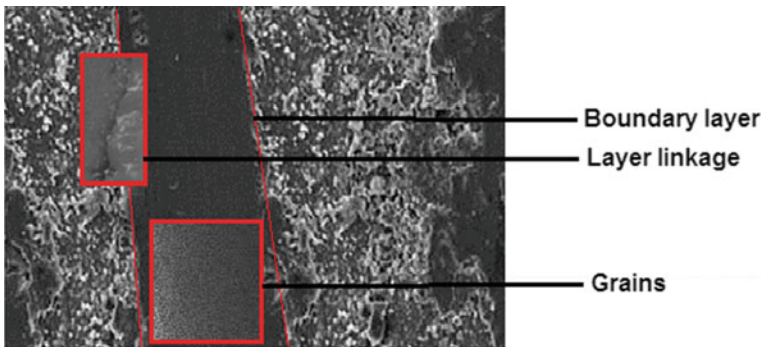


Fig. 7 SEM image of titanium–graphite interface

### 3.5 Machinability Analysis of Titanium–Graphite

Titanium–graphite composite has been machined by electrical discharge machining (EDM) process. Graphite is considered as an electrode material. Diameter 8 mm holes have been produced on the surface of the titanium–graphite composite shown in Fig. 8. During the machining process, peak current (10–15 A), voltage (45–50 V) and pulse on time (100–120  $\mu$ s) have been considered as the control parameters. Material removal rate is considered as the response parameters. The EDM experimental results are shown in Table 1.

Figure 9 shows the variation of MRR with different volume fractions of graphite. Material removal rate is increased in 3 and 5% volume fraction of graphite. Higher

**Fig. 8** EDM drilled holes

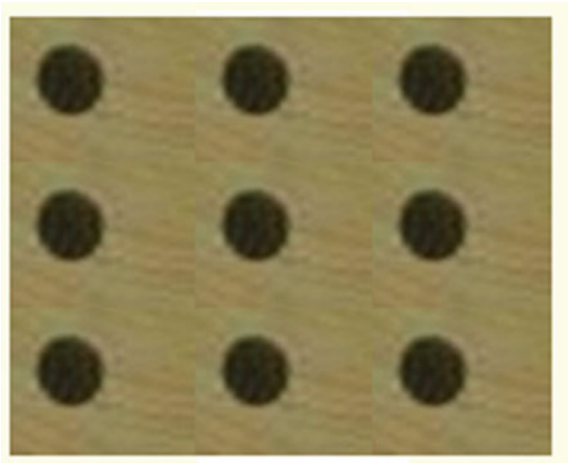


**Table 1** EDM experimental results

S. No.	Current (A)	Voltage (V)	Pulse ON time ( $\mu$ s)	3% VF graphite	5% VF graphite	10% VF graphite
				MRR (g/min)	MRR (g/min)	MRR (g/min)
1	10	45	100	8.11	5.12	3.45
2	10	48	110	9.12	4.31	4.42
3	10	50	120	9.56	5.12	3.32
4	12	45	110	12.23	6.25	7.43
5	12	48	120	13.65	7.39	5.66
6	12	50	100	11.33	8.44	7.12
7	15	45	120	14.65	10.32	7.67
8	15	48	100	12.31	9.36	5.43
9	15	50	110	16.16	12.33	10.12



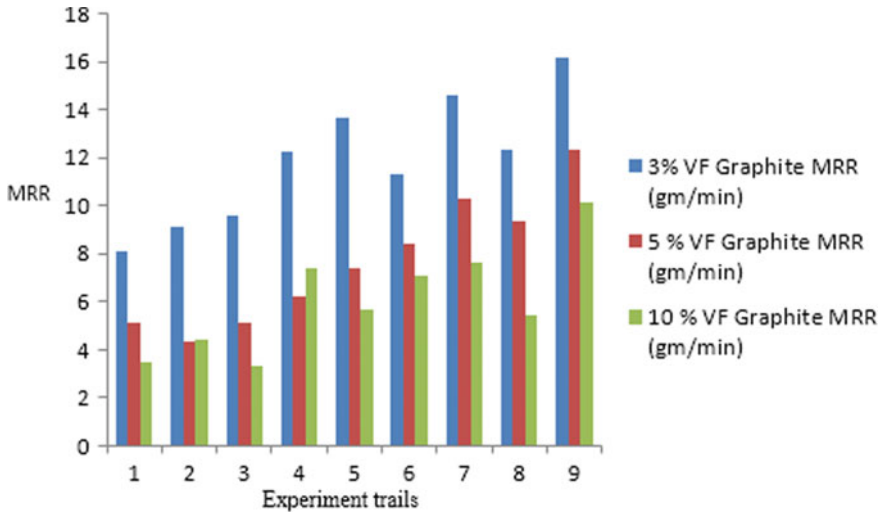


**Fig. 9** Variation of MRR with different volume fraction of graphite

MRR is achieved when low hardness of metal matrix due to fewer amounts of Graphite particles are present on the material. Material removal rate is decreased by 10% volume fraction of graphite. Lower MRR is achieved when high hardness of metal matrix due to large amount of graphite particles present in the material.

## 4 Conclusion

- Titanium–graphite composite samples with the volume fraction of graphite in the mixture are 3, 5 and 10% prepared by SPS process.
- It has been observed that the addition of graphite into titanium provides a higher amount of density and hardness.
- Metal matrix characterization has been studied through scanning electron microscope (SEM) and X-ray diffraction (XRD).
- Titanium–graphite composite has been machined by EDM process.
- Material removal rate is increased in 3 and 5% volume fraction of graphite.
- Material removal rate is decreased by 10% volume fraction of graphite.

## References

1. Peters M, Kumpfert J, Ward CH, Leyens C (2003) Titanium alloys for aerospace applications. *Adv Eng Mater* 5:419–427

2. Garbiec D, Siwak P, Mróz A (2016) Effect of compaction pressure and heating rate on microstructure and mechanical properties of spark plasma sintered Ti6Al4V alloy. *Arch Civ Mech Eng* 16:702–707
3. Zadra M, Girardini L (2014) High-performance, low-cost titanium metal matrix composites. *Mater Sci Eng A* 608:155–163
4. Koo MY, Park JS, Park MK, Kim KT, Hong SH (2012) Effect of aspect ratios of in situ formed TiB whiskers on the mechanical properties of TiB w/Ti–6Al–4V composites. *Scripta Mater* 66:487–490
5. Lieberman SL, Gokhale AM, Tamirisakandala S, Bhat RB (2009) Three-dimensional micro structural characterization of discontinuously reinforced Ti64–TiB composites produced via blended elemental powder metallurgy. *Mater Charact* 60:957–963
6. Ma W, Lu J (2011) Effect of surface texture on transfer layer formation and tribological behavior of copper–graphite composite. *Wear* 270:218–229
7. Tjong SC, Mai Y-W (2008) Processing-structure-property aspects of particulate and whisker-reinforced titanium matrix composites. *Compos Sci Technol* 68:583–601
8. Radhakrishna Bhat BV, Subramanyam J, Bhanu Prasad VV (2002) Preparation of Ti–TiB–TiC & Ti–TiB composites by in-situ reaction hot pressing. *Mater Sci Eng A* 325:126–130
9. Musa C, Licheri R, Locci AM, Orrù R, Cao G, Rodriguez MA, Jaworska L (2009) Energy efficiency during conventional and novel sintering processes: the case of Ti–Al<sub>2</sub>O<sub>3</sub>–TiC composites. *J Clean Prod* 17:877–882. <https://doi.org/10.1016/j.jclepro.2009.01.012>
10. He D, Fu Z, Wang W, Zhang J, Munir Z, Liu P (2012) Temperature-gradient joining of Ti–6Al–4V alloy by pulsed electric current sintering. *Mater Sci Eng A* 535:182–188. <https://doi.org/10.1016/j.msea.2011.12.061>
11. Muñoz S, Anselmi-Tamburini U (2010) Temperature and stress fields evolution during spark plasma sintering processes. *J Mater Sci* 45:6528–6539. <https://doi.org/10.1007/s10853-010-4742-7>
12. Diouf S, Menapace C, Molinari A (2013) Study of effect of particle size on densification of copper during spark plasma sintering. *Powder Metall* 55(3):228–234
13. Kodash VY, Groza JR, Cho KC, Klotz BR, Dowding RJ (2004) Field-assisted sintering of Ni nanopowders. *Mater Sci Eng A* 385(1–2):367–371
14. Shi X, Yang H, Wang S (2009) Spark plasma sintering of W-15Cu alloy from ultrafine composite powder prepared by spray drying and calcining-continuous reduction technology. *Mater Charact* 60(2):133–137
15. Kwon DH, Huynh KX, Nguyen TD et al (2006) Mechanical behavior of TiB<sub>2</sub> nanoparticles reinforced Cu matrix composites synthesized by in-situ processing. *Mater Sci Forum* 510–511:346–349
16. Zou C, Kang H, Wang W, Chen Z, Li R, Gao X, Li T, Wang T (2016) Effect of La addition on the particle characteristics, mechanical and electrical properties of in situ Cu–TiB<sub>2</sub> composites. *J Alloy Compd* 687:312–319
17. Sorkhe YA, Aghajani H, Taghizadeh Tabrizi A (2014) Mechanical alloying and sintering of nanostructured TiO<sub>2</sub> reinforced copper composite and its characterization. *Mater Des* 58: 168–174
18. Wang F, Li Y, Wang X, Koizumi Y, Kenta Y, Chiba A (2016) In-situ fabrication and characterization of ultrafine structured Cu–TiC composites with high strength and high conductivity by mechanical milling. *J Alloy Compd* 657:122–132
19. Manotas-Albor M, Vargas-Uscategui A, Palma R, Mosquera E (2014) In situ production of tantalum carbide nano dispersoids in a copper matrix by reactive milling and hot extrusion. *J Alloy Compd* 598:126–132
20. Tang C, Wang C, Zhang L, Choy M, Chow T, Chan K et al (2013) In situ formation of Ti alloy/TiC porous composites by rapid microwave sintering of Ti6Al4V/MWCNTs powder. *J Alloy Compd* 557:67–72
21. Diouf S, Molinari S (2012) Densification mechanisms in spark plasma sintering: effect of particle size and pressure. *Powder Technol* 221:220–227

22. Diouf S, Fedrizzi A, Molinari A (2013) A fractographic and microstructural analysis of the neck regions of coarse copper particles consolidated by Spark Plasma Sintering. *Mater Lett* 111:17–19
23. Gülsoy H, Özbey S, Pazarlioglu S, Çiftci M, Akyurt H (2015) Sintering and mechanical properties of titanium composites reinforced nano sized  $\text{Al}_2\text{O}_3$  particles

# Effect on Bearings in Rotating Components by Vibration Analysis: A Case Study in Steel Plant



B. K. Pavan Kumar, Yadavalli Basavaraj and M. J. Sandeep

**Abstract** In the present work, the condition of machines and structures are determined by the condition monitoring technique of rotating machineries through vibration analysis. Here, the amplitude and frequencies of vibrating machines play a key role in the judgement of predicting the condition of the machineries. Henceforth, we have selected critical equipment for the testing which includes mill stands of bar rod mill (BRM-2) from the steel manufacturing industry. Now the amplitude of the equipment was taken by using vibrometer at different parts of the equipment, then by the FFT analyzer, the comparison was made between the parameters like amplitude versus time and amplitude versus frequencies. At the end with the help of the plots obtained the critical part of the equipment which was responsible for vibration was identified. Finally, with the remedial methods, the vibration was reduced to the acceptable level.

**Keywords** Condition monitoring · Bar rod mill · Vibrometer · FFT analyzer

## 1 Introduction

The vibration plays an important parameter in the rotating machineries which can be sort out by using vibration measuring instruments which are plenty available. The equipment selected for the present work is vibrometer due to the availability and easiness in handling. This device provides the details of the vibrations from the machines, which are used for fault diagnosis and maintenance. The main aim of vibration monitoring is to make maximum availability, reliability, and efficiency from the installed plant machines, aiming at excellent results. Vibration monitoring has been used in the areas of steel, chemical, sugar, paper, textile, etc. A reduction in maintenance and management costs along with the increase of machine availability is usually expected when preventive maintenance is performed in parallel with condition-based maintenance [1]. The vibration signal analysis is one of the most important methods used for

---

B. K. Pavan Kumar (✉) · Y. Basavaraj · M. J. Sandeep  
Mechanical Department, BITM, Ballari, Karnataka, India  
e-mail: [pk22586@gmail.com](mailto:pk22586@gmail.com)

© Springer Nature Singapore Pte Ltd. 2020  
L. Vijayaraghavan et al. (eds.), *Emerging Trends in Mechanical Engineering*,  
Lecture Notes in Mechanical Engineering,  
[https://doi.org/10.1007/978-981-32-9931-3\\_27](https://doi.org/10.1007/978-981-32-9931-3_27)

condition monitoring and fault diagnostics, because they always carry the dynamic information of the system. Utilization of the vibration signals effectively depends on the applied signal processing techniques for fault diagnosis [2]. The reason for collecting the statistics regarding the machine through system analysis is to check the strength of the plant or equipment. Vibration monitoring is a useful technique for application to rotating machines and provides valuable information regarding symptoms of machinery failures which in practice may avoid costly breakdowns [3]. The experiments conducted on the machine or equipment on a particular place reveals best results regarding the working parameters of the machine or equipment. Therefore, the information obtained from the monitoring can prevent and predict the failure by cutting down the cost incurred in maintenance.

## 2 Literature Survey

- 2.1 Mayoof et al. [4]. The author in this paper has discussed about the beating phenomenon and the bearing defect frequencies using SKF Micro log CMXA 50 and accelerometer CMSS 2200 vibration measuring instrument. The diagnosis of their conditions is essential matter for downtime reduction and saving cost of maintenance with the focus on a beating phenomena observed in the waveform of a cylindrical rolling element bearing.
- 2.2 Venu Padmavathi et al. [5]. The author in this paper presents the analysis of cause due to high level of vibrations and spectrum analysis which reveals that the problem might be due to misalignment or unbalance. phase analysis was done, which shows the root cause of abnormal vibration of machine.
- 2.3 Mendel et al. [6]. The author in this paper presents vibration analysis techniques for fault detection in rotating machines. Signal processing techniques, like frequency filters, Hilbert transform, and spectral analysis are used to extract features used later as a base to classify the condition of machines.

Based on the literature survey, the problem was identified in the inner race of motor bearing and to overcome this issue many techniques have been adopted among which Fast Fourier Transform analysis is selected.

## 3 Problem Identification

In a steel manufacturing industry, products of various cross-sections are to be produced. Our observation is on the mill stands of Bar Rod Mill (BRM). The purpose of mill stand is to convert the billets of rectangular cross-section into bars of required circular cross-section. Mill stand is driven by the electric motor which has to be run at different speeds depending on the load and size of the bars to be produced, which can be achieved by using variable frequency drives (VFD). Steel mills are designed to produce products with various cross-sections; therefore, the mill motors run with variable frequency drive in order to achieve the required speed. Bar Rod

Mill-2 produces 12–40 mm size TMT bars. It consists of breakdown, roughing and finishing stands, which contains electrical motor coupled with gear box. After the commissioning of plant, during scheduled vibration monitoring it was observed at mill stands where a whistling sound observed physically and later vibration values were increasing. The Fast Fourier Transform analysis was interpreting the outer and inner race defect of bearings. After crossing vibration alarm limits, took for maintenance and inspected gear box input bearings, the inspection revealed that the bearings are damaged due to electrical discharge and found electrical fluting marks on bearing outer race and on rolling element.

#### 4 Root Cause Analysis Methodology

The VFD motor is fitted with insulated bearings on drive end and non-drive end, the rotor shaft doesn't have any arrangement to ground the induced current in the rotor, therefore, it travelled through coupling and discharged through gear box input bearings. There are few reasons for electrical damage to bearings, i.e., electric welding with common lead applied to wrong spot, locomotive grounding through bearings, circulative current through shaft and bearings, electrostatic discharge through bearings. Increased use of VFD's is the dominating reason for bearing damages. Our challenge was to reduce the bearing damage through current leakage which was occurring at both motor and gearbox of mill stands. Through vibration analysis and peak method, we collected the vibration and peak data of all mill stands at different rolling sections and analyzed using Fast Fourier Transform.



Fig. 1 VFD motor with insulated bearings



**Fig. 2** Motor bearing inner race

The above Figs. 1 and 2 show the effect of the fluctuating electric current on the inner race of the motor bearing.

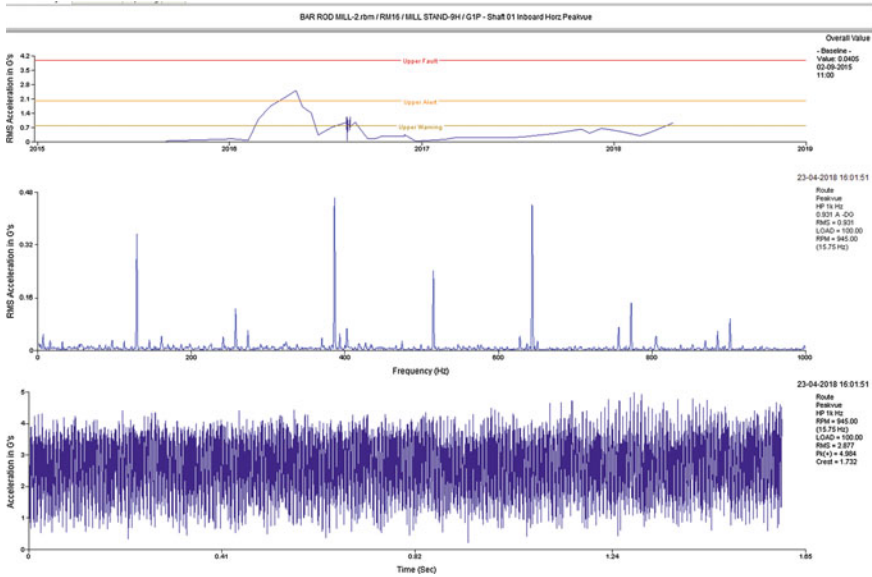
Table 1 shows the reading of the motor and gear box taken from the vibrometer instrument with respect to the horizontal, vertical, and axial positions.

**Table 1** Vibration data taken at BRM-2 Mill Stand-3H @motor and gearbox

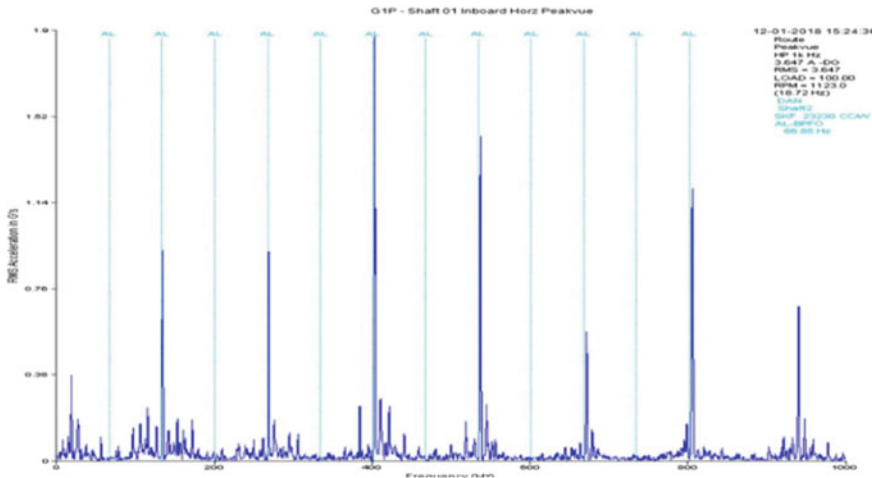
S. No.	Measurement point	Overall level (mm/s)	Equipment speed
1	M1H	1.273	1094.0 rpm
2	M1V	979	
3	M1A	928	
4	M2H	983	
5	M2V	787	
6	M2A	970	
7	G1H	5.529	
8	G1V	2.123	
9	G1A	3.858	
10	G2H	1.998	
11	G2V	2.437	
12	G2A	1.727	

### 5 Results and Discussions

From the above Graph 1 represents amplitude spectrum of BRM-2 Mill Stand for a shaft which has the 1X, 2X, 3X values, respectively, shows the high level of vibration in a motor bearing. Graphs 2 and 3 represent the onboard spectrums, which is taken

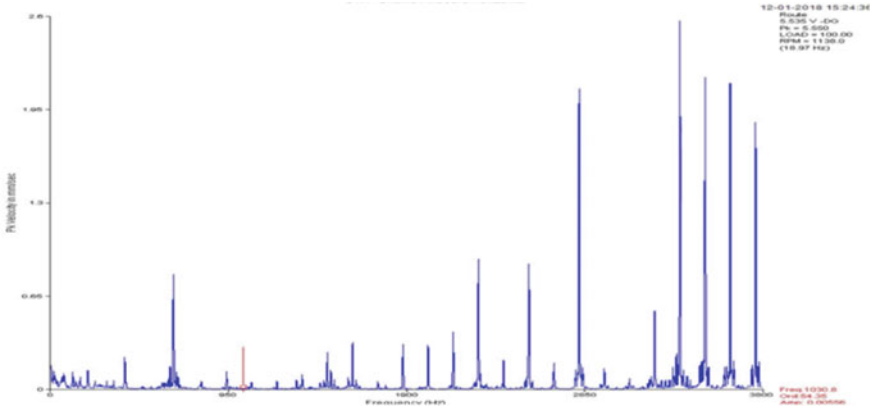


Graph 1 Amplitude spectrum of BRM-2 Mill Stand for a shaft

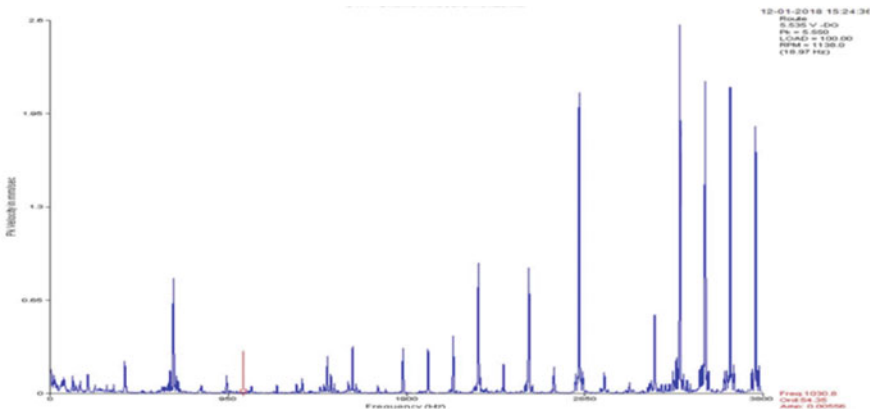


Graph 2 Onboard vibration of shaft in vertical position





**Graph 3** Onboard vibration of shaft in horizontal position

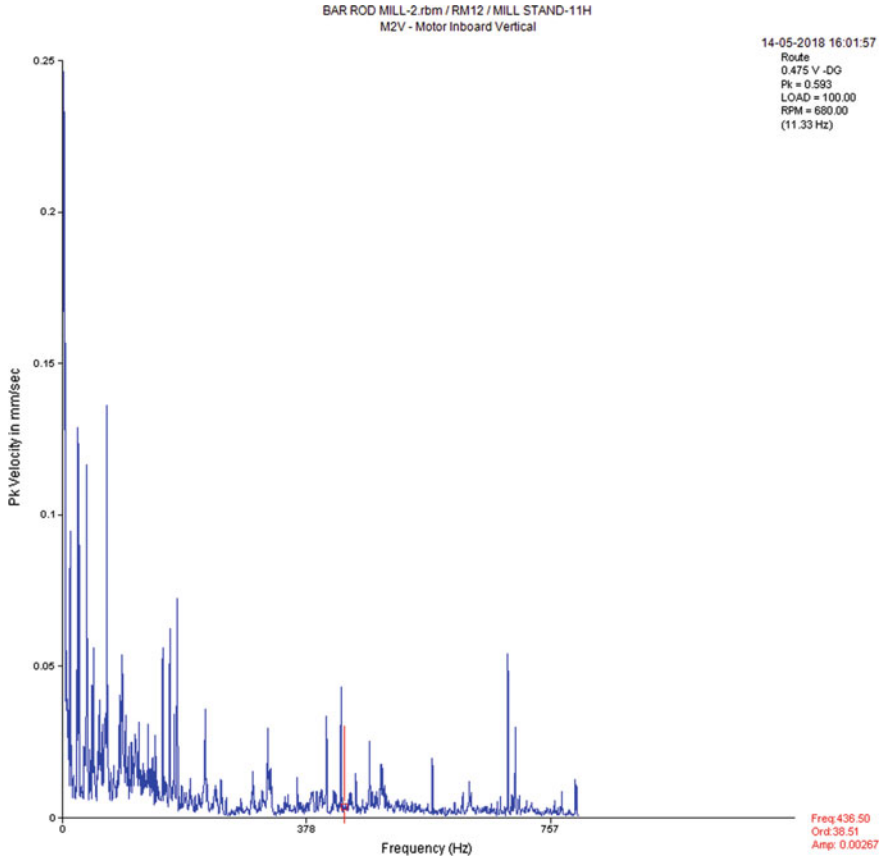


**Graph 4** Amplitude spectrum before rectification

at horizontal and vertical position, respectively. Graph 4 represents the amplitude spectrum which shows the high level of 1X frequencies which leads to failure of motor and root cause analysis is applied to reduce the vibration level as shown in Graph 5.

## 6 Conclusion

From the aspect of motor and driven equipments health condition, it is essential to prevent the premature bearing failure due to electrical fluting by conventional shaft grounding method which is represented in the Graph 1 for BRM-2 Mill Stand. By having these high current capable rings with slim design and flexible installation



**Graph 5** Amplitude spectrum after rectification

option it can be easily adapted for large motors. Apart from the conventional vibration analysis approach, there is a need of process parameters analysis, which will help in prolonged machinery life, and lesser breakdown. As statistical analysis gives the best optimized output to read the machine behavior with respect to variation of its operating parameters.

## References

1. Pinelli M, Spina PR, Venturini M (2012) Gas turbine health state determination: methodology approach and field application. *Int J Rotating Mach* 1–6
2. Bendjama H, Bouhouche S, Boucherit MS (2017) Application of wavelet transform for fault diagnosis in rotating machinery. *Int J Mach Learn Comput* 2(1)
3. Pandey S, Nakra BC (2015) Vibration monitoring of a rotor system using RMS accelerations. *Int J Eng Sci* 3(4)

4. Mayoof FN (2009) Beating phenomenon of multi-harmonics defect frequencies in a rolling element bearing: case study from water pumping station. *Int J Mech Mechatron Eng* 3(9)
5. Venu Padmavathi G, Diwakar G, Satyanarayana MRS (2011) Vibration monitoring of crusher in coal handling plant of Dr NTTPS. *Int J Eng Sci Technol* 3(8)
6. Mende E, Rauber TW, Varejao FM, Batista RJ (2009) Rolling element bearing fault diagnosis in rotating machines of oil extraction rigs. Scotland, 24–28 Aug 2009
7. Metwalley SM, Hammad N, Abouel-Seoud SA (2018) Vehicle gearbox fault diagnosis using noise measurements. International Energy Foundation
8. Kabiri P, Ghaderi H (2017) Automobile independent fault detection based on acoustic emission using wavelet. In: Singapore international NDT conference & exhibition, 3–4 Nov 2017
9. Vahaoja PO, Pikkarainen HVS (2017) Trends in industrial oil analysis—a review. *Int J Condition Monit* 1(1)
10. Elez A, Tomčić B, Petričić M (2010) Detection of inter-coil short circuits in coils. In: International conference on renewable energies and power quality, Granada (Spain), 23–25 Mar 2010
11. Doguer T, Strackeljan J (2009) Vibration analysis using time domain methods for the detection of small roller bearing defects. In: 8th international conference on vibrational analysis

# Multi-objective Optimization of Photochemical Machining Parameters Using Taguchi Grey Relational Analysis



Rashed Mustafa Mazarbhuiya and Maneswar Rahang

**Abstract** This research paper describes the multi-objective optimization of process parameters of photochemical machining process. Aluminium was selected as workpiece for obtaining maximum rate of material removal, minimum surface roughness and minimum edge deviation of predefined pattern. The selected machining parameters were etching concentration, etching temperature and etching time. To determine optimal solution, grey relational analysis was performed. To determine the most significant input parameter, analysis of variance of grey relational grade was carried out. The optimal condition of input parameters was found to be 400 g/L of concentration, 60 °C of temperature and 8 min of etching time. Etching temperature was found to be the most dominant parameter on the output response followed by etching time, while concentration being the least significant. ANOVA of grey relational grade showed the etching temperature was the only significant factor for machining of aluminium workpiece.

**Keywords** PCM · GRA · ANOVA · MRR · Ra · ED

## 1 Introduction

Photochemical machining (PCM) is one machining process which produces burr-free and stress-free complex metal of flat parts. The stresses and defects that arise normally from any other non-conventional machining process are absent in the final part. The PCM process has been explored for its wide applications and its process capability for the purpose of pattern generation with desired geometric dimensions. The PCM is also used to generate user-defined pattern. It gives the idea for the generation of simple-to-complex-shaped pattern for engineering purpose and decorative or ornamenting purpose. Using soft lithography technique, the moulds for fabrication of a microchannel can be manufactured by PCM process. Apart from

---

R. M. Mazarbhuiya (✉) · M. Rahang

Department of Mechanical Engineering, National Institute of Technology Meghalaya, Meghalaya 793003, India

e-mail: [rashedmazar@nitm.ac.in](mailto:rashedmazar@nitm.ac.in)

© Springer Nature Singapore Pte Ltd. 2020

L. Vijayaraghavan et al. (eds.), *Emerging Trends in Mechanical Engineering*,

Lecture Notes in Mechanical Engineering,

[https://doi.org/10.1007/978-981-32-9931-3\\_28](https://doi.org/10.1007/978-981-32-9931-3_28)

this the process can be used for surface treatment and reduction of plat thickness purpose. The PCM is a chemical etching process through a photoresist stencil for material removal over predefined areas by chemical action [1]. Cakir reported that ferric chloride ( $\text{FeCl}_3$ ) is a suitable etchant for aluminium at different etching temperatures. He also reported  $\text{FeCl}_3$  to be efficient etchant for any other materials to enhance the etching rate and to produce smooth surface [2]. Other works also carried out based on etchant, etching temperature and etchant time on different workpieces [3]. Various characteristics of  $\text{FeCl}_3$  etchants were studied for industrial purpose. Although  $\text{FeCl}_3$  is most commonly used etchant, there are different grades of variety in  $\text{FeCl}_3$  [4]. The cost involved for PCM defines standards for industrial etchants and methods to analyse and to monitor them [5]. Many researchers studied the effect of etching time and etchant temperature on the surface finish and rate of etching of PCM on the workpieces of aluminium, copper and Inconel 718 using ferric chloride and cupric chloride as etchants [2, 6, 7]. The current work has explored new aspects of the PCM process. It has described the parametric study for the purpose of pattern generation. Moreover, it has described about the surface roughness of the newly generated surface, which can give the idea of surface treatment of workpiece according to the process requirements. The objective of the present work is to determine the optimal condition of the process parameters using Taguchi approach. This work was carried out on aluminium workpiece. Grey relational analysis (GRA) was applied to determine the multi-objective optimization value of the process parameters. Etching concentration, etching temperature and etching time were analysed with the multiple performance characteristics such as removal rate of material (MRR), surface roughness (Ra) and edge deviation (ED) of predefined pattern on the work surface. To determine the most significant input parameter(s), analysis of variance (ANOVA) was performed.

## 2 Material Selection and Methodology

### 2.1 Material

In this experimental work, aluminium was selected as workpiece in suitable size such as 20 mm × 20 mm × 3 mm.

### 2.2 Experimental Procedure

To carry out this experimentation, the aluminium workpiece was prepared in some suitable shape and size. Then, the desired pattern was formed on a photographic film, termed the photo tool. Using computer-aided design (CAD), the required pattern was designed, which was used as primary image for the photo-tool. Photo tool is

**Table 1** Controlling parameters with their levels

Control parameters	Level 1	Level 2	Level 3
Etching concentration (g/L)	400	500	600
Etching temperature (°C)	40	50	60
Etching time (min)	4	6	8

negative replica of the image to be produced. The workpiece was chemically cleaned to remove the contaminants to get maximum surface for adhesion of photoresist solution. The workpiece was then immersed in a dip coater photoresist for 1 s; after that, the specimen was dried for four minutes. The coated workpiece is then placed in contact with photo tool and then exposed to an UV light source. The next step was developing the pattern on work surface by dipping into the developer solution around 60 s. This operation removed the unexposed areas of photoresist. Finally, the developed workpiece was sent for post baking for about 2 min. The material erosion from the work surface depends on concentration, temperature and etchant time.

### 2.3 Selection of Parameter

Based on the literature survey, for the current experimentation, three controlling parameters at three different levels were considered as shown in Table 1. The effects of input parameters were observed on MRR, Ra and ED.

### 2.4 Taguchi Design of Experiment

The experimental design includes proper selection of process parameters and their interactions. Using Taguchi  $L_9$  orthogonal array, the PCM on aluminium workpiece was carried out. The weights of the workpiece before and after machining are tabulated in Table 2. Using optical microscope, edge deviation of desired shape and size was measured. By calculating the volume of material removed from the workpiece and then dividing it by the etching time, the MRR was obtained. Figure 1 shows the machined specimen, measurement of edge deviation and measurement of surface roughness of work samples.

### 2.5 Multi-objective Optimization Using GRA

GRA is performed to obtain the multi-optimal setting of process parameters to get the best operating level. The first step for optimization is to convert the original response

**Table 2** Taguchi L<sub>9</sub> matrix with weights of workpieces

Sl. No.	Conc. (g/L)	Temp. (°C)	Time (min)	Trial 1		Trial 2		Trial 3	
				Initial weight	Final weight	Initial weight	Final weight	Initial weight	Final weight
1	400	40	4	1.8939	1.8926	1.9476	1.9468	1.9231	1.9225
2	400	50	6	1.7620	1.7463	1.8832	1.8730	1.8831	1.8772
3	400	60	8	1.9334	1.8790	1.9743	1.9438	2.0303	2.0044
4	500	40	6	1.9670	1.9463	1.7527	1.7490	2.0056	1.9973
5	500	50	8	1.8257	1.7814	1.8685	1.8612	1.8596	1.8473
6	500	60	4	1.9168	1.8923	2.1074	2.0974	1.9211	1.9158
7	600	40	8	1.7648	1.7557	1.9557	1.9427	1.9915	1.9846
8	600	50	4	1.9390	1.9306	1.9723	1.9654	1.8928	1.8908
9	600	60	6	1.8449	1.8184	2.0142	1.9923	1.6964	1.6807

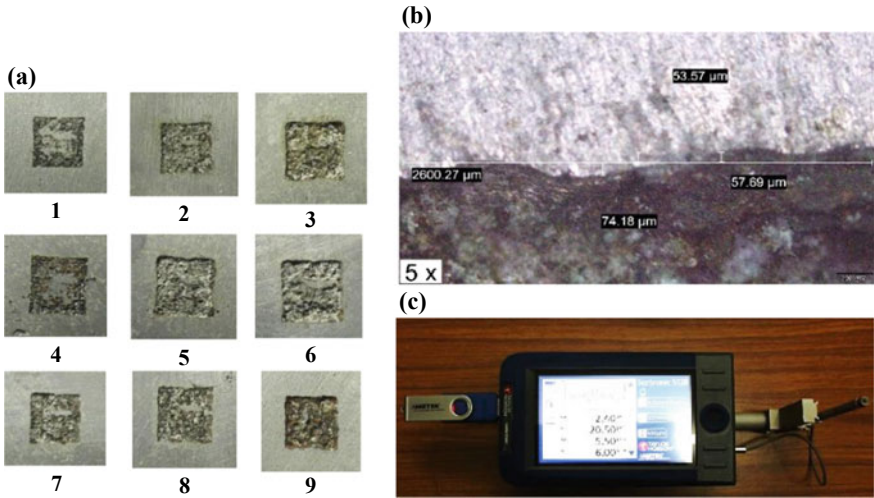


**Fig. 1** a Photochemically machined sample specimen. b Edge deviation measurement. c Measurement of surface roughness

value into *S/N* ratio. Depending on the type of the quality characteristic, “larger the better” was used for MRR and “smaller the better” was used for Ra and ED values.

For larger-the-better characteristics,

$$S/N = -10 \log \left[ \frac{1}{n} \sum_{i=1}^n \frac{1}{Y_i^2} \right] \tag{1}$$

For smaller-the-better characteristics,

$$S/N = -10 \log \left[ \frac{1}{n} \sum_{i=1}^n Y_i^2 \right] \tag{2}$$

where  $Y_{ij}$  is the response value of “*j*” in the *i*th experiment, with  $i = 1, 2, 3, \dots, n; j = 1, 2, \dots, k$ .

After computing *S/N* ratio values, normalize these values as  $Z_{ij}$  ( $0 \leq Z_{ij} \leq 1$ ) by below two equations. *S/N* ratio values and normalized *S/N* ratio values are tabulated in Table 3.

For normalizing output parameter corresponding to the larger-the-better criterion, equation can be expressed as

$$Z_i = \frac{Y_{ij} - \min(Y_{ij}, i = 1, 2, \dots, n)}{\max(Y_{ij}, i = 1, 2, \dots, n) - \min(Y_{ij}, i = 1, 2, \dots, n)} \tag{3}$$



**Table 3** Calculation of *S/N* ratio and normalized *S/N* ratio for MRR, Ra and ED

Sl. No.	<i>S/N</i> ratios			Normalized <i>S/N</i> ratio		
	MRR	Ra	ED	MRR	Ra	ED
1	-14.201	-0.946	-33.93	0	0	0
2	2.766	-8.256	-36.03	0.646	0.849	0.499
3	12.078	-9.558	-36.29	1	1	0.561
4	-0.326	-3.021	-34.3	0.528	0.241	0.103
5	2.574	-8.561	-35.83	0.638	0.884	0.452
6	5.984	-7.604	-38.13	0.768	0.773	1
7	0.795	-7.951	-34.63	0.571	0.813	0.165
8	-1.822	-8.006	-36.82	0.471	0.819	0.688
9	10.420	-8.490	-36.83	0.937	0.876	0.690

And for normalizing output parameters corresponding to the smaller-the-better criterion, equation can be expressed as

$$Z_i = \frac{\max(Y_{ij}, i = 1, 2, \dots, n) - Y_{ij}}{\max(Y_{ij}, i = 1, 2, \dots, n) - \min(Y_{ij}, i = 1, 2, \dots, n)} \tag{4}$$

After computing normalize *S/N* ratio values, deviation sequence for the reference and comparability sequence are found out for computing grey relational coefficient (GC) using below formula.

$$GC_{ij} = \frac{\Delta_{\min} + \lambda \Delta_{\max}}{\Delta_{ij} + \lambda \Delta_{\max}} \tag{5}$$

where

$i = 1, 2, \dots, n$  and experiments and  $j = 1, 2, \dots, m$  responses.

$GC_{ij} = GC$  for the  $i$ th experiments and  $j$ th responses.

$\Delta$  = deviation from target value and can be treated as a quality loss, i.e., absolute difference between  $Y_{oj}$  and  $Y_{ij}$ .

$Y_{oj}$  = ideal normalized value of  $j$ th response.

$Y_{ij}$  =  $i$ th normalized value of the  $j$ th response.

$\Delta_{\min}$  = minimum value of  $\Delta$ .

$\Delta_{\max}$  = maximum value of  $\Delta$ .

$\lambda$  = is the distinguishing coefficient in the range  $0 \leq \lambda \leq 1$  (the value may be adjusted on the practical needs of the system).

And lastly compute the grey relational grade ( $G_i$ ) using the below formula. This  $G_i$  value shows the overall performance characteristic of the multiple responses.  $GC_{ij}$  along with deviation sequence and  $G_i$  values were given in Table 4.

**Table 4** Calculation of grey relational grade

Sl. No.	$\Delta$ MRR	$\Delta$ Ra	$\Delta$ ED	GCMRR	GCRa	GCED	$G_i$	Rank
1	1	1	0	0.5	0.5	1	0.667	8
2	0.354	0.151	0.501	0.7383	0.869	0.666	0.758	5
3	0	0	0.439	1	1	0.695	0.898	1
4	0.472	0.759	0.897	0.679	0.568	0.527	0.592	9
5	0.362	0.116	0.548	0.734	0.896	0.646	0.759	4
6	0.232	0.227	0	0.812	0.815	1	0.876	2
7	0.429	0.187	0.835	0.699	0.843	0.545	0.696	7
8	0.529	0.180	0.312	0.654	0.847	0.762	0.754	6
9	0.063	0.124	0.309	0.941	0.889	0.763	0.865	3

$$G_i = \frac{1}{m} \sum GC_{ij} \quad (6)$$

where  $m$  is the number of responses.

### 3 Results and Discussion

From this experiment, it is observed (from Table 4) that the experiment no. 3 has the highest  $G_i$  value which showed the best multi-performance characteristic for the optimal process parameters setting for maximum MRR, minimum Ra and minimum ED simultaneously. The ED increases with an increase in concentration and temperature, whereas it decreases with increasing etching time. The ED always should be lesser. The MRR increases when the etching rate increases. With increase in etching concentration, etching temperature and also etching time, the MRR increases [8]. With increase in etching time, the uneven surface is obtained due to collisions for a longer time which results in higher Ra. When the etching concentration is more, then higher number of molecules of reagents is present in the concentration, so fast reaction occurs. So, the increase in concentration generally leads to increase in the rate of reaction which results in increase in surface roughness, and this gives more MRR and poor surface finish. When molecules collide with one another in a dynamic way, then chemical reactions take place. As the temperature is a measure of the kinetic energy present in molecules, the movement of molecules is governed by etching temperature. The energy level of molecule increases with the increase in the etching temperature of solution [9].

Figure 2 and Table 5 show the main effect plots for  $G_i$  and ANOVA, respectively. From the ANOVA for  $G_i$ , it is observed that temperature was the most significant parameter. The main effect plots also showed the higher contribution of temperature to the variability of  $G_i$ . The second higher contribution was found to be concentration. The time has less effect compared to other parameters. The results show that the

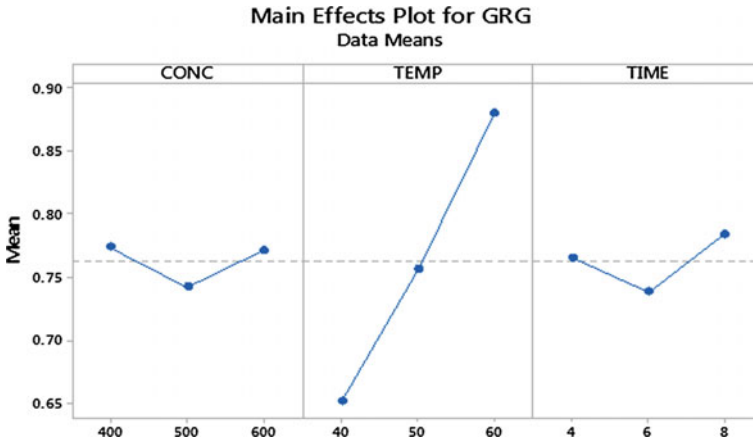


Fig. 2 Main effect plot of GRG

Table 5 Analysis of variance (ANOVA) for GRG

Source	Sum of square	DOF	Mean square	F-ratio	Contribution (%)	Rank
Concentration	0.001998	2	0.000999	1.1307	2.36	3
Temperature	0.0774	2	0.0387	43.803	91.59	1
Time	0.00335	2	0.001668	1.8873	3.95	2
Error	0.00177	2	0.0008835			
Total	0.0845	8				

optimization of photochemical machining of aluminium can be improved effectively through the GRA.

## 4 Conclusions

From the carried-out experimental work, the following points can be concluded:

- The optimum parameter setting is found to be as 400 g/L for etching concentration, 60 °C for etching temperature and 8 min for etching time.
- MRR increases drastically with increase in temperature.
- The study of the ANOVA for GRG reveals that the etching temperature is the most dominant parameter on the output response followed by etching time, while etching concentration being the least contributing.

## References

1. Allen DM (2004) Photochemical machining: from manufacturing's best kept secret' to a \$6 billion per annum, rapid manufacture process. *CIRP J Manuf Syst* 53(2):559–572
2. Cakir O (2008) Chemical etching of aluminum. *J Mater Process Technol* 199:337–340
3. Yadav RP, Teli SN (2014) A review of issues in photochemical 450 machining. *Int J Modern Eng Res* 4:49–53
4. Allen DM, Almond HJ (2004) Characterization of aqueous ferric chloride etchant used in industrial photo chemical machining. *J Mater Process Technol* 149:238–245
5. Roy R, Allen DM, Zamora O (2004) Cost of photochemical machining. *J Mater Process Technol* 149:460–465
6. Cakir O, Temel H, Kiyak M (2005) Chemical etching of Cu-ETP copper. *J Mater Process Technol* 162–163:275–279
7. Wagh DV, Dolas DR, Dhagate MD (2014) Experimental investigation of photochemical machining on Inconel 600 using ferric chloride. *Int J Eng Res Technol* 4(2):289–293
8. Wangikar SS, Patowari PK, Misra RD (2016) Parametric optimization for photochemical machining of copper using grey rational method. In: *International conference on advanced technologies for societal applications*, pp 933–943
9. Wangikar SS, Patowari PK, Misra RD (2017) Effect of process parameters and optimization for photochemical machining of brass and German silver. *Mater Manuf Process* 32(15):1747–1755

# Experimental Investigations on Microstructure, Mechanical and Wear Behavior Under Dry Sliding of Al6061 with Particulate-Reinforced SiC and TiB<sub>2</sub> Metal Matrix Composite Developed by Stir Casting



G. Srinivas Kumar, Y. V. Mohan Reddy and B. Chandra Mohan Reddy

**Abstract** In recent years, the auto industry has been widely using the aluminum alloy in lightweight vehicles. Aluminum-alloying components like pistons, cylinder heads, brake rotor, carburetors, transmission housings, and wheels are used. Most of the work in automobile sector is on reduction of weight, especially in case of braking system. Brake rotors, which are available, are in heavyweight. Al6061 alloy has many applications in the transportation sector. Excellent mechanical properties can be achieved for Al6061 in addition to good ceramics like SiC and TiB<sub>2</sub> as a reinforcement, due to which the alloy finds a wide range of applications (or many applications). Al6061 + SiC and Al6061 + TiB<sub>2</sub> are the two particulate metal matrix composites, which are fabricated with different weight proportions (3, 5, and 7%) by in situ stir casting technique. With addition of ceramics (or the ceramics mentioned above), the alloy properties are highly improved. In contrast to the microstructure, mechanical and wear behavior on these two AMMCs will give the best material for manufacturing of a brake rotor.

**Keywords** Al6061 · Stir casting · Wear behavior · SEM analysis · Brake rotor

---

G. Srinivas Kumar (✉)  
JNTUCEA, Anantapuramu, India  
e-mail: [srin.8045@gmail.com](mailto:srin.8045@gmail.com)

Y. V. Mohan Reddy  
G. Pulla Reddy Engineering College, Kurnool, India  
e-mail: [yvmr06@gmail.com](mailto:yvmr06@gmail.com)

B. Chandra Mohan Reddy  
Jawaharlal Nehru Technological University, Anantapuramu, India  
e-mail: [cmr\\_b@yahoo.com](mailto:cmr_b@yahoo.com)

## 1 Introduction

Aluminum metal matrix composites (AMMC's) offer high fulfillment and applications over pure metals and metallic alloys. The properties of AMMCs give them many advantages in areas such as the automobile, aircraft, and sporting goods industries. AMMCs are classified into three types that are based on reinforcement, namely particulate-reinforced, discrete fiber-reinforced and continuous fiber-reinforced AMMCs. Among all of these, particulate AMMCs are becoming crucial due to their applications and are light in weight; therefore, it is employed in aerospace and automotive manufacturing industries. Using composites rather than conventional material like steel usually provides major weight savings. Due to the specific properties and low weight, it is possible to manufacture composite materials for special purposes. For example, a composite material can be designed specifically for a particular type of load. It is highly advantageous over conventional materials due to the resistance to chemical, thermal, and electrical insulation properties.

## 2 Materials

Aluminum alloy Al6061 has as numerous engineering applications including transportation and construction where the desired mechanical and thermal properties are required like UTS, wear resistance, and conductivity. It is mainly suitable for automobile industry applications, due to its highly corrosive resistance. Chemical composition of Al6061 is represented in the tabular column mentioned in Table 1.

Al6061 is a precipitation-hardened aluminum alloy, containing magnesium and silicon having its major alloying elements. Originally called "Alloy 61S", it was developed in 1935 [1]. It has good mechanical properties; exhibits weldability; and is very commonly extruded. In general, it is one of the most widely used aluminum alloys among all of this series (Table 2).

The only chemical compound of carbon and silicon is SiC. In an Acheson furnace, a mixture of carbon material (usually petroleum coke) and a silica or quartz sand is reacted chemically at high temperatures in the range of 1700–2500 °C resulting in the formation of  $\alpha$ -SiC. It is most better abrasive and has been produced and made under grinding wheels. Presently, it is considered as high functional graded ceramic due to its excellent mechanical properties technically, shown in Table 3.

Titanium diboride ( $\text{TiB}_2$ ) is also one of the ceramics having excellent properties like thermal conductivity, stability of oxidation, and highly corrosive resistance. It is the most attractive material in the Al industry as substance due to refinement of grain

**Table 1** Chemical composition of pure Al6061 alloy

Element	Mg	Fe	Si	Cu	Mn	V	Ti	Al
Weight %	1.08	0.17	0.63	0.32	0.52	0.01	0.02	Remainder

**Table 2** Properties of Al6061

Physical properties	Density			
	2.700 gm/cm <sup>3</sup>			
Mechanical properties	Modulus of elasticity ( <i>E</i> )	UTS	Elongation	Poisson’s ratio
	68.9 GPa	124–290 MPa	12–25%	0.33
Thermal properties	Melting temperature	Thermal conductivity	Thermal expansion	Specific heat capacity
	585 °C	$2.23 \times 10^{-5} \text{ K}^{-1}$	897 J/kg K	32.5–39.2 Ωm

**Table 3** Mechanical properties of SiC

Density	3.1 gm/cc
Ultimate tensile strength	162.5 MPa
Young’s modulus	137 GPa
Brinell hardness	2800 kg/mm
Poisson’s ratio	0.37
Thermal conductivity	3.80–20.60 W/m K
Melting point	1682 °C

**Table 4** Mechanical properties of TiB<sub>2</sub>

Density	4.52 gm/cm <sup>3</sup>
Ultimate tensile strength	126.9 MPa
Young’s modulus	366 GPa
Brinell hardness	33.7
Poisson’s ratio	0.15
Thermal conductivity	25 W/m K
Melting point	2970 °C

size when casting aluminum alloys, because of its extensive properties like wettability, low solubility, and electrical conductivity. It can be used as a cladding for better wear and corrosive resistance. Presently, it is considered as high functional graded ceramic due to its excellent mechanical properties technically, shown in Table 4.

### 3 Methodology

Al6061 having the chemical composition is shown in Table 1. It is melted in a resistance furnace. The crucibles were made of graphite. Before fabrication of composite, melting losses of alloy constituents are taken into consideration. The composite was

**Fig. 1** Photograph of composite material Al6061 + SiC and Al6061 + TiB<sub>2</sub>



fluxed with coverall to prevent dressing. The molten alloy was degasified by tetrachlorethane. The crucible which is modified with the sodium is taken out of the furnace. Bring the molten liquid of matrix into semisolid state, by cooling down it. During this process, the molten liquid is added by the preheated reinforcements (which is 480 °C for ½ h) SiC and TiB<sub>2</sub> particulates. The volume fractions are SiC (3, 5, 7%) and TiB<sub>2</sub> (3, 5, 7%). The average size of SiC and TiB<sub>2</sub> is 10 μm. Molten SiC and Al6061 particles are stirred manually at regular intervals. After sufficient stirring manually over a period of time, semisolid state of liquid is reheated to a fully liquid state in resistance furnace; simultaneously, an automatic mechanical stirring is also carried out for about 15 min at 600 rpm to turn the liquid into homogeneous mixture. Using a thermocouple which is of dipping type, temperature is measured. Finally, after attaining a proper mixing of matrix and reinforcement, it is poured into the preheated cast iron mold in the presence of gravity and procedure is repeated for TiB<sub>2</sub> cast composites (Fig. 1).

## 4 Experimentation

### 4.1 Microstructure

To study the microstructure of fabricated composites, standard metallographic procedure is followed and the samples are prepared. Samples are grinded and then polished by surface grinder and emery paper, respectively. Mirror finish is obtained by polishing with alumina powder. Keller's reagent is applied to the samples, and then their microstructure is investigated by the help of scanning electron microscope (SEM) [2] (Fig. 2).



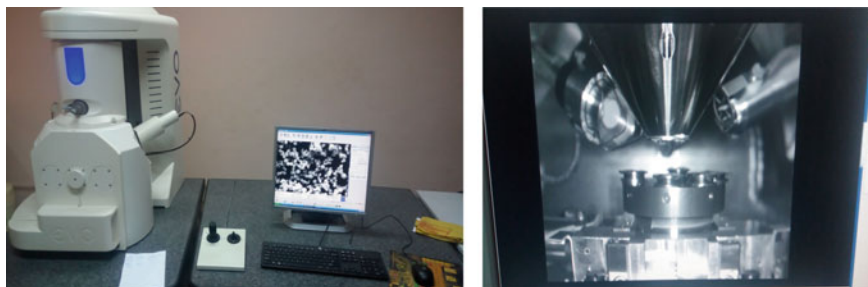


**Fig. 2** Photograph of SEM analysis equipment and its inner view

## **4.2 Microhardness**

Aluminum metal matrix composites with different proportions of various reinforcement (3, 5, and 7% of SiC; 3, 5, and 7% of TiB<sub>2</sub>) particles in Al6061 are taken for microhardness test. The test is conducted on Rockwell microhardness tester (Model-RAS) with 100 kg-f for duration of 15 s using a 1/16" of ball indenter [2].

## **4.3 Tribological Analysis**

Al6061 + SiC and Al6061 + TiB<sub>2</sub> composites are made as per the ASTM E8 standard for studying of wear analysis, under constant load condition. In this study, flattened specimens of length 30 mm having dia of 6 mm are made. The tracking radius of pin on the disc, which slides is about 60 mm. to get a fully contact of specimen with a disc, which is rotating, should be pressed against a rotating EN31 carbon steel disc having 65 HRC, by loading with a known weights. Each specimen is polished by alumina powder, and the rotating disk is by 4000 emery paper before going for test. Wear resistance under dry sliding condition test is carried out on each cast composite specimen by applying a constant load of 10 N-force and sliding distance of 848 m at a velocity of 2.82 m/s. The test duration is about 300 s at a constant velocity of disk, having 900 rpm. Wear rate, frictional force, and coefficient of friction versus sliding distance analysis are carried on each specimen.

# **5 Results and Discussion**

## **5.1 Results**

The samples of metallographic procedure were sectioned from the cylindrical cast composites to observe the difference of distribution of SiC and TiB<sub>2</sub> particulates in

the Al6061 matrix; for these samples, etching is done whenever required by the help of 0.5% HF solution and is observed for any developments under EVO<sup>®</sup> HD Scanning Electron Microscope from Carl Zeiss. All the samples were cast composites which are having different weight fractions (3, 5, and 7% of SiC; 3, 5, and 7% of TiB<sub>2</sub>) as a reinforcement.

In the second step, mixing is needed to improve the particle distribution; i.e., slurry is heated above the liquidus temperature and then stirred well for 15 min at 600 rpm using an automatic stirring device.

From Fig. 3, it reveals that the cast composite is having a wt proportion (7% of TiB<sub>2</sub>) as reinforcement, and cluster formation takes place at different locations. Particulates which are added to the molten alloy were observed on the top layer of molten surface, though they have a more value of specific density than the molten alloy. Having higher surface tension and poor wetting properties makes it to float on the surface. Wettability between the ceramics and molten liquid alloy is poor, and it is improved by applying mechanical force on the particles, by overcoming the surface tension.

From Figs. 4 and 5, it revealed that microstructure of specimens has wt proportion (5 and 7% TiB<sub>2</sub>) as reinforcement. It clearly observed that the resulting of cluster formation & non uniform distribution of particulates in the samples.

From Figs. 6, 7, and 8, it revealed that microstructure of specimens has wt proportion (5, 7, and 15% SiC) as reinforcement. It clearly observed the uniform distribution of particulates in all the specimens.



**Fig. 3** Micrograph of Al6061 + 3% of TiB<sub>2</sub> with 15KX, 10KX, and 7.5KX

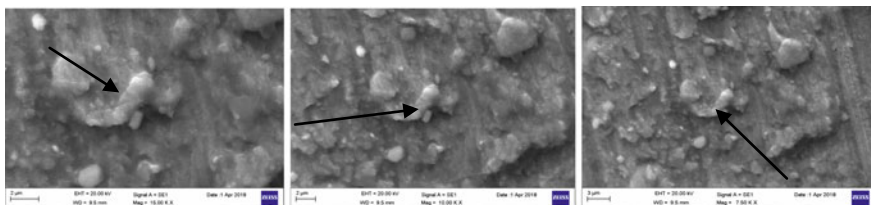


**Fig. 4** Micrograph of Al6061 + 5% of TiB<sub>2</sub> with 15KX, 10KX, and 7.5KX

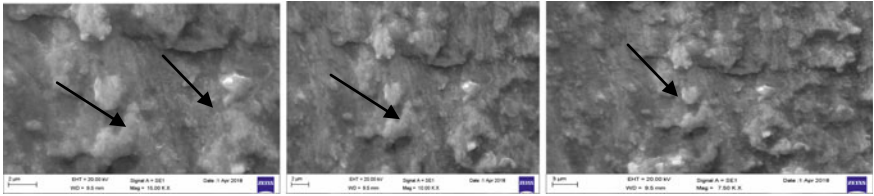


**Fig. 5** Micrograph of Al6061 + 7% of TiB<sub>2</sub> with 15KX, 10KX, and 7.5KX

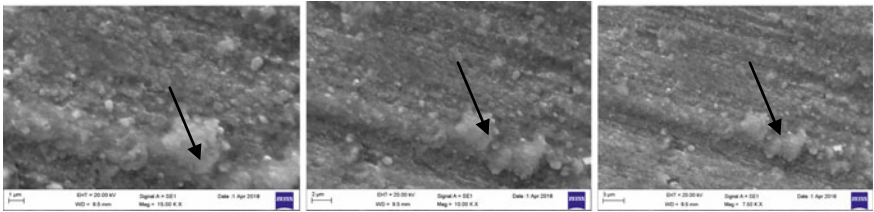


**Fig. 6** Micrograph of Al6061 + 3% of SiC with 15KX, 10KX, and 7.5KX

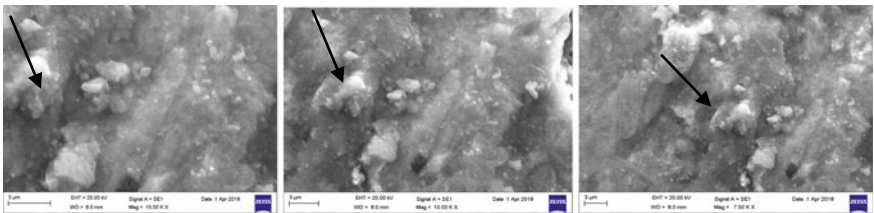


**Fig. 7** Micrograph of Al6061 + 5% of SiC with 15KX, 10KX, and 7.5KX

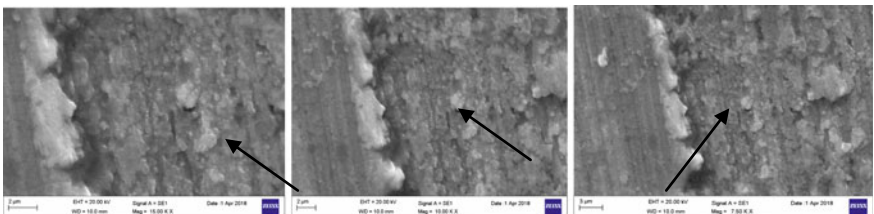
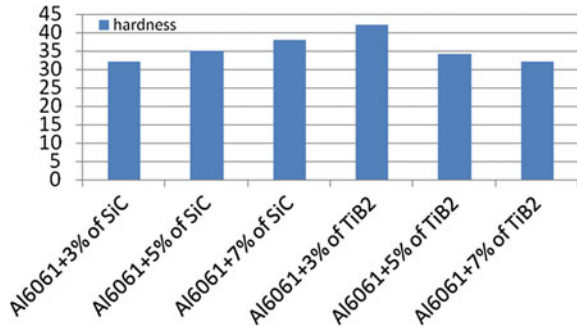


**Fig. 8** Micrograph of Al6061 + 7% of SiC with 15KX, 10KX, and 7.5KX

### Hardness

Testing has been conducted on all the specimens, with different weight fractions of SiC (3, 5, and 7%) and TiB<sub>2</sub> (3, 5, and 7%) as a reinforcement in Al6061 which are fabricated by stir casting. Hardness is recorded, and graph is plotted for the obtained values.

**Graph 1** Cast composite hardness



Graph 1, indicates the results of hardness, it reveals that increases of hardness with increase in weight fraction of SiC, while the weight fraction of TiB<sub>2</sub> increase, hardness decrease, due to cluster formation or non uniform distribution of TiB<sub>2</sub> particulate. Beyond certain weight fraction of particles, the hardness starts decreasing, because ceramic particles start bonding with each other, lead to cluster formation, and stagnate itself [3, 4].

**Wear Analysis**

In order to observe the qualitative proof on the particulate distribution in the matrix, among the two ceramic reinforcements (SiC and TiB<sub>2</sub>) wear rate is to be employed. On wear resistance testing machine, which is under dry sliding condition, testing was conducted at ambient temperature, and the specimens are loaded against the rotating disk by applying the known weights. The graphs that are obtained by the experimentation would reveal the coefficient of friction, frictional force, and wear rate of fabricated composites [1] (Tables 5, 6 and 7).

The wear rate of all specimens (mm<sup>3</sup>/Nm) is obtained and is plotted against the sliding distance, as shown in Graph 2 for a constant load of 10 N-force for different reinforcements of SiC (3, 5, and 7%) and TiB<sub>2</sub> (3, 5, and 7%). In Graph 2, it reveals

**Table 5** Wear rate and sliding distance

Distance	wt%					
	7% of SiC	5% of SiC	3% of SiC	7% of TiB <sub>2</sub>	5% of TiB <sub>2</sub>	3% of TiB <sub>2</sub>
100	34.2	18	33.3	72	25.5	62
200	40	28	53	92	30	66
300	42.3	41	64	109	37	70
400	46	48	85	126	48	72
500	42.5	52	98	136	54	73
600	47	62.5	118	151	62	78
700	20.7	70	128	162.5	69	81
800	62	74	138	180	72	85
848	64	76	140	186	70	85

**Table 6** Frictional force and sliding distance

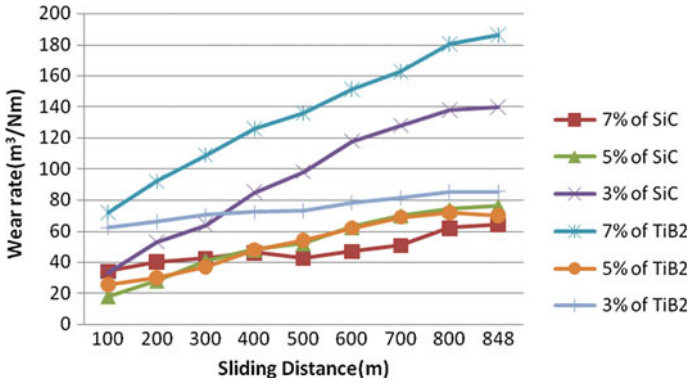
Distance	wt%					
	7% of SiC	5% of SiC	3% of SiC	7% of TiB <sub>2</sub>	5% of TiB <sub>2</sub>	3% of TiB <sub>2</sub>
100	2.2	1.5	3	2.1	2.7	1.6
200	2.4	2.5	3.1	2.4	2.9	2
300	3.1	2.4	3.1	3.1	2.9	1.8
400	3.5	2.6	3.2	3.2	3	1.5
500	3.5	2.5	3.3	3.4	3.2	1.5
600	2.7	2.5	3.3	3.5	3.4	1.7
700	2.7	2.4	3.3	3.4	1.9	1.4
800	2.8	2.1	2.1	4.1	1.5	1.5
848	2.9	2.3	2.25	4.2	2.1	1.7

**Table 7** Frictional coefficient and sliding distance

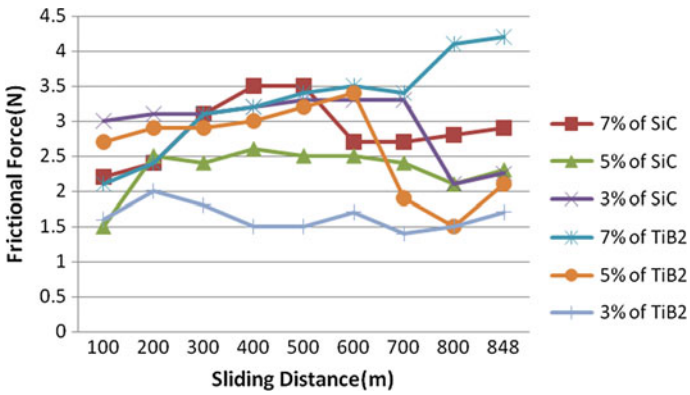
Distance	wt%					
	7% of SiC	5% of SiC	3% of SiC	7% of TiB <sub>2</sub>	5% of TiB <sub>2</sub>	3% of TiB <sub>2</sub>
100	0.023	0.014	0.029	0.023	0.027	0.016
200	0.029	0.024	0.031	0.03	0.029	0.02
300	0.033	0.025	0.032	0.033	0.031	0.017
400	0.035	0.027	0.033	0.035	0.031	0.015
500	0.035	0.025	0.033	0.038	0.034	0.015
600	0.027	0.027	0.036	0.04	0.031	0.017
700	0.027	0.023	0.037	0.039	0.018	0.014
800	0.028	0.022	0.025	0.048	0.015	0.016
848	0.029	0.024	0.025	0.043	0.022	0.018

that at constant load application, wear rate increases, against the sliding distance of all the specimens. Special characteristics were observed in Graph 2 that Al6061 + 7% of SiC has less wear rate among all cast composites, having maximum of 64 mm<sup>3</sup>/m at a sliding distance of 848 m.

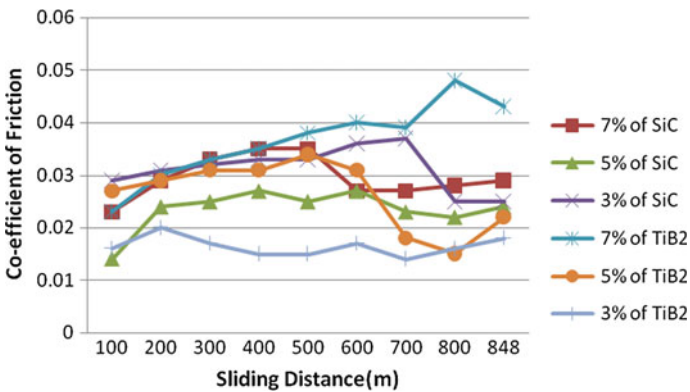
The frictional force of the specimens will give frictional coefficient values directly and is plotted against the sliding distance as shown in Graphs 3 and 4 for a constant load of 10 N for different % by wt proportion of reinforcement SiC and TiB<sub>2</sub>. From Graphs 3 and 4, it is shown that coefficient of friction and frictional forces were drastic changes in the cast composites of TiB<sub>2</sub> as a reinforcement because of non-uniform distribution of particulates in the matrix. It was observed that Al6061 + 7% of SiC has more frictional force and coefficient of friction among all cast composites, having maximum of 3.5 N and 0.035, respectively, over a sliding distance of 848 m.



**Graph 2** Wear rate versus sliding distance of cast composites



**Graph 3** Frictional force versus sliding distance of cast composites



**Graph 4** Frictional coefficient and sliding distance of cast composites

## 5.2 Conclusions

Here, experimental study reveals that:

1. For different % by wt proportion of reinforcement of SiC and TiB<sub>2</sub> particle with Al6061 as a matrix, SiC with 7% by wt would have better frictional force, coefficient of friction, and wear rate.
2. SiC as reinforcements in Al6061 matrix, as a homogenous distribution of particles without agglomeration, was achieved rather than TiB<sub>2</sub>. Strong bonding was observed due to preheating of reinforcements SiC and TiB<sub>2</sub> particulates.
3. Due to the formation of cluster, when TiB<sub>2</sub> is used as reinforcement in the Al6061 matrix which is observed in SEM photograph, the hardness values are higher, but in case of SiC as a reinforcement, due to homogenous distribution of particles, hardness value is better.
4. The best results have been obtained at 7% by wt proportion of SiC as a reinforcement.

**Acknowledgements** This work was completed in part with resources provided by the Jawaharlal Nehru Technological University, Anantapuramu; G. Pulla Reddy Engineering College, Kurnool; and S.V. University, Tirupati, permitting us to perform the tests in their esteem laboratory.

## References

1. Pazhouhanfar Y, Eghbali B (2018) Microstructural characterization and mechanical properties of TiB<sub>2</sub> reinforced Al6061 matrix composites produced using stir casting process. *Mater Sci Eng, A* 710:172–180
2. Mahajan G, Karve N, Patil U, Kuppan P, Venkatesan K (2015) Analysis of microstructure, hardness and wear of Al-SiC-TiB<sub>2</sub> hybrid metal matrix composite. *IJST* 8(suppl-2)
3. Singla M, Dwivedi DD, Singh L, Chawla V (2009) Development of aluminium based silicon carbide particulate metal matrix composite. *J Minerals Mater Charact Eng* 8(6):455–467
4. Srinivas Kumar G, Viswanath Chari V (2017) Comparison of mechanical characterization of Al metal matrix composite and Gray Cast iron of an automobile brake rotor. *Int J Eng Innov Res* 6(5):2277–5668. ICEMS-2017, ISSN (Online)
5. Mishra AK, Srivastava RK (2017) Wear behaviour of Al-6061/SiC metal matrix composites. Springer, Berlin. <https://doi.org/10.1007/s40032-016-0284-3>
6. “Selection and Applications”—The Aluminum Association, Inc. Dec-1998
7. Ghosh S, Sahoo P, Sutradhar G (2014) Tribological properties of Al–SiC metal matrix composites: a comparison between sand cast and squeeze cast techniques. *J Inst Eng India Ser D* 95(2):161–171
8. Kumar N, Gautam G et al (2015) Synthesis and characterization of TiB<sub>2</sub> reinforced aluminium matrix composites: a review. *J Inst Eng India Ser D* (2015)
9. Agbeleye AA, Esezobor DE et al (2017) Tribological properties of aluminium-clay composites for brake disc rotor applications. *J King Saud Univ Sci*. <http://dx.doi.org/10.1016/j.jksus.2017.09.002>

10. Nakanishia H, Kakihara K et al (2002) Development of aluminum metal matrix composites (Al-MMC) brake rotor and pad. *JSAE Rev* 23:365–370
11. Mohan Krishna SA, Shridhar TN et al (2015) Research significance, applications and fabrication of hybrid metal matrix composites. *IJSET Int J Innov Sci Eng Technol* 2(5)



# Investigations on Material Removal Rate During Wire Electrodischarge Machining of Nickel–Titanium Alloy



Vinayak N. Kulkarni, V. N. Gaitonde, Rohit Sureban and M. S. Patil

**Abstract** Nickel–titanium (NiTi) shape-memory alloys (SMA) are being extensively used in high-end and crucial applications in the fields like aerospace, bioengineering, robotics, and automobile, and the areas of their application are growing at a high rate due to their unique characteristics. For all such applications, the machining of NiTi SMA is a crucial task. In this study, the machining of NiTi SMA using wire electrodischarge machining (WEDM) and copper wire as the electrode has been studied for the various input parameters. The quality and the time duration for the machining depend on the selection of input parameters such as pulse on/off time, wire feed rate and servo voltage. The experiments for the study were planned according to the full factorial design (FFD), and then, it was analyzed by response surface methodology (RSM) mathematical models. It was found that with the increase in pulse on and pulse off duration, the material removal rate increased accordingly. In the present experimental studies, for the higher wire feed rate, the MRR increased initially and then decreased thereafter.

**Keywords** Nickel–Titanium · Shape-memory alloy · Wire feed rate · Material removal rate · Response surface methodology

## 1 Introduction

Nickel–titanium (NiTi) shape-memory alloys (SMAs) are the advanced grade of materials widely used in aerospace, biomedical, and automobile industries [1]. The reasons for the use of SMAs in these fields are their special properties called shape-memory and superelastic effect in which the material after getting deformed tends to regain its original state upon heating and also its high resistance to corrosion and biocompatibility [2, 3]. NiTi SMA has a strain recovery of more than 8%. The applications of NiTi SMAs are so crucial that there cannot be any compromise of the

---

V. N. Kulkarni (✉) · V. N. Gaitonde · R. Sureban · M. S. Patil  
School of Mechanical Engineering, KLE Technological University, Hubballi, Karnataka 580031,  
India  
e-mail: [vinayak33me@gmail.com](mailto:vinayak33me@gmail.com)

© Springer Nature Singapore Pte Ltd. 2020  
L. Vijayaraghavan et al. (eds.), *Emerging Trends in Mechanical Engineering*,  
Lecture Notes in Mechanical Engineering,  
[https://doi.org/10.1007/978-981-32-9931-3\\_30](https://doi.org/10.1007/978-981-32-9931-3_30)

305

quality as it might affect the properties of these alloys, and also, the machining of these alloys must be precise. Conventional machining of NiTi SMA would result in high wear of the material resulting in a decrease in quality on the special properties and even may affect the internal structure of the alloy [4].

The applications of NiTi SMAs require intricate shapes to be machined, which is possible by wire electrodischarge machining (WEDM) process. The WEDM process uses metallic wire as the electrode tool. The gap is maintained between the nozzle and the workpiece to minimize the vibrations and also between the wire and workpiece material as it is a non-contact-type machining. When the voltage passes through the electrode (tool), a dielectric field is generated between the electrode and the workpiece which is greater than the dielectric constant of the material, hence eroding the material into the path that is programmed. The dielectric liquid performs the action of both carrying away the debris formed during machining and also as the coolant. The use of various dielectric fluids also influences the machining characteristics as studied by Chakraborty et al. [5]. The machining in WEDM is effected by various input parameters such as pulse on duration, pulse off duration, and wire feed rate, and these in turn have a variable effect on the output parameters such as surface roughness, tool wear rate, and material removal rate (MRR) [6]. The effect on machining parameters on the surface integrity has been studied by Liu et al. [7], and the study indicates that surface integrity is widely dependent on selection of proper input parameters and also the effect of input machining parameters on the material removal rate (MRR) has been studied. It was observed that the discharge current and the pulse on/off duration are the major contributors to the MRR. Manjiaiah et al. [8] studied the MRR and surface roughness behavior by Taguchi method using utility concept.

Some work has been carried on the study of WEDM machining of NiTi alloys using brass- and zinc-coated brass wire [9]. The studies on material removal rate for WEDM of NiTi shape-memory alloys using copper wire electrode have not been explored, and therefore, the present study focuses on machining of NiTi alloy using copper wire as the electrode material in WEDM process.

## 2 Experimental Details

### 2.1 Work and Tool Material

For the current experimental study, a medical grade NiTi SMA of 100 mm × 180 mm × 2 mm rectangular plate has been considered. It has 53.74% nickel and 44.13% titanium by atomic percentage weight as major constituents. The electrode wire for machining in WEDM selected for the study is a copper wire of 0.25 mm diameter.

**Table 1** Selected system parameters and their levels

Code	Parameter	Symbol	Level 1	Level 2	Level 3
A	Pulse on time ( $\mu\text{s}$ )	$T_{\text{on}}$	105	115	125
B	Pulse off time ( $\mu\text{s}$ )	$T_{\text{off}}$	25	40	55
C	Wire feed (m/min)	WF	4	6	8

## 2.2 Design of Experiments and Methodology

A systematic study for the research was planned and designed based upon the full factorial design concept using Taguchi's  $L_{27}$  array. And the analysis was based upon the response surface methodology (RSM) which is suited to compare several variables to one response variable. The main and interaction effects of the system variables on performance characteristics can be studied using RSM model [10].

## 2.3 Process Parameters

The current study aims toward the study and analysis of performance characteristics of NiTi SMA with respect to the input variables during WEDM. The improper selection of the input parameters may lead to lower MRR and uneconomical machining practices or may cause the breakage of electrode wire. Hence, the selection of input parameters plays an important role in the present study. Based upon the literature studies and trial-and-error method, the system parameters, i.e.,  $T_{\text{on}}$ ,  $T_{\text{off}}$ , and wire feed (WF) at three different levels as shown in Table 1 are selected. For the present study, the servo voltage has been set to 40 V with a peak current of 12 A; and the dielectric fluid used is the deionized water.

## 2.4 Experimentation

The experiments for the present study were carried out in CNC WEDM Electronica Ecocut Elpuls-15 model. It has a wide range of parameters to choose from and provides flexibility for the operator. The copper wire electrode of diameter 0.25 mm is used with deionized water as the dielectric fluid to machine the NiTi SMA which is held rigidly to the worktable using fixtures as shown in Fig. 1. The external noise during machining is reduced by having the air-conditioned atmosphere in the machining room. Circular profiles of diameter 10 mm have been machined according to the  $L_{27}$  array, and these specimens were further used for the analysis.

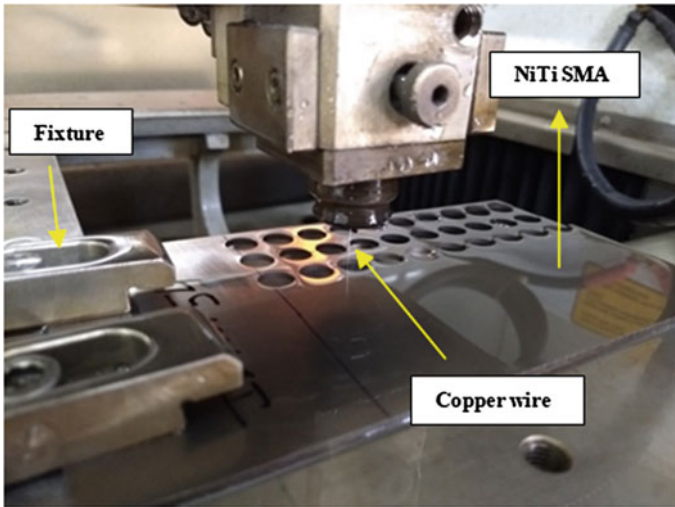


**Fig. 1** Experimental setup

## 2.5 Monitoring of Output Responses

The material removal rate (MRR) was calculated by knowing the total time taken to machine the profile and the kerf width which is measured using a coordinate measuring machine. The equation used to calculate MRR is given by Eq. 1.

$$\text{MRR} = V_c \times b \times h \text{ mm}^3/\text{min.} \quad (1)$$

where

$V_c$  Cutting speed =  $\pi D/(T_m)$  in mm/min.

$T_m$  Machining time in s.

$D$  Diameter in mm.

$b$  Kerf width (width of cut) in mm.

$h$  Plate thickness in mm.

## 3 Response Surface Modeling

To study the performance variable, i.e., MRR, a second-order regression model was developed using RSM. The RSM method is preferred as it makes easy to analyze the effect of two or more parameters on the response.  $T_{\text{on}}$ ,  $T_{\text{off}}$ , and WF were taken as input variables for regression modeling given in Eq. 2.

**Table 2** ANOVA for MRR (mm<sup>3</sup>/mm)

Source	Degrees of freedom	Sequential sum of square	Adjusted sum of square	Adjusted mean square	<i>F</i>	<i>P</i>
Regression	9	19.8619	19.8619	2.20688	6.86	0.0
Residual error	17	5.4702	5.4702	0.3218		
Total	26	25.3322				

$$\begin{aligned}
 \text{MRR} = & 24.4 - 0.448 T_{\text{on}} - 0.120 T_{\text{off}} + 0.73 \text{WF} + 0.00160 T_{\text{on}} * T_{\text{on}} \\
 & - 0.00284 T_{\text{off}} * T_{\text{off}} - 0.0431 \text{WF} * \text{WF} + 0.00365 T_{\text{on}} * T_{\text{off}} \\
 & + 0.00201 T_{\text{on}} * \text{WF} - 0.00907 T_{\text{off}} * \text{WF} \quad (2)
 \end{aligned}$$

The analysis of variance (ANOVA) method is used to check the adequacy of the developed model at 95% confidence level. The ANOVA for MRR is given in Table 2. Since the *P*-value is less than 0.05, the developed regression model is adequate.

## 4 Results and Discussions

The plan for the study in uncoded units and measure of experimental performance characteristic MRR for the present study are summarized in Table 3. The plan was based upon the full factorial design using Taguchi's  $L_{27}$  orthogonal array.

### 4.1 Main Effect Plot

The main effect graphs are used to analyze the influence of process parameters at different levels of the mean of response data.

Figure 2 shows the influence of input parameters ( $T_{\text{on}}$ ,  $T_{\text{off}}$ , and WF) on the MRR. From Fig. 2, it can be inferred that there is a constant increase in MRR when the pulse on time changes from 105 to 115  $\mu\text{s}$ , and there is a sudden increase in MRR when  $T_{\text{on}}$  changes from 115 to 125  $\mu\text{s}$ ; this is because of increase in spark discharge energy that increases with increase in pulse duration. Further looking at pulse off timing ( $T_{\text{off}}$ ), there is an increase in MRR when  $T_{\text{off}}$  changes from 25 to 40  $\mu\text{s}$ ; this might be due to the proper erosion of material from the machined area and then decreases considerably. The wire feed causes an increased MRR from 4 to 6 m/min but then remains almost constant on the further increase. The increase in MRR may be due to the rate of fresh wire being available for machining.

**Table 3** Experimental study plan and results

Exp. No.	$T_{on}$ ( $\mu s$ )	$T_{off}$ ( $\mu s$ )	WF (m/min)	MRR ( $mm^3/min$ )
1	105	25	4	2.302
2	105	25	6	2.337
3	105	25	8	2.236
4	105	40	4	3.011
5	105	40	6	2.971
6	105	40	8	3.054
7	105	55	4	1.687
8	105	55	6	1.538
9	105	55	8	1.709
10	115	25	4	0.486
11	115	25	6	3.706
12	115	25	8	2.761
13	115	40	4	3.496
14	115	40	6	3.312
15	115	40	8	3.536
16	115	55	4	2.992
17	115	55	6	3.076
18	115	55	8	3.024
19	125	25	4	2.640
20	125	25	6	3.030
21	125	25	8	3.520
22	125	40	4	4.075
23	125	40	6	3.821
24	125	40	8	3.908
25	125	55	4	4.728
26	125	55	6	4.591
27	125	55	8	4.498

## 4.2 Analysis of the Interaction Effects of Process Parameters

The interaction plots were developed using the regression model developed for the MRR response. The interaction of the various input parameters ( $T_{on}$ ,  $T_{off}$ , and WF) can be studied using these plots. Figure 3 shows the combined effect of  $T_{on}$  and  $T_{off}$  on MRR. It can be inferred that with the increase in  $T_{on}$  and  $T_{off}$  the MRR increases. But for higher  $T_{off}$  and lower  $T_{on}$  duration, the MRR is least because of insufficient time to generate the spark required for the erosion of the material.

Figure 4 shows the influence of  $T_{on}$  and WF on MRR; it can be clearly observed that the MRR increases with an increase in both  $T_{on}$  and WF. The increase in pulse

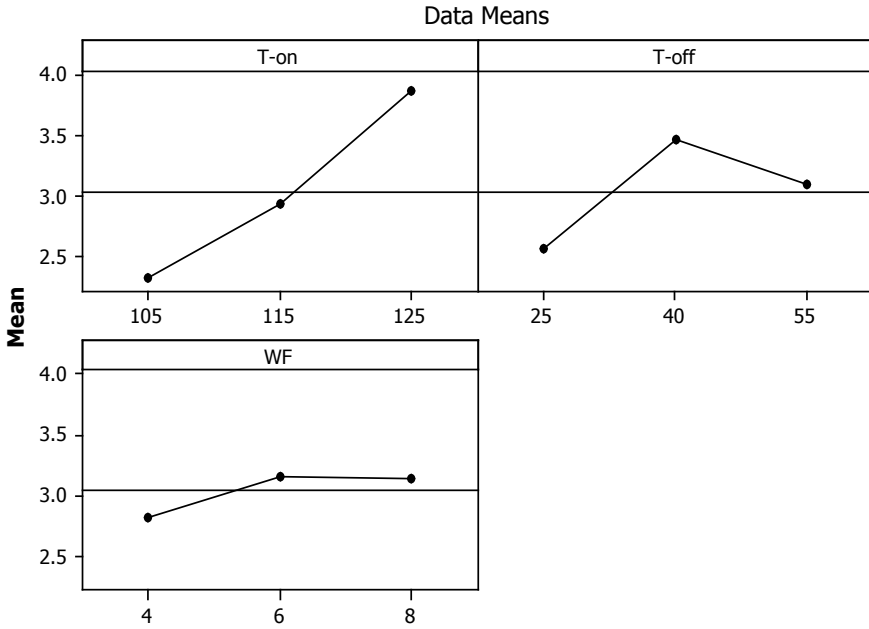
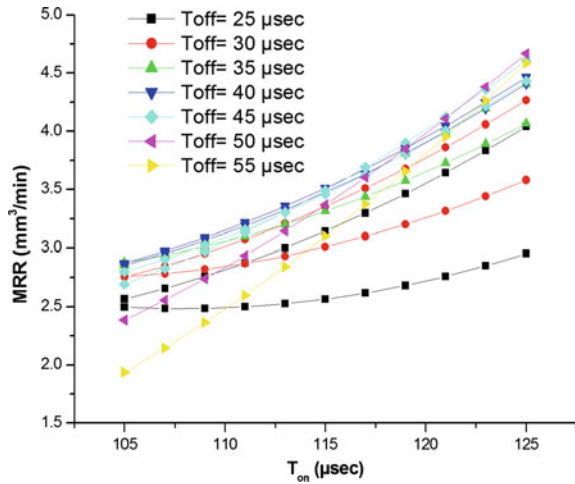
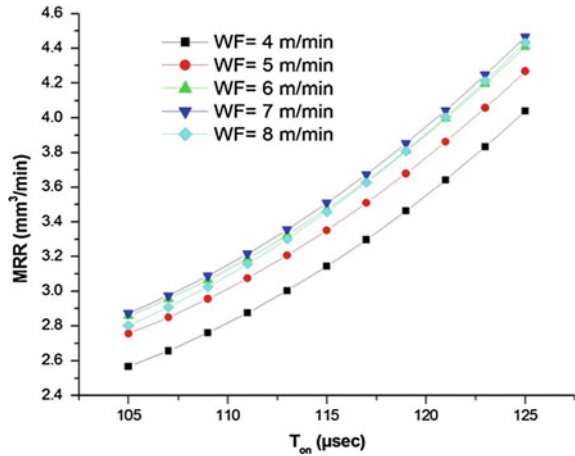


Fig. 2 Main effect plots for MRR

Fig. 3 Influence of  $T_{on}$  and  $T_{off}$  on MRR



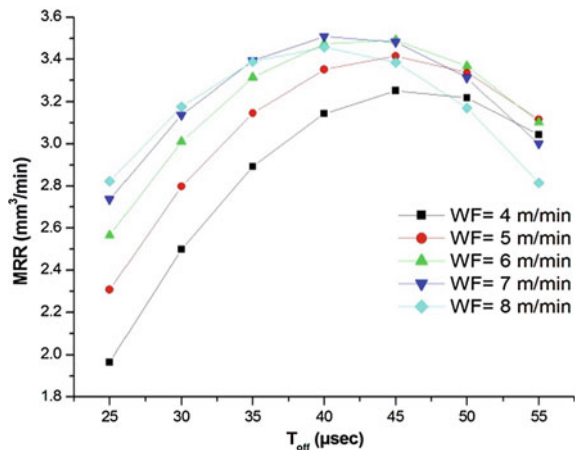
**Fig. 4** Influence of  $T_{on}$  and WF on MRR



on duration provides more time for the spark to erode the material, and also wire feed rate provides more electrode tool material to machine the surface, hence increasing the MRR.

Figure 5 shows the influence of  $T_{off}$  and WF on MRR. Both  $T_{off}$  and WF have a varying effect on the MRR. Initially, for the lower values of both  $T_{off}$  and WF, the MRR increases, but after the pulse off duration of 40  $\mu$ s, the MRR decreases for the increased value of  $T_{off}$  and WF. This is because of insufficient duration attained for the generation of spark as the wire feed rate is also high. Hence, there is a considerable decrease in MRR.

**Fig. 5** Influence of  $T_{off}$  and WF on MRR





## 5 Conclusion

The present work focused on the experimental studies of machining of NiTi SMA during WEDM process. The influence of input parameters such as  $T_{on}$ ,  $T_{off}$ , and WF on the output parameter, i.e., material removal rate (MRR) during machining of NiTi SMA, was modeled and analyzed using RSM and ANOVA techniques. It can be concluded from the various graphs obtained based upon the experimental readings that pulse on ( $T_{on}$ ) duration and pulse off ( $T_{off}$ ) duration are the most influencing input process parameters for MRR using copper wire as an electrode material. With an increase in both  $T_{on}$  and  $T_{off}$ , there is an increase in MRR. But the interaction of wire feed rate with  $T_{off}$  shows that the MRR first increases and then decreases. It is witnessed that maximum MRR is obtained at  $T_{on} = 125 \mu\text{s}$ ,  $T_{off} = 50 \mu\text{s}$ , and  $\text{WF} = 7 \text{ m/min}$ . Further with more research and experimental studies, the researchers can carry out the analysis of remaining output responses such as surface roughness and tool wear rate as per their applications.

**Acknowledgements** This work has been fully supported by capacity building funds 2018–19 granted by KLE Society and KLE Technological University, Hubballi.

## References

1. Chembath M, Balaraju JN, Sujata M (2015) Surface characteristics, corrosion, and bioactivity of chemically treated biomedical grade NiTi alloy. *Mater Sci Eng C56*:417–425
2. Kulkarni VN, Gaitonde VN, Aiholi V, Viranna H (2018) Multiperformance characteristics optimization in wire electric discharge machining of superelastic alloy. *Mater Today Proc 5/9P3*:18845–18854
3. Yoneyama T, Miyazaki S (2009) Shape memory alloys for biomedical applications. Woodhead Publications Limited
4. Manjaiah M, Narendranath S, Basavarajappa S (2014) Review on non-conventional machining of shape memory alloys. *Trans Nonferrous Met Soc China 24*:12–21
5. Chakraborty S, Dey V, Ghosh SK (2015) A review on the use of dielectric fluids and their effects I electrical discharge machining characteristics. *Precis Eng 40*:1–6
6. Sharma N, Khanna R, Gupta R (2013) Multi quality characteristics of WEDM process parameters with RSM. *Procedia Eng 64*:710–719
7. Liu JF, Li L, Guo YB (2014) Surface integrity evolution from the main cut to finish trim cut in W-EDM of shape memory alloy. *Procedia CIRP 13*:137–142
8. Manjaiah M, Narendranath S, Basavarajappa S, Gaitonde VN (2014) Wire electro discharge machining characteristics of titanium-nickel shape memory alloy. *Trans Nonferrous Met Soc China 24*:3201–3209
9. Kulkarni VN, Gaitonde VN, Viranna H, Vasant A (2018) Analysis of wire EDM process parameters in machining of NiTi superelastic alloy. *Mater Today Proc 5/9P3*:19291–19300
10. Montgomery DC (2017) Design and analysis of experiments. Wiley, Hoboken

# A Study on the Development of Aluminum Alloys Using the Mechanical Surface Improvement Method Using the Taguchi Method



Suleyman Cinar Cagan, Bellam Venkatesh and Berat Baris Buldum

**Abstract** The surface quality of the manufactured parts is an important factor affecting the functional properties such as corrosion resistance and fatigue strength of the part. For this reason, this study aims to develop surface roughness of Al 7075-T6 material which is generally used in the aviation and aerospace industry. In order to enhance the surface quality of the parts, the ball burnishing apparatus was designed and experiments were carried out at different parameters (force, feed rate, and medium). The design of the experiments was carried out using the Taguchi method, and the  $L_9$  orthogonal array was chosen. Also, the contributions of the parameters on surface roughness have been calculated with an analysis of variance (ANOVA). Consequently, the optimum surface roughness value was reached with parameters of the force 200 N, mineral oil, and feed rate of 0.1 mm/min. The most important parameters affecting the surface quality are found to be the burnishing force, feed rate, and medium, respectively.

**Keywords** Mechanical surface improvement · Aluminum alloy · Taguchi method · Ball burnishing

## 1 Introduction

Aluminum and its alloys have become increasingly industrialized due to their lightweight as well as their strength and easy forming ability [1–3]. Aluminum alloys play a significant role in the development of space, aviation, weapons, and defense

---

S. C. Cagan (✉) · B. B. Buldum  
Mechanical Engineering Department, Engineering Faculty, Mersin University, Ciftlikkoy  
Campus, 33343 Yenisehir, Mersin, Turkey  
e-mail: [cinarcagan@mersin.edu.tr](mailto:cinarcagan@mersin.edu.tr)

B. B. Buldum  
e-mail: [barisbuldum@mersin.edu.tr](mailto:barisbuldum@mersin.edu.tr)

B. Venkatesh  
Mechanical Engineering, CMR Institute of Technology, Hyderabad, India  
e-mail: [b.venkatesh995@gmail.com](mailto:b.venkatesh995@gmail.com)

© Springer Nature Singapore Pte Ltd. 2020  
L. Vijayaraghavan et al. (eds.), *Emerging Trends in Mechanical Engineering*,  
Lecture Notes in Mechanical Engineering,  
[https://doi.org/10.1007/978-981-32-9931-3\\_31](https://doi.org/10.1007/978-981-32-9931-3_31)

industry due to their mechanical properties as well as their lightweight (density is  $2.81 \text{ g/cm}^3$ ). Within these alloys, the importance and application areas of 7075-T6 grade aluminum alloys are increasing especially in the defense and aerospace industry [2, 3].

Surface roughness is important in determining the quality of the product to be obtained as it affects the mechanical properties, performance, and cost of production of the mechanical parts [4, 5]. Characteristic irregularities occur on the surface of the workpiece after many machining processes [6]. Ball burnishing process is an elementary, quick, and inexpensive finishing process used to remove these irregularities [7, 8]. The finishing process is a recognized mechanical surface treatment method for imparting certain physical, mechanical, and tribological properties to the workpiece [9]. In this process, the surface of the workpiece is compressed by applying an apparatus in order to obtain a smooth surface by removing irregularities in the surface by plastic deformation [9, 10]. As a result, this process can substitute for other conventional surface treatment techniques such as turning, milling, honing, and grinding.

The parameters affecting surface quality when applying to finish to the workpiece are workpiece materials, ball materials, ball types, burnishing forces, number of passes, ball sizes, lubricants, feed rates, and burnishing speed. When the literature is searched, it is seen that researchers are studying different material and burnishing process parameters (force, speed, etc.) [8, 10–17]. There is no study about the application of ball burnishing under different medium conditions in the literature.

In this experimental study, the optimum surface roughness value of the aluminum alloy was investigated using three different burnishing forces, three different feed rates, and three different burnishing medium. Also, the experimental design was planned by selecting  $L_9$  orthogonal Taguchi method.

## 2 Materials and Methods

### 2.1 Material and Experiments

The experiments were carried out using Al 7075-T6 aluminum bar. This workpiece material's sizes were  $\text{Ø}50 \times 280 \text{ mm}$ . The chemical content of the Al 7075-T6 used as the workpiece is indicated in Table 1. This workpiece is divided into 9 equal parts. Different parameters have been applied to each part.

The experiments were carried out on a conventional lathe as shown in Fig. 1. The Al 7075-T6 workpiece was turned to make the surface suitable for testing. Experiments have been carried out with a conventional lathe. In addition, using a force gauge, the burnishing force is accurately determined (Fig. 1). The force gauge equipment is calibrated every 3 months. No chip penetration between the tool and the contact surface is prevented. This is because the penetration of anything between

**Table 1** Chemical content of Al7075-T6 magnesium alloy (wt%)

Workpiece	Al	Cu	Fe	Mg	Si	Mn	Ti	Zn	Cr
Al7075-T6	Balance	1.94	0.45	2.71	0.37	0.25	0.19	5.63	0.21

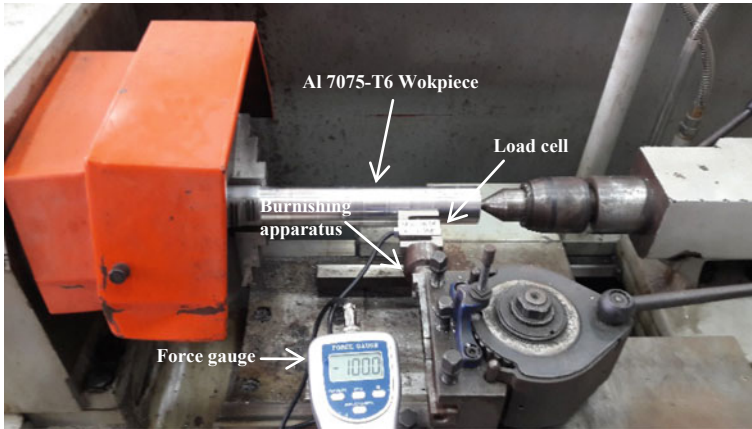


**Fig. 1** Experimental setup

the interface between the tool and the sample adversely affects the quality of the surface.

The Taguchi method is used to determine optimal, reliable, and optimized parameter combinations by reducing the number of experiments [18, 19]. The Taguchi method is a low-cost, simple, and effective method to save time [19]. Therefore, experiment design was done using the Taguchi method in this study. Experimental design was planned using three different levels of three control factors. As a result, the total degree of freedom grade is equal to 6. Basically, the degree of freedom must be calculated in order to be able to select the appropriate index in the Taguchi method. In this study, since the degree of freedom is smaller than 9, there is no problem in selecting  $L_9$  Taguchi orthogonal array [19]. The effect of three important parameters for surface roughness of specimens was selected: mediums, forces, and feed rates. According to the Taguchi experimental design, nine experiments defined for three factors and three levels belong to each factor (Table 2). The factors and levels used in

**Table 2** Taguchi experimental design

	Medium	Force	Feed rate
1. Trial	1	1	1
2. Trial	1	2	2
3. Trial	1	3	3
4. Trial	2	1	2
5. Trial	2	2	3
6. Trial	2	3	1
7. Trial	3	1	3
8. Trial	3	2	1
9. Trial	3	3	2

**Table 3** Process parameters and their limits

Factors	Units	Levels		
		1	2	3
Burnishing medium	–	Dry	Boron oil	Mineral oil
Force	N	100	200	300
Feed rate	mm/min	0.05	0.1	0.2

the experiments are depicted in Table 3. For the analysis of the experimental results, the interactions between the main factors were not taken into consideration and the S/N ratio was calculated for each experiment.

### 2.2 Measurements

The surface roughness is used as a measure in determining the surface texture of the material [20]. After any test procedure applied to the workpiece, changes in the surface topography of the material occur at the micro level. The determination of these changes is very important in terms of the mechanical properties of the part [20]. Surface roughness helps to determine the performance of any mechanical component as having the strategic designation because surface irregularities can cause cracks or corrosion initiation. The surface roughness value is generally calculated by taking into account the arithmetic mean values of the absolute values ( $R_a$ ) [21]. Referring to Fig. 2, the  $R_a$  value can be expressed by the following equations:

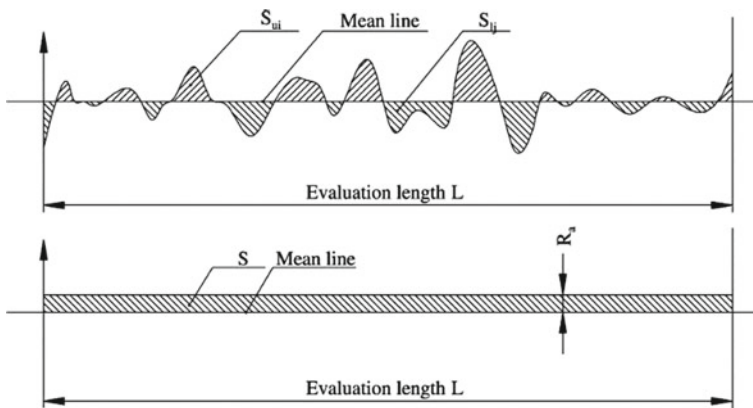


**Fig. 2** Scheme of surface roughness [21]

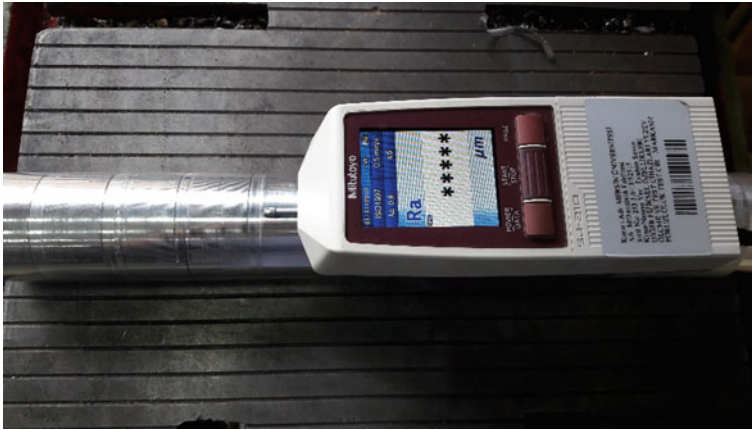


**Fig. 3** Surface roughness meter

$$R_a = \frac{1}{L} \int_0^L |y| dx = \frac{1}{L} \left( \sum S_{ui} + \sum S_{lj} \right) = \frac{S}{L} \tag{1}$$

Therefore,

$$R_a = R_t(S_u + S_l) \tag{2}$$

The surface roughness of the specimens is taken from five different parts of the Al 7075-T6 workpiece. Surface roughness tests were performed using a Mitutoyo portable roughness meter (Fig. 3).

### 3 Results and Discussion

#### 3.1 Experimental Results

The surface roughness values and calculated S/N ratios obtained after burnishing process to determine the surface roughness of Al 7075-T6 aluminum alloy in different parameters (force, feed rate, environment) are presented in Table 4.

The signal-to-noise ratios of the surface roughness obtained in the experiments were calculated, and the variation of the results according to the parameters is shown in Fig. 4. As a result of the tests performed, it is seen that the medium with the optimum surface roughness is the mineral oil medium. Subsequently, it is seen that surface roughness values obtained in experiments performed in boron oil medium and dry medium, respectively, are better. When the graph is examined, it is understood

**Table 4** Results of experiments and *S/N* ratio values

Experiments	Parameters			Results		
	Medium	Force	Feed rate	R <sub>a</sub> (μm)	Standard deviation	S/N R <sub>a</sub> (μm)
1	Dry	100	0.05	1.68	0.0682	-3.82343
2	Dry	200	0.1	0.61	0.0639	-2.54210
3	Dry	300	0.2	1.26	0.0425	-5.29636
4	Boron	100	0.1	1.33	0.0704	-3.72782
5	Boron	200	0.2	0.41	0.0550	-1.63415
6	Boron	300	0.05	0.86	0.0633	-2.75973
7	Mineral	100	0.2	2.12	0.0947	-3.07020
8	Mineral	200	0.05	0.79	0.0491	-3.40523
9	Mineral	300	0.1	0.20	0.0253	0.38176

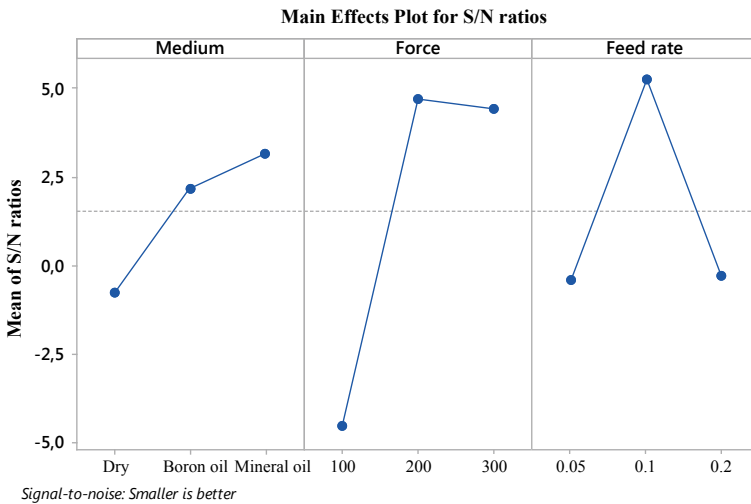


**Fig. 4** Change of surface roughness results to calculated signal-to-noise ratios

that surface roughness value generally decreases as the force value increases. The change in the surface roughness was negligible since the force value increased from 200 to 300 N. This is due to the increase of the compression on the surface of the Al 7075-T6 aluminum alloy workpiece and the processing of the subsurface layer by compression of the cavitation [22, 23]. The surface roughness value in experiments with a force value of 200 N is the most appropriate value. When the graph is analyzed in terms of progress, it is observed that the surface roughness value is the best in the case where there is no significant difference in the surface roughness values between the speed of progression of 0.05 and 0.2, but the speed of progression is



0.1. Considering the *S/N* ratio, the optimized parameters of burnishing process for fulfillment optimum surface roughness are the burnishing force: 200 N, medium: mineral oil, and feed rate: 0.1 mm/min. The *S/N* ratios to surface roughness results were obtained using the Minitab 18 program.

### 3.2 Analysis of Variance (ANOVA)

From ANOVA, the aim is to determine how the examined factors influence the selected output values to measure quality and how the different levels cause variability. According to the applied ANOVA in this study, it is observed that the burnishing medium (4.8%), the force (68.9%), and feed rate (15.6%) play roles in minimizing the surface roughness (Table 5). When the results of the tests applied to the Al 7075-T6 workpiece are analyzed, it is determined that the factor that most impresses the surface roughness value is the force. Contribution ratio of the burnishing parameters is shown in Fig. 5. The *F* test is used to determine which finishing parameters are more effective for outputs. In general, there is a relationship between the numerical

**Table 5** ANOVA results for surface roughness

Parameters	Degrees of freedom	SS	MS	<i>F</i> value	Contribution (%)
Burnishing medium	2	0.1507	0.07534	0.46	4.8
Force (N)	2	2.1310	1.06548	6.56	68.9
Feed rate (mm/min)	2	0.4834	0.24168	1.49	15.6
Error	2	0.3247	0.16234		
Total	8	3.0897			

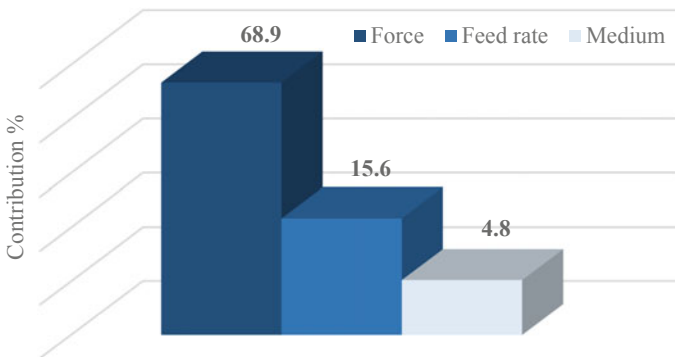


**Fig. 5** Contribution percentage of the burnishing parameters

value of  $F$  and the output effect of the burnishing parameters. The greater the numerical value of the  $F$  value of any parameter, the greater the effect of that parameter on the output. It has been determined that the most effective factor contributing to surface roughness is the burnishing force.

## 4 Conclusions

In this chapter, a study has been carried out on the improvement of the surface of the Al 7075-T6 workpiece by mechanical methods. Experiments were carried out using the burnishing process, which is one of the mechanical surface improvement processes. The Taguchi method was used in the experimental design. This method is preferred because it decreases the number of experiments and provides advantages in terms of time and money. The results obtained in this study in which different parameters (medium, force, and feed rate) are examined are given below.

- Optimum parameters were determined according to the analysis of the  $S/N$  ratios calculated by considering the surface roughness values. The optimum surface roughness according to the experiments was obtained in the following parameters: the burnishing force: 200 N, the medium: mineral oil, and feed rate: 0.1 mm/min.
- According to the results of ANOVA, the effect of the force on the surface roughness was 68.9%. Feed ratio and the effect of the medium on surface roughness are 5.6 and 4.8%, respectively. The force and feed rate are substantial for surface roughness of Al 7075-T6 workpiece material.
- Generally, the surface roughness of the Al 7075-T6 workpiece material used in the experiments is improved as the force increases. This is due to the increase of the compression on the workpiece surface and the processing of the subsurface layer by compression of the cavitation. However, as the force increases too much, the surface quality is beginning to deteriorate. The surface quality does not seem to be very good when the feed rate is low or high.
- The optimum surface roughness was derived from the experimental results in mineral oil medium. Boron oil is the medium where the best surface roughness value is obtained after mineral oil medium. The dry medium was also found to have the worst results.

## References

1. Zainol A, Yazid M (2018) Review of development towards minimum quantity lubrication and high speed machining of aluminum 7075-T6. *J Adv Manuf Technol* 12(1):129–142
2. Rao KSS, Allamraju KV (2017) Effect on micro-hardness and residual stress in CNC turning of aluminium 7075 alloy. *Mater Today Proc* 4(2):975–981

3. Maximov J, Anchev AP, Duncheva GV, Ganev N, Selimov KF (2017) Influence of the process parameters on the surface roughness, micro-hardness, and residual stresses in slide burnishing of high-strength aluminum alloys. *J Braz Soc Mech Sci Eng* 39(8):3067–3078
4. Kulakowska A, Kukielka L, Kaldunski P, Bohdal L, Patyk R, Chodor J, Kukielka K (2018) Burnishing rolling process of the surface prepared in the turning process. In: AIP conference proceedings, vol 1960, no 1, pp 070016-1–070016-6
5. Hemant S, Harish A, Bharadwaj RN, Bhat AB, Sriharsha C (2018) Design of roller burnishing tool and its effect on the surface integrity of Al 6061. *Mater Today Proc* 5(5):12848–12854
6. Yuan X, Sun Y, Li C, Liu W (2017) Experimental investigation into the effect of low plasticity burnishing parameters on the surface integrity of TA2. *Int J Adv Manuf Technol* 88(1–4): 1089–1099
7. Amdouni H, Bouzaiene H, Montagne A, Van Gorp A, Coorevits T, Nasri M, Iost A (2017) Experimental study of a six new ball-burnishing strategies effects on the Al-alloy flat surfaces integrity enhancement. *Int J Adv Manuf Technol* 90(5–8):2271–2282
8. Patel KA, Brahmabhatt PK (2015) Surface roughness prediction for roller burnishing of Al alloy 6061 using response surface method. *Int J Sci Eng Res* 6(3):636–640
9. Pacana A (2018) Application of function of quality losses G. Taguchi for study of roller burnishing parameters. In: MATEC web of conferences, vol 183, p 03007
10. Rodríguez A, de Lacalle LL, Celaya A, Lamikiz A, Albizuri J (2012) Surface improvement of shafts by the deep ball-burnishing technique. *Surf Coat Technol* 206(11–12):2817–2824
11. Buldum BB, Bayhan B (2018) Effect of ball-burnishing parameters on surface roughness and surface hardness of aluminum alloy 6013. *Mater Test* 60(4):418–422
12. Ugurlu M, Cagan SC, Buldum BB (2017) Improvement of surface roughness using ANOVA for AZ31B magnesium alloy with ball burnishing process. *Int J Engine Res Technol* 6(9):216–221
13. Amini S, Bagheri A, Teimouri R (2018) Ultrasonic-assisted ball burnishing of aluminum 6061 and AISI 1045 steel. *Mater Manuf Process* 33(11):1250–1259
14. Ye H, Lai L-S, Li J, Liu S-Z, Xiong H (2018) Surface properties of 7075 aluminum alloy workpieces after ultrasonic burnishing processing. *Surf Technol* 2:002
15. López de Lacalle LN, Rodríguez A, Lamikiz A, Celaya A, Alberdi R (2011) Five-axis machining and burnishing of complex parts for the improvement of surface roughness. *Mater Manuf Process* 26(8):997–1003
16. García-Granada AA, Gomez-Gras G, Jerez-Mesa R, Travieso-Rodríguez JA, Reyes G (2017) Ball-burnishing effect on deep residual stress on AISI 1038 and AA2017-T4. *Mater Manuf Process* 32(11):1279–1289
17. Denkena B, Grove T, Maiss O (2017) Surface texturing of rolling elements by hard ball-end milling and burnishing. *Int J Adv Manuf Technol* 93(9–12):3713–3721
18. Cicek A, Kivak T, Ekici E (2015) Optimization of drilling parameters using Taguchi technique and response surface methodology (RSM) in drilling of AISI 304 steel with cryogenically treated HSS drills. *J Intell Manuf* 26(2):295–305
19. Dehnad K (2012) Quality control, robust design, and the Taguchi method. Springer Science & Business Media
20. He C, Zong W, Zhang JJ (2018) Influencing factors and theoretical modeling methods of surface roughness in turning process: State-of-the-art. *Int J Mach Tools Manuf* 129:15–26
21. Aldas K, Ozkul I, Akkurt A (2014) Modelling surface roughness in WEDM process using ANFIS method. *J Balkan Tribol Assoc* 20(4):548–558
22. El-Taweel T, El-Axir M (2009) Analysis and optimization of the ball burnishing process through the Taguchi technique. *Int J Adv Manuf Technol* 41(3–4):301–310
23. Nemat M, Lyons A (2000) An investigation of the surface topography of ball burnished mild steel and aluminium. *Int J Adv Manuf Technol* 16(7):469–473

# A Review on 4D Printing—the Next Industrial Revolution



L. Vamsi Krishna Reddy and Kode Jaya Prakash

**Abstract** Additive manufacturing is initially developed to meet the needs in the field of aerospace engineering. As the cost of sending a component into the space to replace the failed part is more than the actual cost of the product the researchers started working on printing machines. This effort of the researchers and research organization bought a 3D printing machine into the picture. Taking the 3D model as reference, the 3D printing machine prints the component by adding the material in layers. Later, the application of 3D printing was extended in many fields like medicine, automobile, and textile industry. Taking a step forward, a private research organization in Cambridge, Massachusetts institute of technology (MIT), has developed a 4D printing machine in 2013. 4D printing is printing a 3D component with smart material to add a fourth dimension called intelligence. Hence, this gave rise to programmable printing. This paper deals with 4D printing technology, materials suitable for printing the component, materials that add strength to the component, applications, challenges, and future scope.

**Keywords** 3D printing · 4D printing · Additive manufacturing · Fourth dimension · Smart materials · Programmable printing

## 1 Introduction

4D printing was developed by a private research organization, The Massachusetts institute of technology (MIT) of Cambridge in 2013 [1–3]. 4D printing is printing a 3D component with a smart material to add a fourth dimension called intelligence. The basic difference between 3D & 4D printing is the 3D printing technology produces a rigid model which remains rigid throughout the product lifetime. Whereas

---

L. Vamsi Krishna Reddy (✉)  
Srinivasa Ramanujan Institute of Technology, Anantapur, India  
e-mail: [vamsi.mech306@gmail.com](mailto:vamsi.mech306@gmail.com)

Kode Jaya Prakash  
V.N.R. Vignana Jyothi Institute of Engineering & Technology, Hyderabad, India  
e-mail: [kodejayaprakash@gmail.com](mailto:kodejayaprakash@gmail.com)

© Springer Nature Singapore Pte Ltd. 2020  
L. Vijayaraghavan et al. (eds.), *Emerging Trends in Mechanical Engineering*,  
Lecture Notes in Mechanical Engineering,  
[https://doi.org/10.1007/978-981-32-9931-3\\_32](https://doi.org/10.1007/978-981-32-9931-3_32)

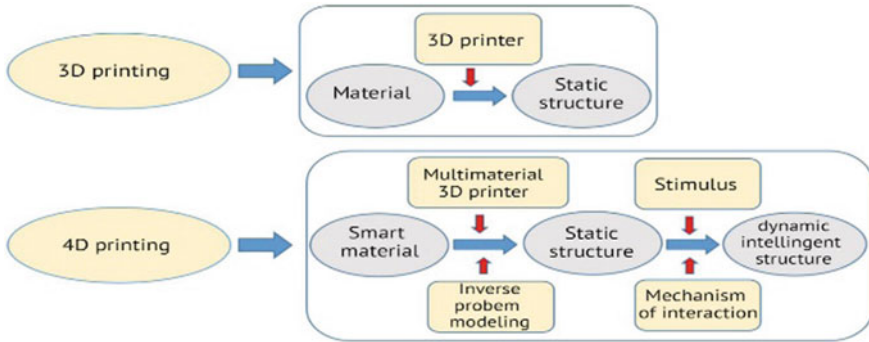


Fig. 1 Flowchart of 3D and 4D printing sources

the components printed using 4D printing technology will have a flexible, dynamic, and intelligent structure because of its smart materials used and its kinematic design. Figure 1 shows the difference between 3D and 4D printing technology.

Generally, smart materials are printed in the key areas in order to obtain the desired structure [4, 5]. 4D printing can be done in 3D printing machine with the help of two or more smart materials. The printing of smart material will help in obtaining the special properties like stretching, twisting, and bending. Figure 2 will show the flat plate that forms a cube when dipped in water.

4D printing follows the same layer-by-layer printing technique that is done in the 3D printing. The only thing that makes the 4D printing different from the 3D printing is its programmable printing with the help of smart materials which are aligned, controlled, and oriented in different key areas. Figure 3 shows the printing of smart material in key areas. Taking special care while printing the material in key areas will give best results.

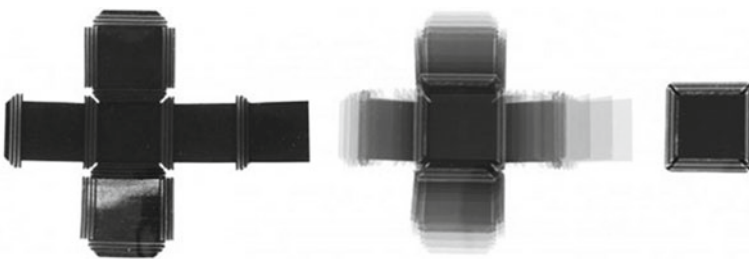
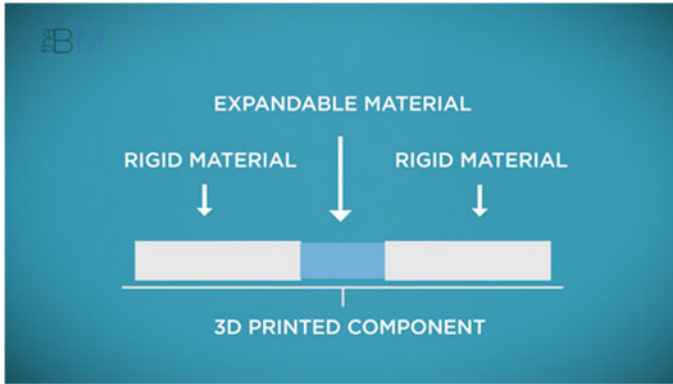


Fig. 2 Self-folding of a flat plate into a cube in water printed by using 4D printing technology



**Fig. 3** Printing of smart material in key areas using 4D printing

## 2 Materials Suitable for 4D Printing

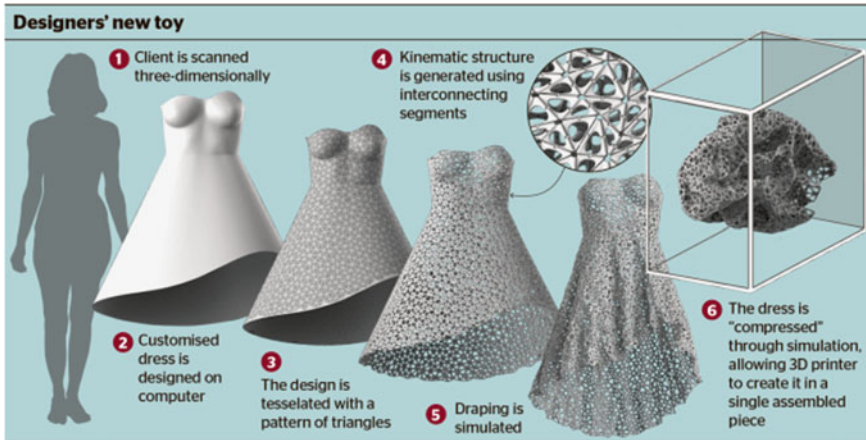
Generally, smart materials are used for 4D printing [6–11]. Smart materials are designed materials which show different properties at different working conditions. The smart materials usually change their properties with respect to temperature, pressure, pH value, stress, and application of electric and magnetic fields. Depending on the physical behavior, chemical composition, and reaction to the external environment, the smart materials are classified as piezo-electric material, shape memory alloys, magnetostrictive materials, pH-sensitive polymers, temperature-responsive polymers, halochromic materials, chromogenic materials, photomechanical materials, photochromic materials, self-healing materials, smart gels, etc. The selection of material depends upon the type of component required.

### 2.1 Applications in Various Fields

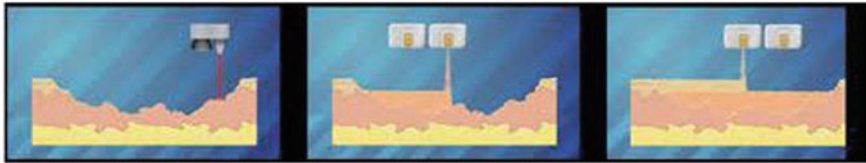
4D printing has a wide range of applications in the field of medicine, aerospace, textile, manufacturing, jewelry making, etc [12–14]. The main advantage of 4D printing is the component which is much larger than the printing machine can be printed by compressing through computational folding and can be enlarged due to its kinematic structure.

Figure 4 shows a dress of women that is folded by computational folding and printed in its compressed state.

The Wake forest university's Military research Centre has already developed a skin-printing machine in order to heal the burnt wounds [15]. The wound is first scanned by the 3D scanner, and then the layers of skin are printed on the wound. This method of skin printing with the help of cells eliminates the extraction of skin from donor site on the body. Figure 5 shows the three stages of skin printing.



**Fig. 4** Computational folding of a dress designed with kinematic linkage for 4D printing



**Fig. 5** Three stages of skin printing (scanning, printing first layer of skin, printing second layer of skin) using 4D printing technology

## 2.2 Working of 4D Printed Components

The shape memory alloys are deposited at the key areas of the component by carefully controlling the location and orientation of fiber which fold, twist, curl, or stretch in the expected manner when placed in the working medium [16–18]. As a part of research, the students of MIT have developed a single stand that folds into MIT when dipped into the water and regains its shape when removed from water. This property is achieved because of shape memory alloy that is used for printing the structure. Later, it was extended to other components. Figure 6 shows a flat surface that folds into truncated octahedron when dipped into the water. The component is printed with two different materials in order to obtain the required self-folding property. Polypyrrole forms a hard but flexible matrix that provides structural strength to the component and all the edges are printed with polyol-borate a soft gel that swells when it absorbs water. As a result of this material combination, the flat surface folds into truncated octahedron when dipped into water and regains its flat structure by ejecting the water when removed from the working medium. The ionic covalent entanglement (ICE) gel is used in 4D printing in order to avoid the mechanical failures and cracks. The use of

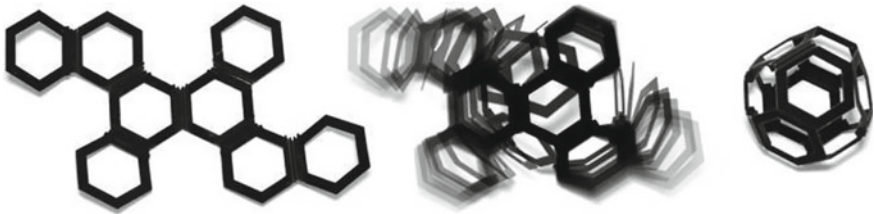


**Fig. 6** 4D printing of a self-folding truncated octahedron

these gels will save the material up to 20%. The material selection, application, and working vary with respect to the material used, working medium, and application.

### 2.3 Strength and Weakness of 4D Printing

The following are the strength and weakness of 4D printing as mentioned in Table 1 as follows:

**Table 1** Strength and weakness of 4D printing

S. No.	Strength	Weakness
1	Efficiency of material, manufacturing process and positive market growth forecast	New technology in the field of 3D printing
2	Multi-color print, multi-material print	Smart materials are expensive and limited
3	Smart material (programmable material)	Accuracy in shape change, complex shapes
4	Multi-color print, multi-material print	Smart materials are expensive and limited
5	Smart material (programmable material)	Accuracy in shape change, complex shapes

### 2.4 Opportunities and Threats of 4D Printing

The following are the opportunities and threats of 4D printing as mentioned in Table 2 as follows:



**Table 2** Opportunities and threats of 4D printing

S. No.	Opportunities	Threats
1	Helps in logistic problems and transportation	Machine compatibility
2	Helpful in extreme places, i.e., warzone and space	Public safety and health problems
3	Useful for implants and medical field	Impact on environment, ethical issues and system vulnerable to software hack, piracy
4	Multi-color print, multi-material print	Smart materials are expensive and limited
5	Concept of smart city, buildings, and structures	Intellectual property rights, copyright, patent, and trademark

## 2.5 Limitations

- 4D printing is a time-consuming and expensive method of printing.
- A wide knowledge of materials and its behavior under working medium should be studied.
- There is a difficulty in orientating, controlling, and aligning the materials at the key areas.
- Adhesion between two different materials needs to be studied thoroughly.
- A wide study of external forces and extent that should be applied to get the required self-folding structure should be studied thoroughly.
- Recycling of components is difficult.
- The durability of smart nature of material cannot be predicted.

## 2.6 Future Scope

- In the field of medicine, there is a future scope of printing all the organs of human body with the cells of the patient who is in need of organ replacement. This eliminates the need and difficulty of searching for donor.
- In the field of aerospace engineering, an aerodynamic structure of planes can be designed with smart materials which change its structure with respect to temperature and pressure.
- In the field of textile industry, there is a scope of developing a multi-seasonal dust-proof textile which can expand and contract with respect to temperature and can be elongated or compressed depending on the requirement.
- In the field of manufacturing, universally suitable components can be printed by making the use of size increasing property of smart materials.
- Tyres that change their shape depending on the road conditions can be developed.
- Self-healing materials can be used for construction of roads and bridges.

## 2.7 Conclusion

4D printing has made a revolutionary change in the field of medicine, aerospace, textile industry, automobile industry, etc. Invention of smart materials and speeding up of printing method may help in improving the production, decreasing the wastage, eliminating the mechanical failure of structure, predicting the life expectancy of the product, designing the aerodynamic structures of aerospace components, printing of human organs, etc. However, a rapid growth in the field of additive manufacturing is a remarkable change which leads the technology to take a step forward in the field of manufacturing.

## References

1. Eujin P (2014) 4D printing - revolution or fad. *Assembly Autom* 34:123–127
2. Eujin P (2014) 4D Printing: dawn of an emerging technology cycle. *Assembly Autom* 34: 310–314
3. Ge Q, Dunn C, Qi H (2014) Active origami by 4D printing. *Smart Mater Struct* 23:187–197
4. Ge Q, Qi H, Dunn M (2013) Active materials by four-dimension printing. *Appl Phys Lett* 103:1–5
5. Walton Z (2013) 4D printing is the future of 3D printing and it's already here. *WebPro New*
6. Tibbits, S (2013) 4D printing multi-material shape change. *Architectural Design High Definition* 116–121
7. Wei F, Zhang H, Zhang X (2006) The application and development of intelligent materials. *Mater Rev* 20:375–379
8. Ge Q et al (2014) Active origami by 4D printing. *Smart Mater Struct* 23:094007
9. Khoo ZX et al (2015) 3D printing of smart materials: a review on recent progresses in 4D printing. *Virtual Phys Prototyping* 10:103–122
10. Figuring TI Curved crease origami, <http://www.theiff.org/oexhibits/paper04.html>. Retrieved on 2016/07/21
11. Goldy Katal NT (2013) Digital light processing and its future applications. *Int J Sci Res Publications* 3(4) (2013)
12. Mearian L How 4D printing is now saving lives, <http://www.coputerworld.com/article/3071666/3d-printing/how-4d-printing-is-now-saving-lives.html>. Retrieved on 2016/07/20
13. Org P Materials science, <https://phys.org/news/2016-06-self-assembly-shape-changing-smart-material.html>. Retrieved on 2016/07/05
14. Shannon E, Bakarich RG (2015) 4D printing with mechanically robust. Thermally actuating hydrogels. Wiley Online Library, New Jersey, USA
15. Aniwaa (2014) Objet260 Connex3 Stratasys-3D printer, <http://www.aniwaa.com/product/3d-printers/stratasys-objet260-connex3/>. Retrieved on 2017/05/08
16. Novel HU WYSS Institute. 4D printing method blossoms from botanical inspiration, <https://wyss.harvard.edu/novel-4d-printing-method/>. Retrieved on 2016/07/20
17. EBM electron beam melting-in the forefront of additive manufacturing, <http://www.arcam.com/technology/electron-beam-melting/>. Retrieved on 2016/03/06
18. Etherington D Techcrunch, <https://techcrunch.com/2016/10/11/mits-new-software-makes-multi-material-3d-printing-easy/73>. Retrieved on 2017/05/02

# Parametric Investigations on Friction Stir Welding of Aluminium Alloys



Bazani Shaik, G. Harinath Gowd and B. Durgaprasad

**Abstract** FSW process are widely used in various automobile and aerospace industries nowadays, which encouraged us to take up this work for doing research. This paper reports the experimental investigations on the effects of process parameters, i.e., tool rotational speed, weld speed and tilt angle on the responses, i.e., tensile strength, impact strength, and elongation in dissimilar welding of Aluminum alloys of different grades using the solid-state welding technique Friction Stir Welding process. In view of the costlier process, Taguchi L9 is used for carrying out the research. As it is a complex process, to identify the significant variables, initial trial experiments are done on the same parent materials. Based on them, ranges are also found out for each input process parameter. A total of three input process parameters (tool rotational speed, weld speed, and tilt angle) are chosen for study and the output responses measured are tensile strength, impact strength, and elongation. ASTM standards are used in preparing the work pieces. After measuring its output responses, main effects are studied between the input process parameters versus output responses. This analysis can be further used in predicting the empirical equations with which the process can be automated based on the optimal values and microstructural investigations done.

**Keywords** Friction stir welding · Aluminum alloys · Square tool · Taguchi L9 · Microstructural investigations

## 1 Introduction

Friction stir welding nowadays is widely using in aircraft industries for welding wings, fuel tanks, aircraft structure, and marine industries in structure work, automotive industries to weld wheel rims, chassis, fuel tanks, chemical industries for

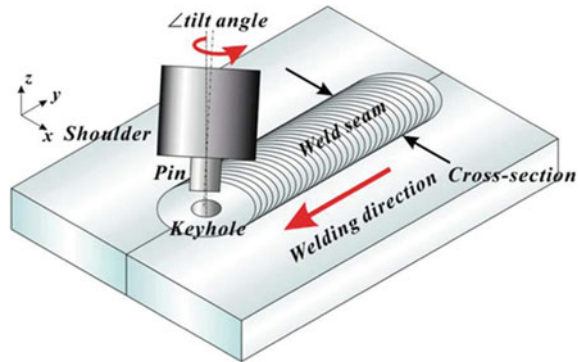
---

B. Shaik (✉) · G. Harinath Gowd · B. Durgaprasad  
Department of Mechanical Engineering, JNTUA, Anantapur 515002, India  
e-mail: [bazanimits@gmail.com](mailto:bazanimits@gmail.com)

G. Harinath Gowd  
Department of Mechanical Engineering, Madanapalle Institute of Technology & Sciences,  
Madanapalle 517325, India

© Springer Nature Singapore Pte Ltd. 2020  
L. Vijayaraghavan et al. (eds.), *Emerging Trends in Mechanical Engineering*,  
Lecture Notes in Mechanical Engineering,  
[https://doi.org/10.1007/978-981-32-9931-3\\_33](https://doi.org/10.1007/978-981-32-9931-3_33)

**Fig. 1** Schematic diagram of friction stir welding process



joining pipelines, heat exchanger, air conditioner, electronic industries for joining bus bar, aluminum to copper, connectors, electronic equipment fabrication industries, etc. The advantage of friction stir welding is that it can be used to weld both similar and dissimilar metals having no flux and no filler metal [1]. Also, the entire process consumes less power consumption, can be made automated easily, less maintenance is required, process easy to operate and environmental pollution-free. The principle of operation is for without reaching melting point of material for soften tool pin and tool shoulder enables deformation of heat for low plasticized material. The work piece material and rotating tool generates friction and joining the work pieces nonconsumable tool is used shown in (Fig. 1).

The base materials heating takes place because of plasticity by friction force, deformation of joining process with rotating tool takes place and the continuous weld is formed. The shoulder of weld direction is on the advancing side. The shoulder which moves opposite direction is on retreating side and different parameters play a major role of input parameters on tool as rotational speed rpm, line at rotating tool on welding speed mm/min, tool tilt angle degree. The welding material mainly affected due to heat on mechanical deformation and welding unaffected material zone with no deformation. The heat effects of different zones occur on heat-affected zone involves unaffected zone and thermos mechanical affected zone.

## 2 Literature Survey

Various related studies are present in this section and are as follows. Patel et al. [2] are investigated corrosion resistance of alloy structural of structure grains turns stronger alloy and having development of aluminium alloys at fatigue resistance of aluminum alloys of complex structures of development and application of arc electric and extrusion constructions civil. Das and Toppo [3] studied of thickness 3 mm AA6061-T6 of temperature metal and melt and welding speed, micro hardness, and rotational speed. Dalwadi et al. [4] are investigated joining of dissimilar

metals of Al6351T6 and Al6101T6 of 12 mm plates of welding speed 16 mm/min, rotational speed 900 rpm and fracture of fibrous pattern examine of scanning electron microscope. Fallahi et al. [5] of modeling process method taguchi studied the modeling process of taguchi method, composition factor method, grey relation analysis, response surface methodology observed and Design experiments are capable reliable tools [6] examined behavior propagation scattering velocities waves guided of brass plates of welds material scattering of different zones crack of smooth. KepiGangway [7] studied metallographic of welding speed 40 mm/min of values time travel on process of friction stir welding. Moradi et al. [8] suggested industry of aerospace on temperatures of titanium plates and sheets of sizes of tool and composition material of zone nugget and challenges of evolution texture of microstructural and mechanical properties. Pabandi et al. [9] examined dissimilar aluminum alloys technique and structural changes AA6061 and AA2024 of different grain structures and crystallization of identical profile. Based on the literature survey, the research gap is found that FSW is a suitable process for getting welds with high quality. Hence the present work focused mainly on finding the relationship between the input and output variables so that the entire process can be further optimized based on this experimental data. The literature covers mainly the experimental investigations and its effects on the output responses. To improve the process more focused research should be carried out on the parameters in FSW process. This gap is being covered with the proposed work.

### 3 Experimental Work

The experiments are carried out on the Friction Welding Setup and maximum load capacity of the machine is 5 Tones. The dissimilar butt welding samples are prepared on the two base materials, i.e., AL7075-T651 and AL6082-T651 using the FSW setup which is controlled with the help of a computer unit. The experiments are carried out over the FSW unit as per the experimental design prepared using Taguchi method. A total of 9 experiments are carried out based on L9 orthogonal array method. Figure 2 gives the ready to weld position after fixing and aligning the two-parent materials using the special made fixtures which helps to hold the work pieces in positions.

AL7075-T651 and AL6082-T651 are chosen as the work piece materials because of the growing importance in terms of its usage in many aerospace and automobile industries.

Figure 3 shows the butt welded samples.

The chemical compositions of base materials are given in Table 1 and its mechanical properties are listed in Table 2.

The plates were finished to a dimension of 100 mm × 50 mm × 6 mm. A butt weld is being made by clamping the materials using fixtures by placing AA7075 and AA6082 on Advancing Side and Retreating Side, respectively, by opting the parametric values as mentioned in central composite design matrix. The M2 Grade SHSS tool is used for experimentation having shoulder dia 18 mm and probe length 6 mm. The specimens used are prepared as per the ASTM Standards. Out of two

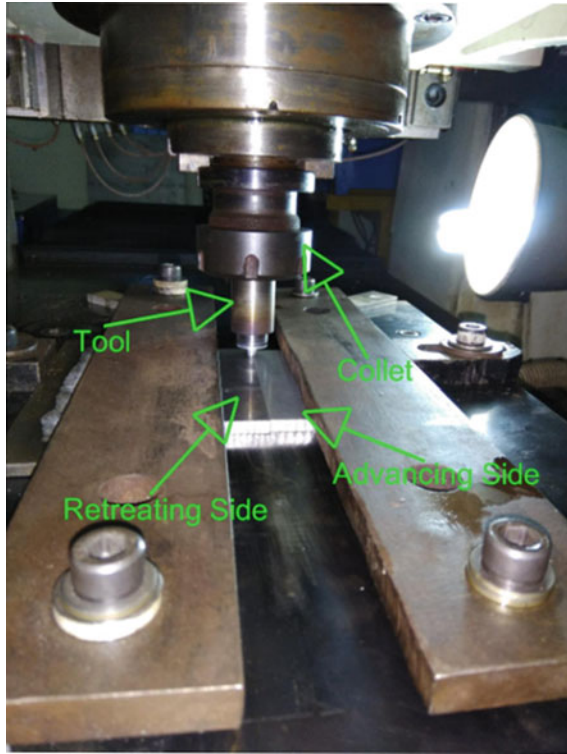


Fig. 2 FSW setup weld position

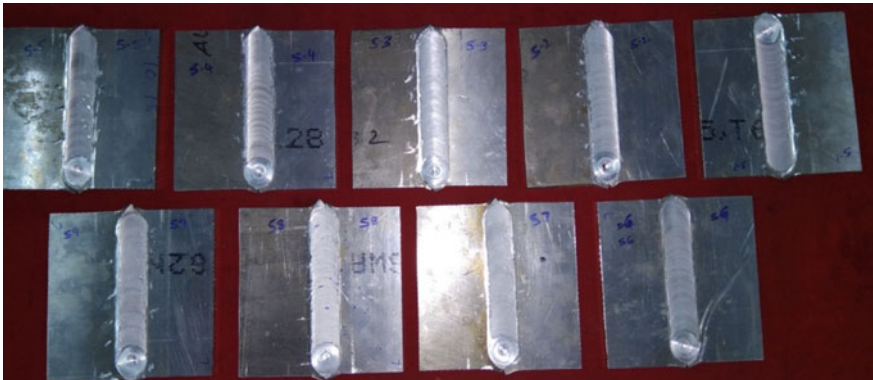


Fig. 3 Butt welded samples

**Table 1** Chemical composition of 7075-T651 and 6082-T651 Al alloys (wt%)

Elements	Si	Fe	Cu	Mn	Mg	Cr	Ni	Zn	Ti	Al
Al7075-T651	0.12	0.2	1.4	0.63	2.53	0.2	0.004	5.62	0.03	89.26
Al6082-T651	1.05	0.26	0.04	0.68	0.8	0.1	0.005	0.02	0.01	97.03

**Table 2** Mechanical properties of Aluminum Alloys

Al alloy	Tensile Strength (MPa)	Impact Strength (J)
7075-T651	220	17
6082-T651	330	10

base materials used, Al7075-T651 placed in the advancing side and Al6082-T651 placed in the retreating side in order to improve mechanical properties of Joint. The butt joints in total of 9 are prepared as per the taguchi L9 design experiment. For conducting the experiments only, the major influencing parameters are taken into consideration, as the minor influencing parameters account to the less variations in output responses. Major influencing parameters are identified based on the literature survey and also based on the trail experiments. The parameters chosen and its ranges and various other notations are given in Table 3.

In this research, Tool rotational speed, welding speed, and Tilt angle are the three significant process parameters chosen to vary. After completion of experiments, the output responses are measured and recorded and is shown in Table 4. In order to measure the output responses, the welded specimens are prepared using metallographic techniques. Hydro Fluoric Solution is used as the etching agent. Each output is measured at three different points along the weld zone and the averages of three

**Table 3** The coded and actual values of input variables

S. No.	Parameters	Notation	Unit	Levels		
				1	2	3
1	Rotational speed	<i>RS</i>	rpm	1150	1250	1350
2	Welding speed	<i>WS</i>	mm/min	40	50	60
3	Tilt angle	<i>TA</i>	°	1	2	3

**Table 4** Experimental Design of Taguchi Model

S. No.	Rotational speed	Weld speed	Tilt angle	Tensile strength	Impact strength
1	1150	40	1	142.00	7.80
2	1250	50	1	181.20	9.45
3	1350	60	1	175.00	10.40
4	1150	40	2	153.00	7.40
5	1250	50	2	165.10	9.50
6	1350	60	2	160.20	8.10
7	1150	40	3	155.00	9.00
8	1250	50	3	160.00	7.40
9	1350	60	3	158.00	8.00



values are calculated and are taken as the final value which is recorded. Microstructural examination and material mixing observation were carried out using optical microscope.

## 4 Analysis of Input Process Parameters Over Output Responses

The plots were drawn between the selected inputs (i.e., Rotational speed, Weld speed, and tilt angle) and the chosen output responses, i.e., Tensile strength, Impact strength and elongation. The experimental data is used for plotting the graphs and are shown below. Only the main effects are studied.

### 4.1 Influence of Rotational Speed on Tensile Strength

The influence of rotational speed over the tensile strength is shown in (Fig. 4). It is shown that as the tool rotational speed increases, the tensile strength increases and it reaches a maximum of 168.76 MPa at the tool rotational speed of 1250 rpm. Afterwards it decreases. The lower rotational speed 1150 rpm with tensile strength 150 MPa produce insufficient heat input and also affects the tensile properties.

### 4.2 Influence of Weld Speed on Tensile Strength

The influence of weld speed over the tensile strength is shown in (Fig. 5).

The variation of tensile strength with welding speed at different constant rotary speed is presented in Fig. 5. It is evident from the plotted graph that, with the increase in welding speed 60 mm/min with 164.4 MPa tensile strength increases and then decreases at all rotary speeds. On the other hand, the trend of variation of tensile strength with different constant welding speeds is opposite to that of the welding speed.

**Fig. 4** Effect of tool rotational speed on tensile strength

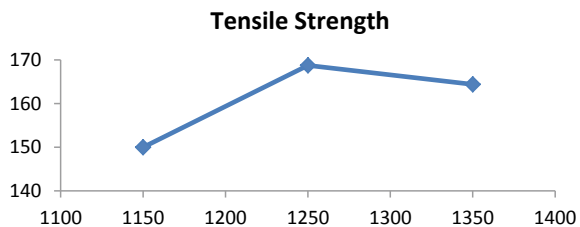


**Fig. 5** Effect of weld speed on tensile strength

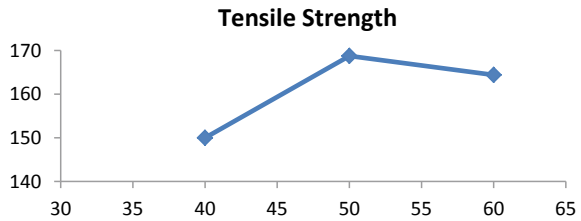
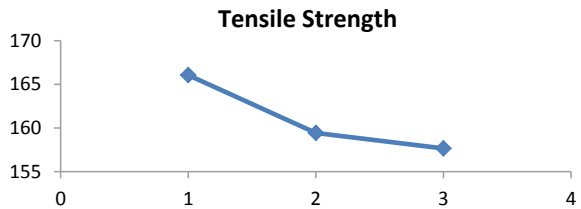


**Fig. 6** Effect of tilt angle on tensile strength



### 4.3 Influence of Tilt Angle on Tensile Strength

The influence of tilt angle over the tensile strength is shown in (Fig. 6).

The decrease of tool tilt angle 1° with tensile strength 166.067 MPa leads to poor bonding due to high frictional heat generation and the increase in tilt angle 3° with impact strength 157.667 MPa leads to poor bonding due to very low frictional heat generation.

### 4.4 Influence of Rotational Speed on Impact Strength

The influence of rotational speed over the impact strength is shown in (Fig. 7).

During low rotation speeds of 1150 rpm with Impact Strength 8.066 J, the desired amount of heat to make the proper welds is not generated and therefore the obtained welds have lower mechanical properties, in contrast, higher rotational speed 1350 rpm with impact strength 8.833 J leads to higher friction between the tool and sample, therefore, more heat is generated and the softening of materials is enhanced.

**Fig. 7** Effect of rotational speed on impact strength

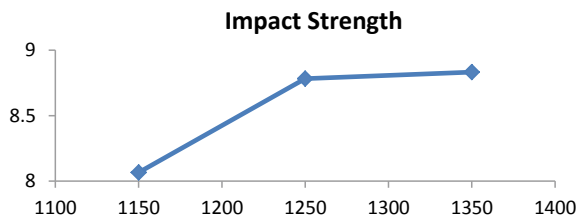


**Fig. 8** Effect of weld speed on impact strength

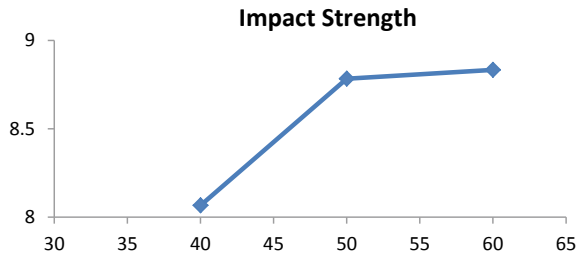
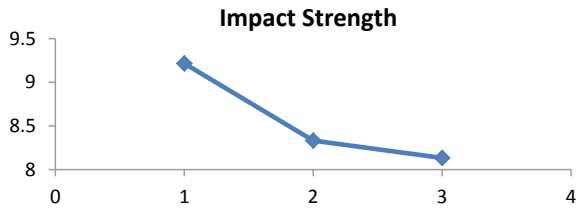


**Fig. 9** Effect of tilt angle on impact strength



#### ***4.5 Influence of Weld Speed on Impact Strength***

The influence of weld speed over the impact strength is shown in (Fig. 8).

The higher Weld Speed 60 mm/min with Impact Strength 8.833 J means a shorter welding duration, in this type of situation, there will not be enough time for mixing and joining the process of materials therefore by minimizing the Weld Speed 40 mm/min with Impact Strength 8.066 J more time is given to materials to soften and mixed.

#### ***4.6 Influence of Tilt Angle on Impact Strength***

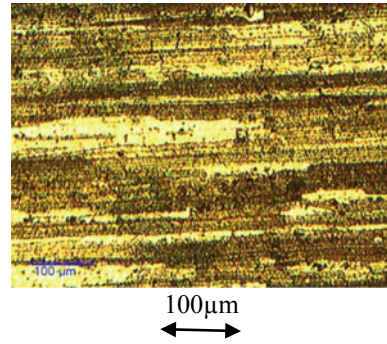
The influence of tilt angle over the impact strength is shown in (Fig. 9).

The impact strength reduces 8.13 J with the increase 3° in tilt angle. At lower tilt angles 1° the impact strength 9.2 J is more and it gradually reduces with a gradual increase of tool tilt angle, while keeping the other rotational speed and weld speed constant.

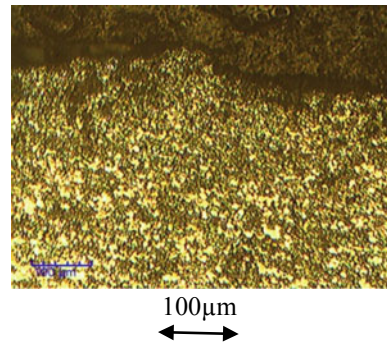
### **5 Microstructural Investigations**

Figure 10 shows microstructures of magnification 100X and etchant hydrofluoric solution used its Shows microstructure of AA 7075 parent metal at the advancing

**Fig. 10** AA 7075 parent metal on advancing side



**Fig. 11** Shoulder zone of eutectic constituents



side of the FSW process. The parent metal shows microstructure in rolled temper condition. The sheet has been cold worked by rolling process, and the primary grains of alpha aluminum are elongated along the direction forming. The eutectic constituents like  $\text{Cu-Al}_2$ ,  $\text{Mg}_2\text{Si}$ ,  $\text{Zn-Al}_2$ , and  $\text{Mg-Al}_2$  precipitated along the rolling direction and elongated. Figure 11 shows the shoulder zone of the FSW process and the metal matrix undergone fragmentation due to the stirring and the frictional heat of the process facilitated the dissolution of the eutectic constituents of two 7075 of advancing side and retreating side. Complete dynamic re-crystallization of the two observed. Figure 12 shows the thermomechanical transformation zone of the AA 7075 where the heat of the process increases the plasticity of the parent metal and metal has undergone plastic deformation in the direction of tool. The direction of the grains at the nugget zone is perpendicular to the parent metal grains of 7075. The flow of grains shows marginal plasticity caused due to temperature at this zone and due to mechanical parameters. The eutectic constituents have also undergone deformation. Figures 13 and 14 show two microstructures of the nugget zone at different locations of top and bottom. Figure 15 shows the interface zone of the retreating side with 7075 and the nugget zone. The left is 7075 and right is the nugget zone and center line is the fusion line. Figure 16 shows the retreating side heat-affected zone with deformed grains due to the heat of the process. Partial recovery of the grain had taken place. Figure 17 shows microstructure of AA 7075 parent metal at the retreating side of

**Fig. 12** Thermo mechanically treated zone of AA7075

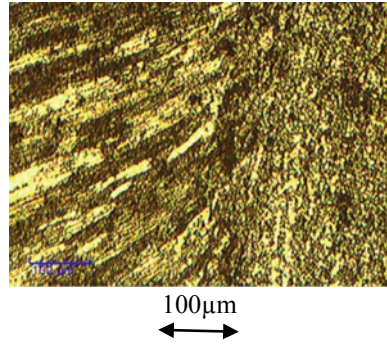


**Fig. 13** Nugget zone at top

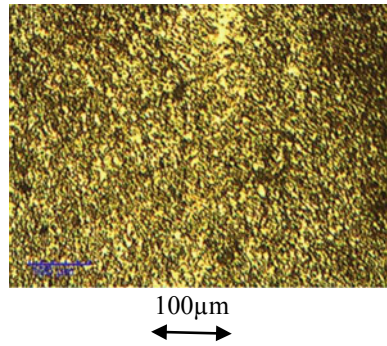
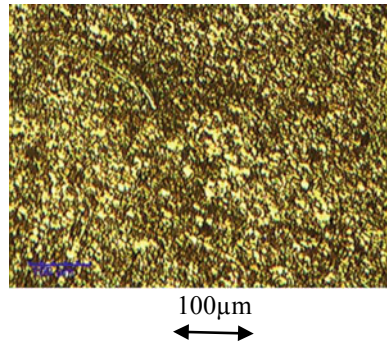


**Fig. 14** Nugget zone at bottom



the FSW process. The parent metal shows microstructure in rolled temper condition. The sheet has been cold worked by rolling process, and the primary grains of alpha aluminum are elongated along the direction forming. The eutectic constituents like  $\text{Cu-Al}_2$ ,  $\text{Mg}_2\text{Si}$ ,  $\text{Zn-Al}_2$ , and  $\text{Mg-Al}_2$  precipitated along the rolling direction and elongated.

**Fig. 15** Interface zone

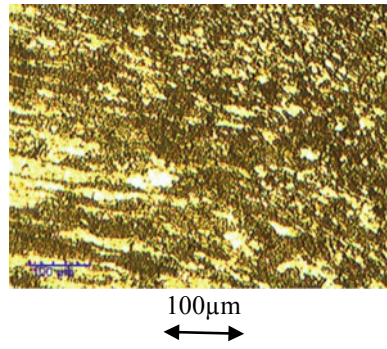


**Fig. 16** Heat affected zone

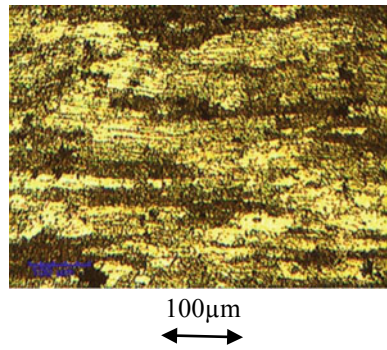
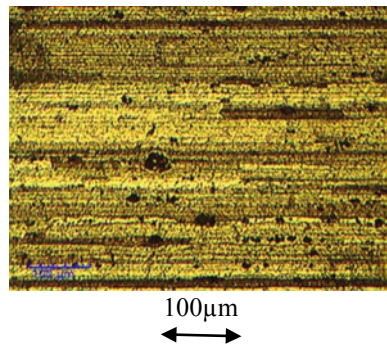


**Fig. 17** Elongated of rolling direction



## 6 Conclusions

In this work, the important weld strength characteristics, i.e., tensile strength, impact strength is analyzed after conducting experiments using the Friction Stir welding setup. The 2d plots are analyzed and found that the selected input process of Tilt angle  $1^\circ$  with Impact strength 9.2 J of best output response, rotational speed of 1350 rpm

with 164 MPa tensile strength and weld speed 60 mm/min with 8.8 J of Impact strength parameters are influencing over the output responses. That is using the experimental data empirical models can be developed and then these models can be used for finding the optimal process parameters to get the best output characteristics of welded joints. Then the problem can be solved by using any optimization algorithm after formulating the objective function. Later the entire process can be automated which helps to increase the product rate without increasing the unit cost of the welded joints and microstructural changes of Nugget Zone Top and bottom, TMT zone of the AA 7075T651 where the heat of the process increases the plasticity of the parent metal and metal has undergone plastic deformation in the direction of tool and eutectic constituents of Cu–Al, Mg–Al, Mg–Si of different grains formation is developed.

## References

1. Ma ZY, Feng AH, Chen DL, Shen J (2017) Recent advances in friction stir welding/processing of aluminum alloys: microstructural evolution and mechanical properties. *Crit Rev Solid State Mater Sci*. <https://doi.org/10.1080/10408436.2017.1358145>
2. Patel AR, Dhruval J et al (2018) Investigation of mechanical properties for hybrid joint aluminium to polymer using friction stir welding. *Mater Today Proc* 5:4242–4249
3. Das U, Toppo V (2018) Effect of tool rotational speed on temperature and impact strength of friction stir welded joint of two dissimilar aluminum alloys. *Mater Today Proc* 5:6170–6175
4. Dalwadi CG, Patel AR, Kapopara JM, Kotadiya DJ, Patel ND, Rena HG (2018) Examination of mechanical properties for dissimilar friction stir welded joint of Al alloy (AA-6061) to PMMA (Acrylic). *Mater Today Proc* 5:4761–4765
5. Fallahi AA, Shokuhfar A, Moghaddam AO, Abdolazadeh A (2017) Analysis of SiC nanopowder effects on friction stir welding of dissimilar Al–Mg alloy to A316L stainless steel. *J Manuf Process* 30:418–430
6. Morgan R, Thirumalaisamy N (2018) Experimental and numerical analysis of friction stir welded dissimilar copper and bronze plates. *Mater Today Proc* 5
7. Kepingway MR (2017) Friction stir, welding of titanium alloys, Jade. <https://doi.org/10.1016/j.matdes.2017.12.033>
8. Moradi MM, Aval HJ, Jamaati R, Amir Khanlou S, Ji S (2018) Microstructure and texture evolution of friction stir welded dissimilar aluminum alloys: AA2024 and AA6061. *J Manuf Process* 32:1–10
9. Pabandi HK, Jashnani HR, Paidar M (2018) Effect of precipitation hardening heat treatment on mechanical and microstructure features of dissimilar friction stir welded AA2024-T6 and AA6061-T6 alloys. *J Manuf Process* 31:214–220

# A Study of Direct and Inverse Problems in Force Sensing of Elastic Bodies



Saurav Kumar Dutta, Annem Narayana Reddy  
and Santosha Kumar Dwivedy

**Abstract** The estimation of contact forces in elastic bodies leads to an inverse problem, and its solution procedure is different as compared to a direct problem. This paper discusses how a direct problem becomes an inverse problem and how these problems depend on boundary conditions of the elastic bodies. A cantilever beam for different boundary conditions is also investigated in the framework of finite element method. The numerical results show how a problem becomes direct or inverse for different boundary conditions. They also indicate the extreme sensitivity of forces to the input data for both direct and inverse problems.

**Keywords** Dirichlet problem · Ill-posed problem · Boundary conditions · Force estimation

## 1 Introduction

Direct and inverse problems are commonly used terms, and these terms are used to explain many different phenomena in wide variety of fields like geophysics, heat conduction problems, and vibration problems. However, this paper writes about the direct and inverse problems only with the reference of force sensing in elastic bodies. It is important to know about the direct and inverse problems because the estimation of forces in the direct problems is different than that of the inverse problems. The solution procedure for direct problems is easy while that of the inverse problems is intensive and involves the use of optimization techniques [1, 2].

For force sensing in elastic bodies, a problem is direct only if the boundary conditions of the elastic bodies are properly specified. The same problem becomes inverse if the boundary conditions are improperly specified [2]. The direct problem is also called a Dirichlet problem, whereas the inverse problems tend to be ill-posed and can

---

Saurav Kumar Dutta (✉) · Annem Narayana Reddy · Santosha Kumar Dwivedy  
Department of Mechanical Engineering, Indian Institute of Technology Guwahati,  
Guwahati 781039, India  
e-mail: [d.saurav@iitg.ac.in](mailto:d.saurav@iitg.ac.in)

© Springer Nature Singapore Pte Ltd. 2020  
L. Vijayaraghavan et al. (eds.), *Emerging Trends in Mechanical Engineering*,  
Lecture Notes in Mechanical Engineering,  
[https://doi.org/10.1007/978-981-32-9931-3\\_34](https://doi.org/10.1007/978-981-32-9931-3_34)



also be called as an ill-posed problem [3]. The solution of an ill-posed problem is not continuous with respect to the input information. The existence and uniqueness of the solution of an ill-posed problem can also be not guaranteed, as stated by Tikhonov and Arsenin [4]. Due to these reasons, the solution procedure of an ill-posed problem becomes different and requires the use of rigorous numerical techniques than that of a direct problem.

Ill-posed problems in force sensing arise because of difficulties in placing sensors at the points of application of forces [5, 6]. Reddy and Ananthasuresh [1] found the application of inverse problems in the determination of gripping forces between the gripper and the cell in biomanipulation. Determination of cutting forces between cutting tool and workpiece, contact forces between railway tracks and rolling stock for safety of railway systems, tire design are some of the examples of the ill-posed inverse problems in force sensing.

## 2 Association of Problems with Boundary Conditions

In most of the deformation problems concerning the elastic bodies, the boundary conditions are not properly specified. There might be a part of the boundary of an elastic body where both displacements and tractions are specified. Similarly, there might be some other part of the boundary of the same elastic body, where neither the displacements nor the tractions are specified. This may give rise to an ill-posed problem. This type of ill-posed problem is basically a Cauchy inverse problem or reconstruction-type inverse problem. It is called a Cauchy problem as both the field variable and its derivative are specified at the same boundary. It is also called a reconstruction-type inverse problem as the boundary tractions in the under-specified boundaries are reconstructed from displacements in the over-specified boundaries [5]. Figure 1a shows an elastic body which is fixed at one end and being subjected to an unknown force  $P$  at the opposite end. Figure 1b and c shows the same elastic body with demarcated boundary conditions.

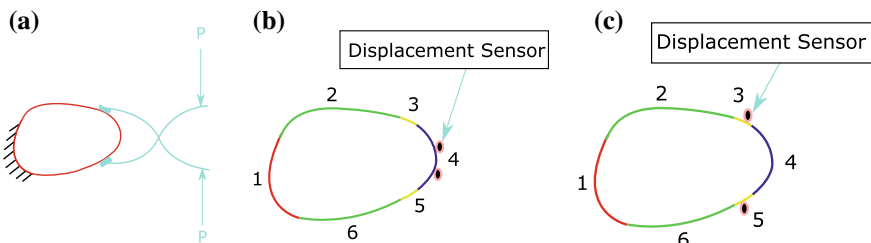


**Fig. 1** a Elastic body with b properly specified boundary conditions and c improperly specified boundary conditions

As can be seen in Fig. 1b, boundary conditions of boundaries 1, 2, and 6 are properly specified but those of boundaries 3, 4, and 5 are improperly specified. On boundary 1 (fixed end), displacements are known (zero). The boundary 1 has a properly specified displacement boundary condition. On boundaries 2 and 6, tractions are known (zero). The boundaries 2 and 6 have properly specified traction boundary conditions. On boundaries 3 and 5, neither the displacements nor the tractions are known. On boundary 4, both displacements and tractions are known. A boundary can have either the displacement boundary condition or the traction boundary condition. The presence or absence of both displacements and tractions on a boundary makes the boundary conditions improperly specified.

If displacements are known at boundaries 3 and 5, Fig. 1b would look like Fig. 1c. With the change in the position of the displacement sensors, the boundary conditions get properly specified. Hence, the ill-posed problem becomes a well-posed problem with the change in the position of the sensors. As can be seen in Fig. 1c, on boundaries 1, 3, and 5, displacements are known, and on boundaries 2, 4, and 6, tractions are known.

It is very difficult to measure displacements or strains at points, where forces are being applied. So, the displacements are measured at points where forces are not applied. These points are located either on the boundary or in the domain. By using that input data, the forces on the boundary are computed. So, this is how most of the deformation problems become an inverse problem rather than a direct problem.

### 3 Solution Strategy

The direct problems can be solved either in displacement-based approach or stress-based approach. If displacements on the boundary are known, Navier’s equation of elasticity, as given in Eq. (1), is used. If tractions are known on the boundary, Beltrami–Michell compatibility conditions are used along with equilibrium equations, as given in Eqs. (2) and (3), respectively.

$$(\lambda + \mu)\nabla(\nabla \cdot \mathbf{u}) + \mu\nabla^2\mathbf{u} + \rho\mathbf{b} = \rho\frac{\partial^2\mathbf{u}}{\partial t^2} \tag{1}$$

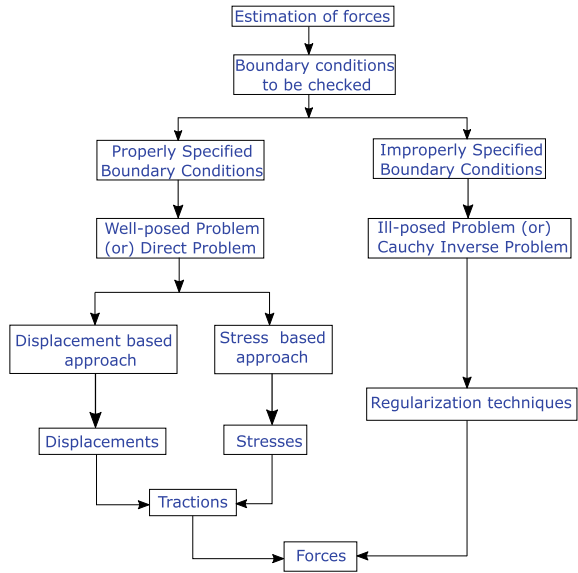
$$\nabla^2\boldsymbol{\tau} + \frac{1}{1 + \nu}\nabla(\nabla(\text{tr } \boldsymbol{\tau})) = -\frac{\nu}{1 - \nu}\rho(\nabla \cdot \mathbf{b})\mathbf{I} - \rho\nabla\mathbf{b} - \rho(\nabla\mathbf{b})^T \tag{2}$$

$$\nabla \cdot \boldsymbol{\tau} + \rho\mathbf{b} = \rho\frac{\partial^2\mathbf{u}}{\partial t^2} \tag{3}$$

where  $\rho$  is the density of the elastic body,  $\lambda$  and  $\mu$  are Lamé constants,  $\mathbf{b}$  is the body force per unit mass,  $\boldsymbol{\tau}$  is the stress tensor,  $\mathbf{u}$  is the displacement vector,  $\nu$  is the Poisson’s ratio,  $\text{tr}$  is the trace of a tensor, and  $\nabla$  is the differential operator.

These differential equations can be solved analytically or by using numerical techniques like the finite element method. The solution of a direct problem, obtained

**Fig. 2** Flowchart depicting the processes involved in the estimation of forces



using the displacement-based approach, the stress-based approach or the finite element method, ensures that the solution exists and is unique [7].

In the case of inverse problems, the unknown forces are obtained by using any one of the frameworks of finite element method, finite difference method, boundary element method, etc. Then, the unknown forces, which are generally incorrect, are conditioned using regularization techniques. The displacements that are obtained from the sensors experimentally always have some noise associated with them. These input data tend to give hugely deviated results. To overcome this, techniques like least squares minimization are used along with the regularization schemes. The entire process of force estimation can be shown with the help of a flowchart as shown in Fig. 2.

### 4 Example

In this section, a steel cantilever beam is taken and subjected to a point load at the free end, as shown in Fig. 3a. The length of the beam is 30 cm, and its width is 1 cm. The out-of-plane width of the beam is 1 cm. The Young’s modulus and Poisson’s ratio of the beam are 200 Gpa and 0.3, respectively. The applied load P is equal to 100 N. The self-weight of the beam has been neglected.

The beam here is considered as an Euler–Bernoulli beam. The deflection of the beam is calculated using the following equation.

$$\delta = \frac{PL^3}{3EI} \tag{4}$$

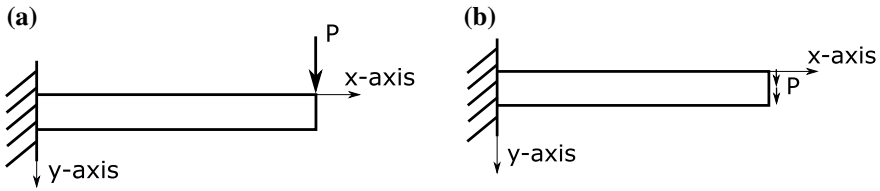


**Fig. 3** A cantilever beam with **a** point load at the free end and **b** distributed load at the free end

where  $\delta$  is the deflection,  $L$  is the length,  $E$  is Young’s modulus, and  $I$  is the second moment of area of the cross-sectional area of the beam.

A generalized finite element code is generated for four-noded quadrilateral elements, using Eq. (3). The stiffness matrix is denoted by  $[K\_original]$ , and the force vector is denoted by  $\{F\_original\}$ . After the imposition of boundary conditions into  $[K\_original]$  and  $\{F\_original\}$ , the stiffness matrix is denoted by  $[K]$  and the force vector is denoted by  $\{F\}$ . The displacement vector,  $\{u\}$ , is obtained by using the following equation.

$$\{u\} = [K]^{-1}\{F\} \tag{5}$$

After getting the displacements, the reaction forces at the fixed ends can be obtained by using the following equation.

$$\{F\_unknown\} = [K\_original]\{u\} \tag{6}$$

As can be seen in Fig. 3a, a point load,  $P$ , is acting at the free end. Since a point load is acting, it is difficult to state the boundary conditions of this beam. So, by Saint-Venant’s Principle, the point load is replaced by a distributed load, as shown in Fig. 3b. The loading of cantilever beam of Fig. 3b is equivalent to the loading of cantilever beam of Fig. 3a. The point load is replaced by a distributed load which would produce the same deflection as for the point load. The boundary conditions of the beam can now be stated easily. As is evident from Fig. 3b, the left surface of the beam is having a properly specified displacement boundary condition and the top, bottom, and right surfaces are having properly specified traction boundary conditions.

## 5 Numerical Results

The deflection of the beam using Eq. (4) is found to be 0.54 cm. The cantilever beam is discretized into  $120 \times 4$  elements, 120 elements along  $x$ -axis, and four elements along  $y$ -axis. The mesh and the node numbers at the fixed and free ends are shown in Fig. 4a. Since 100 N load is uniformly distributed at the free end of the beam,

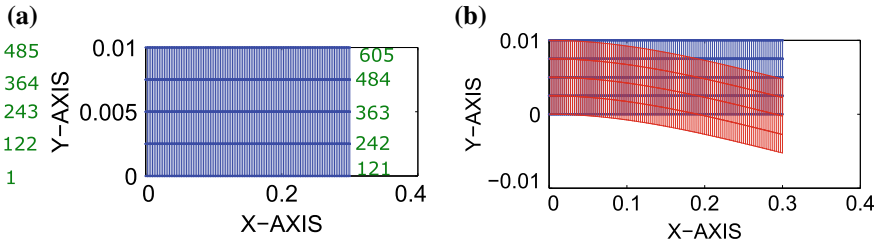


**Fig. 4** Discretized cantilever beam with **a** undeformed mesh and the green-colored node numbers at the free and fixed ends, **b** undeformed and deformed mesh

100N is divided equally among the five nodes of the free end of the beam. Thus, a load of 20N is acting at each of the nodes of the free end, i.e., nodes 121, 242, 363, 484, 605. By using Eq. (5), the displacements of all the nodes are obtained. The displacement along y-axis corresponding to node 605 comes out to be 0.52 cm. Thus, the deflection of the beam comes out to be almost same both by the deflection formula and the finite element method.

### 5.1 Direct Problem

In Fig. 4a, it is assumed that the magnitude of the forces acting at the nodes 121, 242, 363, 484, 605 is not known. But the displacements at the nodes 121, 242, 363, 484, 605 are known. It is a direct problem as now in Fig. 3b, the left and right surfaces are having properly specified displacement boundary conditions and the top and bottom surfaces are having properly specified traction boundary conditions. The displacements at nodes 121, 242, 363, 484, 605 were stored when the displacements of all the nodes were found for knowing the deflection of the beam in the previous case. MATLAB can store values up to 16 decimal places. In the present case, the magnitude of the forces is to be found at the nodes 121, 242, 363, 484, 605. By solving the problem in the framework of finite element method, the displacement vector is reproduced by using Eq. (5). Then, the unknown forces are obtained by using Eq. (6). The results can be found in Table 1.

In this particular case, the magnitude of the unknown forces at nodes 121, 242, 363, 484, 605 was recovered by knowing the displacements at these nodes. Since the boundary conditions were properly specified, the magnitude of the unknown forces could be directly found by using finite element method. In the results of Table 1, the displacements along x and y axes were free from noises. However, experimentally if the displacements were extracted at points corresponding to those nodes, the displacements would have had noises. It is found that in direct problems also, a little perturbation of the input data causes a huge deviation in the values of the computed forces. No noise is introduced into the displacements along x and y axes,

**Table 1** Results of the direct problem

Nodes	Displacement along $x$ -axis (cm)	Displacement along $y$ -axis (cm)	Unknown forces along $x$ -axis (N)	Unknown forces along $y$ -axis (N)
121	-0.013097409169197	-0.524117536724479	0	-20
242	-0.006547147693617	-0.524115866712624	0	-20
363	-3.441610341175686e - 14	-0.524115036210672	0	-20
484	0.006547147693548	-0.524115866712624	0	-20
605	0.013097409169129	-0.524117536724480	0	-20

**Table 2** Results of the direct problem with perturbed input data

Nodes	Displacement along $x$ -axis (cm)	Displacement along $y$ -axis (cm)	Unknown forces along $x$ -axis (N)	Unknown forces along $y$ -axis (N)
121	-0.0131	-0.5241	-245.3685	107.0620
242	-0.0065	-0.5241	517.6594	-61.2238
363	0	-0.5241	5.7335e-09	-192.3442
484	0.0065	-0.5241	-517.6594	-61.2238
605	0.0131	-0.5241	245.3685	107.0620

but the displacements are rounded off to 4 decimal places. The results obtained are given in Table 2.

It is evident from the results of Table 2 that a little perturbation of the input data causes a huge deviation in the values of the computed forces in the direct problems as well.

### 5.2 Inverse Problem

In Fig. 4a, it is assumed that the magnitude of the forces acting at nodes 121, 242, 363, 485, 605 is not known. Unlike in direct problem, the displacements at nodes 121, 242, 363, 485, 605 are also not known. The displacements at some other nodes are known. In this case, the boundary conditions get improperly specified. Thus, in Fig. 3b, in the right surface of the beam, neither the displacements nor the tractions are known. Traction are related to the forces. If the forces are not known, so are the tractions. By knowing the displacements at some other nodes, it is possible to get  $\{u\}$  by using Eq. (5), but it is not possible to correctly know the magnitude of the forces acting at nodes 121, 242, 363, 485, 605, by using Eq. (6). It is assumed that the displacements at nodes 115 and 500 are known. The magnitude of the forces at the nodes 121, 242, 363, 485, 605 is to be found out by utilizing the displacements at nodes 115 and 500. The results obtained are shown in Table 3.

**Table 3** Results of the inverse problem

Nodes	Displacement along $x$ -axis (cm)	Displacement along $y$ -axis (cm)	Unknown forces along $x$ -axis (N)	Unknown forces along $y$ -axis (N)
115	-0.013064023818795	-0.484841221688367	-120.3222	-105.1613
500	0.003064188826504	-0.011807632562045	517.6594	-61.2238
121	Not known	Not known	-3.0850e-09	2.4214e-08
242	Not known	Not known	2.5408e-08	8.8476e-09
363	Not known	Not known	2.2585e-08	-6.9384e-08
484	Not known	Not known	-4.9680e-08	8.2422e-08
605	Not known	Not known	-2.9337e-08	-3.9116e-08

It can be seen from the results of Table 3 that the forces cannot be obtained by using only finite element method in the case of inverse problems. After obtaining the incorrect values of the forces, regularization techniques are to be used. The presence of noise in the input data would also require the use of least squares minimization.

In the results of Tables 1, 2, and 3, it was found that in each case, the displacement vector, obtained using Eq. (5), is almost same and that is why the deformed mesh of the beam, as shown in Fig. 4b is same for all the three cases. But the unknown forces obtained using Eq. (6) are correct only for the results of Table 1, i.e., for the direct problem with noiseless input data.

## 6 Conclusion

This paper discussed the direct and inverse problems in force sensing and showed their relationship with boundary conditions. A cantilever beam was taken, and it was numerically investigated for different boundary conditions. It was established that for direct problems, the solution procedure is equivalent to solving a finite element problem but for inverse problems, merely using finite element method did not give the correct results. Moreover, in the literature, it was reported that in inverse problems, the forces are not continuous functions of displacements. However, it was found that for direct problems as well, the forces deviated greatly from their actual solution, whenever there was noise in the displacements.

## References

1. Reddy AN, Ananthasuresh G (2008) On computing the forces from the noisy displacement data of an elastic body. *Int J Numer Methods Eng* 76(11):1645–1677
2. Maniatty A, Zabarar N, Stelson K (1989) Finite element analysis of some inverse elasticity problems. *J Eng Mech* 115(6):1303–1317

3. Reddy AN (2010) Two inverse problems in linear elasticity with applications to force-sensing and mechanical characterization. PhD thesis, Citeseer
4. Tikhonov A, Arsenin VY (1977) Solution of ill-posed problems
5. Bezerra LM, Saigal S (1995) Inverse boundary traction reconstruction with the BEM. *Int J Solids Struct* 32(10):1417–1431
6. Maniatty A, Zabaras N (1989) Method for solving inverse elastoviscoplastic problems. *J Eng Mech* 115(10):2216–2231
7. Timoshenko S, Goodier J (1951) *Theory of elasticity*, vol 412



# Linear Heat Transfer and Structural Analysis of a Railway Wheel



A. N. Borade  and A. J. Keche

**Abstract** The railway transportation system plays a very important role in society. In railway engineering, structural stresses, thermal stresses, contact stresses, surface cracks, plastic deformation and wear of the railway wheel have a serious issue, and also increasing speed and axle loads of the wheel reduces strength and creates wear. Thermal stresses are generated usually while breaking the operation of the vehicle. Present study deals with S-shaped wheel profile analysed by using finite element method and considered factors are displacement, stress distribution, temperature and deformation. The Hypermesh software is used for simulation; the maximum displacement obtained from simulation is 0.66 mm. The maximum stress obtained from simulation is 314 MPa. The maximum grid temperature obtained from simulation is 545 K. The result of FEA shows good agreements with real-life problems related to railway wheel.

**Keywords** Structural · Thermal · Wear · Stress · Displacement

## 1 Introduction

The railway transportation system plays a tremendous role in connectivity. In a railway vehicle various types of component such as rail axle, spring, break, pads etc. But railway wheel has been one of the most intensive loaded components in a railway vehicle. The railway wheel is subjected to various types of loading during running conditions. In recent years, speed and load carrying capacity are improved due to the effect of larger wheel—rail contact force produce. As a result, there has been increase in structural and thermal stress—strain on the vehicle. The railway wheel-related problems are structural and thermal stress parameter, plastic deformation, wear, fracture, creeps and rotating interaction fatigue.

---

A. N. Borade (✉) · A. J. Keche  
Department of Mechanical Engineering, Maharashtra Institute of Technology, Aurangabad,  
Maharashtra 431028, India  
e-mail: [abhijeetbrd890@gmail.com](mailto:abhijeetbrd890@gmail.com)

© Springer Nature Singapore Pte Ltd. 2020  
L. Vijayaraghavan et al. (eds.), *Emerging Trends in Mechanical Engineering*,  
Lecture Notes in Mechanical Engineering,  
[https://doi.org/10.1007/978-981-32-9931-3\\_35](https://doi.org/10.1007/978-981-32-9931-3_35)

In recent years, a couple of case studies have been done and possibilities are tested to investigate thermal overload of a wheel–rail characteristic of the area of interest. Taraf [1] investigated rail–wheel contacting defect with the help of two-dimensional elastic–plastic finite element model. Seo [2] studied residual stress analysis of S-shaped wheel and flat wheel, during manufacturing and braking operations. The cyclic stress of fatigue analysis is investigated by applying the finite element method. Mohan [3] simulated thermal and structural behaviour of the rail–wheel due to the breaking of the wheel, leading to thermal overloading which results in fatigue. Crack propagation leads to fracture. Aalami [4] investigated rail–wheel interaction problem, structural stress distribution of a railway wheel-set component by using finite element method. Milosevic [5] carried out thermal analysis of a solid railway wheel using analytical and numerical modelling of the thermal effect of the braking system of the railway vehicle. Jigan [6] investigated the effects of the tangential surface force in the shear direction on residual stress–strain with the help of three-dimensional elastic–plastic rolling contact simulation.

This study evaluates coupled linear heat transfer and structural stress analysis of an S-shaped solid railway wheel by using the finite element analysis method. The Hypermesh software is used for simulation of solid railway wheel.

## 2 Finite Element Modelling

A commonly used 983-mm-diameter S-shaped wheel is created in Hypermesh software, meshed with hex element having a quadratic displacement behaviour. The FE model mesh is obtained having a total of 23,017 elements and total number of nodes 26,320 of the S-shaped wheel as shown in Fig. 1. The slope of the rail in international

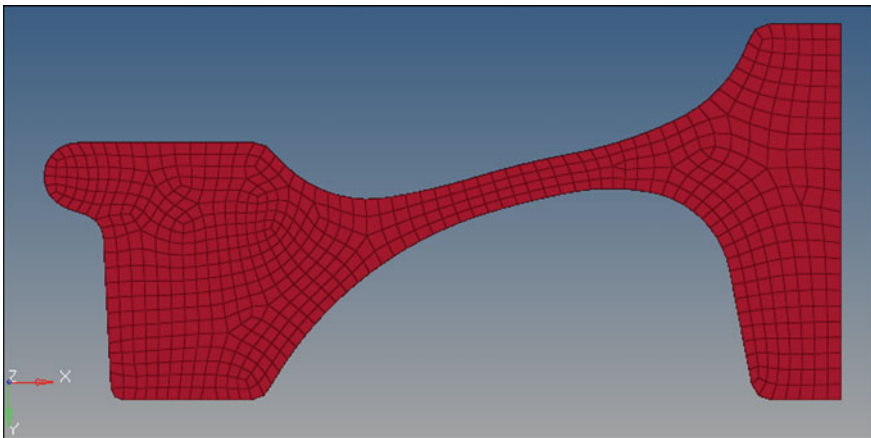


**Fig. 1** FE mesh model of an S-shaped wheel

**Table 1** Mechanical properties of materials

S. No.	Property	Unit
1	Modulus of elasticity(Gpa)	200
2	Density (Kg/m <sup>3</sup> )	7850
3	Poisson’s ratio	0.3
4	Thermal conductivity (W/mm K)	0.0049

railway can be 1:20 or 1:40. In this study, the slope of 1:20 is utilized for a flat wheel and s-shaped wheel profile diameter.

### 2.1 Material Properties

The material selected for the analysis is IRS-R-34/99 is of ductile nature, high-carbon steel having carbon percentage of 0.50–0.67. Mechanical properties of materials are shown in Table 1.

## 3 Finite Element Analysis

The railway wheel residual stress created wear and reduced the hardness of the tread. The residual stress affected rail–wheel changing stress distribution and shape of wheel. A coupled heat transfer structural analysis initial temperature wheel applied 70° F and constant value film coefficient are used. The heat flux is implemented on the faces of solid wheel. The railway wheel hub position is fixed. As the air comes in contact with the wheel, the rail undergoes a heat generation due to friction. The heat flux is calculated as,

The diameter of the wheel from the hub is 491.5 mm. The width of the rim which is in contact with the rail is approximately 96.06 mm for the S-shaped solid wheel. The load acting on four wheels is 240 KN. The load acting on one wheel is (*M*) 6118.297 kg. The velocity of bogie is 16.67 m/s. Time taken bogie brought to rest at 30 s. The heat flux generation is calculated as 0.19096 W/mm<sup>2</sup>.

$$\text{The Kinetic Energy Generated at wheel} = 0.5(M v^2) \tag{1}$$

$$\text{Power Generation} = \text{K.E/Time Taken} \tag{2}$$

$$\text{Area} = [\pi \times \text{Diameter of wheel} \times \text{Width}] \tag{3}$$

$$\text{Heat Flux Generation} = \text{Power Generation/Area} \tag{4}$$

## 4 Results and Discussion

The finite element model runs successfully to visualize post processing stress–strain distribution level of S-shaped railway wheel profile. In Fig. 2, displacement magnitude is plotted for S-shaped wheel. As expected, maximum displacement found 0.66 mm of rim which is in the outer portion of the wheel. This displacement is provided to the wheel because of significant reasons. First, it is ensured that the route of wheel includes two setting pads which are important for nature of contact force along the wheels route. And secondly, this distance is required for the rolling contact of the wheel. Figure 3 shows maximum signed von Mises stress on the rolling motion. It is the perpendicular section to the axis of the wheel and contact surface. The maximum amount of the stress web portion is 314.11 MPa as illustrated in Fig. 3. The amount of the elemental stress created by the wheel motion on the rail exceeds the yield point. According to Fig. 4, the maximum von Mises stress for the S-shaped wheel 1610 MPa at the flange portion of the wheel along with the pre-stressed state has induced the maximum stress in the region; due to higher stress region at flange portion, there are maximum possibilities of crack, wear deformation.

In Fig. 5, heat transfer grid temperature analysis for S-shaped wheel profile is shown. The steady model includes heat transfer by conduction through the web of the wheel and convection heat transfer via a flange. The flange is an angular disc of uniform thickness, connected to the surrounding by convection. The rim and flange portion of the wheel is in contact with the rail due to friction between flange, rim and rail; during breaking, heat generation is more. The maximum temperature at the flange is 545.37 K.

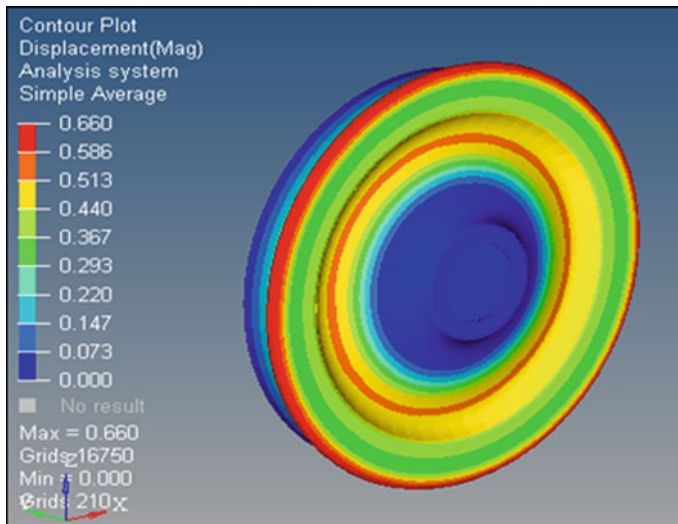


Fig. 2 Maximum displacement of S-shaped wheel

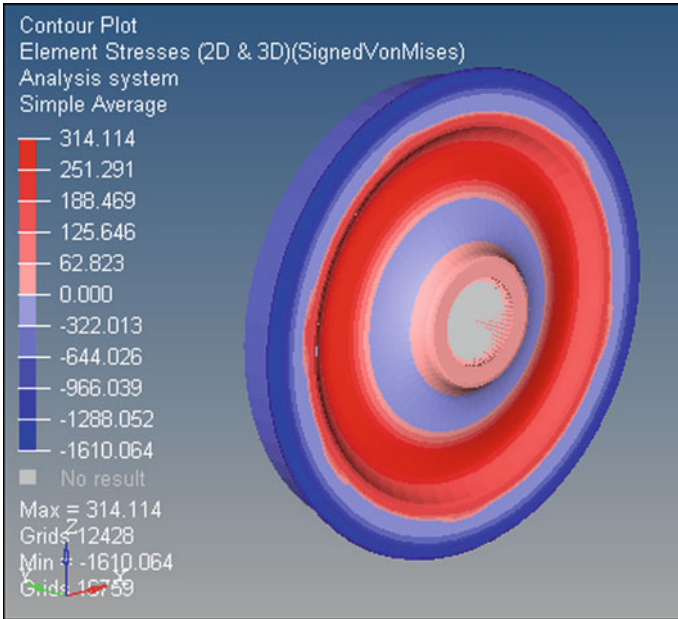


Fig. 3 Maximum signed von Mises stress of an S-shaped wheel

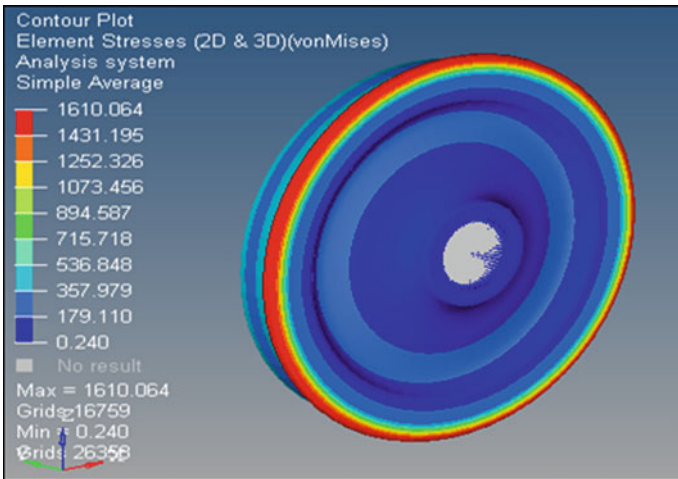
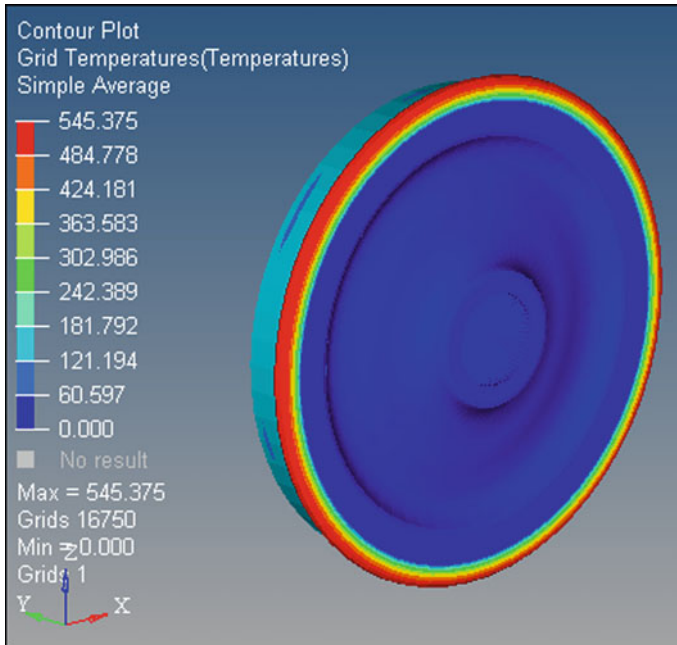


Fig. 4 Maximum von Mises stress of an S-shaped wheel



**Fig. 5** Heat transfer analysis grid temperature

Figure 6 shows element temperature gradients and heat transfer analysis of outer surface of the flange. The maximum temperature of outer surface flange is 16.47 K. This thermal stress analysis is obtained during braking and running operation of the vehicle. If effective cooling is not employed and due to excessive braking, residual thermal stress will get induced which will lead to wear and fatigue failure of the wheel.

## 5 Conclusions

The finite element analysis is a numerical technique used to determine applied stress which will affect the material, design or modelling and simulation of the railway wheel. In this paper, the structural load and the effect of the thermal residual stress variation on the *S*-shaped railway wheel are evaluated through the FEA. The following conclusions are obtained:

- 1 The maximum displacement of *S*-shaped wheel is observed to be 0.66 mm from the rim portion of the wheel.
- 2 Result shows that von Mises stress on the wheel exceeds the yield point and also maximum grid temperature 545 K at the flange portion of wheel.

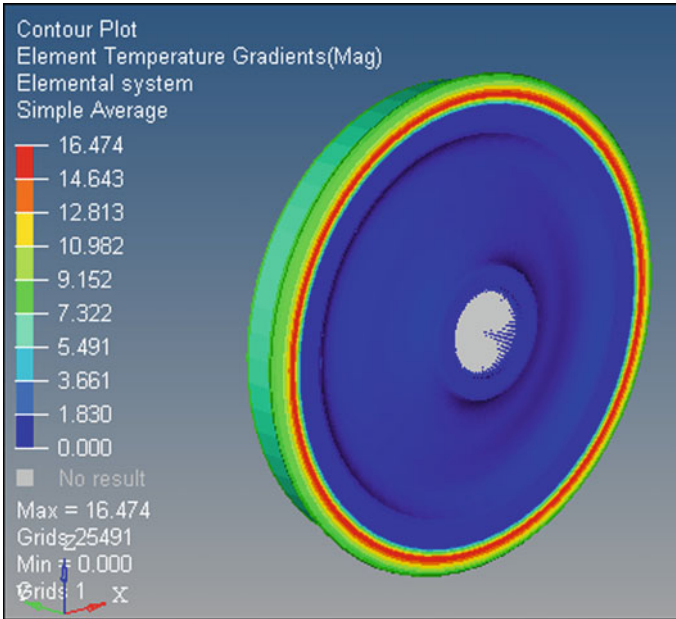


Fig. 6 Element temperature gradients, heat transfer analysis

- 3 It is observed that if effective cooling is not conducted as resulted wear, corrugation, fracture, creep, crack propagation and dynamic vibrations are created on the railway wheel.

## References

1. Taraf M, Zahaf EH, Oussouaddi O, Zegloul A (2010) Numerical analysis for predicting the rolling contact fatigue crack initiation in a railway wheel steel. *Tribol Int* 43:124–129
2. Seo JW, Seok JK, Hyen KJ (2009) Effects of residual stress and shape of web plate on the fatigue life of railway wheels. *Eng Fail Anal* 16:2493–2507
3. Mohan PM (2012) Analysis of railway wheel to study thermal and structural behaviour *IJSER* 11
4. Aalami M.R., Anari A., Shafighfad T, A robust finite element analysis of the rail wheel rolling contact, *Advances in Mechanical Engineering*. (2013)
5. Milosevic MS, Stamenkovic DS, Milojevic AP (2012) Modelling thermal effect in braking system of railway vehicles. *Therm Sci* 16:515–526
6. Jiang Y, Biqiang X, Sehitoglu H (2002) Three dimensional elastic plastic stress analysis of rolling contact. *Tribol Int* 124/699
7. Sharma S (2016) Anilkumar, Dynamic analysis of wheel rail contact using FEA. *Procedia Eng* 144:1119–1128
8. Magel E, Kalousek J, Caldwell R (2005) A numerical simulation of wheel wear. *Wear* 258: 1245–1254

# Performance Optimization of VCR Diesel Engine Using Soybean Oil-Based Biodiesel



Hrushikesh B. Kulkarni and Pravin R. Kubade

**Abstract** In the present work, the performance of four-stroke variable compression ratio diesel engine is evaluated using soybean-based biodiesel. Blends of biodiesel are prepared by varying percentage of biodiesel in diesel (*B20*, *B40*, *B60*). Engine input parameters such as compression ratio (13:1, 15:1, 17:1) and load (4, 8, 1.2 kg) are varied to optimize the results. Taguchi method of optimization is used to study the effect of various combinations of input parameters on performance of VCR engine. Analysis of variance (ANOVA) is done to identify significance of individual input parameter on brake power, brake-specific fuel consumption, and exhaust emission. The optimization helps to select optimum values of compression ratio and load that would minimize exhaust emission and brake-specific fuel consumption but also maximize brake power. Engine performance is highly influenced by load.

**Keywords** Soybean-based biodiesel · VCR engine · Brake power · Brake-specific fuel consumption · NO<sub>x</sub> emission

## 1 Introduction

Energy is the backbone of sustainable development. Conventional fuels such as petrol and diesel are burned under controlled conditions to produce energy. This energy can be used for power production and transportation. The present demand of oil is 90 millions of barrels per day which will shoot it to 111.1 millions of barrels per day in 2040. Petroleum products such as coal, oil, and natural gas are limited in quantity and may not be available in future. Problems associated with the use of natural energy resources are global warming, environmental pollution, human health, and

---

H. B. Kulkarni (✉)

Department of Mechanical Engineering, NBN Sinhgad College of Engineering, Solapur, Maharashtra 413001, India

e-mail: [lhbkulkarni.coeo@gmail.com](mailto:lhbkulkarni.coeo@gmail.com)

P. R. Kubade

Department of Mechanical Engineering, KIT's College of Engineering, Kolhapur, Maharashtra 416234, India

© Springer Nature Singapore Pte Ltd. 2020

L. Vijayaraghavan et al. (eds.), *Emerging Trends in Mechanical Engineering*,

Lecture Notes in Mechanical Engineering,

[https://doi.org/10.1007/978-981-32-9931-3\\_36](https://doi.org/10.1007/978-981-32-9931-3_36)



climate change. For satisfying increasing energy demand, maintaining sustainable development and reducing environmental issues, there is a need to identify and manufacture new and renewable energy resources [1–4]. Biodiesel is a renewable fuel manufactured from various sources [5].

Transesterification is the process of conversion of oils into biodiesel; further, it can be blended with diesel at various percentages (0, 15, 20, 40, and 60). Biodiesel can be used in compression ignition internal combustion engine without or with small modifications. Soybean oil [6], canola oil [7], corn oil [8], sunflower oil [9], rapeseed oil [10] and palm oil [11], algae [12, 13], jatropha [14, 15] are other major resources of biodiesel worldwide. Recycled grease, oils, and animal fats can also be used for manufacturing biodiesel [16–19]. A huge amount of the literatures are available on jatropha, algae, etc., but very few literatures are available on soybean-based biodiesel. So, novelty of the present work is to study and optimize the performance of CI engine using soybean-based biodiesel [20–37].

Although biodiesel is renewable and environmentally friendly, it has few disadvantages such as low energy content, high cost as compared to petroleum products, high exhaust emission, need to develop infrastructure for biodiesel production and distribution network.

In the present work, the performance of diesel engine using blend of diesel and biodiesel is optimized using Taguchi optimization technique. The main objective of this work is to improve the performance of VCR engine and reduce the exhaust emissions.

Dr. Taguchi has developed a technique based on ‘Orthogonal Array’ which reduces variation by keeping control by optimum setting of control parameters. Taguchi method employs the signal-to-noise (S/N) ratio and the analysis of variance (ANOVA) to evaluate the performance characteristics. It combines design of experiments (DOE) and optimized control parameters to obtain best optimal solution with a set of minimum experiments. Minitab 17 is a very powerful statistical tool used for design analysis of Taguchi method.

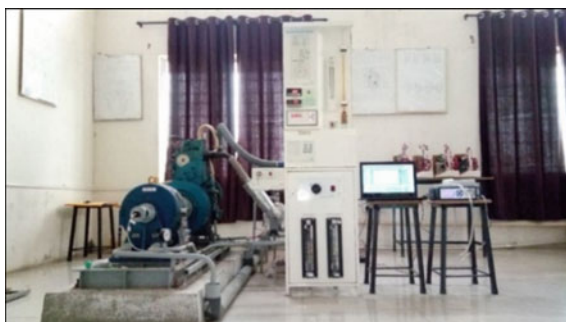
## 2 Test Setup

For the present work, a computerized variable compression ratio (4-stroke, single-cylinder, VCR, Product Code 234) diesel engine fitted with eddy current-type dynamometers manufactured by Apex Innovation is used for conducting experiment. Gas analyzer of (Digas 444) type is used for exhaust gas analysis. Initially, VCR engine is fueled with pure diesel to start the engine, and further, it is operated on biodiesel. Soybean-based biodiesel was purchased from SVM Agro Processor, Nagpur, India. Output parameters such as brake power, brake-specific fuel consumption,  $\text{NO}_x$ , and  $\text{CO}_x$  are optimized. Table 1 gives the VCR engine specification, and Fig. 1 shows the test setup for experimentation work.

Table 2 gives properties of diesel and soybean-based biodiesel [6].

**Table 1** VCR engine specification

Sr. No.	Information	Specification
1	Manufacturer	Kirloskar Oil Engines Ltd, India
2	No of cylinders	1
3	No of strokes	4
4	Fuel	Diesel
5	Rated power	3.5 kW @ 1500 rpm
6	Cylinder diameter	87.5 mm
7	Stroke length	110 mm
8	Connecting rod length	234 mm
9	Compression ratio range	12–18.1

**Fig. 1** Computerized VCR engine test setup**Table 2** Diesel and biodiesel properties [6]

Sr. No.	Properties	Diesel (Petroleum)	Soybean-based Biodiesel
1	Specific gravity	0.825	0.78
2	Kinematic viscosity	4.35	5.16
3	Flash point (°C)	42.5	166.5
4	Fire point (°C)	67	193

### 3 Performance Optimization Using Taguchi Method

Taguchi method is a statistical method developed to improve quality of goods manufactured, but further it is used to reduce the number of experiments and variation in the output. The results of these experiments are based on careful selection of input parameters which nullifies the effect of noise in output. Orthogonal arrays (OA) of different size are selected to conduct the set of experiments. Results are the then

**Table 3** Selection of input parameters with levels

Sr. No.	Parameters	Level 1	Level 2	Level 3
1	Compression ratio	13	15	17
2	Load (Kg)	4	8	12
3	Biodiesel blend (%)	B20	B40	B60

analyzed to identify the factor which badly affects the output and which parameters support to improve the results.

### ***3.1 Selection of Input Parameters and Levels***

VCR engine operates on various input parameters with wide working range. So as to achieve higher power output with less exhaust emission, the selection of parameters and their levels with optimum combination is very important. From the available literature, it is observed that compression ratio and load are two very important factors which are need to be optimized and third is blend of biodiesel with pure diesel. Table 3 shows the selection of parameters with their levels decided for the present work.

### ***3.2 Selection of Orthogonal Array and Experimental Results***

In Taguchi method, standard orthogonal arrays are available which are decided on the basis of number of parameters and levels [20]. For the present work, three process parameters with three levels are selected; then, L9 orthogonal array is the best choice. Total nine experiments were conducted as per the combinations provided by Taguchi orthogonal array. Output parameters, i.e., results obtained by actual experiments, are mentioned as brake power (KW), brake-specific fuel consumption (BSFC), and NO<sub>x</sub> mentioned in Table 4.

### ***3.3 Analysis of Variance (ANOVA)***

Analysis of variance (ANOVA) is a statistical method used for decision making. ANOVA computes the relation between each parameter and detects the variation in the average performance of parameters selected for optimization. ANOVA also helps to identify significant and insignificant parameter which affects the performance of the engine.

**Table 4** Taguchi L9 orthogonal array

Experiment No.	Compression ratio (CR)	Load (Kg)	Biodiesel blend (%)	Brake power, BP (KW)	Brake-specific fuel consumption, BSFC (Kg/KWh)	Nitrogen oxide, NO <sub>x</sub> (ppm)
1	13	4	B20	1.19	0.419	15
2	13	8	B40	1.87	0.266	19
3	13	12	B60	2.50	0.199	35
4	15	4	B40	1.38	0.325	21
5	15	8	B60	2.12	0.247	26
6	15	12	B20	2.49	0.208	26
7	17	4	B60	1.51	0.270	31
8	17	8	B20	1.87	0.260	29
9	17	12	B40	2.57	0.179	37

### 3.4 Signal-to-Noise Ratio (S/N Ratio)

The main objective of Taguchi method is to minimize the variations in the performance or output though there is presence of undesirable or uncontrollable factors called noise. Signal-to-noise ratio is the ratio of signal, i.e., input to noise. If S/N ratio is high, there is minimum effect of the noise of experiments. There are three different categories of S/N ratio such as larger the better, smaller the better, and nominal the best. The choice of S/N ratio depends on aim of experiment [21].

Smaller the better is considered when the small output is expected from experimentation; in the equation mentioned below  $y_i$  is the observed response value and  $n$  is the number of replications.

$$\frac{S}{N} \text{ ratio}(\eta) = -10 \log_{10} \frac{1}{n} \sum_{i=1}^n y_i^2 \tag{1}$$

Nominal the best is considered when output is expected to be nominal and minimum variation of in the output value. Here,  $\mu$  is mean and  $\sigma$  is variance

$$\frac{S}{N} \text{ ratio}(\eta) = -10 \log_{10} \frac{\mu^2}{\sigma^2} \tag{2}$$

Higher the better considered when high value of output is expected. In the equation mentioned below  $y_i$  is the observed response value and  $n$  is the number of replications.

$$\frac{S}{N} \text{ ratio}(\eta) = -10 \log_{10} \frac{1}{n} \sum_{i=1}^n \frac{1}{y_i^2} \tag{3}$$

### 4 Results and Discussion

In the present work, brake power, brake-specific fuel consumption, and nitrogen oxide emission are the output parameters considered for optimization.

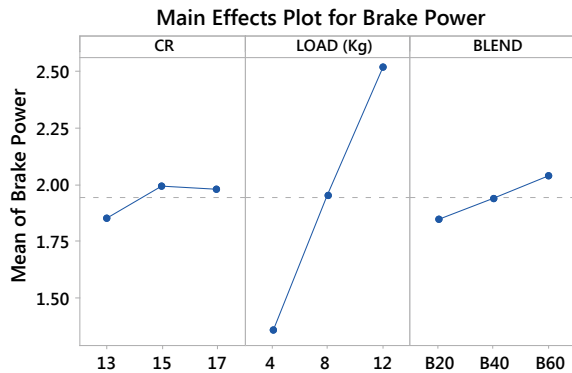
Brake power of the engine should be high as possible, so ‘larger is better’ S/N ratio is considered. In case of brake-specific fuel consumption and nitrogen oxide, ‘smaller is better’ S/N ratio is considered because fuel consumption and exhaust emission should be lower. In addition, analysis of variance (ANOVA) is done to study the effect of input parameters on the performance. Response curve is the graphical representation of engine performance.

Figure 2 shows the main effect plot for brake power; mean value for brake power has maximum value 1.99 at 15 CR, 2.52 at 12 kg load, and 2.04 at B60 blend. Mean value for brake power has minimum value 1.85 at 13 CR, 1.36 at 4 kg load, and 1.85 at B20 blend. Difference between maximum and minimum value of mean is called delta value. Maximum value of delta is for load, i.e., 1.16 having rank 1 and minimum, i.e., 0.143 for compression ratio having rank 3; it means load is having maximum and compression ratio is having minimum effect of on brake power [22]; this results can be confirmed with S/N ratio and ANOVA [23, 24] (Fig. 3).

From S/N ratio and ANNOVA, it is clear that load affects at about 95.40% on brake power of VCR engine. Regression equation for brake power is given below:

$$\begin{aligned} \text{BP(KW)} = & 1.9444 - 0.0911 \text{ CR}_{13} + 0.0522 \text{ CR}_{15} \\ & + 0.0389 \text{ CR}_{17} - 0.5844 \text{ LOAD(Kg)}_4 \\ & + 0.0089 \text{ LOAD(Kg)}_8 + 0.5756 \text{ LOAD(Kg)}_{12} \end{aligned}$$

Fig. 2 Main effect plot for brake power



**Fig. 3** Main effect plot for S/N ratio for brake power

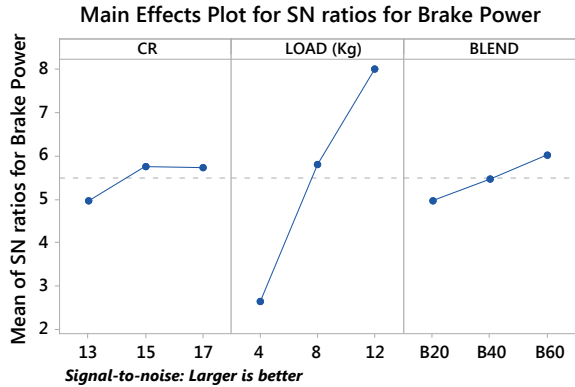
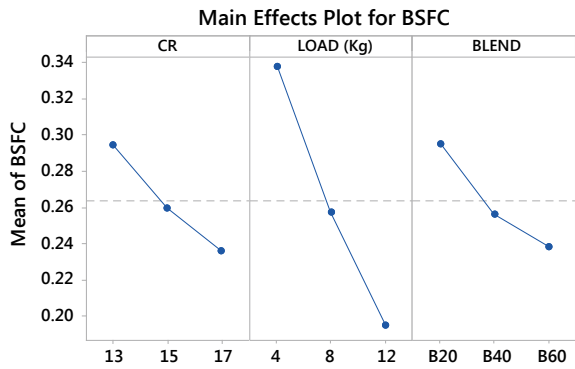


**Fig. 4** Main effect plot for BSFC



$$\begin{aligned}
 & - 0.0944 \text{ BLEND\_B20} - 0.0044 \text{ BLEND\_B40} \\
 & + 0.0989 \text{ BLEND\_B60}
 \end{aligned}
 \tag{4}$$

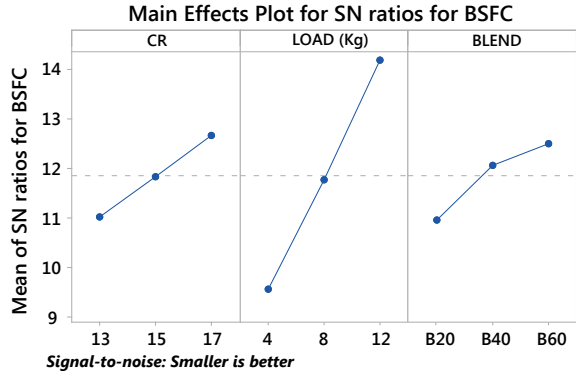
Figure 4 shows the main effect plot for BSFC; mean value for brake power has maximum value 0.2947 at 13 CR, 0.3380 at 4 kg load, and 0.2957 at B20 blend. Mean value for brake power has minimum value 0.2363 at 17 CR, 0.1953 at 12 kg load, and 0.2387 at B60 blend. Difference between maximum and minimum value of mean is called delta value.

Figure 5 shows the main effect plot for S/N ratio for BSFC. From mean effect plot and S/N ratio, it is clear that maximum value of delta is for load, i.e., 4.638 having rank 1 and minimum, i.e., 1.549 for blend having rank 3; it means load is having maximum and blend is having minimum effect of on brake power. These results can be confirmed with S/N ratio and ANOVA. Load affects at about 71.92% on BSFC of VCR engine.

Regression equation for BSFC is given below:

$$\text{BSFC(Kg/Kwh)} = 0.26367 + 0.0310 \text{ CR\_13} - 0.0037 \text{ CR\_15}$$

**Fig. 5** Main effect plot for S/N ratio for BSFC



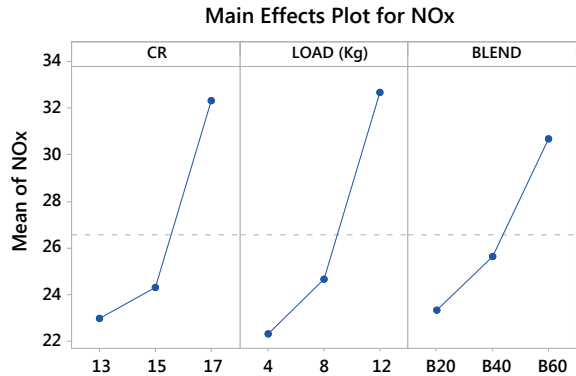
$$\begin{aligned}
 & - 0.0273 \text{ CR}_{17} + 0.0743 \text{ LOAD(Kg)}_4 \\
 & - 0.0060 \text{ LOAD(Kg)}_8 - 0.0683 \text{ LOAD(Kg)}_{12} \\
 & + 0.0320 \text{ BLEND}_{B20} - 0.0070 \text{ BLEND}_{B40} \\
 & - 0.0250 \text{ BLEND}_{B60}
 \end{aligned} \tag{5}$$

Figure 6 shows the main effect plot for NO<sub>x</sub>; mean value for NO<sub>x</sub> has maximum value 32.33 at 17 CR, 32.67 at 12 kg load, and 30.67 at B60 blend. Mean value for brake power has minimum value 23 at 13 CR, 22.33 at 4 kg load, and 23.33 at B20 blend. Difference between maximum and minimum value of mean is called delta value.

From Fig. 7, mean effect plot and S/N ratio, it is observed that delta values of load are 10.33 and 3.58, respectively, and have rank 1. ANOVA shows that load is having 41.15% contribution on exhaust emission (NO<sub>x</sub>). As load on engine increases, exhaust emission increases.

Regression equation for NO<sub>x</sub> is given below:

**Fig. 6** Main effect plot for NO<sub>x</sub>



**Fig. 7** Main effect plot for S/N ratio for NO<sub>x</sub>



$$\begin{aligned}
 \text{NO}_x(\text{ppm}) = & 26.556 - 3.56 \text{CR}_{13} - 2.22 \text{CR}_{15} \\
 & + 5.78 \text{CR}_{17} - 4.22 \text{LOAD}(\text{Kg})_4 - 1.89 \text{LOAD}(\text{Kg})_8 \\
 & + 6.11 \text{LOAD}(\text{Kg})_{12} - 3.22 \text{BLEND}_{B20} - 0.89 \text{BLEND}_{B40} \\
 & + 4.11 \text{BLEND}_{B60}
 \end{aligned} \tag{6}$$

## 5 Conclusion

Biodiesel can be considered as a best alternative fuel for petroleum diesel. As it is renewable fuel, it can be manufactured by the process of transesterification. Biodiesel produced from soybean seed oil is used in the present work for performance evaluation of variable compression ratio diesel engine. Performance tests were conducted by varying engine parameters such as compression ratio and load as well as changing percentage of blend of biodiesel in pure diesel.

Taguchi method is used to analyze the results as it reduces the number of trials to be taken and helps to identify the input factors which directly affect the output. Contribution of individual factor of output parameters such as brake power, brake-specific fuel consumption, and NO<sub>x</sub> emission is evaluated.

The results of experimentation show that load is the crucial factor which directly affects the engine performance. Compression ratio and biodiesel blend are the secondary factors. Brake power increases as compression ratio increases, but it decreases as load increases. Exhaust emission, i.e., nitrogen oxide emission, increases as compression ratio, load, and percentage of biodiesel increase. Regression equation drawn is helpful for optimizing the output of VCR engine.



## References

1. Huang D, Zhou H, Lin L (2012) Biodiesel: an alternative to conventional fuel. *Energy Procedia* 16:1874–1885
2. Kulkarni HB (2016) Design and development of prototype cylindrical parabolic solar collector for water heating application. *Int J Renew Energy Development* 5(1):49
3. Bhujangrao KH (2016) Design and development of cylindrical parabolic collector for hot water generation. *Iranica J Energy Environ* 7(3):226–232
4. Sieminski A (2014) International energy outlook. *Energy Information Administration (EIA)* 18
5. Pathak RK, Pereira DNE, Sharma A, Trivedy R, Yavarzadeh M (2016) Various sources for production of biodiesel. *J Ind Pollution Control*
6. Gupta R, Gupta P, Bhalla J, Mourya S (2016) Performance analysis of a diesel engine using the soybean oil based biodiesel. *Indian J Sci Technol* 9(36)
7. Ge JC, Yoon SK, Choi NJ (2017) Using canola oil biodiesel as an alternative fuel in diesel engines: a review. *Appl Sci* 7(9):881
8. Mendez A (2011) Production of biodiesel from corn oil and ethanol by homogeneous alkali catalyzed transesterification
9. Prathmesh MS, Kulkarni HB (2017) Evaluation of performance characteristics and exhaust gas analysis of VCR engine at different compression ratio and loads. *Iranian J Energy Environ* 8(3):230–233
10. Solis JL, Berkemar AL, Alejo L, Kiros Y (2017) Biodiesel from rapeseed oil (*Brassica napus*) by supported  $\text{Li}_2\text{O}$  and  $\text{MgO}$ . *Int J Energy Environ Eng* 8(1):9–23
11. Khalizani K, Khalisanni K (2011) Transesterification of palm oil for the production of biodiesel. *Am J Appl Sci* 8(8):804–809
12. Shalaby EA (2011) Algal biomass and biodiesel production. In *biodiesel-feedstock and processing technologies*. InTech, Rijeka, Croatia
13. Sing SF, Isdepsky A, Borowitzka MA, Moheimani NR (2013) Production of biofuels from microalgae. *Mitig Adapt Strat Glob Change* 18(1):47–72
14. Parawira W (2010) Biodiesel production from *Jatropha curcas*: a review. *Sci Res Essays* 5(14):1796–1808
15. Raja SA (2011) Biodiesel production from jatropha oil and its characterization. *Res J Chem Sci* 1:81–87
16. Groschen R (2011) Overview of the feasibility of biodiesel from waste/recycled greases and animal fats. *Minnesota Department Agriculture*
17. Guo Y, Leung YC, Koo CP (2002) A clean biodiesel fuel produced from recycled oils and grease trap oils (BAQ 2002). In: *Better Air Quality in Asian and Pacific Rim Cities*, 16, pp 55–1
18. Demshemino S, Yahaya MF, Nwadike I, Okora LN (2013) Comparative analysis of biodiesel and petroleum diesel. *Int J Educ Res* 1:8
19. Firoz S (2017) A review: advantages and disadvantages of biodiesel. *Int Res J Eng Technol (IRJET)* 04(11)
20. Rajage S, Waghmare S, Pathan S, Shinde A, Kubade PR (2016) effect of laser cutting parameters on surface quality and kerf width of high-carbon high-chromium steel (AISI D3). *Int J Innov Res Sci Eng* 3:571–580
21. <https://support.minitab.com/en-us/minitab/18/help-and-how-to/modeling-statistics/doe/supporting-topics/taguchi-designs/what-is-the-signal-to-noise-ratio/>. Last Accessed 07 June 2018
22. Modi MA, Patel TM, Rathod GP (2014) Parametric optimization of single cylinder diesel engine for palm seed oil & diesel blend for brake thermal efficiency using Taguchi method. *IOSR J Eng* 4(05)
23. Kshirsagar G (2016) Parametric optimization of abrasive water jet machining of inconel-718 material. *Int Res J Eng Technol (IRJET)* 03(08)

24. Rao SR, Padmanabhan G (2012) Application of Taguchi methods and ANOVA in optimization of process parameters for metal removal rate in electrochemical machining of Al/5% SiC composites. *Int J Eng Res Appl* 2(3):192–197
25. Mohan M, Verma V (2017) Optimization of performance of VCR engine blended with palm oil biodiesel using taguchi method
26. Prajapati JM, Patel PR, Patel TM (2017) Parametric optimization of single cylinder diesel engine fueled with karanja biodiesel & diesel blend for brake thermal efficiency using taguchi method. *IOSR J Mech Civil Eng* 14(2):107–111
27. Sivaramkrishnan K, Ravikumar P (2012) Performance optimization of karanja biodiesel engine using taguchi approach and multiple regressions. *ARPN J Eng Appl Sci*, 7:507–516
28. Patel DV, Patel TM, Rathod GP (2015) Parametric optimization of single cylinder diesel engine for jatropha biodiesel and diesel blend for brake specific fuel consumption using taguchi method. *IOSR J Mech Civil Eng (IOSR-JMCE)*, 12(2):66–72
29. Rambabu V, Prasad VJJ, Subramanyam T (2012) Evaluation of performance and emissions of a VCR DI diesel engine fuelled with preheated CsME. *Global J Res Eng*, 12(7-A). *Global J Res Eng Mech Mech Eng* 12(7)
30. Palanisamy PS (2014) Performance of single cylinder ci engine using blends of rubber seed biodiesel-taguchi method. *UPB Sci Bull Series D* 76(4)
31. Patel MKB, Patel TM, Patel MSC (2012) Parametric optimization of single cylinder diesel engine for pyrolysis oil and diesel blend for specific fuel consumption using taguchi method. *IOSR J Mech Civil Eng* 6(1):83–88
32. Rao KS, Kumar MP, Prasad SS, Teja BS, Chandh YVS (2017) design of chassis of two-wheeled electrical vehicle by optimization of design parameters using taguchi method. *Int J Mech Eng Technol(IJMET)* 8(1):62–69
33. Özener O, Yüksek L, Ergenç AT, Özkan M (2014) Effects of soybean biodiesel on a DI diesel engine performance, emission and combustion characteristics. *Fuel* 115:875–883
34. Rao PV (2013) The effects in performance and emissions of DI diesel engine using biodiesel (PPME)-Blends as fuel. *Asian J Sci Appl Technol* 2(2):1–4
35. Dahiya AP, Berwal AK, Khan BK (2015) Combustion analysis in a compression ignition engine powered by biodiesel. *Int J Eng Technol Manage Appl Sci* 3(9)
36. Wilson VH (2012) Optimization of diesel engine parameters using Taguchi method and design of evolution. *J Brazilian Soc Mech Sci Eng* 34(4):423–428
37. Mohammed EK, Nemit-allah MA (2013) Experimental investigations of ignition delay period and performance of a diesel engine operated with Jatropha oil biodiesel. *Alexandria Eng J* 52(2):141–149

# Vibration Response of Sandwich Beam with Viscoelastic Core and FGM Face Sheets Using Finite Element Method



I. Ramu, M. Raghuraman and K. V. G. R. Seshu

**Abstract** The present work explains about the vibration response of a viscoelastic sandwich beam with functionally graded material constraining layers. These layers are formed by varying the ceramic ( $Al_2O_3$ ) and stainless steel (SUS304) composition along the thickness direction. The basic kinematics is considered from Timoshenko beam theory due to inertia effect. The sandwich beam is formulated. Three-layered sandwich beam is modelled using the finite element method. The top and bottom layers are FGM layers and the middle layer as a viscoelastic core. The linear displacement field is assumed to model the FGM layers and also the core layer displacement field as non-linear. Hamilton's principle is used to derive the governing equation of motion of the viscoelastic sandwich beam. The vibration analysis has been carried out by using the derived governing equation of motion with cantilever and fixed-fixed boundary conditions. The obtained results are compared with the available literature results. The natural frequencies are calculated with different boundary conditions by varying the core thickness. The influence of core thickness and FGM constraining layer index value on natural frequencies are observed.

**Keywords** Sandwich FGM beam · Timoshenko beam theory · Viscoelastic core · Finite element method · Free vibrations

## Nomenclature

$h$	Thickness of FGM face sheet
$u$	Displacement in $x$ direction
$w$	Displacement in transverse direction
$N$	Shape function
$\{q\}$	Final displacement vector
$\{q^{(e)}\}$	Element displacement vector

---

I. Ramu (✉) · M. Raghuraman · K. V. G. R. Seshu  
Vishnu Institute of Technology, Bhimavaram 534202, India  
e-mail: [ramuinala@gmail.com](mailto:ramuinala@gmail.com)

© Springer Nature Singapore Pte Ltd. 2020  
L. Vijayaraghavan et al. (eds.), *Emerging Trends in Mechanical Engineering*,  
Lecture Notes in Mechanical Engineering,  
[https://doi.org/10.1007/978-981-32-9931-3\\_37](https://doi.org/10.1007/978-981-32-9931-3_37)

$[K]$	Final stiffness matrix
$[K^{(e)}]$	Element stiffness matrix
$[K_C]^{(e)}$	Element stiffness matrix of a viscoelastic core
$[K_{FG}]^{(e)}$	Element stiffness matrix of a constraining layer of FGM
$[M]$	Final mass matrix
$[M^{(e)}]$	Element mass matrix
$[M_C]^{(e)}$	Element mass matrix of a viscoelastic core
$[M_{FG}]^{(e)}$	Element mass matrix of a constraining layer of FGM
$\rho_{FG}$	Density of FG
$\rho_C$	Density of viscoelastic core
$V_C$	Volume fraction of ceramic
$V_M$	Volume fraction of metal
$\eta$	Loss factor
$\eta_v$	Core loss factor

## 1 Introduction

Vibration characteristics of sandwich structures are vital precise to study the dynamics analysis of structural members. The sandwich beam is one of the important structural members which is made up of two face sheets joined by viscoelastic core member as a middle layer. To reduce vibration, damping mechanism of a viscoelastic core is introduced for a sandwich beam. These sandwich structures have many applications such as railways, bridges, satellites, aeroplane wings and robotic arms etc.

Sandwich beam vibration analysis with exact solutions has been studied by Rao [1], and the various boundary conditions are used to calculate the frequency result, loss factors and the shear modulus assumed as a complex in the core model. Ganapathi et al. [2] studied the dynamic analysis of laminated composite and sandwich beam with loss factors. Arikoglu and Ozkol [3] examined the effect of viscoelastic core thickness on natural frequencies of three-layered sandwich beam model. A meshless method using penalty approach was studied by ChehelAmirani et al. [4] for vibration analysis of FG core sandwich beam with various boundary conditions. Abdoun et al. [5] studied the harmonic response of sandwich viscoelastic beam using an asymptotic numerical method.

Bilasse et al. [6] proposed a numerical solution using finite element approach for linear and non-linear vibration analysis of viscoelastic sandwich beam. Multi-layered sandwich beam modelled using finite element formulation for free vibration analysis has been presented by Mohanty [7]. Long et al. [8] where the finite element formulation is explained for sandwich structure and compared the obtained numerical simulation results of ANSYS with the reference results. Kpeky et al. [9] examined the solid-shell finite element formulation for sandwich structures modal analysis. Long [10] studied the active constraining layer of FG beam using finite element approach.

In the literature, there is no survey on bounds and soundness assortment of the sandwich structures damping responses. The numerical assessment related to this work is to improve a vibrant representation for vibration characteristics of damped sandwich beams. The main aim of the present work is to develop a finite element approach of a three-layered sandwich beam with cantilever and fixed–fixed boundary conditions and to investigate its vibration responses. The bottom and top face sheets are assumed to be FGM sheets, while the core is assumed as a viscoelastic layer. The FGM face sheets are made up of two materials, i.e. stainless steel and alumina, the viscoelastic core is assumed as polyurethane foam. The frequency response curves are obtained for various core loss factors, boundary conditions and different thickness ratios.

## 2 Mathematical Formulation

Sandwich beam with viscoelastic core as a middle is illustrated in Fig. 1. Timoshenko beam theory is adopted to model the bottom and top face FGM constraining layers.

The FGM constraining layer field variables are expressed as

$$\begin{aligned}
 u(x, z, t) &= u(x, t) - z\phi(x, t) \\
 w(x, z, t) &= w(x, t)
 \end{aligned}
 \tag{1}$$

The displacement vector of an element can be represented as:

$$q_e^T = \begin{bmatrix} u_{t1} & w_{t1} & \phi_{t1} & u_{c2,1} & u_{c3,1} & w_{c,1} & u_{b,1} & w_{b,1} & \phi_{b,1} \\ w_{t2} & w_{c2} & w_{b2} \\ u_{t3} & w_{t3} & \phi_{t3} & u_{c2,3} & u_{c3,3} & w_{c3} & u_{b,3} & w_{b,3} & \phi_{b,3} \end{bmatrix}
 \tag{2}$$

The axial displacement of the viscoelastic core layer is denoted with a cubic function and the displacement of transverse direction is incorporated by the quadratic function.

Shape functions are represented as

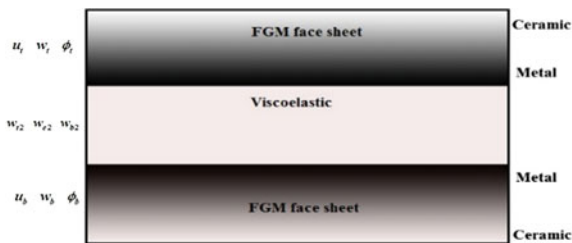


Fig. 1 Viscoelastic sandwich beam with FGM constraining layers

$$\begin{aligned}
 N_1 &= \frac{1 - \zeta}{2}, N_2 = \frac{1 + \zeta}{2} \quad \text{for } -1 \leq \zeta \leq 1 \\
 N_3 &= \frac{\zeta^2 - \zeta}{2}, N_4 = 1 - \zeta^2, N_5 = \frac{\zeta^2 + \zeta}{2} \quad \text{for } -1 \leq \zeta \leq 1
 \end{aligned}
 \tag{3}$$

### 2.1 The Material Properties of FGM Face Sheet

The material properties of FGM face sheets are varying in the thickness direction, the effective material properties such as ( $E_{FG}$ ) Young’s modulus, ( $\rho_{FG}$ ) mass density and ( $\nu_{FG}$ ) Poisson’s ratio is obtained as.

$$\begin{aligned}
 E_{FG}(z) &= E_C V_C + E_M V_M \\
 \rho_{FG}(z) &= \rho_C V_C + \rho_M V_M \\
 \nu_{FG}(z) &= \nu_C V_C + \nu_M V_M
 \end{aligned}
 \tag{4}$$

The relationship between the ( $V_M$ ) metal and ( $V_C$ ) ceramic volume fractions is represented using simple rule of mixture obtained as

$$V_C + V_M = 1
 \tag{5}$$

The volume fraction of ceramic varies by using the simple power-law function is obtained as

$$V_C = \left( \frac{z + h}{2 \times h} \right)^k
 \tag{6}$$

In which,  $k$  is an index of the power law and  $h$  is the thickness of face sheet. The variation of index value  $k$  varies the ceramic volume fraction content. It causes to change the material properties of the FGM constraining layer.

### 2.2 FGM Face Sheet

The constraining elemental FGM beam layer kinetic energy is expressed as:

$$K E_{FG}^{(e)} = \frac{1}{2} \rho_{FG} \iiint_v \left[ \left( \frac{\partial u}{\partial t} \right)^2 + \left( \frac{\partial w}{\partial t} \right)^2 \right] dv$$

$$= l_b \int_x \rho_{FG} \partial u_{FG} \ddot{u}_{FG} dx + l_b \int_x \rho_{FG} \partial w_{FG} \ddot{w}_{FG} dx + \alpha l_b \int_x \rho_{FG} \partial \phi_{FG} \ddot{\phi}_{FG} dx \tag{7}$$

The kinetic energy of constraining layer of FGM beam element is expressed as

$$\begin{aligned} KE_{FG}^{(e)} &= l_b \int_0^{l_e} \rho_{FG} (\delta q_{(e)}^T [N_{FG}]^T [I_{FG}] [N_{FG}] \delta \ddot{q}_{(e)}) dx \\ &= \delta q_{(e)}^T [M_{FG}]^{(e)} \delta \ddot{q}_{(e)} \end{aligned} \tag{8}$$

where  $[M_{FG}]^{(e)}$  is mass matrix of FGM face sheet of beam element.

The stiffness matrix of FGM face sheet is expressed from the potential energy

$$\begin{aligned} PE_{FG}^{(e)} &= \iiint_v (\varepsilon^T \sigma) dv = l_b \int_0^{l_e} (\delta q_{(e)}^T [B_{FG}]^T [D_{FG}] [B_{FG}] \delta q_{(e)}) dx \\ &= \delta q_{(e)}^T [K_{FG}]^{(e)} \delta \ddot{q}_{(e)} \end{aligned} \tag{9}$$

where  $[K_{FG}]^{(e)}$  is element stiffness matrix of FGM face sheet.

### 2.3 Viscoelastic Core

Viscoelastic core element kinetic energy can be represented as

$$\begin{aligned} KE_C^{(e)} &= l_C \int_0^{l_e} \rho_C (\delta q_{(e)}^T [N_C]^T [I_C] [N_C] \delta \ddot{q}_{(e)}) dx \\ &= \delta q_{(e)}^T [M_C]^{(e)} \delta \ddot{q}_{(e)} \end{aligned} \tag{10}$$

where  $[M_C]^{(e)}$  is element viscoelastic core mass matrix.

The elemental strain energy of viscoelastic core is expressed as

$$\begin{aligned} PE_C^{(e)} &= l_b \int_0^{l_e} (\delta q_{(e)}^T [B_C]^T [D_C] [B_C] \delta q_{(e)}) dx \\ &= \delta q_{(e)}^T [K_C]^{(e)} \delta \ddot{q}_{(e)} \end{aligned} \tag{11}$$

where  $[K_C]^{(e)}$  is viscoelastic core element stiffness matrix.

## 2.4 Governing Equation of Motion

Hamilton's principle is used to derive the governing equation of motion of viscoelastic sandwich beam element.

$$\delta \int_{t_1}^{t_2} (\text{KE}^{(e)} - \text{PE}^{(e)}) dt = 0 \quad (12)$$

The equation of motion of sandwich beam element is represented as

$$[M^{(e)}]\{\ddot{q}^{(e)}\} + [K^{(e)}]\{q^{(e)}\} = 0 \quad (13)$$

Sandwich beam element's potential energy is equal to the sum of the potential energy of the constraining layers and viscoelastic layer. Similarly, the kinetic energy of sandwich beam element is the sum of a viscoelastic element and FGM face sheets.

The equation of motion of sandwich beam by assembling of mass and elastic stiffness matrix is obtained as

$$[M]\{\ddot{q}\} + [K]\{q\} = 0 \quad (14)$$

## 3 Results and Discussion

Vibration response of sandwich beam with viscoelastic core can be studied using finite element method. The viscoelastic behaviour of a core material is assumed in a simple way by considering Young's modulus  $E = E_v(1 + i\eta\nu)$ , where  $E_v$  and  $\eta\nu$  are constant. The derived equation of motion is used to determine the natural frequencies and loss factors for various modes. The first six modes of natural frequencies of a viscoelastic sandwich beam with a clamped-free boundary condition for various core loss factors are presented in Table 1. These results are reasonably good of those provided by the literature of references Bilasse et al. [6] and Abdoun et al. [5] observed in Table 1.

Material properties which are used for this analysis are presented below.

Young's modulus of elastic face sheet =  $6.9 \times 10^{10} \text{ Nm}^{-2}$

Poisson ratio of elastic face sheet = 0.3

Density of elastic face sheet =  $2766 \text{ kg m}^{-3}$

Viscoelastic material properties:

Young's modulus  $E = 1.794 \times 10^6 \text{ Nm}^{-2}$

Poisson ratio  $\nu_c = 0.3$

Density  $\rho_c = 968.1 \text{ kg m}^{-3}$

The material properties of the ceramic and metal are as follows:



**Table 1** Cantilever viscoelastic sandwich beam natural frequencies and loss factors

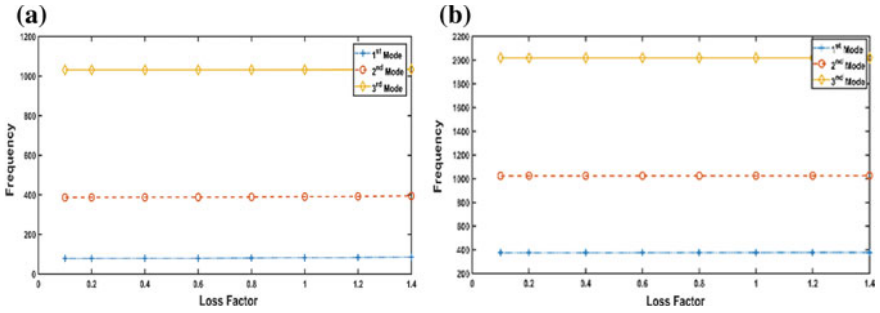
Core's loss factor ( $\eta_v$ )	Bilasse et al. [6]		Abdoun et al. [5]		Present	
	Frequency	Loss factor ( $\eta$ )	Frequency	Loss factor ( $\eta$ )	Frequency	Loss factor ( $\eta$ )
0.1	64.1	0.281	64.5	0.281	64.2	0.281
	296.7	0.242	298.9	0.242	297.4	0.242
	744.5	0.154	746.5	0.154	749.0	0.153
	1395.7	0.089	1407.7	0.089	1412.1	0.088
	2264.5	0.057	2286.2	0.057	2308.8	0.056
	3349.8	0.039	3385.7	0.039	3448.1	0.037
0.6	65.5	0.246	65.9	0.247	65.7	0.246
	299.2	0.232	303.1	0.224	300.6	0.232
	746.3	0.153	752.3	0.150	751.5	0.152
	1396.6	0.089	1412.7	0.088	1413.5	0.087
	2265.2	0.057	2290.6	0.057	2309.47	0.056
	3350.2	0.039	3389.5	0.039	3448.7	0.037
1	67.5	0.202	67.8	0.204	67.8	0.203
	303.1	0.218	309.1	0.201	305.5	0.218
	749.4	0.150	761.1	0.142	755.9	0.149
	1398.3	0.088	1420.6	0.086	1416.0	0.086
	2266.3	0.057	2297.9	0.057	2311.4	0.055
	3350.9	0.039	3395.9	0.037	3449.8	0.037
1.5	69.9	0.153	70.3	0.155	70.4	0.153
	309.1	0.198	317.4	0.176	313.1	0.198
	755.2	0.146	777.2	0.131	764.0	0.145
	1401.4	0.087	1432.8	0.083	1420.6	0.086
	2268.5	0.057	2310.1	0.056	2314.5	0.055
	3352.3	0.039	3307.0	0.039	3451.8	0.037

$$\text{SUS304, } \rho_c = 7800 \text{ kg/m}^3, E = 201 \text{ GPa, } \nu = 0.3$$

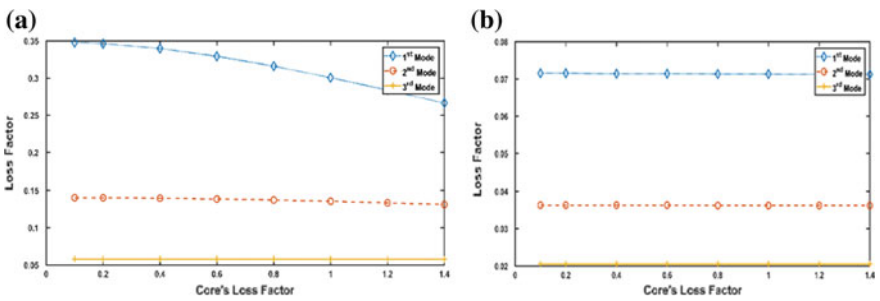
$$\text{Al}_2\text{O}_3, \rho_m = 2707 \text{ kg/m}^3, E = 380 \text{ GPa, } \nu = 0.3$$

Figure 2a, b represents the frequency variation with respect to the loss factor of the viscoelastic sandwich beam with FGM face sheets of a cantilever and both sides fixed boundary conditions, respectively. It is noticed that the first three mode frequencies are reduced with an increase of loss factor. The increase of loss factor reduces its overall stiffness matrix of the sandwich beam, which may cause marginally reduces its frequencies.

The variation of loss factor with respect to the core loss factor is shown in Fig. 3a, b, correspondingly. The loss factor is decreased with an increase of core loss factor.



**Fig. 2** **a** First three-mode frequencies variation with loss factor for cantilever beam. **b** First three-mode frequencies variation with loss factor for fixed beam



**Fig. 3** **a** First three-loss factors variation with a core loss factor of cantilever beam. **b** First three-loss factor variation with core loss factor of both sides fixed beam

This is because of increase of core loss factor. The first mode loss factor decrease of variation can be observed in these figures. Similarly, the other two modes are also varied to a certain extent.

Figure 4a, b illustrated the frequency versus thickness ratio (FGM face sheet to the core) for cantilever and both sides fixed boundary conditions. It indicates that the increase of thickness ratio reduces the first three mode frequencies. There is

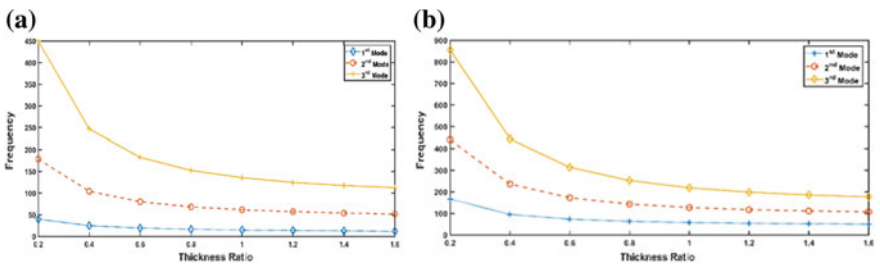


**Fig. 4** **a** First three-mode frequencies variation with thickness ratio of cantilever beam. **b** First three-mode frequencies variation with thickness ratio of both sides fixed beam

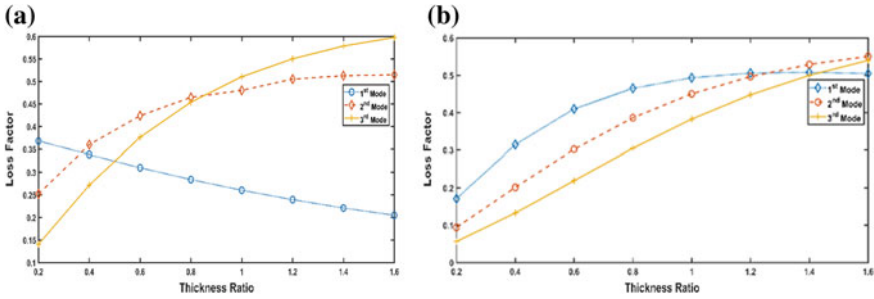


**Fig. 5** **a** Loss factor versus thickness ratio of cantilever beam. **b** Loss factor versus thickness ratio of both sides fixed beam

no effect of the bending moment and displacement for fixed–fixed condition on the frequencies. Hence, higher frequency values.

The variation of loss factor against thickness ratio of a sandwich beam for cantilever and both sides fixed boundary conditions is shown in Fig. 5a, b. Here, the increase of thickness ratio may decrease the first mode frequency; similarly, the increase of thickness ratio increases the second and third mode frequencies of FGM constraining layer sandwich beam. The reasons might be the effect of eigenvalues.

### 4 Conclusions

Vibration responses and loss factors are obtained for a viscoelastic sandwich beam with various boundary conditions by using the present developed finite element modal. Timoshenko beam theory is assumed for basic kinematics. In the presently developed modal of the finite element method with three layer sandwich beam. The governing equation of motion of viscoelastic sandwich beam is derived by Hamilton’s principle. The influence of loss factor on the natural frequencies is observed. The natural frequencies are reduced with an increase of loss factor. The effect of loss factor on the thickness ratio also calculated. An increase of core thickness will decrease the first mode and correspondingly, increase the second and third mode frequency of cantilever sandwich beams.

### References

1. Rao DK (1975) Frequency and loss factors of sandwich beams under various boundary conditions. *J Mech Eng Sci* 20(5):271–282
2. Ganapathia M, Patel BP, Boisse P, Polit O (1999) Flexural loss factors of sandwich and laminated composite beams using linear and nonlinear dynamic analysis. *Compos: Part B* 30:245–256

3. Arikoglu A, Ozkol I (2010) Vibration analysis of composite sandwich beams with viscoelastic core by using differential transform method. *Compos Struct* 92:3031–3039
4. ChehelAmirani M, Khalili SMR, Nemati N (2009) Free vibration analysis of sandwich beam with FG core using the element free Galerkin method. *Compos Struct* 90:373–379
5. Abdoun F, Azrar L, Daya EM, Potier-Ferry M (2009) Forced harmonic response of viscoelastic structures by an asymptotic numerical method. *Comput Struct* 87:91–100
6. Bilasse M, Daya EM, Azrar L (2010) Linear and non-linear vibrations analysis of viscoelastic sandwich beams. *J Sound Vib* 329:4950–4969
7. Mohanty SC (2011) Finite element modeling of a multilayered sandwich beam with viscoelastic core for vibration analysis, vol 10. In: *International Conference on modeling, simulation and control, IPCSIT*, pp 103–108
8. Long R, Barry O, Oguamanam DCD (2012) Finite element free vibration analysis of soft-core sandwich beams. *AIAA J* 50(1):35–38
9. Kpeky F, Boudaoud H, Abed-Meraim F, Daya EM (2015) Modeling of viscoelastic sandwich beams using solid-shell finite elements. *Compos Struct* 133:105–116
10. Long R (2010) A finite element formulation of active constrained-layer functionally graded beam. Ryerson University, Toronto

# Heat Transfer Enhancement with Different Nanofluids in Heat Exchanger by CFD



T. Sreedhar, B. Nageswara Rao and D. Vinay Kumar

**Abstract** Nanofluids play a prominent role in heat transfer applications. The thermophysical phenomenon is additionally necessary for these fluids. Many researchers' have been measured these fluids, in terms of preparation, stability and thermal properties. Most of the industries measure mistreatment of different types of heat exchangers. In order to interchange this drawback, we tend to square measure mistreatments completely for different coolants like water with ethylene glycol, nanofluid, and hybrid nanofluid. These fluids have high thermophysical properties. The design and modeling of a double pipe heat exchanger is finished by creo 2.0 and temperature distribution, heat transfer constant is simulated by ANSYS Fluent.

**Keywords** H<sub>2</sub>O · MWCNT · Creo 2.0 · CFD

## 1 Introduction

The nanoparticles utilized in nanofluids are usually made from metals, oxides, carbides, or carbon nanotubes. Common base fluids are water, glycol, and oil. The mixture of nanoparticle and base fluid is known as nanofluids. Two different base fluids (mixing water/EG/oil with different weight ratio) or two different nanoparticles are suspended in base fluid is known as hybrid nanofluid. These fluids have highest thermal conductivity compared to conventional fluids, so these are effectively used in different applications like heat exchangers, fuel cells, solar, engines, and space. Formulation of nanolubricants from the several metals, oxides, and allotropes of carbon helps to improve anti-wear property of base oils, and thermal conductivity will enhance during the addition of nanoparticles [1] (Fig. 1).

---

T. Sreedhar (✉) · B. Nageswara Rao · D. Vinay Kumar  
Department of Mechanical Engineering, Vignan's Foundation for Science Technology & Research, Vadlamudi, Guntur 522213, Andhra Pradesh, India  
e-mail: [sreedharthotti@gmail.com](mailto:sreedharthotti@gmail.com)

© Springer Nature Singapore Pte Ltd. 2020  
L. Vijayaraghavan et al. (eds.), *Emerging Trends in Mechanical Engineering*,  
Lecture Notes in Mechanical Engineering,  
[https://doi.org/10.1007/978-981-32-9931-3\\_38](https://doi.org/10.1007/978-981-32-9931-3_38)

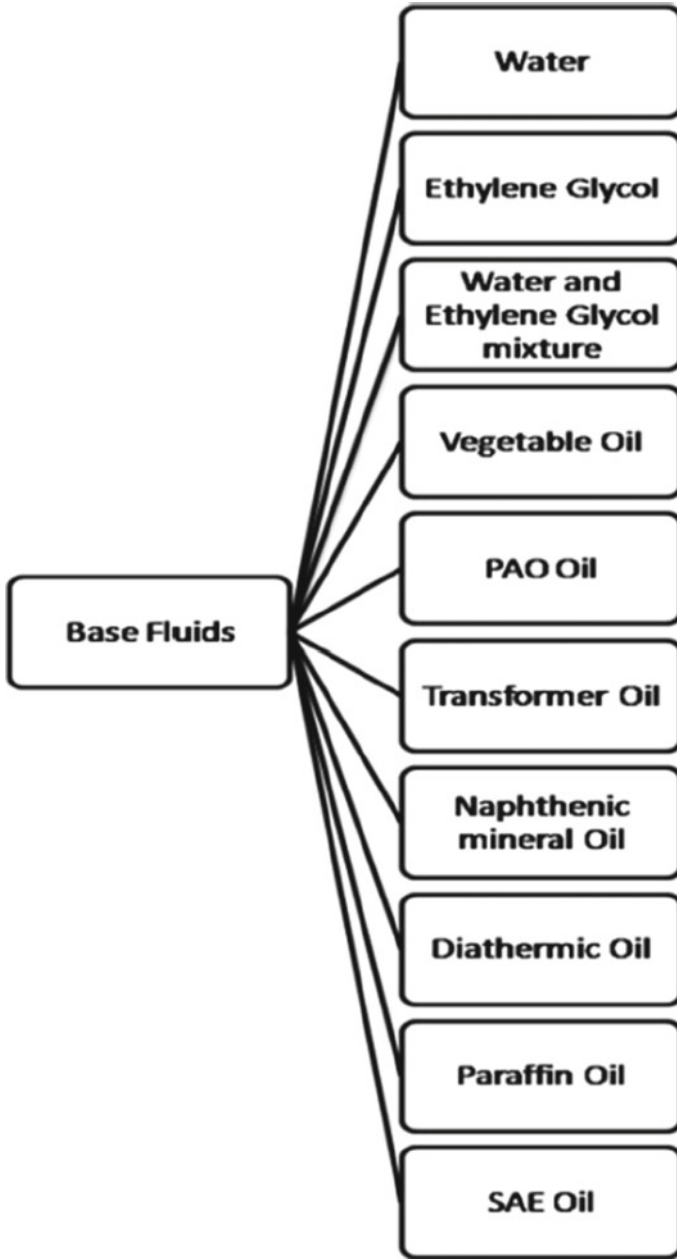


**Fig. 1** Base fluids were used by researches to prepare nano- and hybrid nanofluids

## 1.1 Preparation and Stability of Nanofluids

We have two different types of methods to prepare the nano/hybrid nanofluids; they are single-step and two-step methods or dispersion method. The single-step methodology has the benefits in terms of dominant particle size, reducing the particles agglomeration, and manufacturing nanofluids containing aluminiferous nanoparticles. But, many of the researchers focus on the two-step method because of the high-accuracy results [2].

Using UV–Vis spectrophotometer, Hwang et al. [3] conducted many experiments on MWCNT, fullerene, CuO, and SiO<sub>2</sub> to know the stability and thermophysical properties of the nanofluid. The results noticed increasing sedimentation time with decrease in fullerene in oil. By using centrifugal method, Sing et al. [4] conducted experiments on Ag nanofluid. In this experimentation, PVP is used as a stabilizer. Ag nanofluid has good stability while utilizing PVP. Jain et al. [5] conducted different experiments on Al<sub>2</sub>O<sub>3</sub> nanoparticles which are suspended in DI water and EG. Thermal conductivity of Al<sub>2</sub>O<sub>3</sub> nanofluid is found with help of hot-wire method, and stability of the nanofluid was found by using 3 omega method.

## 2 Literature Survey

Dong et al. [6] conducted the experiment on pool boiling heat transfer from surfaces with micro/nanostructures. The results stated that at low heat fluxes, surfaces with microstructures have a way higher density of active nucleation sites than that on a smooth surface, enhancing the heat flux and reducing the heat. Usri and Azmi [7] conducted an experiment on Al<sub>2</sub>O<sub>3</sub> nanoparticles which were randomly dispersed into mixture of water: EG (different volume ratios are 40:60, 50:50, and 60:40) using a two-step method. The activity information of the nanofluids provides most improvement in thermal conductivity. Phanindra et al. [8] performed the experiment on Al<sub>2</sub>O<sub>3</sub> and Cu/oil hybrid nanofluid. In this experiment, he found the heat transfer and flow characteristics of hybrid nanofluids. Amin and Asadi [9] conducted experiment on Mg (OH)<sub>2</sub>/MWCNT engine oil. In this, dynamic viscosity and thermal conductivity are increased with increase in volume concentration.

Yousef et al. [10] conducted many experiments on multiwall carbon nanotubes (MWCNT) which are dispersed in water. From the experimental results, pH value of the MWCNT is 7.4 which is small difference isotropic point and nanofluid which causes a interparticle repulsion force. Rahimi et al. [11] performed many experiments on DWCNT which are suspended in water as a base fluid. The experimental results analyzed high heat transfer rate and entropy of the nanofluid. Timofeeva et al. [12] conducted experiments on large size of the SiC nanoparticles which are suspended in water. The results give little enhancement of heat transfer and high viscosity. To improve the heat transfer, we need to work on small nanoparticle size. Bastian Aguila and Vasco [13] performed experiment on the CuO nanofluid. Thermal conductivity

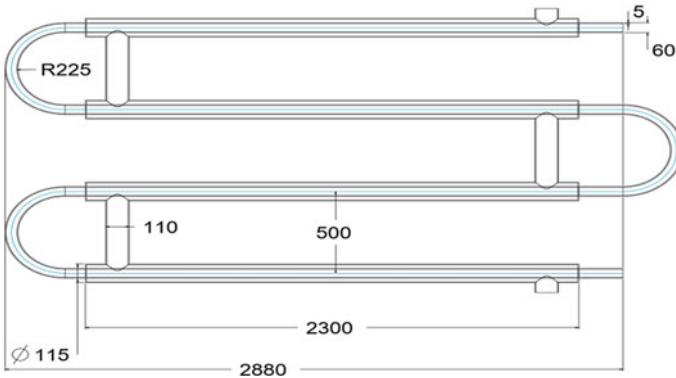


**Fig. 2** D drafting of heat exchanger; the dimensions are in millimeters

of the nanofluid is observed by using thermal analyzer. Different experiments were conducted by i.e., varying of temperature (30–40 °C and viscosity was 30–55 °C) of CuO nanofluid were performed and observed the 9–11% of increment of thermal conductivity of nanofluid. Garg and Alvarado [14] worked on the MWCNT with base fluid water. There are definite optimum process conditions (ultrasonication time during this case) that can provide the enhancement in heat transfer.

### 3 Modeling of Heat Exchanger Using Creo 2.0

For the development of this type of equipment, generally we use Sweep in Creo software. In this operation, basically we require diameters and length. Then, the model is saved in part file and step file (Fig. 2).

### 4 Boundary Conditions

Fluids: water and ethylene glycol

Nanoparticles: copper (Cu), copper oxide (CuO), and multiwall copper nanotube (MWCNT)

Conditions for heat exchangers: parallel flow

Inlet temperature of pipe = 345 K

Inlet temperature of shell = 303 K

Inlet mass flow rate = 1.5 kg/s [8].



## 5 Thermophysical Properties

Wang et al. [15] conducted a review on theoretical and numerical investigations and found many formulas based on different investigators on the thermophysical properties.

Density ( $\text{kg/m}^3$ )

$$\rho_{\text{nf}} = \varnothing * \rho_{\text{np}} + (1 - \varnothing) * \rho_{\text{bf}} \quad (1)$$

Specific heat ( $\text{J/kg K}$ )

$$C_{p_{\text{nf}}} = \frac{\varnothing * (\rho C p)_{\text{np}} + (1 - \varnothing) * (\rho C p)_{\text{bf}}}{\varnothing * (C p)_{\text{np}} + (1 - \varnothing) * (C p)_{\text{bf}}} \quad (2)$$

Thermal conductivity ( $\text{W/m}^2 \text{K}$ )

$$K_{\text{eff}} = \frac{k_{\text{np}} + 2k_{\text{bf}} + 2(k_{\text{np}} - k_{\text{bf}})\phi}{k_{\text{np}} + 2k_{\text{bf}} - (k_{\text{np}} - k_{\text{bf}})\phi} K_{\text{bf}} \quad (3)$$

Viscosity ( $\text{kg/ms}$ )

$$\mu_{\text{nf}} = \text{Pr} * \frac{k_{\text{nf}}}{c_{p(\text{nf})}} \quad (4)$$

Similarly, the calculations of thermophysical properties for the MWCNT were investigated. For the density, Laurent et al. [16] explained the weight and density of carbon nanotubes.

$$D_{\text{mw}} = 1000 \frac{W_{\text{mw}}}{V_{\text{mw}}} \quad (5)$$

where

$$W_{\text{mw}} = \frac{1}{1315} \pi L \left[ n d_{\text{out}} - 2 d_{s-s} \sum_{i=0}^{n-1} i \right] \quad (5.1)$$

$$V_{\text{mw}} = \pi L \frac{d_{\text{out}}^2}{4} \quad (5.2)$$

For the calculation of thermal conductivity, Xue et al. [17] investigated the model for thermal conductivity of carbon nanotube-based composites.

$$K_{\text{eff}} = k_{\text{bf}} \frac{1 - \varnothing + 2\varnothing \frac{k_{\text{np}}}{k_{\text{np}} - k_{\text{bf}}} \ln \frac{k_{\text{np}} + k_{\text{bf}}}{2k_{\text{bf}}}}{1 - \varnothing + 2\varnothing \frac{k_{\text{bf}}}{k_{\text{np}} - k_{\text{bf}}} \ln \frac{k_{\text{np}} + k_{\text{bf}}}{2k_{\text{bf}}}} \quad (6)$$

## 6 Fluent for Heat Exchanger

The step file is imported to this ANSYS Fluent. Here, we have to assign the fluid and solid body to the imported assembly file, i.e., step file (Fig. 3).

Figure 4 represents that the body is undergone with meshing to split number of elements and nodes. In this, 185,600 nodes and 216,358 elements are generated because the minimum edge length is 0.32 mm and maximum face size is 16.3 mm (Table 1).

Figure 5 shows the fluid flow in pipe and shell both inlet and outlet of fluid, where A is hot fluid at inlet, B is cold fluid at inlet, C is hot fluid at outlet, and D is cold fluid at outlet. Here, the hot fluid is water which is constant for 3 cases and cold fluid

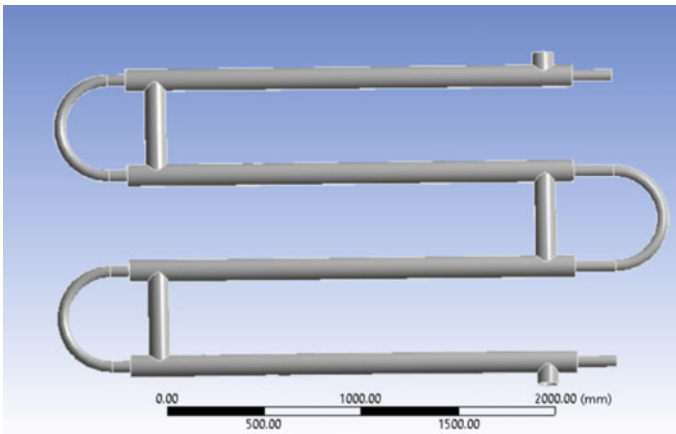


Fig. 3 Imported model

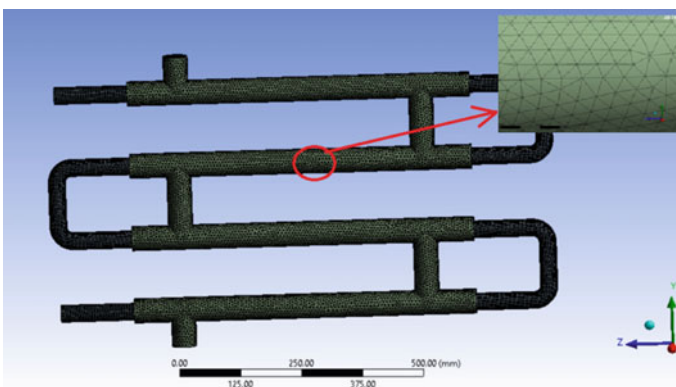
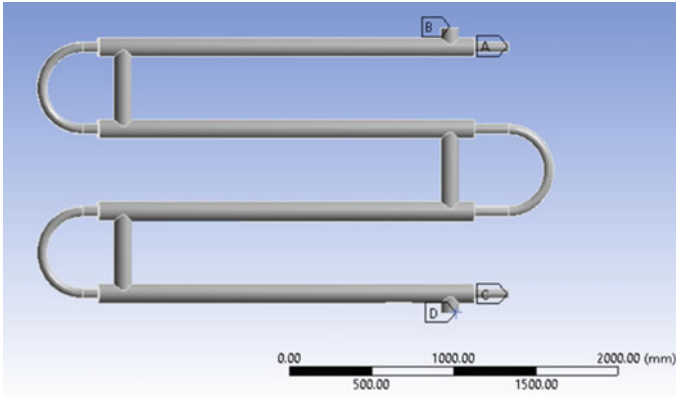


Fig. 4 Meshed body

**Table 1** Quality of meshing taken from the ANSYS Fluent

Mesh quality	Orthogonal	Aspect ratio	Skewness	Element quality
Minimum	0	1.1694	2.9678e – 4	9.1839e – 6
Maximum	0.9999	31,154	0.999	0.9997
Average	0.8239	3.8680	0.2807	0.7901
Standard deviation	0.1434	58.7492	0.1630	0.1586

**Fig. 5** Input conditions

(water + ethylene glycol, water + SiO<sub>2</sub> and water + Cu) with 3 volume fractions (0.05, 0.15 and 0.25) is considered to be replaced for every case of simulation.

## 7 Results and Discussions

From Fig. 6, it was noticed that the temperature is reduced for hot fluid at pipe and temperature is gained the cold fluid at shell. The temperature difference for the cold fluid region is almost 20 °C. Loss of temperature at hot fluid region is almost 7 °C.

From Fig. 7, it was noticed that the maximum heat transfer coefficient is at cold fluid region and minimum is at hot fluid region. The highest value was obtained at corners of shells.

Figure 8 explains the temperature differences from inlet to the outlet of the nanofluid for the different volume fractions.

For the water plus ethanol glycol (EG) mixture, the temperature difference is 10 K for the volume fraction 0.05, and if an increment of volume fraction takes place, then temperature of difference also increases. Similarly, water plus CuO nanofluid has obtained 13 K difference at volume fraction 0.05 and also water plus Cu has 14 K;

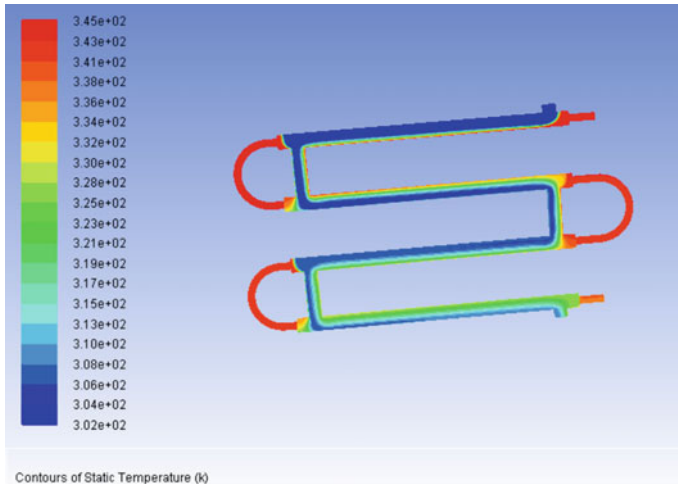


Fig. 6 Temperature differences for the double-pipe heat exchanger

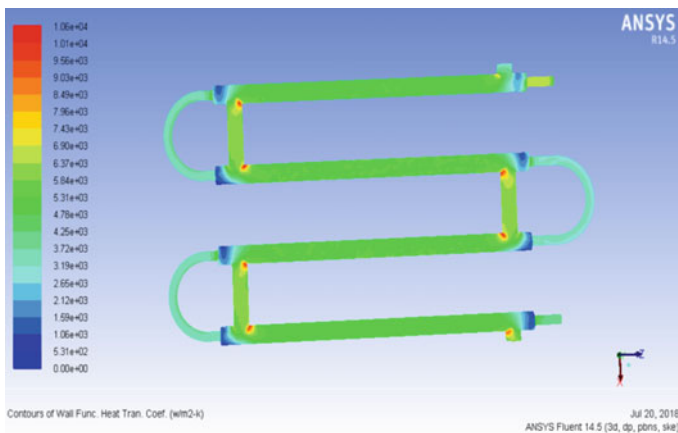


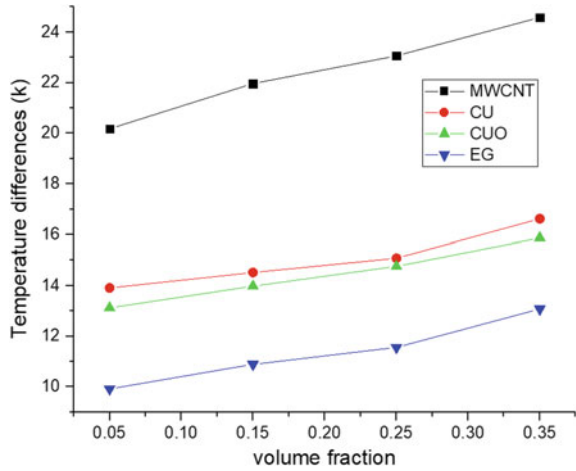
Fig. 7 Heat transfer coefficient

however, water plus MWCNT has 20 K temperature difference; it happens due to good thermal conductivity of nanoparticle.

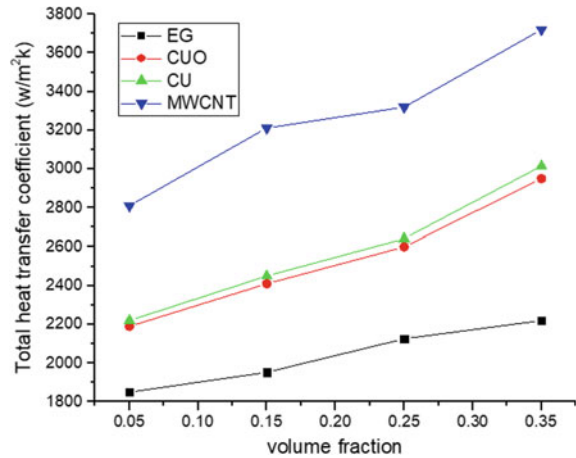
While the volume fraction increases, the temperature difference also increases due to the increment of the nanoparticles in base fluid. Therefore, thermal conductivity increases with an increase in volume fraction.

Figure 9 explains the heat transfer coefficient of the nanofluid for different volume fractions.

**Fig. 8** Temperature difference



**Fig. 9** Heat transfer coefficient

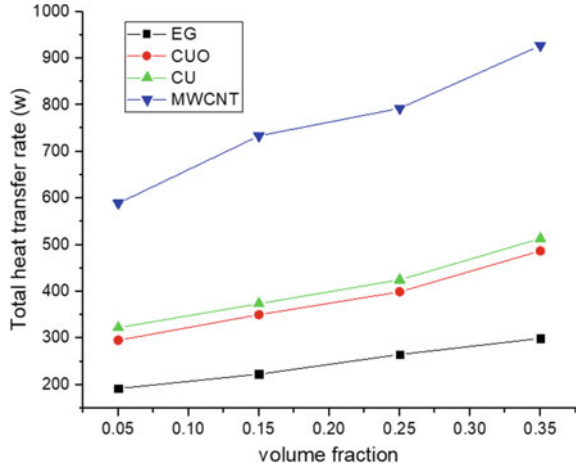


The combination of water and MWCNT has given the heat transfer above  $2800 W/m^2 K$  at 0.05 volume fraction, whereas it was less for the remaining fluids. Other two combinations have obtained near values around  $2200 W/m^2 K$ . But, for the metallic nanoparticle, ‘Cu’ has little high value. Therefore, water plus EG has low heat transfer capacity compared to other combinations, because of its slow thermal conductivity.

If thermal conductivity of the material/fluid is more, then the result of the heat transfer coefficient also increases along with the volume fraction. Same principle is observed in Fig. 8. In this figure, MWCNT has more heat transfer coefficient happened due to highest thermal conductivity.

Figure 10 explains the difference of the theoretical and simulation results of total heat transfer rate of the nanofluid for the different volume fraction.

**Fig. 10** Total heat transfer rate



In theoretical and simulation results for the MWCNT, total heat transfer rate is more for MWCNT. It happens only because of highest thermal conductivity for the MWCNT compared to others.

Total heat transfer rate of the nanofluids for the different volume fractions is calculated using the following formula, and output parameters are taken from the results mentioned in Figs. 7 and 8.

$$Q = UA \Delta T \tag{7}$$

where

- $U$  Overall heat transfer coefficient ( $W/(m^2 K)$ )
- $A$  Heat transfer surface area ( $m^2$ )
- $\Delta T$  Logarithmic mean temperature difference (K)

## 8 Conclusion

Based upon the results, the volume fraction has been maintained with an interval of 0.1% for all types of combinations. In addition to it, temperature difference at inlet condition has been maintained at constant difference for all fluid combinations. The output parameters which are exit temperature difference, overall heat transfer coefficient, and heat transfer rate have been analyzed and found the significant outcomes. For every volume fraction, the superior heat transfer rate was observed through the combination of  $H_2O$  plus MWCNT nanofluid. With reference to Sarafraz and Hormozi [18], the thermal conductivity of water plus MWCNT has been increased to 68%, whereas with the same approach, in the current study for all kinds of volume

fractions, the thermal conductivity of water plus MWCNT is obtained about 85%. Therefore, for an efficient application, the water plus multiwall carbon nanotube fluid may be suggested.

## References

1. Sajid MU et al (2018) Thermal conductivity of hybrid nanofluids: a critical review. *Int J Heat Mass Transfer* 126:211–234. <https://doi.org/10.1016/j.ijheatmasstransfer.2018.05.021>
2. Yu W, Xie H (2012) A review on nano fluids: preparation, stability mechanisms, and applications. *J Nanomaterials* 17. <https://doi.org/10.1155/2012/435873>
3. Hwang Y, Lee JK, Lee CH et al (2007) Stability and thermal conductivity characteristics of nanofluids. *Thermochim Acta* 455(1–2):70–74
4. Singh K, Raykar VS (2008) Microwave synthesis of silver nanofluids with polyvinylpyrrolidone (PVP) and their transport properties. *Colloid Polym Sci* 286(14–15):1667–1673
5. Oh DW, Jain A, Eaton JK, Goodson KE, Lee JS (2008) Thermal conductivity measurement and sedimentation detection of aluminum oxide nanofluids by using the 3 omega method. *Int J Heat Fluid Flow* 29:1456–1461
6. Dong L, Quan X, Cheng P (2014) An experimental investigation of enhanced pool boiling heat transfer from surfaces with micro/nano-structures. *Int J Heat Mass Transfer* 71:189–196
7. Usri NA et al (2015) Thermal conductivity enhancement of Al<sub>2</sub>O<sub>3</sub> nanofluid in ethylene glycol and water mixture. *Energy Procedia* 79:397–402
8. Phanindra Y, Kumar SD, Pugazhendhi S (2018) Experimental investigation on Al<sub>2</sub>O<sub>3</sub> & Cu/Oil hybrid nano fluid using concentric tube heat exchanger. *Mater Today Proc* 5(5):12142–12150
9. Asadi Amin et al (2018) An experimental and theoretical investigation on heat transfer capability of Mg (OH)2/MWCNT-engine oil hybrid nano-lubricant adopted as a coolant and lubricant fluid. *Appl Therm Eng* 129:577–586
10. Yousefi T, Shojaeizadeh E, Veysi F, Zinadini S (2012) An experimental investigation on the effect of pH variation of MWCNT-H<sub>2</sub>O nanofluid on the efficiency of a flat-plate solar collector. *Sol Energy* 86(2):771–779
11. Rahimi A, Kasaeipoor A, Malekshah EH, Palizian M, Kolsi L (2018) Lattice Boltzmann numerical method for natural convection and entropy generation in cavity with refrigerant rigid body filled with DWCNTs-water nanofluid-experimental thermo-physical properties. *Therm Sci Eng Prog* 5:372–387
12. Timofeeva EV, Smith DS, Yu W, France DM, Singh D, Routbort JL (2010) Particle size and interfacial effects on thermo-physical and heat transfer characteristics of water-based  $\alpha$ -SiC nanofluids. *Nanotechnology* 21(21)
13. Bastian Águila V et al (2018) Effect of temperature and CuO-nanoparticle concentration on the thermal conductivity and viscosity of an organic phase-change material, vol 120. Elsevier. ISSN 00179310
14. Garg P, Alvarado JL, Marsh C, Carlson TA, Kessler DA, Annamalai K (2009) An experimental study on the effect of ultrasonication on viscosity and heat transfer performance of multi-wall carbon nanotube-based aqueous nanofluids. *Int J Heat Mass Transf* 52(21–22):5090–5101
15. Wang XQ, Mujumdar AS (2008) A review on nanofluids—Part I: theoretical and numerical investigations. *Braz J Chem Eng* 25(4):613–630. ISSN 0104-6632
16. Laurentet C et al (2010) The weight and density of carbon nanotubes versus the number of walls and diameter. Elsevier. <https://doi.org/10.1016/j.carbon.2010.04.010>
17. Xue QZ (2005) Model for thermal conductivity of carbon nanotube-based composites. *Phys B Condens Matter* 368(1–4):302–307
18. Sarafraz MM, Hormozi F (2016) Heat transfer, pressure drop and fouling studies of multi-walled carbon nanotube nano-fluids inside a heat exchanger, vol 72. Elsevier Inc.

# Adopting SDR Fluctuations to Non-premixed Turbulent Combustion by Varying Swirl Ratio



S. M. Jameel Basha

**Abstract** It is known that the CI engine combustion process is complex phenomenon. The rapid progress has been made in multidimensional modeling of in-cylinder processes by suitable combination of assumptions and equations that can analyze the critical features. The CFD models gives us the complete understanding of the in-cylinder processes, reduce the cost of the expensive and time consuming experimental techniques. FLUENT is one of the versatile tools which is used for modeling of in-cylinder flows as well as exhaust pollutants. FLUENT has a set of assumptions and restriction. One such restriction is that the effect of Scalar Dissipation Rate Fluctuations (SDRF) is ignored. In the present paper an attempt has been made for the inclusion of SDRF by writing the User Defined Function and appending the same to the existing code FLUENT. Three swirl ratios 2, 3 and 4 with spherical bowl have been chosen and runs are made for these swirl ratios with and without SDRF. The simulated results are compared with the experimental results for validation.

**Keywords** SDRF · Flamelet equation · Swirl ratio

## 1 Introduction

Swirl refers to a rotational flow within the cylinder about its axis. The swirl can be generated either by decreasing the flow tangentially into the cylinder or by pre-swirling the incoming flow by use of helical port [1]. The swirling motion inside the combustion chamber will enhance the mixing ratio of fuel and air in a DI Diesel engine. High swirl may result in convective heat losses and poor volumetric efficiencies. An optimization of swirl will be helpful in improving the performance of engine. Swirl ratio is normally used to define the swirl. It is defined as the angular velocity of a solid body rotating flow, which has equal angular momentum to the actual flow, divided by the crank shaft angular rotational speed. In this present work

---

S. M. Jameel Basha (✉)

Srinivasa Ramanujan Institute of Technology, Anantapur, India  
e-mail: [jameeljunaid@gmail.com](mailto:jameeljunaid@gmail.com); [mechod@srit.ac.in](mailto:mechod@srit.ac.in)

© Springer Nature Singapore Pte Ltd. 2020  
L. Vijayaraghavan et al. (eds.), *Emerging Trends in Mechanical Engineering*,  
Lecture Notes in Mechanical Engineering,  
[https://doi.org/10.1007/978-981-32-9931-3\\_39](https://doi.org/10.1007/978-981-32-9931-3_39)



three different swirl ratios 2, 3 and 4 are considered and the computational results are presented in the subsequent sections.

## 2 Problem Definition

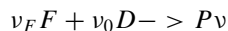
Large amount of works have been reported using multi dimensional modeling till date. The commercially available code FLUENT is used in the present work. All the codes run with their own assumptions and restrictions. It is seen in the present code that, Scalar Dissipation Rate Fluctuation herewith called as SDRF is ignored [2]. SDRF been accounted by modeling the diffusion term in the Flamelet equation. An UDF has been written and appended to the existing code and runs were made for the injection timing of 28° bTDC, injection duration of 23.5°, Hemispherical piston is used with and without considering the effect of SDRF. The swirl ratios considered for the present work are 2, 3 and 4. The simulated results are validated with the experimental data.

## 3 Theory of Computation

Turbulence is a feature of high Reynolds number flow phenomenon controlled by nonlinearity and since each individual flow has unique characteristics associated with its initial and boundary conditions; there is no general solutions to the equations governing turbulent flows. The turbulence and laminar flows goes orthogonal to each other. All engineering flows except few have a turbulent flows because of their Reynolds number [3]. The three dimensional Navier Stokes equation which is time dependent can explain about turbulent flow in the comprehensive manner [4]. Turbulence in the flows greatly enhances the mass transfer, momentum, energy and swirl in the combustion phenomenon. Stress developed in the turbulent flow is grater in magnitude compared with the corresponding laminar flows [5–7].

## 4 Theory of Computation

Flamelet equations: Assuming an irreversible one-step reaction of the form



where  $F$ ,  $O$  and  $P$  denote the fuel, oxidizer and reaction product respectively, the flamelet equations for the mass fractions of fuel  $y_F$ , oxidizer  $y_O$  reaction product  $y_P$  and temperature  $T$

$$\frac{\partial y_i}{\partial t} - \frac{x}{2} \frac{\partial^2 y_i}{\partial Z^2} + v_i W_i \omega = 0.0 \quad (1)$$

$$i = F, 0, P$$

$$\frac{\partial T}{\partial t} - \frac{x}{2} \frac{\partial^2 T}{\partial Z^2} - \frac{Q}{cp} \omega = 0.0 \quad (2)$$

where

$$Q = - \sum_{i=1}^N v_i W_i h_i \quad (3)$$

The non-dimensional scalar dissipation rate  $x$ , the Damkohler's number  $D_a$  and the zeldovich number  $Z_e$  are defined as

$$x = \frac{X}{X_{st,0}} \quad (4)$$

$$D_a = \frac{v v_{Fa} P_{st,u} y_0}{(1+v) W_0} \frac{A}{X_{st,D}} \exp(-\beta_{ref}) \quad (5)$$

$$Z_e = \alpha \beta \quad (6)$$

$$\alpha = \frac{(T_{st,b} - T_u)}{T_{st,b}} \quad (7)$$

$$\beta = \frac{E}{RT_{st,b}} \quad (8)$$

Introducing these definitions into the flamelet equations

$$\frac{\partial y_F}{\partial \tau} - \frac{ax}{2} \frac{\partial^2 y_F}{\partial Z^2} + \frac{1}{[1+v]} \omega = 0.0 \quad (9)$$

$$\frac{\partial y_0}{\partial \tau} - \frac{ax}{2} \frac{\partial y_0}{\partial Z^2} + \left( \frac{v}{1+v} \right) \omega = 0.0 \quad (10)$$

$$\frac{\partial y_P}{\partial \tau} - \frac{ax}{2} \frac{\partial^2 y_P}{\partial Z^2} - \omega = 0.0 \quad (11)$$

$$\frac{\partial \theta}{\partial \tau} - \frac{ax}{2} \frac{\partial^2 \theta}{\partial Z^2} - \omega = 0.0 \quad (12)$$

where the non-dimensional chemical source term is given by

$$\begin{aligned} \omega &= D_a \frac{(1 + \nu)^2 (1 - \alpha) \exp(\beta_{\text{ref}} - \beta)}{1 - \alpha(1 - \theta)} y_F y_0 \exp\left(-\frac{Z_e(1 - \theta)}{1 - \alpha(1 - \theta)}\right) \\ \omega &= D_a \frac{(1 - \alpha) \exp(\beta_{\text{ref}} - \beta)}{1 - \alpha(1 - \theta)} \left(\frac{z}{z_{\text{st}}} - \theta\right) \exp\left(-\frac{z_e(1 - \theta)}{1 - \alpha(1 - \theta)}\right) \end{aligned} \quad (13)$$

Here a joint pdf of the temperature and the scalar dissipation rate are derived. A stochastic differential equation (SDE) given by strantonovich is needed that governs the evolution of the scalar dissipation rate [8]. The diffusion term evaluated at stoichiometric conditions can be written using Taylor series of approximation

$$\begin{aligned} \frac{\partial^2 T}{\partial Z^2} &\approx -\frac{(T_{\text{st},b} - T_{\text{st},u})}{\Delta Z Z_{\text{st}}(1 - Z_{\text{st}})} \theta_{\text{st}} \\ \frac{d\theta_{\text{st}}}{d\tau} + x(\tau)\theta_{\text{st}} - \omega(\theta_{\text{st}}) &= 0.0 \end{aligned}$$

with

$$\omega = \frac{D_a(1 - \alpha) \exp(\beta_{\text{ref}} - \beta)}{1 - \alpha(1 - \theta_{\text{st}})} (1 - \theta_{\text{st}})^2 \exp\left(-\frac{Z_e(1 - \theta_{\text{st}})}{1 - \alpha(1 - \theta_{\text{st}})}\right) \quad (14)$$

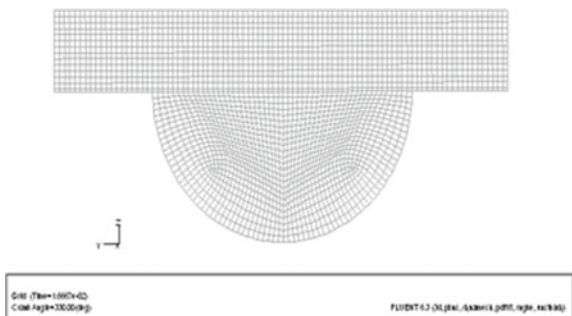
The above equation elucidates how the scalar dissipation rate fluctuations can influence the non-premixed combustion process.

## 5 Test Computations

### 5.1 Effect of Initial Swirl Ratio

These computations were carried with the engine fitted with the hemispherical piston bowl. Figure 1 gives the details of the computational mesh which represents the in-

**Fig. 1** Computational mesh of hemispherical bowl



cylinder flow. Meshing is done by using hexahedral elements and 654,400 cells are considered for meshing in case of Hemispherical bowl.

## 5.2 Comparison of Predicted and Experimental Pressure Histories

The Fig. 2 gives the comparison of predicted with and without considering the effect of SDRF and experimental pressure histories. There is a very marginal difference in the pressures at the start of the compression between the three curves but noticeable deviation can be seen at the peak pressure. From the graph it can be seen that predicted pressure are high without SDRF, then followed by considering the effect of SDRF and then by the experimental value. Practically prior to the combustion the cylinder is occupied with the residual gases of the previous stroke whereas in case of the predicted values this residual gases effect is not considered. The predicted values without considering the effect of SDRF is 7.147 MPa, with considering the effect of SDRF is 7.01 MPa and experimental [9, 10] value is 6.829 MPa. The percentage error is 4.449% when the comparison is made between predicted peak pressure without SDRF and experimental value and the percentage error is 2.58% when comparison is made between predicted peak pressure with SDRF and experimental value. The later part of the compression stroke for all the three are almost same.

## 5.3 Comparison of Predicted and Experimental Temperature Histories

Figure 3 gives the comparison between predicted with SDRF, without SDRF and experimental values for the temperature histories. The maximum value of the cylinder temperatures are 2610 K with SDRF, 2620 K without SDRF and 2601 K for

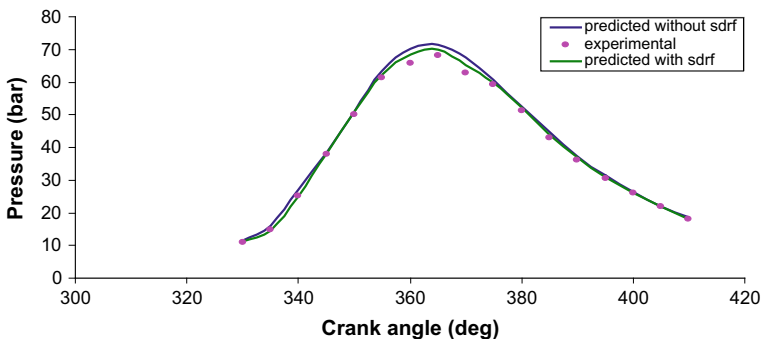
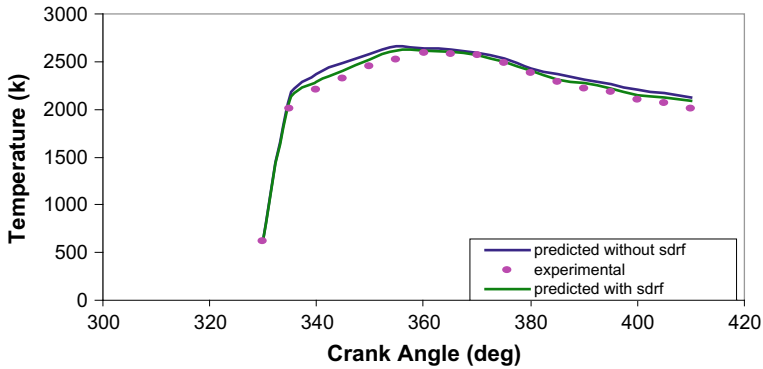


Fig. 2 Variation of cylinder pressure with crank angle (spherical bowl)



**Fig. 3** Variation of cylinder temperature with crank angle

experimental. It is seen that the value of maximum temperature is for without considering the effect of SDRF owing to the fact that crank case dilution is not considered during the run and next maximum temperature is in case of considering the effect of SDRF again for the same reason.

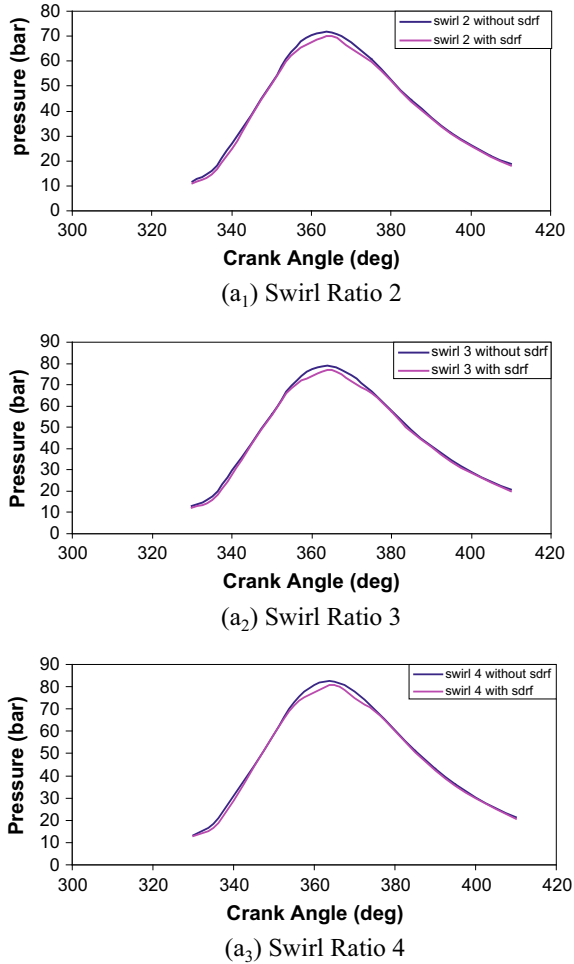
#### **5.4 Effect of Initial Swirl Ratio on in-Cylinder Pressure**

Figure 4a<sub>1</sub>, a<sub>2</sub>, a<sub>3</sub> gives the comparison of predicted peak pressures for three different initial swirl ratios 2, 3 and 4. Peak pressures increase with increase in swirl. The predicted peak pressures are 8.85 MPa and 8.67 MPa for initial swirl ratios of 4 and 3 respectively. With an initial swirl ratio 2 the peak pressure attained is 7.14 MPa. The occurrence of peak pressure is at same crank angle for all the swirl ratios. The predicted peak pressures for initial swirl ratios 2, 3 and 4 considering the effect of SDRF is 7.01, 7.711 and 8.061 MPa respectively. By considering the effect of SDRF reduced predicted pressures can be observed.

#### **5.5 Effect of Initial Swirl Ratio on in-Cylinder Temperature**

As the cylinder pressure shows the raise in peak pressure with the increase in swirl it is obvious that the same trend follows for the temperature also. The same is shown in the Fig. 5a<sub>1</sub>, 5a<sub>2</sub>, a<sub>3</sub>. The peak pressure noted for the swirl ratios 2, 3 and 4 are 2620.61, 2664 and 2673 K respectively. It can be noticed that there is a little difference in the variation of peak temperatures for various swirl ratios. However the effect of increase in initial swirl ratio will have more impact on inlet temperature compared to that of the peak temperatures. Marginally reduced temperatures can be observed

**Fig. 4** Effect if initial swirl ratio on pressure

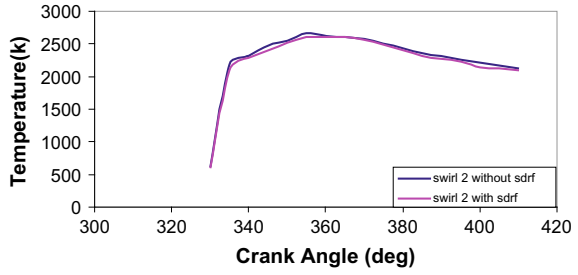


due to effect of SDRF. The peak pressure noted for the swirl ratios 2, 3 and 4 are 2613.7, 2645.6 and 2664.87 K respectively.

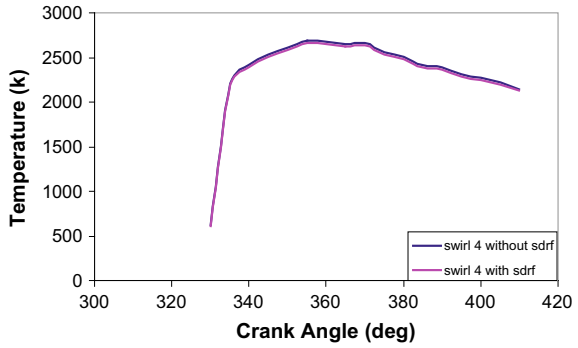
### 5.6 Effect of Initial Swirl Ratio on Total Energy

Total energy represents the heat release rate during the combustion and total energy also gives us the idea where exactly the start of combustion precisely happens in the cylinder. Figure 6a<sub>1</sub>, a<sub>2</sub>, a<sub>3</sub> gives the variation in total energy with respect to crank angle for various swirl ratios. It is noticed that there is larger difference in swirl 2, with and without considering the effect of SDRF, marginal in case of swirl 3 and swirl

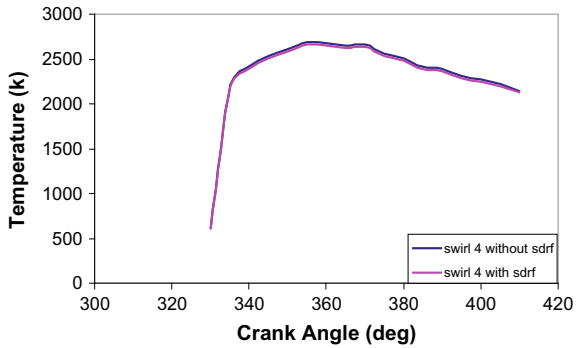
**Fig. 5** Effect of initial swirl ratio on cylinder temperature



(a<sub>1</sub>) Swirl Ratio 2



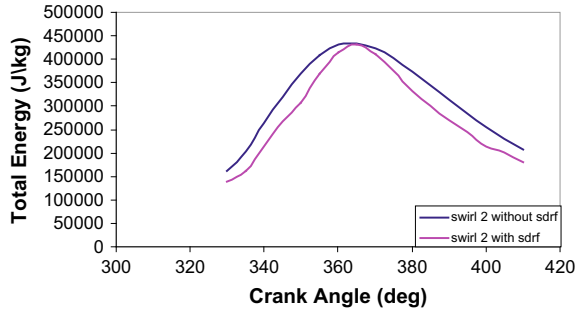
(a<sub>2</sub>) Swirl Ratio 3



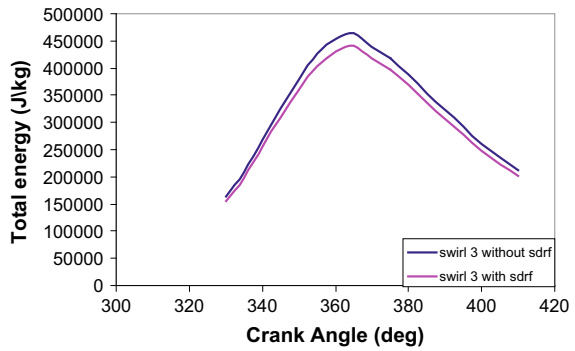
(a<sub>3</sub>) Swirl Ratio 4

4. The value of maximum energy for the initial swirl ratio of 2, 3 and 4 are 434.2, 464.6 and 465.5 kJ/kg respectively. As the expansion stroke proceeds, the difference in swirl ratio got bridged at crank angle 25° aTDC all the curves proceeds further with a little variation. Reduced total energies can be noticed by the application of SDRF. The values of total energy with the application of SDRF are 432, 441.4 and 442.24 kJ/kg for swirl ratios 2, 3 and 4 respectively.

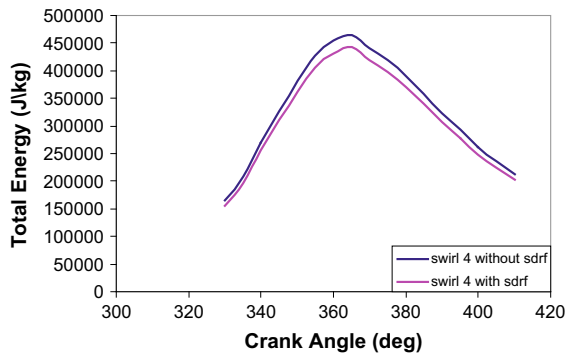
**Fig. 6** Effect of initial swirl ratio on total energy



(a<sub>1</sub>) Swirl Ratio 2



(a<sub>2</sub>) Swirl Ratio 3



(a<sub>3</sub>) Swirl Ratio 4



### ***5.7 Effect of Initial Swirl Ratio on Turbulent Kinetic Energy***

Figure 7a<sub>1</sub>, a<sub>2</sub>, a<sub>3</sub> shows the effect of initial swirl ratio on turbulent kinetic energy. It is evident from the figure that turbulence increases with the swirl. The peak values of TKE attained are 93.96, 136.24 and 138.24 m<sup>2</sup>/s<sup>2</sup> for the swirl ratios 2, 3 and 4 respectively. The increasing trend in TKE is due to availability of more energy due to shear in mean flow. The variation among all the swirl ratios can be seen at the crank angle 5° bTDC. The peak values of TKE attained are 88.45, 100.21 and 104.09 m<sup>2</sup>/s<sup>2</sup> for the swirl ratios 2, 3 and 4 respectively considering the effect of SDRF.

### ***5.8 Effect of Initial Swirl Ratio on HC Emission***

Figure 8a<sub>1</sub>, a<sub>2</sub>, a<sub>3</sub> gives the comparison of predicted HC emissions for initial swirl ratios 2, 3 and 4. It is noticed that the HC emission in case of swirl ratio 2 is maximum (0.306% without SDRF and 0.299% with SDRF). This is due to incomplete combustion. Because of this reason, lower peak cylinder pressure is resulted. HC emission is least in case of swirl ratio 3 (0.2754% without SDRF and 0.269% with SDRF) and slightly higher in case of swirl ratio 4 (0.2876% without SDRF and 0.281% with SDRF).

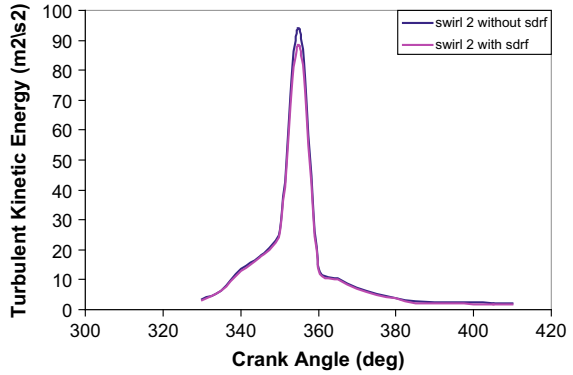
### ***5.9 Effect of Initial Swirl Ratio on CO Emission***

Figure 9a<sub>1</sub>, a<sub>2</sub>, a<sub>3</sub> gives the comparison of CO emissions for swirl ratios 2, 3 and 4. It is noticed that the predicted CO emission without SDRF is maximum in case of swirl ratio 2(0.27%) almost half of this value equal to 0.135% for the swirl ratio of 3 and less than this value equal to 0.108% for swirl ratio 4. Less amount of oxygen is responsible for the production of CO during combustion. As the swirl ratio increases, the abundance of oxygen will reduce the formation of CO. The predicted CO emission with SDRF for swirl ratios 2, 3 and 4 are 0.264%, 0.132% and 105% respectively.

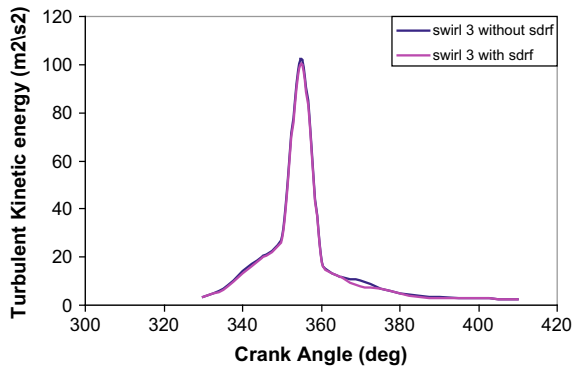
### ***5.10 Effect of Initial Swirl Ratio on CO<sub>2</sub> Emission***

Figure 10a<sub>1</sub>, a<sub>2</sub>, a<sub>3</sub> gives the comparison of CO<sub>2</sub> emissions for swirl ratios 2, 3 and 4. Presence of CO<sub>2</sub> represents efficient combustion as discussed earlier. In this context swirl ratio 3 has the maximum value of CO<sub>2</sub> as 0.1772%, secondly with swirl ratio 2 with the value of 0.1693% and lastly with swirl ratio 4 equal to 0.1689%. The predicted CO<sub>2</sub> emission with SDRF for swirl ratios 2, 3 and 4 are 0.165, 0.173 and 0.164% respectively.

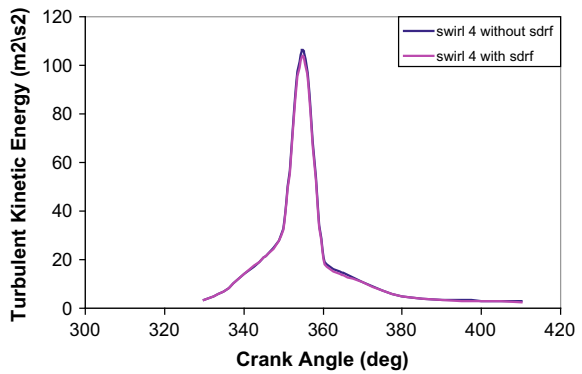
**Fig. 7** Effect of initial swirl ratio on Turbulent kinetic energy



(a<sub>1</sub>) Swirl Ratio 2

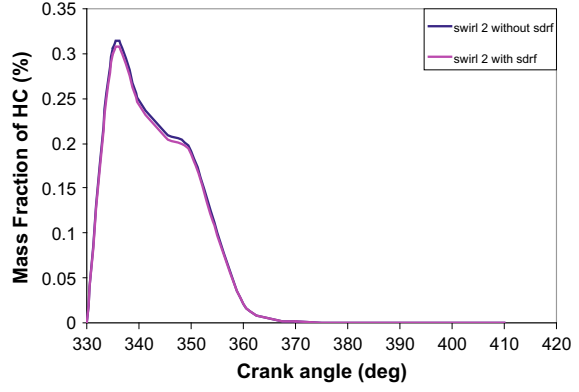


(a<sub>2</sub>) Swirl Ratio 3

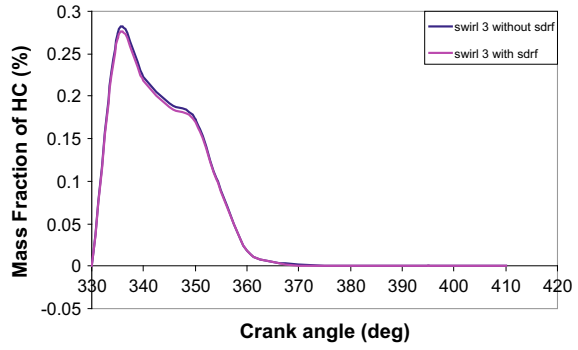


(a<sub>3</sub>) Swirl Ratio 4

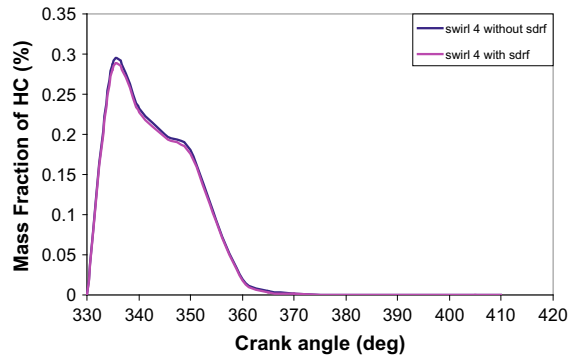
**Fig. 8** Effect of initial swirl ratio on HC emission



(a<sub>1</sub>) Swirl Ratio 2

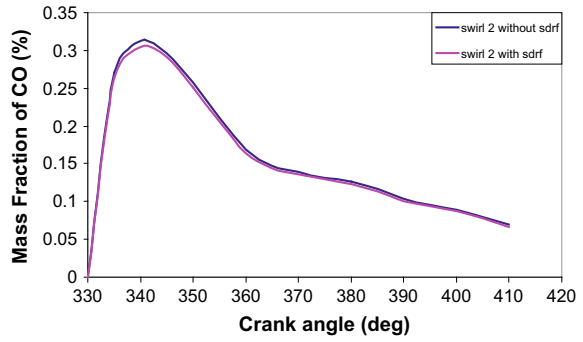


(a<sub>2</sub>) Swirl Ratio 3

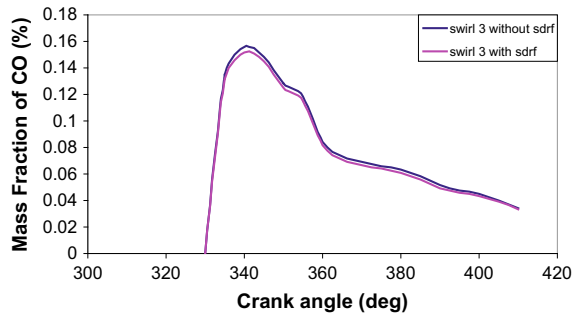


(a<sub>3</sub>) Swirl Ratio 4

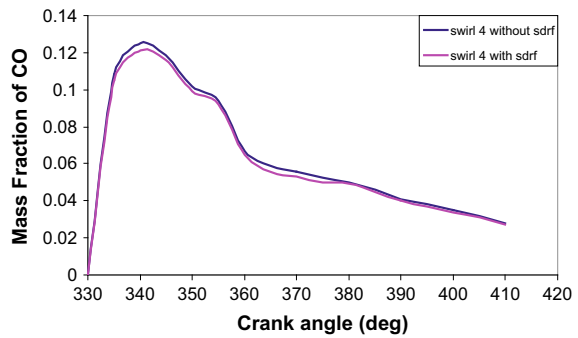
**Fig. 9** Effect of initial swirl ratio on CO emission



(a<sub>1</sub>) Swirl Ratio 2

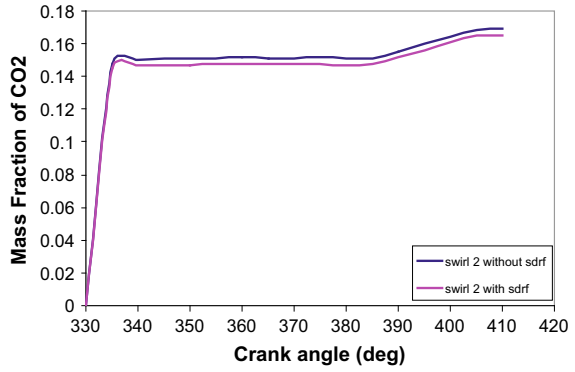


(a<sub>2</sub>) Swirl Ratio 3

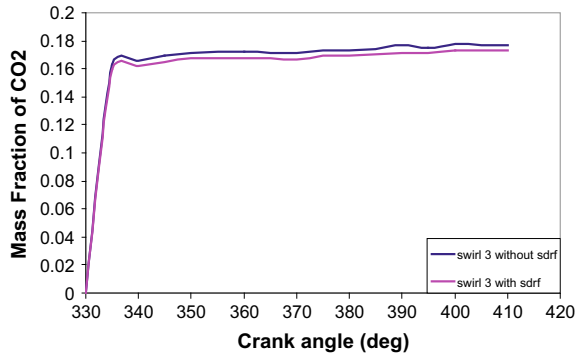


(a<sub>3</sub>) Swirl Ratio 4

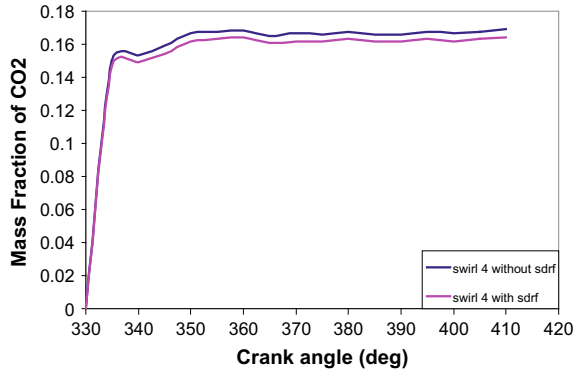
**Fig. 10** Effect of initial swirl ratio on CO<sub>2</sub> emission



(a<sub>1</sub>) Swirl Ratio 2



(a<sub>2</sub>) Swirl Ratio 3



(a<sub>3</sub>) Swirl Ratio 4

## 6 Conclusions

The following are the important conclusions drawn from the present work with the modified code accounting SDRF using FLUENT.

- The error is 5.91% in predicted peak pressure without SDRF and experimental value and the error is 4% in predicted peak pressure with SDRF and experimental value.
- The maximum cylinder temperature attained for without SDRF is 2590.11 K, with SDRF is 2538.3 K and experimental is 2486.5 K.
- Good agreement can be noticed in pressure and temperature histories with noticeable reduction in percentage error.
- Increase in swirl up to a moderate level increases the in-cylinder average peak pressure. SDRF is found to have moderate impact in the variation of in-cylinder peak pressures.
- Increase in swirl ratio reduces CO emission and moderately reduces HC emissions. Increased swirls also tend to have more CO<sub>2</sub> formation.

## References

1. John Heywood B (1990) Internal combustion engine fundamentals. McGraw Hill International Editions
2. FLUENT Users Manual, FLUENT 6.3 documentation, FLUENT International Corporation Limited, USA
3. Morel T, Monsour NN (1982) Modeling of turbulence in internal combustion engines, SAE paper 820040
4. Hault DP, Wong VW (1978) The generation of turbulence in an internal combustion engine. In: General Motors Research Laboratories symposium on combustion, modeling in reciprocating engines, Warren, Michigan
5. Wei R, Li X, Zhang G, Du W (2000) A new Double Swirls Combustion System for DI diesel engine, SAE paper 2000-01-2915
6. Bray KNC, Libby PA (1995) Turbulent transport in flames. Proc R S Lond A 541:231–256
7. Libby PA, Williams FA (1994) Fundamental aspects and a review in turbulent reacting flows. Academic Press, London, pp 1–61
8. Linan A, Williams FA (1993) Fundamental aspects of combustion. Oxford University Press, New York
9. Rajagopal K (1991) Three dimensional modeling of in-cylinder flows, fuel-air mixing and combustion in a four stroke compression ignition engine. Ph.D. theses, IIT Madras
10. Jameel Basha SM (2016) Accounting SDR fluctuations to non-premixed turbulent combustion for better predictions of in-cylinder processes. Int J Adv Res (IJAR) 4(5):1656–1671. ISSN:2320-5407

# Flat-Fire Trajectory Simulation of AK-47 Assault Rifle 7.82-mm Bullet



D. Siva Krishna Reddy, Bibhu Prasad Padhy and Bharani Kumar Reddy

**Abstract** The present work discusses the computation of the trajectory of a projectile with flat-fire trajectory approximation. The test case corresponds to 7.82-mm bullet of assault rifle AK-47. Initially, computational fluid dynamics (CFD) simulations are performed over the bullet with commercial CFD software, ANSYS Fluent. Density-based solver is employed to solve coupled continuity, momentum, and energy equations for Mach number of 2. The corresponding velocity of bullet is 680 m/s. The effect of turbulence on flowfield is accounted by using k- $\epsilon$  turbulence model. Flow features over the bullet and associated surface pressure distribution obtained from the simulations are explained. Predicted drag coefficient of bullet is validated against available experimental data, and the deviation is below 5%. Flat-firing approximation is used for simulating the trajectory of the bullet for which drag coefficient is an input parameter. Initially, the flat-fire trajectory code is validated against published trajectory data. The error between the predicted velocity and published data is below 0.05%. Next, flat-fire trajectory simulation is performed for bullet. Velocity, range, and height of the bullet are predicted as a function of time. It is found that the bullet travels a distance of 280 m before hitting the ground. During the course of travel, there is 33% reduction in its velocity and corresponding flight time is 0.63 s. The effect of variation in density with respect to altitude on range of bullet is also investigated. Range of the bullet at 4 km altitude is 16% higher than that of sea level.

**Keywords** External ballistics · Terminal ballistics · Computational fluid dynamics · Shock waves · Aerodynamic drag

---

D. Siva Krishna Reddy (✉) · B. P. Padhy  
Department of Mechanical Engineering, SRM Institute of Science and Technology,  
Kattankulathur, Tamil Nadu 603203, India  
e-mail: [sivakrishna.v@ktr.srmuniv.ac.in](mailto:sivakrishna.v@ktr.srmuniv.ac.in)

B. K. Reddy  
Department of Mechanical Engineering, Srinivasa Ramanujan Institute of Technology, Anantapur,  
Andhra Pradesh 515701, India

© Springer Nature Singapore Pte Ltd. 2020  
L. Vijayaraghavan et al. (eds.), *Emerging Trends in Mechanical Engineering*,  
Lecture Notes in Mechanical Engineering,  
[https://doi.org/10.1007/978-981-32-9931-3\\_40](https://doi.org/10.1007/978-981-32-9931-3_40)

## 1 Introduction

External ballistics is the field in which motion of an object under the influence of drag and gravity is studied. Many engineering problems such as prediction of range of an artillery shell, flight time of a bullet fired from assault rifle, range of a missile can be determined from principles of external ballistics. The object whose motion is being studied is termed as projectile. The range of projectile for the given initial momentum to the large extent depends on shape of the object. If the drag coefficient of a given geometry is lower compared to other geometries, then range of the given projectile will be higher. Hence, there is a need to optimize the shape of the bullet for minimum drag coefficient.

McCoy [1] presented comprehensive review of geometries of different projectiles. The applications considered in the review are: bullets and artillery shells. As the projectiles travel at supersonic Mach numbers, a slender forebody is preferred to reduce the drag. Charles [2] performed wind tunnel testing on 155-mm artillery shell to determine the drag coefficient as function of the Mach number. The data is presented in the form of tables and curvefits, which can be used to simulate the trajectory parameters. Paul [3] investigated the stability characteristics of 20-mm bullet using CFD. The aerodynamic coefficients, Magnus coefficients, and pitch-damping coefficients are calculated by doing extensive CFD simulations.

Wei and Xiaobing [4] simulated muzzle flow around the revolving barrel using CFD. The computed muzzle velocity and maximum bore pressure are validated with measured values and comparisons found to be good. The lateral velocities of the projectiles fired from the gun barrel are determined. Klatt et al. [5] performed wind tunnel testing and numerical simulations to determine the effect of Magnus forces on a generic projectile at Mach number of 3. The angle of attack of the projectile varied from  $0^\circ$  to  $16^\circ$ .

The objective of the present work is to compute the flowfield over the 7.82-mm bullet and drag coefficient for freestream Mach number of 2. The geometry of the bullet and its dimensions are shown in Fig. 1. With the predicted drag coefficient, trajectory of the bullet will be simulated with flat-firing approximation. The range, velocity, and height of the projectile will be calculated as a function of flight time. Effect of variation in density with respect to altitude on range of the bullet is also investigated. The organization of the paper is as follows. First CFD simulations are presented. Next trajectory simulations are presented. Finally, conclusions drawn from the present work are given.

## 2 CFD Results

ANSYS Fluent 18.1 [6] is used for simulating the axisymmetric flowfield over the projectile. The freestream conditions for the simulations are mentioned below. The velocity corresponds to that of firing condition of AK-47. Simulations are performed



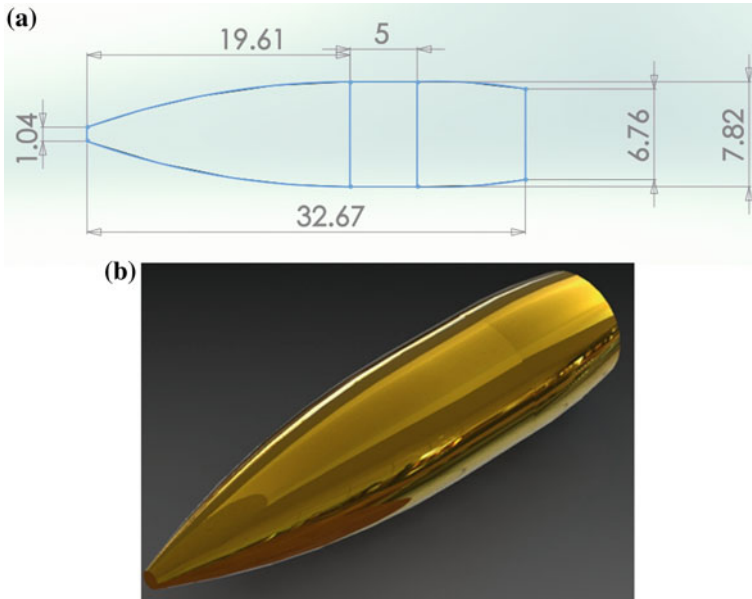


**Fig. 1** **a** Geometry of the 7.82-mm bullet. All dimensions are shown in mm, **b** three-dimensional model of the bullet

on structured grids, which are generated using ANSYS-CFD meshing tool. The compressible RANS equations are solved with density-based algorithm. The inviscid fluxes are discretized using AUSM scheme. Standard  $k-\epsilon$  turbulence model without compressibility correction [7] is used to close the turbulence terms in RANS equations. At the inlet, freestream conditions are imposed. Extrapolation boundary conditions were applied at outlet boundary. No-slip boundary conditions were applied on walls of the bullet. The outlet boundary is located at a distance of 13 times the diameter of the bullet from the inlet. At this location, flow supersonic and hence location of outlet boundary do not influence accuracy of the predictions. The boundary of the computational domain above the bullet axis is located at a distance of five times bullet diameter. As the geometry of the bullet is symmetry, axisymmetric simulations are performed.

Reynolds number based on the bullet diameter is  $3.643 \times 10^5$ . As the Reynolds number is close to transition Reynolds number of  $5.0 \times 10^5$ , fully turbulent computations are performed. The computed flowfield is mirror imaged about the symmetry axis using post-processing software ParaView [8] to obtain the flowfield over entire bullet.

Figure 2 shows the computed flowfield in terms of the Mach number contours for freestream Mach number of 2. Critical flow features are identified. As the shape of the nose region is blunt and freestream flow is supersonic, a bow shock wave is formed ahead of the projectile and decelerates the flow. In the nose stagnation region, across the bow shock wave Mach number decreases to subsonic values. The Mach

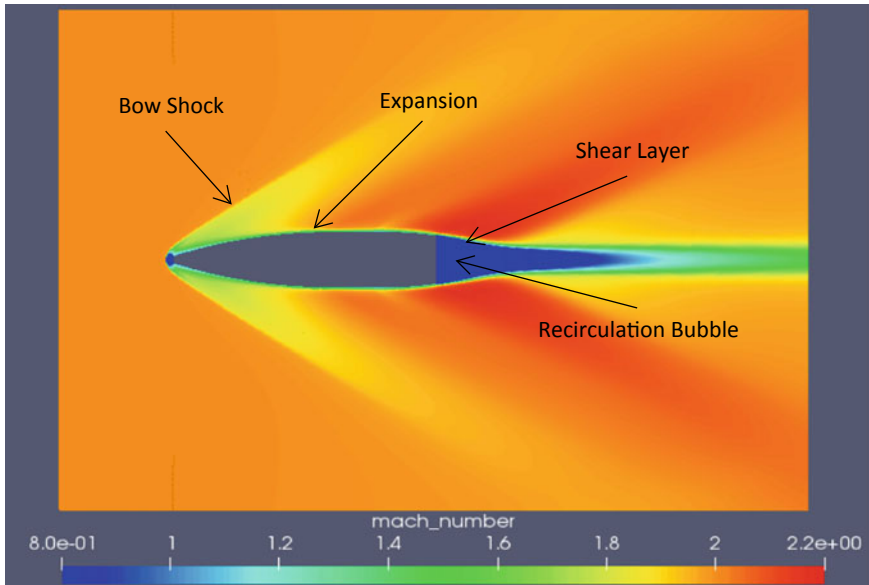


**Fig. 2** Computed Mach number contours over the bullet for freestream Mach number of 2

number of the shock layer that prevails away from the nose region is supersonic. The flow accelerates over the expansion fan that originates at the end of ogive region. This results in increase of Mach number of the flow to above 2. The boundary layer is attached on majority of the bullet and separates in the downstream of the boat-tail. This results in the formation of recirculation bubble. Flow in the recirculation bubble is subsonic. A shear layer separates the inner recirculation bubble and outer inviscid flow. A recompression shock wave originates in the near-wake and turns the flow to freestream direction. In the far-wake, the flow is again supersonic.

Figure 3 shows velocity vectors in the downstream of the boat-tail. It can be noticed that boundary layer separates in the downstream of the boat-tail. A single recirculation bubble is formed. The velocity of the flow in the recirculation bubble is about 200 m/s, whereas velocity of the flow in the outer inviscid is about 748 m/s.

Figure 4 shows surface pressure distribution over the bullet. X-axis represents the non-dimensional arc length ( $s/D$ ) from the nose of the bullet. Bullet diameter is used to non-dimensionalize the arc length. At fore stagnation point  $s/D = 0.0$ . The other critical regions of the bullet are identified in the figure. Surface pressure obtained from the simulation is non-dimensionalized with freestream pressure and plotted as Y-coordinate. The non-dimensional pressure at nose stagnation point is about 6.11. As the flow expands over the nose, pressure decreases sharply. Over the ogive region, pressure still continues to decrease as the flow continues expansion. Oblique shock that is generated at the beginning of the ogive region results in the increase of pressure locally at  $s/D = 0.3$ . On the flat region, the decrease in pressure is marginal. There

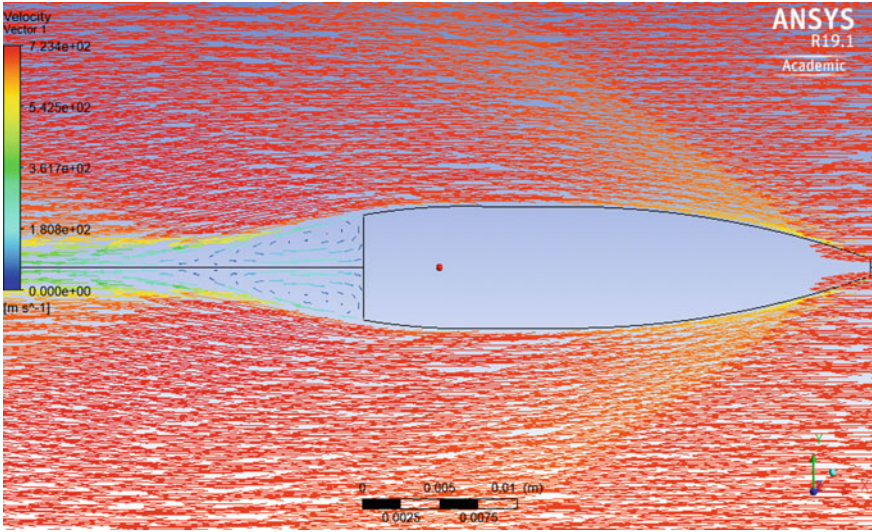


Fig. 3 Velocity vectors in flowfield over the bullet. Flow is from right to left

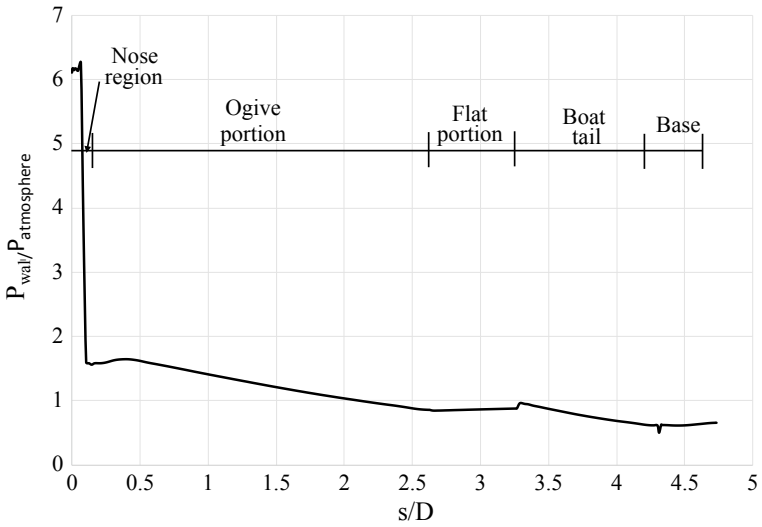


Fig. 4 Non-dimensional surface pressure distribution over the bullet. Critical regions over the bullet are identified

is a significant reduction in pressure over the boat-tail due to flow expansion. On the base, pressure marginally increases.

The computed drag coefficient from the simulations is about 0.312. The measured drag coefficient for the chosen bullet is 0.3 [1]. The error in the predicted drag coefficient is about 4%.

### 3 Trajectory Computation

The trajectory of the bullet is computed with flat-firing approximations [1]. For short-range supersonic projectiles which are fired parallel to ground, flat-firing approximation accurately describes the trajectory. The flat-firing trajectory equations, taken from Ref. [1], are reproduced here.

$$k1 = (\rho \times S \times C_d)/(2 \times m) \quad (1)$$

$$V_x = V_{x0}/(1 + V_{x0} \times k1 \times t) \quad (2)$$

$$X = V_x \times t \quad (3)$$

$$V_y = V_x \times (\tan(\phi) - gt(1 + 0.5 \times V_{x0} \times k1 \times t)/V_{x0}) \quad (4)$$

$$r = V_{x0}/V_x \quad (5)$$

$$Y = h - (0.5 \times g \times t^2) \times (0.5 + (1/(r - 1)) - (1/(r - 1)^2) \times \log(r)) \quad (6)$$

In the above equations,  $k1$  is constant,  $t$  is time,  $\rho$  is density,  $S$  is surface area of the bullet,  $C_d$  is coefficient of drag of the bullet,  $m$  is mass of the bullet,  $V_x$  is instantaneous velocity in  $X$ -direction,  $V_{x0}$  is muzzle velocity,  $V_y$  is velocity in the vertical direction,  $\phi_0 = \text{angle of projection} = 0^\circ$ ,  $\phi = \text{instantaneous angle}$ ,  $h$  is initial vertical distance, and  $Y$  is instantaneous vertical distance.

A program in ‘C++’ was developed to solve the above equations. To validate the present trajectory code, initially simulations are performed for a case that is reported in Ref. [1] and corresponding initial conditions are  $V_{x0} = 262.128$  m/s,  $H = 1.7$  m, and  $C_d = 0.205$ . The data taken from Ref. [1] is also given in Table 1. It can be noticed that error is below 0.001% for the entire trajectory. Next trajectory simulations are performed for firing conditions of AK 47 bullet, and the initial conditions are:  $V_{x0} = 680$  m/s,  $\rho = 1.22$  kg/m<sup>3</sup>,  $S = 0.0000456$  m<sup>2</sup>,  $C_d = 0.312$ ,  $m = 0.0079$  kg,  $\phi_0 = 0^\circ$ ,  $h = 1.7$  m.

Flat-fire trajectory simulations are performed for these conditions, and predicted range of the bullet as a function of the time is shown in Fig. 5. As the time increases, range of bullet increases. The bullet continues to travel in the  $X$ -direction against

**Table 1** Comparison of predicted instantaneous velocity with the data given in Ref. [1]

S. No.	Range (X) (m)	Velocity given in Ref. [1] $V_x$ (m/s)	Computed velocity $V_x$ (m/s)	Error (%)
1	0	262.128	262.128	0
2	22.86	256.946	256.9458	0.0000
3	45.72	251.765	251.764	0.0003
4	68.58	246.888	246.887	0.0004
5	91.44	242.011	241.999	0.004
6	114.3	237.439	237.4387	0.0001
7	137.16	232.562	232.5619	0.00002

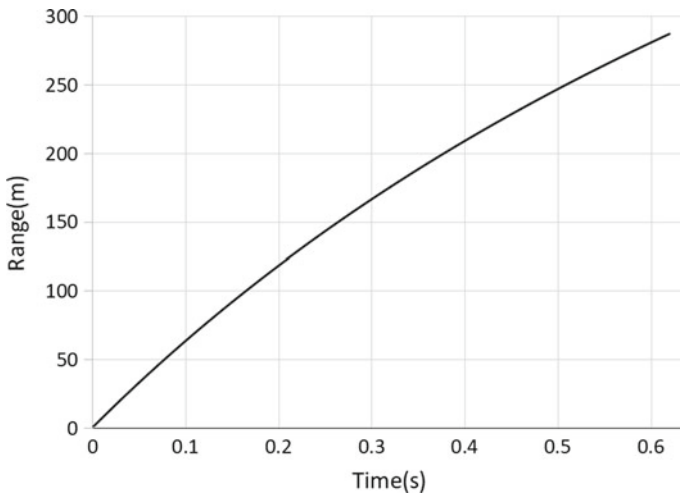


**Fig. 5** Trajectory of bullet about horizontal axis with respect to time for initial velocity of 680 m/s

aerodynamic drag due to momentum given at initial conditions. As a result, range of the bullet continues to increase with respect to time. The bullet takes 0.16 s and 0.357 s to travel a distance of 100 m and 200 m, respectively.

Figure 6a shows the trajectory of the bullet in X (range) and Y (height) coordinates. Initial height of the projectile is 1.7 m, and the vertical distance of 0 m represents ground. The height of the projectile continuously decreases as the range increases. The decrease in height is mainly due to the effect of gravity. Note that rate of fall in height is less compared to that of range. When the projectile travels a distance of 100 m in the X-direction, the decrease in height is 0.1 m. This reconfirms the accuracy of flat-fire trajectory approximation for the chosen problem. The bullet travels a distance of 285 m before falling on the ground.

Velocity of the bullet as a function of range is shown in Fig. 6b. Velocity continuously decreases as the bullet travels in the forward direction, and its value is about

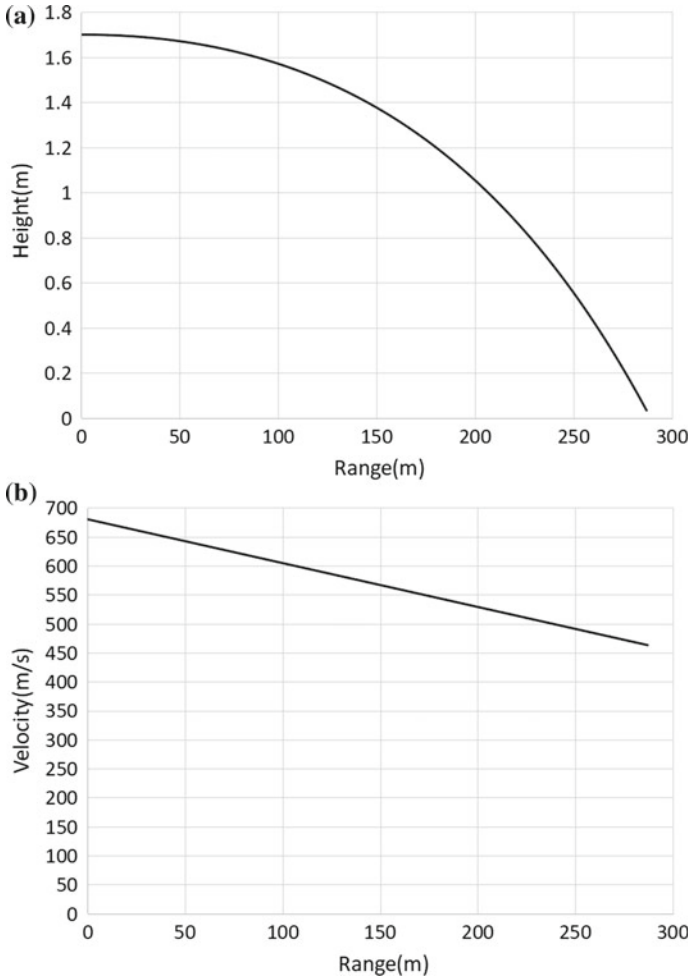


**Fig. 6** Variation of the **a** height and **b** velocity of projectile as a function of the range

600 m/s when the range is about 100 m. The decrease in velocity is caused by the aerodynamic drag. When the bullet hits at ground, velocity is 460 m/s or terminal velocity is 460 m/s. The reduction in velocity of the bullet at the time of hitting the ground is about 33%.

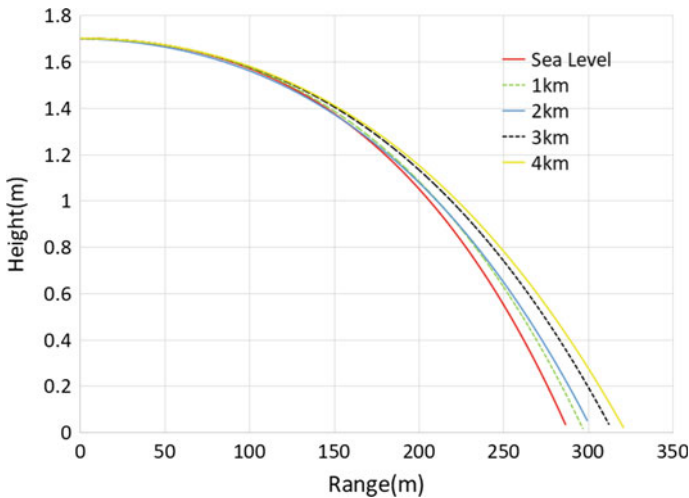
The trajectory of the bullet is simulated at altitudes of 1, 2, 3, and 4 km. Atmospheric conditions at these altitudes are taken from Ref. [7] and are listed in Table 2. CFD simulations are performed to determine the drag coefficient of the bullet for these conditions and are given in Table 2. Reynolds number calculated based on bullet diameter, initial velocity, and atmospheric density is also shown in the table. The reduction in density and temperature with respect to altitude does not yield significant changes in the Reynolds number and drag coefficient.

**Table 2** Predicted drag coefficient of the bullet as a function of the altitude. The atmospheric conditions at these altitudes are taken from Ref. [9]

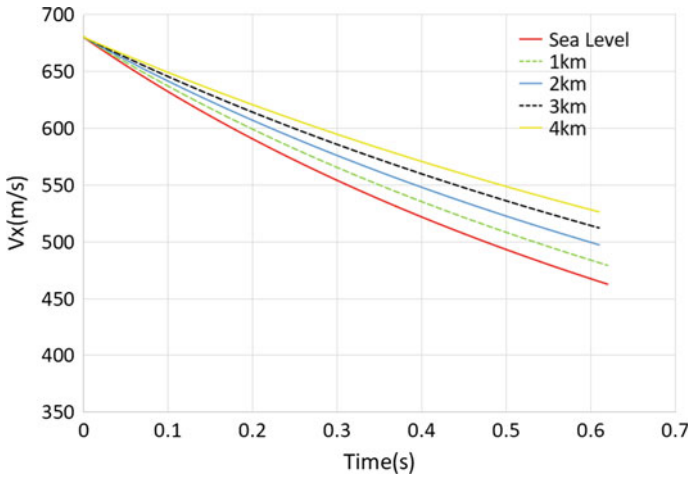
S. No.	Altitude (km)	Density ( $\rho$ ) (kg/m <sup>3</sup> )	Pressure (bar)	Temperature (K)	Reynolds No. (Re) $\times 10^5$	Coefficient of drag ( $C_d$ )
0	0	1.225	1.0133	288.15	3.633	0.3132
1	1	1.111	0.898	281.65	3.354	0.3145
2	2	1.006	0.795	275.15	3.095	0.3154
3	3	0.909	0.701	268.65	2.851	0.3163
4	4	0.819	0.616	262.15	2.62	0.3182

Figure 7 shows trajectory computed at these four altitudes for the initial velocity of 680 m/s. The maximum range is obtained for 4 km altitude. The range progressively increases as the altitude increases. As the altitude increases, density decreases and hence drag force action on the projectile also decreases. The reduction in drag force propels the projectile to a longer distance. The change in density between sea level and 4 km is 33%, and this results in increase in range of the bullet by 16%.

Instantaneous velocity of bullet for the four altitudes is shown in Fig. 8. Maximum terminal velocity is observed at 4 km, and minimum terminal velocity is observed at sea level. As the drag force acting on the bullet is lower at higher altitudes, the loss of momentum will be lower. This results in higher terminal velocity.



**Fig. 7** Comparison of trajectory of the bullet at altitudes of 1, 2, 3, and 4 km for initial velocity of 680 m/s



**Fig. 8** Instantaneous horizontal velocity of the projectile at altitudes of 1, 2, 3, and 4 km for initial velocity of 680 m/s

## 4 Conclusions

Flowfield over AK 47 assault rifle bullet is simulated for a Mach number of 2. The diameter and velocity of the bullet are 7.82 mm and 680 m/s, respectively. CFD simulations are performed ANSYS Fluent. The flowfield is dominated by bow shock wave, expansion fan, and recirculation bubble. At nose stagnation point, surface pressure is 6.14 times the atmospheric pressure. In the downstream of the nose, surface pressure decreases sharply due to flow expansion. The predicted drag coefficient is 0.312, and deviation from the published drag data is about 4%. The velocity of a projectile as a function of the range is predicted for an initial velocity of 260.12 m/s. Flat-firing approximation was used in the trajectory simulation. The error between the predictions and published data is below 0.01%. The validated code is used to predict trajectory parameters of bullet for an initial velocity of 680 m/s. The instantaneous velocity of the bullet decreases with respect to time, due to aerodynamic drag. For the chosen conditions, bullet travels a distance of 280 m in 0.63 s. The terminal velocity of the bullet is 450 m/s and drop in its height during the flight is about 1.7 m. At higher altitudes, atmospheric air density is lower. This results in increase in range and terminal velocity. At 4 km altitude, the reduction in density compared to sea level is 37%, and corresponding increases in range and terminal velocity are 16% and 13%, respectively.



## References

1. McCoy RL (1012) Modern exterior ballistics, 2<sup>nd</sup> edn. Schiffer Military History, Atglen. ISBN 978-0764338250
2. Charles CT (1958) A drag coefficient  $K_D$  based on the 155 mm Shell HE, M101. Ballistic Research Laboratory, Memorandum Report No. 1167, Maryland, U.S.A.
3. Weinacht P (2003) Prediction of projectile performance, stability and free-flight motion using computational fluid dynamics. Army Research Laboratory, Aberdeen Proving Ground, MD ARL-TR-3015
4. Wei W, Zhang X (2013) Numerical simulation and analysis of the muzzle flow during the revolving barrel gun firing. *J Appl Mech* 80(3):03162-1-6
5. Klatt D, Hruschka R, Leopold F (2013) Investigation of the Magnus effect of a generic projectile at Mach 3 Up to 16 degrees Angle of Attack. *J Appl Mech* 80(3):031603-1-9
6. ANSYS FLUENT 18.0 user guide, © Fluent Inc. January, 2017
7. Launder BE, Spalding DB (1974) The numerical computation of turbulent flows. *Comput Methods Appl Mech Eng* 3(2):269–289
8. ParaView 5.5 guide, ©ParaView June, 2018
9. Yahya SM (2014) Gas tables for compressible flow calculations, 6<sup>th</sup> edn. New Age International Publishers, New Delhi

# Optimum Annular Plane Fin Profile with Uniformly Varying Thickness



Abhijit Deka and Dilip Datta 

**Abstract** Motivated by research gap, an annular fin of plane profile is investigated here as a multi-objective optimization problem primarily considering the maximization of the heat dissipation rate and, at the same time, minimization of the maximum induced thermal stress. The minimization of the fin volume and maximization of fin efficiency and effectiveness are studied further for assessing the fin performance. The fin base and tip half thickness along with fin external radius are considered as three design variables. Evaluating the temperature and the thermal stress field through the hybrid spline difference method, the non-dominated sorting genetic algorithm II is utilized in optimizing the problem. The obtained results are analyzed from the angle of a practicing designer.

**Keywords** Annular plane fin profile · Heat dissipation rate · Thermal stress · Multi-objective optimization

## 1 Introduction

Fin, by extending the effective heat dissipation surface, enhances the heat dissipation from the primary surface [1]. A significant number of studies on heat dissipation analysis in fins are found in the literature [2–4]. The temperature variations developed in a fin induce thermal stress. However, the development of thermal stress in a fin is not desirable as it may cause mechanical failures. Hence, a systematic analysis of the developed thermal stress is essential to enhance the life expectancy and performance of a fin [5]. However, because of the mathematical complexity involved with the nonlinearity of the problem, a very limited number of studies on thermal stress analysis in annular fins are found in the specialized literature [6–8]. In view of the above, the main role of a designer is to design a fin that would dissipate heat at the

---

A. Deka (✉) · D. Datta  
Department of Mechanical Engineering, Tezpur University,  
Tezpur 784028, India  
e-mail: [adeka13@tezu.ernet.in](mailto:adeka13@tezu.ernet.in)

© Springer Nature Singapore Pte Ltd. 2020  
L. Vijayaraghavan et al. (eds.), *Emerging Trends in Mechanical Engineering*,  
Lecture Notes in Mechanical Engineering,  
[https://doi.org/10.1007/978-981-32-9931-3\\_41](https://doi.org/10.1007/978-981-32-9931-3_41)

maximum rate but induce the minimum thermal stress. This can be achieved simply by modifying the geometry of a fin [9]. However, such a modification may lead to a complex fin profile from the manufacturing point of view. Further, it is found that the heat dissipation rate and developed maximum thermal stress are conflicting in nature; i.e., a solution favoring the heat dissipation rate would be inadmissible concerning the maximum thermal stress and vice versa. Hence, a sensible methodology would be to optimize both the measures simultaneously to arrive at a compromise solution. It is to be mentioned that although annular fins are optimized by maximizing the heat dissipation for constant volume [10] or constant fin height [11], no work could be found in the specialized literature optimizing concurrently both the heat dissipation rate and the thermal stress of an isolated annular fin of plane profile with variable volume and thickness.

## 2 Problem Statement and Formulation

The multi-objective optimization of plane profile annular fin is studied considering one-dimensional heat conduction, and fin internal and external radii are free of traction. Further, it is considered that steady-state heat dissipation from the fin surface takes place by both natural convection and radiation. A constant base temperature, a constant heat dissipation coefficient, and negligible internal heat generation are other assumptions adopted in the analysis. Also, Poisson's ratio ( $\nu$ ), thermal expansion coefficient ( $\alpha$ ), and modulus of elasticity ( $E$ ) of the fin material are considered constant. Figure 1 depicts an annular fin of plane profile, where  $r$  represents the radial coordinate of the fin with  $r_b$  and  $r_o$  being the internal and external radii of the fin, respectively, while  $t$  represents the half thickness of the fin with  $t_b$  and  $t_o$  being its quantities at the base and tip, respectively. Note that profile of the fin will be rectangular if  $t$  is constant (i.e.,  $t_o = t_b$ ); otherwise, it will be tapered as shown in Fig. 1.

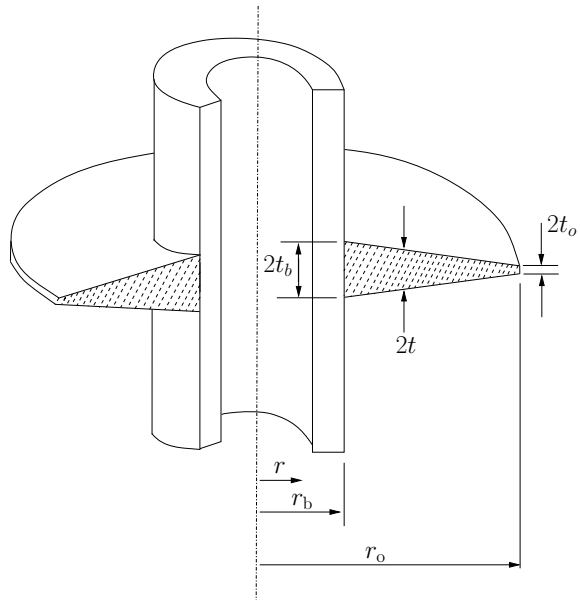
### 2.1 Heat Dissipation Modeling

Since the thermal conductivity ( $k$ ) for most of the fin materials varies linearly with fin temperature ( $T$ ), it can be expressed as given by Eq. (1), where  $T_\infty$  is the ambient temperature,  $k_a$  is the thermal conductivity of the fin material at ambient temperature, and  $\beta$  is a constant characterizing the change in  $k$  with  $T$ .

$$k = k_a \{1 + \beta (T - T_\infty)\} \quad (1)$$

Incorporating Eq. (1), the one-dimensional heat balance equation and boundary conditions in a thin annular fin can be represented by Eqs. (2) and (3), respectively, where

**Fig. 1** An annular fin of plane profile



$h$  represents the convective heat dissipation coefficient,  $\epsilon$  represents the emissivity of the fin material, and  $\sigma$  represents the Stefan–Boltzmann constant.

$$\frac{d}{dr} \left[ r \{1 + \beta (T - T_\infty)\} \frac{dT}{dr} \right] + \left[ r \{1 + \beta (T - T_\infty)\} \frac{dT}{dr} \right] \frac{t'}{t} - \frac{hr}{k_a t} \left\{ T - T_\infty + \frac{\sigma \epsilon (T^4 - T_\infty^4)}{h} \right\} (1 + t'^2)^{\frac{1}{2}} = 0 \quad (2)$$

$$T = T_b, \quad \text{at } r = r_b \quad (3a)$$

$$-k_a \{1 + \beta (T - T_\infty)\} \frac{dT}{dr} = h (T - T_\infty) + \sigma \epsilon (T^4 - T_\infty^4), \quad \text{at } r = r_o \quad (3b)$$

### 2.2 Thermal Stress Modeling

Since an annular fin of small thickness can be studied by considering it under the action of an axisymmetric plane stress system [12], the stress–displacement relationships for such an annular fin can be expressed by Eq. (4), where  $\sigma_r$  and  $\sigma_\theta$  are, respectively, the radial and circumferential thermal stress,  $u$  being the radial displacement.

$$\sigma_r = \frac{E}{1 - \nu^2} \left\{ \frac{du}{dr} + \nu \frac{u}{r} - (1 + \nu)\alpha T \right\} \tag{4a}$$

$$\sigma_\theta = \frac{E}{1 - \nu^2} \left\{ \frac{u}{r} + \nu \frac{du}{dr} - (1 + \nu)\alpha T \right\} \tag{4b}$$

Further, from the classical theory of elasticity, the equilibrium condition for a fin of plane profile is given by Eq. (5).

$$\frac{d\sigma_r}{dr} + \frac{\sigma_r}{t} \frac{dt}{dr} + \frac{\sigma_r - \sigma_\theta}{r} = 0 \tag{5}$$

Combining Eqs. (4) and (5), the equilibrium condition of a fin can be expressed as given by Eq. (6) with boundary conditions given by Eq. (7).

$$\frac{d^2u}{dr^2} + \left(1 + \frac{rt'}{t}\right) \frac{1}{r} \frac{du}{dr} - \left(1 - \frac{rt'}{t}\nu\right) \frac{u}{r^2} - \left(\frac{dT}{dr} + \frac{t'}{t}T\right) (1 + \nu)\alpha = 0 \tag{6}$$

$$\frac{du}{dr} + \nu \frac{u}{r} - (1 + \nu)\alpha T_b = 0, \quad \text{at } r = r_b \tag{7a}$$

$$\frac{du}{dr} + \nu \frac{u}{r} - (1 + \nu)\alpha T_o = 0, \quad \text{at } r = r_o \tag{7b}$$

### 3 Optimization Modeling

The multi-objective fin design optimization problem is formulated, as expressed by Eq. (8), by considering the three independent geometric parameters, i.e., the external radius ( $r_o$ ), half thickness at the base ( $t_b$ ), and half thickness at the tip ( $t_o$ ) as the design variables and the five performance parameters, i.e., heat dissipation rate,  $f_1(\mathbf{x})$ , induced maximum thermal stress,  $f_2(\mathbf{x})$ , fin volume,  $f_3(\mathbf{x})$ , fin efficiency,  $f_4(\mathbf{x})$ , and fin effectiveness,  $f_5(\mathbf{x})$ , as the objective functions.

$$\left. \begin{array}{l} \text{Determine} \quad \mathbf{x} \equiv (r_o, t_b, t_o)^T \\ \text{to maximize} \quad \mathbf{z}(\mathbf{x}) \equiv \{f_1(\mathbf{x}), f_4(\mathbf{x}), f_5(\mathbf{x})\} \\ \text{minimize} \quad \mathbf{f}(\mathbf{x}) \equiv \{f_2(\mathbf{x}), f_3(\mathbf{x})\} \\ \text{subject to} \quad g_1(\mathbf{x}) \equiv r_o > r_b \\ \quad \quad \quad g_2(\mathbf{x}) \equiv t_o < t_b \\ \quad \quad \quad r_o, t_b, t_o \geq 0 \end{array} \right\} \tag{8}$$

In Eq. (8), constraint  $g_1(\mathbf{x})$  ensures the existence of the fin, and constraint  $g_2(\mathbf{x})$  restricts the increase in fin thickness in the outward direction while the last line

ensures that the design variables are positive. The objective functions are formulated as given by Eq. (9), where  $A_b$  is the fin base area and the subscript max represents the maximum value.

$$f_1(\mathbf{x}) = -kA_b \left. \frac{dT}{dr} \right|_{r=r_b} \quad (9a)$$

$$f_2(\mathbf{x}) = \left[ (\sigma_r^2 - \sigma_r \sigma_\theta + \sigma_\theta^2)^{\frac{1}{2}} \right]_{\max} \quad (9b)$$

$$f_3(\mathbf{x}) = V \quad (9c)$$

$$f_4(\mathbf{x}) = \frac{f_1(\mathbf{x})}{hA_s(T_b - T_\infty) + \sigma \epsilon A_s(T_b^4 - T_\infty^4)} \quad (9d)$$

$$f_5(\mathbf{x}) = \frac{f_1(\mathbf{x})}{hA_b(T_b - T_\infty) + \sigma \epsilon A_b(T_b^4 - T_\infty^4)} \quad (9e)$$

where,

$$A_b = 4\pi r_b t_b \quad (9f)$$

The fin volume  $V$  in Eq. (9c) and the heat dissipation area  $A_s$  in Eq. (9d) are evaluated using Simpson's  $\frac{1}{3}$  rule for numerical integration and from the fin geometry, respectively [9].

## 4 Solution Procedure

The non-dominated sorting genetic algorithm II (NSGA-II) [13] is applied to solve the multi-objective fin design optimization problem formulated in Eq. (8). In the cycles of NSGA-II, the problem governing Eq. (2) and its boundary conditions in Eq. (3) are solved numerically to compute the heat dissipation rate  $f_1(\mathbf{x})$  given by Eq. (9a). Similarly, the problem governing Eq. (6) along with its associated boundary conditions in Eq. (7) is solved to compute the induced maximum thermal stress  $f_2(\mathbf{x})$  given by Eq. (9b). For these, the sets of Eqs. (2) and (3), and Eqs. (6) and (7) are solved first by employing the hybrid spline difference method (HSDM) [14], to evaluate the temperature field and displacement field, respectively [9].

## 5 Experimentation and Discussion

For numerical experimentation, the considered parameters are as follows: ambient temperature ( $T_\infty$ ) = 300 K, fin base temperature ( $T_b$ ) = 600 K, convective heat dissipation coefficient ( $h$ ) = 50 W/m<sup>2</sup> K, thermal conductivity of the fin material at  $T_\infty$  ( $k_a$ ) = 186 W/mK, variable thermal conductivity parameter ( $\beta$ ) =

$-0.00018 \text{ K}^{-1}$ , emissivity of the fin material ( $\epsilon$ ) = 0.8, base radius of the fin ( $r_b$ ) = 2.0 cm, range of external radius of the fin ( $r_o$ ) = [3.5, 15.0] cm, range of half thickness of the fin at the base ( $t_b$ ), and tip ( $t_o$ ) = [0.01, 0.3] cm. The algorithmic parameter settings for NSGA-II fixed based on some trial runs are as follows: Over 400 generations, a population of size 100 is evolved considering 90% crossover probability and (0, 1%) as the range of random mutation probability. After fixing the sets of input parameters, the fin size optimization problem as formulated in Eq. (8) is investigated as a bi-objective optimization problem for maximizing the heat dissipation rate ( $f_1$ ) separately with minimizing the induced maximum thermal stress ( $f_2$ ), minimizing the fin volume ( $f_3$ ), maximizing the fin efficiency ( $f_4$ ), and maximizing the fin effectiveness ( $f_5$ ). The respective Pareto fronts are shown in Fig. 2a–d.

The solutions of the Pareto front in Fig. 2a depict the trade-off nature of the heat dissipation rate with thermal stress. Similar conflicting nature of the heat dissipation rate with fin volume, fin efficiency, and fin effectiveness is also shown in Fig. 2b–d, respectively.

Six selective optimum fin profiles, corresponding to trade-off solutions A–F of Fig. 2a, are shown in Fig. 3, where the distinctions in the patterns of the fin profiles are prominent. Calculating the values of  $f_3$ – $f_5$  for these fin configurations, which

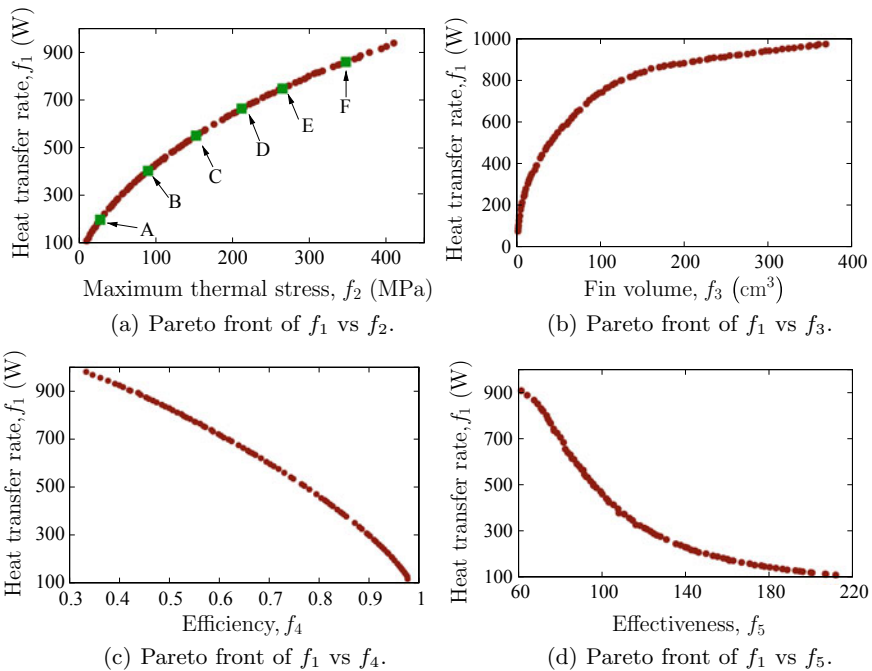


**Fig. 2** Pareto fronts of  $f_1$  vs  $f_2$ ,  $f_3$ ,  $f_4$ , and  $f_5$

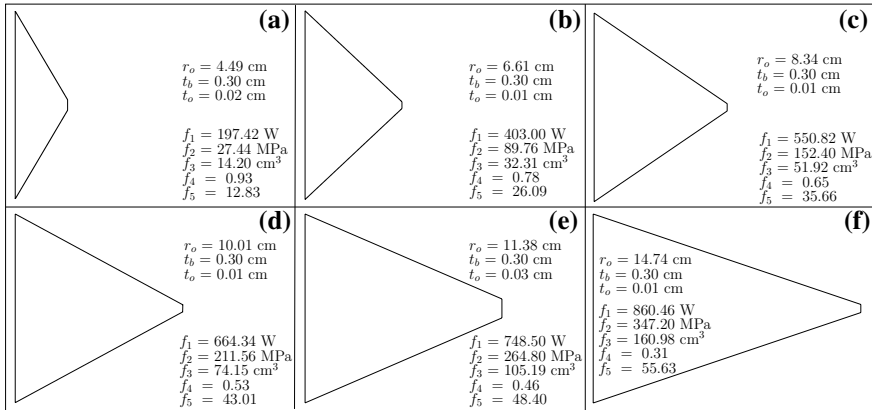


**Fig. 3** Configurations corresponding to trade-off solutions A–F of Fig. 2a. (Scale along the axial direction is 15 times larger than that along the radial direction)

are also shown in Fig. 3 along with the optimized values of  $f_1$  and  $f_2$ , it is observed in these particular six profiles that with increasing  $f_1$  and  $f_2$ ,  $f_3$  and  $f_5$  also increase continuously, while  $f_4$  decreases.

### 5.1 Sensitivity Analysis

Finally, to investigate the effect of each design variable on the heat dissipation rate and maximum thermal stress developed in the fin, a sensitivity analysis is performed. For this purpose, the design variables are allowed to vary  $\pm 40\%$  from a chosen particular point in the design space ( $t_b^\dagger = 0.20$  cm,  $t_o^\dagger = 0.10$  cm, and  $r_o^\dagger = 9.25$  cm) having  $f_1^\dagger = 573.51$  W and  $f_2^\dagger = 268.24$  MPa. For this, the problem is solved three times, every time enabling a design variable to alter from its chosen value while retaining the other two design variables' constant. The plots of the variation of the heat dissipation rate and the maximum thermal stress developed against the characteristic variation of the corresponding design variables are shown in Fig. 4a, b, respectively. It is observed in the plots that both the heat dissipation rate and the maximum thermal stress developed are more sensitive to the external radius ( $r_o$ ) of the fin, followed by that to the fin half thickness at the base ( $t_b$ ), while the influences of the fin half thickness at the tip ( $t_o$ ) are comparatively very less in both the cases. Accordingly, to acquire the desired heat dissipation effect maintaining the maximum thermal stress, a designer will have the freedom to choose economic combinations of the design variables based on the accessibility of resources. It may be noticed in Fig. 4 that, with an increment in  $t_b$ , the heat dissipation rate in the fin raises and the induced maximum thermal stress falls. Since all other parameter values related to the problem ( $r_o$ ,  $t_o$ ) were kept constant, this happened because an increase in  $t_b$  decreases the conductive



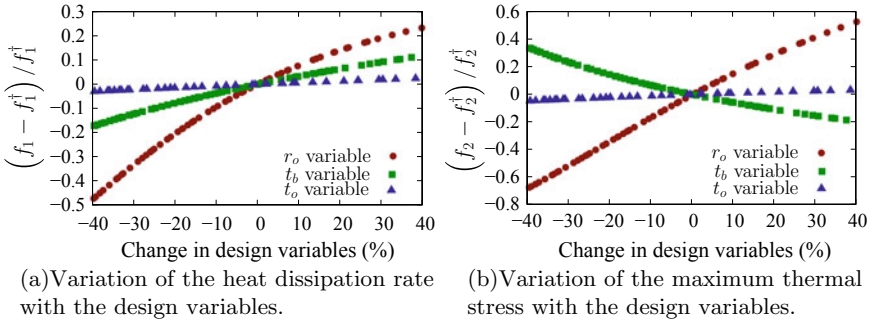


**Fig. 4** Sensitivity analysis of the heat dissipation rate and maximum thermal stress developed in terms of the design variables

resistance to heat flow, thus increasing the heat dissipation rate. Further increased heat dissipation rate results in a more uniform temperature distribution along the radial direction of the fin, which leads to decreasing thermal stress in the fin.

## 6 Conclusion

The present work demonstrates multi-objective design optimization of an annular fin of plane profile considering steady-state one-dimensional heat dissipation in a convective and radiative environment. Analyzing the trade-off solutions of the obtained Pareto fronts, useful information could be gathered regarding the active design space and the effects of the objective functions on efficient fin geometries. Further, performing a sensitivity analysis, the influences of individual design variable on the heat dissipation rate and induced maximum thermal stress are also studied in regard to economic and viable fin design from the industrial perspective point.

## References

1. Kraus AD, Aziz A, Welty J (2001) Extended surface heat transfer. John Wiley & Sons, New York
2. Kundu B, Lee KS, Campo A (2015) An ease of analysis for optimum design of an annular step fin. *Int J Heat Mass Transf.* 85:221–227
3. Deka A, Datta D (2017) Geometric size optimization of annular step fin using multi-objective genetic algorithm. *J. Thermal Sci. Eng. Appl.* 9:0210131–0210139
4. Deka A, Datta D (2017) A comparative investigation of annular fins of different profiles using multi-objective genetic algorithm. In: 2017 international conference on advances in mechanical, industrial, automation and management systems (AMIAMS), Allahabad, India. IEEE, pp 74–79

5. Mallick A, Ranjan R, Das R (2016) Application of homotopy perturbation method and inverse prediction of thermal parameters for an annular fin subjected to thermal load. *J Thermal Stress* 39:298–313
6. Chiu CH, Chen CK (2002) Thermal stresses in annular fins with temperature-dependent conductivity under periodic boundary condition. *J Thermal Stress* 25:475–492
7. Bas H, Keles I (2015) Novel approach to transient thermal stress in an annular fin. *J Thermophys Heat Transf* 29:705–710
8. Deka A, Datta D (2018) Multi-objective optimization of annular fin array with B-spline curve based fin profiles. *J Thermal Stress* 41:247–261
9. Deka A, Datta D (2017) B-spline curve based optimum profile of annular fins using multiobjective genetic algorithm. *J Thermal Stress* 40:733–746
10. Arslanturk C (2005) Simple correlation equations for optimum design of annular fins with uniform thickness. *Appl Thermal Eng* 25:2463–2468
11. Kang HS (2009) Optimization of a rectangular profile annular fin based on fixed fin height. *J Mech Sci Technol* 23:3124–3131
12. Timoshenko SP, Goodier JN (1970) *Theory of elasticity*. McGraw-Hill, New York
13. Deb K, Pratap A, Agarwal S, Meyarivan T (2002) A fast and elitist multi-objective genetic algorithm: NSGA-II. *IEEE Trans Evol Comput* 6:182–197
14. Wang CC, Liao WJ, Yang CY (2013) Hybrid spline difference method for heat transfer and thermal stresses in annular fins. *Numer Heat Transf Part B: Fundam* 64:71–88

# Experimental Study on Effect of Green Cutting Fluid and Surfactant on Temperature in Turning Operation



Rahul Katna, Mohammed Suhaib, Narayan Agrawal, Swati Jain, Kanwarjeet Singh and S. Maji

**Abstract** Cutting fluids play a major role in the metal industry. They are used for having increased material removal rates and increasing the quality of the machined product. The cutting fluids have been used for many decades after their efficacy in increasing productivity was established. Since the advent of cutting fluids the market has flooded with different composition of cutting fluids. All these are mineral oil based and comprise different additives or performance enhancers. However, the latest trend in cutting fluids use is employing vegetable oils as base oil for formulating cutting fluids. Cutting fluids formulated from vegetable oils are a promising source of increasing productivity in the industry because of their thermal properties. It is, however, difficult to formulate stable water-soluble cutting fluid. Also, it has been observed that the chemical constituent of a cutting fluid behaves differently on the surface of the workpiece during machining operation. In this study different cutting fluids were formulated from edible oil and non-edible oil and the performance in terms of temperature was compared and reported.

**Keywords** Edible oil · Non -edible oil · Temperature · Tool · Workpiece · Specific heat capacity · Thermal conductivity

## 1 Introduction

Metal machining operations are of various types. Most widely used metal removal operations are turning, milling, grinding etc. In every metal removal material operation, huge amount of heat is generated. The major source of heat generation is the shear zone (from where the chips get sheared) and the rake face where the metal

---

R. Katna (✉) · N. Agrawal · K. Singh · S. Maji  
Delhi Institute of Tool Engineering, Okhla, New Delhi, India  
e-mail: [katnarahul@gmail.com](mailto:katnarahul@gmail.com)

R. Katna · M. Suhaib  
Jamia Millia Islamia, New Delhi, India

S. Jain  
Integrated Institute of Technology, Dwarka, Delhi, India

© Springer Nature Singapore Pte Ltd. 2020  
L. Vijayaraghavan et al. (eds.), *Emerging Trends in Mechanical Engineering*,  
Lecture Notes in Mechanical Engineering,  
[https://doi.org/10.1007/978-981-32-9931-3\\_42](https://doi.org/10.1007/978-981-32-9931-3_42)

chip rubs and the zone of rubbing between tool and workpiece [1]. The total heat generated is distributed among the tool, workpiece and the chips. The cutting tool carries around 15–20% of the heat, the workpiece also absorbs some heat, and the rest of the heat is carried away by the chips [2–4]. The material of the workpiece and the cutting tool is affected by the temperature. High temperature has many negative effects on the workpiece integrity as well as on the properties of the cutting tool. Temperature also has a direct relation with the cutting forces in machining as the coefficient of friction depends on the temperature [5].

Heat also affects the workpiece by distorting it from its original dimensions. High heat generation may also cause reduced surface finish of the workpiece. It can also influence the surface toughness of the workpiece. High heat generation also affects the cutting tool. Thermal softening of the cutting edges occurs at high temperatures and this causes loss of the cutting property of the cutting tool and thereby causing tool failure [4–7]. The heat generated has high influence on the integrity of the surface being machined [8]. Heat generation is a major performance indicator of machining [9]. Hence temperature control by use of cutting fluids can also be used as an indicator of machining performance. Also, heat generation is a controlling as well as a limiting factor for material removal rates in machining operation. Heat generation is also important for controlling the life of the cutting tool [10–12].

The use of cutting fluids helps in reducing the temperature rise in machining. Cutting fluids help in keeping the machining cool and thus prevents the negative thermal effects due to temperature. A cool machining operation can help in increasing the material removal rates and thereby increasing the productivity. However, the cutting fluids formulated from mineral oils as base oils have harmful effect on environment as well as on worker [7, 12–14]. Researches done with vegetable oil based cutting fluids show that these perform better in reducing temperature as compared to the mineral oil based cutting fluid. It is also important to formulate cutting fluid which is safe for environment [12, 13]. Use of vegetable oil and a surfactant selection should be made properly in a way that a stable emulsion is formed for use in machining. Proper emulsion formulation is of utmost importance because the manner in which the cutting fluid constituents interact with the surface is important. Also the thermal properties play a major role in keeping the temperature rise in control. Higher thermal conductivity helps in carrying away the heat effectively from the cutting zone and high specific heat capacity of the liquids helps in keeping the temperature of cutting fluid low after absorbing heat from the cutting zone.

## 2 Materials and Method

In this study one edible oil and one non-edible oil were taken as base oils. Six different samples of cutting fluids were formulated by varying the percentage of a commonly used surfactant. The edible oil taken was mustard oil and the non-edible oil taken was neem oil. The surfactant concentration was taken as 5, 10, and 15% for both the oils.

## 2.1 Cutting Fluid Preparation

The cutting fluid concentrate was prepared by mixing the measured quantity of oil and surfactant in a magnetic stirrer. Each oil and surfactant mixture was blended in a magnetic stirrer for 15 min. The samples made from mustard oil and 5, 10, and 15% surfactant were coded as MS05, MS10, and MS15.

3 different samples were prepared from neem oil similarly. Same surfactant was used and its concentration varied as 5, 10 and 15%. The mixture was blended in magnetic stirrer for 15 min.

The samples were coded as NS05, NS10, and NS15. The concentrates were diluted with water to 5%.

## 2.2 Cutting Condition

In order to determine the effect of surfactant on temperature in machining, same cutting conditions were kept for all samples. The machining operation was carried out on a conventional lathe machine HMT make, available in the workshop. Average cutting speed of 60 m/min, feed rate at 0.1 mm/rev and depth of cut as 0.3 mm was taken for all the samples.

The workpiece material takes for machining was Mild steel and the machining was done by single point HSS tool. A constant flow rate of one liter per minute was maintained throughout the experiment. The flow rate was maintained using a submersible pump with a tube attached to its outlet and a control valve at the end of the tube in order to control the flow rate of the cutting fluid. For measuring the temperature rise during machining a thermal infrared thermometer make MK was used.

The range of the infrared thermometer, as specified by the manufacturer, was -55 to 800 °C. The laser was pointed directly at the cutting zone for measuring the temperature rise during machining. The temperature was recorded during the entire machining time and the average temperature was reported. The temperature of cutting fluid before machining and after machining was also recorded by the thermal infrared thermometer.

## 3 Results and Discussion

The formulated cutting fluids were observed immediately for stability and after 72 h. Figures 1 and 2 show the results of cutting fluid stability formulated from neem oil after 1 day and 3 days, respectively. Figures 3 and 4 show emulsion stability of cutting fluid formulated from mustard oil after 1 day and 3 days, respectively.

**Fig. 1** Cutting fluid formulated from neem oil after 1 day

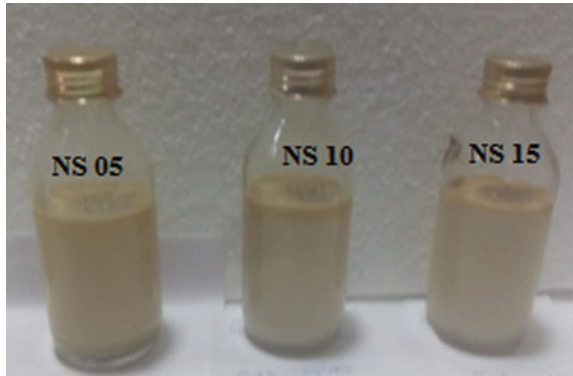


**Fig. 2** Cutting fluid formulated from neem oil after 3 days

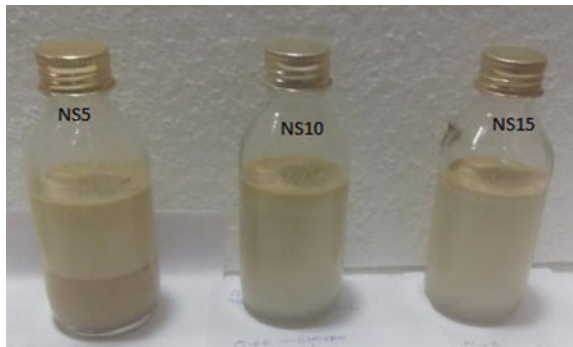


**Fig. 3** Cutting fluid formulated from mustard oil after 1 day

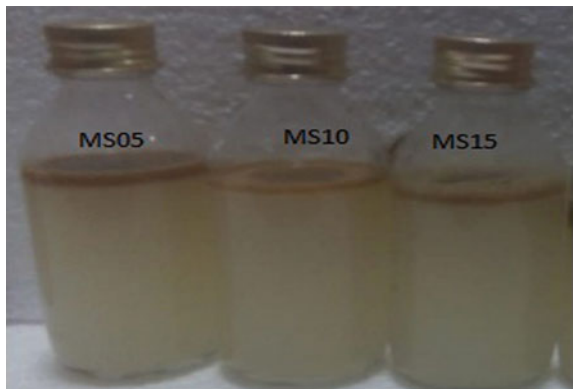
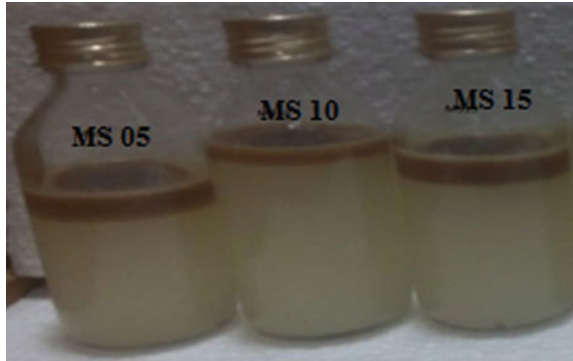


**Fig. 4** Cutting fluid formulated from mustard oil after 3 days



It is observed from Figs. 1, 2, 3, and 4 that the emulsions formulated under the conditions as described in the material and method section are stable only for one day. The temperature rise during machining is reported from Figs. 5, 6, 7, 8, 9, 10,

**Fig. 5** Temperature rise for cutting fluid formulated from neem oil and 5% surfactant

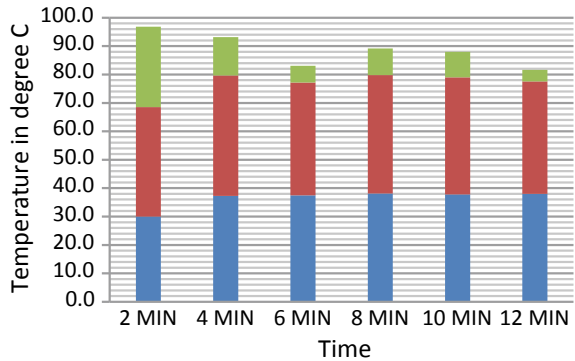


**Fig. 6** Temperature rise for cutting fluid formulated from mustard oil and 5% surfactant

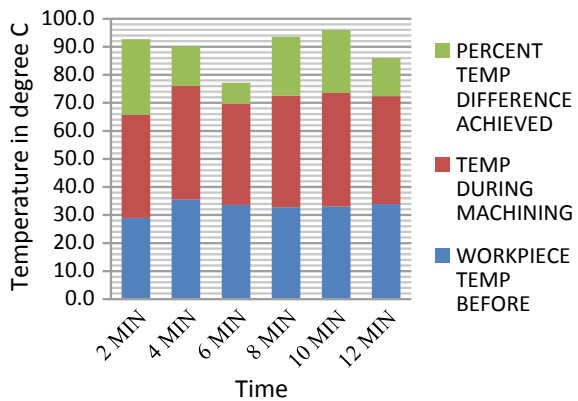


**Fig. 7** Temperature rise for cutting fluid water

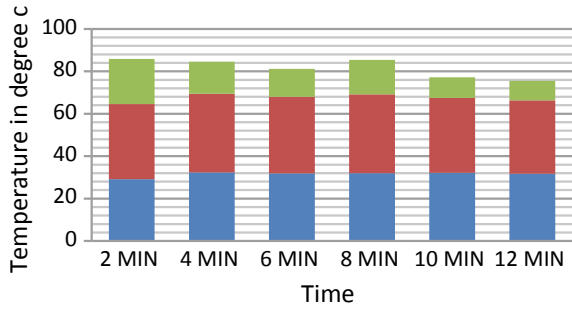


**Fig. 8** Temperature rise without any cutting fluid

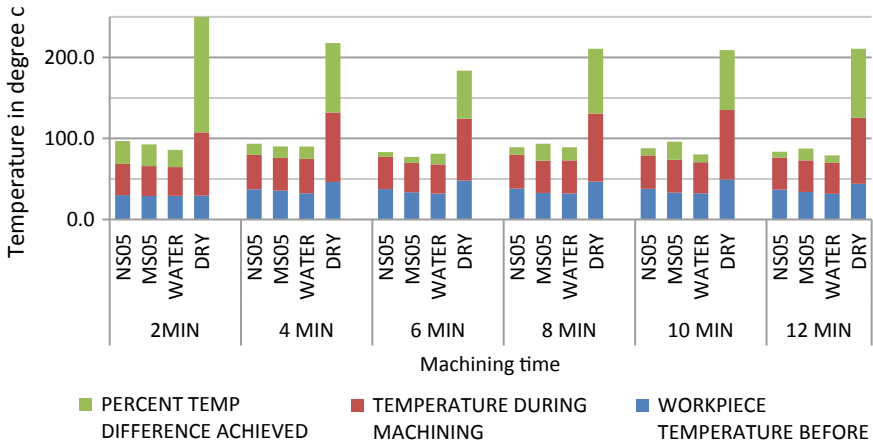
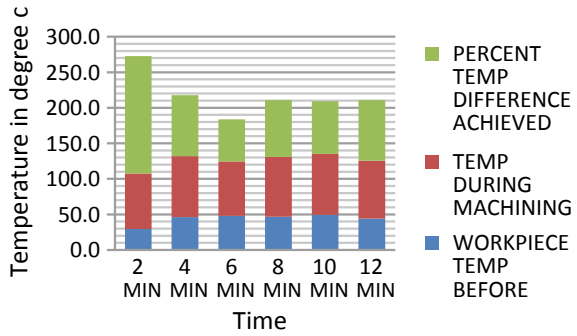


**Fig. 9** Effect of different cutting fluid environment on temperature with surfactant concentration 5%



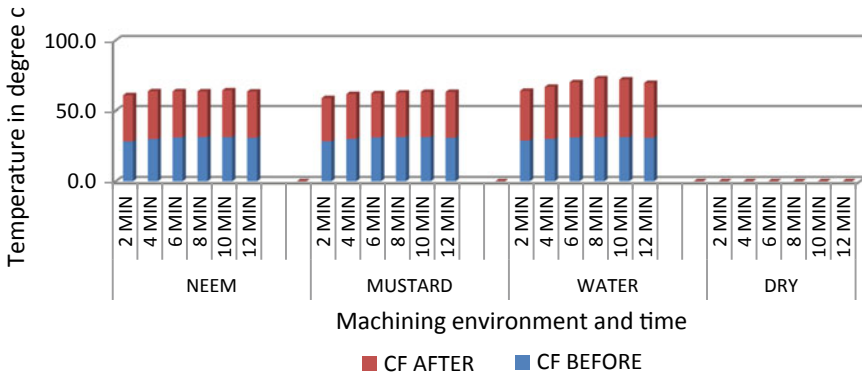


**Fig. 10** Difference in fluid temperature with machining environment (5% surfactant)

11, 12, 13, 14, 15, 16, 17, 18, 19, 20, 21, and 22. Figures 5, 6, 7, and 8 show the temperature rise during machining with individual cutting fluid environment with 5% surfactant concentration. The comparison between different cutting fluids is shown in Fig. 9.

**Fig. 11** Temperature rise for cutting fluid formulated from neem oil and 10% surfactant

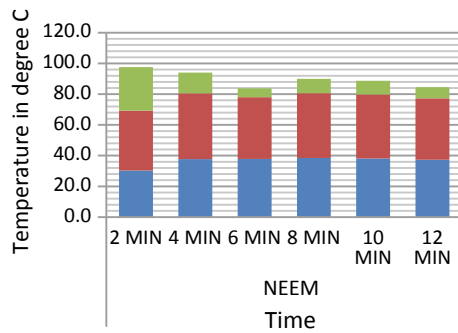


**Fig. 12** Temperature rise for cutting fluid formulated from mustard oil and 10% surfactant

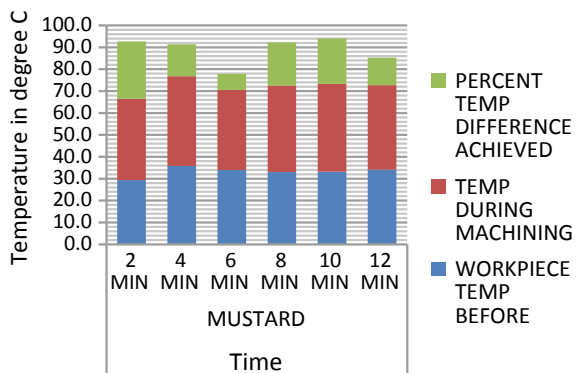


**Fig. 13** Temperature rise for cutting fluid—water

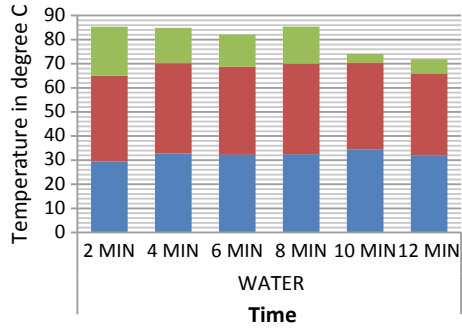


**Fig. 14** Temperature rise without any cutting fluid

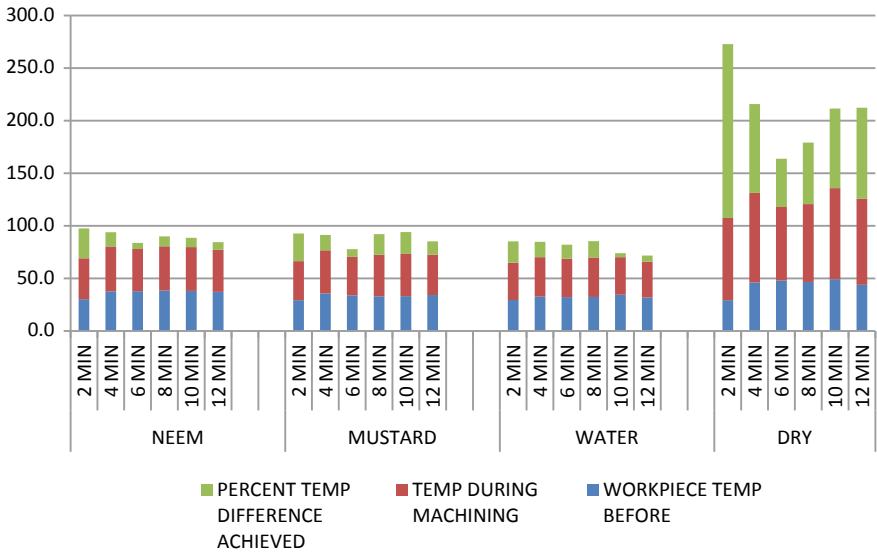
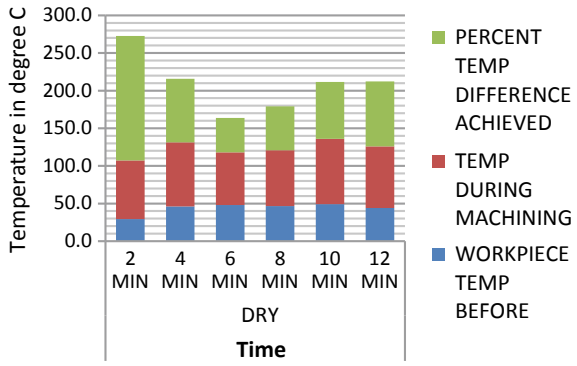


**Fig. 15** Effect of different cutting fluid environment on temperature with surfactant concentration 10%

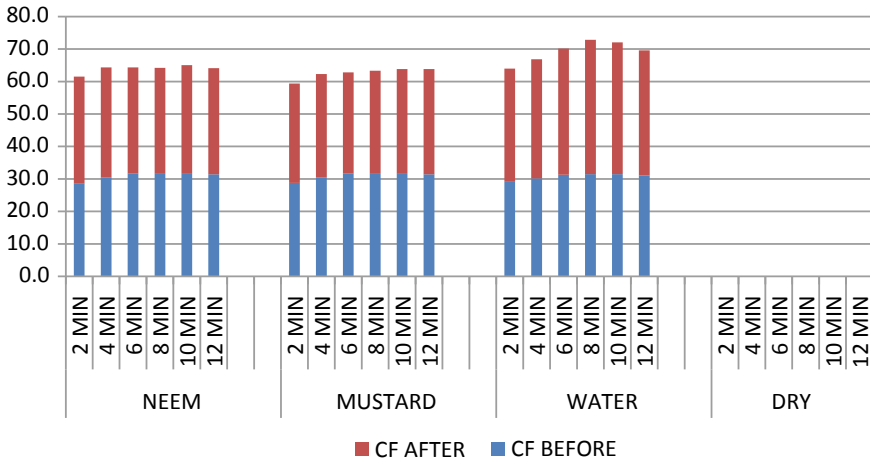


Fig. 16 Difference in fluid temperature with machining environment and time with 10% surfactant

Fig. 17 Temperature rise for cutting fluid formulated from neem oil and 15% surfactant

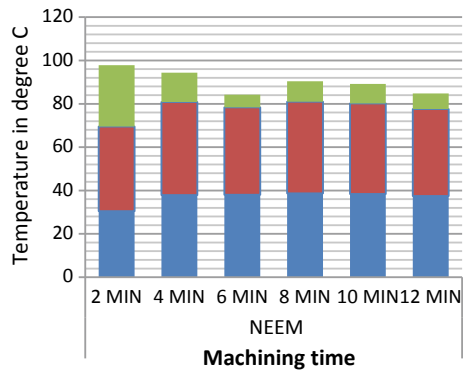
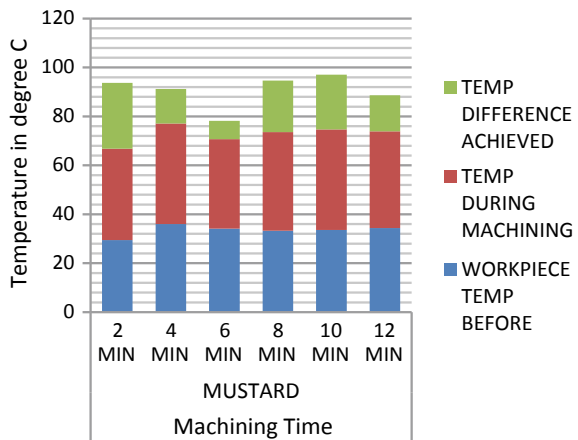
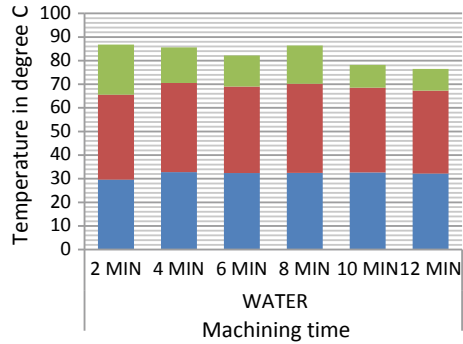


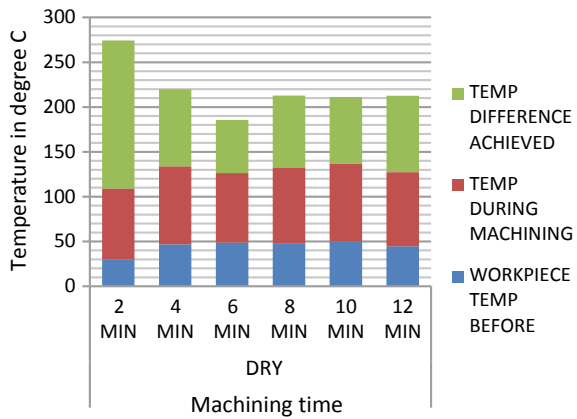
Fig. 18 Temperature rise for cutting fluid formulated from mustard oil and 15% surfactant



**Fig. 19** Temperature rise for cutting fluid water



**Fig. 20** Temperature rise without any cutting fluid



As can be seen from the observations, water acts as the best coolant among all the cutting fluid samples used. It was followed by mustard oil based cutting fluid and the least performance was obtained by neem oil based cutting fluid at 5% surfactant concentration.

Figure 10 shows the rise in temperature of cutting fluid after the machining has been done. The rise in temperature is an indicator of the specific heat capacity of the formulated cutting fluid. Figures 11, 12, 13 and 14 show temperature rise with cutting fluid formulated from neem oil, cutting fluid formulated from mustard oil, cutting fluid with water only and no cutting fluid, i.e., dry condition, respectively. Figure 15 shows the comparison between different cutting fluid conditions at 10% concentration of surfactant.

As observed in Fig. 15, water performs the best in terms of reduction of temperature during machining followed by mustard oil based cutting fluid and the least performance was of the neem oil based cutting fluid. The trend remains the same as in the case when the surfactant concentration was kept 5%. However, an increase of 1% average temperature was observed in the temperature with 5% increase in surfactant concentration which could be due to decrease in thermal conductivity by the addition

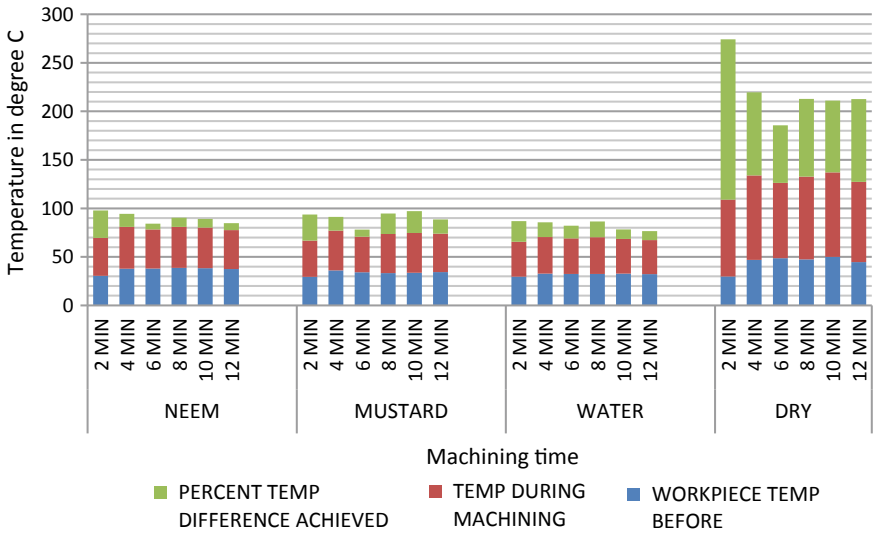


Fig. 21 Effect of different cutting fluid environment on temperature with surfactant concentration 15%

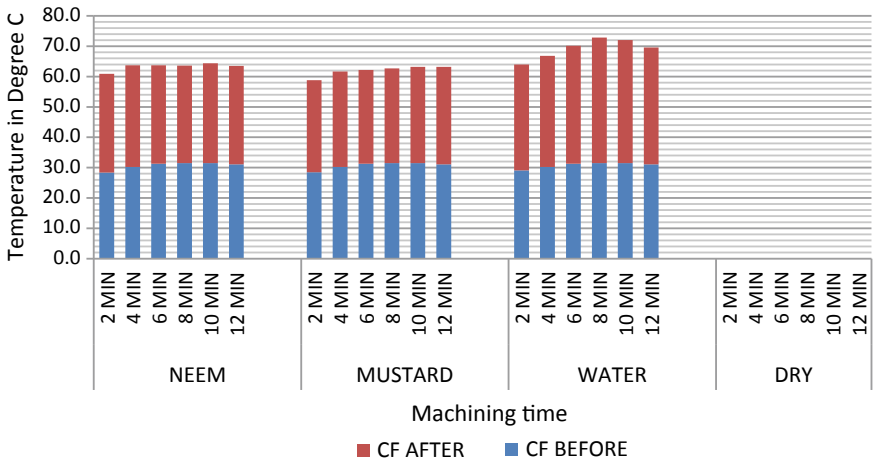


Fig. 22 Difference in fluid temperature with machining environment and time with 15% surfactant

of surfactant. Similar rise is observed in the rise of cutting fluid temperature after machining process. This could be attributed to decrease in specific heat capacity of the cutting fluid by increasing the percentage of the surfactant.

Figures 17, 18, 19 and 20 show temperature rise with cutting fluid formulated from neem oil and 15% surfactant concentration, cutting fluid formulated from mustard oil and 15% surfactant concentration, cutting fluid with water only and no cutting fluid, i.e., dry condition, respectively. Figure 21 shows the comparison between different cutting fluid conditions at 15% concentration of surfactant. Similar trend is observed. Mustard oil based cutting fluid with 15% surfactant concentration performs better than the neem oil based cutting fluid with 15% surfactant concentration.

However, in this case, also an average 1.5% increase in temperature rise was observed during machining. This is attributed to the effect of increasing the surfactant concentration in the cutting fluid. Figure 22 shows the difference in cutting fluid temperature. Here also the temperature rise is almost 1.5% than the cases with 5 and 10% surfactant concentration. It is clear indication of decrease in the specific heat capacity of the cutting fluid due to addition of surfactant.

## 4 Conclusion

Following conclusions can be drawn from this study: Surfactant plays an important role to emulsify the oil. Amount of surfactant plays an important role in long term emulsion stability. However, increasing the amount of surfactant can cause agglomeration of the excess surfactant particles and thereby causing emulsion instability. Same surfactant does not work equally for all the oils for emulsification. Water has the highest thermal conductivity. However, use of water only as cutting fluid is not recommended because in metal removal operations lubricity is also required. Hence, cutting fluids, which are a combination of oil and water, should be used. Change in concentration of surfactant has direct effect on the temperature rise in machining operation.

**Acknowledgements** This work is a part of the project funded by Department of Science and Technology, Govt of India. Under grant number SP/YO/060/2017. The authors are grateful to DITE, Delhi for providing workshop facilities to execute the studies. Special thanks to Mr. Kamal Kataria and Ms. Pranjal Vats, B. Tech Tool Engineering, DITE, Delhi, students for extending help in carrying out this work in the workshop.

## References

1. Boothroyd G (1988) Fundamentals of metal machining and machine tools. CRC Press, 15 Nov 1988
2. Krishnan MS (2009) NPTEL: a programme for free online and open engineering and science education. InTechnology for Education, 2009. T4E'09. International Workshop on 2009 Aug 4, pp. 1–5. IEEE

3. Merchant ME (1945) Mechanics of the metal cutting process. I. orthogonal cutting and a type 2 chip. *J Appl Phys* 16(5):267–275
4. Shaw MC, Cookson JO (2005) Metal cutting principles. Oxford University Press, New York
5. Sutherland JW, Gunter KL (2001) Environmental attributes of manufacturing processes. In *Handbook of Environmentally Conscious Manufacturing*, pp. 293–316. Springer, Boston, MA
6. Brinksmeier E, Heinzl C, Wittmann M (1999) Friction, cooling and lubrication in grinding. *CIRP Ann* 48(2):581–598
7. Brinksmeier E, Meyer D, Huesmann-Cordes AG, Herrmann C (2015) Metalworking fluids—mechanisms and performance. *CIRP Ann* 64(2):605–628
8. Shouckry AS (1982) The effect of cutting conditions on dimensional accuracy. *Wear* 80(2):197–205
9. Trent EM (1984) Metal cutting, 2nd edn. Butterworth's & Co. London, UK, limited. ISBN 0-408-34-38
10. Bhatia SM, Pandey PC, Shan HS (1980) The thermal condition of the tool cutting edge in intermittent cutting. *Wear* 61(1):21–30
11. Chakraverti G, Pandey PC, Mehta NK (1984) Analysis of tool temperature fluctuation in interrupted cutting. *Precis Eng* 6(2):99–105
12. Isik Y (2010) An experimental investigation on effect of cutting fluids in turning with coated carbides tool. *J. Mech. Eng.* 56(3):195–201
13. Amrita M, Srikant RR, Sitaramaraju AV, Prasad MM, Krishna PV (2014) Preparation and characterization of properties of nanographite-based cutting fluid for machining operations. *Proc Inst Mech Eng Part J: J Eng Tribol* 228(3):243–252
14. Srikant RR, Ramana VS (2015) Performance evaluation of vegetable emulsifier based green cutting fluid in turning of American Iron and Steel Institute (AISI) 1040 steel—an initiative towards sustainable manufacturing. *J Clean Prod* 1(108):104–109

# Comparative Investigation of Alloy Plates Against Ballistic Impact, Blast, and Fire Loading



Jaykumar Gadhiya, Rahul Singh Dhari , Milanpuri Goswami and Nirav Patel 

**Abstract** The materials such as Al 2024-T3, Mg AZ31B, and Ti-6Al-4V are mostly used in various mechanical components that subject to very harsh operating environment. These components may be prone to various kinds of loadings such as impact, blast, and fire. The behavioral study of the response of these components under such loadings is complex due to dynamic nature of the loadings. It becomes more challenging when it is under a thermal environment that means at various temperatures. In the present study, a Continuum Damage Mechanics model is used to predict the behavior of these materials subjected to ballistic impact, blast and fire loading considering various levels of plate temperatures. The temperature and strain rate dependent Johnson–Cook model is implemented in ABAQUS/Explicit using VDLOAD and VDFLUX user subroutines for blast and fire loading, respectively. The localized temperature rises in the plates due to plasticity is studied at various plate temperatures. The comparative investigation is performed by varying plate temperatures and loading conditions. The results can be interpreted for usage of these materials in various aerospace and structural applications.

**Keywords** Blast · Fire · Impact · Metals · Temperature

---

J. Gadhiya · R. S. Dhari · M. Goswami · N. Patel (✉)  
Department of Mechanical Engineering, School of Technology, Pandit Deendayal Petroleum University, 382007 Gandhinagar, Gujarat, India  
e-mail: [nirav.npp@gmail.com](mailto:nirav.npp@gmail.com)

J. Gadhiya  
e-mail: [jay.gadhiyamc14@sot.pdpu.ac.in](mailto:jay.gadhiyamc14@sot.pdpu.ac.in)

R. S. Dhari  
e-mail: [rahul4194@gmail.com](mailto:rahul4194@gmail.com)

M. Goswami  
e-mail: [milanpuri.gmc14@sot.pdpu.ac.in](mailto:milanpuri.gmc14@sot.pdpu.ac.in)

© Springer Nature Singapore Pte Ltd. 2020  
L. Vijayaraghavan et al. (eds.), *Emerging Trends in Mechanical Engineering*,  
Lecture Notes in Mechanical Engineering,  
[https://doi.org/10.1007/978-981-32-9931-3\\_43](https://doi.org/10.1007/978-981-32-9931-3_43)



## 1 Introduction

The Al 2024-T3, Mg AZ31B, and Ti-6Al-4V are widely used in wings, fuselage of aircraft, and biomedical industries due to its high strength to weight ratio and stiffness. These materials encounter high strain rate loading which is a very interesting domain of research from a long time. The behavior of material is different under these loading conditions compared to other loadings. In addition to this, the dependency of various parameters makes it more difficult to develop a closed form analytical solution. Hence, it is imperative to exploit modern numerical or simulation models to understand this complex phenomenon.

The material modeling for metallic plates was initially presented by Johnson and Cook [1] applied to Copper, Brass, Nickel, Iron, and Tungsten. Several researchers have used Johnson–Cook model for simulation of material response under dynamic loading conditions like ballistic impact [2–4] and blast loading [5, 6]. The model is popular due to simplicity in equations and determination of constants [7]. Duodu et al. [2] compared the impact resistance of steel plate with composite laminates. Sitnikova et al. [6] investigated the behavior of aluminum-based fiber metal laminates under high impulse loading. In order to protect against ballistic attack, a solid homogeneous plate could suffice while this is not necessary in case of blast [8]. Liu et al. [9] studied the impact response of sandwich panels with metal fiber laminate skins and aluminum foam core. Few researchers [10, 11] have also attempted to study the damage response of metals under fire loadings. The resistance of steel columns and steel plates against fire loading is explored by Choe et al. [10] and Erbay et al. [11], respectively.

Finite element calculations are performed using fully meshed geometries with a square honeycomb [5], prismatic corrugations [12], and corrugated core [13] topologies made from different materials. The study of yield strength, strain hardening rate, and strain rate sensitivity have been conducted [3, 5] that indicate a complex response of mechanical components under ballistic impact and blast loads. Majority of these articles addressed the behavior of materials at constant temperatures but generally, the plastic deformation gives rise to a temperature of the material. Klepaczko et al. [14] conducted experiments on TRIP Steels to study the heat generation during plastic deformation. The study of damage behavior of metals under various loadings such as impact, blast, and fire are interesting domain of research and study of these materials under different thermal environment is also challenging.

In the present paper, an attempt has been made to study behavior of Aluminum Al 2024-T3, Titanium Ti-6Al-4V, and Magnesium AZ31B subjected to dynamic loading conditions such as ballistic impact, blast loading, and high-intensity fire loading. The paper provides insights on behavior of flat plates made up of these materials at a series of various temperatures considering various ballistic loadings, some of which are discussed in the paper. In addition to this, the damage behavior of plate is also studied for various levels of impact velocity, blast and fire loads. The damage behavior of materials over change in temperature is taken into account to study the response of plates using Johnson–Cook plasticity and damage model that executed in ABAQUS/Explicit. The blast wave and fire loading are applied over the

plate using VDLOAD and VDFLUX. The effects of temperature variation due to plastic deformation are also addressed.

## 2 Mathematical Modeling

The Johnson–Cook model is one of the most suitable methods to simulate high strain rate loading over materials, mostly metallic in nature and in adiabatic transient conditions. It contains failure criteria to initiate damage and damage evolution laws to compute damage which degrades stiffness of materials and the elements are removed from the analysis once the element erosion conditions are met. Johnson–Cook model [1] has three parts namely, hardening model, strain rate model and damage model.

The static yield stress ( $\sigma^0$ ), under Johnson–Cook hardening model is assumed to be of the following form [15]:

$$\bar{\sigma} = \left[ A + B(\bar{\varepsilon}^{pl})^n \right] \left( 1 + \hat{\theta}^m \right), \quad (1)$$

where  $\hat{\varepsilon}^{pl}$  is the equivalent plastic strain and  $A$ ,  $B$ ,  $n$ , and  $m$  are material parameters measured at or below the transition temperature ( $\Theta_{\text{transition}}$ ).  $\hat{\theta}$  is the non-dimensional temperature defined as follows [15]:

$$\hat{\theta} = \left\{ \begin{array}{l} 0, \text{ for } \theta < \theta_{\text{transition}}; 1, \text{ for } \theta > \theta_{\text{melt}}; \\ (\theta - \theta_{\text{transition}}) / (\theta_{\text{melt}} - \theta_{\text{transition}}), \text{ for } \theta_{\text{transition}} \leq \theta \leq \theta_{\text{melt}}, \end{array} \right\} \quad (2)$$

where  $\Theta$  is the current temperature,  $\Theta_{\text{melt}}$  is the melting temperature, and  $\Theta_{\text{transition}}$  is the transition temperature at which there is no dependency of the yield stress to temperature. The Johnson–Cook dynamic failure model works on the criteria having the value of the equivalent plastic strain. The damage parameter  $\omega$  is defined as [15]:

$$\omega = \sum (\Delta \bar{\varepsilon}^{pl} / \bar{\varepsilon}^{pl}), \quad (3)$$

where  $\Delta \bar{\varepsilon}^{pl}$  is an increment of the equivalent plastic strain.

Generally, high mechanical load on materials results in the variation in localized temperature. In order to study the temperature change, a relationship is established between mechanical loading and heat generation during elastic and plastic deformation ( $Q_p$ ). The ratio of plastic work ( $W_p$ ) converted to heat is given by the ratio  $\beta$  as follows [14]:

$$\beta = Q_p / W_p. \quad (4)$$

The Johnson–Cook model controls the degradation of the material properties based on the load application, i.e., impact, blast, and fire loads. The blast wave is

made up of high pressure interacting with nearby objects over a very short period of time. However, the pressure is so high that it results in causing significant damage. The heat flux ( $H$ ) and pressure [6] ( $P$ ) incident on target plate is expressed as:

$$H, P(r, t) = P_0 P_d(r) P_t(t), H_0 H_d(r) H_t(t), \quad (5)$$

where  $P$  is the incident pressure as a function of radius and time. The pressures  $P_r$  and  $P_t$  are decay terms function of radius and time, respectively. At the center of the plate,  $r_0$  is the radius of the area with constant pressure,  $k$  is a decay constant, and  $r_b$  is the distance from the center of the plate at where the pressure value is negligible. At starting, the heat flux,  $H$  and pressure,  $P$  is constant up to a distance of  $r_0$  then reduce exponentially up to a distance of  $r_b$  [6]. Various values are written as below [6],

$$H_d, P_d(r) = \left\{ \begin{array}{l} 1, r \leq r_0; 0, r > r_b \\ e^{-k(r-r_0)}, r_0 < r \leq r_b \end{array} \right\}, H_t, P_t(t) = \left\{ \begin{array}{l} t/t^* \quad t \leq t^* \\ e^{-2(t-t^*)}/t_0 \quad t > t^* \end{array} \right\}. \quad (6)$$

where  $t_0$  and  $t^*$  are time constants.

### 3 Results and Discussion

The objective of the present study is to investigate the behavior of flat plates of materials Al 2024-T3, Ti-6Al-4V, and Mg AZ31B under three types of loading conditions: (1) Ballistic impact loading, where projectiles are impacted on plates at various velocities from 150 to 450 m/s with plate temperatures ranging 223 K to 358; (2) Blast loading, where three different pressure waves are incident upon the plate over various temperatures; (3) Fire loading, where heat flux of different magnitudes are applied over the plate considering time and spatial decay over the plate. The properties for alloys along with its Johnson–Cook parameters are adopted from previous literature [16–19]. Equations (5) and (6) is coded into ABAQUS as a VDLOAD and VDFLUX subroutine for blast and fire loads, respectively that compute the spatial and time decay for the pressure wave and the load is thereupon applied to the plate.

In order to validate the results obtained by the present study, an analysis is carried out on steel plate considering similar loading and boundary condition as work done by Duodu et al. [2]. The damage patterns are plotted in Fig. 1a which can be compared with the results of Duodu et al. [2] (Fig. 9). In addition to this, the initial results of plate subjected to blast loading using the model similar to Dharmasena et al. [5] (Fig. 15) are compared to results obtained in present work and the same is depicted in Fig. 1b. The results are found to be in good agreement with previous results.

All analysis are executed by considering a target plate of size 200 × 200 mm and thickness of 12 mm for ballistic impact and 4 mm for blast and fire loadings. A 0.22

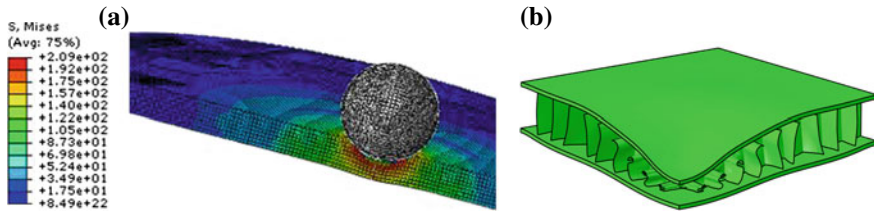


**Fig. 1** **a** Stress pattern of impact of circular plate of steel at  $t = 25$  ms, **b** blast loading response of sandwiched aluminum plate under 1 kg TNT

caliber projectile of diameter 20 mm with a rigid mass of 8 g is impacted on the target with varying velocity of 150, 225, 300, 375 and 450 m/s. The projectile is impacted perpendicularly by keeping both sides of the plate fixed. Model is discretized using eight-node linear brick element with reduced integration (C3D8R) having mesh size of  $0.5 \text{ mm} \times 0.5 \text{ mm}$  and  $3 \times 3 \text{ mm}$  and R3D4 is used for the projectile. The general contact algorithm is used to formulate contact between plate and projectile with a penalty contact of friction coefficient 0.3. The temperature-dependent properties are inserted directly in terms of values of Young modulus. Figure 2 depicts the velocity–time histories from the impact of rigid projectiles on different materials at 450 m/s over different temperature cases –223 to 358 K. The impactor has rebounded for the other cases of impact velocities such as 150 and 300 m/s, but has penetrated completely for the case of 450 m/s for Al 2024-T3 (refer Fig. 3) and Ti–6Al–4V

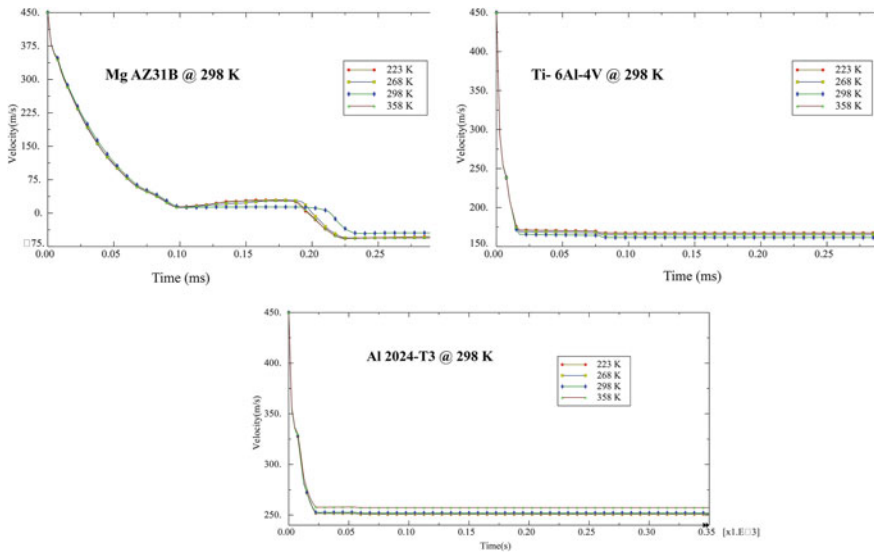


**Fig. 2** Velocity time histories for various temperatures at impact velocity 450 m/s

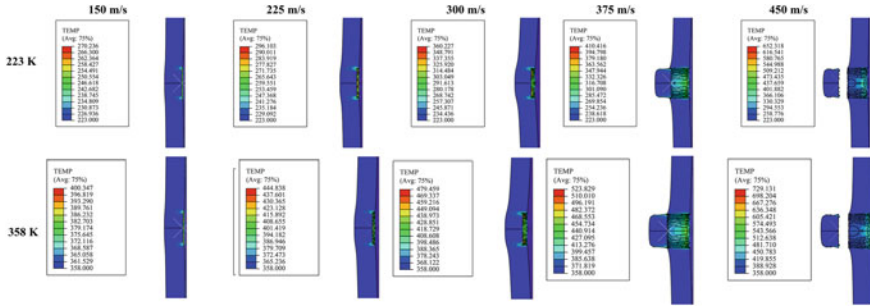


**Fig. 3** Deformation for Al-2024 at various impact velocities and temperatures  $t = 0.05$  ms

materials. However, the projectile fails to penetrate the Mg-AZ31B plate at 450 m/s. Similar observations regarding Mg AZ31B were made by Jones et al. [20].

It is observed from the results that, Mg AZ31B has more potential to sustain against impact loading compare to other two materials. As velocity increased, temperature rise also increases due to increment in plastic deformation. At 150 m/s case, localized temperate rise in Al 2024-T3 is more than the other two material and lowest for Ti-6Al-4V. For velocities of 225, 300 and 375 m/s, the trends are opposite where the rise in temperature for Ti-6Al-4V is higher and lower for Al 2024-T3. At an impact velocity of 450 m/s, Ti-6Al-4V has the highest localized temperature rise and lowest for Mg AZ31B. The difference of temperature rise is almost the same for low velocity at different plate temperatures but not same at high velocities. At low temperature, a difference of rising in temperature is higher compared to the higher plate temperatures. The figure shows that temperature affected area is more at low velocity because of availability of more interaction time. The velocities of impactor for ballistic impact loading (150 m/s) for Al 2024-T3, Mg AZ31B, and Ti-6Al-4V at various temperature is shown in Table 1. It can be observed that Ti-6Al-4V is absorbing the most energy from the projectile during the impact and hence the velocity of impactor is least for the Ti-6Al-4V cases at the recorded times.

The blast loading is executed over 4 mm thick plates of dimensions  $200 \times 200$  mm of three different alloys for three different magnitudes considering different temperatures. The blast wave parameters are adopted from the work performed by Sitnikova et al. [6]. The damage pattern of all three alloys is presented in Fig. 4. It can be inferred from Fig. 4 that the Ti-6Al-4V has sustained least amount of damage under

**Table 1** Velocity of projectile for ballistic impact velocity = 150 m/s at time  $t = 1.5$  E-5s

Mat.\Temp. (K)	223	238	298	313	328	358
Al 2024-T3	49.6	49.7	50.2	50.7	51.2	49.7
Mg AZ31B	61.2	61.4	61.8	62.9	64.1	66.4
Ti-6Al-4V	8.8	9.0	9.6	9.7	10.2	8.6

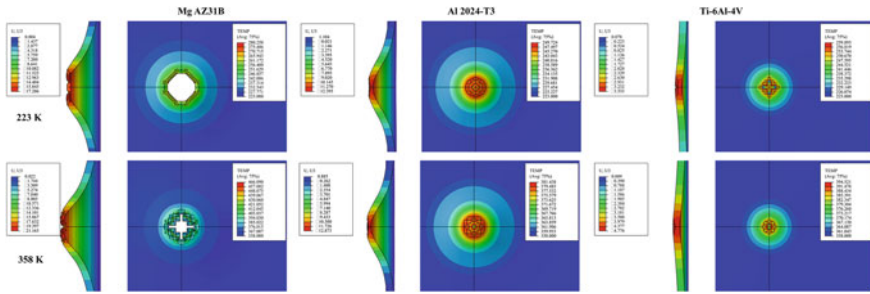


**Fig. 4** Perforation failure of Al 2024-T3, Mg AZ31B, and Ti-6Al-4V under blast loading ( $P = 716$  MPa) at various temperatures

impulse loading of 716 MPa at various temperatures. It is observed that more perforation failure is induced in Mg AZ31B (Fig. 4) at 223 K than at 358 K temperature which implies that Mg AZ31B works better at higher temperature as compared to other temperatures. However, in the case of Al 2024-T6, the plate has taken a similar amount of damage at all 3 temperatures. Further, Fig. 4 also indicates the rise in temperature of the plates due to plastic deformation. By comparing the cross-section and the side face of the plates, it can be observed that region from where the plate bent or has been dented exhibits rise in local temperature. In the case of Ti-6Al-4V, the rise in temperature is very low compared to the other two alloys and different of temperatures (rise) is in range of 34–55 K for all blast loading cases which implies the lesser amount of plastic deformation. Just around 5–6 mm dents are generated at 716 and 940 MPa blast loadings, which are greater for other two alloys (12–17 mm for Al 2024-T3 and 17–26 mm for Mg AZ31B).

The rise in air pressure due to blasts also gives rise to fire in most cases. In the present article, an attempt has been made to study the response of the materials under fire loading. Simulations have been performed for fire loading of 20–356 MJ/kg. The magnitude of flux relates roughly to the amount of heat generated during the explosion event at the various magnitudes. The damage pattern of plates under fire loading at room temperature is presented in Fig. 5. The damage pattern indicates that Mg AZ31B has sustained more damage as compared to the other two alloys. The damage has been least in the case of Ti-6Al-4V. Ti-6Al-4V has shown least perforation failure across the temperature range which is due to the high melting temperature of Ti-6Al-4V.

## 4 Conclusions

The response of Al 2024-T3, Mg AZ31B, and Ti-6Al-4V to high strain loading over various temperatures is investigated considering various impact velocities and

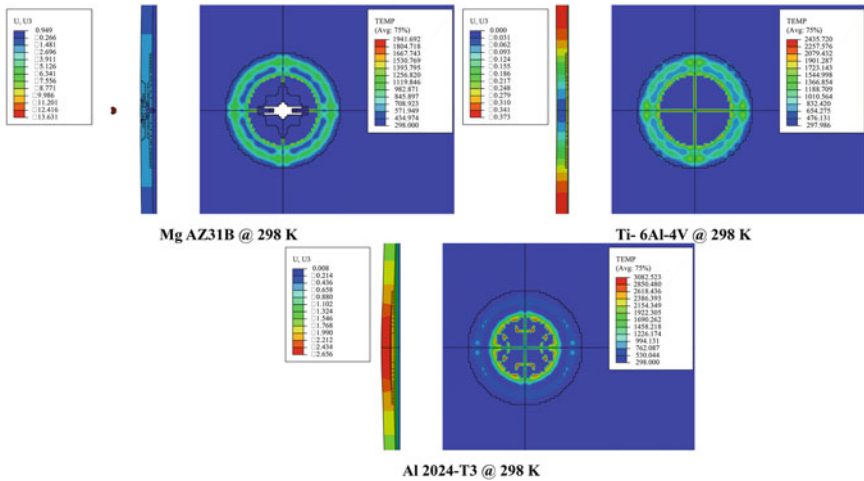


**Fig. 5** Damage pattern of Al 2024-T3, Mg AZ31B, and Ti–6Al–4V at room temperature due to fire loading (20 MJ/kg)

levels of blast and fire loads. Very considerable solution is obtained using Johnson–Cook plasticity and damage model in ABAQUS/explicit that includes VLOAD and VDFLUX subroutine. The results are obtained for three types of loadings at various temperatures ranging from 223 to 358 K. It has been observed that the material response is greatly affected by temperature variation as the energy absorption capacity is changed. Mg-AZ31B is absorbed more energy than Al-2024-T3 and Ti–6Al–4V during impact loading for all temperature cases considered, however, it was found to take more damage against blast and fire loadings. Localized Temperature rise is also highest in Mg AZ31B compare to other two alloys and lowest for Ti–6Al–4V during blast loading which implies Mg AZ31B had the most plastic deformation as compared to the Titanium and Aluminum alloy. It is observed that Ti–6Al–4V is performed good comparatively for fire and blast loading having sustained least amount of damage and smallest dents. The material has exhibited resistance against deformation during fire loading due its high melting point.

## References

1. Johnson GR, Cook WH (1985) Fracture characteristics of three metals subjected to various strains, strain rates, temperatures and pressures. *Eng Fract Mech* 21:31–48. [https://doi.org/10.1016/0013-7944\(85\)90052-9](https://doi.org/10.1016/0013-7944(85)90052-9)
2. Duodu EA, Gu J, Ding W, Shang Z, Tang S (2017) Comparison of Ballistic impact behavior of carbon fiber/epoxy composite and steel metal structures, Iran. *J Sci Technol Trans Mech Eng.* <https://doi.org/10.1007/s40997-017-0072-6>
3. Yen CF (2002) Ballistic impact modelling of composite materials. *Proc. 7th Int. LS-DYNA Users Conf.* 15–26

4. Banerjee A, Dhar S, Acharyya S, Datta D, Nayak N (2017) Numerical simulation of ballistic impact of armour steel plate by typical armour piercing projectile. *Proced. Eng.* 173:347–354. <https://doi.org/10.1016/j.proeng.2016.12.028>
5. Dharmasena KP, Wadley HNG, Xue Z, Hutchinson JW (2008) Mechanical response of metallic honeycomb sandwich panel structures to high-intensity dynamic loading. *Int J Impact Eng* 35:1063–1074. <https://doi.org/10.1016/j.ijimpeng.2007.06.008>
6. Sitnikova E, Guan ZW, Schleyer GK, Cantwell WJ (2014) Modelling of perforation failure in fibre metal laminates subjected to high impulsive blast loading. *Int J Solids Struct* 51: 3135–3146. <https://doi.org/10.1016/j.ijsolstr.2014.05.010>
7. Banerjee A, Dhar S, Acharyya S, Datta D, Nayak N (2015) Determination of Johnson cook material and failure model constants and numerical modelling of Charpy impact test of armour steel. *Mater Sci Eng, A* 640:200–209. <https://doi.org/10.1016/j.msea.2015.05.073>
8. Hazell PJ (2016) *Armour: materials, theory, and design*
9. Liu H, Cao ZK, Yao GC, Luo HJ, Zu GY (2013) Performance of aluminum foam-steel panel sandwich composites subjected to blast loading. *Mater Des* 47:483–488. <https://doi.org/10.1016/j.matdes.2012.12.003>
10. Choe L, Varma AH, Agarwal A, Surovek A (2011) Fundamental behavior of steel beam-columns and columns under fire loading: experimental evaluation. *J Struct Eng* 137:954–966. [https://doi.org/10.1061/\(ASCE\)ST.1943-541X.0000446](https://doi.org/10.1061/(ASCE)ST.1943-541X.0000446)
11. Erbay OO, Sarawit T, Zarghamee MS (2010) Modeling behavior and failure of steel connections subject to elevated temperatures 136:2361–2368. [https://doi.org/10.1061/41130\(369\)214](https://doi.org/10.1061/41130(369)214)
12. Kooistra GW, Deshpande VS, Wadley HNG (2004) Compressive behavior of age hardenable tetrahedral lattice truss structures made from aluminium. *Acta Mater* 52:4229–4237. <https://doi.org/10.1016/j.actamat.2004.05.039>
13. Liu J, He W, Xie D, Tao B (2017) *The effect of impactor shape on the low-velocity impact behavior of hybrid corrugated core sandwich structures*. Elsevier Ltd., Amsterdam
14. Rusinek A, Klepaczko JR (2009) Experiments on heat generated during plastic deformation and stored energy for TRIP steels. *Mater Des* 30:35–48. <https://doi.org/10.1016/j.matdes.2008.04.048>
15. SIMULIA: Abaqus/CAE User's Manual (2016)
16. Ati TD (2012) Technical data sheet ATI Ti–6Al–4V. Grade 5(1):4–7
17. Kay GJ (2003) Failure Modelling of Titanium 6Al–4V and Aluminum 2024-T3 with the Johnson-Cook material model. DOT Rep. DOT/FAA/AR, 1–24. <https://doi.org/10.1080/14786436808223020>
18. Pereira JM, Revilock DM, Ruggeri CR, Emmerling WC, Altobelli DJ (2014) Ballistic impact testing of aluminum 2024 and titanium 6Al–4V for material model development. *J Aerosp Eng* 27:456–465. [https://doi.org/10.1061/\(ASCE\)AS.1943-5525.0000356](https://doi.org/10.1061/(ASCE)AS.1943-5525.0000356)
19. Feng F, Huang S, Meng Z, Hu J, Lei Y, Zhou M, Yang Z (2014) A constitutive and fracture model for AZ31B magnesium alloy in the tensile state. *Mater Sci Eng, A* 594:334–343. <https://doi.org/10.1016/j.msea.2013.11.008>
20. Jones TL, Burkins MS, Gooch WA (2008) Analysis of magnesium alloy Az31B-H24 for ballistic applications. *Mater. Soc. Annu. Meet.* 81–84



# Inverse Kinematics and Trajectory Planning of Planar Redundant Manipulators in Cluttered Workspace



V. V. M. J. Satish Chembuly and Hari K. Voruganti

**Abstract** Redundant manipulators have high degrees of freedom (DOF) which enables the robot to work in cluttered environments. Inverse kinematics (IK) of redundant manipulators have multiple solutions, finding the best solution among the possible solutions is called redundancy resolution. Redundancy resolution can be performed by solving it as an optimization problem, the optimization criterion can be joint distance, joint-torque, and energy consumption. This paper focusses on inverse kinematics, redundancy resolution and trajectory planning of redundant manipulators for pick and place and path traversing applications. Case studies of IK solutions with obstacles in the workspace are shown for 5-DOF planar redundant manipulators. Simulations have also been carried out for redundancy resolution by taking joint distance minimization as objective and reaching the task space location without colliding obstacles, as constraints of the optimization. Results are reported on trajectories in joint space and these ensure smooth end-effector velocities in task space.

**Keywords** Redundancy resolution · Obstacle avoidance · Inverse kinematics · Trajectory planning

## 1 Introduction

Redundant manipulators have high joint space dimension ( $m$ ) compared to the dimensions of the workspace ( $n$ ) [1], which enhances the capability of the robot to work in complex environments. Inverse kinematic equations of redundant manipulators involve nonlinear and transcendental equations, which makes the problem tedious and arising of multiple solutions. Identifying the best solution, satisfying the condition of reaching task space by choosing a secondary criterion such as joint-torque minimization, avoidance of obstacles, joint limits and singular configurations is called Redundancy resolution.

---

V. V. M. J. Satish Chembuly · Hari K. Voruganti (✉)  
Department of Mechanical Engineering, NIT Warangal, Warangal, Telangana 506004, India  
e-mail: [harikumar@nitw.ac.in](mailto:harikumar@nitw.ac.in)

© Springer Nature Singapore Pte Ltd. 2020  
L. Vijayaraghavan et al. (eds.), *Emerging Trends in Mechanical Engineering*,  
Lecture Notes in Mechanical Engineering,  
[https://doi.org/10.1007/978-981-32-9931-3\\_44](https://doi.org/10.1007/978-981-32-9931-3_44)

The most widely suggested methods for solving inverse kinematics and redundancy resolution of manipulators involves the usage of pseudo-inverse of Jacobian [2, 3], where the secondary criterion is achieved by including null space term. The extended Jacobian inverse is also used extensively, in this approach an additional set of equations are provided that are equal to a number of unknown joint rates. These Jacobian inverses are sensitive at singular configurations and computationally expensive. Iterative methods have also been widely used for finding inverse kinematics of redundant manipulators. Nearchou et al. [4], proposed a modified genetic algorithm solution to the IK problem of redundant robots manipulating in environments with obstacles. Koker [5] suggested a hybrid approach which combines the attributes of neural networks and evolutionary techniques to obtain more exact solutions. The solutions to these approaches are mostly dependent on the initial guess. As the inverse kinematics of redundant manipulators have multiple solutions, Kalra et al. [6] proposed an evolutionary-based real-coded genetic algorithm to find the solution of the multi-modal inverse kinematics of industrial robots.

Another important aspect of concern is the trajectory planning of redundant manipulators, in which smooth joint trajectories are obtained which reduces mechanical vibrations at the joints which in turn avoids the failure at the joints. Francisco Valero et al. [7] proposed a trajectory planning algorithm for the workspaces with obstacles, in which, joint velocities can be obtained with an optimality criterion of minimum time. Marcos et al. [8] presented a new approach which integrates pseudoinverse with genetic algorithm for trajectory planning of redundant manipulators.

The use of redundant manipulators fulfills the task of reaching workspace without collision of obstacles. A lot of research has been performed on serial manipulators avoiding obstacles. Artificial potential field method is widely used for obstacle avoidance which is proposed by Khatib [9] where the robot manipulator maneuver in the field of forces that draws the end-effector towards the target location and drives away the links of the manipulator from the obstacles. But this method stuck with the local minima. Kim et al. [10] proposed a real-time obstacle avoidance by the formulation of artificial potential approach, harmonic functions are used to build artificial potential field which ignores local minima in presence of obstacles. Khoogar et al. [11] presented an approach to avoiding obstacles based on genetic algorithms, in which obstacle avoidance is carried out by simply adding a weighted factor in fitness value. Chirikjian et al. [12] proposed an obstacle avoidance algorithm for hyper-redundant manipulators, his method has a benefit of getting an active set of kinematic equations based on differential geometry, which allows less computational time, unlike artificial potential field. Maciejewski et al. [13] proposed an efficient numerical implementation for obstacle avoidance of redundant manipulators in dynamically varying environments. Menon and Goshal [14] implemented a tractrix-based motion planning algorithms in which obstacles are modeled as smooth differentiable surfaces and Lagrangian constraints are used during optimization.

This paper proposed a classical optimization technique for obtaining an inverse kinematic solution and the joint trajectories without collision of obstacles in the workspace.

Trajectory planning is carried out for planar redundant manipulator for point to point applications. Trajectory planning is performed at joint level by interpolating them as cubic polynomial function and distance minimization of the end-effector as optimization criteria. Collision avoidance in this approach is computationally efficient, because of the effective modeling of obstacles and efficient collision detection technique.

## 2 Problem Formulation

Consider a  $n - DOF$  planar robotic manipulator shown in Fig. 1, where, the length of  $i$ th link corresponds to  $l_i$ ,  $\theta_i$  corresponds to the angle between the link  $l_i$  and the  $x$ -axis and  $E(x_{te}, y_{te})$  is the position of the end-effector. The forward kinematic equations of a planar manipulator in the 2-dimensional workspace can be described as

$$x_{te} = l_1 \cos \theta_1 + l_2 \cos \theta_2 + l_3 \cos \theta_3 + \dots + l_n \cos \theta_n \tag{1}$$

$$y_{te} = l_1 \sin \theta_1 + l_2 \sin \theta_2 + l_3 \sin \theta_3 + \dots + l_n \sin \theta_n \tag{2}$$

As the redundant manipulators possess high joint space dimension than the task space dimension the IK solutions are not unique and cannot obtain closed-form solutions. Hence, the inverse kinematics of planar redundant manipulators can be posed as an optimization problem, which can be described as the minimization of the distance between the desired point in the task space  $D(x_{tp}, y_{tp})$  and end-effector position  $E(x_{te}, y_{te})$  shown in Fig. 1. Mathematically it can be shown as minimize

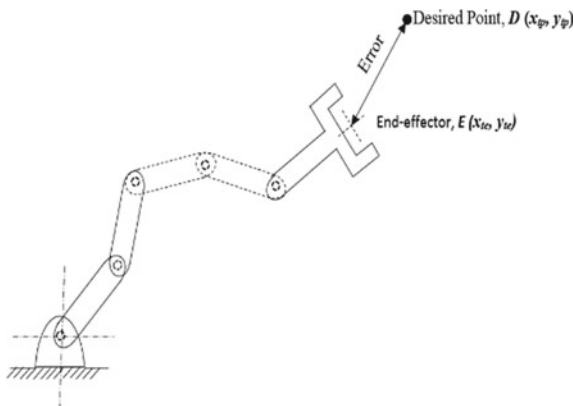


Fig. 1 Modelling of planar redundant manipulator

$$\Delta e = (x_{te} - x_{tp})^2 + (y_{te} - y_{tp})^2 \quad (3)$$

After formulating the forward kinematic model and then posing it as an optimization problem, classical optimization technique has been adopted to solve the IK of planar redundant manipulators.

## 2.1 Inverse Kinematics and Trajectory Planning

Inverse kinematics of redundant manipulators is solved as an optimization problem with the objective of minimization of the geometric distance between the end-effector position and the target location in the task space shown in Eq. 3. Classical optimization technique, Nelder and Mead simplex algorithm is adopted to find the joint configurations for a given point in the task space.

Trajectory planning is performed for a pick and place applications of the robot. The joint configuration of the target location is determined using inverse kinematics and then trajectories of joints are evaluated between the configurations of the robot at home position and desired location. Joint trajectories are evaluated by interpolating it as a cubic polynomial function. Joint positions and velocities at home position and target locations are chosen as end conditions for trajectory planning.

## 2.2 Obstacle Avoidance

Robot manipulators while performing various tasks in the cluttered environment they must be under control to trace the desired end-effector path by avoiding obstacles in the workspace. Collision avoidance of robots is crucial and requires collision detection techniques. Collision detection is performed between the links of the robots and obstacles in the workspace, for which links of the robot were cast as line segments and obstacles as polygons. The problem of collision detection reduced by evaluating the intersection point of the line segment and polygons. Intersections are determined by using a ray casting algorithm where an infinite ray is projected along the links of the robot and finds the intersection of the ray with the edges of the polygonal obstacles. Collision check algorithm is integrated into the optimization algorithm, the configurations associated with the collision are recognized and those particular configurations need to be avoided. Collision avoidance is handled by penalty approach, i.e., by including the penalty to the objective function. The reformed objective function with a penalty is described as

$$g = (x_{te} - x_{tp})^2 + (y_{te} - y_{tp})^2 + \text{penalty} \quad (4)$$

A constant value of *penalty* is chosen, which is scaled relative to the value of objective function.

*penalty* = 0; when there is no collision detection;

*penalty* = *constant*; when there is a collision.

### 2.3 Redundancy Resolution

Redundant manipulators possess more joint space dimension than the task space dimension. Inverse kinematic solutions of the particular manipulators are not unique and have infinite solutions. The process of identifying the best solution from the multiple solutions by choosing optimization criteria is called redundancy resolution. The issue of redundancy resolution has framed as a nonlinear constrained optimization. Such a formulation yields a configuration which desires the minimal amount of joint displacements from the current configurations. The objective function of the problem is expressed as

*Minimize*

$$\sum_{j=1}^{j=n} (\theta_{ij} - \theta_{fj})^2 \quad (5)$$

*Subject to*

$$(x_{te} - x_{tp})^2 + (y_{te} - y_{tp})^2 + \text{penalty} \geq 0 \quad (6)$$

where  $\theta_{in}$  is the initial joint configuration of the corresponding  $n$ th joint,  $\theta_{fn}$  is the final joint configuration of the corresponding  $n$ th joint. The optimization problem is dealt with a gradient-based classical optimization algorithm. The constraints of the problem are handled by the sequential quadratic algorithm.

## 3 Methodology

The classical method of optimization such as Nelder and Mead simplex algorithm is adopted for solving the inverse kinematics of redundant manipulators. Coordinates of the task space are given as inputs to the defined objective function. Collision avoidance is implemented in the algorithm by handling it as a penalty approach. Joint configurations from the inverse kinematics are taken as input for trajectory planning of redundant manipulator. The joint displacements are interpolated as a cubic polynomial, the joint positions and velocities are evaluated for a sequence of the time interval by taking home configuration and desired target configuration as

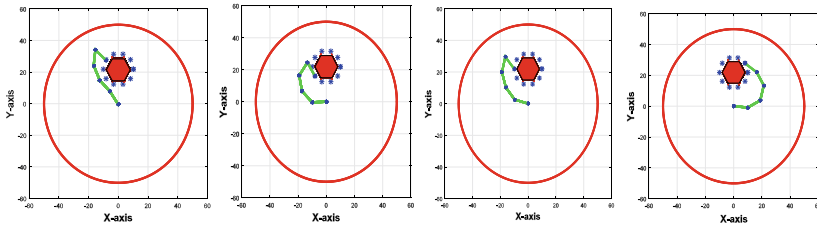


**Fig. 2** Robot configurations with a polygonal obstacle while traversing a circular path

an end condition. Redundancy resolution has been carried out by formulating it as a nonlinear constrained optimization problem.

## 4 Results and Discussion

To validate the optimization approach for solving the inverse kinematics and trajectory planning of redundant manipulators, the following cases of robot simulations has been performed.

### 4.1 A 5-Link Robot with One Polygonal Obstacle

Here, simulations of inverse kinematics are performed for redundant manipulators with five links and link length of 10 unit each. Obstacle avoidance is implemented with a polygonal obstacle in the workspace. Figure 2 shows the joint configurations for different points chosen closer to the obstacle. The forward kinematic Eqs. (1) and (2) shows that for given coordinates in task space it is required to find five joint variables. The home position of the robot, in this case, is considered as  $0^\circ$ . Here the robot is required to trace the path which is taken a series of points around the obstacle without colliding with the obstacle. For each point in the path, the optimization problem is solved to find the values of joint variables to reach that point. These configurations show that the positional error is very less and the robot is positioned accurately. The computational time for solution of this problem is 85.43 s.

### 4.2 Inverse Kinematics and Trajectory Planning of 5-DOF Robot

Inverse kinematics of redundant manipulator is carried out for point to point application and trajectories of joints are also evaluated for the corresponding end-effector

position without obstacles. In this case, a five-link planar manipulator is considered, with a uniform link length of 10 units. Figure 3a shows the joint configurations from the home position to the task location in the workspace. The joint configurations at the target location of the manipulator are evaluated using optimization approach and then trajectories of each individual joint are determined when the robot is moving from home position to target position, by taking initial, final configurations of joints and velocities at the start and end position of the robot as an end condition. Whereas Fig. 3b shows the joint configurations of the robot for an end-effector trajectory by minimizing the objective given in Eq. 3.

Joint displacement of Fig. 4a shows the variation of all joint displacements for a given interval of time. Figure 4b shows that the variation joint displacements, which

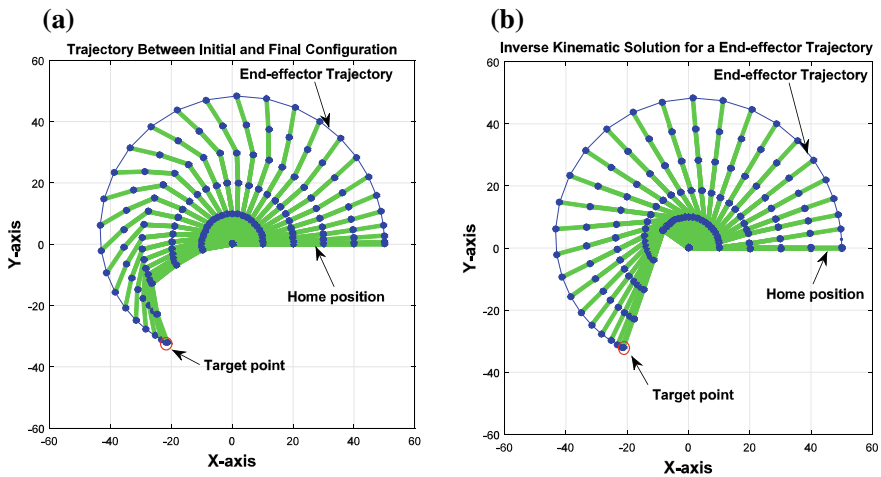


Fig. 3 Joint configurations and trajectory for point to point application, a polynomial interpolation, b polynomial interpolation, and optimization

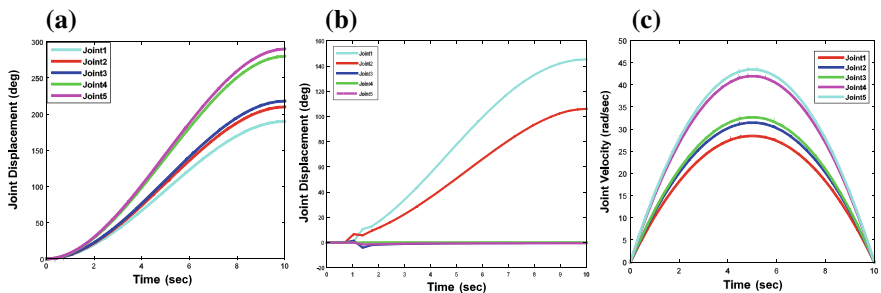
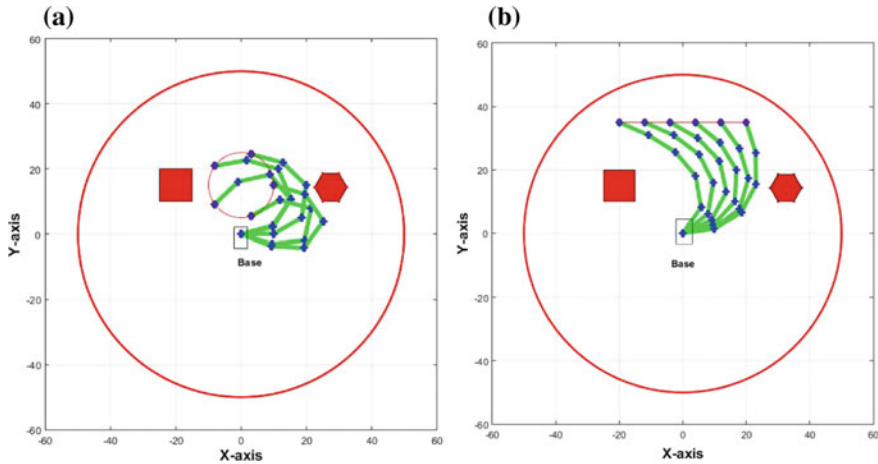


Fig. 4 Joint trajectories, a joint displacement using polynomial interpolation, b joint displacement using polynomial interpolation and optimization, c joint velocities



**Fig. 5** Evaluation of joint configuration of the robot while traversing a path with obstacles, **a** circular path, **b** straight line path

are observed only at two joints, for remaining joints the variation is zero. Figure 4c shows the variation of joint velocities for a given time interval.

### 4.3 Redundancy Resolution with Polygonal Obstacles

These simulations show the redundancy resolution scheme of a redundant manipulator. A five-link serial manipulator is considered for tracing two different paths in the workspace without colliding the obstacles. The constrained optimization algorithm is implemented by choosing joint distance minimization as an optimization criterion shown in Eq. 5. The constraints of the problem are shown in Eq. 6. Figure 5a shows the joint configurations while tracing a circular path. Figure 5b shows the joint configurations while tracing a straight line path. Both cases show that the robot is traversing the paths by avoiding obstacles.

## 5 Conclusions

This paper presents a classical approach of the constrained optimization problem for solving inverse kinematics and trajectory planning of serial redundant manipulators. Results are reported on point to point and path traversing applications, in which the end-effector is accurately positioned in task space and gives the best solution while satisfying the constraints of optimization. Trajectory planning algorithm is also included to bring smooth joint and effector velocities. Obstacle avoidance



has also considered, simulations were carried out on serial redundant manipulators while traversing a given path with polygonal obstacles in the workspace. A direct search optimization algorithm is used for solving IK of redundant manipulators, which avoids the calculation of the pseudo-inverse of Jacobian. This reduces the computational burden and makes the manipulator non-sensitive at singular configurations. Simple and effective modeling of obstacles makes this approach suitable for convex and non-convex obstacles. This approach can be easily extended to redundant manipulator with more number of degrees of freedom.

## References

1. Patel RV, Shadpey F (2005) Control of redundant robot manipulators: theory and experiments, vol. 316. Springer Science & Business Media
2. Buss SR (2004) Introduction to inverse kinematics with Jacobian transpose, pseudoinverse, and damped least squares methods. *IEEE J Robot Autom* 17:1–19
3. Dułęba Ignacy, Opałka Michał (2013) A comparison of Jacobian-based methods of inverse kinematics for serial robot manipulators. *Int J Appl Math Comput Sci* 23(2):373–382
4. Nearchou AC (1998) Solving the inverse kinematics problem of redundant robots operating in complex environments via a modified genetic algorithm. *Mech Mach Theor* 33(3):273–292
5. Köker Raşit (2013) A genetic algorithm approach to a neural-network-based inverse kinematics solution of robotic manipulators based on error minimization. *Inf Sci* 222:528–543
6. Kalra P, Mahapatra PB, Aggarwal DK (2006) An evolutionary approach for solving the multimodal inverse kinematics problem of industrial robots. *Mech Mach Theor* 41(10):1213–1229
7. Valero Francisco, Mata Vicente, Besa Antonio (2006) Trajectory planning in workspaces with obstacles taking into account the dynamic robot behavior. *Mech Mach Theory* 41(5):525–536
8. Da Graça Marcos M, Machado JT, Azevedo-Perdicoulis TP (2009) Trajectory planning of redundant manipulators using genetic algorithms. *Commun Nonlin Sci Numer Simul* 14(7):2858–2869
9. Khatib Oussama (1986) Real-time obstacle avoidance for manipulators and mobile robots, autonomous robot vehicles. Springer, New York, pp 396–404
10. Kim J-O, Khosla PK (1992) Real-time obstacle avoidance using harmonic potential functions. *IEEE Trans Robot Autom* 8(3):338–349
11. Khoogar AR, Parker JK (1991) Obstacle avoidance of redundant manipulators using genetic algorithms. In: *IEEE Proceedings of Southeastcon'91, IEEE 1991*
12. Chirikjian GS, Burdick JW (1990) An obstacle avoidance algorithm for hyper-redundant manipulators. In: *IEEE international conference on robotics and automation proceedings 1990, IEEE 1990*
13. Maciejewski AA, Klein CA (1985) Obstacle avoidance for kinematically redundant manipulators in dynamically varying environments. *Int J Robot Res* 4(3):109–117
14. Menon MS, Ghosal A (2015) Obstacle avoidance for hyper-redundant snake robots and one dimensional flexible bodies using optimization. In: *14th world congress in mechanism and machine science*

# Investigation on Mechanical Properties of Equal Channel Angular Formed Al6061 and Graphite Metal Matrix Composite



M. K. Ravishankar, H. R. Vitala and B. P. Dileep

**Abstract** Continual interest, recent research, and development in the field of Composite Materials motivated to entitle “Comparative Study of the Mechanical Properties of Al6061 with Graphite undergoing Equal Channel Angular pressing”. The title introduces Equal channel angular pressing process in comparative study. The present work incorporates a stir casting technique in preparation of Al6061 with varying percentage of graphite and further undergoing Equal channel Angular pressing process to compare hardness and corrosion properties between them. This study comprises of comparative microstructural study. The comparative study results showed that the Al6061 with graphite undergone equal channel angular pressing process has increased strength, hardness, weight of material and fine microstructure.

**Keywords** Aluminium metal matrix composites · Equal channel angular pressing · Hardness · Corrosion · Microstructure

## 1 Introduction

Equal channel angular pressing forming process [1] is one of the unique metal forming processes in which an ultra-large plastic deformation [2] is achieved on material in order to get ultra-fine grains and nano-crystalline structure, the same procedure can also be adopted for alloys too. This technique claims to be a unique forming procedure to extrude almost all metal by using specially designed various sectional

---

M. K. Ravishankar  
PES University, Electronic City Campus, Bengaluru, India

H. R. Vitala  
Department of Mechanical Engineering, SJB Institute of Technology, Bangalore, Karnataka  
560060, India

B. P. Dileep (✉)  
Department of Mechanical Engineering, School of Engineering, Amrita Vishwa Vidyapeetham,  
Bengaluru Campus, Bengaluru, India  
e-mail: [bp\\_dileep@blr.amrita.edu](mailto:bp_dileep@blr.amrita.edu)

channel dies [3] without substantially changing the geometry to achieve severe plastic deformation. This forming process is in big demand to get high strain rate super plasticity by highly effective grain refinement [4] to the great extent of submicron scale or nano-scale.

The Equal channel angular pressing die [5–7] is consists of two identical circular cross-section channels [8] interconnected at a various angle; usually between 90° and 120° [9–11]. The cross-section channels can also be rectangle or square [12] depending on requirement. The work piece is machined to the diameter which is equal to the diameter of die channel and extruded by applying hydraulic press [13] through two interconnecting channels with the same cross-section using a single straight solid plunger in the same way as regular direct extrusion [14–17].

During this forming process, adequate lubrication either solid or liquid is highly recommended [18, 19] to reduce frictional influences of die wear and the required load for plastic deformation of specimen [20]. One most important advantage of this forming process is that it can be repeated many times on same preprocessed specimen without changing the dimensions with a very small change in its length [21], and the applied strain can be increased to next level after every pass hence the material has undergone this process show significant improvement in its mechanical properties [22] and proved to be stronger than base material [23].

## 2 Material Selection

Brief descriptions of the raw material as well as reinforcement materials used in synthesis of composites are as follows:

### (a) Aluminium 6061 alloy

6061 is a precipitation-hardened aluminium alloy, containing magnesium and silicon as their major alloying element which belongs in the 6000 series. Their compositions are as in Table 1.

### (b) Reinforcement-Graphite (Gr)

The key properties of Graphite selected are as shown in Table 2.

## 3 Preparation of the Composites

Al 6061 and graphite metal matrix composites were prepared by using stir casting process. The casting tools including reinforcements are preheated to 200 °C to eliminate moisture and dirt from the surface of the reinforcements and equipment before using them for casting. Then pre-calculated amount of Al6061 is placed inside the

**Table 1** Composition of Al6061

Component	Amount (weight %)
Aluminium	95.8–98.6
Silicon	0.4–0.8
Magnesium	0.8–1.2
Iron	Max. 0.7
Copper	0.15–0.40
Zinc	Max. 0.25
Titanium	Max. 0.15
Manganese	Max. 0.15
Chromium	0.04–0.35
Others	0.05

**Table 2** Key properties of graphite composition of Al6061

Property	Commercial graphite
Bulk density (gm/cm <sup>3</sup> )	1.3–1.95
Porosity (%)	0.7–53
Modulus of elasticity (GPa)	8–15
Compressive strength (MPa)	20–200
Flexural strength (MPa)	6.9–100
Coefficient of thermal expansion ( $\times 10^{-6}$ °C)	1.2–8.2
Thermal conductivity (W/m K)	25–470
Specific heat capacity (J/kg K)	710–830
Electrical resistivity ( $\Omega$ m)	$5 \times 10^{-6}$ – $30 \times 10^{-6}$

crucible and heated to 700 °C to get molten matrix using electric resistance furnace followed by adding a degassing tablet to minimize the coating film defects by separating the volatile components present in the molten bath during casting process. The tablet assists in elimination of entrapped air in the matrix metal bath and thus avoids most probable casting defects. Then the molten matrix Al6061 is added with graphite reinforcements of different varying percentages of 3, 6 and 9%.

Now the produced composite is subjected to equal channel angular pressing by passing it through a die which is cylinder in shape having a passage of 90° and further subjected to various tests. Now the tests are conducted on both the set of specimens, i.e., the casted material and the casted material undergoing 900 Equal channel angular pressing.

The top, middle, and the bottom portion of the material were taken for Microstructural characterization to note the distribution of second phase particulates. Then specimens for various mechanical property tests are prepared as per ASTM standards.

The mechanical property will be evaluated using the results of various tests to note the extent of improvement of matrix behavior after Equal channel angular pressing. Finally, the improvements in the properties are obtained which are studied.

## 4 Equipment Details

Equipments used in the project process are as shown in Table 3. Figure 1 shows the front view and side view of the die used for the Equal Channel angular pressing which consists of a passage through which the casted material is forced out. As it is seen that there is a hole present at the top and side of the cylinder which is connected to form L shaped channel that helps processed material to exhibit improved properties by reducing burrs and residual stresses present in the material due to the casting.

**Table 3** Equipment used

S. No.	Instrument/equipment	Specification	Use in the present investigation
1	Resistance furnace	Capacity—5 kg Operating temp—1000 °C Power rating—7.5 kW Heating element—Sic	To melt the aluminium 6061
2	Electric oven	Volts—2.30 A.C Power rating—3.5 kW Max temp—3000 °C	Preheating the reinforcement, degassing tablet, die, and stirrer
3	Two disk polishing machine	RPM—0 to 1000 Coolant nozzle and Table top type	To carry out the mirror image to get microstructure
4	Computerized optical microscope	Digital camera for microscope with 3.3 M pixel CCD system	For viewing the microstructure in different optical lens magnification
5	Brinell's hardness machine	Max force—10 to 500 g, resolution—0.0001 to 0.1 μm Max testing height—380 mm, Depth of throat—200 mm	Testing hardness for materials in microns
6	Die	Cast iron	To prepare the specimens
7	Universal testing machine	Loading accuracy as high as + 1%	The universal testing machine is used to push the material out of the die by transmitting a constant increasing force on the plunger of the die which in turn forces the material to pass through the 90° passages

(continued)

**Table 3** (continued)

S. No.	Instrument/equipment	Specification	Use in the present investigation
8	Salt spray chamber	ASTM B 117-2007	For the corrosion test on the casted material
9	Electronic weighing machine	Capacity—2.2 kg Accuracy—0.02 g	Weighing of different materials like matrix (Al-4.5% Cu), reinforcement, wear test specimen etc.
10	Crucible	Graphite crucible	For melting purpose
11	Stirrer	Stainless steel coated with zirconia	Used for getting uniform distribution reinforcement in matrix phase
12	Die	ES 31	For the equal channel angular pressing process
13	Plunger of the equal channel angular pressing die	High carbon chromium steel	For the equal channel angular pressing process

**Fig. 1** Die for equal channel angular pressing

The detail of die and plunger used during the process is as shown below and Fig. 2.

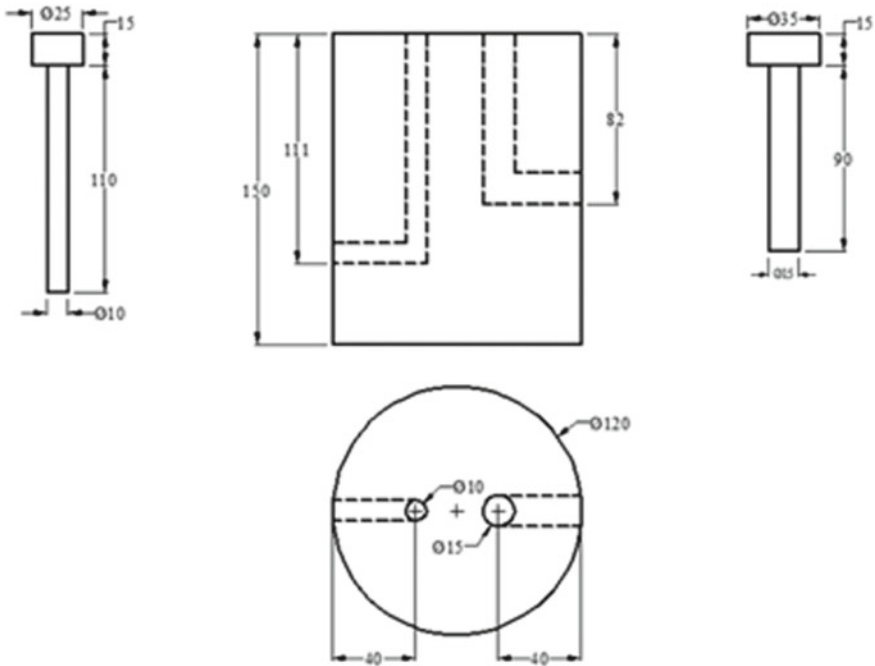


Fig. 2 Dimension of die and plunger

## 5 Test Results and Discussion

The results obtained from the following tests conducted are as discussed below.

### 5.1 Micro Structural Study

Microstructure was visualized with the help of optical microscope. For the specimen preparation, first of all specimens, were cut into small cylindrical shape and then the different samples were ground on different grit size papers sequentially i.e. 220, 400, 600, 800 and 1000. After grinding, the specimens were rubbed mechanically by alumina paste and then etched by Keller's reagent to obtain better contrast. The specimens were visualized on different magnifications ( $100\times$ ,  $200\times$ ) to show the presence of reinforcement and its distribution on the metal matrix. The microstructures of all the samples, i.e., as cast and with different combination of reinforcement of Graphite are shown in Fig 3. In the present work, a good attempt was made to prepare Al6061-Gr aluminium metal matrix composites with micro size Graphite particles as reinforcement by liquid metallurgy process.

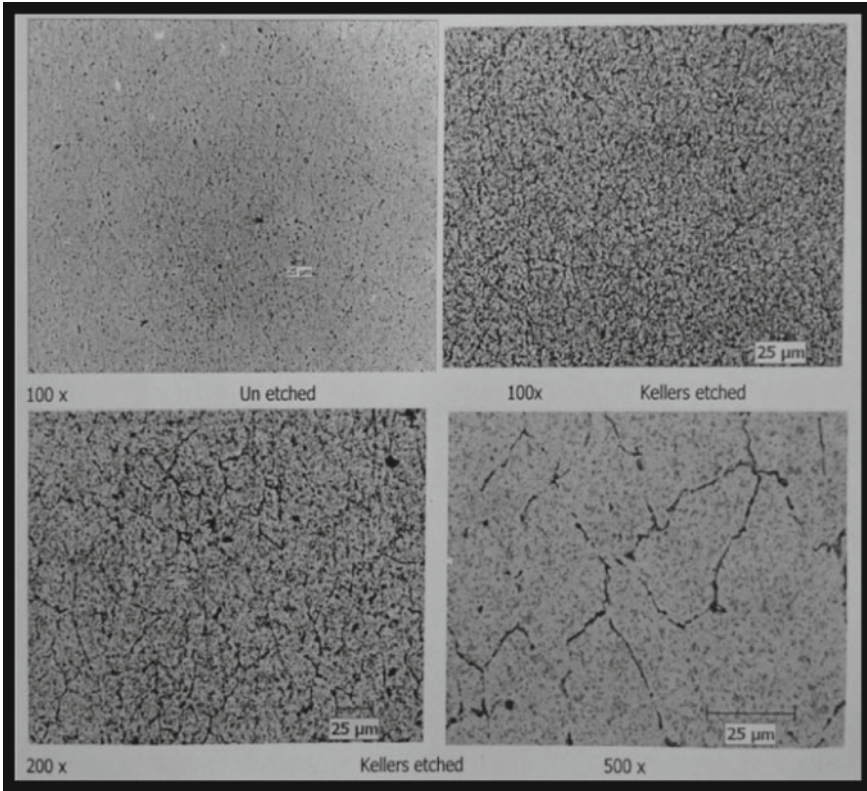


**Fig. 3** Microstructure of Al6061-Gr composites

The optical micrographs of as-cast Al6061-Gr alloy reinforced with 6 wt% and Al6061-Gr alloy reinforced with 6 wt% undergoing Equal channel angular pressing, are shown in Fig. 3. Optical micrographs of Al6061-Gr with 6 wt% after Equal channel angular pressing, composites exhibited uniform distribution of Graphite particulates in the Al6061 matrix, and no void and discontinuities were found all across the specimen volume. Very common defects during metal casting like porosity and shrinkages were also not found in the micrographic studies. There was a good noticeable interfacial bonding is been achieved between the Graphite particles reinforcements with Al6061 alloy matrix.

## 5.2 Hardness Test

The Brinell hardness test on all compositions was conducted using 10 mm steel ball indenter using 60 kgf applied load, same load is maintained for period of 10 s on each sample at different locations. During the hardness test, it is found that the hardness of



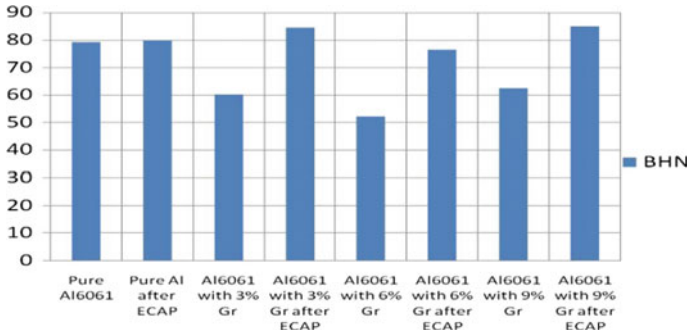


**Fig. 4** The Brinell hardness number of Al6061 + Gr composites before and after ECAP

the specimens processed by Equal channel angular pressing is much greater than that of its just casted specimens; the graphs also show that the hardness decreases with the increasing wt% of graphite. This decrease in hardness number is due to softness of the graphite particles, but most importantly it also noticed that hardness increases when the casted material undergoes Equal channel angular pressing. Al6061 + Gr composite specimen with 9% graphite after ECAP showed a maximum increase in hardness of 88BHN in comparison with purest Al6061 specimen hardness of 79BHN (Fig. 4).

### 5.3 Corrosion Test

The casted materials after undergoing the salt spray test were inspected and the results are obtained as shown in Table 4. The casted materials after Equal channel angular pressing are tested and the results are shown in Table 5. It is seen that time taken by the specimens to initiate the corrosion is not affected greatly neither by adding graphite nor by equal channel angular pressing process. The test method used is ASTM B 117-2007.

**Table 4** Results of corrosion test before equal channel angular pressing

Date	Total hours	Pure Al	Al with 3% Gr	Al with 6% Gr	Al with 9% Gr
21.06.2017-initial	0	1.4117	1.4789	1.3123	1.4025
21.06.2017	12	1.3461	1.3617	1.2974	1.3317
22.06.2017-final	24	1.2221	1.3717	1.1147	1.2716

**Table 5** Results of corrosion test after equal channel angular pressing

Date	Total hours	Pure Al	Al with 3% Gr	Al with 6% Gr	Al with 9% Gr
21.06.2017- initial	0	1.1471	1.5741	1.6002	1.5789
21.06.2017	12	1.3461	1.4476	1.4476	1.4964
22.06.2017- final	24	1.2221	1.3717	1.3711	1.3141

## 6 Conclusion

Stir casting techniques were successfully adopted in the preparation of Al6061 with graphite varying from 0, 3, 6 and 9%. It is seen that Equal channel angular pressing process has increased the strength, hardness, and fine microstructure formation. Equal channel angular pressing process is carried out in 90° which results in reducing the burrs and residual stresses present in the material after the process of casting. The microstructural study confirms the uniform distribution of the reinforcement particles in the matrix. The hardness of the casted materials before Equal channel angular pressing was lesser (79BHN) compared to that of the casted materials that have undergone equal channel angular pressing (88BHN), it showed a total of 11.4% increase in hardness number compared to base material. The corrosion test using salt spray mechanism which showed that adding graphite to Al6061 or processing the casted specimens by equal channel angular pressing process will not have a noticeable effect on corrosion resistance property of Al6061.

## References

1. Author F (2010) Contribution title. In: 9th International proceedings on proceedings, pp. 1–2. Publisher, Location (2010)
2. LNCS Homepage. <http://www.springer.com/lncs>. Last accessed 2016/11/21
3. Niranjana KN, Shivaraj BN, Sunil Kumar M, Deepak AR (2017) Study of mechanical properties on AL6061 hybrid composite by stir casting method. *Int Res J Eng Technol (IRJET)*, 01 Jan 2017
4. Dileep BP, Sridhar BR (2018) A investigation on mechanical and metallurgical properties of steel EN24 and SiC MMCs. *Int J Mech Prod Eng Res Dev (IJMPERD)* 8(2):189–194. ISSN(P): 2249–6890; ISSN(E): 2249-8001, Apr 2018
5. Fisher G (1984) Composite: engineering the ultimate material. *Am Ceram Soc Bull* 63(2): 360–364
6. Rack HJ (1990) Metal matrix composites. *Adv Mater Processes* 137(1):37–39
7. Urquhart AW (1991) Molten metal's sire MMCs, CMCs. *Adv Mater Process* 140(7):25–29
8. Roos JR, Celis JP, Franser J, Buelens C (1990) The development of composite plating for advanced materials. *JOM* 42(11):60–63
9. Dietrich Herbert (1991) Carbon/carbon, protected/ protedted. *Mater Eng* 108(8):34–35
10. Ravi Kumar V, Dileep BP, Mohan Kumar S, Phanibhushana MV (1859) Effect of metal coatings on mechanical properties of aluminium alloy. In: AIP conference proceedings 1859–2017, 020037-1-020037-6

11. Taya M, Arsenault RJ (1989) Metal matrix composite thermo mechanical behavior. Pergamon press
12. Dileep BP, Ravikumar V, Prashanth M, Phanibhushana MV (2014) Effect of Zinc coating on mechanical behavior of Al 7075. *Appl Mech Mater* 592–594:255–259
13. Kainer and Prasad (1991) Composite material technology. 37:191
14. Wei W (1992) High temp. MMCs for aero engines; challenges and potential. *Metals Mater J*, pp 430–435
15. Demeis R (1988) New life for aluminium. *Aerospace America*, Mar 1989, pp. 26–29
16. Doychak J (1992) Metal and intermetallic matrix composites for aerospace propulsion and power systems. *JOM* 44(6):46–51
17. Hunt E, Pitcher PD, Grayson PJ *Advanced Al and Mg alloys*. In: Khanand T, Effenberg G (eds) ASM
18. Nixon TD, Cawley JD (1992) Oxidation inhibition mechanisms in coated carbon-carbon composites. *J Am Ceram Soc* 75(3):703–708
19. Eustathopoulos N, Chatain D, Coudurier L (1991) Wetting and interfacial chemistry in liquid metal ceramic systems. *Mat Sci and Engg* 135A:83–88
20. Adeqoyin I, Mohamed FA, Lavernia EJ (1991) Particulate reinforced MMCs-A review. *J Mat Sci* 26:1137–1156
21. Ravi Kumar V, Dileep BP, Vital HR (2017) Tribological and mechanical characterization of Al–Ni–SiC metal matrix composites. In: AIP conference proceedings 1859–2017, 020020R
22. Mehan L (1968) Fabrication and evaluation of sapphire reinforced Al composites. *Metal Matr Compos*, ASTM-STP 438:29–58
23. Chester TS (1991) Non-metallic materials for gas turbine engines: are they real? *Adv Mater Process* 139(6):32–39

# The Effect of Heat Treatment on Mechanical Properties of Aluminium Alloy 7075 with Nano B<sub>4</sub>C



T. H. Manjunatha, Yadavalli Basavaraj, V. Venkataramana and Madeva Nagaral

**Abstract** The mechanical behavior of Al7075 alloy composite reinforced with 3%, 6% by weight ratio nanosized B<sub>4</sub>C particulate is investigated with and without heat-treatment process. The composite is prepared by liquid casting—stirring method and mechanical behavior of alloy Al7075-3% weight (wt) and B<sub>4</sub>C, 6% wt and B<sub>4</sub>C nanocomposites were deliberated. Hardness, ultimate tensile strength; yield strength, percentage elongation and compression strength were evaluated and compared as per ASTM standards. The findings yielded in significant enhancement of properties after heat-treatment process. Only percentage elongation of the composite showed declined value relatively.

**Keywords** Al7075 alloy · B<sub>4</sub>C nano particulates · Heat treatment · Yield strength · Stir casting · Percentage elongation

## 1 Introduction

Evaluation of aluminium-based metal matrix composites (AMCs) paved a way for wider applications in auto, aerospace industries due to their better wear resistance, strength to weight and stiffness to weight ratios, along with anti-corrosion, thermal conductivity properties [1]. AMCs are customized by incorporating micro and nano-sized particles (SiC, Al<sub>2</sub>O<sub>3</sub>, and B<sub>4</sub>C), into the aluminium matrix. Boron carbide an advanced fortification material due to its specific properties play vital role for fabricating newer material with high performance. Al7075 with B<sub>4</sub>C alloy is strong compared to many steels with good strength, machinability, etc [2]. Several methods presently applied to formulate the nanocomposites, viz mechanical blending, high-energy ball milling, mist deposition, powder metallurgy, and various casting techniques [3]. For the present study mechanically stirring (casting) method is selected

---

T. H. Manjunatha (✉) · Y. Basavaraj · V. Venkataramana  
Mechanical Department, BITM, Ballari, Karnataka, India  
e-mail: [manjuforeverthree@gmail.com](mailto:manjuforeverthree@gmail.com)

M. Nagaral  
Aircraft R & D Centre, HAL, Bengaluru, Karnataka 560037, India

© Springer Nature Singapore Pte Ltd. 2020  
L. Vijayaraghavan et al. (eds.), *Emerging Trends in Mechanical Engineering*,  
Lecture Notes in Mechanical Engineering,  
[https://doi.org/10.1007/978-981-32-9931-3\\_46](https://doi.org/10.1007/978-981-32-9931-3_46)

**Table 1** Elements of Al7075 alloy

Element	Al+	Cu	Mg	Si	Fe	Mn	Ni
wt%	Bal	1.22	2.20	0.09	0.16	0.05	0.01
Element	Al+	Sn	Ti	Cr	Pb	Zn	
wt%	Bal	0.01	0.06	0.24	0.01	5.62	

to diffuse 3 and 6 wt% of nano B<sub>4</sub>C particles in molten aluminium (Al7075) without agglomeration and clustering to analyze the influence of heat treatment towards mechanical properties.

## 2 Experimental Work

### 2.1 Material

For the study, nanosized B<sub>4</sub>C as reinforcement, Aluminium 7075 as base material having element composition (using optical emission spectrometer-BAIRD—DV 6E) as shown in Table 1.

### 2.2 Preparation of Nano Composite—Al7075–B<sub>4</sub>C

The nano combination containing 3% and 6 wt% of B<sub>4</sub>C particulates made from mechanical stirring, casting technique. Initially preheating of nano B<sub>4</sub>C and the cast iron die to 300–400 °C subsequently calculated amount of Al7075 by weight is placed in a crucible (graphite) inside an electric arc furnace and heated to 750 °C. To vent out adsorbed gases from melt C<sub>2</sub>Cl<sub>6</sub> is added. Zirconium coated mechanical stirrer is used to swirl liquid metal (300 rpm), vortex is observed nano particulates are introduced at constant feed rate to avoid clustering and promote uniform homogenous distribution after continues stirring, the entire melt is poured into a preheated die. The prepared nanocomposites were shaped as per the standards for characterization purpose [4].

### 2.3 Testing of Composites

Microstructural study made with scanning electron microscope on test sample with the range having 10–12 mm diameter cut from the castings and polished thoroughly, for etching Keller's reagent was used, indentation response is evaluated by Brinell hardness tester. The specimens are cut as per metallographic standard method and

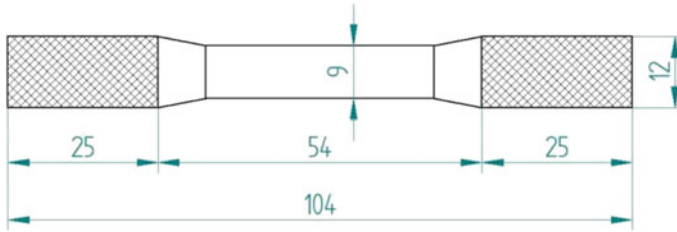


**Fig. 1** Specimen for tensile testing (all dimensions are in “mm”)

experimentation (3 times) is done with load 250 kgf, dwell period 30 s, average results were documented and hardness is determined. The tensile specimens of 9 mm diameter and 45 mm gauge length (as per ASTM E8 standard) prepared, tested with Universal Testing Machine (Instron make)—displacement control mode rate of 0.1 mm/60 s. Various tensile properties and percentage elongation were assessed for Al7075-3%, 6 wt%. B<sub>4</sub>C composites [5]. Compression test (ASTM E9 standard) also conducted. Figure 1 shows tensile work specimen applied for experimentation.

### 3 Outcomes and Discussion on Microstructure

#### 3.1 Microstructure Study

The microstructural survey was carried out on the prepared composites using Vegas Tescan made scanning electron microscope. The test sample is 10–12 mm in diameter cut from the castings and polished thoroughly, for etching the sample Keller’s reagent was used.

Figure 2a, b substantiates homogeneous distribution of B<sub>4</sub>C particles (SEM micro snaps of Al7075 alloy as cast and Al7075 with 6 wt% of nano B<sub>4</sub>C models) along with very little agglomeration and isolation of elements. Figure 2b certainly exhibits flat distribution of nano B<sub>4</sub>C particles in alloy matrix; further zero defects indicate soundness of castings.

The EDS spectrum discloses the presence of Al, Zn, Cu, Mg, B, and C at interface reaction layer (Fig. 3) to authenticate the presence of B<sub>4</sub>C.

#### 3.2 Tensile Properties

Figure 4, shows there is gradual increase in the UTS from 227.2 to 279.2 MPa with the inclusion of B<sub>4</sub>C from 3%, 6 wt% initially and the values crept up from 292.4 to 350.6 MPa after heat treatment. From this it is evident that the presence of B<sub>4</sub>C nano

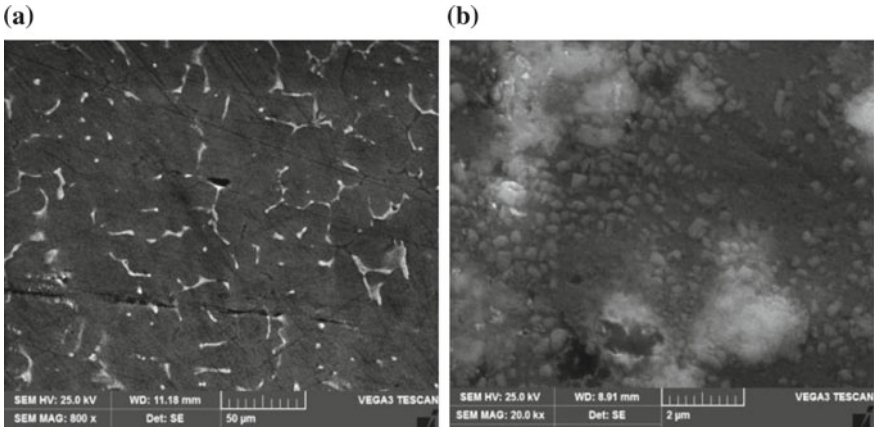


Fig. 2 a–b Scanning electron microphotographs of a as cast Al7075 alloy b with 6 wt% of B<sub>4</sub>C

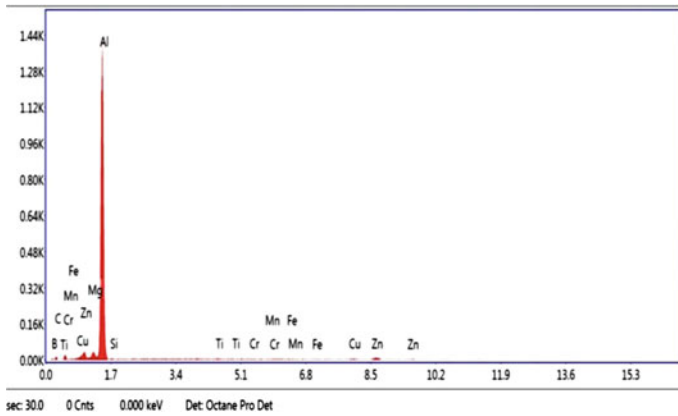


Fig. 3 EDS spectrum of Al7075-6% B<sub>4</sub>C nano composites

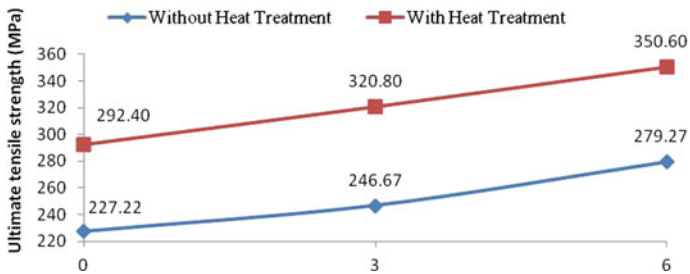


Fig. 4 Ultimate tensile strength of Al7075 and nano B<sub>4</sub>C composites

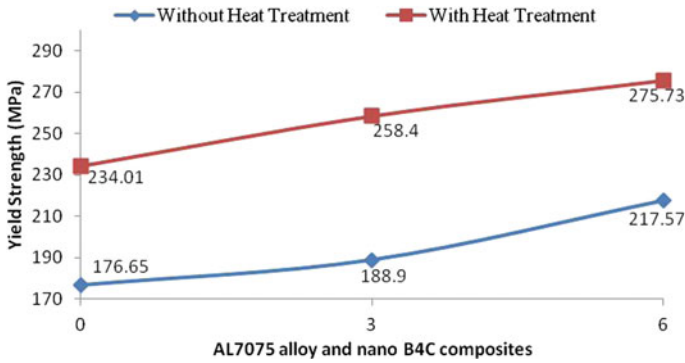


Fig. 5 Yield strength of Al7075-3% and 6 wt% of nano B<sub>4</sub>C composites

particulates with heat treatment show significant positive enhancement in mechanical properties of the composite.

In the similar way Fig. 5 indicates the comparative values of yield strength, 176.65–217.57 MPa (3%–6%B<sub>4</sub>C) without heat treatment and 234.01–275.73 MPa (3%–6%B<sub>4</sub>C) with heat treatment authenticating the importance of heat treatment process to boost the yield strength.

Figure 6 depicts the impact of B<sub>4</sub>C (3%, 6 wt%) in terms of malleability and is observed, graph is declining from 12.15 to 8.92% without heat treatment and further down to 8.76% after heat treatment, it is obvious from the graph there is no much difference in the %of elongation for both conditions.

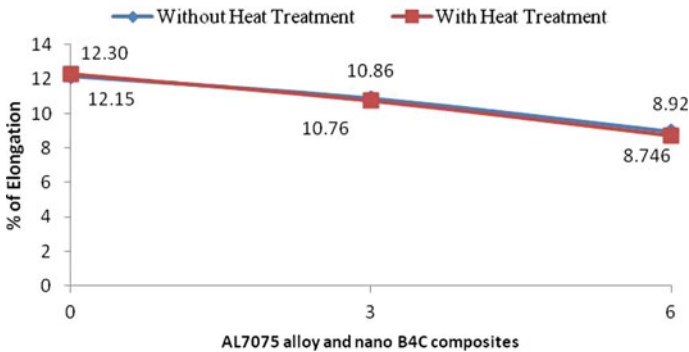


Fig. 6 Elongation of Al7075-3% and 6 wt% of nano B<sub>4</sub>C composites



### 3.3 Compression Strength

Figure 7 shows the compression strength of specimens with and without heat treatment with 3 wt% and 6 wt% B<sub>4</sub>C in Al7075 alloy. The data obtained from the testing, map a conclusion increase in compression strength from 629.53 to 788.36 MPa with the increase in % wt of B<sub>4</sub>C. Also, compression strength is comparatively more (788.36 MPa) after heat treatment.

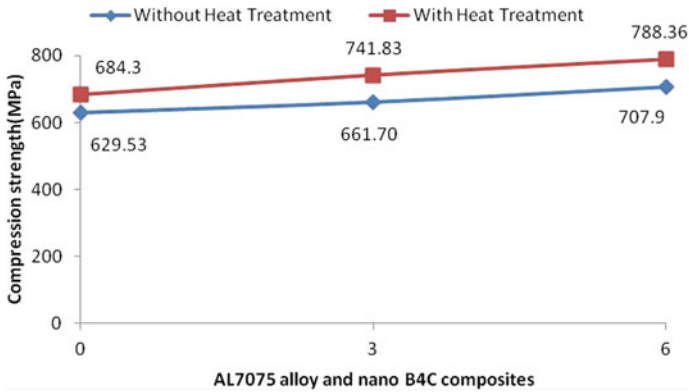


Fig. 7 Compression strength of Al7075-3% wt and 6 wt% of nano B<sub>4</sub>C composites

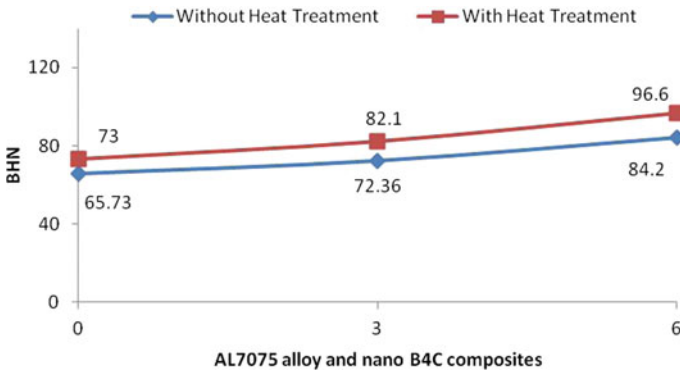


Fig. 8 Hardness of Al7075-3, 6 wt% of nano B<sub>4</sub>C composites

### 3.4 Hardness Study

The BHN test carried out with 5 mm ball diameter, load 250 kg and the values obtained are in the range of 65.7–96.66 BHN presented in Fig. 8. BHN 96.6 is maximum value obtained with heat-treated specimen.

## 4 Conclusions

The effect of heat treatment on mechanical properties of the Al7075 with addition of 3 and 6% wt of nano B<sub>4</sub>C composite are analyzed and following remarks were made:

- The stir casting process was successfully adopted in the preparation of Al7075-3 and 6% wt nano B<sub>4</sub>C composites.
- The microstructural studies revealed the uniform distribution of the nano B<sub>4</sub>C particulates in Al7075 alloy matrix.
- The ultimate tensile strength, compressive strength, and yield strength properties have shown significant increment with addition of B<sub>4</sub>C percentage (from 3 to 6% wt.), further escalation with heat treatment. In addition, Hardness of the composite is high contrast to base Al matrix. Only percentage elongation showed declined values in both the cases.

## References

1. Zebarjad SM, Sajjadi SA (2007) Dependency of physical and mechanical properties of mechanical alloyed Al–Al<sub>2</sub>O<sub>3</sub> composite on milling time. *Mater Des* 28(7):2113–2120
2. Alizadeh A et al (2017) Preparation and investigation of Al 4 wt% B<sub>4</sub>C nano composites powers using mechanical milling. *Indian Acad Sci* 34:1039–1048
3. Topton F, Kilicarslan A, Karaaslan A, Cigdem M, Kerti I (2010) Processing and micro structural characterization of AA 1070 and AA 6063 matrix B<sub>4</sub>Cp reinforced composites. *Mater Des* 31:S87–S91
4. Jadhav PR, Sridhar BR, Nagaral M, Harti JI (2017) Evaluation of mechanical properties of B<sub>4</sub>C and graphite particulates reinforced A356 alloy hybrid composites. Published by Elsevier Ltd., Science Direct materials today proceedings 4
5. Dama K, Prashanth L, Nagaral M, Mathapati R, Hanumantharayagouda MB (2017) Microstructure and mechanical behavior of B<sub>4</sub>C particulates reinforced ZA27 alloy composites. In: Science direct materials today proceedings, vol 3. Elsevier Ltd., Amsterdam
6. Khakbiz M, Akhlaghi F (2009) Synthesis and structural characterization of Al–B<sub>4</sub>C nanocomposite powders by mechanical alloying. *J Alloys Comp* 479(1/2):334–341
7. Nie C-Z, Gu J-J, Liu J-L, Zhang D (2007) Production of boron carbide reinforced 2024 aluminium matrix composites by mechanical alloying. *Mater Trans* 48(5):990–995
8. Alizadeh A (2011) Hot extrusion process effect on mechanical behavior of stir cast Al based composites reinforced with mechanically milled B<sub>4</sub>C particles. *J Mater Sci Technol* 27(12): 1113–1119

# Comparison of Various Types of Lubrication During Hard Turning of H13 Tool Steel by Analysing Flank Wear Using ANOVA



Anil Raj, K. Ramesha, Joel U. Sajan, Danish Mohammed Khan and U. A. Varshini

**Abstract** Hard machining of components has been a new attraction in the field of manufacturing, as it avoids the need for multiple cost inculcation processes for a single part. Hard machining attracts a wide attention to the researchers because of the usage of hard tools, tougher machinery and enormous quantities of cutting fluids. Optimized use of any of these functionaries' can result in reduction of cost as well as safer and clean working environments. In this research new cutting fluid reduction processes were compared along with the use of hard metal inserts. These two methods suggest an enormous amount of cost reduction along with cleaner shop floor. Minimal quantity lubrication (MQL) and minimal cutting fluid application (MCFA) capacities in cutting fluid reduction as mentioned by various researchers in past two decades. These methods were compared in this research paper for finding out the best possible system. Flank wear is considered as a crucial parameter in hard machining as the wear rate affects other deserving product qualities such as surface finish and job profiles. In this research tungsten carbide coated hard metal inserts were used instead of conventional CBN or diamond tipped tools, which are of higher in price margin. The study comprised of Taguchi's L9 orthogonal array, which was advised by previous researchers as good tool for optimisation. MQL and MCFA assisted experimentation were performed with same cutting conditions, which were then again compared with dry hard machining and wet machining. Influence of each input parameters were critically evaluated using ANOVA. The results revealed that a promising reduction in tool wear was noticed in MCFA assisted hard machining.

**Keywords** MCFA · MQL · Hard turning · Flank wear · ANOVA · SEM

---

A. Raj (✉) · K. Ramesha · J. U. Sajan · D. M. Khan · U. A. Varshini  
Department of Mechanical and Automobile Engineering, Faculty of Engineering, Christ University, Bangalore 560074, India  
e-mail: [anil.raj@christuniversity.com](mailto:anil.raj@christuniversity.com)

K. Ramesha  
e-mail: [ramesha.k@christuniversity.in](mailto:ramesha.k@christuniversity.in)

© Springer Nature Singapore Pte Ltd. 2020  
L. Vijayaraghavan et al. (eds.), *Emerging Trends in Mechanical Engineering*,  
Lecture Notes in Mechanical Engineering,  
[https://doi.org/10.1007/978-981-32-9931-3\\_47](https://doi.org/10.1007/978-981-32-9931-3_47)

## 1 Introduction

Hard Machining, which is considered as a machining operation conducted with geometrically defined cutting edges and has a Rockwell hardness value of 39–42 HRc Range. Hard Machining uses tools which are composed of the carbides of titanium, tantalum, tungsten, or some combination of these materials. Then it is sintered or cemented in a matrix binder, usually cobalt. With the advancement in Hard Machining throughout the past decade has opened door for conduction of complex operation including various geometries. Development in the field of advanced machining technology brought a new era. Hard machining technology brought modifications to the present milling and turning operations. With the change in rpm ranging from 600 to 1,000 were used in working up of 45 HRc [1]. Regarding the depth of cut, cutting speed and the feed rate the formation of friction within the layers of the tool and workpiece was formed. This led to the formation of temperature rise due to shear force within the work. This rise in temperature was controlled using cutting fluid which is made from oils made from petroleum products, animal fats, plant oils, water, and air, or other raw ingredients. The function of lubricant is to absorb heat developed in the cutting zone and to lubricating the tools cutting edge and the chip, preventing friction and welding of chip on the tool, thus reducing surface distortion, deformation and better job profile. The relation with the cutting fluid and the hard metal insert is concentrated in this paper. Sometimes the cutting fluid costs constitute 7–17% of total production cost in industry [2]. The form of using minimum quantity of cutting fluid for better optimisation was tested on tungsten carbide coated hard metal for cleaner and safer workplace [3]. The introduction of an active idea of reduction in the use of cutting fluid started two decades ago. The different forms of reduction in cutting fluid include minimal quantity lubrication (MQL) and minimal cutting fluid application (MCFA) [4]. Both of the above-mentioned systems can endorse green surroundings in the shop floor. MQL and MCFA were considered as lubricating technologies that are environmentally friendly, safe and make manufacturing process more proficient [5].

Minimal quantity lubrication (MQL) uses Units Coolube where minute quantities of the high-efficiency lubricant is used for lubrication applied directly to the tool and work interface. With recent study proved that coolubes exhibit superior mechanical properties like an ideal lubricant [6]. These coolants are made from pure biodegradable materials and reduces fluid usage and eliminates the need for coolant treatment and disposal. In case of units coolube the coolube added is controlled by unit's system where the added coolube is less than 1 drop per cycle and compressed air is injected into it for maximising productivity [7]. Due to the polar properties of the coolube on the metallic surface strong bonds are formed on the surface leading to reduction of friction 50% better than the ordinary coolant increasing tool life, better cut finish and minimising heat formation.

Minimal cutting fluid application (MCFA) [8] the working process is different from the conventional methods. This process uses a fluid application system developed in-house. This system helps in delivering the cutting fluid directly to the cutting

zone at a very low rate. Here the cutting fluid is applied at high pressure and velocity due to which it is able to penetrate into the cutting zone. This helps in actuating rebinder effect which, in turn, reduces tool wear and reduces cutting force.

## 2 Selection of Work Material

The material selected for this experimentation was AISI H13 tool steel of hardness 18 HRc. This tool steel was often employed in manufacturing industries to make tools, dies, and moulds for specific operation. The material was heat-treated to get a through hardness of 45 HRc for this research. This material's chemical composition is revealed in Table 1, which was obtained after testing it in a NABL accredited lab.

**Table 1** Composition of H13 tool steel

Element	C	Cr	Mo	V	Si	Mn	Fe
Weight %	0.39	5.15	1.25	1.1	1.0	0.5	Balance

## 3 Selection of Cutting Tool

The research was supported by Taegu Tec Private Ltd. The tool manuals provide by Taegu Tec facilitated in selecting tool for this particular research. Tool insert selected for this research was SNMG 120408 MT TT 5100 hard metal insert with tool holder PSBNR 2525 M12. The tool insert has eight edges with a nose radius of 0.8 mm and orthogonal rake angle of 8°.

## 4 Experimental Setup

The experimental set up is shown in Fig. 1 Experimental setup, it was developed for this research purpose at CRDM lab by Varadarajan et al. [7] at Karunya University. The lathe used for this research was also modified to give variable feed and speed rates without any steps. The speed and feed can be controlled independently controlled by using servo motors and controllers. The experimental set up consists of a lubrication pumping system developed in-house to supply lubricant at very high pressure. The system can provide a maximum of four outlets which can deliver cutting fluid at a maximum pressure of 150 bar. Cutting fluid injector helps to regulate the pressure of cutting fluid and convert it to high-velocity fine stream. The fine stream of cutting fluid can easily enter the tool work and top side of chip, which promotes Rebinder

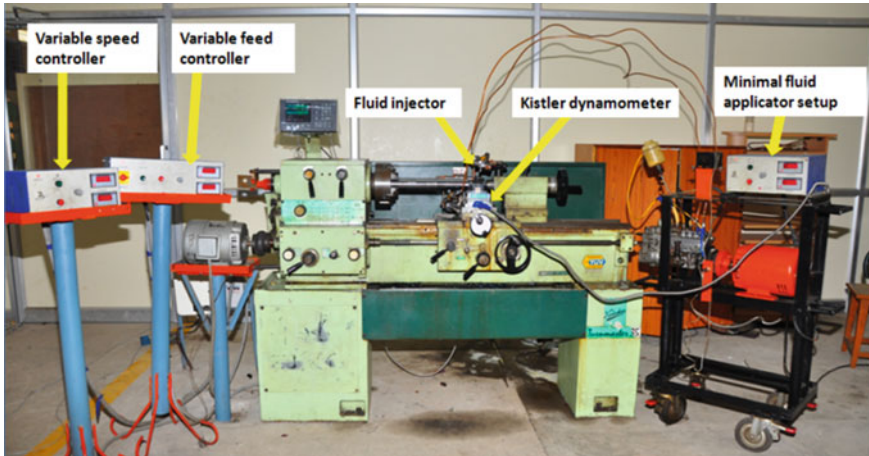


Fig. 1 Experimental setup

effect. The pulsating action of cutting fluid pump also accelerates chip breakages, which in turn reduces cutting force as well as flank wear rate.

In Fig. 2, a MQL system that was developed in CRDM is shown. The system uses compressed air and cutting fluid together to give a high-velocity continuous stream of cutting fluid. The system uses a fluid application gun which can be actuated automatically. The MQL system can be operated at a maximum pressure of 5 bar and minimum quantity of cutting fluid can be regulated as 2 mL/min was also developed to supply cutting fluid in which the cutting fluid was propelled by a stream of compressed air [9, 10]. A constant pressure of 5 bar was kept throughout the experimentation. The quantity of cutting fluid was kept at 8 mL/min as that of MCFA system. Both of these systems used petroleum-based cutting fluid emulsion of 20% in water.



Fig. 2 Minimal quantity lubrication setup and spray gun

## 5 Experimental Procedure

### 5.1 Design of Experiment

The parameters that play an important role in the flank wear of the tool inserts during hard machining were extensively studied. Similar investigation conducted earlier showed that the cutting speed, feed rate and depth of cut played a precarious role in reducing surface roughness (Anil Raj et al.). Table 2 shows the parameters and levels of experimentation.

A Taguchi's L9 orthogonal array of experimentation was used for this research. This design matrix (Table 3) favoured the use of three input parameters in three levels of actuation and flank wear values obtained after measuring with SEM images are given. This L9 table helps to optimise the results of research with less number of trials.

**Table 2** Cutting parameters and its levels

Parameters	Level 1	Level 2	Level 3
Cutting speed (m/min)	75	95	115
Feed rate (mm/rev)	0.05	0.075	0.1
Depth of cut (mm)	0.05	0.75	1

**Table 3** L9 orthogonal array table with input parameter and responses

Run order	Cutting speed (m/min)	Feed rate (mm/rev)	Depth of cut (mm)	Flank wear during MCFA (mm)	Flank wear during MQL (mm)
1	50	0.05	0.5	0.015	0.020
2	50	0.075	0.75	0.035	0.040
3	50	0.1	1	0.055	0.065
4	75	0.05	0.75	0.037	0.045
5	75	0.075	1	0.057	0.067
6	75	0.1	0.5	0.045	0.056
7	100	0.05	1	0.04	0.059
8	100	0.075	0.5	0.059	0.066
9	100	0.1	0.75	0.07	0.085

### 5.2 Measurement of Tool Wear

Scanning electron microscope was used for the Flank wear measurement purpose. This microscopic images also helped to study the patterns of wear occurred on the tool under various cutting conditions. Joel JSM 6390 electron microscope was employed for the capture of images for each edge after machining. Image-J software was used for the measurement of flank wear happened areas.

## 6 Results and Discussion

Flank wear measure during each set of experimentation is shown in Table 3. Both the conditions of cutting fluid application are mentioned in this table.

### 6.1 Relative Significance Graphs for Flank Wear

Figure 3 shows relative significance of input parameter at three levels and its effect on flank wear during MQL fluid application. Cutting speed at level 1 ( $v_1$ ) Feed rate at level 1 ( $f_1$ ) and depth of cut at level 1 ( $d_1$ ) pertains to give the minimum flank wear.

Figure 4 indicates effects of input parameters on the flank wear when the cutting fluid is applied using MCFA system. The flank wear was found to be minimum when all the parameters are at level 1 ( $v_1, f_1, \text{ and } d_1$ ).

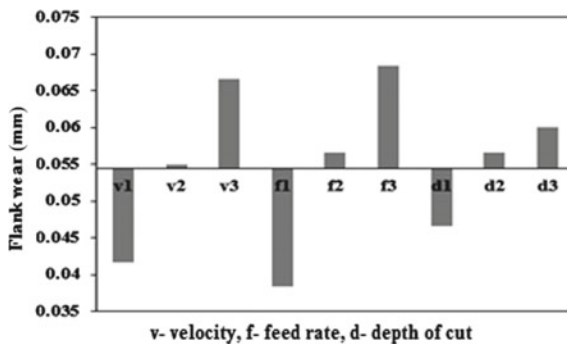


Fig. 3 Flank wear during MQL ( $v$ —cutting speed,  $f$ —feed rate,  $d$ —depth of cut)



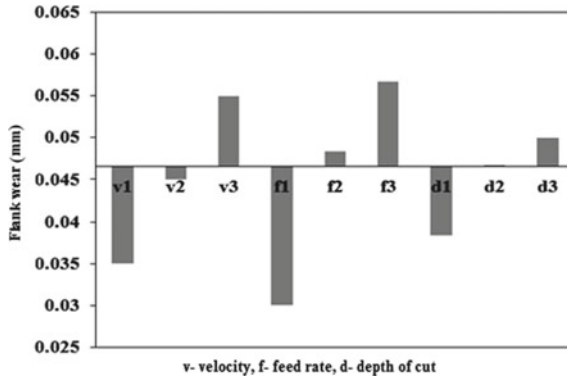


Fig. 4 Flank wear during MCFA (*v*—cutting speed, *f*—feed rate, *d*—depth of cut)

Table 4 MQL and MCFA ANOVA analysis results

Factors	Effect on flank wear MQL (%)	Effect on flank wear MCFA (%)
Cutting speed	27.655	23.57
Feed	43.286	48.78
Depth of cut	16.89	10.878
Other error	9.559	7.923
Total %	100.00%	100.00%

### 6.2 Analysis of Variance (ANOVA) Results for Flank Wear

The analysis was carried out with the help of MINITAB 14 software. The effects of each input parameter to the output were reflected in this process. Table 4 shows the % effect of input parameters towards flank wear during MCFA and MQL assisted hard turning after ANOVA analysis. Both cases feed rate was found to be prominent factor to affect the flank wear. It is 43.3% during MQL and 48.8% during MCFA assisted hard turning of H13 tool steel. Cutting speed was found to be 27.65% during MQL and 23.57% during MCFA, it was the next prominent factor. The depth of cut was found to have least significance of 16.9% during MQL and 10.9% during MCFA.

### 6.3 Comparison of Flank Wear During MCFA and MQL

Figure 5 reveals the comparison graph of flank wear during MCFA and MQL assisted hard turning. The results plotted in the graph shows there was a noticeable difference in flank wear.

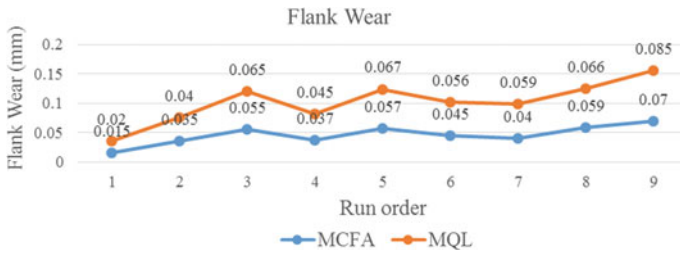


Fig. 5 Graph comparing flank wear during MCFA and MQL

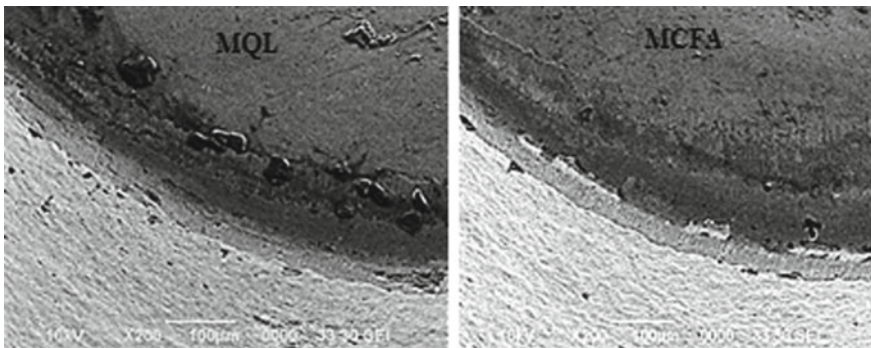


Fig. 6 Sample images of SEM analysis result of MQL and MCFA

The graph points out that MCFA assisted process was superior than MQL assisted hard turning. Flank wear was found to be at least 10% lower during MCFA assisted hard turning of H13 tool steel.

Figure 6 shows the sample SEM analysis result of flank wear during MQL and MCFA. MQL image shows the chip inclusions and more wear rate of the insert. MCFA image shows SEM image of less wear rate and lesser inclusions.

## 7 Conclusions

Detailed experimentations conducted by comparing cutting fluid application system helped to reveal the following details.

- Flank wear irrespective of cutting fluid application condition was very much dependent on feed rate.
- Cutting speed and depth of cut were found to be effective in a lower tone for controlling flank wear.
- MQL system was not promising as that of MCFA system in reducing flank wear.

- Pressure of cutting fluid applied and pulsating fluid application in MCFA system was giving the upper edge for this system.
- It was observed that MCFA system produced very less oil mist during operation compared to MQL system.

## References

1. Tönshoff HK, Arendt C, Amor RB (2000) Cutting of hardened steel. *CIRP Annals Manuf Technol* 49(2):547–566
2. Soković M, Mijanović K (2001) Ecological aspects of the cutting fluids and its influence on quantifiable parameters of the cutting processes. *J Mater Process Technol* 109:181–189
3. Quinn LJ (1992) Metalworking fluids: at the cutting edge of health and safety. *ASTM Stand News (USA)* 20(5):40–43
4. Dixit US, Sarma DK, Davim JP (2012) Machining with minimal cutting fluid. In: *Environmentally friendly machining*, Springer, US, pp 9–17
5. NIOSH, Metal working fluids—recommendation for chronic inhalation studies, National Institute for Occupational Safety and Health (NIOSH), Cincinnati, OH USA 45226
6. Tai BL, Stephenson DA, Furness RJ, Shih AJ (2014) Minimum quantity lubrication (MQL) in automotive powertrain machining. *Procedia CIRP* 14:523–528
7. Varadarajan AS, Philip PK, Ramamoorthy B (2000) Investigations on hard turning with minimal cutting fluid application (HTMF) and its comparison with dry and wet turning. *Int J Mach Tools Manuf* 42(2):193–200
8. Wins KLD (2010) Optimization of surface milling of hardened AISI 4340 steel with minimal fluid application using a high velocity narrow pulsing jet of cutting fluid. *Engineering* 56(4):241–249
9. Tousun N, Pihtili H (2010) Gray relational analysis of performance characteristics in MQL milling of 7075 Al alloy. *Int J Adv Manuf Technol* 46(5):509–515
10. Tosun N, Huseyinoglu M (2010) Effect of MQL on surface roughness in milling of AA7075-T6. *Mater Manuf Process* 25(8):793–798

# Study of Wear Properties of Vinyl Ester Polymer Filled with Micro-Gr-Nano-CuO Particles



S. N. Vasantha Kumar, Govardhan Goud and P. C. Sharath

**Abstract** The Vinyl ester (VE) particulate composites find a wide range of applications in chemical industries and wastewater treatment plants, due to their excellent mechanical properties combined with chemical resistance. The present work focuses on the wear resistance of VE composite reinforced with two different fillers materials (i) nano-copper oxide (CuO) and (ii) micrographite (Gr). The fabrication was done by hand lay-up technique by adding different wt% of pure CuO, Gr and hybrid CuO-Gr into the VE resin with the help of ultrasonicator and magnetic stirrer. The wear behaviour of VE composites was found by using VE composite pin against EN31 steel disc on a computerised pin on disc (POD) operator by varying sliding speed. Effect of CuO and Gr particles on VE composite alters the wear behaviour by changing the morphology. The specific wear rate increases with the increase of wt% of Gr, whereas in the case of CuO, it increases up to 6 wt% and decreases for further addition. The composite containing 5 wt% of Gr and 4 wt% of CuO exhibits highest wear resistance 2.69 m<sup>3</sup>/N-m. This result shows that the synergistic effect of hybrid filler Gr-CuO is to improve the wear resistance when compared with that of pure Gr/CuO. The micrograph by SEM showed uniform distribution of graphite and copper oxide particles in the VE composites.

**Keywords** Polymer · Wear · Microstructure

---

S. N. Vasantha Kumar (✉)

Mechanical Engineering Department, Canara Engineering College, Mangalore, India  
e-mail: [Vasanth.kumar385@gmail.com](mailto:Vasanth.kumar385@gmail.com)

G. Goud

Mechanical Engineering Department, Bahubali College of Engineering, Shravanabelagola, India  
e-mail: [pgovardhan0@yahoo.com](mailto:pgovardhan0@yahoo.com)

P. C. Sharath

Metallurgical Engineering Department, Jain University, Bangalore, India  
e-mail: [pcsharath1988@gmail.com](mailto:pcsharath1988@gmail.com)

© Springer Nature Singapore Pte Ltd. 2020

L. Vijayaraghavan et al. (eds.), *Emerging Trends in Mechanical Engineering*,  
Lecture Notes in Mechanical Engineering,  
[https://doi.org/10.1007/978-981-32-9931-3\\_48](https://doi.org/10.1007/978-981-32-9931-3_48)

## 1 Introduction

For different working conditions in various industrial and automobile applications, the polymers are increasingly used. Because of its good tailoring properties and high strength-to-weight ratio, polymer composites are replacing metal parts. Along with its other advantages, the material must have unique mechanical and tribological properties for safety and financial efficiency purpose [1, 2]. The polymer composite prepared by using different inorganic fillers is the today's most common material (bearing and breaking system). The incorporation of particles and/or fibres to the polymers provides versatile improvements in terms of tribological and mechanical properties [3, 4]. Earlier attempts were made to understand the wear behavior of polymer with the incorporation of particles/fibers [5, 6]. Vinyl ester resin is the most attractive thermosetting material that is widely used in engineering application because of high mechanical, chemical properties, and superior resistance to moisture [7]. The different solid lubricants, such as graphite, MoS<sub>2</sub> and PTFE (polytetrafluorethylene) are helpful in enhancing wear performance and reducing frictional coefficient have been reported by different authors [8–10]. On the counterpart, the transfer film layers are formed which are promoted by solid lubricants, which avoid the direct contact of sliding objects and thereby reduce the wear rate and frictional coefficient [11]. The polymers loaded with nanoparticles have attracted recently because of many advantages like high specific surface area and even at very low filler loading a strong interaction takes place between matrix and filler. For instance, Bahadur et al. have reported that the addition of fillers such as CaO, CuS, CuF<sub>2</sub> and CaS reduced the wear rate of polyamide, whereas other fillers such as CuAc and CaF<sub>2</sub> fillers increased the wear rate [12, 13]. Also, addition of fillers such as CuS and CuF<sub>2</sub> fillers to PEEK decreases the wear rate [14]. Q. Wang et al. have reported that the incorporation micro-sized Gr alone improved the friction-reducing and anti-wear abilities of the polyimide (PI) composites, whereas addition of nano-sized CuO alone deteriorated the wear resistance of PI composites because of its abrasive effect. Addition of both CuO and Gr together results in synergistic effect which leads to the best wear properties [15]. They also showed that wear rate and friction coefficient of PEEK composite filled with nanoparticles of SiC, Si<sub>3</sub>N<sub>4</sub>, ZrO<sub>2</sub> and SiO<sub>2</sub> [16–19]. Recently, Wenxiang XU et al. studied the significant effect of morphology and physical properties of interface on overall mechanical properties of composites loaded with nano- and microparticles [20]. The effect of slurry concentration on wear properties of GF-reinforced Vinyl ester composites was studied by Essi Serlin et al. and they quoted that an increase in the erodent concentration of the slurry (10–20 wt%) or in the total kinetic energy of the erodent particles (30–770 kJ) increases the wear rate [21].

Vinyl ester particulate composite finds wide application in the field of tribology (Bearings, breaking system, and so on). To meet the quality of practical application, reinforcements (fibres/particulates) are used along with solid lubricants (Gr, PTFE, etc.). In the previous studies, it is shown that reinforcement in micrometre affects the property at a greater level when the addition level is increased by 5 wt%. But,

for reinforcement which is in nanometre affects greatly when varied by 2 wt%. In the present work, the different wt% of micro-sized Gr and nano-sized CuO (Order of 5 and 2 wt%) were incorporated into thermoset polymer (Vinyl ester). The effect of sliding speed and filler wt% on the wear property of VE composite is discussed in detail. It is expected that result will broaden the application of solid lubricant and nanofillers-filled composites.

## 2 Experimentation

### 2.1 Materials

Vinyl Ester resin, supplied by Naphtha Resins and Chemicals, Bengaluru, India, was used as matrix with density of  $1.05 \text{ g/Cm}^3$ , ultimate tensile strength of 60 MPa, flexural strength of 130 MPa, and heat distortion temperature of  $125 \text{ }^\circ\text{C}$ . Graphite microparticles (supplied by Fenge Metallurgical, Bengaluru, India) of average grain size  $50 \text{ }\mu\text{m}$  with density of  $1.27 \text{ g/Cm}^3$ , compression strength of 20–200 MPa and flexural strength of 6.9–100 MPa are used as solid lubricant. Nano-particles of Copper oxide supplied by Nano Research Lab, Jharkhand, India was used as reinforcement. It is having an average particle size of 30–50 nm with specific surface  $>10 \text{ m}^2/\text{g}$ , true density of  $6.4 \text{ g/Cm}^3$  and atomic weight of  $79.54 \text{ g/mol}$ . The promoter used was dimethylacetamide with density of  $0.94 \text{ g/cm}^3$ , cobalt naphthalate with density of  $0.94 \text{ g/Cm}^3$  was used as accelerator and methyl ethyl ketone peroxide (MEKP) was used as catalyst with density of  $1.17 \text{ g/Cm}^3$ . The promoter, accelerator and catalyst are supplied by Naphtha Resins and Chemicals, Bengaluru, India. The ratio 10:2 by weight was taken for resin and hardener mixing.

### 2.2 Specimen Preparation

The composite specimens were prepared by hand lay-up method by taking different wt% of Gr and CuO particles. The calculated amount of fillers were preheated in an oven to remove the moisture content present in it and were uniformly dispersed in VE matrix. The uniform dispersion of micro-Gr into VE resin was done by using mechanical stirring machine for about 5 h. The mixture was placed in oven at  $85 \text{ }^\circ\text{C}$  for few minutes to remove the air bobbles entered during mixing. Then, catalyst (2.0 wt%) was added into the Gr-VE solution, which was degassed by stirring about for 2 minutes. Next, promoter (0.3 wt%) was added and mixed quickly. Then, the mixture was poured into prepared mould as shown in Fig. 1. At room temperature, the specimens were allowed to cure for 24 h in mould. The nano-CuO was uniformly dispersed into VE resin using bath-type ultrasonicator around 1 h. The temperature of the suspended solution which was increased during sonication process was cooled



**Fig. 1** Specimen fabrication

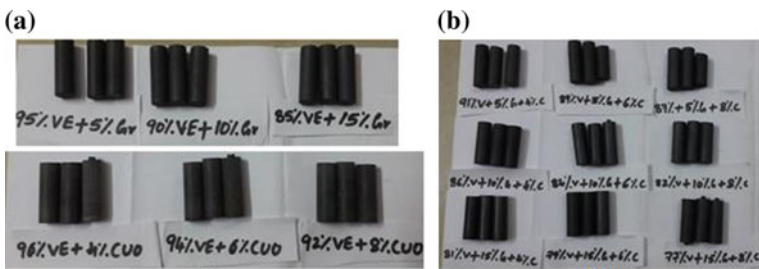


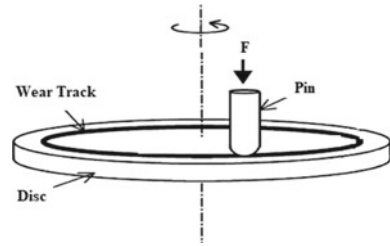
**Fig. 2** Specimens, **a** pure Gr/CuO-VE composites, **b** hybrid Gr-CuO-VE composite

down by dipping the solution in ice water bath. The next procedures are similar to those used for Gr/resin solution. In the preparation of hybrid Gr-CuO-VE composite, the selected amount of Gr was added to the VE resin. Then, the mixture was stirred using magnetic stirring followed by ultrasonic stirring by adding selected amount of nano CuO to it, rest all the procedures are similar to those used for both Gr/resin and CuO/resin. The prepared samples of size 30 mm height and 10 mm diameter are shown in Fig. 2.

### 2.3 Characteristics

To conduct a wear test, computerized pin-on-disc (Magnum make) type wear tester was used. Figure 3 shows the diagram (schematic) of POD type wear tester used in this work. The specimens for wear testing are prepared with a geometry 30 mm height and 10 mm diameter. The stainless steel EN31 disc served as counterpart whose surface was hardened and smoothly polished. The wear test was performed under ambient conditions at a sliding velocities 2, 3 and 5 m/s, with normal load of 30 N for a track radius of 0.04 m and sliding distance chosen was 1500 m. No. 600 super fine abrasive paper was used to abrade the disc surface before conducting each

**Fig. 3** Schematic diagram of pin-on-disc operator



test, then cleaned with acetone, followed by drying. The wear test data recorded were wear loss. Using Eq. (1) the specific wear rate were calculated,

$$K_s = \frac{\Delta m}{\rho * S * F} \quad (1)$$

where  $K_s$  = Specific wear rate in  $\text{m}^3/\text{N}\cdot\text{m}$ ,  $\Delta m$  = Mass loss in g,  $\rho$  = density of the composite in  $\text{g}/\text{Cm}^3$ ,  $S$  = Sliding distance in m and  $F$  = applied load in N.

The experiments were repeated for three times. The SEM (ZEISS SIGMA) was used to examine the worn surface of the pin sliding against disc. The worn surface of pin were coated with a platinum layer using rotary pumped coating system to increase the resolution of SEM observations. To understand the effect of filler loading and wear mechanism, the morphology of worn surfaces was studied.

### 3 Results and Discussion

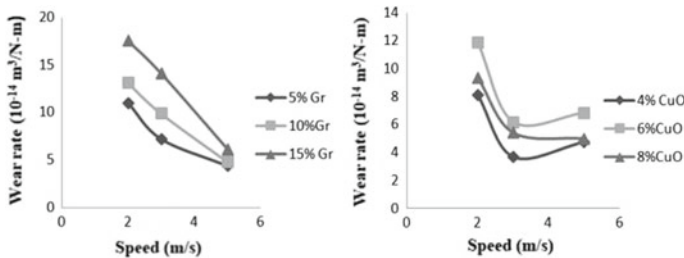
#### 3.1 Effect of Speed on Specific Wear Rate of the Composites

Table 1 represents the specific wear rate of different compositions of VE composites. The wear test was conducted under dry sliding condition at 2, 3 and 5 m/s with normal load of 30 N for a track radius of 0.04 m and a sliding distance of 1500 m. Improvement in the wear properties of VE composites was observed in case of solid lubricant Gr as a single filler. On the other hand, the nano-CuO was not showing improvement in wear properties as a single filler. The incorporation of nano-CuO in VE composites resulted in many effects on wear characteristics. The actual contact between pin and counterpart would be increases because of nanoparticle rolling effect, which resulted in higher wear rate. Another important effect of nanoparticle was abrasive wear which would deteriorate the wear characteristics of VE composite. Therefore, these effects would be responsible for ultimate wear. The addition of both Gr and CuO into VE matrix would result in synergistic effect which would result in adhesive wear. This adhesive wear is less dangerous than abrasive wear. Also, reaction between CuO and Fe are important parameter in improvement of wear parameters. Figure 4 shows shows the wear rate of Gr- and CuO-filled VE composite under dry sliding condition for different filler content with constant loading condition of 30



**Table 1** Different compositions of VE composite

Composition	Specific wear rate ( $10^{-14} \text{ m}^3/\text{N}\cdot\text{m}$ )		
	2 m/s	3 m/s	5 m/s
5%Gr	11.02	7.21	4.41
10%Gr	13.13	9.89	4.8
15%Gr	17.57	14.13	6.16
4%CuO	8.11	3.7	4.76
6%CuO	11.87	6.18	6.83
8%CuO	9.36	5.44	5.02
5%Gr + 4%CuO	10.54	5.05	2.69
5%Gr + 6%CuO	12.32	9.82	3.74
5%Gr + 8%CuO	11.36	7.7	2.76
10%Gr + 4%CuO	7.74	5.16	4.35
10%Gr + 6%CuO	9.28	6.29	5.39
10%Gr + 8%CuO	8.26	5.74	4.65
15%Gr + 4%CuO	8.96	4.33	5.25
15%Gr + 6%CuO	13.99	6.77	7.63
15%Gr + 8%CuO	10.24	4.7	6.74



**Fig. 4** Effect of speed on sp. wear rate of VE/Gr and VE/CuO composite

N. In VE-Gr composite, better wear resistance was observed as the sliding speed increases because of transfer film formation on the disc which intern act as barrier between pin and disc and thereby reduces the further loss of material. Because of abrasive wear in case of CuO filled VE composites, the nano particles are under rolling effect hence fresh surface comes in contact with counterpart which leads to loss of materials. It can be observed that the 4%CuO-filled VE composite exhibits lowest specific wear rate/highest wear resistance. This is mainly due to the uniform distribution of CuO in the composite. As the nanofiller loading increases in VE composite, the handling becomes difficult which leads to agglomeration of particle. This agglomeration induces defects in VE composites which intern deteriorate the wear properties.

Figure 5a–c illustrates the combined effect of CuO-Gr fillers on wear behaviour of VE composites. Figure 5a shows increase in wear rate as CuO filler content increases

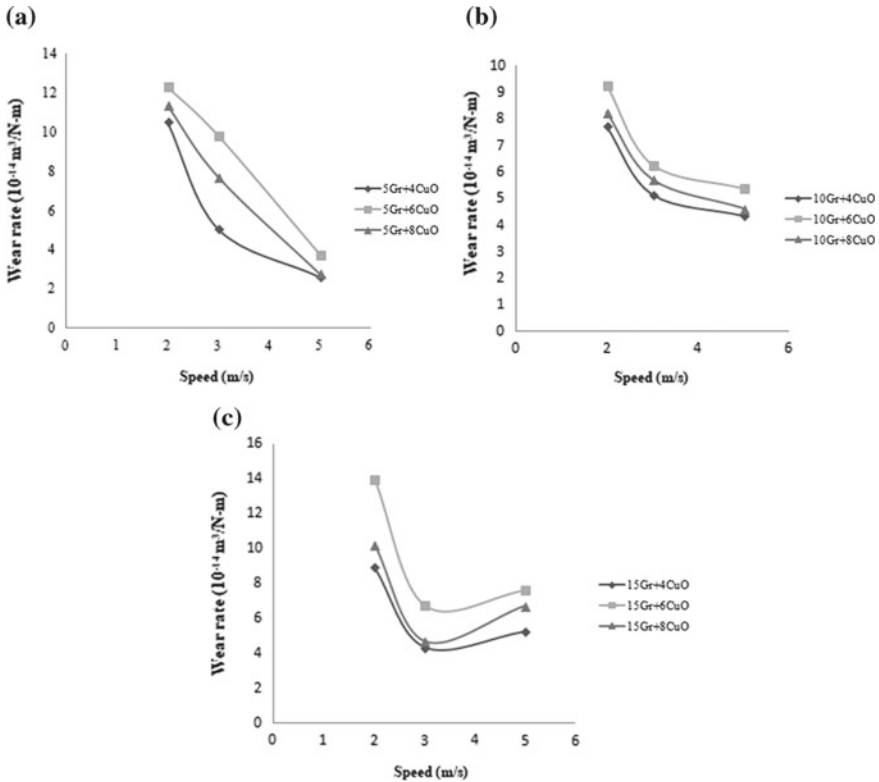


**Fig. 5** Effect of speed on sp. wear rate of **a** 5%Gr/CuO composite, **b** 10%Gr/CuO composite and **c** 15%Gr/CuO composite

in the VE-Gr-CuO composite. Uniform distribution of 4%CuO and 5%Gr into VE composite results in very low wear rate. It is also noted that as the sliding speed increases which induces the formation of transfer film thereby reduces further loss of material. Figure 5b shows VE/Gr composite reinforced with 4%CuO exhibits lowest wear rate or highest wear resistance. 10%Gr-4%CuO-reinforced VE composite exhibits highest wear rate when compared to 5%Gr-4%CuO-reinforced VE composite. This is because as the graphite content increases, the hardness of the composite increases, which in turn reduces the wear rate. It can be observed from the Fig. 5c VE composite reinforced with 15%Gr and 4%CuO exhibits lowest wear rate and 15%Gr-6%CuO reinforced VE composite exhibits highest wear rate. Further addition of Gr and CuO into the VE cannot be fabricated by hand lay-up technique.

Highest wear rate was observed for higher loading of individual fillers in VE composites at lower sliding speed. This is because of agglomeration of particles due to mutual attraction between them. But as the sliding speed increases, the wear debris acts as barrier between pin and disc and thereby slightly reduces the wear rate.

Figure 6 shows the specific wear rate of the 5%Gr-4%CuO-filled VE composite at a sliding speed of 5 m/s. It can be observed that the 4%CuO-reinforced VE composite

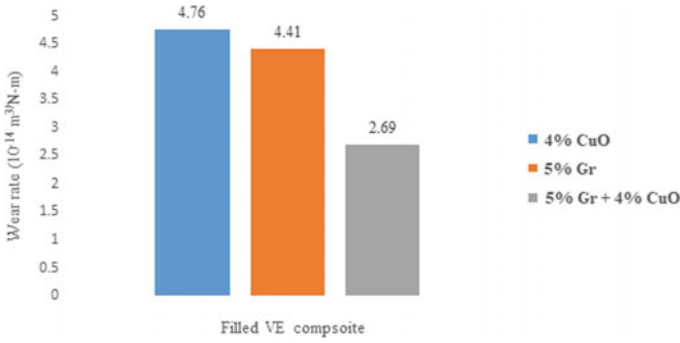


Fig. 6 Effect of different fillers on sp. wear rate of VE composite

exhibits highest wear rate while 5%Gr-reinforced VE composite exhibits slightly lesser wear rate. This is because the oxide layer formed at this speed range was thick. The synergistic effect of 5Gr and 4CuO resulted in lesser wear rate when compared with VE composite filled with 5%Gr and 4%CuO alone.

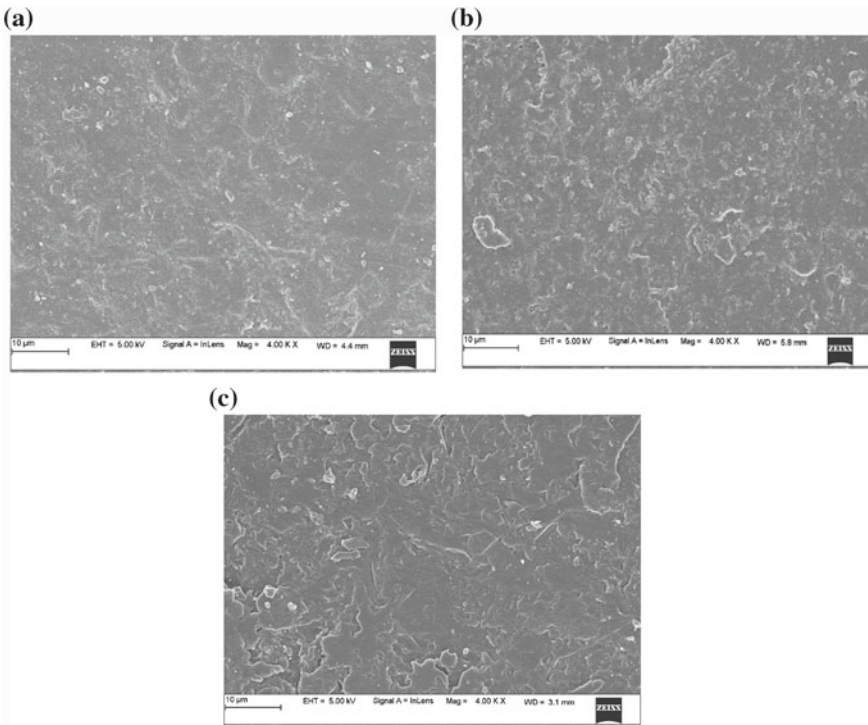
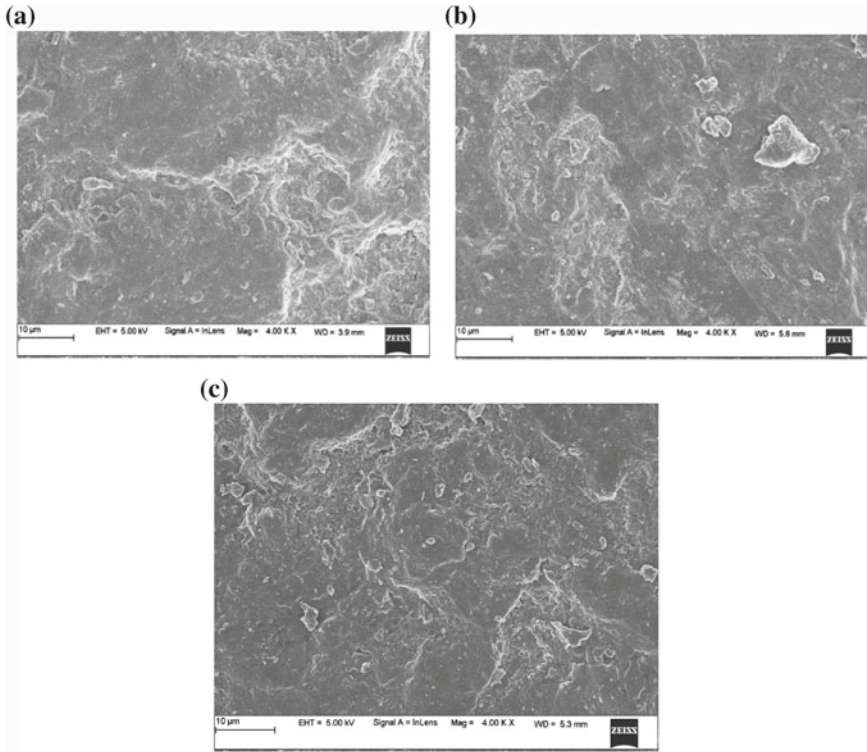


Fig. 7 Worn surface, SEM images of Gr/VE composites. a 5%Gr-VE; b 10%Gr-VE; c 15%Gr-VE



**Fig. 8** Worn surface, SEM images of nano-CuO VE composites. **a** 4%CuO-VE; **b** 6%CuO-VE; **c** 8%CuO-VE

SEM images of worn surface of filled composites are shown in Figs. 7, 8 and 9. The SEM images show the differences in the morphologies (surface) of VE composites loaded with different wt% of Gr and CuO Particles. The worn surfaces of Gr-VE were relatively smooth and thick transfer film was observed (Fig. 7a). Sever abrasion was observed in case of CuO-VE composites worn surface and VE debris was observed on the disc surface, which is in tern responsible for increase in the wear rate (Fig. 8a). The worn surface of micro-Gr and nano-CuO-filled VE composite was relatively smooth and very less scuffing was observed, and transfer film was relatively uniform and thus reduces the direct contact, hence reduces the wear rate (Fig. 9a).

In case of 10%Gr-6%CuO-VE composite, the abrasive and fatigue wear was observed in worn-out surface (Fig. 9b). With increase in sliding speed, the wear rate is increasing in case of 15%Gr-8%CuO-VE composite which is due to saviour abrasive wear which was characterised by rough surface of worn surface (Fig. 9c).

Direct contact between pin and disc can be avoided by developing a transfer film which is possible by the addition of 5%Gr and 4%CuO into VE composite owing to synergistic effect, which is corresponding for the better wear properties.

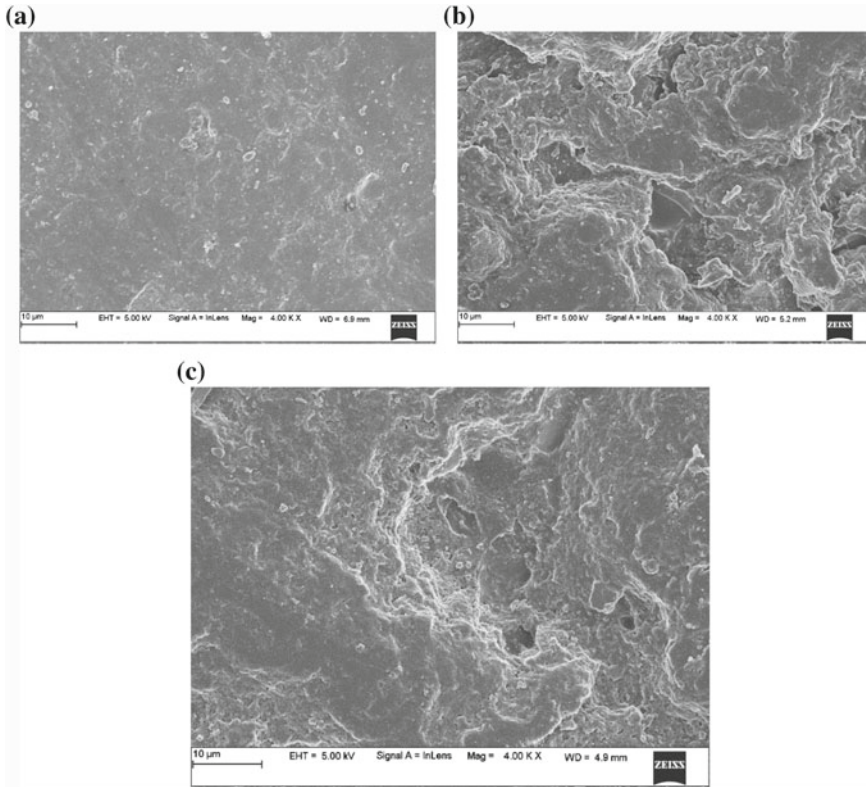


**Fig. 9** Worn surface and SEM images of Gr-CuO-VE composites. **a** 5%Gr-4%CuO-VE; **b** 10%Gr-6%CuO-VE; **c** 15%Gr-8%CuO-VE

## 4 Conclusions

The wear characteristics of micro-Gr, nano-CuO-filled and hybrid Gr-CuO-filled VE composites were investigated systematically in this work. The synergistic effects of the particles play an important role in changing and controlling the wear properties of filled composites. The addition of micro-Gr and nano-CuO together is most effective in changing the tribological properties of VE composites. The VE composites filled with particles exhibit worse wear property under higher filler loading and sliding speed. The 5%Gr-4%CuO showed uniform disruption of particle in VE matrix, which in turn responsible for better wear resistance under dry sliding condition.

## References

1. Vinson JR, Sierakowski RL (2002) The behaviour of structures composed of composites materials. New Jersey, USA, pp 155–200
2. Hollaway L (1995) Handbook of polymer composites for engineers, vols 24–28, 1st edn. Jaico Publishing House, Mumbai, pp 73–76
3. Friedrich K (1986) Wear of reinforced polymers by different abrasive counterparts. In: Friedrich K (ed) Friction and wear of polymer composites, vol 1, pp 233–287
4. Richardson GC, Sauer JA (1976) Effect of reinforcement on the mechanical properties of polypropylene composites. *Polym Eng Sci* 16(4):252–256
5. Bijwe J, Logani CM, Tewari US (1990) Influence of fillers and fiber reinforcement on abrasive wear resistance of some polymeric composites. *Wear* 138:77–92
6. Wang J, Gu M, Songhao B, Ge S (2003) Investigation of the influence of MoS<sub>2</sub> filler on the tribological properties of carbon fiber reinforced nylon 1010 composites. *Wear* 255:774–779
7. Guo Z, Pereira T, Choi O, Wang Y, Hahn HT (2006) Surface functionalized alumina nanoparticle filled polymeric nanocomposites with enhanced mechanical properties. *J Mater Chem* 16:2800–2808
8. Bahadur S (2000) The development of transfer layers and their role in polymer tribology. *Wear* 245:92–99
9. Donnet C, Erdemir A (2004) Historical developments and new trends in tribological and solid lubricant coatings. *Surf Coat Technol* 180:76–84
10. Teer DG (2001) New solid lubricant coatings. *Wear* 251:1068–1074
11. Zhang XR, Pei XQ, Wang QH (2009) Friction and wear studies of polyimide composites filled with short carbon fibers and graphite and micro SiO<sub>2</sub>. *Mater Des* 30:4414
12. Bahadur S, Gong D, Anderegg JW (1993) Tribochemical studies by XPS analysis of transfer films of nylon 11 and its composites containing copper compounds. *Wear* 165:205–212
13. Bahadur S, Gong D, Anderegg J (1996) Investigation of the influence of CaS, CaO, and CaF<sub>2</sub> fillers on the transfer and wear of nylon by microscopy and XPS analysis. *Wear* 197:271–279
14. Bahadur S, Gong D (1993) The investigation of the action of fillers by XPS studies of the transfer films of PEEK and its composites containing CuS and CuF<sub>2</sub>. *Wear* 160:131–138
15. Wang Q, Zhang X, Pei X (2010) A synergistic effect of graphite and nano-CuO on the tribological behavior of polyimide composites. *J Macromol Sci Part B Phys* 50(2):213–224
16. Wang QH, Wang QH, Xu JF, Xue QJ (1997) The effect of nanometer SiC filler on the tribological behaviour of PEEK. *Wear* 209:316
17. Wang QH, Xu JF, Shen WC, Liu WM (1996) An investigation of the friction and wear properties of nanometer Si<sub>3</sub>N<sub>4</sub> filled PEEK. *Wear* 196:82
18. Wang QH, Xue QJ, Shen WC, Liu HW, Xu JF (1996) The effect of particle size of nanometer ZrO<sub>2</sub> on the tribological behaviour of PEEK. *Wear* 198:216
19. Wang QH, Xue QJ, Shen WC (1997) The friction and wear properties of nanometer SiO<sub>2</sub> filled PEEK. *Tribol Int* 30:193
20. Xu W, Wu F, Jiao Y, Liu M. A general micromechanical framework of effective moduli for the design of non-spherical nano and micro-particle reinforced composites with interface properties. <https://doi.org/10.1016/j.matdes.2017.04.075>
21. Sarlin E, Lindgren M, Suihkonen R, Siljander S, Kakkonen M, Vuorinen J (2015) High-temperature slurry erosion of vinyl ester matrix composites—the effect of test parameters. *Wear* 328:488–497

# Experimental Modeling of EDMed Aluminum Metal Matrix Composite: A Review



Rama Nand Yadav, Rajesh Kumar Porwal and J. Ramkumar

**Abstract** Electrical discharge machining is uttermost exploited material removal process broadly used in manufacturing industries for variegate shapes and difficult-to-machine electrically conductive materials. The nascent materials such as metal matrix composites, ceramic composites, duplex stainless steels, and titanium alloys have a vast demand in the area of automobiles, aircraft, aerospace, railways, and micro industries. The machining of these materials using conventional machining process is bonded to linear cutting to overcome this problem EDM was introduced. Many researchers have presented a vast work to understand the material removal mechanism of EDM and conclude that machining performance is mostly affected by process parameters. The machining performance can predict in appropriate way using process modeling techniques. The process modeling of materials like carbon nano-tube reinforced MMC is still needed a lot of research work. This paper includes review of AMC machining and experimental modeling using various methods such as RSM and ANN.

**Keywords** Electrical discharge machining (EDM) · Metal matrix composite (MMC) · Aluminum metal matrix composite (AMC) · Artificial neural network (ANN) · Response surface method (RSM)

## 1 Introduction

Metal matrix composites are known as real engineering materials. They are obtained from composite materials with at least two constituent segments. The high strength material such as SiC and Al<sub>2</sub>O<sub>3</sub> are reinforced into a metal to produce MMC materials. The resulting materials have properties such as higher strength, good stiffness, better temperature capability, and better radiation resistance. Consistently, MMC materials

---

R. N. Yadav · R. K. Porwal (✉)  
Faculty of Mechanical Engineering, Shri Ramswaroop Memorial University, Lucknow, India  
e-mail: [porwal.me@srmu.ac.in](mailto:porwal.me@srmu.ac.in)

J. Ramkumar  
Department of Mechanical Engineering, IIT Kanpur, Kanpur, India

© Springer Nature Singapore Pte Ltd. 2020  
L. Vijayaraghavan et al. (eds.), *Emerging Trends in Mechanical Engineering*,  
Lecture Notes in Mechanical Engineering,  
[https://doi.org/10.1007/978-981-32-9931-3\\_49](https://doi.org/10.1007/978-981-32-9931-3_49)

in which AMC materials are fulfilling the applications in the field of space, electrical, and automotive industries to make the products like space shuttle orbiter frames, rib truss member, automotive disc-brakes, drive-shaft, engines, electronic packing, integrated circuit, and dielectric substance because of their significant advance properties such as high wear impedance, better strength, high temperature wear capability and low density. The machining of AMC materials is difficult by conventional process because of their hard and abrasive nature. Hence, EDM is a more appropriate machining technique for AMC as there is no direct contact between electrodes and material is removed by thermal erosion due to which problems like stresses, vibrations, and chatters are not generated in case of electric discharge machine [1, 2].

In the present era, manufacturing industries demand precise and higher performance under minimum time in order to sustain their position in the global market competition including customer satisfaction. If we talk about EDM, the most popular and versatile non-conventional method compare to the others, provide more precise efficiency during machining of advance manufacturing metals. In EDM process, machining takes place through spark erosion between electrodes. The erosive impact of the electric discharges concept was found by English scientist Joseph Priestly during 1770s, with this research electrical discharge machining process started. Further, B. R. Butinzky and Lazarenko, scientists from Russia derived a controlled process of electrical discharge that prevent unwanted erosive during EDM. The introduction of CNC program in electrical discharge machine provided appropriate improvement in the field of machining [3]. The schematic diagram of electrical discharge machining process with its components is presented in Fig. 1. This process has also some drawbacks such as low MRR and surface quality, to resolve this some researchers presented new concepts such as powder-mixed EDM, tool and workpiece rotation, and vibrational EDM [4–6].

EDM is a thermal electrical process in which potential difference is developed between electrodes as shown in Fig. 2. The machining of workpiece is done with the help of generated electric spark between spark gap. As the space portion between electrodes are getting smaller, the strength of potential difference getting stronger and stronger as shown in figure.

At some point, critical value is achieved then dielectric medium got broken due to excessive value of electric field strength and spark generated. As the spark developed, a high pressure and high-temperature plasma channel are formed that helps to melt

**Fig. 1** Graphical representation of EDM process [5]

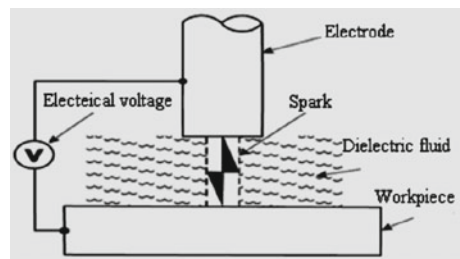
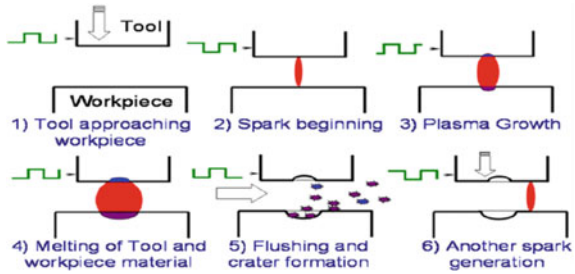




**Fig. 2** EDM process mechanism [7]



and evaporate of both electrodes surface. The duration of each spark is very short while frequency for each spark is very high as thousands spark per second. The material is removed in crater form from machined portion and crater size depends upon the volume of current. From the previous study, it is found that crater size is increased with the increase of discharge.

There are various parameters in EDM such as pulse on time, pulse off time, arc gap, peak current, voltage, polarity, flushing pressure, tool geometry, tool material, and rotation of electrodes that are basically utilized for improving material removal rate, surface quality, and lowering tool wear rate [8, 9]. The techniques such as grey rational analysis, neural network, genetic algorithm, artificial bee colony optimization, and fuzzy set theories are used for performance measurement of EDM [10–12]. Variants of EDM are vibration assisted EDM, electrochemical discharge machining, electrical discharge grinding, and electrical discharge coating are also introduced for high performance of EDM [13, 14]. The objective of this literature survey is to highlight the work that has been done for modeling of EDMed AMC and to conclude various approaches that are going on for modeling purpose.

## 2 Research Developments of Aluminum Metal Matrix Composite Materials

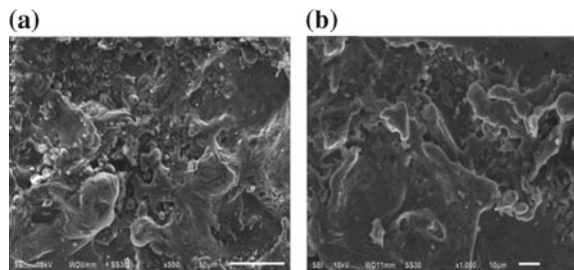
AMC is the advanced developed engineering materials and widely used in manufacturing field due to their smart qualities. Researchers have done significant work for the improvement of machining performance for AMC materials. The use of nanoparticles into dielectric fluid, rotary motion techniques, vibrational machining, RSM methodology, and ANN models are the latest trends about EDM machining process. A brief literature survey about development in the research field of EDM process is discussed below.

Electrical discharge machining of AMC was performed with brass as tool material in kerosene dielectric fluid by Narendra et al. They used current,  $T_{on}$ , and flushing as input parameters for the observation of material removal and TWR. They found that maximum value of input parameters provides higher MRR but tool wear was also high than MRR at higher current setting [15]. Singar et al. experiment was on

hybrid metal matrix composite (Al/SiCp/B4Cp) material using electric discharge diamond peripheral surface grinding to study the behavior of MRR and SR. They found a 289% improved MRR with increasing spark current at 20  $\mu\text{s}$   $T_{\text{on}}$ . They also found that SR and MRR was affected by  $T_{\text{on}}$ ,  $T_{\text{off}}$ , grit number, and wheel speed [16]. Pramanik conducted an experiment on 10 vol% 700 nm SiCp reinforced 6061 aluminum alloy MMC material using wire-EDM process. They used a 0.25 mm diameter zinc-coated brass wire for the experiments. The kerf width, SR, and wire wear were the performance parameters, whereas the input parameters such as wire speed, flushing rate, open-circuit voltage, and servo voltage were fixed. On the other hand wire tension and  $T_{\text{on}}$  were varying during the experiment. He observed that MRR improved with increasing value of  $T_{\text{on}}$ . Further, they revealed that shorter  $T_{\text{on}}$  provides better SR at lower wire tension and longer  $T_{\text{on}}$  provides better SR at higher wire tension. Further, he found that increase in  $T_{\text{on}}$  increases the both top and bottom kerf width [17]. An experimental study for PMEDM on AA6061/10%SiC composite was conducted by Balbir et al. for surface characteristics using  $T_{\text{on}}$ , current and gap voltage as input parameters. They found that SR directly affected by input parameters and best surface finish was obtained at 50 V gap voltage, 1–3 A current, with 60–90  $\mu\text{s}$   $T_{\text{on}}$  and 90–100  $\mu\text{s}$   $T_{\text{off}}$ . They explained the existence of C and W in recast layer at EDMed surface. They also observed a reduction in recast layer during powder-mixed EDM from 54.67 to 47.5  $\mu\text{m}$  as compare to normal EDM as shown in Fig. 3. According to them, the hardness of powder-mixed EDMed surface increased as white recast layer thickness got reduced during machining [18].

Mohinder et al. used wire-EDM for the machining of ZrSiO<sub>4</sub>p/6063 aluminum MMC. A 0.25 mm diameter brass tool electrode and deionized water as dielectric medium were used for experiments. The input parameters used to conclude their influences at dimensional deviation (DD). They observed that an increased in  $T_{\text{on}}$  and peak current increased the DD, whereas there was not any remarkable effect of  $T_{\text{off}}$  and servo voltage on DD [19]. Satish et al. presented an experiment on Al6063 composite material reinforced with SiCp with 5, 10, and 15% volume fractions using wire-EDM. The input parameters were investigated to observe the performance parameters such as MRR and SR. An L9 orthogonal array was used for the experiment design. They found that increasing value of SiC vol% results reduction in MRR and improvement in SR. They also found that the increasing value of  $T_{\text{on}}$  due to higher intensity of the spark during machining provides higher MRR [20]. An experiment

**Fig. 3** Machined zone micrograph by SEM, **a** normal EDM and **b** powder-mixed EDM [18]



was explored for wire-EDM of Al/SiC material reinforced with 20% SiC particulate by Patil and Brahmankar. A coated 0.25 mm diameter brass tool wire was used in machining. The process parameters such as  $T_{on}$ ,  $T_{off}$ , wire tensions, flushing, ignition pulse current, and speed of wire were observed for material removal and SR. They found a higher cutting speed required for unreinforced alloy as compared to reinforced alloy, while SR was superior in reinforced alloy. They also revealed that wire breakage was reduced because of more  $T_{on}$  and flushing pressures [21]. An experimental work was conducted for wire-EDM of MMC materials to investigate the machining feed rate and SR by Rozenek et al. They observed that as current increases the value of feed rate and SR increases, but decreasing value of voltage dominates the feed rate and SR slowly. They also observed that higher  $T_{on}$  value provided a higher value of feed rate and SR. According to them, the cutting speed was 3 and 6.5 times lower in SiC and Al<sub>2</sub>O<sub>3</sub>-based MMC machining, respectively on comparing to aluminum alloy [22]. An experiment was conducted using EDM for 15 vol% and 25 vol% SiC whisker/2124 AMC materials to observe the behavior of material removal and SR by Ramula et al. They used brass and copper as tool electrode materials and Cutzol EDM 220-30 fluid as a dielectric medium for experimental investigation. They observed that brass electrode provide 5–10% more MRR than copper electrode. Further, they conclude that MRR was higher in 25 vol% SiC AMC during brass electrode than using copper electrode while machining time was more in 15 vol% SiC whisker/2124 Al. They also observed that fast cutting speed provide micro-damage at machined surface and slow speed cutting provide soft surface [23].

### 3 Experimental Modeling of EDM of AMC Materials

EDMed of AMC modeling by means of mathematical techniques provide an appropriate way to relate the machining performance. Modeling techniques such as RSM methodology, grey relational techniques, Taguchi method, principal component analysis (PCA), and ANN helps to predict the performance parameters such as surface roughness, MRR, TWR, and also the discharge phenomena of EDM. Automatically optimum conditions can be generate at high precise with the help of adaptive control system. A brief discription of EDM machined AMC materials modeling conducted by various researchers is presented below.

A mathematical model was developed for machining of aluminum SiC composite materials using EDM by Dhar. They used rotatable second-order CCD. The process parameters like  $T_{on}$ , peak current, gap voltage, and the vol% of SiC were considered for MRR, TWR, gap size, and SR. From the ANOVA analysis, they observed that as  $T_{on}$  and peak current increase the MRR got increased, on the other hand increases in SiC percentage and gap voltage reduced MRR. Further, they found that an increase in both  $T_{on}$ , and peak current increases TWR, but an increase in SiC% and gap voltage provides low TWR. They also found that SR got increased with the increase of  $T_{on}$ , SiC%, peak current, and gap voltage [24]. Pragya et al. presented RSM and ANN-based mathematical modeling for AMC using wire-EDM. The parameters

like servo voltage,  $T_{on}$ ,  $T_{off}$ , and wire feed rate for the cutting speed of EDM were selected for machining. They found that the prediction of ANN models was more precise than RSM models. There was three time less error in ANN models. They observed that voltage influenced more on average cutting speed than  $T_{off}$  and wire feed rate [25]. A mathematical modeling work of AMC machining was proposed by Karthikeyan et al. using EDM. They investigated the influence of vol% of SiC, current and  $T_{on}$  for electrodes wear rate and SR. They found that output parameters are mostly influenced by the vol% of SiC,  $T_{on}$  and current. According to them, as current increased material removal rate increased and decreased with increase in vol% of SiC and  $T_{on}$ . On other hand, tool wear was increased with an increase in current and vol% of SiC, but decreased in higher  $T_{on}$ . They also found that SR was improved with improve in current, vol% of SiC and  $T_{on}$  [26].

A FEA-based model for EDMed AMC material was developed by Vishwakarma et al. to analyze the temperature distribution and material removal effect. They made a comparison between the predicted and experimental value of MRR and found an appropriate agreement between them. They also observed that material removal during second discharge was better as compare to single discharge. According to them, there was higher temperature during machining of workpiece still that was not enough to melt reinforced materials so materials got evacuated without melting. Further, they revealed that presented developed model would be useful to obtain residual and thermal stress distribution mechanism of particles reinforcement [27]. Dabade et al. derived optimization using Taguchi-based GRA method to improve SR of AMC material workpiece. They optimize the parameters like cutting forces, SR, residual stresses, and microhardness. As a result, they found an enhanced surface quality of machined specimen at 0.8 mm-tool nose radius, 0.05 mm/rev-feed rate, 40 m/min-cutting speed, and 0.2 mm-cutting depth [28].

Velmurugan et al. used rotatable CCD for experiments and least-squares technique to obtain the regression coefficients for their proposed model. They also used ANOVA and SEM for analysis of experiments. They observed that MRR increases with increase in current,  $T_{on}$ , and flushing, but decreases with increase in voltage. In case of tool wear, the increase value of current and voltage, improve the wear ratio and increased  $T_{on}$  decreases it. They also observed that machined SR increases with increase in current,  $T_{on}$ , voltage, and flushing [29]. Wang et al. worked on the blind hole drilling of AMC using rotary EDM using Taguchi method. They confirmed that copper material electrode with an eccentric through hole using injection flushing performance was the best compared to stationary solid electrode and rotary solid electrode. According to them either polarity or peak current mostly affected electrodes wear rate and surface quality [30]. Rajesh et al. consist a setup of EDM mounted with rotary tool attachment for machining of 6061Al/Al<sub>2</sub>O<sub>3</sub>. They observed that electric discharge surface grinding provides more surface finish as compare to EDM, they also found that SR increases with increase in  $T_{on}$ , peak current and abrasive particle concentration of tool. Further, they conclude that best surface finish can be obtained at peak current 3 A, polarity negative,  $T_{on}$  60  $\mu$ s,  $T_{off}$  15  $\mu$ s, abrasive particle size 220 mesh, abrasive particle concentration 5%, and speed 1400 rpm [31].

## 4 Conclusion

A lot of researches have been done in the field of EDM, although seldom literatures are available on modeling of EDMed AMC. The outcomes of present work are as:

- From the survey it is found that the most modeling researches are focused only on aluminum MMC materials. Therefore, a lot of scope is available in other MMCs such as magnesium, titanium, and copper metal matrix composites for further research.
- The most modeling researches are focused on optimization of EDMed AMC rather than prediction of performance parameters. Therefore, modeling of EDMed AMC has lots of scope to work upon.
- In the current scenario, RSM and ANN are the most used methodology for the modeling of EDM. From the present review work, it is also found that ANN is the most precise method comparing to other modeling methods.

## References

1. Teti R (2002) Machining of composite materials. *CIRP-Ann Manuf Technol* 51:611–634
2. Abhay SG, Nilesh GP (2018) Wire-electro discharge machining of metal matrix composites: a review. *Procedia Manuf* 20:41–52
3. Abulais S (2014) Current research trends in electric discharge machining (EDM). *Int J Sci Eng Res* 5:100–118
4. Ho KH, Newman ST (2003) State of the art electrical discharge machining (EDM). *Int J Mach Tools Manuf* 43:1287–1300
5. Elman JC (2001) Electro discharge machining. *Soc Manuf Eng (SME)*
6. Anand P, Shankar S (2010) Current research trends in variants of electrical discharge machining: a review. *Int J Eng Sci Technol* 2(6):2172–2191
7. Rajurkar KP, Levy G, Malshe A, Sundaram MM, Mc Geough J, Hu X, Resnick R, DeSilva A (2006) Micro and nano machining by electro-physical and chemical processes. *CIRP-Ann Manuf Technol* 55:643–666
8. Shivam G, Ambesh J, Ravi P (2016) Optimization of process parameters in electro-discharge machining using Taguchi method. *Carbon* 100:0–14
9. Goyal S, Ravi S (2014) Parametric study of powder mixed EDM and optimization of MRR & surface roughness. *Carbon* 100:0–43
10. Kuo Y, Yang T, Huang GW (2008) The use of grey relational analysis in solving multiple attribute decision-making problems. *Comput Ind Eng* 55(1):80–93
11. Haykin S, Network N (2004) A comprehensive foundation. *Neural Netw* 2:41
12. Klocke F, Beck T, Hoppe S, Krieg T, Müller N, Nöthe T, Raedt HW, Sweeney K (2002) Examples of FEM application in manufacturing technology. *J Mater Process Technol* 120(1–3):450–457
13. Shih HR, Shu KM (2008) A study of electrical discharge grinding using a rotary disk electrode. *Int J Adv Manuf Technol* 38(1–2):59–67
14. Gupta K, Jain NK, Laubscher RF (2016) Assisted hybrid machining processes. In: *Hybrid machining processes*. Springer, Berlin, pp 45–65
15. Singh PN, Raghukandan K, Rathinasabapathi M, Pai BC (2004) Electric discharge machining of Al-10%SiCp as-cast metal matrix composites. *J Mater Process Technol* 155–156:1653–1657

16. Yadav RS, Yadava V (2017) Experimental investigations on electrical discharge diamond peripheral surface grinding (EDDPSG) of hybrid metal matrix composite. *J Manuf Process* 27:241–251
17. Pramanik A (2015) Electrical discharge machining of MMCs reinforced with very small particles. *Mater Manuf Process* 31(4):397–404
18. Balbir S, Jatinder K, Sudhir K (2014) Experimental investigation on surface characteristics in powder-mixed electro discharge machining of AA6061/10% SiC composite. *Mater Manuf Process* 29(3):287–297
19. Sharma A, Garg MP, Goyal KK (2014) Prediction of optimal conditions for WEDM of Al 6063/ZrSiO<sub>4</sub> (p) MMC. *Procedia Mater Sci* 6:1024–1033
20. Satishkumar D, Kanthababu M, Vajjiravelu V, Anburaj R, Sundarrajan NT, Arul H (2011) Investigation of wire electrical discharge machining characteristics of Al6063/SiCp composites. *Int J Adv Manuf Technol* 56:975–986
21. Patil NG, Brahmkankar PK (2010) Determination of material removal rate in wire electro-discharge machining of metal matrix composites using dimensional analysis. *Int J Adv Manuf Technol* 51:599–610
22. Rozenek M, Kozak J, Dabrowski L, Łubkowski K (2001) Electrical discharge machining characteristics of metal matrix composites. *J Mater Process Technol* 109(3):367–370
23. Ramula M, Taya M (1989) EDM machinability of SiCw/Al composites. *J Mater Sci* 24:1103–1108
24. Dhar S, Purohit R, Saini N, Sharma A, Kumar GH (2007) Mathematical modeling of electric discharge machining of cast Al-4Cu-6Si alloy-10 wt.% SiCp composite. *J Mater Process Technol* 194:24–29
25. Pragya S, Jain PK, Jain NK (2013) RSM and ANN modeling approaches for predicting average cutting speed during WEDM of SiCp/6061 Al MMC. *Procedia Eng* 64:767–774
26. Karthikeyan R, Lakshmi NPR, Naagarazan RS (1999) Mathematical modeling for electric discharge machining of Al-silicon carbide particulate composites. *J Mater Process Technol* 87:59–63
27. Vishwakarma UK, Dvivedi A, Kumar P (2012) FEA modeling of material removal rate in electrical discharge machining of Al6063/SiC composites. *Int J Mech Aero Eng* 6:398–403
28. Dabade UA (2013) multi objective process optimization to improve surface integrity on turned surface of Al/SiCp metal matrix composites using grey relational analysis. *Procedia CIRP* 7:299–304
29. Velmurugan C, Subramanian R, Thirngnanam S, Ananadavel B (2011) Experimental investigations on machining characteristics of Al-6061 hybrid metal matrix composites processed by electrical discharge machining. *Int J Eng Sci Technol* 8(3):87–101
30. Wang CC, Yan BH (2000) Blind hole drilling of Al<sub>2</sub>O<sub>3</sub>/6061Al composite using rotary electro-discharge machining. *J Mater Process Technol* 102:90–102
31. Choudhary R, Kumar H, Singh S (2018) Experimental investigation on surface characteristics in electrical discharge surface grinding (EDSG) of 6061Al/Al<sub>2</sub>O<sub>3p</sub> 10% composite. *Adv Mater Process Technol* 1–24

# Numerical Simulation of Transient Temperature and Stresses During Friction Stir Welding of AA 7075 T651



Md. Parwez Alam and A. N. Sinha

**Abstract** A three-dimensional finite element model has been developed by using ANSYS APDL to study of transient temperature distribution and von Mises stresses during friction stir welding of AA 7075 T651. A cylindrical tool on the workpiece is created. A pilot node has defined on the tool for governing the rotational and translational speed of the tool. Heat is generated due to frictional contact and plastic deformation of the workpiece. Temperature-dependent material properties and friction coefficient were considered in this model. The cooling effect caused by the free convection in ambient air, backing plate and clamping bar is taken into account. It has been observed that temperature profile below the moving tool is an oval shape. It had also observed that the maximum value of von Mises stress has little variation during welding.

**Keywords** Friction stir welding · Temperature · ANSYS · Von Mises stress · Aluminium alloy

## 1 Introduction

Friction stir welding (FSW) was invented in 1991 by Wayne Thomas and his colleagues for joining of lightweight metal [1]. At that time, 2xxx and 7xxx series of aluminium alloy were considered impossible to weld by conventional welding. But, it had found easily weldable by FSW. Now, it is proven suitable joining process of metals, polymers, metal matrix composites and dissimilar materials. So, it is frequently used in several industries. Some examples of the application fields, where FSW mostly used are aerospace, railway, automotive and shipbuilding. For

---

Md. P. Alam (✉) · A. N. Sinha  
Mechanical Engineering Department, National Institute of Technology Patna, Ashok Rajpath  
Patna, Patna 800005, India  
e-mail: [parwez.me13@nitp.ac.in](mailto:parwez.me13@nitp.ac.in)

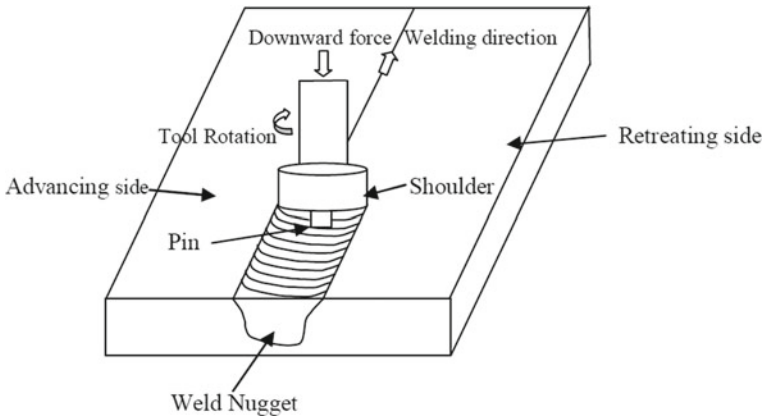


**Fig. 1** Schematic representation of FSW [7]

any welding processes, proper heat input is primary factor for sound welding. Various process parameters are responsible for heat generation in friction stir welding. Heat distribution is also considered as a key factor for joint quality. It depends on environment condition and cooling rate. Many researchers have been working in the area of numerical, analytical and experimental studies to predict temperature, stress and material flow in welding processes. Numerical modelling is assumed as an efficient tool to understanding the complex phenomena in welding. It does not only save time and money but also helps in temperature measurement in stir zone. Schematic representation of FSW is shown in Fig. 1.

Friction stir welding was considered fully coupled thermomechanical process due to severe plastic deformation [2] and strength of material decrease when temperature increases [3]. Zhang et al. [4] developed a 3D model by considering contact condition between tool and workpiece during FSW and reported that heat is mainly generated within the region close to the shoulder. Sun et al. [5] developed a 3D computational fluid dynamics model and determined heat generated at the tool–workpiece interface by interfacial friction stress. Shi and Wu [6] developed a model to study heat transfer during different stages in FSW, and they reported that peak temperature reached in plunge stage, peak temperature decreases monotonically in dwell stage and attained quasi-steady state in welding stage.

## 2 Description of Numerical Simulation

Two rectangular plates with dimension 52 mm × 45 mm × 3 mm were created and meshed. For accurate results, finer mesh is created along the weld line. The total number of nodes and elements are 6481 and 6453, respectively. A rigid tool, without the pin is created on the weld joint. In this model, thermophysical properties



**Table 1** Thermophysical property of workpiece

Workpiece property	Elastic modulus (GPa)	Poisson's ratio	Coefficient of thermal expansion ( $^{\circ}\text{C}^{-1}$ )
AA7075 T651	71.1	0.33	$25.2 \times 10^{-6}$

**Table 2** Thermophysical property of tool

Tool property	Elastic modulus (GPa)	Poisson's ratio	Thermal conductivity (W/mC)	Specific heat (J/KgC)	Density ( $\text{Kg/m}^3$ )
H13	210	0.3	24.4	460	7750

of AA7075 T651 are considered. Thermal conductivity, specific heat and density are considered as temperature-dependent, and Poisson's ratio and the coefficient of thermal expansion are considered as temperature-independent properties in this model. Tables 1 and 2 show material property of tool and workpiece.

It is also assumed that the workpiece behaves as rate-independent plastic material. In this analysis, 3D 20-node couple field element SOLID226 was selected because it is capable of large deflection, large strain capabilities, plasticity and stress stiffness. For contact pair, element CONTA174 and element TARGE170 are used [8]. A pilot node is also created on the top surface of the tool for governing welding speed and rotational speed. Detail of FSW modelling is shown in Fig. 2 as a flowchart.

## 2.1 Governing Equation

In friction stir welding, heat is generated by friction plastic deformation, whereas heat transfer during friction stir welding is a typical nonlinear instant heat conduction process which is governed by Fourier law of heat conduction. It is expressed as Eq. (1)

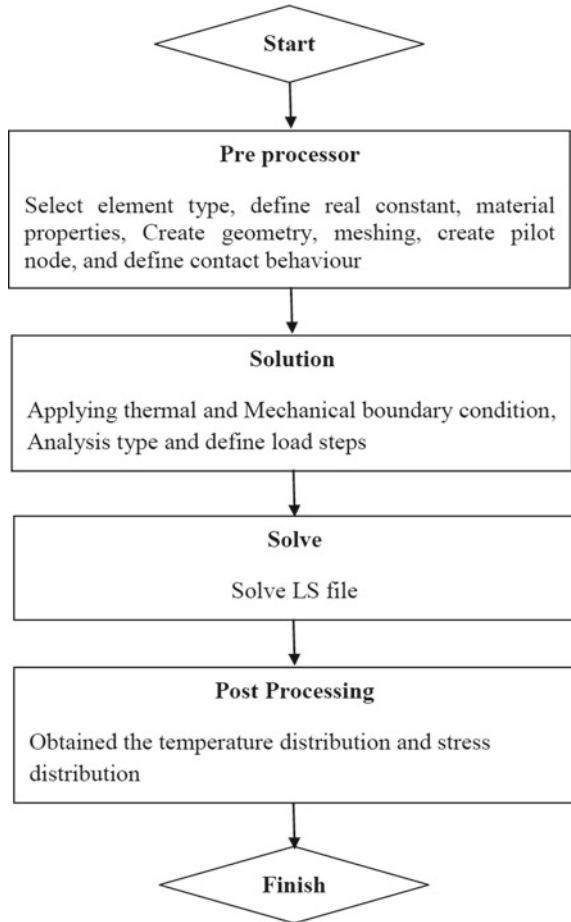
$$\frac{\partial}{\partial x} \left( K_x \frac{\partial T}{\partial x} \right) + \frac{\partial}{\partial y} \left( K_y \frac{\partial T}{\partial y} \right) + \left( K_z \frac{\partial T}{\partial z} \right) + \dot{Q} = \rho C_p \left( \frac{\partial T}{\partial t} \right) \quad (1)$$

where  $\rho$ ,  $C_p$ ,  $K$  and  $\dot{Q}$  represent density, specific heat, directional thermal conductivity and rate of heat generation, respectively.

In the present simulation only convective heat transfer is considered. The heat loss from free surfaces of workpiece and tool are calculated as Eq. (2)

$$q = h_{\text{conv}}(T - T_0) \quad (2)$$

**Fig. 2** Flowchart for modelling of FSW



where  $T$ ,  $T_0$  and  $h_{conv}$  refer absolute workpiece temperature, ambient temperature and convection coefficient of workpiece and tool. Value of heat transfer coefficient for aluminium alloy to air is taken  $30 W/m^2$ . Heat loss through backing plate and clamping bar is also considered as convection loss with high convection coefficient. In this model, heat transfer coefficient is taken  $100 W/m^2$  and  $300 W/m^2$  for clamping bar and backing plate, respectively.

The mechanical boundary condition applied as clamping bar on the plate and bottom support. The bottom portion of the workpiece is a constraint in the normal direction and taken  $U_z = 0$ , whereas the clamped portion is taken as a complete restraint as real; i.e., there is no movement in any direction.  $U_x = U_y = U_z = 0$  is applied. Figure 3 shows the mechanical and thermal boundary condition.

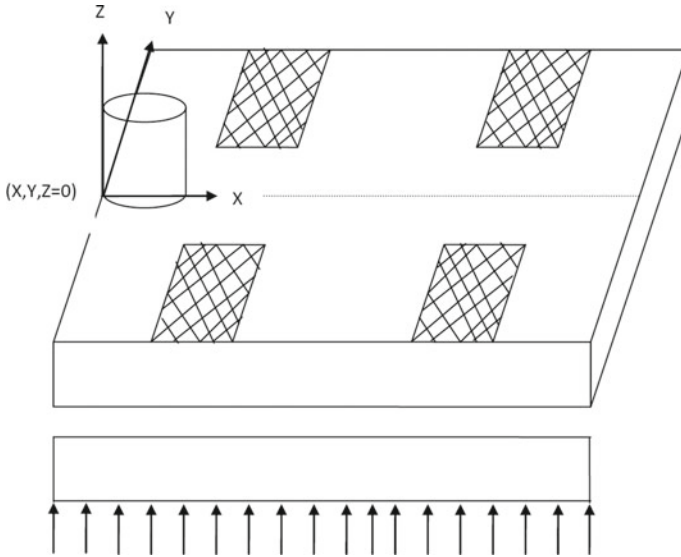


**Fig. 3** Boundary condition of FSW

### 3 Result and Discussion

In the present study, ANSYS APDL has been using for transient thermal analyses and von Mises stress. Total five load steps were defined. It contains plunge stage, dwell or preheat stage, travel or welding stage, tool plunge out stage and cooling stage. Figure 4a, b show temperature distribution in the workpiece. In this figure, it observed the oval shape of the weld zone.

Figure 5 shows the temperature distribution profile which is obtained from numerical simulation. In the current analysis, three different locations are chosen. These locations are 7.8, 16 and 23 mm from weld line. It was observed that the peak temperature achieves in dwell stage and then it decreases. The peak temperature at a distance 7.8 mm away from the weld line is 490 °C.

ANSYS provides two methods for heat stress analysis, the direct method and the indirect method [9]. In this analysis, direct method is applied. Figure 6 shows von Mises stresses at 9.98 s, and maximum stresses were found near the tool region due to thermal stress and by structural loading. In this region, compressive stress is generated due to thermal expansion and contraction by the clamping fixture.

Stresses also are found near the clamping region due to contraction in the cooling stage, but it is restricted by clamping fixture. From Fig. 7, it can be seen that stresses near the clamping region are more than those of Fig. 6.

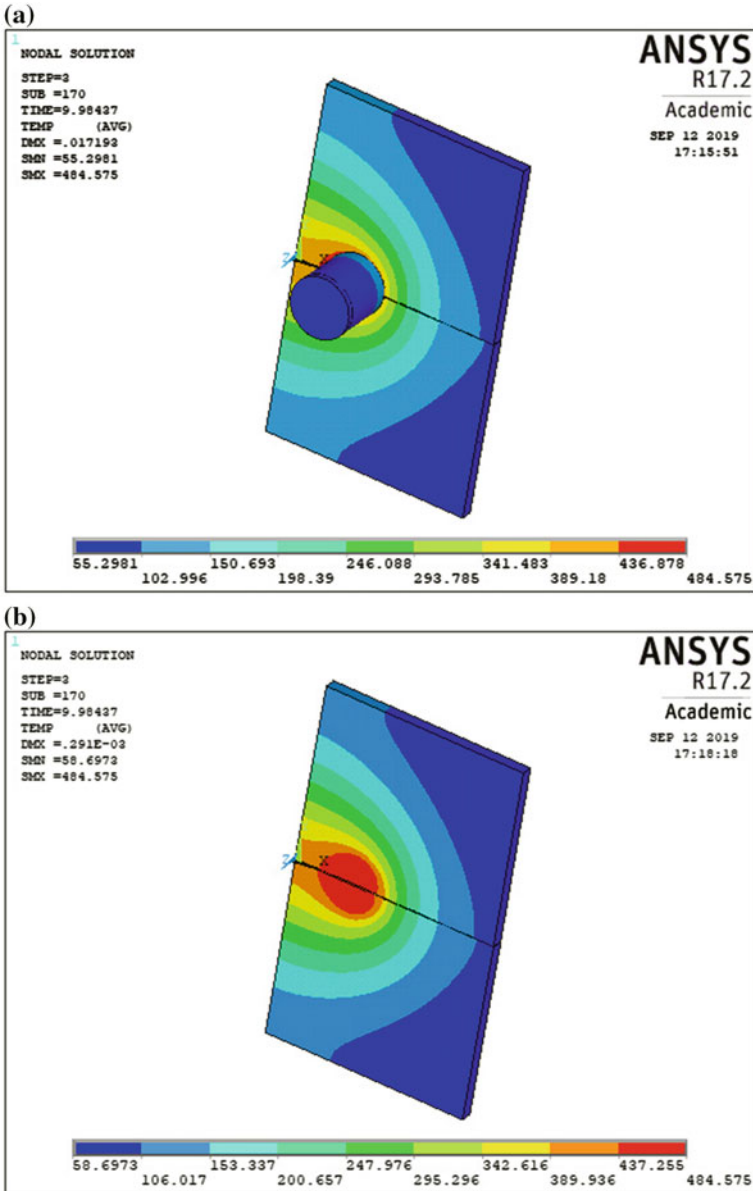


Fig. 4 Temperature distribution in workpiece at 9.98 s. **a** with tool. **b** without tool

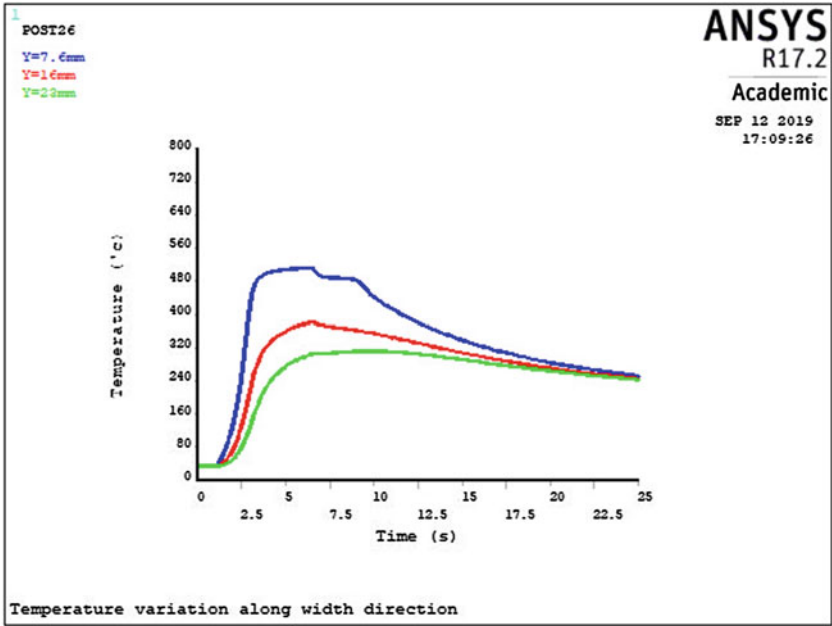


Fig. 5 Temperature distribution profile at various distances away from the weld line

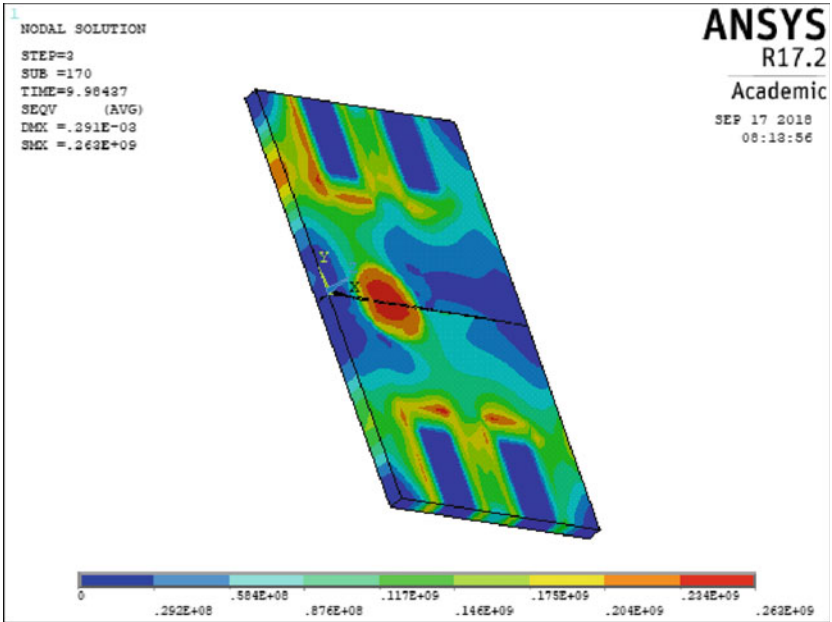


Fig. 6 Von Mises stress distribution at 9.98 s

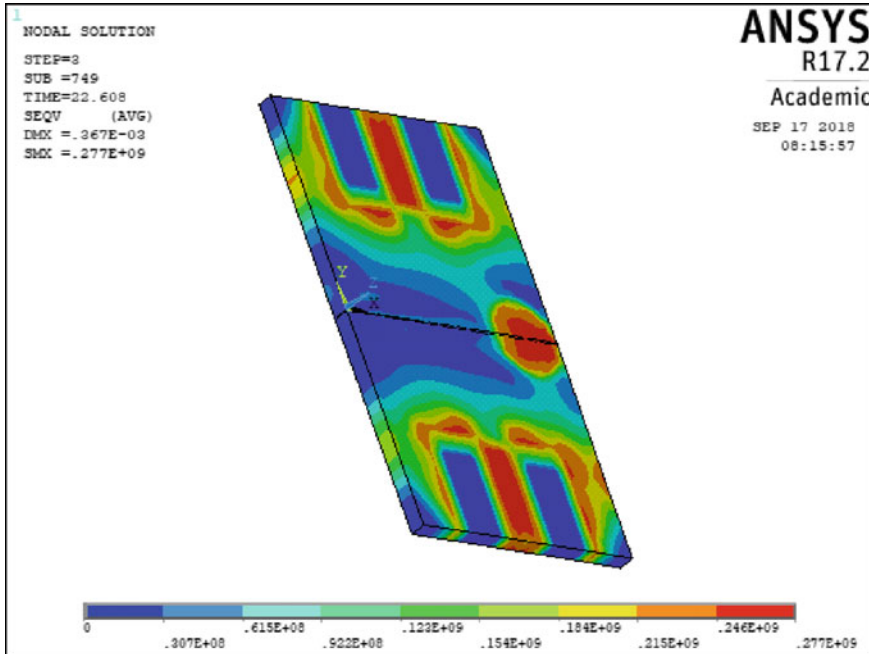


Fig. 7 Von Mises stress distribution at 22.6 s

## 4 Conclusion

In the present work, a finite element model in ANSYS APDL is developed for studying the temperature distribution and stresses during friction stir welding. It was found from the present studies that peak temperature at workpiece and tool interface is 490 °C. It was also observed that temperature profile below the moving tool is an oval shape. In addition, it was observed that the maximum value of von Mises stress has little variation during welding.

## References

1. Thomas WM, Nicholas ED, Needam JC, Murch MG, Templesmith P, Dawes CJ (1995) GB Patent Application No 9125978.8, and US Patent 5460317 Dec 1991
2. Chen GQ, Shi QY, Li YJ, Sun YJ, Dai QL, Jia JY,... & Wu JJ (2013) Computational fluid dynamics studies on heat generation during friction stir welding of aluminum alloy. *Comput Mater Sci* 79:540–546
3. Bisadi H, Rasae S, Farahmand M (2013) Thermal analysis of plunge stage in friction stir welding: simulation and experiment. *Int J Basic Sci Appl Res* 2(11):968–975
4. Zhang J, Shen Y, Li B, Xu H, Yao X, Kuang B, Gao J (2014) Numerical simulation and experimental investigation on friction stir welding of 6061-T6 aluminum alloy. *Mater Des* 60:94–101

5. Sun Z, Wu CS, Kumar S (2018) Determination of heat generation by correlating the interfacial friction stress with temperature in friction stir welding. *J of Manuf Process* 31:801–811
6. Shi L, Wu CS (2017) Transient model of heat transfer and material flow at different stages of friction stir welding process. *J Manuf Process* 25:323–339
7. Alam MP, Sinha AN (2018) Studies on temperature distribution in friction stir welding of AA7075 T651. In *International Conference on Computational and Characterization Techniques in Engineering & Sciences (CCTES)* 119–121 IEEE
8. Ansys Inc., ANSYS Mechanical APDL Theory Reference
9. Xue C, Ren X, Zhang Q (2013) Heat production simulation and heat-force couple analysis of FSW pin. *Eng Rev* 33(2):85–91

# Energy Production Through Gasification of Waste Biomass in Punjab Region



Rohtash Goswami, Sunirmit Verma and Ranjan Das

**Abstract** This paper presents useful energy (gas and power) production from the three waste biomass (dried grass, leaves, and dead branches) through gasification technology. These waste biomasses were collected in the Indian Institute of Technology Ropar, Punjab and air-dried. The feasibility of the studied biomass for thermochemical conversion process in a downdraft biomass gasifier has been investigated by characterization of biomass. The average higher heating values based on the ultimate and proximate analysis correlation were evaluated as 15.58 MJ/kg for dried grass, 17.075 MJ/kg for leaves and 15.785 MJ/kg for dead branches. The performance of downdraft biomass gasifier has been investigated in terms of calorific value (3.52 MJ/m<sup>3</sup> for dried grass, 5.14 MJ/m<sup>3</sup> for leaves and 4.15 MJ/m<sup>3</sup> for dead branches) and cold gas efficiency (50.83%, for dried grass, 64.72% for leaves and 59.15% for dead branches). The results show that these waste biomass are a reliable source for energy production through gasification technology having dual benefits of easy waste management and low-cost power production.

**Keywords** Waste biomass · Gasification · Calorific value · Cold gas efficiency

## 1 Introduction

The fast-growing industrial sector and increasing energy demand for commercial use have led to accelerated depletion of fossil fuels. Due to the limited existence of these resources, practical use of renewable energy is a favorable option for survival in the near future. The use of waste biomass for energy production has many advantages such as easy waste management and low-cost power production. Also, utilization

---

R. Goswami · S. Verma · R. Das (✉)  
Indian Institute of Technology Ropar, Rupnagar 140001, India  
e-mail: [ranjandas@iitrpr.ac.in](mailto:ranjandas@iitrpr.ac.in)

R. Goswami  
e-mail: [rohtash@iitrpr.ac.in](mailto:rohtash@iitrpr.ac.in)

S. Verma  
e-mail: [sunirmit.verma@iitrpr.ac.in](mailto:sunirmit.verma@iitrpr.ac.in)

© Springer Nature Singapore Pte Ltd. 2020  
L. Vijayaraghavan et al. (eds.), *Emerging Trends in Mechanical Engineering*,  
Lecture Notes in Mechanical Engineering,  
[https://doi.org/10.1007/978-981-32-9931-3\\_51](https://doi.org/10.1007/978-981-32-9931-3_51)



of waste biomass for energy production can fulfill the energy demand not only in rural areas but also in the industrial sector and this in turn can increase the economic strength of the developing countries. According to McKendry [1], the design of gasifier depends upon the properties of the fuel being gasified. An analysis of the gasification of waste biomass has also been carried out under different mediums namely air, oxygen, steam, and the calorific values were found to be in the range of 4–6 MJ/Nm<sup>3</sup>, 10–15 MJ/Nm<sup>3</sup> and 13–20 MJ/Nm<sup>3</sup> in the respective cases. Arena et al. [2] studied the gasification of three separately prepared fuels made from natural wood, sawdust, and furniture waste, respectively in a 500 kW capacity fluidized bed gasifier under a gasification temperature of 850 °C. They investigated the feasibility of all above biomass as a fuel for gasification. Yoon et al. [3] compared the properties and gasification quality of rice husk and pellet of rice husk under similar conditions in a fixed bed downdraft gasifier. Gasification results proved that the pellet is a better fuel as compared to rice husk. Zainal et al. [4] studied the effect of equivalence ratio on the performance of gasifier when furniture wood was used as a fuel for gasification in a downdraft biomass gasifier. They obtained nearly 80% cold gas efficiency with a specific fuel consumption rate of 2 kg/kWh. Dogru et al. [5] calculated the optimum level of gasification process using hazelnut shells in a 5 kWe pilot scale downdraft biomass gasifier. They observed high quality gas production of 5 MJ/m<sup>3</sup> GCV (Gross calorific value) at optimum fuel feeding range of 4.06–4.48 kg/h. Lapuerta et al. [6] investigated the feasibility of various biomass waste for power production (Grapevine pruning, sawdust, forestry waste etc.). Further, the analysis was also carried out by blending the biomass wastes with coal at different weight concentrations and the effect of different parameters (air-fuel ratio, gasification temperature) on the quality of gas produced was reported. Pathak et al. [7] successfully tested (agro-residue briquette and babul wood at consumption rates of 125 kg/hr and 122 kg/h, respectively) in a modular throat biomass gasifier and obtained a cold gas efficiency of 70% with briquettes and 71% with babul wood.

In this paper, characterization of waste biomass (dried grass, leaves, and dead branches) available in Indian Institute of Technology Ropar, Punjab has been studied for their feasibility for energy production. Also, the performance of a 10 kW downdraft biomass gasifier has been investigated for all above-mentioned biomasses. The study involves analysis of parameters including gas calorific value, gas composition and cold gas efficiency.

## 2 Methodology

### 2.1 Experimental Details

A 10 kW Enersol downdraft biomass gasifier (Model No.: ESB-R10) as shown in Fig. 1 is used for the gasification of leaves, dried grass and dead branches for power generation. The produced power is supplied to a control panel where all

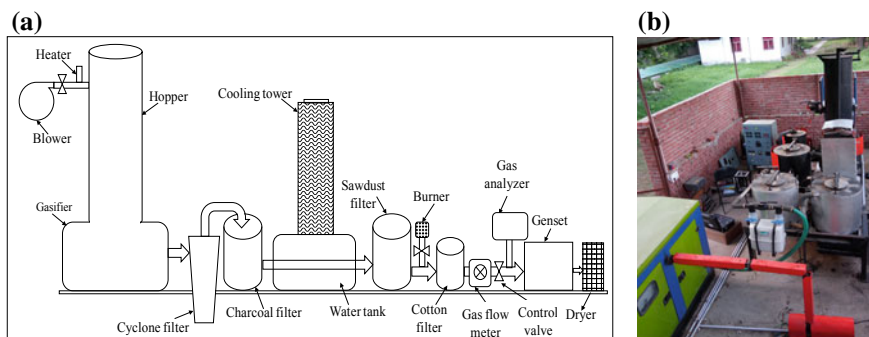


**Fig. 1** a Line diagram and b experimental setup of a biomass gasifier system

mechanical components such as a gas blower, pump, motor, etc. are operated. The hopper, reduction chamber with a gas collector and ash tank, filters, cooling tower, gas analyzer, control panel, and genset are the main components of the gasifier system used for the present study. The functions of various components are mentioned in Table 1.

**Table 1** Functions of different components used in the gasifier setup

Component	Function
Hopper with a blower (air) and heater	The biomass fuel is retained in the hopper. The required air to gasify the biomass is supplied by a blower and heater is used to ignite the biomass
Reduction chamber	Charcoal gasifies in the reduction chamber to produce flammable gas
Gas collector and ash tank	Biochar collection is done here by gravity above which gas collection is accomplished
Filter	The cyclone, charcoal, sawdust, and cotton filters are connected in series to eliminate dust particles, moisture/water, tar and ash content
Cooling tower	Gas is continuously cooled by a cooling tower through circulation of the water by a pump
Gas analyzer	The calorific value and gas composition are assessed using this instrument
Genset	The engine connected with the generator runs on the producer gas to produce electricity for powering the gasifier system
Control panel	Mechanical components are controlled here and temperatures at various points are displayed
Dryer	To eliminate moisture contents from raw biomass by using heat from the engine exhaust

## 2.2 Characterization of Biomass

In Indian Institute of Technology Ropar, Punjab, significant amount of waste biomass gets collected daily in the form of leaves (collected from the bottom of trees), grass (harvested from cricket and football ground) and dead branches (branches cut off from the trees) and is dumped at the landfill area. This generated waste biomass has been used as a energy resource through gasification technology. The waste biomass (leaves and dead branches) were air-dried for two weeks while harvested grass was air-dried for one month before use in the biomass gasifier. Three samples (of leaves, dried grass and dead branches of trees) were converted into powder form of approximate size 2–5 mm as shown in Fig. 2. Using this powdered form, a characterization study of biomass has been carried out to find fixed carbon (FC), volatile matter (VM), moisture and ash contents as per ASTM D121 standards [8, 9]. The composition of biomass (C, H, O) has been found out by the relation between fixed carbon and volatile matter (Eqs. 1, 2, and 3) reported by Parikh et al. [10]. The higher heating value (HHV) of the biomass was estimated by two correlations, Eq. 4 based on proximate analysis (PA) and Eq. 5 based on ultimate analysis (UA) as suggested by Yin [11].

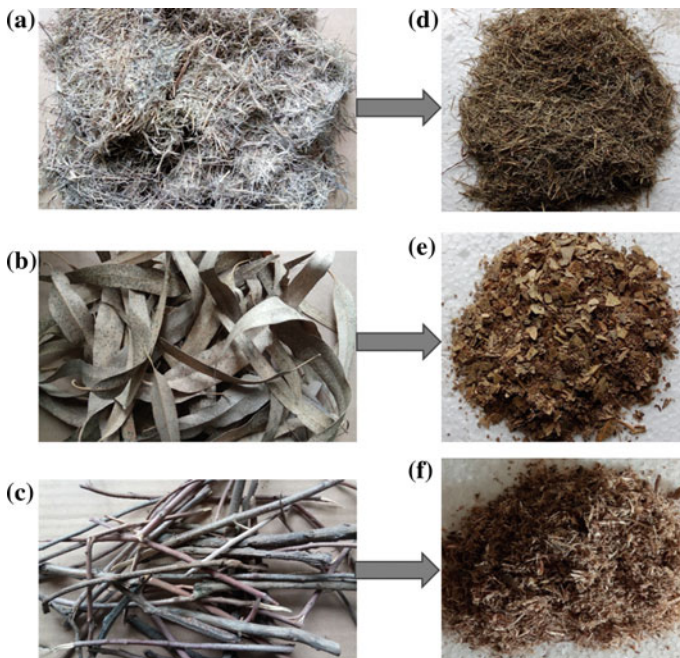


**Fig. 2** Specimens of dried grass, leaves and dead branches used for gasification (a,b,c) and characterization (d,e,f)

$$\text{Carbon (\%)} = 0.637 \times \text{FC (\%)} + 0.455 \times \text{VM (\%)} \quad (1)$$

$$\text{Hydrogen (\%)} = 0.052 \times \text{FC (\%)} + 0.062 \times \text{VM (\%)} \quad (2)$$

$$\text{Oxygen (\%)} = 0.304 \times \text{FC (\%)} + 0.476 \times \text{VM (\%)} \quad (3)$$

$$\text{HHV}_{\text{PA}}(\text{MJ/kg}) = 0.2521 * \text{FC (\%)} + 0.1905 * \text{VM (\%)} \quad (4)$$

$$\text{HHV}_{\text{UA}}(\text{MJ/kg}) = 0.2949 * \text{C (\%)} + 0.8250 * \text{H (\%)} \quad (5)$$

### 3 Results and Discussion

The disposal of waste biomass not only requires large dumping grounds but also proves to be inconvenient to the humankind. The processing of waste biomass for the creation of energy enhances the economics of power generation and encourages the use of renewable energy. The waste biomass (dried grass, leaves and dead branches) produced by the institute has been successfully converted into syngas to run an I.C. engine for power generation. However, dead branches need to be preprocessed (reduced in size up to 5–8 cm in length) before they can be used in the biomass gasifier while dried grass and leaves can be directly used as it is.

#### 3.1 Characterization Analysis of Biomass

The proximate analysis of the biomass as summarized in Table 2 shows that leaves and dead branches contain higher volatile matter as compared to dried grass. Gasification temperature and gas quality are affected by moisture and ash contents present in the biomass [5]. Amongst the studied biomass, leaves have the lowest moisture content (7.07%) and ash content (5.61%) as compared to the other two. Table 3 shows the composition of biomass and HHV of biomass. The calculated average HHV (arithmetic mean of  $\text{HHV}_{\text{PA}}$  and  $\text{HHV}_{\text{UA}}$ ) of dried grass (15.58 MJ/kg) and dead

**Table 2** Proximate analysis of dried grass, leaves and dead branches

Parameters (%)	Dried grass	Leaves	Dead branches
Fixed carbon	11.50	12.52	10.54
Volatile matter	68.16	74.80	70.23
Moisture content	8.46	7.07	11.16
Ash content	11.88	5.61	8.07

**Table 3** Ultimate analysis and HHV estimated by Eqs. 1–5 [10, 11]

Parameters (%)	Dried grass	Leaves	Dead branches	Source eq.
Carbon (%)	38.33	42.01	38.67	1
Hydrogen (%)	4.82	5.29	5.01	2
Oxygen (%)	35.94	39.41	36.63	3
HHV <sub>PA</sub> (MJ/kg)	15.88	17.40	16.03	4
HHV <sub>UA</sub> (MJ/kg)	15.28	16.75	15.54	5

branches (15.785 MJ/kg) are approximately the same, but leaves possess a relatively higher amount of average higher heating value (17.075 MJ/kg).

### 3.2 Gas Composition

The composition of gas was analyzed by a gas analyzer (Model no. PFGCOM, made by AMB Electronics Pvt. Ltd., Delhi) This analysis involved the evaluation of four gas parameters, namely the carbon monoxide (CO), carbon dioxide (CO<sub>2</sub>), methane (CH<sub>4</sub>) and hydrogen (H<sub>2</sub>) content. For dried grass, the suitable gasification was observed to occur in the temperature range of 300–600 °C and the maximum concentration of CO (19.48%) and H<sub>2</sub> (7.11%) in this temperature range is shown in Fig. 3a.

Figure 3b indicates the syngas composition derived from gasification of leaves biomass. The suitable range of gasification temperature was found to be 250–550 °C where the maximum concentration of CO (18.73%) and H<sub>2</sub> (7.42%) was observed. The gasification of dead branches provides the highest value of CO (18.43%) and H<sub>2</sub> (9.83%) as shown in Fig. 3c within the temperature range of 300–500 °C. However, the concentration of CH<sub>4</sub> is relatively lower than other species and it decreases with increase in gasification temperature.

### 3.3 Gas Calorific Value and Cold Gas Efficiency

The calorific value of gas describes the quality of gas produced through the gasification process and is affected by the characteristics of biomass, the design of gasifier and gasification temperature. The variation of gas calorific value relative to the temperature of the reduction chamber for three waste biomass (dried grass, leaves, and dead branches) is shown in Fig. 4. The gasification of leaves and dead branches produce high calorific value gas relative to dried grass due to low ash content. The average calorific value of gas generated from dried grass, leaves and dead branches were calculated as 3.52 MJ/m<sup>3</sup>, 5.14 MJ/m<sup>3</sup>, and 4.15 MJ/m<sup>3</sup>, respectively. The cold gas efficiency defines the optimum design of biomass gasifier for producing best

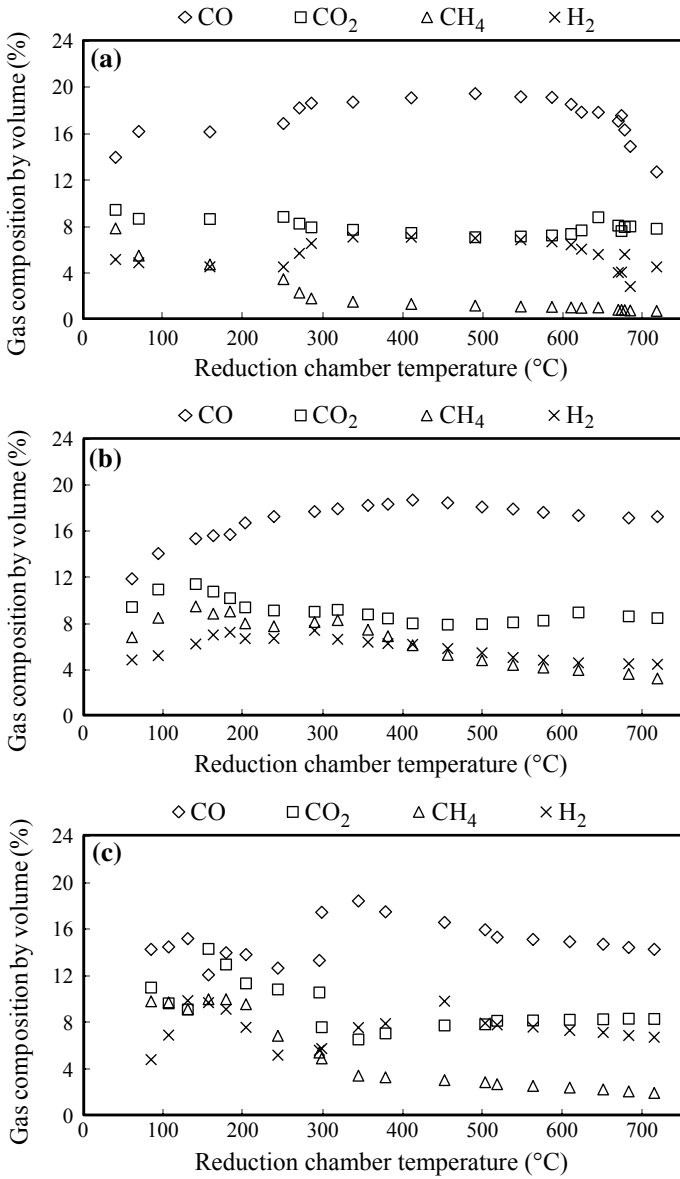
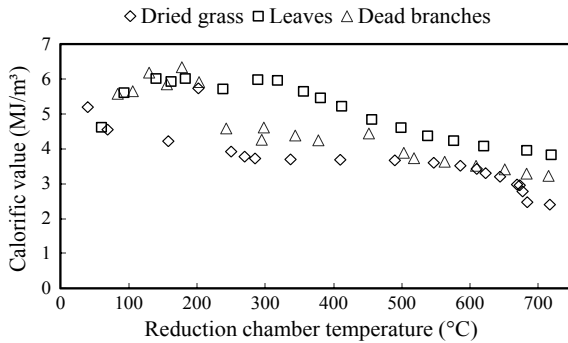


**Fig. 3** Gas composition at various temperatures of reduction chamber (°C) for gasification of **a** dried grass, **b** leaves and **c** dead branches

**Fig. 4** Calorific value of gas at various temperatures of reduction chamber ( $^{\circ}\text{C}$ ) for dried grass, leaves, and dead branches



quality gas and is related to the calorific value of gas, specific gas flow rate and the higher heating value of biomass used. Average cold gas efficiency derived from dried grass, leaves and dead branches' gasification is found as 50.83%, 64.72%, and 59.15%, respectively.

## 4 Conclusion

The characterization of waste biomass shows that dried grass, leaves and dead branches possess considerable potential towards energy production. The appropriate gasification temperature was found to be in the 300–500  $^{\circ}\text{C}$  for all waste biomass. The average calorific values calculated for dried grass, leaves and dead branches were 3.52  $\text{MJ}/\text{m}^3$ , 5.14  $\text{MJ}/\text{m}^3$ , and 4.15  $\text{MJ}/\text{m}^3$ , respectively. For all waste biomass, gasifier provides appreciable cold gas efficiency of 50.83% for dried grass, 64.72% for leaves and 59.15% for dead branches. It has been observed that these waste biomasses can play an important role in strengthening the economy of developing countries where such type of waste biomass is regularly generated and disposed off.

**Acknowledgements** Authors thank Science & Engineering Research Board (SERB), Department of Science & Technology, Govt. of India for providing the financial support for sponsored project EEQ/2016/000073 titled “Design and Development of a Solar Pond and Biomass Driven Thermo-electric Unit for Domestic Power Generation using Inverse Method”. Authors also thank IIT Ropar for providing other research facilities.

## References

1. McKendry P (2010) Energy production from biomass (part 3): gasification technologies. *Biores Technol* 83(1):55–63
2. Arena U, Zaccariello L, Mastellone ML (2010) Gasification of natural and waste biomass in a pilot scale fluidized bed reactor. *Combust Sci Technol* 182(4–6):625–639

3. Yoon SJ, Son Y, Kim YK, Lee JG (2012) Gasification and power generation characteristics of rice husk and rice husk pellet using a downdraft fixed-bed gasifier. *Renew Energy* 42:163–167
4. Zainal ZA, Rifau A, Quadir GA, Seetharamu KN (2002) Experimental investigation of a downdraft biomass gasifier. *Biomass Bioenerg* 23(4):283–289
5. Dogru M, Howarth CR, Akay G, Keskinler B, Malik AA (2002) Gasification of hazelnut shells in a downdraft gasifier. *Energy* 27(5):415–427
6. Lapuerta M, Hernández JJ, Pazo A, López J (2008) Gasification and co-gasification of biomass wastes: effect of the biomass origin and the gasifier operating conditions. *Fuel Process Technol* 89(9):828–837
7. Pathak BS, Patel SR, Bhave AG, Bhoi PR, Sharma AM, Shah NP (2008) Performance evaluation of an agricultural residue-based modular throat-type down-draft gasifier for thermal application. *Biomass Bioenerg* 32(1):72–77
8. ASTM D 121-09a (2009) The standard terminology of coal and coke. Pennsylvania: American Society for Testing and Materials. <https://www.astm.org/Standards/D121.htm>. Accessed: 23.07.2018
9. Lenka R (2016) Characterization of the properties of some biomass species and estimation of their power generation potentials. Ph.D. dissertation, NIT Rourkela, India, <http://ethesis.nitrkl.ac.in/8386/>. Accessed 23 July 2018
10. Parikh J, Channiwala SA, Ghosal GK (2007) A correlation for calculating elemental composition from proximate analysis of biomass materials. *Fuel* 86(12–13):1710–1719
11. Yin CY (2011) Prediction of higher heating values of biomass from proximate and ultimate analyses. *Fuel* 90(3):1128–1132



# Image Correlation Technique for Slope and Curvature of a Cantilever Beam Using Light Intensity



M. Raghuraman and I. Ramu

**Abstract** Image correlation technique is an optical method based on grey value digital images that can determine the shape, displacement and the strain of an object under load. In this technique, the slope and curvature of a cantilever beam can be obtained based on the intensity values of loaded and unloaded images. According to the conservation principle, for small deformation, the total amount of light reflected for the specified area on the surface would be the same before and after loading when the illumination is unaltered. The method, image correlation technique is obtained on this basis.

**Keywords** Intensity · Light · Slope · Curvature · Image · Cantilever

## 1 Introduction

In non-contact optical method, the shape and displacements can be determined for an object under load in three dimensions. The method can be compared with the results of finite element method. Digital image correlation works by comparing the pixel positions of two images, one before and after deformation (Fig. 1).

This technique is a variable and useful tool for deformation analysis. The digital image correlation method for experimental mechanics can be applied to rigid body mechanics and for finding the equidistant line displacements of a cantilever beam by correlating the spot of intensity patterns.

### 1.1 Image Correlation Technique

For a completely polished surface which is reflective for a small deflection, the assumption of the total light falling on the specimen for a region would be the

---

M. Raghuraman (✉) · I. Ramu  
Vishnu Institute of Technology, 534202 Bhimavaram, India  
e-mail: [raghuraman262@gmail.com](mailto:raghuraman262@gmail.com)

© Springer Nature Singapore Pte Ltd. 2020  
L. Vijayaraghavan et al. (eds.), *Emerging Trends in Mechanical Engineering*,  
Lecture Notes in Mechanical Engineering,  
[https://doi.org/10.1007/978-981-32-9931-3\\_52](https://doi.org/10.1007/978-981-32-9931-3_52)

539

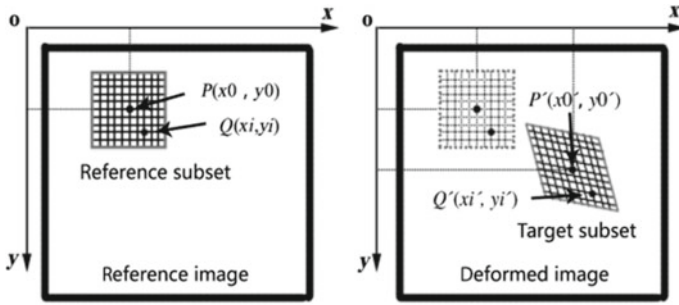


Fig. 1 Image showing the change in pixel positions

same quantity before loading and unloading of the specimen when illumination is unchanged. The intensity which is reflected from the specimen can be used to obtain slope contour and curvature contour with the help of shift in pixel positions. Subramanian et al. [3] state that if we know the pixel location in one state we can obtain the values of slope can be obtained by computing the difference between the pixel positions of two states of the specimen (loaded and unloaded). Subramanian and Arunagiri [1] explain the principle of conservation of light reflected can be expressed as integration of intensities over small regions. Basically, this technique finds curvature and slope by comparing the pixel positions along the length of specimen for loaded and unloaded states of the specimen.

Figure 2 described in [2] shows  $I_1$  and  $I_2$  where these intensities denote the distribution functions of intensities before and after loading. Taking two points A and B on the specimen, the intensities of loaded and unloaded specimens are assumed to be the same over the finite portion PQ and P'Q'. The equation can be written as

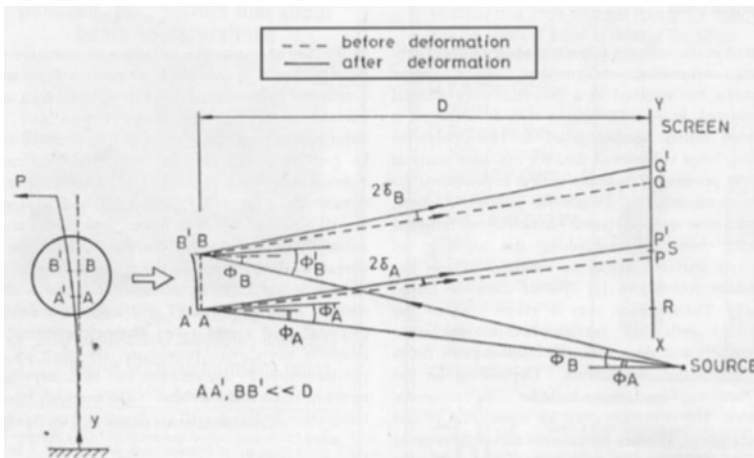


Fig. 2 Experiment setup for image correlation technique

$$I_1PQ = I_2P'Q'$$

$$I_1/I_2 = 1 + [2D(d^2w/d^2y)/(1 + D\chi a)] \quad (1)$$

From the above Eq. (1) described in [2], the intensity values of loaded image can be related to intensity values of unloaded image where  $d^2w/d^2y$  is curvature and  $\chi a$  is apparent curvature.

## 1.2 Relation Between Bending Moment and Curvature

According to beam bending equation,  $\sigma/y = M/I = E/R$

where Stress  $\sigma$  is in  $N/mm^2$

Distance from the neutral axis is  $y$

Moment of Inertia is  $I$  & Young's modulus is  $E$

From the beam bending equation, the curvature  $1/R$  is proportional to the bending moment  $M$  units are N-m. Hence for the maximum bending moment, there will be a maximum curvature for the cantilever beam and vice versa.

## 1.3 Derivation of Slope for a Given Length of Cantilever Beam

Slope at free end is given by

$$\theta_{tip} = PL^2/2EI$$

Deflection at free end is given by

$$\delta_{tip} = PL^3/3EI$$

Equation relating to the slope and deflection at free end is given by

$$\theta_{tip}/\delta_{tip} = 3/2L$$

For a given length the slope is

$$\theta_{eqn} = PLx/EI - Px^2/2EI$$

$$\theta_{eqn}/\theta_{tip} = 2 \times (x/L) - (x/L^2)$$

$$\theta_{eqn}/\theta_{tip} = 2\xi - \xi^2 \quad (2)$$

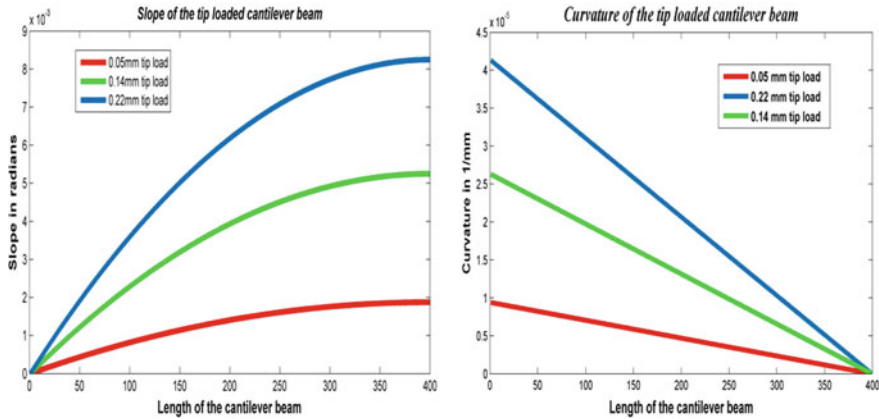


**Fig. 3** Slope contour & curvature contour of cantilever beam for varying tip displacements

Figure 3 is obtained using Eq. (2) where the values of E and I are eliminated and brought to a value which is ratio of its lengths  $\xi$ . Since this method do not use those values for computing the slope and curvature of the cantilever beam. The value of  $L$  is the length of specimen i.e. 40 mm and  $x$  is element length varies from 1 to 40 mm. Substituting the values of  $\xi$  and  $\theta_{tip}$  in the Eq. (2), the slope and curvature are plotted to its length of the specimen.

## 2 Introduction

### 2.1 Optical Bench Setup

The cantilever beam specimen is positioned in a fixture between the light source and matte screen. The light source is passed through the collimating lens, spacial filter and finally it made to fall on the reflective beam specimen (Fig. 4, Table 1).

### 2.2 Capturing of Images for Unloading and Loading Conditions

The reflected images from the screen are captured using Charged Couple Device camera. Figure. 5 shows the image taken from CCD camera setup for loaded and unloaded condition. Reflected image of the specimen will be made to fall on the screen when the tip deflection of 0.05, 0.14 and 0.22 mm is given to the cantilever beam at free end using the dial gauge. The length of the reflected specimen in the

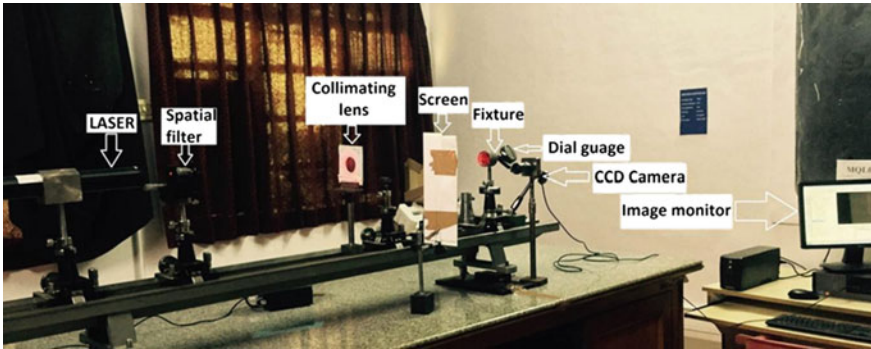


**Fig. 4** Experiment setup in laboratory for image correlation technique

**Table 1** Specifications of optical bench

Description	Specifications
Total length of the bed	170 cm
Accuracy of calibration	0.01%
Guide ways	Lathe type
Laser	He-Ne, 2 m W
Power supply	220 V AC, 50 Hz

**Fig. 5** Reflected images of loaded and unloaded



screen increases when it is unloaded and the distance  $D$  between the object to screen is calculated by using the scale on length of bed.

### 2.3 Experiment Procedure

The camera is placed in front of the screen and the images of loaded and unloaded states are taken. The cantilever beam specimen is placed in the fixture which is kept under illumination for no-load condition. A dial gauge is used to give a displacement in millimeters where the free end of the cantilever beam is displaced towards the light source so there will be a change in specimen's length which is smaller than the unloaded specimen. The images of loaded and unloaded states are stored in the computer and they are used as the inputs for the MATLAB programming. From the Fig. 6 the cumulative intensities of loaded and unloaded grayscale images are shown where the pixel positions of both the conditions are correlated, the differences in the intensity values give the slope, by differentiating the slope curve, the curvature is obtained.

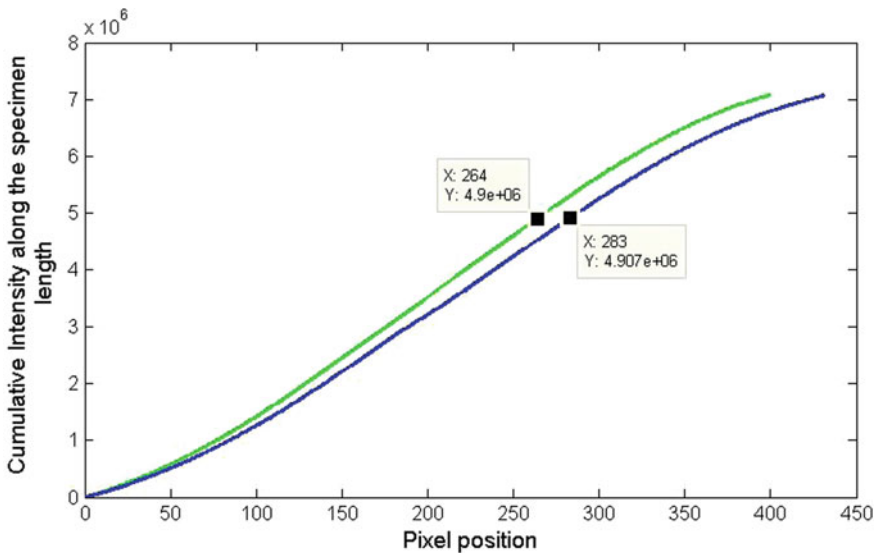


Fig. 6 Cumulative intensities before and after loading the specimen

### 3 Results and Discussion

The values of slope and curvature are computed by using MATLAB image processing toolbox where the comparison is made for values from image correlation technique and the values from the expression derived for theoretical slope. The graph below shows the slope contour and curvature contour comparison between image correlation technique and the theoretical values after normalizing the values for varying tip displacements of 0.05, 0.14, 0.22 mm.

#### 3.1 For 0.05 mm Tip Displacement

Slope contour & curvature contour of cantilever beam with tip displacement of 0.05 mm is shown in Fig. 7.

#### 3.2 For 0.14 mm Tip Displacement

Slope contour & curvature contour of cantilever beam with tip displacement of 0.14 mm is shown in Fig. 8.

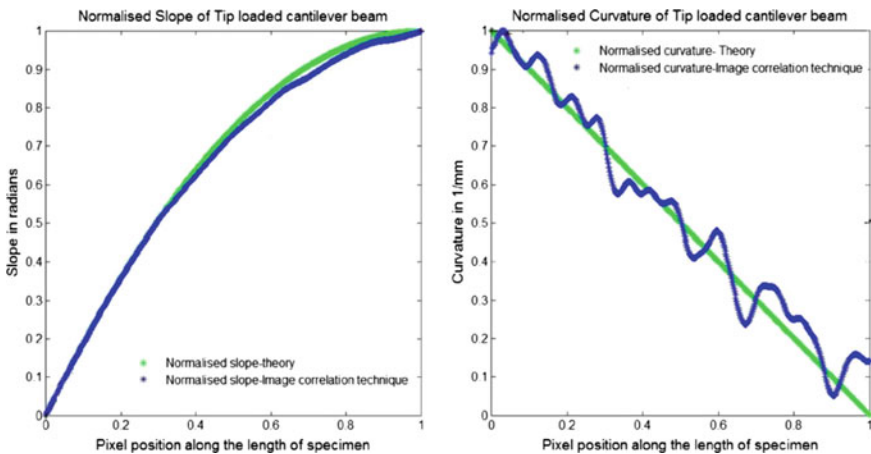


Fig. 7 Normalised slope and curvature contours for 0.05 mm tip displacement

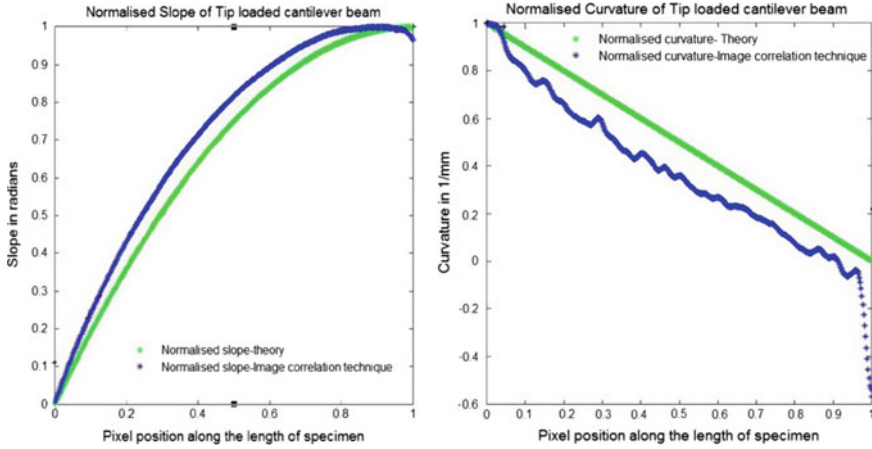


Fig. 8 Normalised slope and curvature contours for 0.14 mm tip displacement

### 3.3 For 0.22 mm Tip Displacement

Slope contour & curvature contour of cantilever beam with tip displacement of 0.22 mm is shown in Fig. 9.

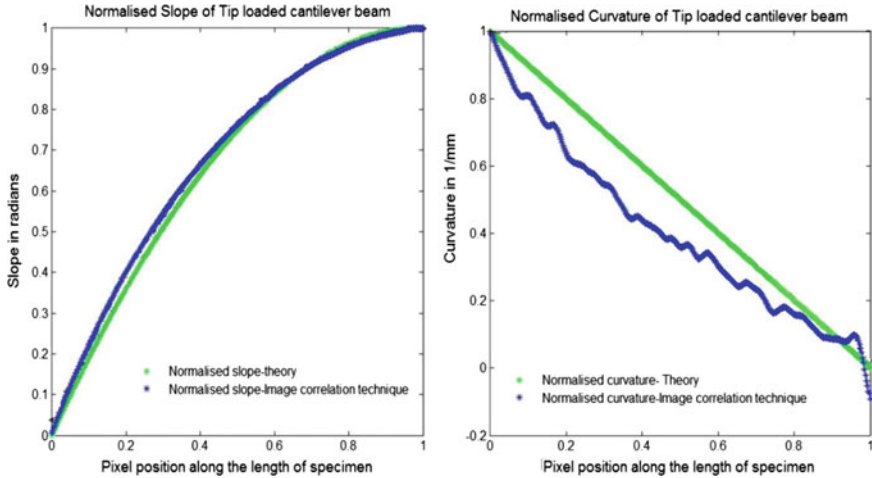


Fig. 9 Normalised slope and curvature contours for 0.22 mm tip displacement



## 4 Results and Discussion

The graphs for 0.05, 0.14, 0.22 mm tip displacements shows the increment in tip displacement and the decrement in the distance between the cantilever beam specimen and screen, the slope and curvature values from the experiment are closer to the theoretical values. One of the reason is the better illumination of the reflective beam when the distance between the screen and specimen is less so more number of pixels will be on the reflected image of the specimen for better correlation of the pixels for loaded and unloaded specimen. This method can be applied to the practical surfaces by applying the epoxy resin coating which makes the specimen reflective and same procedure discussed in this study is repeated for finding the slope and curvature for various beam structures with different cross-sections.

## References

1. Subramanian G, Arunagiri R (1981) Reflecting grid method for curvature and twist. *J Strain* 17(3):87–88
2. Subramanian G, Jagannath VR (2008) Surface contouring of reflecting plates using intensity integration technique. *Int J Exp Mech* 37(4):159–165
3. Subramanian G, Radhakrishnan S, Patel BB (1995) Intensity integration technique for slope contouring of reflecting plates. *J Aero Soc India* 47:234–237

# Influence of the Notch Length on the Optimal Radial Location of Strain Gage in a Single Edged Notched Plate



Pranjol Paul, K. S. R. K. Murthy and Debabrata Chakraborty

**Abstract** For estimation of accurate mode I stress intensity factor in a single edged notched plate, it is important to place the strain gage within a maximum permissible radial distance  $r_{\max}$  [14]. In the present paper, it is aimed to study how the notch length affects this parameter  $r_{\max}$ . A finite element based procedure is developed based on theoretical formulation analogous to Dally and Sanford technique [16] for cracks. Results show that both notch length and the net ligament length have significant influence on  $r_{\max}$  and some interesting observations have been reported.

**Keywords** Sharp V-Notch · Optimal strain gage location · Notch length

## 1 Introduction

Sharp V-notches can be regularly seen in engineering components around us besides other patterns of notches. Notches serve some specific purposes in components such as gears, screws etc. However, notches can also be the consequence of defective fabrication as in case of anisotropic chemical etching processes [1] and injection molding [2].

A sharp V-notch is defined as a notched geometry with almost negligible notch tip radius compared to edge lengths. Williams [3], based on the eigenfunction expansion method, described that stress singularity occurs at the tip of a sharp V-notch in the form of  $\sigma_{ij} = K^V r^{\lambda'-1} f_{ij}(\theta)$  where the order of the singularity  $\lambda' - 1$  and the angular functions  $f_{ij}(\theta)$  are dependent on the notch angle  $\gamma$ . The parameter  $K^V$  is known as the notch stress intensity factor (NSIF). For particular geometrical and loading conditions, the  $K^V$  (the superscript  $V$  representing the V-notch) denotes the state of the stress field near the notch tip. It is influenced by the geometry of the notched body as well as boundary conditions.  $K^V$  had been used extensively for developing many numerical [4–7] and experimental [8–13] methodologies for evaluation of stress intensity factor for multiple notched geometries. Experimental procedures

---

P. Paul (✉) · K. S. R. K. Murthy · D. Chakraborty  
IIT Guwahati, Guwahati 781039, India  
e-mail: [pranjol@iitg.ac.in](mailto:pranjol@iitg.ac.in)

© Springer Nature Singapore Pte Ltd. 2020  
L. Vijayaraghavan et al. (eds.), *Emerging Trends in Mechanical Engineering*,  
Lecture Notes in Mechanical Engineering,  
[https://doi.org/10.1007/978-981-32-9931-3\\_53](https://doi.org/10.1007/978-981-32-9931-3_53)

like strain gage technique, photoelasticity, caustics, coherent gradient sensing and digital image correlation are established to evaluate stress intensity factor (SIF) when subjected to mode I and mixed mode conditions [8–13].

In ref [14], Paul et al. had conceptualized a fascinating approach to obtain the notch stress intensity factor (NSIF) of sharp V-notched configurations by making use of single strain gage. The publication [14] proposes a completely different approach involving strain series (Williams eigenfunction expansion series) having multiple parameters for suitable evaluation of mode I NSIF ( $K_I^V$ ) of isotropic sharp V-notched bodies. It involves the use of a strain gage (i.e. only one) to be pasted away from the notch tip for the determination of  $K_I^V$ . However, before the strain gage pasting, it has to be known *a priori* which radial locations would be the appropriate ones for pasting and the study [14] reveals a methodology (justified by robust theories) justifying the occurrence of a valid or optimal radial location of strain gage and allowing estimation of such optimal location *a priori* for suitable estimation of  $K_I^V$ . The research [14] also relates the valid gage locations with the notch geometry. The authors also showed the influence of material properties on the optimal gage locations as published in [15]. The studies [14, 15] for sharp V-notched configurations are based on the study of Dally and Sanford [16] carried out for cracked configurations. In the present conference paper, the authors (Paul et al.) have attempted to show the influence of the notch length and proximity of boundary on the optimal radial strain gage locations in a single edge notched tensile configuration (abbreviated as SENT configuration). The results, thus obtained, are suitably presented in the results section.

## 2 Theoretical Aspects

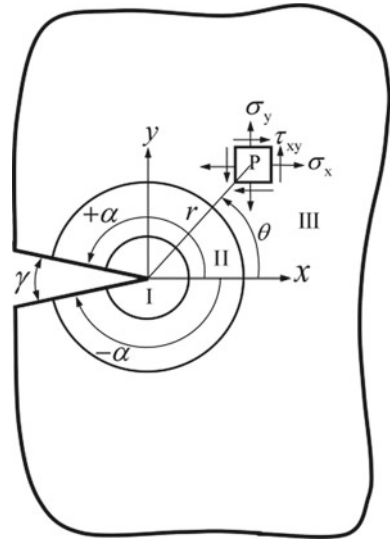
In this section, the mathematical modeling associated with the proposed sharp V-notch analysis technique and the associated theory for determining optimal radial strain gage locations for accurate estimation of notch stress intensity factor is summarized. However, the research articles published by Paul et al. [14, 15] can be gone through for comprehensive understanding.

### 2.1 Elastic Strain Analysis

An isotropic and homogenous two-dimensional object containing a sharp V-notch subjected to loading in mode I condition and plane stress condition (Fig. 1) is considered throughout for carrying out the work.

By considering zero-stress boundary conditions over the surface ( $\sigma_\theta = \tau_{r\theta} = 0$  at  $\theta = \pm\alpha$ , depicted by Fig. 1) of the notched body, the stress components in polar coordinates under mode I loading condition can be written as follows:

**Fig. 1** Schematic representing the zones (I, II and III) in a sharp V-notched (single edge) body



$$\begin{Bmatrix} \sigma_r \\ \sigma_\theta \\ \tau_{r\theta} \end{Bmatrix} = \sum_{n=1}^{\infty} \text{Re} \left\{ \frac{\lambda'_n A'_n}{r^{1-\lambda'_n}} \begin{bmatrix} (3 - \lambda'_n) \cos(\lambda'_n - 1)\theta + (\lambda'_n \cos 2\alpha + \cos 2\lambda'_n \alpha) \cos(\lambda'_n + 1)\theta \\ (\lambda'_n + 1) \cos(\lambda'_n - 1)\theta - (\lambda'_n \cos 2\alpha + \cos 2\lambda'_n \alpha) \cos(\lambda'_n + 1)\theta \\ (\lambda'_n - 1) \sin(\lambda'_n - 1)\theta - (\lambda'_n \cos 2\alpha + \cos 2\lambda'_n \alpha) \sin(\lambda'_n + 1)\theta \end{bmatrix} \right\} \quad (1)$$

where  $n$  denotes the order of the term in the infinite series,  $\lambda'_n$  is the eigenvalue for the notched configuration subjected to mode I loading condition and  $A'_n$  denotes the Williams eigen function coefficient. The boundary conditions as mentioned above lead to a characteristic equation for evaluating the value of the eigenvalue  $\lambda'_n$  as

$$\lambda'_n \sin 2\alpha + \sin 2\lambda'_n \alpha = 0 \quad (2)$$

The solution of the Eq. (2),  $\lambda'_n$ , denotes the singularity order around the notch tip in mode I condition of loading. It is dependent on angle  $\alpha$  (Fig. 1) which is, in turn, dependent on the magnitude of notch angle  $\gamma$  (Fig. 1). The Eq. (2), being a transcendental equation, can be solved numerically. The nature of  $\lambda'_n$ , whether real or complex, is solely governed by the notch angle  $\gamma$  and it is written as

$$\lambda'_n = \lambda_n + i\lambda_n^* \quad (3)$$

The first-order eigenvalue  $\lambda'_1$  is customarily real (i.e.,  $\lambda'_1 = \lambda_1$  and  $\lambda_1^* = 0$ ) and smaller than unity till  $\gamma < 180^\circ$  that represents singular stress behavior, and  $\gamma = 180^\circ$  denotes a notchless solid, i.e.,  $1 - \lambda_1 = 0$  in Eq. (2). However, the nature of  $\lambda'_n$  (order higher than first order), whether real or complex, is governed by the magnitude of the notch angle [14]. The nature of Williams' expansion coefficient  $A'_n$ , whether real or complex, is governed by the nature of notch eigenvalue  $\lambda'_n$ . If the eigen

value is real, then the corresponding Williams expansion coefficient is also real and if the eigen value is complex, then the corresponding Williams expansion coefficient is also complex (ref. [14]).The Williams coefficient  $A'_n$ , therefore, is generalized as

$$A'_n = A_n + iA_n^* \tag{4}$$

In case of  $n = 1, A'_1 = A_1$  ( $A_1^* = 0$  because  $\lambda_1^* = 0$  when  $n = 1$ ) denotes singular term and is associated with the notch stress intensity factor  $K_I^V$  as follows:

$$K_I^V = \lim_{r \rightarrow 0} (\sqrt{2\pi} r^{1-\lambda_1} \sigma_y(\theta = 0)) = \sqrt{2\pi} \lambda_1 (1 + \lambda_1 - \lambda_1 \cos 2\alpha - \cos 2\alpha \lambda_1) A_1 \tag{5}$$

In case of  $n > 1, A'_n$  denotes higher order coefficients (non-singular). In Cartesian coordinate system, the state of stress (Fig. 1) can be expressed as follows (ref. [14]).

$$\begin{Bmatrix} \sigma_x \\ \sigma_y \\ \tau_{xy} \end{Bmatrix} = \sum_{n=1}^{\infty} \text{Re} \left\{ \frac{\lambda'_n A'_n}{r^{1-\lambda'_n}} \begin{bmatrix} (2 + \lambda'_n \cos 2\alpha + \cos 2\alpha \lambda'_n) \cos(\lambda'_n - 1)\theta - (\lambda'_n - 1) \cos(\lambda'_n - 3)\theta \\ (2 - \lambda'_n \cos 2\alpha - \cos 2\alpha \lambda'_n) \cos(\lambda'_n - 1)\theta + (\lambda'_n - 1) \cos(\lambda'_n - 3)\theta \\ -(\lambda'_n \cos 2\alpha + \cos 2\alpha \lambda'_n) \sin(\lambda'_n - 1)\theta + (\lambda'_n - 1) \sin(\lambda'_n - 3)\theta \end{bmatrix} \right\} \tag{6}$$

Using the constitutive relationship, subject to plane stress condition, the strain components at a point  $P(r, \theta)$  can be written as follows:

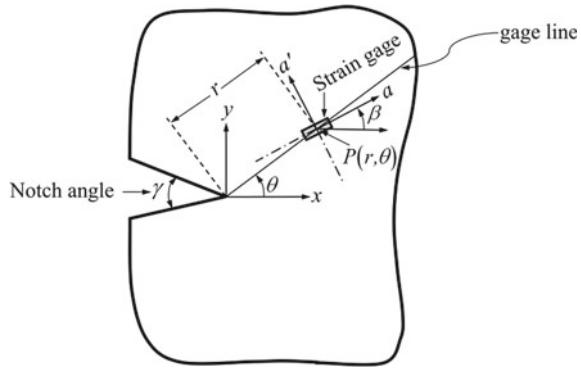
$$\begin{aligned} 2G\varepsilon_x &= \sum_{n=1}^{\infty} \text{Re} \left\{ \frac{\lambda'_n A'_n}{r^{1-\lambda'_n}} \left[ 2\kappa \cos(\lambda'_n - 1)\theta + \lambda'_n \cdot \cos 2\alpha \cdot \cos(\lambda'_n - 1)\theta + \cos 2\lambda'_n \alpha \cdot \cos(\lambda'_n - 1)\theta - (\lambda'_n - 1) \cdot \cos(\lambda'_n - 3)\theta \right] \right\} \\ 2G\varepsilon_y &= \sum_{n=1}^{\infty} \text{Re} \left\{ \frac{\lambda'_n A'_n}{r^{1-\lambda'_n}} \left[ 2\kappa \cos(\lambda'_n - 1)\theta - \lambda'_n \cdot \cos 2\alpha \cdot \cos(\lambda'_n - 1)\theta - \cos 2\lambda'_n \alpha \cdot \cos(\lambda'_n - 1)\theta + (\lambda'_n - 1) \cdot \cos(\lambda'_n - 3)\theta \right] \right\} \\ 2G\gamma_{xy} &= \sum_{n=1}^{\infty} \text{Re} \left\{ \frac{\lambda'_n A'_n}{r^{1-\lambda'_n}} \left[ 2(\lambda'_n - 1) \cdot \sin(\lambda'_n - 3)\theta - 2(\lambda'_n \cos 2\alpha + \cos 2\lambda'_n \alpha) \cdot \sin(\lambda'_n - 1)\theta \right] \right\} \end{aligned} \tag{7}$$

where  $\kappa = (1 - \nu)/(1 + \nu)$  for plane stress condition and  $G$  is the rigidity modulus. The strain series in Eq. (7) is an infinite series.

### 2.2 Single Strain Gage Technique

Locating an optimal zone around the notch tip is very important for measuring the surface strains. Zone I (Fig. 1) will not be optimal for strain measurement because of high strain gradients and 3D state of stress. The notch problems basically deal with solutions in infinite series. Due to this, the zone III, the remotest zone (Fig. 1), also does not support measurement of strains. This is supported by the fact that plenty of

**Fig. 2** Diagram representing the general orientation of strain gage in an isotropic and homogenous two-dimensional body with sharp V-notch



unknown coefficients is needed in the strain series to represent the strains at those distant locations leading to the requirement of plenty of strain gages. Moreover, singularity dominated zone may not exist at those distant locations. So, the intermediate zone or zone II is expected to be an optimal zone for measuring surface strains. It is supposed that strains in zone II comprise the first-order singular term and a few higher order non-singular terms [14]. The zone II is the optimal zone about the notch tip where strains are suitably denoted by the strain series (Eq. (7)). The strain series comprises the first order (singular) term and two higher order (non-singular) terms in case of the infinite strain series up to  $n = 2$  as per Paul et al. [14]. The present problem has been carried out with similar such strain series, i.e., up to  $n = 2$ .

Figure 2 as shown below is the representation of strain gage orientation. The normal strain component along the longitudinal direction  $a$  (making an inclination  $\beta$  with the horizontal axis of notched configuration) of the strain gage at a point  $P$  is expressed as follows [14]:

$$2G\varepsilon_a = r^{\lambda_1-1} A_1 f_1(\theta, \beta, \lambda_1, \nu, \gamma) + r^{\lambda_2-1} A_2 f_2(\theta, \beta, \lambda_2, \lambda_2^*, \gamma, \nu, r) + r^{\lambda_2-1} A_2^* f_2^*(\theta, \beta, \lambda_2, \lambda_2^*, \gamma, \nu, r) \tag{8}$$

where  $\varepsilon_a$  denotes the normal strain along the direction  $a$  as stated above whereas  $f_1$ ,  $f_2$  and  $f_2^*$  are the functions representing the first-order and the second-order terms of the strain series. For notched configurations associated with complex second-order eigen value and Williams' coefficient,  $f_2$  and  $f_2^*$  do occur simultaneously. On the other hand, for notched configurations associated with real second order eigen value and Williams' coefficient, only  $f_2$  does occur and  $f_2^*$  does vanish. Details can be obtained from successive paragraphs and from references [14, 15].

$K_I^V$  can be easily computed using Eq. (5) once  $A_1$  gets computed. The computation of  $A_1$  has been made easier by the proposed strain gage technique for sharp V-notched configurations because a systematic approach has been adopted for transforming the multiple strain gage problem to single strain gage problem [14]. This approach as proposed by the authors for sharp V-notched configurations is predicted to have significantly minimized the effort of the overall analysis. Equation (8), thus, could

be finally expressed as

$$2G\varepsilon_a = r^{\lambda_1-1} A_1 f_1(\theta, \beta, \lambda_1, \nu, \gamma) \tag{9}$$

where

$$f_1(\theta, \beta, \lambda_1, \nu, \gamma) = \lambda_1 \left\{ \begin{array}{l} \cos^2 \beta \left[ \cos \theta(\lambda_1 - 3) + \cos \theta(\lambda_1 - 1) \right] - \\ \quad [2\kappa + \cos \lambda_1(2\pi - \gamma)] \\ \quad \cos \theta(\lambda_1 - 3) \sin^2 \beta + \\ \quad 2\kappa \cos \theta(\lambda_1 - 1) \sin^2 \beta - \\ \quad \cos \theta(\lambda_1 - 1) \cos \lambda_1(2\pi - \gamma) \sin^2 \beta - \\ \quad \sin \theta(\lambda_1 - 3) \sin 2\beta - \\ \quad \cos \lambda_1(2\pi - \gamma) \sin \theta(\lambda_1 - 1) \sin 2\beta - \\ \quad \lambda_1 \cos^2 \beta \cos \theta(\lambda_1 - 3) + \\ \quad \lambda_1 \cos^2 \beta \cos \gamma \cos \theta(\lambda_1 - 1) + \\ \quad \lambda_1 \cos \theta(\lambda_1 - 3) \sin^2 \beta - \\ \quad \lambda_1 \cos \gamma \cos \theta(\lambda_1 - 1) \sin^2 \beta + \\ \quad \lambda_1 \sin \theta(\lambda_1 - 3) \sin 2\beta - \\ \quad \lambda_1 \cos \gamma \sin \theta(\lambda_1 - 1) \sin 2\beta \end{array} \right\} \tag{10}$$

As Eq. (9) comprises only one unknown coefficient  $A_1$ , hence only one strain gage is enough to measure the same.

### 2.3 Optimal Radial Strain Gage Locations

The Eq. (9) substantiates that locating valid or optimal radial location of the strain gage is a prerequisite for the accurate evaluation of  $K_I^V$ . The authors have already devised the systematic procedure for locating valid or optimal gage locations associated with sharp V-notched configurations [14]. The optimal radial strain gage locations can be selected from the range as follows

$$r_{\min} \leq r \leq r_{\max} \tag{11}$$

where

$$r_{\min} = 1.25 \times \text{Plate thickness} \tag{12}$$

Usually the Eq. (11) will yield a valid or optimal radial strain gage location if any radial distance  $r$  from the notch tip along the gage line is found satisfying the criterion

of the equation (Eq. (11)). Equation (11) does not permit pasting of the strain gage beyond the parameter  $r_{\max}$  known as the maximum permissible radial strain gage distance. From the Eq. (11), we may conclude that the parameter  $r_{\max}$  decides the optimal or valid radial gage location for a given SENT (single edge notched tensile) configuration. The methodology to estimate the  $r_{\max}$  can be learned in details from ref. [14]. However, it can be summarized that the value of  $r_{\max}$  is found from the plot of  $\ln(\epsilon_a)$  versus  $\ln(r)$  which is the result of finite element analysis. The results section below will discuss how the  $r_{\max}$  value gets affected by the notch length  $a$  and proximity of boundary.

### 3 Results and Discussions

In the present paper, the influence of the notch length and proximity of boundary on the maximum permissible radial strain gage distance  $r_{\max}$  is studied. As the ratio  $a/b$  increases, the notch length  $a$  also increases and simultaneously the notch tip comes closer to the right boundary for a given plate width  $b$ . In the study presented in this paper, the proximity or the closeness of the right boundary is quantified by the net ligament length  $(b - a)$ . To see the variation of  $r_{\max}$  with the ratio  $a/b$ , the effect of increase in notch length is independently observed by considering higher values of net ligament length  $(b - a)$  i.e. significantly higher distance between the notch tip and the right boundary. To get this, a SENT configuration with  $b = 1200$  mm and  $h/b = 3$  is assumed ( $h$  is the half of the height of sharp V-notched full plate). Notch lengths  $a = 7.5, 15, 30,$  and  $60$  mm are assumed leading to significantly smaller values of  $a/b = 0.00625, 0.0125, 0.025,$  and  $0.05$ . As the  $a/b$  values are significantly smaller, so it could be imagined that the right boundary of the SENT plate would have no or insignificant influence when the notch length increases from  $7.5$  to  $60$  mm. Other input data considered for the present study are available in Table 1. The FEA meshing pattern can be seen in Fig. 3. Figure 4 depicts the plots of  $\ln(\epsilon_a)$  versus  $\ln(r)$  along the gage line for the SENT plates under plane stress condition for  $a/b = 0.00625, 0.0125, 0.025,$  and  $0.05$ . Figure 4 also depicts the points of deviation yielding the values of  $r_{\max}$ . It is seen from the numerical output (Table 2) that when the right boundary is distantly located from the notch tip, then the  $r_{\max}$  values are substantially governed by the notch length in such a fashion that the  $r_{\max}$  increases when notch length increases.

**Table 1** Essential parameters corresponding to the SENT plate

Notch angle ( $\gamma$ )	First eigen value ( $\lambda'_1$ )	$b$ (mm)	$a/b$	$h/b$	$E$ (GPa)	$\nu$	$\sigma$ (MPa)
30°	0.5015	1200	0.00625, 0.0125, 0.025 and 0.05	3	200	1/3	100



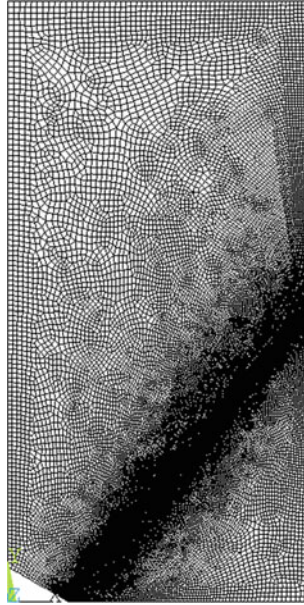


**Fig. 3** Finite element meshing pattern for a SENT plate (half symmetry) showing the strain gage line (darkened portion) along which the strain gage ought to be pasted at suitable location

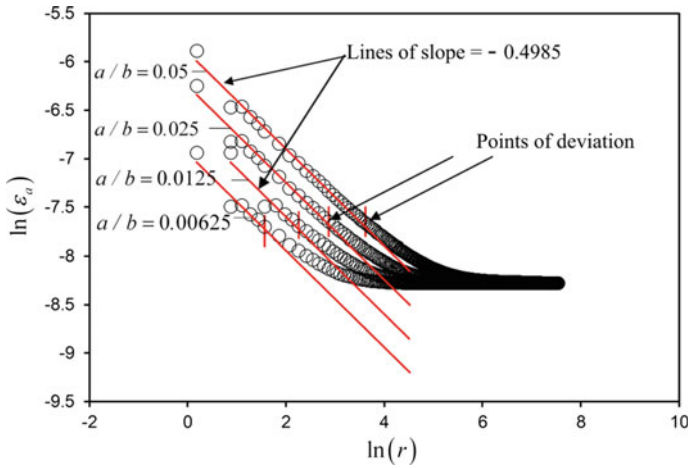


**Fig. 4** Plot of  $\ln(\epsilon_a)$  versus  $\ln(r)$  with  $a/b = 0.00625-0.05$  for a notch angle  $\gamma = 30^\circ$

**Table 2** Variation of the  $r_{\max}$  with notch length  $a$  of the SENT configuration ( $b = 1200$  mm, notch angle  $\gamma = 30^\circ$  and  $h/b = 3$ )

$a/b$	$a$ (mm)	$r_{\max}$ (mm)	$r_{\max}/a$	$r_{\max}/(b - a)$
0.00625	7.5	4.80	0.640	0.004
0.0125	15	9.60	0.640	0.008
0.025	30	17.66	0.589	0.015
0.05	60	37.29	0.622	0.033
0.1	120	57.58	0.480	0.053
0.2	240	118.01	0.492	0.123
0.4	480	488.46	1.018	0.678
0.6	720	126.07	0.175	0.263
0.8	960	24.32	0.025	0.101

Figure 5 depicts the graphical trend of the  $r_{\max}/a$  and  $r_{\max}/(b - a)$  with  $a/b$  shown in Table 2. From Fig. 5 and Table 2, it can be seen that in case of significantly smaller  $a/b$ , the values of  $r_{\max}/a$  are nearly constant as well as finite. On the contrary, the values of  $r_{\max}/(b - a)$  approach zero for lesser  $a/b$  which corroborates that the notch length  $a$  is the governing parameter in determination of  $r_{\max}$ . When the ratio  $a/b$  further increases, then the increase in  $r_{\max}$  values up to an extent and subsequent decrease in  $r_{\max}$  values could be owing to the predominating effect of notch length  $a$  and the net ligament length  $(b - a)$  respectively as shown in Fig. 5.

The effect of the right boundary is predicted to have begun when the ratio  $a/b$  exceeds 0.4. As the notch length  $a$  increases from  $a/b = 0.2$  to 0.4, the  $r_{\max}$  value

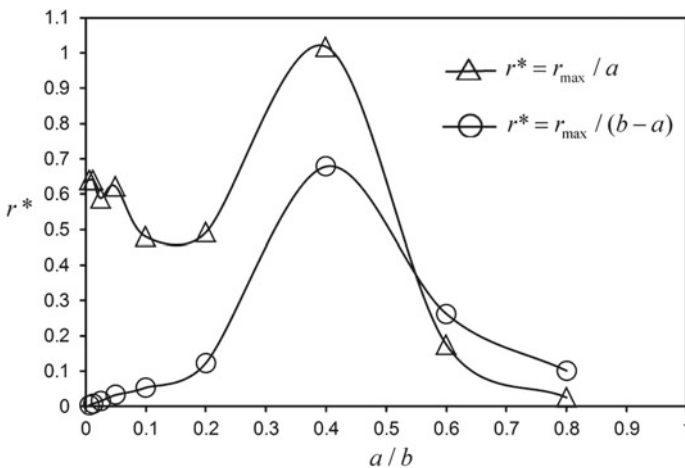


**Fig. 5** Variation of  $r_{\max}$  with the ratio  $a/b$  (ranging from 0.00625 to 0.8) for SENT plates with notch angle  $\gamma = 30^\circ$

continues to increase due to the predominance of notch length over the boundary effects (Table 2 and Fig. 5). Once the value of  $r_{\max}$  reaches a maximum value of 488.46 mm (Table 2) at  $a/b = 0.4$ , the value of  $r_{\max}$  is seen decreasing with successive increase in  $a/b$  which signifies the predominance of the proximity or closeness of right boundary or simply the boundary effect or the net ligament length ( $b - a$ ).

Therefore, the aforementioned comments are briefly explained as: (a) the  $r_{\max}$  value increases with the increase in notch length till the proximity of the right boundary remains ineffective which generally happens at reasonably lower  $a/b$  ratio and (b) the  $r_{\max}$  value decreases with the increase in  $a/b$  due to the predominance of the boundary effects (or the effect of the proximity of the right boundary) which happens at relatively larger values of  $a/b$ .

## 4 Conclusions

An optimal radial strain gage location plays a vital role in estimation of accurate NSIF  $K_I^V$  for a specific geometry containing sharp V-notch using single strain gage. In the sections discussed in this presented paper, it has been reported that an optimal radial strain gage location is further governed by a parameter known as maximum permissible radial distance  $r_{\max}$ . Interestingly, the parameter  $r_{\max}$  value is found to be exhibiting a peculiar behavior in response to two other parameters viz. the notch length  $a$  and the net ligament length ( $b - a$ ). It is to be understood here that when the notch length increases, then the net ligament length decreases at the same time. In summary, the increase in the notch length and the corresponding decrease in the net ligament length occur concurrently and this results into a peculiar behavior of  $r_{\max}$ . A systematic study presented in this paper shows that the  $r_{\max}$  value is greatly influenced by the notch length  $a$  for lesser values of  $a/b$  which results in the increase in  $r_{\max}$  with the increase in notch length. The decreasing net ligament length ( $b - a$ ) shows no influence on the  $r_{\max}$  value up to  $a/b = 0.4$ . However, as the ratio  $a/b$  further increases from  $a/b = 0.4$ , the  $r_{\max}$  value astonishingly starts decreasing showing the influence of decreasing net ligament length. It has been also observed that in cases of extremely smaller  $a/b$  ratios, the increase in  $r_{\max}$  with increasing notch length is relatively less than that in cases of higher  $a/b$  ratios.

## References

1. Dunn ML, Suwito W, Cunningham S (1997) Stress intensities at notch singularities. *Eng Fract Mech* 57:417–430
2. Tomari K, Tonogai S, Harada T, Hamada H, Lee K, Morii T, Maekawa Z (1990) The V-notch at weld lines in polystyrene injection moldings. *Polym Eng Sci* 30:931–936
3. Williams ML (1952) Stress singularities resulting from various boundary conditions in angular corners of plates in extension. *J Appl Mech* 19(4):526–528

4. Stern M, Becker EB, Dunham RS (1976) A contour integral computation of mixed-mode stress intensity factors. *Int J Fract* 12(3):359–368
5. Ayatollahi MR, Nejati M (2011) Determination of NSIFs and coefficients of higher order terms for sharp notches using finite element method. *Int J Mech Sci* 53(3):164–177
6. Gross B, Mendelson A (1972) Plane elastostatic analysis of V-notched plates. *Int J Fract Mech* 8(3):267–276
7. Yu T, Shi L (2012) Determination of sharp V-notch stress intensity factors using the extended finite element method. *J Strain Anal Eng* 47(2):95–103
8. Kondo T, Kobayashi M, Sekine H (2001) Strain gage method for determining stress intensities of sharp-notched strips. *Exp Mech* 41(1):1–7
9. Kondo T, Kurabe Y, Sasaki T, Kurahashi T, Miyashita Y (2014) Use of strain gages for determining generalized stress intensity factors of sharp V-notched plates under transverse bending. *Eng Fract Mech* 124–125:248–261
10. Ayatollahi MR, Nejati M (2011) Experimental evaluation of stress field around the sharp notches using photoelasticity. *Mater Des* 32(2):561–569
11. Prassianakis JN, Theocaris PS (1980) Stress intensity factors at V-notched elastic, symmetrically loaded, plates by the method of caustics. *J Phys D Appl Phys* 13(6):1043–1053
12. Yao XF, Yeh HY, Xu W (2006) Fracture investigation at V-notch tip using coherent gradient sensing (CGS). *Int J Solids Struct* 43(5):1189–1200
13. Dehnavi MRY, Eshraghi I, Soltani N (2013) Investigation of fracture parameters of edge V-notches in a polymer material using digital image correlation. *Polym Test* 32(4):778–784
14. Paul P, Murthy KSRK, Chakraborty D (2018) A strain gage technique for mode I notch stress intensity factor of sharp V-notched configurations. *Theor Appl Fract Mec* 94:57–70
15. Paul P, Murthy KSRK, Chakraborty D (2018) Effect of material properties on optimal radial strain gage locations in sharp V-notched configurations. In: 3rd international conference on design, analysis, manufacturing and simulation, EDP Sciences, Les Ulis
16. Dally JW, Sanford RJ (1987) Strain-gage methods for measuring the opening-mode stress-intensity factor. *KI Exp Mech* 27:381–388

# Mathematical Prediction of Thermal Runaway Conditions During the Nitration of DNT to TNT



Md. Touseef Ahamad, A. Seshu Kumar and A. M. K. Prasad

**Abstract** The reasons for the runaway during the nitration of DNT to TNT have been investigated mathematically. All the data required for chemical kinetics has extracted from Kozak's experimental work. M. M. Khader had proposed a new technique, Picard-Pade method, and this work has been employed in the present work to solve the mathematical model and the results obtained were well substantiated using Kozak's experimental work. The influence of different mixtures on the temperature growth has been investigated and discussed in detail by dividing the temperature curve into three regions depending upon the change in the slope with respect to time. All the mixture compositions considered were within the range of Orlova's work. The influence of DNT's concentration and its dissociation in the presence of sulfuric acid on the runaway reaction has been explained clearly with the numerical solutions. Within the considered mixture compositions, the mixture with controllable temperature growth is a 40–30–18–12 mixture and the mixture with uncontrollable temperature growth is 63–7–25–5. The computational tool used in this work to solve the mathematical model in MATLAB.

**Keywords** Mathematical · MATLAB · Nitration · Picard-Pade · Runaway · DNT · TNT

## 1 Introduction

The essential comprehension of a runaway reaction emerges from the thermal explosion theory as per Semenov. This hypothesis manages the challenge between heat generation by an exothermic reaction and heat removal from the response mass to, for example, the cooling jacket. The heat generation depends, as indicated by

---

Md. Touseef Ahamad (✉) · A. M. K. Prasad  
Department of Mechanical Engineering, University College of Engineering Osmania University,  
Hyderabad 500007, India  
e-mail: [Touseefmd.anu@gmail.com](mailto:Touseefmd.anu@gmail.com)

A. Seshu Kumar  
Head, Engineering Services Division, IICT, Hyderabad 500007, India

© Springer Nature Singapore Pte Ltd. 2020  
L. Vijayaraghavan et al. (eds.), *Emerging Trends in Mechanical Engineering*,  
Lecture Notes in Mechanical Engineering,  
[https://doi.org/10.1007/978-981-32-9931-3\\_54](https://doi.org/10.1007/978-981-32-9931-3_54)

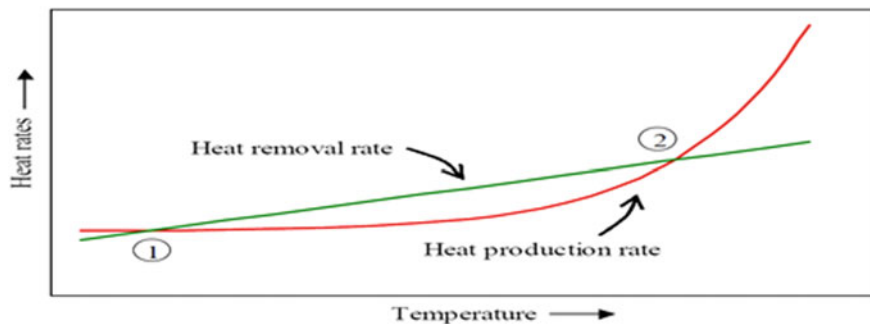


**Fig. 1** Heat flow diagram. Heat production rate by chemical reaction and heat removal rate by cooling [1]. © from Bob Arnold August VAN Woezik

Arrhenius, exponentially on temperature, while the heat removal depends linearly on temperature [1], (see Fig. 1).

A steady state will be reached as soon as the heat production rate is equivalent to the heat removal rate. This will be the situation for both the temperatures of the convergences in (see Fig. 1). The level of control of the heat production rate legitimately pursues from this plot. At the intersection (1), the slope of the heat removal line is more prominent than that of the heat production curve and therefore, a little deviation from this steady state consequently results in a return to its origin. Along these lines, convergence (1) speaks to a stable working point and an exothermic reaction is under control. On the other hand, intersection (2) speaks to a temperamental working point. On the off chance that for reasons unknown, a temperature deviation happens, the first working conditions will never be reached again. In the case of temperature decrease, the steady state of intersection (1) will be attained. In case of an increase, the rate of heat generation will always exceed that of the heat removal. This will prompt an unhindered self-increasing speed of the reaction rate and along these lines of the heat generation rate, which is known as a runaway reaction [1].

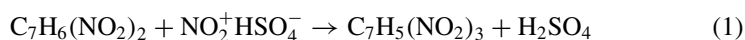
Kozak [2] has done experiments on the nitration of DNT to TNT and found the reasons for the initiation of thermal runaway conditions during the reaction. Governing chemical equations in converting the DNT to TNT and oxidation reactions have been mentioned in this work; the kinetics data that is required during the solving of mathematical model has been taken from this work.

## 2 Methodology

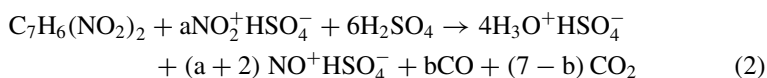
### 2.1 The Basic Chemical Reactions Under Study

This work mainly involves the prediction of the end temperatures for the reactions involved during the nitration of DNT to TNT. There are two reactions involved in the nitration of DNT nitration reaction and oxidation reaction [2, 4].

Nitration is the responsible step for the conversion of DNT to TNT. It is represented as follows



Oxidation is an unwanted secondary reaction which is highly exothermic and has high reaction rate. Therefore, the end temperature will be high due to this oxidation reaction.



### 2.2 Modeling the Selected Chemical Reactions

A mathematical model involving the mass and energy conservations was formulated for predicting thermal runaway conditions.

#### 2.2.1 Mass Conservation

The chemical species that influences both the selected reactions are  $\text{H}_2\text{SO}_4$ ,  $\text{HNO}_3$ , DNT, TNT. A mathematical model consisting of these chemical compounds in the form of ordinary differential equations has been created. The boundary conditions are taken from the experimental work done in Kozak [2]. The chemical kinetic values for nitration reaction were taken from the work of Urbanzki [4], and for oxidation reaction, the data reported by Kozak [2] was used. The heat of reaction for oxidation reaction was estimated based on the heat of formation and bond association enthalpies using the following governing equation.

$$(\Delta h)_{\text{rxn}} = (\Delta h)_{\text{react}} - (\Delta h)_{\text{prod}} \quad (3)$$

As nitration occurs at a temperature of 90 °C so the exothermic value of the reaction will be less and the end temperature will be in control. But the initiation of

secondary oxidation reaction will increase the temperature and results in the thermal runaway condition. As per the literature [2] sulfuric acid, nitric acid, DNT, TNT influences the reactions the most. An attempt has been in the present work to find the appropriate proportions of these four chemical species in the reaction mixture which gives us an idea how the concentration of these species will affect the temperature at that particular time.

The possible reaction rates for both the reactions are as follows:

$$R_n = \alpha \times [v] \times [w] \quad (4)$$

$$R_o = \beta \times [u] \times [v] \quad (5)$$

The following equations were formulated for determining the concentration of the chemical compounds in the selected chemical reactions.

$$\frac{du}{dt} = R_n - R_o \quad (6)$$

$$\frac{dv}{dt} = -R_o \quad (7)$$

$$\frac{dw}{dt} = -R_n - R_o \quad (8)$$

$$\frac{dy}{dt} = R_n \quad (9)$$

### Notations

$u$	Concentration of the sulfuric acid ( $[C_{H_2SO_4}]$ ).
$v$	Concentration of the nitric acid ( $[C_{HNO_3}]$ ).
$w$	Concentration of the dinitrotoluene ( $[C_{DNT}]$ ).
$y$	Concentration of the trinitrotoluene ( $[C_{TNT}]$ ).
$R_n$	Reaction rate of the nitration reaction.
$R_o$	Reaction rate of the oxidation reaction.
$\alpha$	Rate constant for the nitration reaction.
$\beta$	Rate constant for the oxidation reaction.
$(\Delta h)_{rxn}$	Enthalpy of reaction.
$(\Delta h)_{react}$	Enthalpies of reactants.
$(\Delta h)_{prod}$	Enthalpies of the products.

### 2.2.2 Energy Conservation

The main source for the increase in the heat energy is the exothermic nature of the reactions, especially the oxidation reaction as the value of the heat of the reaction is



high and the temperature increases rapidly. The other source is the concentration of the chemical species and the chemical species with a high heat of reaction and high concentration would result in the rise of end temperature.

In this work, the dangerous combination and the safe combination of the mixture have been presented in the results section.

The equation that governs the development of heat due to the reaction [3, 6] can be represented as

$$\frac{dT}{dt} = (R_n \times (\Delta h)_{NIT} + R_o \times (\Delta h)_{OX}) / (\rho \times C_P) \tag{10}$$

*Notations*

- $\frac{dT}{dt}$  Change in temperature ( $T$ ) with respect to time ( $t$ ).
- $(\Delta h)_{NIT}$  Heat of reaction value for nitration reaction.
- $(\Delta h)_{OX}$  Heat of reaction value for the oxidation reaction.
- $\rho$  Density of the mixture.
- $C_P$  Specific heat at constant pressure of the mixture.

Now, these equations have been solved to find the growth of temperature to predict the thermal runaway conditions using a Picard-Pade technique.

### 2.3 Solving the Mathematical Model

#### 2.3.1 Picard-Pade Method

In the present work, the Picard Iteration series will be a function of ‘Time’ that is  $f(t)$ . The order we have chosen to truncate the series is ‘7’ which give us Picard Iteration series up to ‘ $t^6$ .’ A number of iterations employed in the Picard Iteration method in order to obtain the series are ‘5.’ After truncating the Picard Iteration series for the order of ‘7,’ it is used in the Pade approximation to solve the truncated series.

The Pade approximation [4] is a rational fraction approximation to the value of the function. The Pade approximation can be denoted as follows

$$P[n/m](t) = \frac{\sum_0^n P_n \times t^n}{1 + \sum_1^m Q_m \times t^m} \tag{11}$$

where  $P$  and  $Q$  represent the polynomials with degrees ‘ $n$ ’ and ‘ $m$ .’

The crucial step in getting forward with this technique is choosing  $n$  and  $m$  values in order to obtain the best approximation. The choice of these degrees of numerator and denominator can be made based upon the shape of the required thermal profile. The criterion that is best suited in this work is ‘ $n > m$ .’

The system of differential Eqs. (4)–(8) has been formulated as a given blow and solved using Picard Iteration method.

$$u_{i+1} = u(0) + \int_0^t [R_n - R_o] dt \quad (12)$$

$$v_{i+1} = v(0) + \int_0^t [-R_o] dt \quad (13)$$

$$w_{i+1} = w(0) + \int_0^t [-R_n - R_o] dt \quad (14)$$

$$y_{i+1} = y(0) + \int_0^t R_n dt \quad (15)$$

$$T_{i+1} = T(0) + \int_0^t (R_n (\Delta h)_{\text{NIT}} + R_o (\Delta h)_{\text{OX}}) / (\rho C_p) dt \quad (16)$$

### Notations

$R_n$  alpha  $\times$   $v_i$   $\times$   $w_i$

$R_o$  beta  $\times$   $u_i$   $\times$   $v_i$

where  $u(0)$ ,  $v(0)$ ,  $w(0)$ , and  $y(0)$  represent the initial concentration values of the chemical compounds at the starting of the reaction, where  $T(0)$  is the initial temperature. In the present work, the value of  $T(0)$  has been chosen as 90 °C as the reaction tends to start at that temperature. Generally, the reagents dinitrotoluene and trinitrotoluene concentration are maintained at 30% and that of acids form the remaining 70% of the reaction mixture. The proportions of individual species namely DNT, TNT,  $\text{H}_2\text{SO}_4$ , and  $\text{HNO}_3$  may be varied within the set proportion limits.

Kinetic constants and heat of reactions [2, 4] for the two reactions have been taken as alpha =  $1.2 \times 10^{-4}$  and  $(\Delta h)_{\text{NIT}} = -73.15$  kJ/mol, for oxidation reaction, activation energy  $E_a = 132$  kJ/mol, the value of preexponential factor  $A = 3.2 \times 10^{10}$  1/mol.sec at 200 °C and  $(\Delta h)_{\text{OX}} = -788$  kJ/mol.

By solving the above equations, we have obtained a series in 't.' Now, the truncated equation has been used for Pade approximation method. In Pade approximation method, the challenge will be finding the values of polynomials in numerator and denominator that is  $P(t)$  and  $Q(t)$  values. The degree has been chosen and it is  $n = 4$  and  $m = 2$  which satisfies the condition in this work based on the nature of thermal profile reported by Kozak [2] ( $n > m$ ). The total order of the equation can be represented as  $n + m$ .

The Pade approximation for temperature after five iterations of the Picard Iteration method  $T_5(t)$  with  $P[4/2]$  for the mixture with the combination of 65–5–18–12 can be shown as

$$P[4/2] = \frac{80 + 151.7235t + 13.1925t^2 - 0.0588t^3 + 0.0003t^4}{1 + 1.8252t + 0.0365t^2} \quad (17)$$

In the same way, we have obtained the Pade approximation  $P[4/2]$  values for the  $u_5(t)$ ,  $v_5(t)$ ,  $w_5(t)$ , and  $y_5(t)$  and it is iterated for 250 s as the reaction takes place for

250 s. Graphs have been plotted between temperature, concentration, and time in the specified interval.

The MATLAB software was used to solve the selected chemical system in the present work.

### 3 Results and Discussions

For the purpose of analysis, we have considered three types of mixtures of acid mixture and reagent mixture. The variation in acid mixtures is taken as ( $\text{H}_2\text{SO}_4 + \text{HNO}_3$ ), 63%–7%, 55%–15%, 40%–30%. The variation in reagent mixtures (DNT + TNT) is taken as 25%–5%, 22%–8%, 18%–12%.

Keeping the acid concentration constant at 63% sulfuric acid and 7% nitric acid and varying the composition of DNT and TNT in the proportion of 25–5, 22–8, and 18–12, the rise in the temperature was obtained as shown in (see Fig. 2) There are three distinct regions in the temperature profiles: Initial rapidly increasing temperature phase 1 during nitration reaction, steadily increasing temperature phase 2 indicating stabilization of nitration reaction and initiation of the oxidation reaction, and final briskly increasing temperature phase 3 due to the reaction mixture undergoing complete oxidation reaction.

It can be noted from the (see Fig. 2) that the mixture 63–7–25–5 shows faster temperature growth in 63–7–25–5 in phase 1 and the phase 2 occurs at a higher temperature of about 250 °C when compared with the other two compositions. While

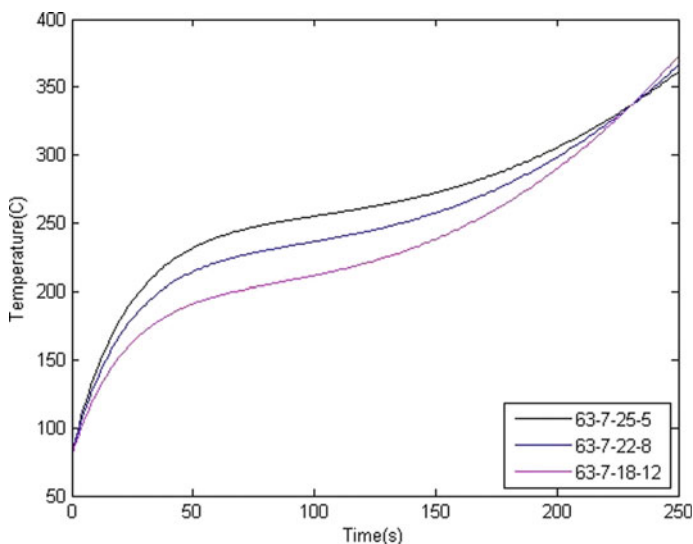
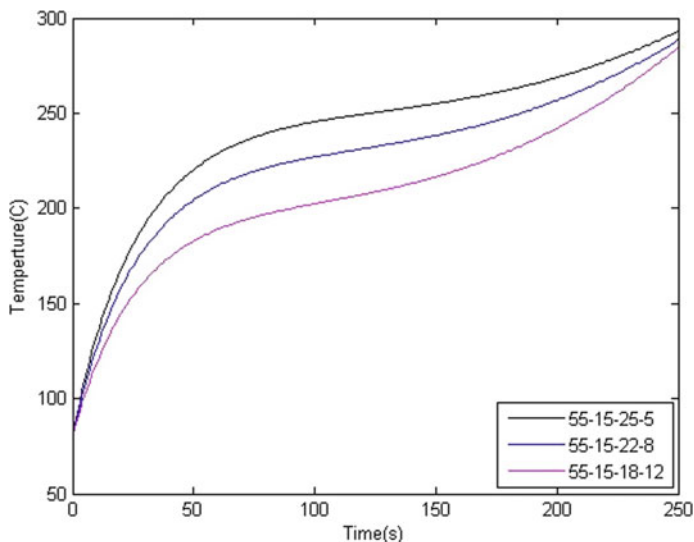


Fig. 2 Change in temperature with respect to time for acid mixture 63%–7%



**Fig. 3** Change in temperature with respect to time for acid mixture 55%–15%

it takes less than 50 s to reach the temperature of 200 °C in case of 63–7–25–5, the mixture 63–7–18–12 takes more than 80 s. On the other hand, by keeping the acid concentration at 55% sulfuric acid and 15% nitric acid and varying the reagent mixtures in the same proportion as earlier, the mixtures behave as shown in (see Fig. 3). It may be seen that the curves shift to the right indicating higher times for the same end temperatures.

With acid concentrations at 40 and 30 and varying the reagent's concentration in the same manner as earlier proportions, the following plot (see Fig. 4) was obtained. In 40–30 plot, it shows that the growth of temperature in phase 1 is less when compared with the other proportions of mixtures. It takes 100 s to reach 220 °C, and phase 3 is absent in 40 and 30 plot which gives us an idea that the temperature rise due to oxidation reaction is absent.

### 3.1 Discussion

In literature [2], it is given that the highest temperature achieved by the reaction is 340–360 °C which will lead to the explosion. That means, the runaway phenomena have already been taken place and it reaches the uncontrollable state. The lowest can be around 160–180 °C but it has the decreasing trend which can be controllable and decreases with time.

This work mainly concentrates on the temperature development in the nitration of DNT to TNT with different composition mixtures. From the literature, it is evident

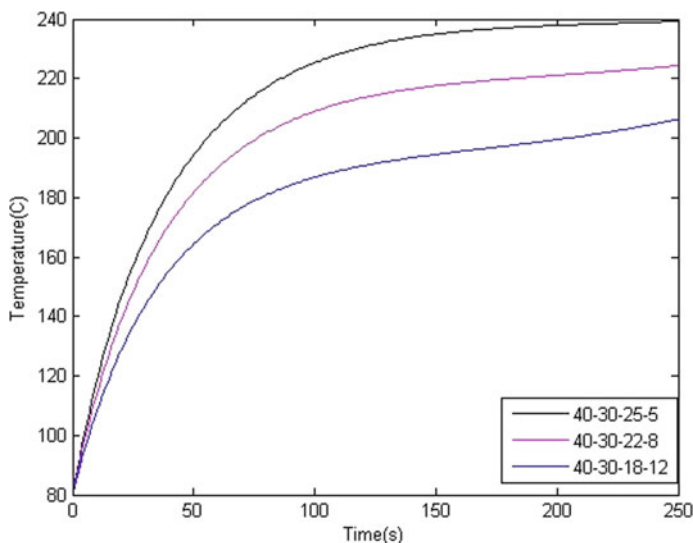


**Fig. 4** Change in temperature with respect to time for acid mixture 40%–30% Discussion

that the main reason for initiating a runaway phenomenon during nitration of DNT is either increase in the acid mixture (sulfuric acid) or increase in reagent's mixture (DNT). If we observe closely, above series of plots shows the same trend. We have investigated the change in temperature with different acid and reagent mixtures as shown in above plots. The first three plots represent the change in temperature due to change in reagent's mixture. The next three plots give us an idea of how temperature is changing due to change in the acid mixture. From these plots, we can observe that the temperature follows a trend of decreasing and increasing slope. The decreasing slope of the curve is when it is executing nitration reaction but the sudden increase in the slope is due to the unwanted oxidation reaction.

In (see Fig. 2) for same acid mixture composition by varying the reagent mixture, we can observe that there is a change in slope. The slope decreases with the decrease in the percentage of DNT in the mixture. Thus, along with acid mixture, DNT dissociation also plays a crucial role in increasing the heat. So, increasing the DNT composition of reagent mixture will increase the temperature growth. We can observe the same with (see Figs. 3 and 4) also.

The first two plots look almost same but if we analyze them with the literature, we can conclude that these two graphs vary in increasing slope that is in the (see Fig. 3), acid mixture has less slope when compared with (see Fig. 2) which says that the increase of temperature in (see Fig. 3) is slow when compared with (see Fig. 2). For explanation, just consider two mixtures with same acid content 63%–7%. If we observe, 63%–7%–25%–5% has more slope than 63%–7%–22%–8%. Now, let us consider (seen Fig. 4) acid mixture graph does not have this increasing slope trend. This gives us an idea that in (see Fig. 4), the effect of oxidation reaction will be negligible and the temperature will increase slowly so that it can be controlled easily.

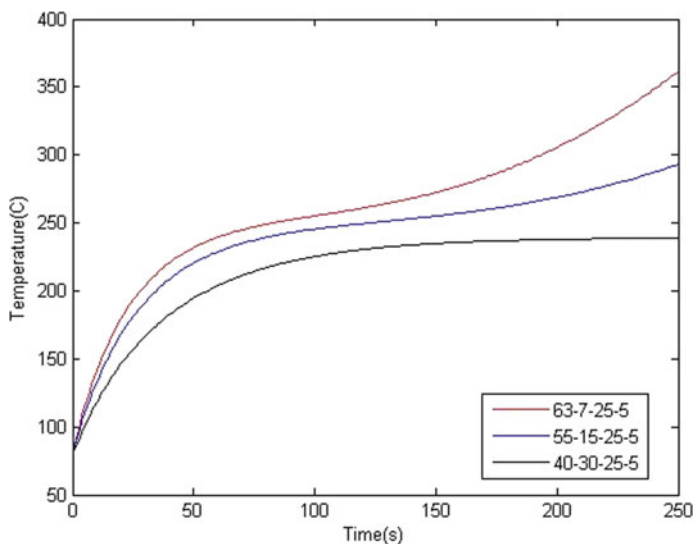


**Fig. 5** Change of temperature with respect to time by keeping reagent's mixture constant at 25%–5%

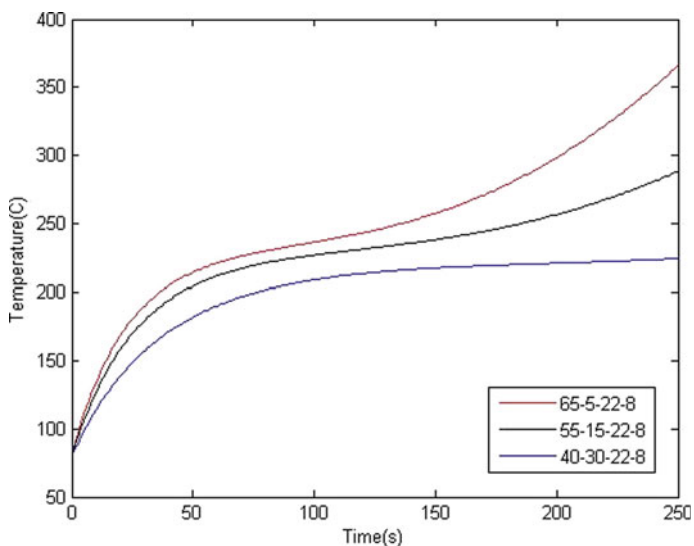


**Fig. 6** Change of temperature with respect to time by keeping reagent's mixture constant at 22%–8%

The next three plots (see Figs. 5, 6, and 7) show us how temperature increases rapidly due to change in the acid's composition. There will be a lot of difference in the end temperatures unlike in (see Figs. 1, 2, and 3). But the only thing is that the

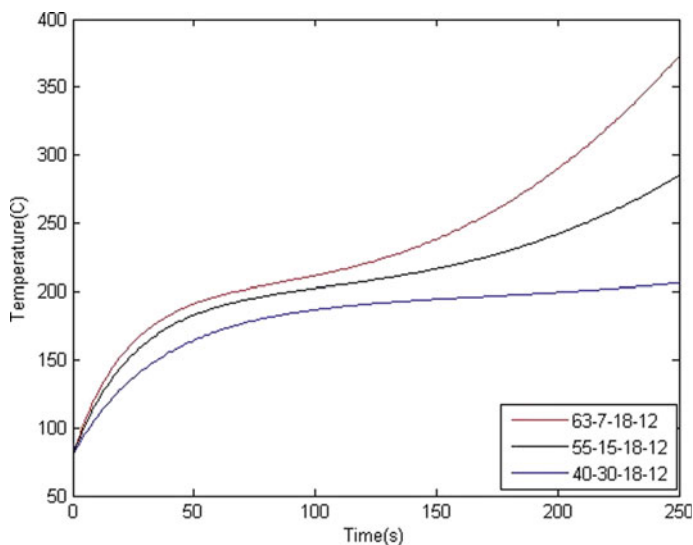


**Fig. 7** Graph showing temperature plots by making reagents concentration 18%–12%

slopes of (see Fig. 6) are slightly less when compared with (see Fig. 7) same as with (see Fig. 7) when compared with (see Figs. 5 and 6).

From these three plots, we have mentioned clearly that which composition is dangerous and uncontrollable and which composition is safest and controllable.

## 4 Conclusion

By using the Picard-Pade technique, the solutions obtained are satisfactory and matching with the literature values. It is evident that with the increase in acid percentage, the end temperature increases. Now, with the increase in reagents content, i.e., DNT's content, the slope of the curve increases rapidly. This shows us that if we increase the DNT's content, the reaction temperature will be uncontrollable as it will be growing in a faster way. The worst mixture or dangerous composition will be 63–7–25–5 if we look at the plot and the observation from result Table 1, and the temperature increases so rapidly after 150 s where the growth of temperature is uncontrollable. The safest mixture is 40%–30%–18%–12% where the slope is in decreasing trend if we look at the plot and the observation from result Table 1 which means that the temperature growth due to this mixture can be controlled.

**Table 1** Observations from results

Proportion of mixtures in %	PHASE-1 (end temperatures)	PHASE-2 (end temperatures)	PHASE-3 (end temperatures)
63–7–25–5	Temp = 250 °C Time = 70 s	Temp = 260 °C Time = 140 s	Temp = 370 °C Time = 250 s
63–7–22–8	Temp = 220 °C Time = 60 s	Temp = 240 °C Time = 130 s	Temp = 370 °C Time = 250 s
63–7–18–12	Temp = 180 °C Time = 80 s	Temp = 220 °C Time = 130 s	Temp = 380 °C Time = 250 s
55–15–25–5	Temp = 240 °C Time = 80 s	Temp = 260 °C Time = 200 s	Temp = 290 °C Time = 250 s
55–15–22–8	Temp = 220 °C Time = 70 s	Temp = 230 °C Time = 170 s	Temp = 280 °C Time = 250 s
55–15–18–12	Temp = 180 °C Time = 60 s	Temp = 210 °C Time = 140 s	Temp = 275 °C Time = 250 s
40–30–25–5	Temp = 230 °C Time = 100 s	Temp = 240 °C Time = 250 s	Doesn't exist
40–30–22–8	Temp = 210 °C Time = 110 s	Temp = 225 °C Time = 250 s	Doesn't exist
40–30–18–12	Temp = 185 °C Time = 120 s	Temp = 205 °C Time = 250 s	Doesn't exist

## References

1. Van Woezik BAA Runaway and thermally safe operation of a nitric acid oxidation in a semi-batch reactor. ISBN 90 - 365 14878
2. Klozak GD, Raikova VM (2010) Hazard of runaway of nitration processes in nitrocompounds production. *Cent Eur J Energ Mater* 7(1):21–32. ISSN 1733-7178
3. Deepak Kumar G, Ahamad MT, Seshu Kumar A, Prasad AMK (2016) Prediction of runaway during the nitration of DNT mathematically-a review. *IJSART* 2(8):68–70. ISSN [ONLINE] 2395-1052
4. Urbanski T Chemistry and technology of explosives. Department of Technology, Politechnika, Pergamon Press, Warszawa
5. Khader MM (2013) On the numerical solutions for chemical kinetics system using Picard-Pade technique. *J King Saud Univ Eng Sci* 25:97–103
6. Bird RB, Stewart WE, Lightfoot EN (2002) Transport phenomena, 2nd edn. Wiley, New York, Chichester, Weinheim, Brisbane, Singapore, Toronto
7. Van Woezik BAA Runaway and thermally safe operation of a nitric acid oxidation in a semi-batch reactor. Thesis University of Twente, Enschede. ISBN 90 - 365 14878
8. Rahman SA, Bakar MZ, Ahmad Z Preliminary study of the heat release from esterification process. *Int J Eng Technol IJET-IJENS* 10(3)
9. Chen C-Y, Wu C-W, Du YS, Yu SW (1998) An experimental study of worst case scenario of nitric acid decomposition in a toluene nitration process. *Institution of Chemical Engineers, Trans I Chem E*, vol 76, Part B, August 1998, 0957–5820



10. Raikova VM, Kozak GD (2009) Safety of exothermal processes in chemical manufacture. Russian University of Chemical Technology, Moscow, p 75
11. Kozak GD, Raikova VM et al (2008) Experimental methods of study of safety of exothermal reactions. Russian University of Chemical Technology, Moscow, p 65
12. Westerterp KR, Molga EJ (2006) Safety and runaway prevention in batch and semi batch reactors—a review. *Chem Eng Res Des* 84(A7):543–552. Institute of Chemical Engineers, *Trans I Chem E, Part A*, July 2006

# Flow Physics Analysis on the Effect of Cambered Airfoil Blades on Vertical Axis Wind Turbines Using CFD



Kanthala Uma Reddy , Bachu Deb , Bidesh Roy   
and Sheikh Mohammad Rashid 

**Abstract** One of the promising kinds of renewable energy is wind energy, but not fully exploited till now because of low efficiency of rotors and no power production at slow wind speeds. A vertical axis wind turbine (VAWT) known as H-Darrieus turbine is capable of working efficiently at low speeds and is capable of solving this issue. The design of turbine blade plays an important role in determining the power produced. Multiple experiments involving NACA series of symmetrical airfoils have been conducted to study the performance, but very few studies are available showing the outcome of using the unsymmetrical blade on an H-Darrieus wind turbine. In this paper, the computational study performed on unsymmetrical NACA airfoil blades of varying camber display improved performance. With the increase in camber, the  $C_L$  value increases up to certain extent, but too much camber can result in decrease in performance.

**Keywords** NACA airfoil · Camber · VAWT · Renewable energy

## 1 Introduction

Growing energy demand and ever-increasing fossil fuel prices combined with environmental pollution has led the researchers to look for alternative sources of energy. Energy resources like solar, wind, biomass, geothermal and tidal energy are renewable and pollution free. Among the different renewable energy, wind energy is the outstanding one, since it is easily available throughout the earth's surface. In order to harvest the dynamic energy of wind into mechanical energy, wind turbines are utilized. Wind turbines can be divided into two major groups, i.e. vertical axis wind turbines (VAWTs) and horizontal axis wind turbines (HAWTs) in which VAWTs are less efficient. In contrast, VAWTs are having the capacity to produce enough power at comparatively lesser wind velocity [1]. These turbines are having the advantages like, simple erection, easy to maintain, less possibility to damage the bird's life,

---

K. Uma Reddy (✉) · B. Deb · B. Roy · S. M. Rashid  
Department of Mechanical Engineering, NIT Mizoram, Aizawl 796012, India  
e-mail: [kanthala.mech@nitmz.ac.in](mailto:kanthala.mech@nitmz.ac.in)

© Springer Nature Singapore Pte Ltd. 2020  
L. Vijayaraghavan et al. (eds.), *Emerging Trends in Mechanical Engineering*,  
Lecture Notes in Mechanical Engineering,  
[https://doi.org/10.1007/978-981-32-9931-3\\_55](https://doi.org/10.1007/978-981-32-9931-3_55)

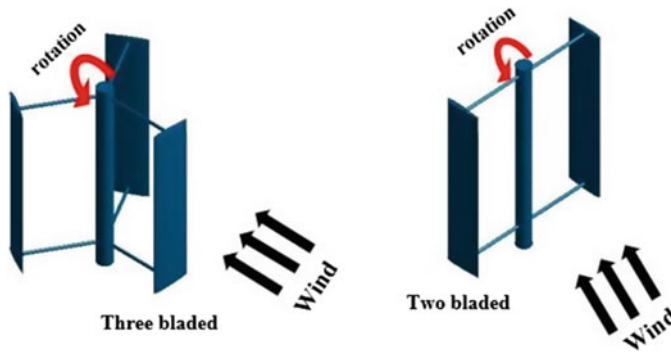


**Fig. 1** Three bladed and two-bladed H-Darrieus rotors

and omni-directional. H-Darrieus rotor, as shown in Fig. 1, falls within the scope of VAWT. H-Darrieus rotor uses the lift forces of the wind to rotate the airfoils of the machine. To increase the performance and efficiency of the VAWT there is a need to select the optimal parameters. Selection of the optimal airfoil shape is one of the vital roles to design an H-Darrieus rotor.

In recent years, it was found that the most of the researches basically concerns about assessment or optimization processes and prediction of coefficient of power ( $C_p$ ), which is the ratio of actual power produced by the rotor to the available wind power, using theoretical methods such as computational fluid dynamics (CFD) and momentum methods. Nevertheless, research on VAWT airfoils is scarcer than those of HAWT airfoils [2]. The aerodynamic performance of 20 various airfoils configurations (symmetrical and unsymmetrical) carried out by Mohamed [3] using 2D CFD to maximize the output power and suggested the S-1046 is one of the promising airfoils to H-Darrieus rotor to generate the power, particularly in urban areas. Chen et al. [3] combine the orthogonal algorithm to automatic computational fluid dynamics analysis (ACFDA) and combine the one factor at a time (OFFAT) with ACFDA to assess an airfoil family and concluded that significant effect is produced on  $C_p$  by the thickness–chord ratio (TCR). Beri and Yao [4] modified the conventional NACA 0018 airfoil at its trailing edge to see the effect on self-starting of VAWT at low wind speed and compared with cambered NACA 2415 airfoil that possess the capacity of self-starting. The researchers confirmed that on modification of NACA 0018 airfoil, superior self-starting abilities was achieved in their modelled turbine. Barker [5], who compared the performances of NACA0012 unsymmetrical (cambered) and symmetrical airfoil, informed that the cambered section provided higher tangential thrust for a larger range of angle of attack (AOA) assuring self-starting ability. Hyun et al. [6] investigated H-Darrieus rotor with cambered NACA 634-021 airfoil under unsteady flow condition and compared the same with the symmetrical NACA 634-021 airfoil. The researchers highlighted that 2.5% larger torque and power coefficients are attained for turbine using cambered airfoil. Deshpande and Li [7] studied

the effect of rotor blade thickness and camber on aerodynamic performance of Darrieus rotor with 3-blades. They used NACA0018 and NACA0022 symmetrical airfoil and also NACA 5522 and LS0421 unsymmetrical airfoil to demonstrate the benefits of cambered blades. Wolff et al. [8] and Ai et al. [9] investigated the aerodynamic performance of the airfoil with morphing trailing edge structures. Generally, for a small thickness airfoil, its lift behaviour is ascertained primarily by its camber [10]. In specific, Bedon et al. [11] and Zamani et al. [12] examined a Darrieus rotor by use of CFD code to evaluate the dynamic and static ability of the rotor in regard to the profile used in its blade. Moreover, by using CFD, the capability of self-starting of VAWTs was analyzed by Worasinchai et al. [13] and Singh et al. [14]. Maruyama et al. [15] and Claessens [16] analyzed the aerodynamic behaviour of the VAWT transforming the existing NACA 0018 airfoil to find out the design goals for the aerodynamic features and to improve the performance.

After going through a number of literatures, three different airfoils having varying camber were chosen to study the aerodynamic characteristics through CFD. This paper aims to study the effect of cambered airfoils blades on the performance of an H-Darrieus VAWT.

## 2 Model Generation and Mathematical Formulation

Generation of models for the numerical study is very crucial during its design stage for proper dimensioning to calculate the results more accurately. Three NACA airfoils namely NACA 0009, NACA 4409 and NACA 7409 were generated by importing coordinates from online airfoil repository [17] to the commercially available designing and simulation software ANSYS Workbench 16.0.

As the study is mostly concentrated on the flow around the airfoils under consideration having air as the working fluid, the equations of continuity and momentum for the fluid in motion are taken into consideration as described in Sect. 2.2.

### 2.1 Generation of Airfoil Models

Three NACA 4-digit airfoils selected, namely NACA 0009, NACA 4409 and NACA 7409 are generated in the design modeller tool of ANSYS Workbench. The three airfoils are as shown in Fig. 2.

The imported coordinates are very small and cannot be used as such, and for simulation, the airfoils are enlarged to fit the test requirements using scaling option within the design modeller.

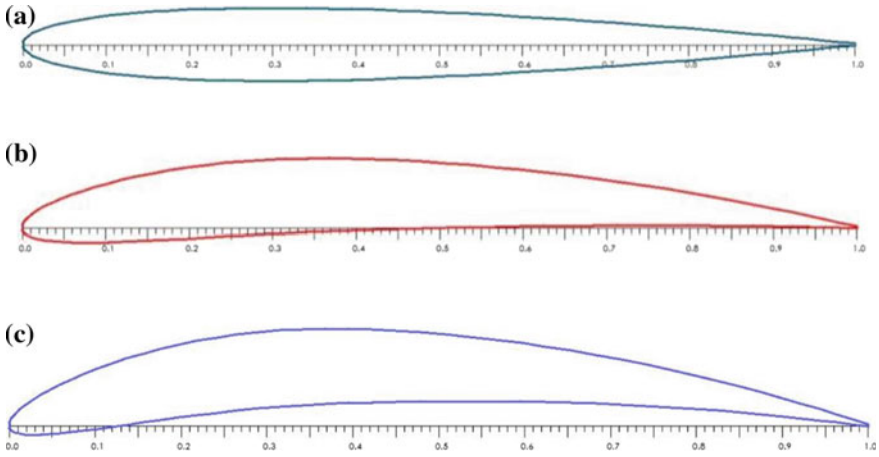


Fig. 2 Airfoils under consideration a NACA 0009, b NACA 4409 and c NACA 7409

### 2.2 Meshing and Boundary Conditions

For this numerical study, CFD is chosen for performance prediction of an H-Darrieus turbine with three different airfoils. The 3D computational fluid domain is generated using ANSYS design modeller with impositions of all boundary conditions as shown in Fig. 3. The model simulation accuracy is affected by the method in which the grid of the mesh is created.

In the present work, discretization of the three-dimensional computational domain is done using unstructured triangular elements by the use of advanced sizing functions in ANSYS meshing module. The grid structure at outer zone and rotating zone are shown in Fig. 3b1, b2, respectively. In the computational domain, meshes were

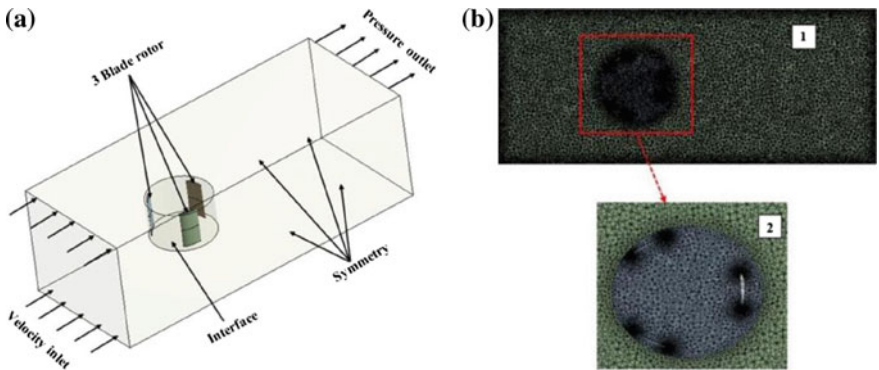


Fig. 3 Computational domain a Boundary condition and b Mesh structure

**Table 1** Boundary specifications

Boundary conditions
Inlet parameter: velocity
Outlet parameter: pressure
Boundary: symmetry
Rotors: wall
Turbulence level: 5%

generated with a growth rate of 1.2 with a smooth transition ratio 0.272 and computations are carried out with different element size of mesh, and each elements size was solved with same set of input parameters, until monitor points reaches steady and imbalance is below 1%, is called grid independence limit. The same procedure was considered for all selected airfoils to predict the flow around the rotor and the boundary specifications which were chosen for flow physics are as shown in Table 1.

### 2.3 Mathematical Formulation

For simulation, 3D models of each airfoil are taken individually to study the flow field around the blade and H-Darrieus rotor consisting of the mentioned airfoil profiles. The simulations are performed in the *Fluent tool* of ANSYS Workbench for predicting the flow behaviour and pressure distribution on the blade geometry. Suitable boundary conditions should be taken to ensure the result obtained is nearly accurate to the field working conditions. The 3D blade model is placed more towards the inlet side of the boundary while the exit side is expanded to have a clear image of the velocity disturbances occurring after the air leaves the rotor blades. Figure 3 represents the actual placement of blade within the boundary and other related dimensions.

For the simulation to work properly, we should choose appropriate numerical model to predict the flow parameters.

The governing equations for the numerical study of fluid flow essentially include the continuity and momentum equations in addition to the appropriate turbulence model, which are expressed as below.

*Continuity equation:*

$$\frac{\partial \rho}{\partial t} + \nabla \cdot (\rho \vec{V}) = 0 \tag{1}$$

*Momentum equation:*

$$\frac{\partial \rho}{\partial t} (\rho \vec{V}) + \nabla \cdot (\rho \vec{V} \vec{V}) = -\nabla p + \nabla \cdot \bar{\bar{\tau}} + \rho \vec{g} + \vec{F} \tag{2}$$

The  $k$ - $\varepsilon$  model and  $k$ - $\omega$  model are the two commonly used 2-equation turbulent-viscosity model. In our study, we have used realizable  $k$ - $\varepsilon$  turbulence model as most of the researchers in this field have used this turbulent model. The two equations of this model comprise of turbulent kinetic energy ( $k$ ) and dissipation rate of turbulent kinetic energy ( $\varepsilon$ ) which are generally expressed as:

*Turbulent kinetic energy ( $k$ ),*

$$\frac{\partial}{\partial t}(\rho k) + \frac{\partial}{\partial x_i}(\rho k u_i) = \frac{\partial}{\partial x_j} \left[ \left( \mu + \frac{\mu_t}{\sigma_k} \right) \frac{\partial k}{\partial x_j} \right] + G_k - \rho \varepsilon - Y_M \quad (3)$$

*Dissipation rate of turbulent kinetic energy ( $\varepsilon$ ),*

$$\frac{\partial}{\partial t}(\rho \varepsilon) + \frac{\partial}{\partial x_i}(\rho \varepsilon u_i) = \frac{\partial}{\partial x_j} \left[ \left( \mu + \frac{\mu_t}{\sigma_\varepsilon} \right) \frac{\partial \varepsilon}{\partial x_j} \right] + C_{1\varepsilon} \frac{\varepsilon}{k} (G_k) - C_{2\varepsilon} \rho \frac{\varepsilon^2}{k} \quad (4)$$

### 3 Results and Discussion

Flow analysis using a Workbench CFD tool Fluent around the airfoils namely NACA 0009, NACA 4409 and NACA 7409. The flow patterns are shown by velocity streamline contours in Fig. 4. With the same airfoils, three different H-Darrieus rotors were analyzed using streamline contours in and around the profile as shown in Fig. 5.

The flow around the symmetrical (non-cambered) NACA 0009 airfoil from the point of entry to exit is mostly constant and attached to the airfoil surface with slight variation in flow velocity near to the surface. Around the medium cambered airfoil, i.e. NACA 4409, the flow is attached to the surface, but the flow velocity is more at the upper surface, which indicates low pressure at the upper surface as compared to the lower surface, i.e. pressure difference exists which is essential for lift generation. High cambered airfoil, NACA 7409, shows the initiation of flow separation from the upper surface just near the maximum camber, which will result in the decreased difference of pressure between the lower and upper surfaces, and hence decreased lift generation. The graph shown in Fig. 4d is a plot between lift coefficient ( $C_L$ ) and AoA of airfoil in regard to the approaching wind stream.

Velocity streamline contours of H-Darrieus rotors having three different NACA airfoils are shown in Fig. 5. The inlet parameter of 6 m/s wind velocity is same for all the three-rotor setup, in which one blade is almost at vertical position to the incoming wind. The leading edge of one blade and the trailing edge of another is facing the incoming wind. The maximum velocity drops from 6 m/s to 3.95 m/s, 3.24 m/s and 3.70 m/s are observed for airfoils NACA 0009, 4409 and 7409, respectively. The drop-in velocity for medium camber blade, i.e. NACA 4409 is more, which indicates more lift generation as compared to other two airfoils.

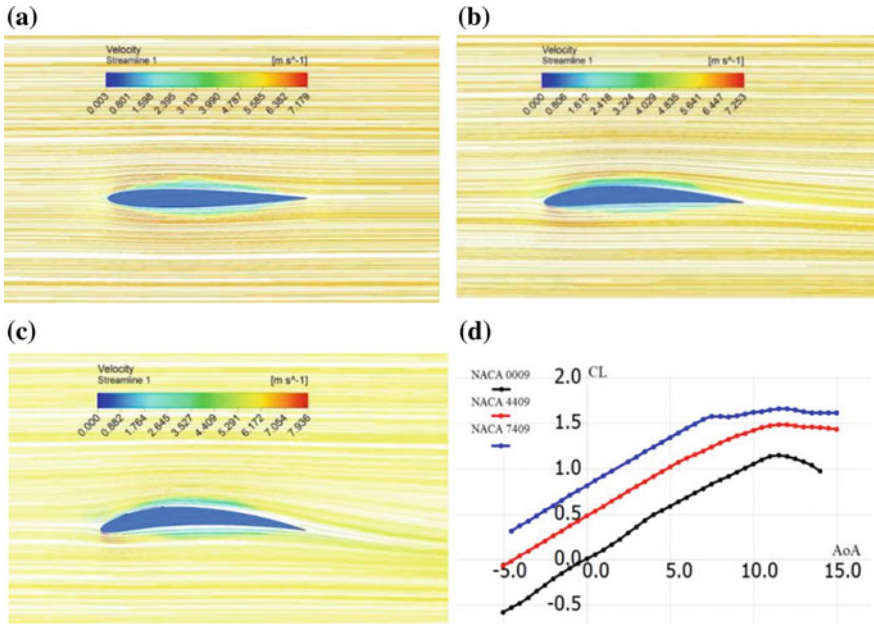


Fig. 4 Velocity streamlines contour plots for a NACA 0009, b NACA 4409, c NACA 7409 and d  $C_L$  versus AoA graph for the three airfoils

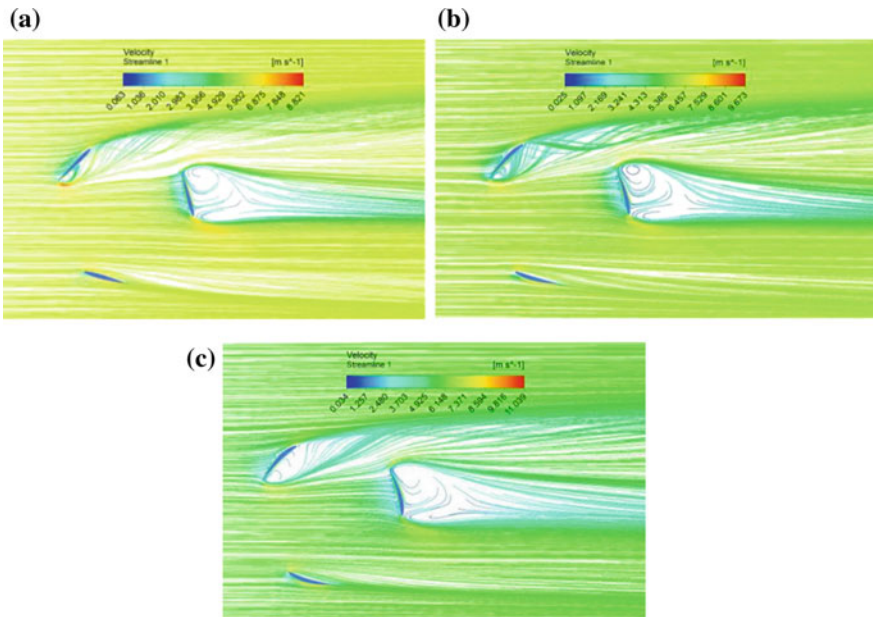


Fig. 5 Velocity streamline contours for H-Darrieus rotor having blade profile a NACA 0009, b NACA 4409 and c NACA 7409



## 4 Conclusion

The numerical study conducted on the NACA 0009, NACA 4409, NACA 7409 airfoils as well as three H-Darrieus rotors with NACA 0009, NACA 4409 and NACA 7409 with varying degree of camber by employing the  $k-\epsilon$  RANS model at an inlet wind speed of 6 m/s. From the velocity streamline contours, the flow around the cambered airfoils is mostly attached to their upper surface creating low pressure and increased velocity at the region, which results in increased lift force for the rotor as compared to the symmetrical rotor. For both NACA 4409 and 7409 airfoils, the lift generation is more, which is reflected in the decreased velocity downstream with NACA 4409 showing maximum drop from 6 to 3.24 m/s.

## References

1. Roy S, Das R, Saha UK (2018) An inverse method for optimization of geometric parameters of a Savonius-style wind turbine. *Energy Convers Manag* 155:116–127
2. Chen J, Xu H, Yang H, Ye C, Liu D (2016) Performance improvement of a vertical axis wind turbine by comprehensive assessment of an airfoil family. *Energy* (11):318–331
3. Mohamed M (2012) Performance investigation of H-rotor Darrieus turbine with new airfoil shapes. *Energy* 47(1):522–530
4. Beri H, Yao Y (2011) Numerical simulation of unsteady flow to show self-starting of vertical axis wind turbine using fluent. *J Appl Sci* 11:962–970
5. Barker JR (1983) Features to aid or enable self-starting of fixed pitch low solidity vertical axis wind turbines. *Wind Eng Ind Aerodyn* 15:369–380
6. Hyun BS, Choi DH, Han JS, Jin JY, Roo CH (2012) Performance analysis and design of vertical axis tidal stream turbine. *J Shipping Ocean Eng* 2:191–200
7. Danao LA, Qin N, Howell R (2012) A numerical study of blade thickness and camber effects on vertical axis wind turbines. *Proc Inst Mech Eng, Part A J Power Energy* 226(7):867–881
8. Wolff T, Ernst B, Seume JR (2014) Aerodynamic behaviour of an airfoil with morphing trailing-edge for wind turbine application. In: *The science of making torque from wind*
9. Ai O, Azarpeyyand M, Lachenal X, Weaver P (2016) Aerodynamic and aerocoustic performance of airfoils using morphing structures. *Wind Energy* 19(7):1325–1339
10. Abbott, IH, von Doenhoff AE (1959) *Theory of wing sections*. Dover Publications Inc., New York
11. Bedon G, DeBetta S, Benini E (2016) Performance-optimized airfoil for Darrieus wind turbines. *Renew Energy* 94:328–340
12. Zamani M, Maghrebi MJ, Varedi SR (2016) Starting torque improvement using J-shaped straight-bladed Darrieus vertical axis wind turbine by means of numerical simulation. *Renew Energy* 95:109–126
13. Worasinchai S, Ingram GL, Dominy RG (2016) The physics of H-Darrieus turbine starting behaviour. *J Eng Gas Turbines Power* 138:1–11
14. Singh MA, Biswas A, Misra RD (2015) Investigation of self-starting and high rotor solidity on the performance of a three s1210 blade H-type Darrieus rotor. *Renew Energy* 76:381–387
15. Maruyama Y, Shimura M, Yoshie R, Wei R, Seki K (2001) Development of vertical axis wind turbine with straight blades suitable for buildings. *J Wind Energy*:265–268
16. Claessens M (2006) *The design and testing of airfoils for application in small vertical axis wind turbines*. Delft University of Technology
17. [www.airfoiltools.com](http://www.airfoiltools.com)

# Application of Additive Dispersed Green Cutting Fluids in Machining



R. Padmini  and Vivek Balakrishnan 

**Abstract** Formulation and application of cutting fluids with additives and natural oils as based fluids during turning of EN8 steel are discussed in this work. Cutting fluids are developed by dispersing amyllum (Amy) in coconut oil (CCO). Performance of biodegradable cutting fluids with amyllum is compared with dry machining, SAE grade oil (synthetic fluid), pure oil-assisted machining initially at constant cutting conditions, and varying percentage additive inclusions in base fluid at 0.3, 0.6, and 0.9%. Before machining, the additive dispersed cutting fluids are examined for thermal conduction and absorbance. Cutting temperatures, surface roughness of workpiece, and tool flank wear roughness are tracked and compared for various machining environments considered. It is discerned that thermal and spectral properties have improved for additive-based fluids compared to pure oils. By examination, it is observed that CC + 0.1% additive resulted in best machining outcome by way of reduced cutting tool temperatures, tool flank wear, and surface roughness.

**Keywords** Machining performance · Biodegradable oils · Additives · Amyllum

## 1 Introduction

During metal cutting due to high cutting temperatures as well as stresses, material deformation is high. Due to cooling plus lubricating actions, cutting fluids play a key role in machining. Technological advancements in manufacturing and environmental consciousness paved the way to seek for compliance in cutting fluids with ecological safety.

Conventional cutting fluids though cool and lubricate during machining these fluids lead to technical and environmental setbacks. Researchers have noticed that wide use of synthetic cutting fluids gave rise to derma-related problems to machinists [1, 2]. They hinder the ecological balance being toxic and non-biodegradable [3, 4]. Enormous amounts of cutting fluids in million metric tons are utilized by

---

R. Padmini (✉) · V. Balakrishnan  
GITAM Institute of Technology, Visakhapatnam, Andhra Pradesh 530045, India  
e-mail: [padhmini.r@gmail.com](mailto:padhmini.r@gmail.com)

© Springer Nature Singapore Pte Ltd. 2020  
L. Vijayaraghavan et al. (eds.), *Emerging Trends in Mechanical Engineering*,  
Lecture Notes in Mechanical Engineering,  
[https://doi.org/10.1007/978-981-32-9931-3\\_56](https://doi.org/10.1007/978-981-32-9931-3_56)

583

manufacturing industries [5]. Hence, to decrease the consumption of such fluids in large quantities and to reduce negativity on operators and environmental alternatives to these fluids are being looked for. Researchers experimented with solid lubricant-assisted machining and pinpointed the friction-reducing ability of MoS<sub>2</sub>. They noted that this behavior is affirmative for machining and it is due to the physical and chemical properties of MoS<sub>2</sub> surface layers [6]. Suresh and Rao [7] worked with solid lubricants like graphite and molybdenum disulfide (MoS<sub>2</sub>). They worked with lubrication of these samples in end milling process. They inferred that milling using MoS<sub>2</sub> minimized friction, main cutting force, and specific energy required by 28%. Graphite's application did not result in such improvement.

Vamsi and Damera [8] applied boric acid (H<sub>3</sub>BO<sub>3</sub>) as solid lubricant during turning. They signified that surface roughness reduced and flank wear also got reduced, besides reduction in cutting tool temperatures and forces. The application of solid lubricants in hard turning operation was reported to be beneficial compared to dry machining as reported by Rao and Krishna [9].

Vegetable oil-assisted machining proved to be a good alternative to conventional cutting fluids as reported by researchers. Susan woods [10] worked with lubricative nature of biodegradable fluids and found that they can be used in machining due to film formation capacity of these fluids on the job. Enhancement in tool life, minimization of cutting tool wear, and forces by using vegetable oils were reported by Belluco and Dechiffire [11].

Cutting fluids formulated using vegetable oils were applied by Skerlos and Hayes [12] in turning. They used carbide tool and austenitic steel and noted a significant improvement in surface finish and traced minimum tool wear. Machining results were found to be encouraging as reported by other researchers by applying different vegetable oils like canola and castor oils [13, 14]. Thus, solid lubricants are found to be viable additives to base fluids in machining applications.

Nanofluids as additives comprise of good thermal and physical properties. This is because of their higher surface area-to-volume ratio. Investigators developed various relations to find the thermal properties of nanofluids [15, 16]. It was noted that due to enhancement in thermal properties nanofluids can reduce the cutting temperatures during machining operations [17, 18]. Nanoparticles do possess good thermal properties and have been applied as additives to cutting fluids in machining applications, but they are toxic and expensive.

In the process of reducing the high quantities of cutting fluids used during machining and to cut down the costs as well as to handle disposal-related issues, researchers have come up with MQL which involves very low quantity of cutting fluid as low as 10 ml/min. Shen et al. [19] estimated the effect of Al<sub>2</sub>O<sub>3</sub>, nanodiamond and zinc oxide (nano) in grinding operation though MQL and found improvement in surface finish and reduction in grinding forces using nanofluids. Researchers observed enhancement in surface integrity of workpiece during turning with high cutting tool pressure by implementing MQL [20]. Another team worked with hardened steel and tracked surface finish and cutting tool flank wear [21]. They also used MQL and observed betterment in machining performance.

Hence, the present work is the result of the literatures pertaining to eco-friendly possibilities to synthetic cutting fluids as a part of which additive-assisted machining is investigated. Abiodun et al. [22] conducted experiments to examine the performance of amyllum starch dispersed cutting fluids in turning and found improvement in machining performance. Flood mode of supply was implemented in this work. Research works on the applicability of natural additives like amyllum or maize starch to biodegradable oils through MQL mode have not been explored, and the present work attempts to address this aspect.

## **2 Materials and Methods**

The methodology implemented to examine the impact of additive-based cutting fluids is discussed in the following sections.

### ***2.1 Formulation of Additive-Based Cutting Fluids***

The cutting fluids are formulated through ultrasonication process using a bath-type sonicator. Pre-weighed quantity of amyllum is dispersed in coconut oil (CCO) and sonicated thoroughly for a period of 60 min for thorough mixing of additive in base oil [23]. These fluids are prepared at different weight percentages varying in the range from 0.3 to 0.9% of amyllum (Amy) additive.

### ***2.2 Absorbance and Thermal Conductivity***

Before being applied as cutting fluids, it is important to understand the level of dispersion of additive in the base fluid. Spectral analysis is one method to assess the absorbance of formulated cutting fluids. Absorbance is analyzed by using a UV-visible spectrometer.

The cutting fluids being applied at machining zone must possess good thermal properties. Thermal conductivity is an important property of cutting fluids due to which heat generated during machining is dissipated. Hence in this research work, thermal conductivity of the pure base fluid and additive-based cutting fluids with varying additive inclusions is tested using PA Hilton apparatus [24].

### ***2.3 Machining***

After evaluation of thermal conductivity of the formulated cutting fluids, experiments are conducted to assess the influence of these fluids while turning AISI 1040 grade

steel at fixed machining conditions, using coated carbide insert. Schematic representation of machining is presented in Fig. 1. Cutting temperatures are measured online using k-type shielded embedded thermocouple. Tool flank wear is obtained by using optical microscope with Olympus analysis software. Surftest SJ-301 equipment is used to measure surface roughness. All the experiments and tests are conducted thrice, and average values are taken to obtain precise results. The details of machining are consolidated and presented in Table 1.

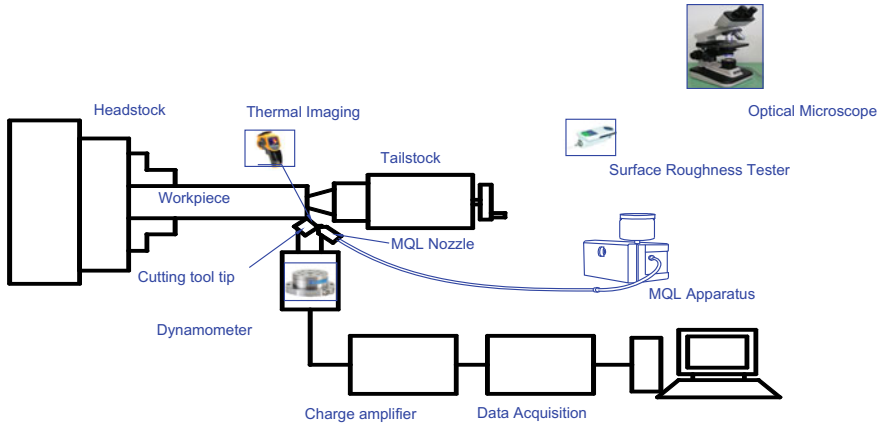


Fig. 1 Schematic representation of machining setup

Table 1 Experimental details

Machine	PSG-124 lathe (10 HP)
Machining operation	Turning
Workpiece	EN8 steel
Cutting tool holder	PSLNR 2020 K12
Cutting tool	CNMG120408NC6110 coated carbide
Machining speed (rpm)	560
Feed rate (mm/rev)	0.17
Depth of cut (mm)	0.5
Machining environment	Dry, CCF, pure oils, CC + % additive
Method of supply of cutting fluid	MQL
Flow rate of cutting fluid	10 ml/min
Machining duration	10 min
% of additive	0, 0.3, 0.6, 0.9

### 3 Results and Discussion

This work aims at investigating the role of additive-based biodegradable cutting fluids in machining using amyllum as additive 0.3, 0.6, 0.9%. Absorbance and thermal conductivity are tested to check the viability of these cutting fluids to be applied in machining. Machining performance is assessed by measuring cutting temperatures, tool wear, and surface roughness at constant cutting conditions. In this section, graphical results are presented and comparative analysis is done and discussed.

#### 3.1 Absorbance

Extent of dispersion of additive particles in coconut oil is presented in Fig. 2. It is observed that absorbance has significantly increased from 0.3% Amy in CCO to 0.6% Amy in CCO approximately by 12%. The increase in absorbance at 0.9% Amy from 0.6% is very less that is 2%. This can be attributed to the agglomeration of additive in base fluid as percentage additive is increased. Hence, increase in percentage of additive does not proportionally increase the absorbance.

#### 3.2 Thermal Conductivity

Results of thermal conductivity of additive-based cutting fluids are shown in Table 2. With increase in % additive, thermal conductivity is also found to increase. Thus, this aspect makes the cutting fluid formulated from amyllum additive in coconut oil to be viable in machining applications. Increase in thermal conductivity makes the cutting fluid reduce the cutting temperatures. Hence, this property is very vital to affirm the applicability of the formulated cutting fluids.

**Fig. 2** Absorbance of additive at varying percentages in base fluid (CCO)

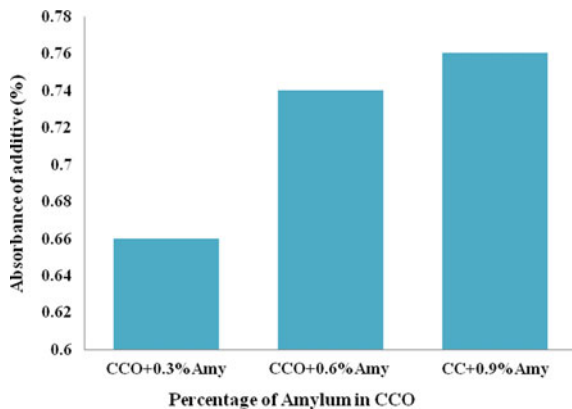
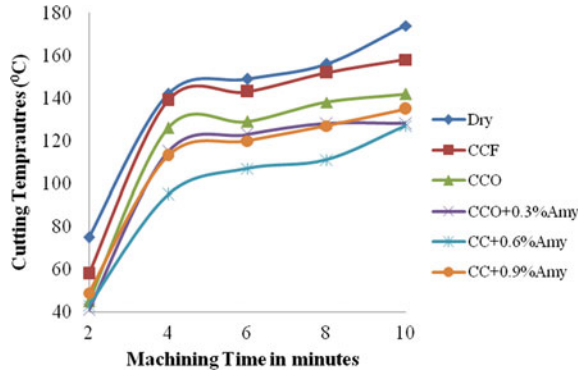


**Table 2** Thermal conductivity (kW/m-K) of additive-based cutting fluids

	Percentage of amylum additive			
	0	0.3	0.6	0.9
CCO	0.1815	0.1826	0.1830	0.1848

**Fig. 3** Variation in cutting temperatures with machining time under various lubricant environments



### 3.3 Cutting Temperatures

Variation of cutting temperatures with machining time during turning of EN8 steel in the present work is reflected in Fig. 3. It is noticed that cutting temperatures increase with increase in machining time. Maximum temperatures are recorded during dry machining. Cutting temperatures are found to be minimum by applying CCO + 0.6% Amy compared to CCO + 0.3% Amy and pure CCO. Increase in % of amylum additive does not show a proportionate reduction in cutting temperatures. This is due to the extent of absorbance of additive in base fluid, though there is increase in thermal conductivity with enhancement in % additive. Due to agglomeration, at higher percentages of additive in CCO ability to reduce friction at the contact surfaces and thereby cutting temperatures, reduction is affected. It can be inferred that inclusion of additive in base fluid has reduced the temperatures to an extent of 28 and 19% when compared to dry and pure oil-assisted machining, respectively.

### 3.4 Tool Wear

Results of tool wear obtained under different lubricant environments are presented in Fig. 4a. It is evident that for all the conditions tool wear has increased with machining time. Under dry cutting condition, tool wear is maximum, under pure oil-assisted machining (CCO) tool wear is found to be less compared to dry machining, and by applying CCO + 0.6% Amy tool wear is found to be least as shown in Fig. 4b(i-iii).

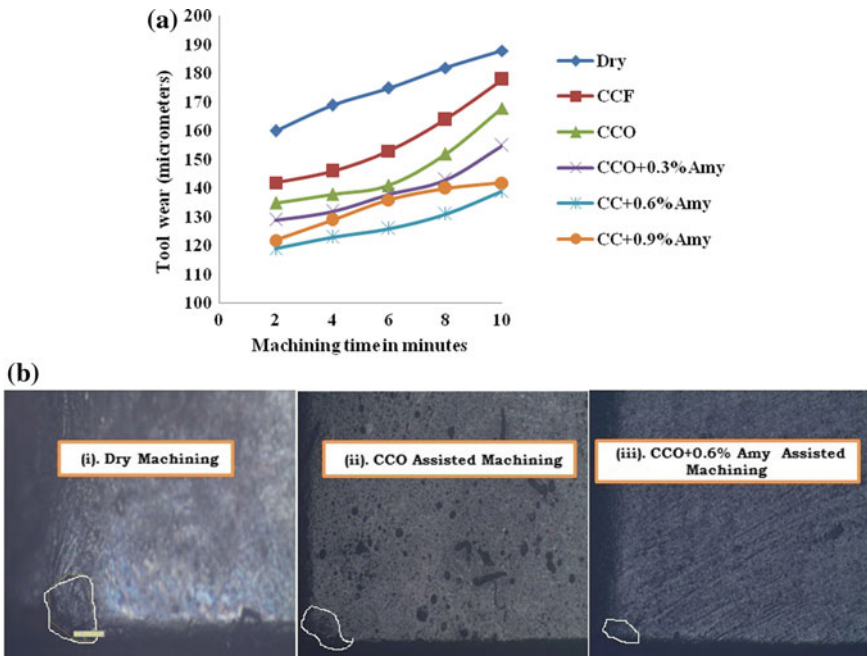


**Fig. 4** a Variation in tool wear with machining time under various lubricant environments and b (i, ii, iii) tool wear with machining time under various lubricant environments

This is due to reduced cutting temperatures and ability of the additive to form a thin film of lubricant between the surfaces in contact. In addition to this, the oiliness and lubricity of CCO also aid in reducing tool wear [25]. Percentage reduction in tool wear is 29 and 13% in comparison with dry and CCO-assisted machining.

### 3.5 Surface Roughness

Surface roughness is an important machining performance parameter to judge the quality of machined surface. It is noticed that amyllum additive-based cutting fluids have reduced surface roughness of workpiece. The results are presented in Fig. 5. It is seen that under dry machining environment maximum the workpiece is subjected to maximum surface roughness, while at 0.6% Amy in CCO it is found to be less compared to other lubricant environments. Reduction in surface roughness can be attributed to the combined effects of reduction in cutting temperatures and tool wear as well. Film formation ability of the additive-based cutting fluids leads to reduction in surface roughness [24]. The extent of reduction in surface roughness by using 0.3% Amy in CCO is observed to be 37 and 12% when compared to dry and pure oil-assisted machining environments.



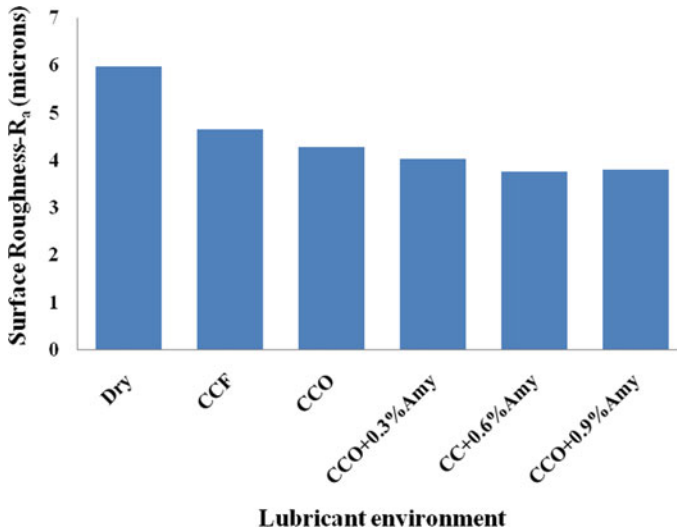


**Fig. 5** Variation in surface roughness— $R_a$  with machining time under various lubricant environments

## 4 Conclusions

- Experimental investigations to examine the performance of amyllum or maize starch-based additive in coconut oil are carried out.
- Absorbance is found to increase with increase in percentage of additive in base fluid up to 0.6% and not beyond. Thermal conductivity increased with increase in % additive.
- Consistent increase in the basic properties with varying amount of additive does not mean that the same behavior should be exhibited by additive-based cutting fluids during machining.
- It is observed that 0.6% Amy in CCO resulted in reduced cutting temperatures, tool wear, and surface roughness.
- Extent of reduction in machining performance parameters is approximately 31% and 12% compared to dry machining while working with CCO + 0.6% Amy.
- Hence, application of natural additives like amyllum to vegetable oils is an amicable alternative to explore eco-friendly and sustainable alternatives to conventional cutting fluids.

## References

1. Passman FJ, Roosmoore HW (2002) Reassessing the health risks associated with employee exposure of metalworking fluid microbes. *Lubr Eng* 58(7):30–38
2. Bennett EO (1983) Water based cutting fluids and human health. *Tribol Int* 16(3):133–136

3. Korde VM, Phelps TJ, Bienkowski PR, White DC (1993) Biodegradation of chlorinated aliphatics and aromatic compounds in total-recycle expanded-bed reactors. *Appl Biochem Biotechnol* 45(46):731–740
4. Zeman A, Sprengel A, Niedermeier D, Spath M (1995) Biodegradable lubricants—studies on thermo oxidation of metal–working fluids by differential scanning calorimetry (DSC). *Thermochim Acta* 268:9–15
5. Kline & Company, Inc (2006) Competitive intelligence for the global lubricants industry, 2004–2014. Kline & Company
6. Dilbag S, Rao PV (2007) Performance improvement of hard turning with solid lubricants. *Int J Adv Manuf Technol* 32:170–177
7. Suresh Kumar Reddy N, Rao PV (2005) Performance improvement of end milling using graphite as a solid lubricant. *Mater Manuf Process* 20:673–686
8. Vamsi Krishna P, Nageswara Rao D (2008) Performance profiling of boric acid as lubricant in machining. *J Braz Soc Mech Sci Eng* 30(3):239–244
9. Vamsi Krishna P, Nageswara Rao D (2008) The influence of solid lubricant particle size on machining parameters in turning. *Int J Mach Tools Manuf* 48(1):107–111
10. Susan W (2005) Vegetable oil-based metalworking fluids can provide better performance and environmental results than mineral oil-based fluids. *Cutting Tool Magazine* 57(2):1–3
11. Belluco W, De Chiffre L (2002) Surface integrity and part accuracy in reaming and tapping stainless steel with new vegetable based cutting oils. *Tribol Int* 35:865–870
12. Skerlos S, Hayes K Vegetable based cutting fluid—a new dimension in research. <http://www.engn.umich.edu/alumni/engineer/03FW/research/holography/index.html>
13. Alves SM, Oliveira JFG (2008) Vegetable based cutting fluids—an environmental alternative to grinding process. In: Proceedings of the 15th CIRP international conference on life cycle engineering. Elsevier, pp 664–668
14. Ion IS, Camelia C, George C (2002) On the future of biodegradable vegetable lubricants used for industrial tribosystems, vol 8. The Annals of University “Dunarea De Jos” of Galati Fascicle, pp 94–98
15. Wong KV, De Leon O (2010) Applications of nanofluids: current and future. *Adv Mech Eng.* (Available online)
16. Das SK, Choi SUS, Yu W, Pradeep T (2008) Nanofluids: science and technology. Wiley-Interscience, USA
17. Putra Nandy, Roetzel Wilfried, Das Sarit K (2003) Natural convection of nano-fluids. *Heat Mass Transf* 39:775–784
18. Xuan Y, Li Q (2000) Heat transfer enhancement of nanofluids. *Int J Heat Fluid Flow* 21:58–64
19. Shen B, Shih A, Tung SC (2008) Application of nanofluids in MQL grinding. *Tribol Lubr Technol* 51:730–737
20. Attanasio A, Gelfi M, Giardini C, Remino C (2006) Minimum quantity lubrication in turning. *Wear* 260:333–338
21. Diniz AE, Ferreira JR, Filho FT (2003) Influence of refrigeration/lubrication condition on SAE 52100 hardened steel turning at several cutting speeds. *Int J Mach Tools Manuf* 43:317–326
22. Abiodun MO, Adetan DA, Oladejo KA (2011) A study of the performance of maize starch based cutting fluids in the turning of AISI 304 stainless steel. *Int J Eng Res Afr* 6:13–24
23. Tarawneh MA, Ahmad SH, EhNoum S, Lau KT (2012) Sonication effect on the mechanical properties of MWCNTs reinforced natural rubber. *J Compos Mater* 47(5):579–585
24. Padmini R, Vamsi Krishna P, Rao GKM (2016) Effectiveness of vegetable oil based nanofluids as potential cutting fluids in turning AISI 1040 steel. *Tribol Int* 94:490–501
25. Srikant RR, Nageswara Rao D, Siva Subrahmanyam M, Vamsi Krishna P (2010) Determination of required quantity of nano cutting fluids for optimized lubrication using artificial intelligence. *Int J Prod Qual Eng* 1(1):1–6

# Investigating the Effect of Metal Working Fluid in Orthogonal Cutting of AISI 420 Stainless Steel Using 3-Dimensional Finite Element Model



Madan Mohan Reddy Nune and Phaneendra Kiran Chaganti

**Abstract** To enhance the efficiency of a machining process, many experiments with several combinations of factors need to be conducted and it is a time consuming and expensive process. Finite element (FE) simulation is the best alternative to reduce the number of experiments. A coupled Eulerian-Lagrangian (CEL) model, which combines fluid and structure is in demand, and it is the nearest representation of the experiment. The present work uses CEL approach to analyse the variation of temperature at shear deformation zones, rake and flank surfaces with and without metal working fluid (MWF) in machining of 420 stainless steel workpiece. The cutting forces were also predicted using these simulations. Some of the simulations were validated with literature and the rest were validated with the experiments. The developed cutting fluid combination was showing a larger reduction in temperature as compared to dry cutting. This methodology will give a scientific base for realistic simulation of the machining process.

**Keywords** Coupled Eulerian-Lagrangian · Metal working fluid (MWF) · Stainless steel 420

## 1 Introduction

Most of the industrial products need to undergo at least one machining operation to get precise tolerance and best surface finish. There is a number of machining parameters which influence the final tolerances and surface finish of a machined part and conducting these experiments are expensive. Finite element modelling (FEM) has been proved to be the best alternative to reduce the number of experiments. FEM and analysis not only gives the optimum cutting conditions but also gives more prominent results by changing material properties and non-linear input parameters [1]. However, a new advance in FEM of the cutting process is always desirable for predicting the real-time situations [2]. There are two types of finite element approaches used in

---

M. M. R. Nune (✉) · P. K. Chaganti  
Department of Mechanical Engineering, BITS Pilani, Hyderabad Campus, Pilani 500078, India  
e-mail: [madan008phd@gmail.com](mailto:madan008phd@gmail.com)

© Springer Nature Singapore Pte Ltd. 2020  
L. Vijayaraghavan et al. (eds.), *Emerging Trends in Mechanical Engineering*,  
Lecture Notes in Mechanical Engineering,  
[https://doi.org/10.1007/978-981-32-9931-3\\_57](https://doi.org/10.1007/978-981-32-9931-3_57)

machining simulations: Eulerian and Lagrangian. In a Lagrangian approach, the work material contains fixed nodes and these nodes are bounded with elements. In this case, work material deforms simultaneously with the elements. In the Eulerian approach, elements do not deform with work material as the nodes are stationary in space, and it allows material flow over non-deformable elements. Combination of these two approaches gives a coupled Eulerian Lagrangian (CEL) model with significant functions of Lagrangian and Eulerian approaches [3]. Compared to 3D, 2D FEM based orthogonal cutting process takes less solving time, lesser meshing issues and reduced distortion during simulations. But, 3D orthogonal FEM gives a more detailed and accurate thermal profile along the width of the chip compared with the 2D orthogonal model. The 2D FEM based cutting forces were deviating by 7% from experimental results [4]. The impact of pressurized coolant at the cutting zone removes the generated chips away from the cutting zone [5]. Hence, CEL based FE model enables the impact of pressurized water at the different zone on a workpiece under various impact loads. The hard to cut material like, AISI 420 is generally used for the manufacturing of turbine blades, housings and their mountings [6, 7], which generates high temperature during orthogonal cutting at the shear zone. The increased heat leads to an increase in the friction coefficient and wear on the tool surface [8]. From the literature, it is evident that CEL based finite element modelling of AISI 420 stainless steel orthogonal cutting along with metal working fluid needs an attention in evaluating new cutting fluids. The present paper investigates the effect of metal cutting fluid at the cutting zone using a 3-dimensional FE model. In the first phase, the developed FE model was validated with the experimental results from the literature. In the second phase, the developed cutting fluid was modelled and the cutting temperatures obtained at the cutting zone were validated with experimental results. In the subsequent phase, the cutting forces were predicted for different cutting parameter combinations.

## 2 Materials and Method

### 2.1 Numerical Model

In adiabatic strain hardening process, the yield stress of material  $\sigma$  is numerically calculated using the J-C model given in Eq. (1) [9]. The Eq. (1) represent three terms: strain, strain rate and heat generated due to the effect of flow stress. The terms  $A$ ,  $B$ ,  $C$ ,  $n$ ,  $m$  are the material constants and  $\varepsilon$ ,  $\varepsilon_0$  are plastic strain rate and reference plastic strain rate.  $T$ ,  $T_f$ , and  $T_a$  are cutting process temperature, workpiece material melting temperature and reference room temperature in °C.

$$\sigma = (A + B^n) \left( 1 + C \ln \frac{\varepsilon}{\varepsilon_0} \right) \left( 1 - \left( \frac{T - T_a}{T_f - T_a} \right)^m \right) \quad (1)$$

Numerically the adiabatic temperature ( $\Delta T_p$ ) generated at the cutting zone for a time interval ( $\Delta t$ ) is obtained using Eq. (2) [10].

$$\frac{\Delta T_p}{\Delta t} = \eta_p \frac{\sigma_e \varepsilon_p}{J c \rho} \tag{2}$$

where  $\sigma_e$ ,  $\varepsilon_p$ ,  $\eta_p$ ,  $J$ ,  $c$  and  $\rho$  are effective stress, plastic strain, the percentage of heat generated due to plastic work, heat conversion factor, specific heat, and mass density.

### 2.2 Developed 3D FE Model

The geometry considered for simulating orthogonal cutting of AISI 420 along with dimensions and boundary conditions is shown in (Fig. 1).

The meshing for workpiece and tool was done using Lagrangian C3D8R element. The workpiece and tool mesh size was 4200 elements (8844 nodes) and 600 elements (858 nodes). The meshing for MWF was done using Eulerian EC3D8R and the number of elements were 54,000 and the nodes were 58,621. The MWF properties Equation of State (EOS)  $C_0 = 1483$  m/s and flow velocity was 3.8 m/s. The material Johnson-Cook (J-C) constants of workpiece and tool, and properties of MWF considered in simulations are given in Table 1.

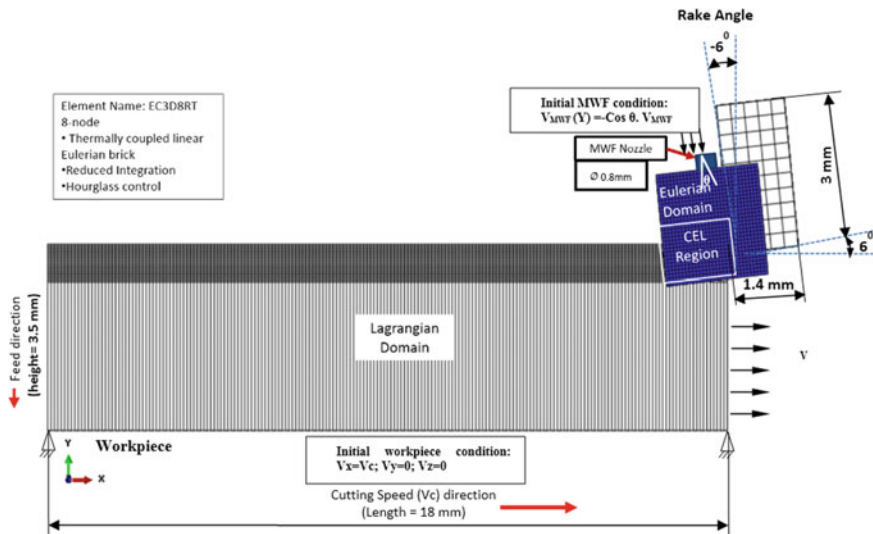
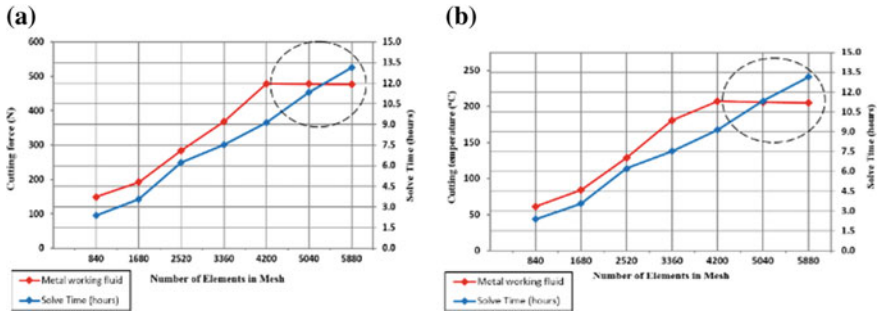


Fig. 1 Comparison of metal working fluid shock speed

**Table 1** The material constants of the workpiece, tool

Material properties	J-C material constants AISI 420SS [4]					Troom (°C)	Tmelt (°C)	Density (kg/m <sup>3</sup> )	Modulus (GPa)
	A (MPa)	B (MPa)	<i>m</i>	<i>n</i>					
Workpiece (AISI420)	450	738	0.8	0.38	27	1454	7800	200	
Tool (carbide)	391	724	0.9	0.3	27	1350	15,000	620	



**Fig. 2** Mesh convergence of developed FE model **a** Cutting force **b** Cutting temperature

### 2.3 Mesh Refinement Test

Mesh refinement test carried out to obtaining the precise output and to reduce CPU time. The mesh refinement test of developed FE model for the outputs cutting force shown in (Fig. 2a) and temperature shown in (Fig. 2b) respectively.

The encircled portion in this graph represents the ineffective mesh, where there is no change in output with an increase in a number of elements. The results were converging for 4200 elements with a CPU time of 9 h 15 min 01 s.

### 2.4 Model Validation

The cutting force results obtained using developed 3D FE model were validated with the published work [8]. Cutting conditions are  $V_c$  values 25, 39, 60, 93 and 145 m/min by keeping  $f$  at 0.1 mm/rev and  $ap$  as 4 mm. For all the simulations-6° rake angle was used. The maximum cutting force 1302 N obtained for a cutting speed of 93 m/min and is shown in (Fig. 3a). A comparison between the simulation results and experimental [8] results of cutting forces are shown in (Fig. 3b).

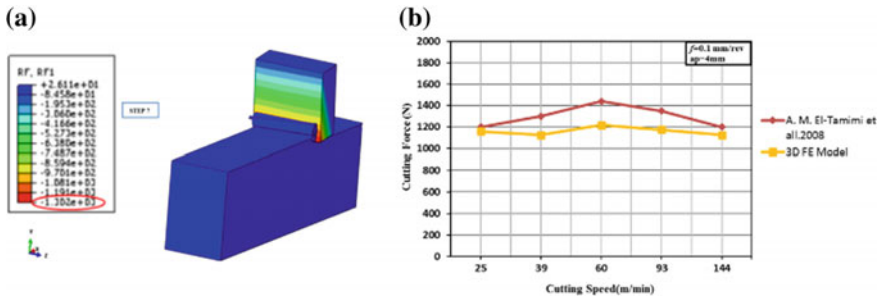


Fig. 3 a Maximum cutting force 1302 N at  $V_c$  93 m/min b Cutting force results

The average deviation of simulation results from experimental results was 10%. Based on the accuracy of these results, developed FE model was used in further sections for prediction of cutting forces for a different process parameter combinations given in Table 2.

### 3 Results and Discussion

The cutting temperature at the cutting zone was measured using Infrared thermal image camera, FLIR make, having a temperature range between  $-100\text{ }^\circ\text{C}$  and  $650\text{ }^\circ\text{C}$ . The measurement of temperature through an experimental setup is shown in (Fig. 4a). A sample temperature result for a  $V_c$  of 175 m/min,  $f$  at 0.15 mm/rev and  $ap$  at 1.52 mm combination was shown in (Fig. 4b) and the value obtained is  $217\text{ }^\circ\text{C}$ . To validate these simulation results, experiments were conducted. In the experiments, a 50 mm diameter 420 stainless steel material was turned with uncoated carbide insert along with PCLNL K12 jet stream tool holder was used for circulating the MWF at a velocity of 3.8 m/s. The validated FE model in the Sect. 2.4 was used to simulate temperature and cutting force at the cutting zone.

The temperature at the cutting zone was recorded using selective nodes in Primary Shear Deformation Zone (PSDZ) and Secondary Shear Deformation Zone (SSDZ). The selected nodes in PSDZ were 112, 1296, 1375, 1452, 1547 and at SSDZ were 1678, 1680, 1695, 1735, 1776 respectively. The identified nodes in the cutting zone were shown in (Fig. 4c) The cutting temperature at each node for different cutting parameter combinations was shown in (Fig. 5a) in the form of a bar chart as shown in (Fig. 5b). This graph shows a little difference between simulation and experimental results. A maximum temperature of  $257\text{ }^\circ\text{C}$  was observed in experiment number 7 and minimum temperature  $176\text{ }^\circ\text{C}$  was observed for experiment number 2 using metal working fluid. The rise of temperature at the cutting zone and the progression of MWF to the cutting zone is demonstrated in four steps as shown in (Fig. 6a).

The total simulation time was 10 ms, out of which, the problem has attained a steady state within 2 ms, which is equal to 2 h 25 min solve time. The temperature

**Table 2** Experimental process parameters

Process parameters	Exp 1	Exp 2	Exp 3	Exp 4	Exp 5	Exp 6	Exp 7	Exp 8	Exp 9
Cutting speed. ( $V_c$ ) m/min	150	150	150	175	175	175	200	200	200
Feed ( $f$ ) mm/rev	0.10	0.15	0.20	0.10	0.15	0.20	0.10	0.15	0.20
Depth of cut ( $a_p$ ) mm	2.67	1.78	1.33	2.29	1.52	1.14	2.00	1.33	1.00



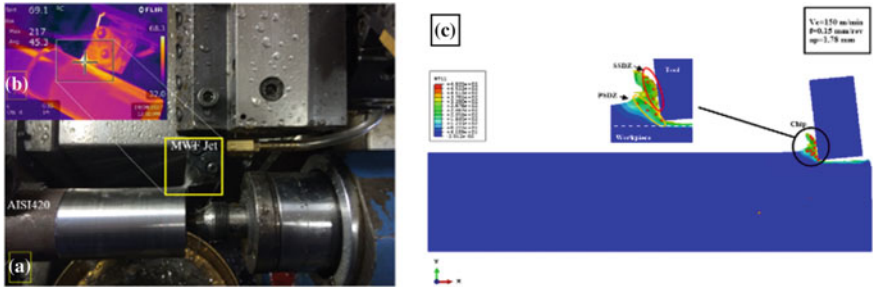


Fig. 4 a MWF flow in turning of AISI 420 SS b Thermal image camera picture c Nodes selection at deformation zone

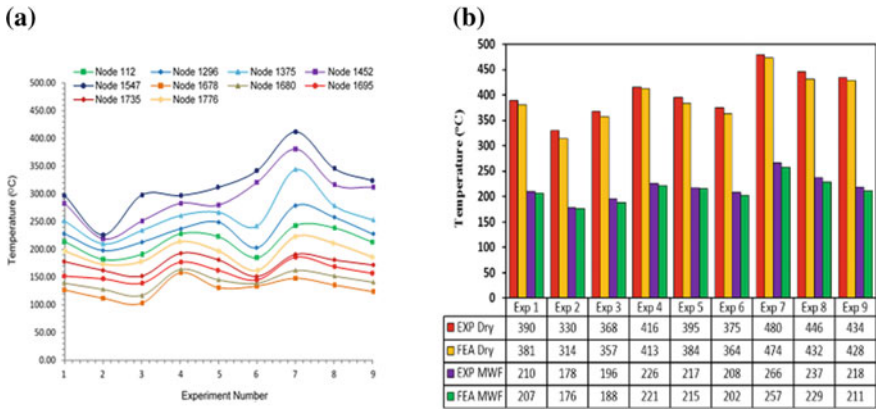


Fig. 5 a Nodal temperature using metal working fluid b Correlation of temperature results

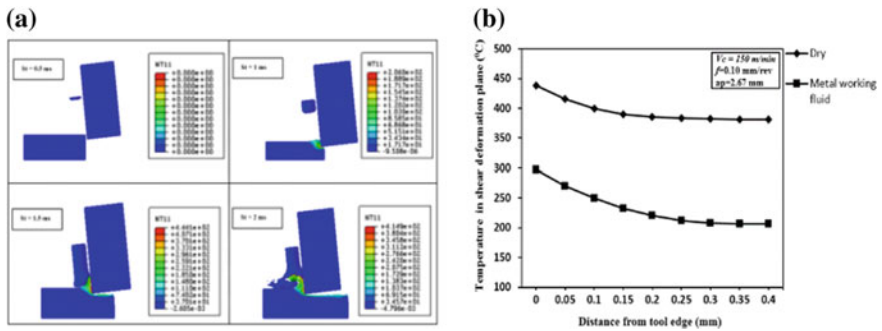


Fig. 6 a MWF supply during  $V_c = 150, f = 0.10, a_p = 2.67$  b Temperature at shear plane

variation at the shear deformation plane with respect to cutting edge distance is shown in (Fig. 6b). At the cutting edge a temperature difference of 150 °C was observed between dry and MWF condition. The reduction of temperature at the points away from the cutting edge attribute to the jet flow of MWF and loss of heat is due to conduction and convection. The simulated cutting force results for all 9 experiments are shown in (Fig. 7a).

It is observed from the bar chart that there is an outstanding reduction in cutting force when MWF was applied. Which removes chips and forms a cooling and lubricating layer between rake face and the workpiece. It is observed from the bar chart that there is an outstanding reduction in cutting force when MWF was applied. Which removes chips and forms a cooling and lubricating layer between rake face and the workpiece. From the different process parameters combination, it is evident that the  $ap$  and  $Vc$  has more influence on the cutting force than  $f$  value. The chips formed in the machining of AISI 420 material for different combinations of process parameters in both dry and MWF condition are clearly represented in (Fig. 7b). The temperature contour profile of a tool insert with the dry cutting condition is shown in (Fig. 8a). A maximum temperature was observed in the auxiliary shear zone and this temperature was estimated in the plane of symmetry.

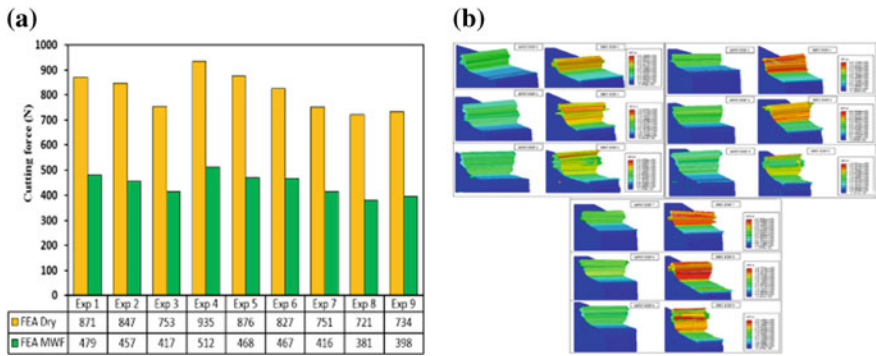


Fig. 7 a FE model predicted cutting forces b Temperature on the chips MWF and dry

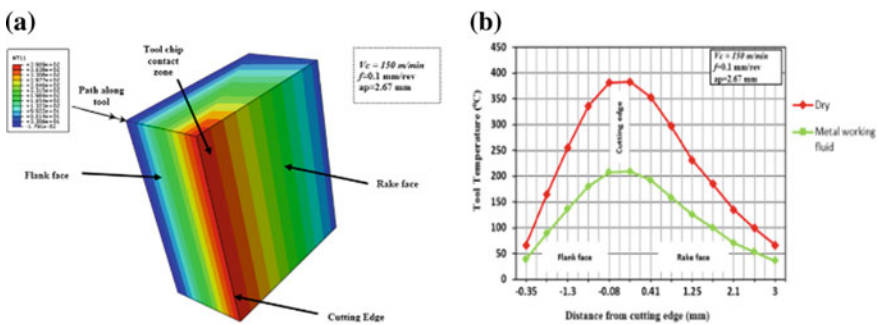


Fig. 8 a Temperature contours on the tool surface b Variation of tool surface temperature

The temperature variation on rake and flank surfaces with respect to distance from cutting edge is represented in (Fig. 8b). The temperature variation for the dry cutting condition is minimum 66 °C recorded at 0.35 mm distance from cutting edge on the flank surface and maximum 383 °C observed at cutting edge. Using MWF a minimum temperature of 39 °C was recorded at 0.35 mm distance from cutting edge on the flank surface and a maximum temperature of 209 °C observed at cutting edge.

This graph emphasizes the role of MWF in reducing the temperature at the cutting zone.

## 4 Conclusion

In this work, the effect of metal working fluid was analysed in orthogonal cutting of 420 stainless steel with developed 3D finite element model. The outcomes made with this study summarized as follows:

- The cutting forces were also predicted using developed FE model with 90% accuracy in orthogonal cutting of 420 stainless steel material under dry, metal working fluid environment condition.
- The present investigation given a new direction to simulate temperature profile at cutting zone (PSDZ & SSDZ), on the generated chips and tool surface with an average accuracy of 98% using developed 3D FE model.
- The developed 3D FE model presented in this work is useful for the manufacturers and researchers to validate the performance of metal working fluids during machining process for different combination of cutting parameters.

**Acknowledgements** The author(s) is/are thankful to BITS Pilani Hyderabad campus for providing Abaqus software facility to carry out this work.

## References

1. Danish M, Ginta TL, Habib K, Rani AMA, Saha BB (2018) Effect of cryogenic cooling on the heat transfer during turning of AZ31C magnesium alloy. *J Heat Transf Eng*:1–41. <https://doi.org/10.1080/01457632.2018.1450345>
2. Li B, Wang Y, Li H, You H (2015) Modelling and numerical simulation of cutting stress in end milling of titanium alloy using carbide coated tool. *Int J Eng Trans A* 28(7):1090–1098
3. Abaqus online documentation, Simulia Abaqus (2014) <http://130.149.89.49:2080/v6.8/books/usb/default.htm?startat=pt05ch18s09abm15.html>. Last accessed 18 May 2018
4. Korkmaz ME, Gunay M (2018) Finite element modelling of cutting forces and power consumption in turning of AISI 420 martensitic stainless steel. *Arab J Sci Eng*:1–8. <https://doi.org/10.1007/s13369-018-3204-4>
5. Debnath S, Reddy MM, Yi QS (2014) Environmental friendly cutting fluids and cooling techniques in machining. *J Cleaner Prod* 83:33–47
6. Madan MR, Kiran CP (2017) Experimental investigation on turning of turbine blade material AISI 410 under minimum quantity cutting fluid. *J Mater Today Proc* 4:1057–1064

7. Kiran CP, Clement S (2013) Surface quality investigation of turbine blade steels for turning process. *J Meas* 46:1875–95
8. El-Tamimi AM, El-Hossainy TM (2008) Investigating the machinability of AISI 420 stainless steel using factorial design. *J Mater Manuf Process* 23:419–426
9. Johnson G, Cook W (1983) A constitutive model and data for metals subjected to large strains, high strain rates and high temperatures. In: *Proceedings of the seventh international symposium on Ballistics*, Netherlands, pp 541–547
10. Davim JP (2012) *Statistical and computational techniques in manufacturing*. Springer-Verlag Berlin Heidelberg Publisher, USA

# Free and Forced Vibration Analysis of Functionally Graded Beams Using Finite Element Model Based on Refined Third-Order Theory



M. Altaf Khan, M. Y. Yasin, Mirza Shariq Beg and A. H. Khan

**Abstract** This work is dedicated toward the development of the finite element (FE) model based on refined third-order theory (TOT) for the dynamic analysis of functionally graded (FG) beams. Variational approach is employed to derive the governing equations as well as consistent boundary conditions. Two-noded beam element is selected for the discretization of FG beam. The variables  $u_0$  and  $\psi_0$  are interpolated using  $C^0$ -continuous linear Lagrangian functions while the presence of the second derivative of the transverse deflection in the variational equation requires  $C^1$ -continuity and is interpolated using  $C^1$ -continuous Hermite interpolation functions. Static deflection and free vibration responses are validated from the literature, and new results have been presented for free and forced vibration of FGM beams.

**Keywords** Functionally graded beam · Third-order theory · Rule of mixture · Finite element method

## 1 Introduction

Functionally graded materials (FGM) have been extensively used as structural member in many engineering applications because of excellent tailor-made properties based on requirement and suitability in different environments. In recent years, the application of FGM as structural components has been significantly increased which find applications in aerospace, biomedical, nuclear, and material research areas. In FGM beams, the material properties are continuously varying through-the-thickness which results in continuous variations in transverse and normal stresses and makes them preferable for the components operating under severe thermal environment where the problem of delamination arises with the laminated composite structures. Sankar [1] obtained elastic solution for FG beam using Euler–Bernoulli beam theory. This theory gives the close results for long, slender beams, but stress concentration occurs when the beams gets thicker. The static and dynamic behavior of FG beams

---

M. Altaf Khan · M. Y. Yasin (✉) · M. S. Beg · A. H. Khan  
Department of Mechanical Engineering, AMU, Aligarh, India  
e-mail: [yaqoob.yasin@gmail.com](mailto:yaqoob.yasin@gmail.com)

© Springer Nature Singapore Pte Ltd. 2020  
L. Vijayaraghavan et al. (eds.), *Emerging Trends in Mechanical Engineering*,  
Lecture Notes in Mechanical Engineering,  
[https://doi.org/10.1007/978-981-32-9931-3\\_58](https://doi.org/10.1007/978-981-32-9931-3_58)

including rotary inertia and shear deformation effects is performed by Li [2]. Sina et al. [3] analyzed free vibration of FG beams based on refined first-order shear deformation theory; however, due to shear locking, it gives unusual transverse shear stress distribution along the thickness. Thai and Thuc [4] presented a comparative analysis of various higher-order theories using analytical solution for static deflection and natural frequencies of FG beams. Simsek [5] investigated the fundamental mode of vibration for FG beam employing classical as well as shear deformable theories with different boundary condition. Kadoli et al. [6] developed finite element (FE) model based on third-order theory (TOT) for static analysis of FG beams. Vo et al. [7] developed FE model based on TOT considering five nodal variables for each node by splitting the transverse deflection into bending and shear deformation components and presented deflection and natural frequencies of FG beam. Chakraborty et al. [8] presented thermo-elastic analysis of Timoshenko FG beam using FE formulation. Kapuria et al. [9] presented a layer-wise theory and its experimental validation for static and dynamic analysis of FG beams.

The present work involves the development of the FE model based on the refined third-order theory (TOT) for free and forced vibration analysis of FG beam. Equations of motion, beam stress resultants, and consistent boundary conditions are derived using variational approach. The variation of the properties across the thickness of FG beam is obtained by varying the ceramic volume fraction, and its effective value is determined using rule of mixtures. Center point deflection and natural frequencies are validated with HOT presented by Vo et al. [7]. New results for free vibration and deflection time histories under various loading and boundary conditions are presented.

## 2 Problem Formulation

The FG beam considered here is composed of metal and ceramic phases with their concentrations smoothly varying with

$$V_u = \left(0.5 + \frac{z}{h}\right)^p \quad (1)$$

where  $V_u$  is the volume fraction with suffix representing the upper surface constituent. The dimensions of beam are shown in Fig. 1. The reference plane is passing through  $z = 0$ , with the upper and lower faces lying at  $z = h/2$  and  $z = -h/2$ , respectively. The beam is subjected to a transverse load  $p_z$  applied on the upper surface. Assuming plane stress condition ( $\sigma_y = \tau_{yz} = \tau_{xy} = 0$ ) and  $\sigma_z \cong 0$ , the constitutive equations for the FGM beam are

$$\sigma_x = Q_{11}(z)\varepsilon_x; \quad \tau_{zx} = Q_{55}(z)\gamma_{zx} \quad (2)$$

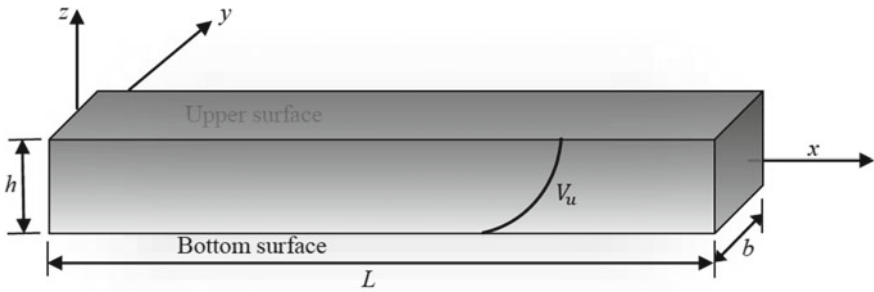


Fig. 1 Geometry and coordinate system for FG beam

where  $\sigma_x$  and  $\varepsilon_x$  are the normal stress and strain along  $x$ -direction and  $\tau_{zx}$  and  $\gamma_{zx}$  are transverse shear stress and shear strain.  $Q_{11}(z)$  and  $Q_{55}(z)$  are reduced stiffness coefficients which are expressed in terms of Young's modulus  $Y(z)$  and Poisson's ratio  $\nu(z)$  as  $Q_{11}(z) = Y(z)$ ;  $Q_{55}(z) = Y(z)/2(1 + \nu(z))$ . The effective values of Young's modulus, Poisson's ratio as well as density are obtained using rule of mixtures as

$$P(z) = P_u V_u + P_b V_b \tag{3}$$

where  $V_u$  and  $V_b$  are the volume fractions of materials lying at the upper and bottom surfaces, respectively, and  $V_u + V_b = 1$ .

The finite element model employed here is based on refined third-order theory

$$u(x, z, t) = f(z)\bar{u}(x, t); \quad w(x, z, t) = w_0(x, t), \tag{4}$$

with

$$\bar{u} = [u_0 \quad -w_{0,x} \quad \psi_0]^T; \quad f(z) = [1 \quad z \quad z^2 \quad -4z^3/3h^2]^T, \tag{5}$$

The strains  $\varepsilon_x$  and  $\gamma_{zx}$  based on linear strain displacement relations are

$$\varepsilon_x = f_1(z)\bar{\varepsilon}_1; \quad \gamma_{zx} = f_2(z)\bar{\varepsilon}_2 \tag{6}$$

where  $f_1(z) = f(z)$ ,  $\bar{\varepsilon}_1 = \bar{u}_{,x} = [u_{0,x} \quad -w_{0,xx} \quad \psi_{0,x}]^T$  and  $f_2(z) = 1 - 4z^2/h^2$  and  $\bar{\varepsilon}_2 = \psi_0$ .

### 2.1 Finite Element Formulation

We employ Hamilton's principle to formulate the dynamics of FG beam. Denoting  $\int_{-0.5h}^{0.5h} (\dots)bdz$  by  $\langle \dots \rangle$ , the Hamilton's principle for FG beam is expressed as

$$\int_x [ \langle (\rho(\ddot{u}\delta u + \ddot{w}\delta w) + \sigma_x \delta \epsilon_x + \tau_{zx} \delta \gamma_{zx}) \rangle - b P_z \delta w(x, 0.5h, t) dx ] - \langle \sigma_x \delta u + \tau_{zx} \delta w \rangle |_x = 0 \tag{7}$$

Based on TOT presented above, the transverse and inplane displacements are interpolated using Hermite ( $\bar{N}$ ) and Lagrangian ( $N$ ) functions, respectively, of 2-noded beam element as [9]

$$u_0 = \mathbf{N}\mathbf{u}_0^e, \quad w_0 = \bar{\mathbf{N}}\mathbf{w}_0^e, \quad \psi_0 = \mathbf{N}\boldsymbol{\psi}_0^e \tag{8}$$

Using Eqs. 6 and 8, substituting strains and displacements in Eq. 7, and denoting generalized displacement vector of element by  $\mathbf{U}^e = [\mathbf{u}_0^{eT} \ \mathbf{w}_0^{eT} \ \boldsymbol{\psi}_0^{eT}]^T$ , the contribution of one element to the area integral is

$$T^e = \delta \mathbf{U}^{eT} [\mathbf{M}^e \ddot{\mathbf{U}}^e + \mathbf{K}^e \mathbf{U}^e] \tag{9}$$

Using the assembly, the global dynamic equation is obtained as

$$\mathbf{M}\ddot{\mathbf{U}} + \mathbf{K}\mathbf{U} = \mathbf{P} \tag{10}$$

where  $\mathbf{M}$  and  $\mathbf{K}$  are the global inertia and stiffness matrices with  $\mathbf{U}$  and  $\mathbf{P}$  denoting the global displacement and force vectors, respectively. Natural frequencies and mode shapes are obtained by converting Eq. 10 into a generalized eigenvalue problem assuming the solution  $\mathbf{U} = \mathbf{U}_0 e^{i\omega_n t}$  where  $\omega_n$  denotes the natural frequency of synchronous free vibration. Using modal approach with the transformation  $\mathbf{U} = \boldsymbol{\Psi}\boldsymbol{\eta}$  where,  $\boldsymbol{\Psi}$  and  $\boldsymbol{\eta}$  are, respectively, the truncated modal matrix and modal coordinate vector, Eq. 10 is expressed as

$$\ddot{\boldsymbol{\eta}} + \boldsymbol{\Lambda}\dot{\boldsymbol{\eta}} + \boldsymbol{\Omega}\boldsymbol{\eta} = \boldsymbol{\Psi}^T \mathbf{P} \tag{11}$$

In Eq. 11,  $\boldsymbol{\Lambda}$  and  $\boldsymbol{\Omega}$  are diagonal matrices with generic terms  $2\xi_i\omega_i$  and  $\omega_i^2$  where  $\xi_i$  is the modal damping ratio and  $\omega_i$  is the undamped frequency of  $i$ th mode. Denoting  $\mathbf{x}(t) = \text{col}(\boldsymbol{\eta}, \dot{\boldsymbol{\eta}})$ ; Eq. 11 is presented in state space format as

$$\dot{\mathbf{x}}(t) = \mathbf{A}\mathbf{x}(t) + \mathbf{B}\mathbf{u}(t) \tag{12}$$

where  $\mathbf{A}$  is the system matrix,  $\mathbf{B}$  the input matrix, and  $\mathbf{u}$  load vector, given by

$$\mathbf{A} = \begin{bmatrix} 0 & \mathbf{I} \\ -\boldsymbol{\Omega} & -\boldsymbol{\Lambda} \end{bmatrix}, \quad \mathbf{B} = \begin{bmatrix} 0 \\ \boldsymbol{\Psi}^T \end{bmatrix}, \quad \mathbf{u} = \mathbf{P} \tag{13}$$



### 3 Numerical Results

Results presented are obtained using 20 regular elements ensuring the convergence of the solution. Static results are presented for FG beam made of Al/ZrO<sub>2</sub>, simply supported at both ends in non-dimensional form using

$$\bar{w}_0 = \frac{Y_{Al} I w_0}{K p_z L^4}; \bar{\sigma} = \frac{\sigma}{S^2 p_z}; \bar{\tau}_{zx} = \frac{\tau_{zx}}{S p_z}; K = \frac{5}{384}; I = \frac{bh^3}{12} \tag{14}$$

Free vibration and transient response are presented for FG beam made of Al/Al<sub>2</sub>O<sub>3</sub> in non-dimensional form using

$$\bar{\omega} = \omega S^2 \sqrt{\frac{h^2 \rho_{Al}}{Y_{Al}}}; \bar{w}_0 = \frac{100 w_0 Y_{Al}}{h S^4 p_z}; \bar{t} = t \sqrt{\frac{Y_{Al}}{h^2 \rho_{Al}}} \tag{15}$$

#### 3.1 Static Response

For verification of the finite element formulation and its computer program, we consider a simply supported FG beam with aluminum [ $Y_u = Y_{Al} = 70$  GPa,  $\nu_u = \nu_{Al} = 0.3$ ] in the upper top surface and zirconia, ZrO<sub>2</sub> [ $Y_l = Y_{ZrO_2} = 200$  GPa,  $\nu_l = \nu_{ZrO_2} = 0.3$ ] in the bottom surface. Uniform load has been applied on the upper surface and the central deflection for different values of  $p$  are presented in Table 1 and compared with published result of [5] and [7] based on HOTS. It can be seen that the present FE model represents good accuracy for all values of  $p$  and thickness parameter  $S$ .

Through-the-thickness variations of  $\bar{\sigma}_x(0.5L, z)$  and  $\bar{\tau}_{zx}(0, z)$  are presented in Fig. 2 for  $S = 16$  and  $p = 0.2; 0.5$  and  $\infty$ . It can be seen that the inhomogeneity

**Table 1** Deflection of simply supported Al/ZrO<sub>2</sub> FG beam

$p$	$S = 4$				$S = 16$			
	TOT FE	FSDT [5]	HOT [5]	HOT [7]	TOT FE	FSDT [5]	HOT [5]	HOT [7]
0	1.1558	1.1300	1.1558	1.1558	1.0097	1.0081	1.0097	1.0097
0.2	0.8791	0.8491	0.8714	0.8710	0.7646	0.7559	0.7574	0.7569
0.5	0.7357	0.7148	0.7326	0.7325	0.6433	0.6395	0.6406	0.6406
1	0.6420	0.6294	0.6427	0.6427	0.5660	0.5661	0.5670	0.5670
2	0.5688	0.5616	0.5714	0.5714	0.5051	0.5072	0.5078	0.5078
5	0.4958	0.4918	0.4998	0.4998	0.4405	0.4439	0.4444	0.4444
$\infty$	0.4045	0.3955	0.4045	0.4045	0.3534	0.3528	0.3534	0.3534

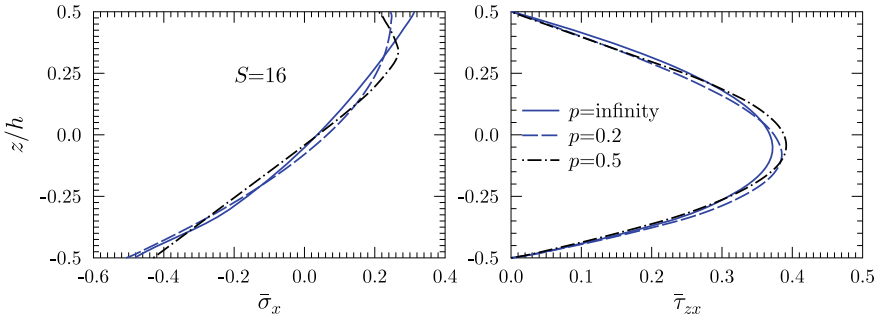


**Fig. 2** Through-the-thickness variation of  $\bar{\sigma}_x(0.5L, z)$  and  $\bar{\tau}_{zx}(0, z)$  for SS Al/ZrO<sub>2</sub> FG beam

index has larger influence on through-the-thickness distribution of stresses. Further, it yields shear-free upper and bottom surfaces.

### 3.2 Dynamic Response

We present first six non-dimensional frequencies of FGM beam with different boundary conditions and inhomogeneity index  $p$  for  $S = 20$  in Table 2. In this case, the beam is made of Al/Al<sub>2</sub>O<sub>3</sub> FG system with upper surface purely ceramic and lower surface purely aluminum. The material properties are Al<sub>2</sub>O<sub>3</sub> is [ $Y_l = Y_{Al_2O_3} = 380$  GPa,  $\nu_l = \nu_{Al_2O_3} = 0.3$ ]. The fundamental frequencies of the FGM beam obtained using analytical solutions based on higher-order theory presented in [7] are also included in Table 2. It is observed that  $\bar{\omega}_1$  of the present FE model is closely matching with one obtained using analytical solutions [7]. Figure 3 illustrates first six free vibration modes taking  $S = 20$  and  $p = 1$ .

Next, we present the displacement time histories of cantilever FGM beam under different types of excitation conditions. The beam is excited with uniform pressure load. The reduced order model is constructed using modal approach considering first six modes. 0.8% damping is given to each mode which is obtained using Rayleigh damping methods.

The displacement time histories of the tip of cantilever beam ( $S = 20$ ) has been presented in Fig. 4 for impulse, step, and sinusoidal pressure loading for undamped ( $\xi = 0\%$ ) and damped ( $\xi = 0.8\%$ ) cases, respectively. For the harmonic excitation, the beam is excited at a forcing frequency  $\omega_f = 0.95\omega_1$ . For the undamped case, well-known beating phenomena are clearly observed for sinusoidal loading case (Fig. 4a part C). When some damping ( $\xi = 0.8\%$ ) has been given to the system, the second peak of the beat is reduced considerably. It can be very well seen in these plots that the contribution of higher modes for the impulse loading is large as compared to the step and sinusoidal excitation.

**Table 2** First six natural frequencies (rad/s) of FGM beams with different thicknesses and inhomogeneity parameter  $p$  and boundary conditions at  $S = 20$

B.Cs	$\bar{\omega}_n$	$p = 0$	$p = 0.2$	$p = 1$	$p = 2$	$p = 5$	$p = \infty$
S-S	$\bar{\omega}_1$	5.4603	5.1061	4.2121	3.8298	3.6269	2.8371
		(5.4603)	(5.0814)	(4.2039)	(3.8343)	(3.6466)	(2.8371)
	$\bar{\omega}_2$	21.573	20.183	16.652	15.118	14.271	11.209
	$\bar{\omega}_3$	47.595	44.550	36.693	33.188	31.120	24.730
	$\bar{\omega}_4$	60.478	57.783	50.279	45.299	39.507	31.424
	$\bar{\omega}_5$	82.453	77.328	64.420	58.586	54.535	42.842
	$\bar{\omega}_6$	124.93	117.27	97.540	88.334	81.840	64.913
C-F	$\bar{\omega}_1$	1.9496	1.8230	1.5040	1.3680	1.2963	1.0130
		(1.9496)	(1.8141)	(1.5011)	(1.36960)	(1.3034)	(1.0130)
	$\bar{\omega}_2$	12.080	11.302	9.3331	8.4833	8.0149	6.2769
	$\bar{\omega}_3$	33.240	31.121	25.738	23.372	21.984	17.271
	$\bar{\omega}_4$	60.478	57.810	49.317	44.672	39.760	31.424
	$\bar{\omega}_5$	63.584	59.600	50.820	46.116	41.968	33.038
	$\bar{\omega}_6$	102.10	95.803	79.593	72.094	66.986	53.049
C-C	$\bar{\omega}_1$	12.230	11.445	9.4596	8.5980	8.1107	6.3546
		(12.223)	(11.384)	(9.4328)	(8.5994)	(8.1460)	(6.3509)
	$\bar{\omega}_2$	33.044	30.954	25.638	23.279	21.839	17.170
	$\bar{\omega}_3$	63.167	59.238	49.185	44.607	41.584	32.821
	$\bar{\omega}_4$	101.36	95.173	79.239	71.773	66.451	52.665
	$\bar{\omega}_5$	121.05	115.72	101.52	91.971	79.646	62.896
	$\bar{\omega}_6$	146.50	137.73	115.02	104.06	95.675	76.119
S-C	$\bar{\omega}_1$	8.4838	7.9362	6.5535	5.9584	5.6328	4.4081
	$\bar{\omega}_2$	27.053	25.326	20.947	19.028	17.909	14.056
	$\bar{\omega}_3$	55.179	51.710	42.859	38.888	36.393	28.671
	$\bar{\omega}_4$	60.478	57.815	50.737	45.973	39.814	31.424
	$\bar{\omega}_5$	91.757	86.091	71.535	64.825	60.269	47.676
	$\bar{\omega}_6$	135.60	127.39	106.15	96.075	88.703	70.459

Note: Values in the parenthesis are taken from Ref. [7] for comparison.

## 4 Conclusions

A two-noded beam element is presented for the dynamic analysis of FG beam using TOT. The FE is validated with the results available in the literature. The numerical study shows that the present FE yields accurate results for static deflection and free vibration. Based on the detailed analysis, it is observed that the central deflection decreases with increase in power law exponent, and it is minimum when power law exponent is infinite (i.e., for pure ceramic beam). The free vibration frequencies

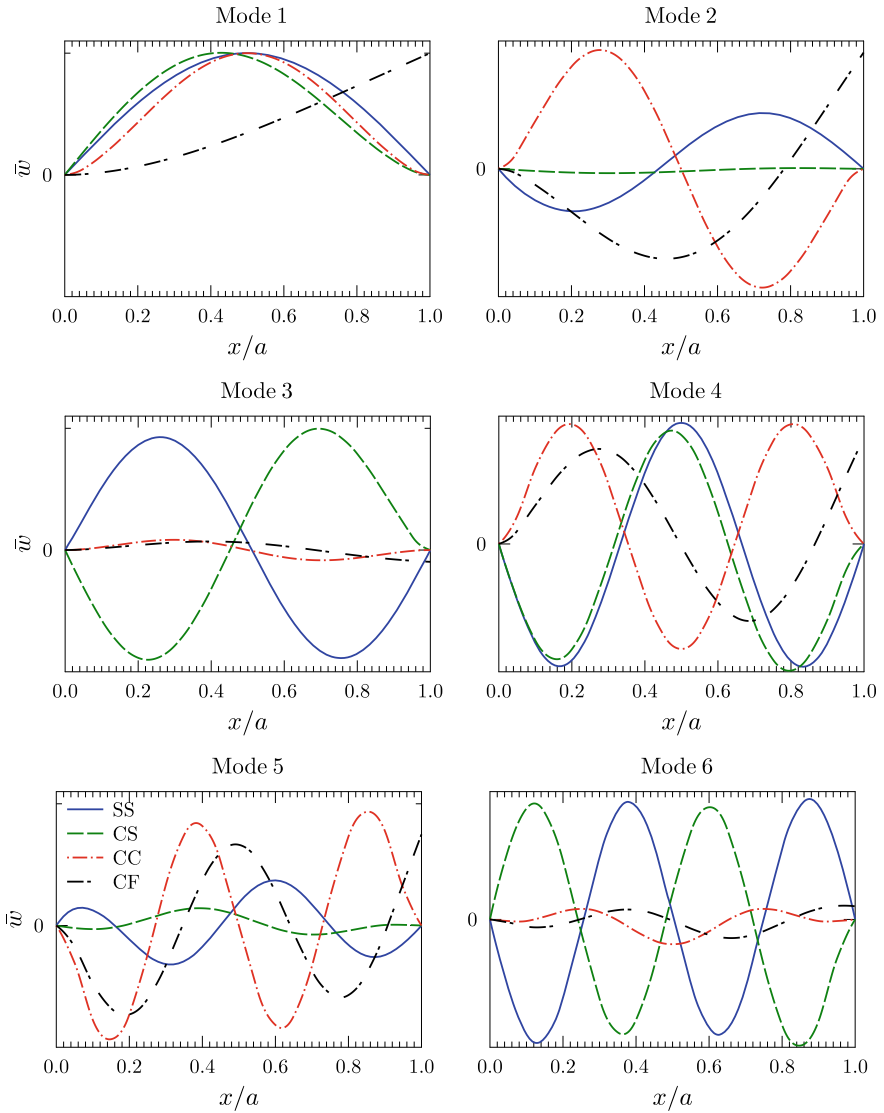


**Fig. 3** First six flexural mode shapes of Al/Al<sub>2</sub>O<sub>3</sub> FG beams with various boundary conditions ( $\nu = 1$ )

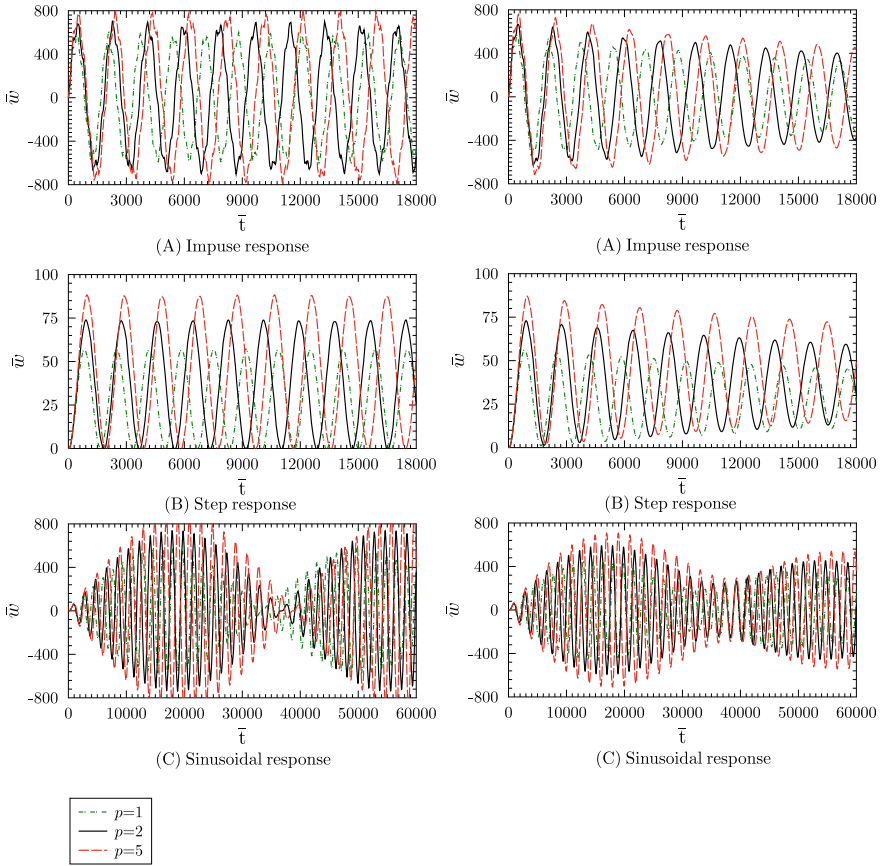


**Fig. 4** Tip deflection time histories of cantilever Al/Al<sub>2</sub>O<sub>3</sub> FGM beam with or without damping under different loading conditions ( $S = 20$ )

decrease as the power law exponent increases. In dynamic response, well-known beating phenomenon is observed when beam is excited with sinusoidal loading at forcing frequency near to resonance. For damped case, the peak of the second beat is considerably reduced in comparison with undamped case. Also, the contribution of higher modes for the impulse loading is large as compared to the step and sinusoidal excitation.

## References

1. Sankar BV (2001) An elasticity solution for functionally graded beams. *Compos Sci Technol* 61:689–696

2. Li XF (2008) A unified approach for analyzing static and dynamic behaviors of functionally graded Timoshenko and Euler-Bernoulli beams. *J Sound Vib* 318:1210–1229
3. Sina SA, Navazi HM, Haddadpour H (2009) An analytical method for free vibration analysis of functionally graded beams. *Mater Des* 30:741–747
4. Thai HT, Vo TP (2012) Bending and free vibration of functionally graded beams using various higher-order shear deformation beam theories. *Int J Mech Sci* 62:57–66
5. Simsek M (2010) Fundamental frequency analysis of functionally graded beams by using different higher-order beam theories. *Nucl Eng Des* 240:697–705
6. Kadoli R, Akhtar K, Ganesan N (2008) Static analysis of functionally graded beams using higher order shear deformation theory. *Appl Math Model* 32:2509–2525
7. Vo TP, Thai HT, Nguyen TK, Inam F (2014) Static and vibration analysis of functionally graded beams using refined shear deformation theory. *Meccanica* 49:155–168
8. Chakraborty A, Gopalakrishnan S, Reddy JN (2003) A new beam finite element for the analysis of functionally graded materials. *Int J Mech Sci* 45(3):519–539
9. Kapuria S, Bhattacharyya M, Kumar AN (2008) Bending and free vibration response of layered functionally graded beams: a theoretical model and its experimental validation. *Compos Struct* 82(3):390–402

# A Statistical Analysis to Optimize Wear Properties of Hybrid Polymer PTFE Composites



G. Harish, P. Harsha Vardhan and Y. P. Deepthi

**Abstract** Polymers are steadily playing a major material role over traditional bearing materials currently being used because of their unique properties including self-lubrication, silent in operation, and less weight. Polytetrafluoroethylene (PTFE) widely known as Teflon is a miracle material in the category of polymers which is found to be best suited for bearing applications. The present work is on tribological behavior of hybrid polymers. Taguchi Orthogonal array is employed for designing the experimental layout. Wear and friction coefficient were measured by pin on disk tribometer. The experimental layout was developed by design of experiments. The difference between the wear and friction values obtained through experimental and mathematical model found to be less than 5%. From the regression table, it is inferred that wear rate is more dependent on load, whereas sliding distance is the most significant factor affecting the coefficient of friction. SEM images were taken in order to study the surface morphology of the PTFE composites, and results have shown that PTFE + Graphite + MoS<sub>2</sub> type of composite is more wear resistant when compared to the PTFE + Graphite and virgin PTFE.

**Keywords** Polytetrafluoroethylene (PTFE) · Wear resistance · Regression analysis

## 1 Introduction

Investigation of bearing material is one of the greatest challenges happening in the field of material science in recent days. Many bearing materials including ceramics, carbides, steels, and many more materials are used as bearing materials because of their good wear resistance, hot hardness, better heat dissipating properties, and excellent thermal conductivity exhibited from them. But, the major property what designer look in these materials is the wear rate of the materials in both wet and dry

---

G. Harish · P. Harsha Vardhan · Y. P. Deepthi (✉)

Department of Mechanical Engineering, Amrita School of Engineering, Amrita Vishwa Vidyapeetham, Bengaluru, India

e-mail: [Deepthi.prajna@gmail.com](mailto:Deepthi.prajna@gmail.com)

© Springer Nature Singapore Pte Ltd. 2020

L. Vijayaraghavan et al. (eds.), *Emerging Trends in Mechanical Engineering*,

Lecture Notes in Mechanical Engineering,

[https://doi.org/10.1007/978-981-32-9931-3\\_59](https://doi.org/10.1007/978-981-32-9931-3_59)

wear condition. Nowadays, use of liquid or semi-solid lubricants has been avoided in the industries because of disposal and additional costs incurred to the industry.

Low coefficient of friction and chemical stability of polymer materials make them best alternate for metals. Polymer has a wide application in the field of lubrication wherever sliding motions are involved [1]. Many researchers have studied wear properties of PTFE composites using graphite, copper, and molybdenum as a filler material and had shown the increase in wear resistance by increase in percent of filler material [2–6].

Wear is reduced significantly when a transfer film formed on counter face of metal. It is also mentioned in the experimental result that increase in temperature during operation can help in postponing the severe wear. Other than transfer film, the counterpart surface roughness, geometry, and material properties are the deciding factors for wear [7]. The wear rate of PTFE composites depends on the type and size of filler added. This added filler contributes the adhesion strength of composite which in turns reduces the wear [8]. The bonding strength between the matrix and filler helps in retaining the structure of PTFE, which adds to the strength of composite [9]. Many researchers worked on PTFE composites filled with various fillers and observed a drastic change in wear behavior. The improved wear resistance can be credited to the load-carrying capacity of fillers [10–17].

Though the composites with single filler can reduce wear, the hardness value of the composites is not improved. Researchers are looking for a novel material to satisfy the design constraints where the material should have high strength as well as high wear resistant. Hybrid composites can able to satisfy these criteria as it has high strength to weight ratio so it can withstand fatigue loads. The glass transition temperatures are high for hybrid composites. Not much work has been reported in polymer composites with hybrid fillers. The work carried out on PTFE composites by addition of graphite and molybdenum as filler material has shown significant improvement in the strength and wear rate. Molybdenum disulfide can be added as filler to PTFE because of its super lubricity property which helps in still reducing the friction and wear.

The current work studies the effect of input parameters like load, composition, and sliding velocity on wear and friction behavior of hybrid composite. Statistical tools like multiple regression analysis technique are employed to study the effect of input parameters on wear and friction coefficient.

## 2 Experimental Details

The PTFE specimens are prepared by compression molding technique. Specimens are fabricated by varying the weight percentage of molybdenum and PTFE where graphite kept constant. The required proportion of material which is added in weight percentages is mixed manually and compacted to a cylindrical shape and sintered in muffle furnace. The friction and wear are measured by pin on disk tribometer [18] as shown in Fig. 1. The input parameters and their different levels are shown in Table 1.



**Fig. 1** Pin on disk tribometer

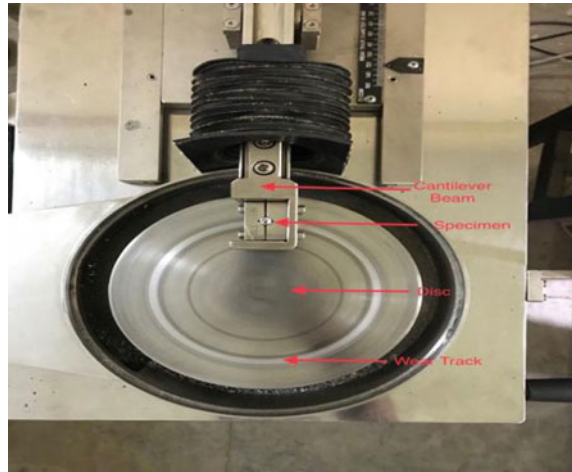


**Table 1** Input factors with levels

Input factors	Notation		Levels			
Composition	C	100	95	90	85	8075
PTFE (wt%)						
Speed (rpm)	S	1.18	1.19	1.20		
Load (N)	L	10	20	30		

### 3 Results and Discussion

Regression analysis is a statistical technique which gives the relationship of input factors to output factors. The regression table for wear and coefficient of friction is shown in Tables 2 and 3.

From the regression table, it can be inferred that the most significant factor, i.e., *p*-value effecting wear is load. It can be inferred that wear increases with increase in load. When it comes to coefficient of friction, the sliding velocity is the most influential factor. The mathematical model obtained through multiple regression method

**Table 2** Regression values for wear

Term	Coefficient	SE coef	T-value	P-value	VIF
L	0.000272	0.000786	0.38	0.785	53,848
C	-0.0101	0.0162	-0.67	0.624	25,077,369
S	-0.40	1.21	-0.33	0.748	53,848
L*C	-0.000007	0.000009	-0.78	0.452	56,896
C*S	0.0092	0.0137	0.67	0.565	25,686,648

**Table 3** Regression values for coefficient of friction

Term	Coefficient	SE Coef	T-Value	P-Value	VIF
C*L	-0.00333	0.0014	-2.38	0.035	56,896
L	0.262	0.123	2.13	0.055	53,848
C	-5.82	2.54	-2.29	0.041	25,077,369
S	-391	189	-2.07	0.061	53,848

for both specific wear rate and coefficient of friction is shown in Eq. 1 and 2.

$$sw = 2.022 E - 05 C + 0.404861 S - 0.000302658 L \tag{1}$$

$$cof = 0.003787 c + 40.55567s - 0.02942 L \tag{2}$$

### 4 Conclusions

Wear tests for the virgin PTFE and hybrid composites with different speeds and loads. The adding of molybdenum and graphite to pure PTFE aided in decreasing the wear. Adding of graphite + MoS<sub>2</sub> facilitated in imparting the strength of hybrid specimen. Also, fillers would have increased the adhesive strength between filler and matrix because of that material loss is decreased during sliding operations.

The SEM images as shown in Fig. 2 were taken for the virgin PTFE and PTFE + Graphite + MoS<sub>2</sub> after the wear test in order to study the surface morphology.

As it can be inferred that the virgin PTFE has a lot of flakes after wear test indicating the less resistance to wear. The hybrid PTFE specimen is better when

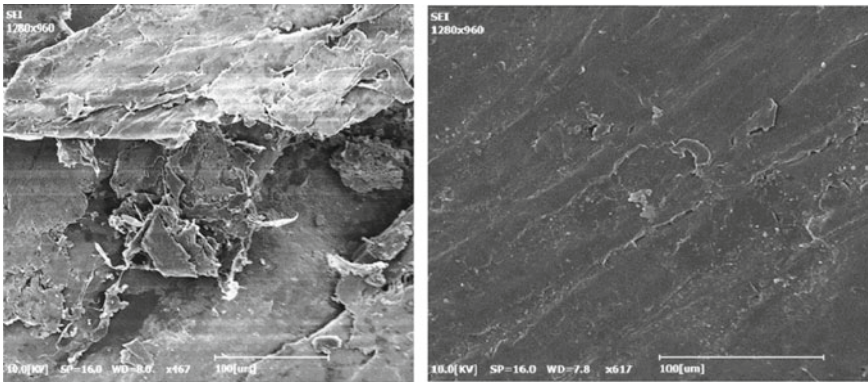


**Fig. 2** SEM pictures of virgin PTFE and hybrid PTFE after wear

compared to the virgin PTFE as the number of flakes is less in this case. It can be concluded that with the addition of the MoS<sub>2</sub>, the wear rate was decreasing and had more wear energy making it suitable in bearing applications.

## References

1. Li F, Yan FY, Yu LG, Liu WM (2000) The tribological behaviors of copper-coated graphite filled PTFE composites. *Wear* 237:33–38
2. Gong D, Xue Q (1989) Study of the wear of filled PTFE. *Wear* 134:283–295
3. Bahadur S, Gong D (1992) The action of fillers in the modification of the friction and wear behavior of polymers. *Wear* 158:41–59
4. Bahadur S, Tabor D (1984) The effect of filled polytetrafluoroethylene. *Wear* 98:1–13
5. Gong D, Zhang B (1990) Study on friction and wear interaction of metals of metal oxides with polytetrafluoroethylene by X-ray photoelectron spectroscopy. *J Appl Polym Sci* 41:2587–2593
6. Li F, Hu K, Li J, Zhao B (2002) The friction and wear of nanometer ZnO filled polytetrafluoroethylene. *Wear* 249:877–882
7. Rhee SH, Ludema KC (1978) Mechanism of formation of polymeric transfer films. *Wear* 46:231–240
8. Bahadur S, Tabor D (1985) Role of fillers in the friction and wear behavior of high-density polyethylene. In: Lee LH (ed) *Polymer wear and its control*. ACS symposium series 287, Washington, pp 253–268
9. Tanaka K (1986) Effect of various fillers on the friction and wear of PTFE-based composites. In: Friedrich K (ed) *Friction and wear of polymer composites*. Elsevier, Amsterdam, pp 137–174
10. Lancaster JK (1972) Polymer-based bearing materials: the role of fillers and fiber reinforcement. *Tribol Int* 5:249–255
11. Evans DC, Lancaster JK (1979) The wear of polymers. In: Scott D (ed) *Treatise on materials science and technology*, vol 13. Academic Press, New York, pp 85–139
12. Cadman P, Gossedge GM (1978) Studies of polytetrafluoroethylene transfer layers produced by rubbing in ultrahigh vacuum using a relatively simple apparatus. *Wear* 51:57–65
13. Cadman P, Gossedge GM (1979) The chemical nature of metal polytetrafluoroethylene tribological interactions as studied by X-ray photoelectron spectroscopy. *Wear* 54:212–215
14. Briscoe BJ (1981) Wear of polymers: an assay on fundamental aspects. *Tribol Int* 14:231–243
15. Briscoe BJ (1985) Wear of polytetrafluoroethylene: a mawerick or not. In: Lee LH (ed) *Polymer wear and its control*. ACS symposium series 287, Washington pp 151–170
16. Deepthi YP, Krishna M (2018) Optimization of electroless copper coating parameters on graphite particles using Taguchi and grey relational analysis. *Mater Today Proc* 5:12077–12082
17. Deepthi YP, Krishna M Effect of process parameters on electroless process of coating copper on graphite powder for PTFE bearing applications. *Int J Eng Technol (UAE)* (in press)
18. Raaj kumar RA, Sriram S, Harikiran reddy R, Deepthi YP Experimental investigation on influence of molybdenum content on tribological properties of hybrid PTFE composite. In *AIP proceedings* (in press)

# Recent Advances in the Development of Aluminium Matrix Composites (AMCs)



V. Anand, M. N. Akshay, S. Abhilash and G. Deepak

**Abstract** Materials development for changing aerospace industry has been the need of time. Composites (metal, ceramic and polymer) materials are proven better than any kind of materials for challenging atmosphere. Aluminium matrix composites (AMCs) are widely used in aerospace applications for variety of accessories. Aluminium composites have good mechanical properties and so they form important materials for structural applications. Processing techniques have an important effect on the overall performance of the AMCs and are directly linked to their mechanical behaviour. This review summarizes the effect of processing techniques, types of reinforcement on the mechanical properties of AMCs.

**Keywords** Aluminium matrix composites · Wear · Stir casting · AMCs

## 1 Introduction

The aluminium matrix composites are materials which comprise of low-weight but exhibit high-performance. These materials also display low density, high specific strength, high specific stiffness, greater wear resistance along with dimensional stability and due to these characteristics, these materials replace standard materials in most of the advanced applications. The properties of these materials can be altered by altering the properties of reinforcement particles such as its type, size and fraction. As AMCs have found vast applications in automotive sector, they have to possess greater wear and frictional resistance. According to recent reports, it has been found that utilization of aluminium matrix composites in components of engine results in significant reduction in fuel consumption due to reduction in overall weight and also pollution levels in automobiles [1]. Aluminium matrix composites also have wide range of applications in aerospace. In the manufacture of Aluminium matrix composites, basically ceramic reinforcements such as Alumina ( $Al_2O_3$ ) and Silicon Carbide

---

V. Anand · M. N. Akshay (✉) · S. Abhilash · G. Deepak  
Department of Mechanical Engineering, Vidyavardhaka College of Engineering, Mysore 570002, India  
e-mail: [akshaymn1998@gmail.com](mailto:akshaymn1998@gmail.com)

© Springer Nature Singapore Pte Ltd. 2020  
L. Vijayaraghavan et al. (eds.), *Emerging Trends in Mechanical Engineering*,  
Lecture Notes in Mechanical Engineering,  
[https://doi.org/10.1007/978-981-32-9931-3\\_60](https://doi.org/10.1007/978-981-32-9931-3_60)

(SiC) are preferred as reinforcements in Aluminium matrix. Enhanced wear resistance is the prime advantage in case of AMCs with ceramic reinforcements. Whereas, increased addition of hard reinforcement in Al-alloy results in increased counterface wear rate and further leading to reduction in wear performance of a tribosystem. Addition of self-lubricating particles as reinforcements in aluminium matrix leads to deterioration of tribological properties as well as mechanical properties of Aluminium matrix composites. Such conditions are overcome with the help of hybrid Al-composites containing both solid-lubricants and hard-ceramic particles that can exhibit enhanced wear performance. Graphite particulates are most efficient for these applications, and their addition enhances the wear resistance and machinability of Aluminium composites with ceramic reinforcements. The content of Graphite particles plays a dominant role in affecting the tribological characteristics of hybrid composites. Basically, the three factors that direct the wear performance of Aluminium matrix composites are mechanical parameters, material factors, and physical parameters. Mechanical parameters include temperature, sliding distance, sliding velocity, applied load and hardness of counterface. The material factors include reinforcement type, shape, contents, and size. With the analysis of influence of all these parameters, the wear performance of the Aluminium matrix composites can be known [1, 2].

## 2 Reinforcement and Processing Techniques

The Aluminium Matrix Composites (AMCs) was produced by Friction Stir Processing (FSP). Aluminium–magnesium–silicon family alloy (AA6082) was utilized as the matrix material. The ceramic particles such as SiC, Al<sub>2</sub>O<sub>3</sub>, WC, B<sub>4</sub>C, and TiC were adopted as reinforcement in the form of particles. By using a set of advanced process criterion AA6082 AMCs were produced. The results clearly indicated that the type of ceramic particle did not considerably vary the ultimate tensile strength (UTS) and microstructure. Homogeneous dispersion was seen in the stir zone for each type of ceramic particle irrespective of the location and good interfacial bonding. Compared to other AMCs, AA6082/TiC AMC exhibited superior hardness and wear resistance. Due to interaction with the rotating tool and severe plastic deformation SiC, WC, B<sub>4</sub>C, and TiC particles encountered fragmentation during FSP [3, 4].

Preparation of a hybrid of AA6061/Al<sub>2</sub>O<sub>3</sub>/graphite composite by additionally incorporating Si<sub>3</sub>N<sub>4</sub> nanoparticles in the material system was carried out. Stir casting method was employed in manufacturing the composites. The wear rate and coefficient of friction of composites with dual ceramic reinforcement were relatively less than that of composites with single ceramic reinforcements. Severe plastic deformation and abrasive wear were found to be the wear mechanism. In unmixed reinforcement composite porosity, particle pullout, crack nucleation in grain boundary was noticed [5].

The effect on the mechanical properties of Al-7072 for different dry weight fraction, when Al<sub>2</sub>O<sub>3</sub> used as ceramic reinforcement was studied in the experiment. The

composite is manufactured using stir casting technique. From the results, it was concluded that when there is increase in percentage of reinforced particles mechanical properties such as breaking strength and compressive strength, hardness and ductility increased significantly. Nanosized titanium carbide (0.5, 1.0 and 1.5 vol.%) reinforced aluminium (Al) metal matrix composites were prepared by powder metallurgical route, viz., hot extrusion and microwave sintering methods. As the amount of TiC particles increases gradually, the surface roughness of Al-TiC nanocomposites decreases. Hot extruded 1.5% TiC-Al composite showed the hardness, tensile strength and the compressive strength of  $103 \text{ GPa}$ ,  $186 \pm 3 \text{ MPa}$ ,  $416 \pm 4 \text{ MPa}$  and  $9.75 \pm 0.5 \text{ GPa}$ , respectively. Young's modulus, hardness, compressive and tensile strengths of the nanocomposites increases with increasing content of titanium carbide, while a reverse pattern was observed in the failure strain of nanocomposites under both compressive and tensile loading [6, 7].

Influence of processing temperature and addition of micron-sized  $\text{B}_4\text{C}$ ,  $\text{ZrSiO}_4$ , and  $\text{TiB}_2$  on the mechanical outcomes of aluminium matrix composites manufactured through stir casting were studied by Shirvanimoghaddam et al. [8]. Tensile strength and hardness of aluminium matrix composites with ceramic reinforcement were found to be superior to monolithic aluminium. Hardness of Al- $\text{B}_4\text{C}$  and Al- $\text{TiB}_2$  composites were greater than Al- $\text{ZrSiO}_4$  composites in same amounts of reinforcements. The 5 vol.% Al $\text{ZrSiO}_4$ , 15 vol.% Al- $\text{TiB}_2$  and 5–10 vol.% Al- $\text{B}_4\text{C}$  composites found to have highest values of hardness and ultimate tensile strength. Al 7075 composite is fabricated with silicon carbide by using one of the common methods, i.e., stir casting. Effect of heat treatment and reinforcement percentage on the physical properties like density, porosity and also on hardness of material was studied and also the size of particle was observed. From this experiment it was observed that density and porosity were directly proportional to the reinforcement content. Another observation in this experiment was the microhardness of AMC's been directly proportional to percentage weight of particulates of silicon carbide as the size decreases gradually. There was a direct proportionality relation between reinforcement fraction and various mechanical properties. If there are cavities in the composites, there will be decrease in the properties. The strength was noted to vary directly with reinforcement fraction up to a certain level, further it decreased. During the fracture study, it was observed that due to small cracks, there was large failure and also ductile failure occurs, when subjected to tension and brittle fracture, overload failure takes place [8].

Processes like forging, rolling and some of the other mechanical processes were carried on nanocomposites and enhances its properties. Upon forging there was significant improvement in metal flow and also in the structural arrangement of grains which could be used for different purposes. When the nano-composites were forged with silicon carbide reinforcements at an elevated temperature it gave the best of results and also it was recommended that a significant amount of aluminium and nano-particle had to be combined. Reinforcement of graphene nanoplatelets is done with aluminium composite with the help of continuous casting and followed by rolling. The master alloy of the reinforced mixture is prepared by milling and pressing operations. The nanoplatelets showed uniformity in cast specimen and then

transformed to fibre form upon deformation and eventually lamellar structure. Due to ball milling, there were damages in the structure of nanoplatelets. In the interface stage due to small cracks, the ductility of the composites reduced. In the inside of the grain, there were stacking faults also. The ultimate strength of GNPs was 36.8% more than for pure Al under same conditions and load. There was a slight dip in the conducting properties. Therefore the Al-GNPs can be used for more strength and conducting purposes [5].

High-pressure torsion (HPT) method was used to process 10 vol.%  $\text{Al}_2\text{O}_3$  particle reinforced Al matrix composite by applying pressure of 6 GPa. The HPT led to grain refinement from 8  $\mu\text{m}$  to 300 nm. Hardness was improved from 163 to 260 Hv after 20 turns. Tensile strength revealed the superplasticity as it causes the elongation of 670% [9]. The Al-6061 reinforced with 10%  $\text{Al}_2\text{O}_3$  by HPT of pressure of 6 GPa for different turns. Grain size was found to reduce from 35  $\mu\text{m}$  to 170 nm after 10 turns. Threefold increase in hardness was observed than without HPT samples [10].

### 3 Computational Framework

An automated computational framework is employed to determine the effect of pre-existing microstructural voids due to the failure response of aluminium composite with ceramic fibre reinforcement subjected to loads in transverse to the fibre direction. With the help of a hierarchical interface-enriched finite element method (HIFEM) automated Numerical simulations were done. A strain-driven integrated depending on the Lemaitre elasto-plastic damage model was developed to imitate the initiation and progress of damage in the aluminium matrix. When subjugated to macroscopic normal strains, including very small volume fraction of voids considerably degenerate the composite strength. The decrease in strength was directly proportional to the volume fragment of voids. Variation of the toughness was highly based on the spatial distribution of voids and does not certainly deteriorate due to the presence of voids [11].

### 4 Mechanical Properties

Pramanik [12] has studied how the reinforcement affects the wear mechanism in Aluminium matrix composites. For this he considered different parameters like sliding distance say 6 km, pressure say 0.14–1.1 MPa, sliding speed of about 230–1480 r/min. 6061 Al MMC which is reinforced with 10%  $\text{Al}_2\text{O}_3$  (in volume fraction) particles of size 6–18  $\mu\text{m}$  and 6061 Al matrix alloy were compared for wear resistance on a pin-on-disc machine. This is conducted under the same conditions. Major outcomes of the test are; the reinforced MMC has high wear resistance than the corresponding matrix material due to the addition of reinforced particles and the MMC wear is linear and can be predicted very easily. Even though the mechanism of wear is similar

for both, excluding three-body abrasion which we see in MMC. From various tests, he concluded that for a monolithic metal, the wear resistance is improved when we add ceramic as reinforcement and they also delay the transition load of particular material. It also stops plastic deformation in the immediate neighbourhood of the particle and higher oxidation is seen in MMC during wearing. As we increase the pressure and sliding speed, debris size is also increased in both the materials. These results divulge the roles of reinforcement in MMC and provide a guide to control wear.

Miao et al. have studied the plastic deformation and cracking behaviour in Band-like Aluminium matrix composites where BAMCs were fabricated with ductile AMC reinforced with the whiskers of  $\text{Al}_{18}\text{B}_4\text{O}_{33}$  (ABO) using powder metallurgy and extrusion process which is followed by annealing and also during fabrication superior elongation are seen. The tests conducted on BAMCs reveals that band like structure in ABO-rich bands cause compressive residual stress and it is seen in the place where nucleation of the crack occurs. The so formed residual stress stops the propagation of cracks and thereby improving BAMC's strain transferring ability. Therefore, during a tensile test as the ABO volume fraction increases, crack becomes denser and smaller in BAMCs. Even though small cracks help in strain non-localization process, improved plastic deformability makes BAMCs a good ductile material [13].

Reddy et al. [14] have studied the characterization and also the fabrication of 6082 Al matrix hybrid composites where the reinforcements are SiC and fly ash, stir casting process is applied to fabricate the same with three different weight fractions, i.e., 2.5, 5, and 7.5% of reinforcements which is in equal proportion. Studies are conducted on its microstructure and also on its mechanical properties like hardness, wear and tensile. The results were compared with the results of Aluminium alloy which is unreinforced. The result of the tests conducted revealed that SiC particles were distributed uniformly whereas fly ash particles are distributed non-uniformly. As the weight fraction of reinforcement's increases, hardness, wear-resistance and ultimate tensile strength also increases. These results obtained are very useful in utilizing industrial wastes like fly ash in the fabrication of hybrid composites.

Illgen et al. have studied the fatigue behaviour of Aluminium MMCs reinforced with 15% volume alumina and short fibres (20 vol.% saffil) at stress amplitudes  $\leq 140$  MPa, by using an ultrasonic fatigue testing machine which helps it to reach fatigue lives of up to  $10^{10}$  cycles. The frequency used for testing is 20 kHz and were operated in a pulse/pause mode. During the test in situ parameters were recorded and a thermography system was used to know the changes in local and global temperature. The results from all the experiments conducted are; VHCF region and LCF/HCF region fits well in the strain-controlled test and it is evident that there is no impact by test frequency. Results also revealed that there is no major difference to the unreinforced Al MMC and the particle reinforced at a stress below 140 MPa. Moreover, up to  $10^{10}$  cycles, no fatigue failure is seen at the stress below 80 MPa. In the VHCF region of two reinforced material, a marginal increase of fatigue life is evident. Spot cooling effects had a positive impact on fatigue performance and also on the scatter of results. For specimens reinforced with short fibres, orientation and heat treatment doesn't affect fatigue life and scatter. Finally, it can be concluded



that there is comparable fatigue lives for short fibre reinforced Aluminium MMCs (AA6061) or particle reinforced in peak aged conditions at a small amplitude of stress (140 MPa) in VHCF regime [15].

Pei et al. [16] investigated thermomechanical properties of aluminium composites (P100/6063, P100/1199, P120/6063, P120/1199) reinforced with 4 unidirectional carbon fiber (67.9–70% in volume) and it is fabricated by pressure infiltration technique. By the end of fabrication composites with low thermal expansion, high thermal conductivity and higher mechanical properties were obtained. After several tests following are the noteworthy observations; P100 fibres and P120 fibres have large dimensioned LMO's which makes it have high thermal conductivity and prevents carbide formation between Al matrix and carbon fiber interface. In P100/6063 composites interfacial gap formation is suppressed when compared to the other system. This is actually due to 6063 alloy's lower viscosity and P100's larger diameter and higher wettability. Due to the residual stress at the interface, with the increase in temperature, the composite's CTE values first decreases till it reaches a temperature of 350 °C and thereafter it starts increasing. And finally, the modulus of elasticity of the composites is very high (greater than 40 GPa) and this is due to the high modulus of carbon fiber (800 GPa). Having high thermal expansion and top-notch mechanical properties, these composites can be a promising material for the production of microelectronic chips.

Afkham et al. have studied the improvement in mechanical properties of aluminium matrix composites fabricated through in situ liquid stir casting process at 1123 K and it is followed by a hot rolling process. Using three metal oxides, i.e., commercial ZnO, recycled Pyrex, and commercial TiO<sub>2</sub> were injected into aluminium metal matrix which is of high grade in terms of purity and ball milling process was examined. The reactions between metal oxides and molten Al which forms Nano alumina particles that act as a reinforcement. Microhardness and tensile test were also done on the rolled composites, this is done to identify the effect of amount and type of metal oxide added on the properties of rolled composites. The results obtained from the series of tests are; with the use of recycled crushed Pyrex powder it was very easy to obtain the composites where alumina nanoparticles are uniformly distributed. Waste Pyrex glass powder having less agglomeration could be distributed uniformly in the Al matrix. After hot rolling process, crack was formed in microstructure due to the addition of ZnO especially TiO<sub>2</sub> powder and this because they were present in a group during stir casting process. With the increase in the amount of Pyrex, we will be able to notice a surge in yield stress, hardness, and ultimate tensile stress but ductility is reduced. At last, we can conclude that using ZnO and TiO<sub>2</sub> powder, no enhancement in the mechanical properties is seen when compared with Pyrex derived powder which is of low cost [17].

Aluminium composites are taken in small amounts to conduct tests on its properties after being reinforced with graphene oxide (GO). Micro-sized purified Al powder with different combinations of GO was combined and specified dimensions of discs were made. These composites were made to undergo compact test at cold conditions. These processes are carried out mandatorily for the sake of observing the homogenous scattering of the GO. Strength and hardness readings were noted

down and it was observed that composites with hardness similar to the ones of rGO composites were obtained only when even mixing was achieved. Compression test was conducted on aluminium matrix composites that are reinforced with micro SiC and nano TiB<sub>2</sub> at high temperature of 350–500 °C. The true stress was found to be directly proportional to true strain and then there is a small decrease when peak value is reached by the true stress. The mechanism involved in softening of hybrid composites was called DRV with little bit of DRX [1, 5].

Jarzabek et al. worked on the adhesion force and fracture strength of the ceramic/metal interface in metal matrix composites with varying ceramic reinforcements. Three samples with different compositions of Cu/Al<sub>2</sub>O<sub>3</sub> were prepared. The results specify that the interface between ceramic particles and metal matrix in 10% Al<sub>2</sub>O<sub>3</sub> composite is notably weaker than 2 and 5% Al<sub>2</sub>O<sub>3</sub> samples. Ceramic/metal interfacial strength was found to be  $59 \pm 8$  MPa and  $59 \pm 11$  MPa in 2 and 5% Al<sub>2</sub>O<sub>3</sub>/Cu, respectively and as the ceramic concentration increases, decrease in Young modulus and hardness was observed. Aluminium metal matrix composites reinforced with single and dual reinforced particles, i.e., SRP and DRP shows varied tribological behaviour at different temperatures when the concentration of ceramic reinforced particles in the matrix is varied. Reinforcements such as Zircon sand and silicon carbide with particle size 18–34 μm were used in LM13 piston alloy of commercial grade. Composites with zircon sand and silicon carbide particle as reinforcement in ratio 1:3 exhibits better wear resistance at both low and high loads across all temperature ranges when compared to other composites. The wear resistance can be enhanced for a composite by adopting DRP instead of SRP in definite proportion. The wear behaviour in a composite shows linear increase when the operating temperature is increased at high load condition. This condition arises due to the formation of oxide film and glazing layer on the sliding components and this actually helps in prevention of contact between metals during sliding [18].

## 5 Conclusion

AMCs have good mechanical properties and so they form important materials for structural applications. Processing techniques have an important effect on the overall performance of the AMCs and are directly linked to their mechanical behaviour. This review summarizes the effect of processing techniques, types of reinforcement on the mechanical properties of AMCs. The more emphasis was given to tribological properties. Friction stir processing, stir casting, high-pressure torsion, and powder metallurgical methods are described and their detail mechanical properties are discussed.

**Acknowledgements** The authors express gratitude towards the assistance provided by CL Educate Ltd. Special thanks to Dr. K. S. Ravi for his constant support and encouragement.

## References

1. Singh J, Chauhan A (2016) Overview of wear performance of aluminium matrix composites reinforced with ceramic materials under the influence of controllable variables. *Ceram Int* 42:56–81
2. Ramnath BV, Elanchezian C, Atreya T, Vignesh V (2014) Aluminum metal matrix composites—a review. *Rev Adv Mater Sci* 38:55–60
3. Dinaharan I (2016) Influence of ceramic particulate type on microstructure and tensile strength of aluminum matrix composites produced using friction stir processing. *J Asian Ceram Soc* 4:209–218
4. Pugazhenthii A, Kanagaraj G, Dinaharan I, Selvam DR (2018) Turning characteristics of in situ formed TiB<sub>2</sub> ceramic particulate reinforced AA7075 aluminum matrix composites using polycrystalline diamond cutting tool. *Meas J Int Meas Confed* 121:39–46
5. Hariharasakthisudhan P, Jose S, Manisekar K (2018) Dry sliding wear behaviour of single and dual ceramic reinforcements premixed with Al powder in AA6061 matrix. *J Mater Res Technol*, 1–9
6. He P, Ma G, Wang H, Yong Q, Chen S, Xu B (2016) Tribological behaviors of internal plasma sprayed TiO<sub>2</sub>-based ceramic coating on engine cylinder under lubricated conditions. *Tribol Int* 102:407–418
7. Mahesh Kumar V, Venkatesh CV (2018) Effect of ceramic reinforcement on mechanical properties of aluminum matrix composites produced by stir casting process. *Mater Today Proc* 5:2466–2473
8. Shirvanimoghaddam K et al (2016) Effect of B<sub>4</sub>C, TiB<sub>2</sub> and ZrSiO<sub>4</sub> ceramic particles on mechanical properties of aluminium matrix composites: experimental investigation and predictive modelling. *Ceram Int* 42:6206–6220
9. Sabbaghianrad S, Langdon T (2016) Developing superplasticity in an aluminum matrix composite processed by high-pressure torsion. *Mater Sci Eng A* 655:36–43
10. Alhajeri S, Al-Fadhalah K, Almazroue A, Langdon T (2016) Microstructure and microhardness of an Al-6061 metal matrix composite processed by high-pressure torsion. *Mater Charact* 118:270–278
11. Ahmadian H, Liang B, Soghrati S (2016) Analyzing the impact of microstructural defects on the failure response of ceramic fiber reinforced aluminum composites. *Int J Solids Struct* 97:43–55
12. Pramanik A (2016) Effects of reinforcement on wear resistance of aluminum matrix composites. *Trans Nonferrous Met Soc China* 26:348–358
13. Miao K et al (2018) High elongation achieved by band-like distribution of reinforcements in aluminum matrix composites. *Mater Charact* 144:42–47
14. Reddy MP et al (2018) Enhancing thermal and mechanical response of aluminum using nanolength scale TiC ceramic reinforcement. *Ceram Int* 44:9247–9254
15. Illgen A, Weidner A, Biermann H (2018) Influence of particle and short-fibre reinforcement on the very high cycle fatigue behaviour of aluminium matrix composites. *Int J Fatigue* 113:299–310
16. Pei R, Chen G, Wang Y, Zhao M, Wu G (2018) Effect of interfacial microstructure on the thermal-mechanical properties of mesophase pitch-based carbon fiber reinforced aluminum composites. *J Alloys Compd* 756:8–18
17. Afkham Y, Khosroshahi RA, Rahimpour S, Aavani C, Brabazon D, Mousavian RT (2018) Enhanced mechanical properties of in situ aluminium matrix composites reinforced by alumina nanoparticles. *Arch Civ Mech Eng* 18:215–226
18. Jarzabek DM, Chmielewski M, Wojciechowski T (2015) The measurement of the adhesion force between ceramic particles and metal matrix in ceramic reinforced-metal matrix composites. *Compos Part A Appl Sci Manuf* 76:124–130

# A Comparative Analysis of LiDAR and Wind Mast Measured Wind Data with the Reanalysis Datasets for an Offshore Location of Gujarat



Hardik K. Jani , Garlapati Nagababu , Ravi P. Patel  
and Surendra Singh Kachhwaha

**Abstract** The wind resource assessment is a decisive process for the development of any wind power generation project. The wind data obtained from any single means may have errors which may lead to the wrong estimation of wind speed and hence the power density. Therefore, the data obtained from any source or method has to be verified and validated with another data source in order to make the resource estimation least erroneous. In the present work, the wind data measured by means of LiDAR and wind mast has been compared with the multiple reanalysis datasets (ERA5, EMD-ERA, MERRA2 and CFSR2) for offshore location in Gujarat, India. From the consequences, the conclusion has been drawn that the reanalysis data provides underestimated wind speeds as compared to LiDAR measurements. Further, among the studied reanalysis datasets, the ERA5 data exhibits highest correlation (0.9329) with the LiDAR measured data, which proves it to be most reliable data source among the other considered reanalysis datasets. The LiDAR measured the mean wind speed of 7.41 m/s at 100 m height, which implies to the mean wind power density of 328.24 W/m<sup>2</sup>. Thus, the study location is highly suitable for the establishment of an offshore wind power project.

**Keywords** Wind energy · LiDAR · Wind mast · Reanalysis data · Offshore · India

## 1 Introduction

Prior to the establishment of a wind power project, it is essential to assess the wind power potential at that particular location. The precise estimation of wind speed at the project site is very crucial, as all the assets of the power project depend on it. The wind resource assessment can be conducted by means of the experimentally measured

---

H. K. Jani (✉) · G. Nagababu (✉) · R. P. Patel · S. S. Kachhwaha  
School of Technology, Pandit Deendayal Petroleum University, Gandhinagar, Gujarat 382007,  
India  
e-mail: [janihardik15@gmail.com](mailto:janihardik15@gmail.com)

G. Nagababu  
e-mail: [garlapatinagu@gmail.com](mailto:garlapatinagu@gmail.com)

© Springer Nature Singapore Pte Ltd. 2020  
L. Vijayaraghavan et al. (eds.), *Emerging Trends in Mechanical Engineering*,  
Lecture Notes in Mechanical Engineering,  
[https://doi.org/10.1007/978-981-32-9931-3\\_61](https://doi.org/10.1007/978-981-32-9931-3_61)

data (through wind mast, atmospheric stations or Light Detection and Ranging) or through the reanalysis data. The Ministry of New and Renewable Energy (MNRE) and National Institute of Wind Energy (NIWE) have made continuous and valuable efforts to promote the offshore wind power generation in India. As a fraction of these efforts, the wind data near the offshore regions of gulf of Khambhat have been measured with the help of Light Detection and Ranging (LiDAR) and wind mast. It is costly and difficult to conduct long term wind measurement projects due to the weather uncertainties, specifically in offshore regions. In the presence of these weather situations, the data recording gets disturbed which leads to the discontinuous data. The offshore wind power generation projects can't be established based on such interrupted data. The reanalysis datasets are the source of readily available continuous wind speed data accessible for long durations. There are multiple numbers of reanalysis datasets available and it is crucial to identify which data source is more reliable than the others. Therefore, the reanalysis data has to be validated with experimentally measured data before use. The core objective of this research work is to identify the most reliable reanalysis data source for the offshore regions of Gujarat by means of the LiDAR measured wind data (Fig. 1). Here, the data measured with LiDAR has been compared to the wind mast measured data and various reanalysis datasets (ERA5, EMD-ERA, MERRA2 and CFSR2), in order to identify the most dependable reanalysis dataset among them.

## 2 LiDAR Measurement Data

The details of the site selected for the LiDAR-based measurement are shown in Table 1. The selected location comes under the Zone-B as identified by FOWIND (Facilitating offshore wind energy project in India) among eight zones recognized

**Table 1** Details of the offshore LiDAR wind monitoring site [1]

Station	Gulf of Khambhat—LiDAR
Location name	Amreli, Gujarat, India
Latitude	20° 45' 19.10" N (20.775°)
Longitude	71° 40' 10.93" E (71.669°)
UTM (Universal Transverse Mercator) location	779721 Easting, 2297392 Northing (UTM WGS84, 42Q)
Depth	15 m depth (as per NHO chart)
Period of data analysis	November 2017–June 2018
Duration	8 months
Time step	10 min
Data recovery (%)	81.9% average at all heights

near Gujarat and Tamil Nadu coastal regions [1]. The wind data has been recorded using Windcube V2 LiDAR. The measured wind speed (WS) and corresponding wind power density (WPD) at 80 and 100 m height is shown in Table 2. The monthly mean wind speeds of 7.05 and 7.18 m/s were observed for 80 m and 100 m height, respectively. The monthly mean wind power density of 308.61 and 328.24 W/m<sup>3</sup> were recorded for 80 m and 100 m height, respectively.

### 3 Wind Mast Data

In order to correlate and validate the wind data measured by the LiDAR, NIWE installed a 100 m height wind mast approximately 25 km away from the LiDAR location (Jafrabad—20° 53' 29.81" N, 71° 27' 35.68" E) (UTM coordinates: WGS84, 42Q zone, 755896 m E, 2312117 m N). The measured WS and corresponding WPD at 80 and 100 m height are shown in Table 2. The mean wind speeds of 6.15 and 6.53 m/s were observed for 80 m and 100 m height, respectively. The wind power density of 200.05 and 243.92 W/m<sup>3</sup> were recorded for 80 m and 100 m height, respectively.

### 4 Reanalysis Datasets and the Comparative Analysis

First, the monthly mean of daily mean wind speeds was acquired from ERA-Interim ECMWF reanalysis dataset. The data having 0.125° × 0.125° spatial resolution and needed to be interpolated for getting the wind speed data for the exact study location. After having 10 m height wind speed at the study location, the wind speeds at 80 and 100 m height is extrapolated with the help of log law as expressed below [2],

$$V = V_{\text{ref}} \frac{\ln(z/z_0)}{\ln(z_{\text{ref}}/z_0)} \quad (1)$$

where,  $V$  stands for wind speed,  $z$  represents height from the surface. The surface roughness factor  $z_0$  is taken as 0.2 mm [3]. The wind power density has been calculated from the following equation,

$$\text{WPD} = \frac{1}{2} \rho V^3 \quad (2)$$

The mass density of air ( $\rho$ ) is considered to be constant as 1.225 kg/m<sup>3</sup> [2]. The derived values of the WS and WPD for 80 and 100 m height are shown in Table 2. The mean wind speeds of 5.90 and 6.00 m/s were observed for 80 m and 100 m height, respectively. The wind power density of 142.67 and 150.20 W/m<sup>2</sup> were recorded for 80 m and 100 m height, respectively.

**Table 2** The wind speed and wind power density for study location observe through LiDAR, wind mast and reanalysis dataset

Month– Year	LiDAR						Wind mast						Reanalysis data (ERA-Interim)					
	80 m			100 m			80 m			100 m			80 m			100 m		
	WS (m/s)	WPD (W/m <sup>2</sup> )	WS (m/s)	WPD (W/m <sup>2</sup> )	WS (m/s)	WPD (W/m <sup>2</sup> )	WS (m/s)	WPD (W/m <sup>2</sup> )	WS (m/s)	WPD (W/m <sup>2</sup> )	WS (m/s)	WPD (W/m <sup>2</sup> )	WS (m/s)	WPD (W/m <sup>2</sup> )	WS (m/s)	WPD (W/m <sup>2</sup> )	WS (m/s)	WPD (W/m <sup>2</sup> )
Nov-17	6.24	179.42	6.44	197.36	5.59	146.82	5.98	184.27	4.90	72.16	4.90	72.16	4.99	75.97				
Dec-17	6.81	251.92	7.04	282.41	6.42	218.08	6.88	271.08	6.15	142.52	6.15	142.52	6.26	150.04				
Jan-18	5.18	137.36	5.28	149.95	5.14	121.92	5.46	153.87	4.70	63.54	4.70	63.54	4.78	66.89				
Feb-18	6.27	227.41	6.36	247.41	5.76	160.36	6.08	193.99	4.94	73.77	4.94	73.77	5.02	77.67				
Mar-18	6.79	260.98	6.97	288.26	6.10	172.09	6.73	238.90	5.39	95.66	5.39	95.66	5.48	100.71				
Apr-18	6.80	279.82	6.87	292.27	6.38	219.93	6.63	252.71	5.64	109.94	5.64	109.94	5.74	115.75				
May-18	8.62	499.65	8.68	515.19	7.64	361.16	7.96	412.64	6.95	205.97	6.95	205.97	7.07	216.85				
Jun-18	9.68	632.28	9.79	653.09	–	–	–	–	8.51	377.79	8.51	377.79	8.66	397.74				
Mean	7.05	308.61	7.18	328.24	6.15	200.05	6.53	243.92	5.90	142.67	5.90	142.67	6.00	150.20				

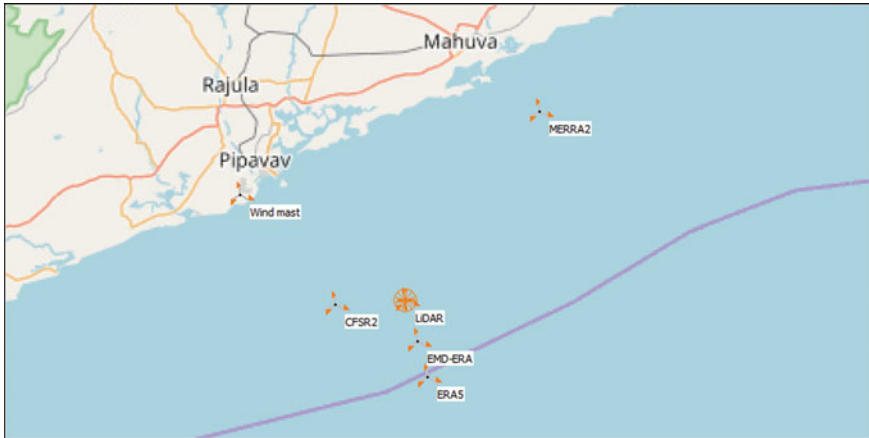


**Fig. 1** Geographical map of the considered offshore region of Gujarat

Now, in order to identify the most suitable reanalysis dataset for the estimation of the wind resources, the LiDAR measurement data has been compared with wind mast measured data and other reanalysis datasets namely ERA5, EMD-ERA, MERRA2 and CFSR2 (Fig. 1). The mean speed and other characteristics (Weibull parameters and standard deviation) of the data are represented in Table 3. The standard deviation of each dataset can be computed through the following equation.

$$SD = \sqrt{\frac{\sum_{i=1}^N (x_i - \bar{x})^2}{N - 1}} \tag{3}$$

**Table 3** The comparative analysis of wind speed data sources for 100 m hub height

Data	Mean wind speed (m/s)	Weibull scale parameter (A) (m/s)	Weibull shape parameter (k)	Correlation with LiDAR data (daily avg.)	Std. error (RMSE) with LiDAR data (daily avg.) (m/s)	Std. deviation (m/s)
LIDAR	7.41	8.34	2.6404	1.0000	0.00	3.09
Wind mast	4.76	5.33	3.0195	0.2046 (*0.964)	0.91	1.76
ERA5	6.77	7.61	2.7348	0.9329	0.68	2.77
EMD-ERA	6.13	6.87	2.9309	0.8371	1.08	2.30
MERRA2	6.82	7.66	2.7671	0.8471	1.00	2.89
CFSR2	6.87	7.72	2.7491	0.8429	1.01	2.60

\*correlation coefficient with LiDAR data for monthly average wind speeds



The considered reanalysis datasets are validated by means of statistical tools: Root mean square error (standard error) and Correlation coefficient. The expression of RMSE can be given by Eq. 4 [4]. The RMSE is a measure of the difference between value predicted by a model and the values actually observed from the environment that is being modelled. RMSE serves to aggregate these differences into a single measure. Generally, the RMSE in wind speed should not be greater than 2 m/s [5].

$$\text{RMSE} = \sqrt{\frac{\sum_{i=1}^N (S_i - M_i)^2}{N}} \quad (4)$$

where  $S$  and  $M$  represent reanalysis data value and measured value, respectively, and  $N$  is for the number of data values. The correlation coefficient of the datasets with the LiDAR data has been computed by means of Eq. 5.

$$R = \frac{\sum_{i=1}^N (M_i - \bar{M})(S_i - \bar{S})}{\left(\sum_{i=1}^N (M_i - \bar{M})^2 \sum_{i=1}^N (S_i - \bar{S})^2\right)^{\frac{1}{2}}} \quad (5)$$

The Weibull distribution of the wind speed data recorded by the LiDAR has been calculated by Eq. 6. The scale parameter  $A$  (in m/s) and shape parameter  $k$  are obtained from the data as depicted in Table 3 and used for the derivation of Weibull distribution function.

$$f(v) = \left\{ \frac{k}{A} \left( \frac{v}{A} \right)^{k-1} \exp \left( - \left( \frac{v}{A} \right)^k \right) \right. \quad (6)$$

## 5 Results Discussion

From the computation of the standard error (RMSE) and the correlation coefficient, it is clear that ERA5 data is the most reliable reanalysis dataset among the considered datasets for the considered locations as it exhibits lowest RMSE of 0.68 m/s and highest correlation coefficient of 0.9329 (Table 3). The correlation coefficients of other reanalysis data range from 0.8371 to 0.8471. Here, it should be noted that the correlation for wind mast is merely 0.2046, which is due to the data unavailability and discontinuity. This value is observed to be 0.964 when the monthly average wind speeds are considered for the correlation computation, which indicated that the wind mast data is fairly reliable when continuous data is available. Further, it is observed that the wind mast data and all the analyzed reanalysis datasets underestimate the wind speed as compared to LiDAR data (Table 3).

Now, as the LiDAR data has been identified as the most accurate data, it has been considered for further analysis. The mean wind power density of 328.24 W/m<sup>2</sup> has

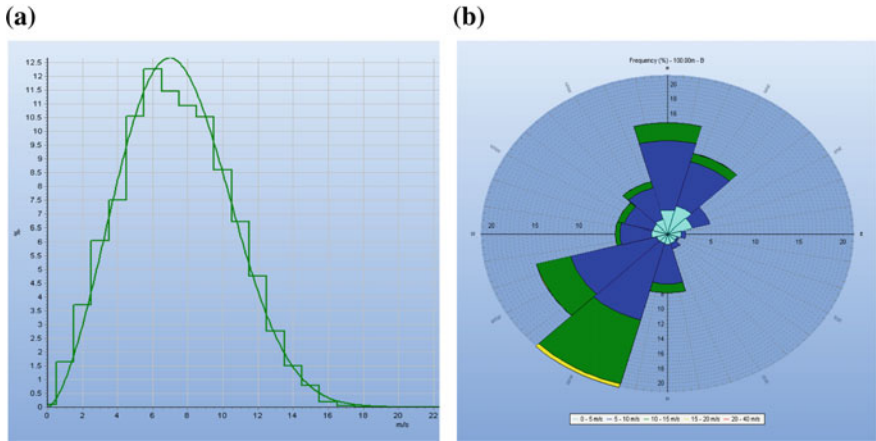


**Fig. 2** (a) Weibull distributions and histograms of LiDAR wind data at 100 m height and (b) Wind rose diagram illustrating wind frequency by direction

been observed at the study location in the offshore region of Gujarat. As presented in the Weibull distribution diagram, the LiDAR data exhibits highest frequency (around 12.5%) between wind speeds of 6–8 m/s (Fig. 2a) with the mean value of 7.41 m/s. The Rose diagram representing the wind speeds along with the directions shows higher wind frequency of over 20% in SSW and about 15% in SSW and N directions as depicted in Fig. 2b.

As the ERA5 reanalysis data presents the most reliable correlation with LiDAR measured wind speed data, the time series distribution of wind speed recorded over the 8 months duration has been plotted and depicted in Fig. 3. It can be seen that there are multiple number of instances where the LiDAR has failed to record the wind speed and displays zero value, especially during first three months of the recording (Nov., Dec. 2017 and Jan. 2018). Hence, for sake of wind resource assessment, the ERA5 reanalysis data should be utilized as it largely correlates with LiDAR data and is available continuously.

## 6 Conclusions

The LiDAR measured wind data has been compared to the wind mast measured wind data and the available reanalysis datasets. The analysis indicated that the ERA5 reanalysis data is the most reliable dataset among the considered datasets as it exhibits fairly high correlation coefficient of 0.9329. The discontinuity of the wind mast data is apparently questionable but the available data shows good agreement with the LiDAR data with monthly average data correlation of 0.964. It can also be observed that all the reanalysis datasets underestimate the wind speeds, which indicates that it is safe to rely on the reanalysis data knowing the actual wind speed won't fall below

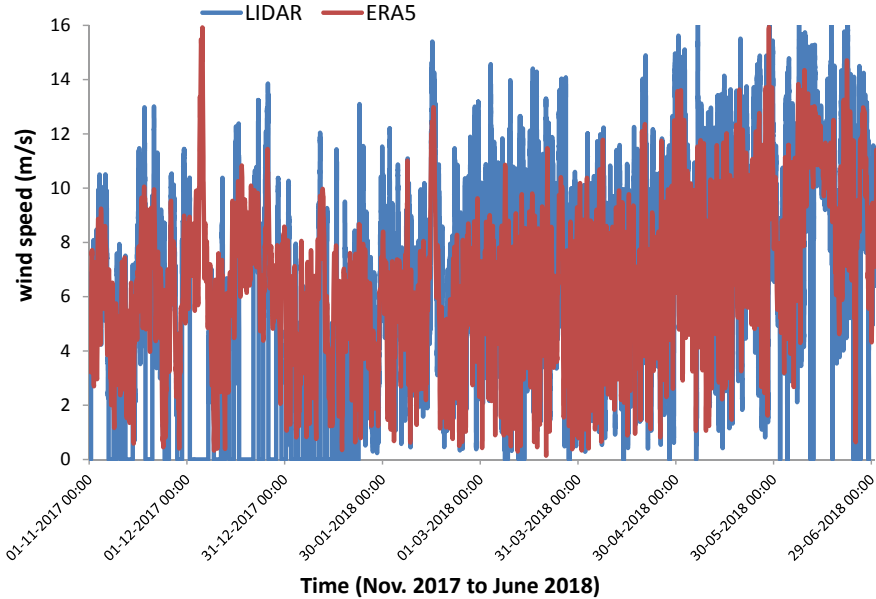


**Fig. 3** Time series wind speed data of LiDAR and ERA5 dataset

that value. The LiDAR measured the mean wind speed of 7.41 m/s at 100 m height, which implies to the mean wind power density of 328.24 W/m<sup>2</sup>. Thus, the study location is highly suitable for the establishment of an offshore wind power project.

**Acknowledgements** The authors wish to acknowledge National Institute of Wind Energy (NIWE) for making the LiDAR and wind mast measurement data available. The authors would also like to thank International A/S, the developers of Wind Pro software for making the different reanalysis data available for the analysis.

## References

1. Wind Resource Assessment Unit & Offshore Unit: National Institute of Wind Energy (NIWE)—Interim Report (First offshore Lidar Wind Data Analysis) (2018)
2. Nagababu G, Kachhwaha SS, Naidu NK, Savsani V (2017) Application of reanalysis data to estimate offshore wind potential in EEZ of India based on marine ecosystem considerations. *Energy* 118:622–631
3. Pimenta F, Kempton W, Garvine R (2008) Combining meteorological stations and satellite data to evaluate the offshore wind power resource of Southeastern Brazil. *Renew Energy* 33:2375–2387
4. Salvação N, Guedes Soares C (2018) Wind resource assessment offshore the Atlantic Iberian coast with the WRF model. *Energy* 145:276–287
5. Ebuchi N, Graber HC, Caruso MJ (2002) Evaluation of wind vectors observed by QuikSCAT/SeaWinds using ocean buoy data. *J Atmos Ocean Technol* 19:2049–2062